Contrôle des vibrations des structures hydroptères avec des absorbeurs shunt piézoélectriques non linéaires

Zein Alabidin Shami

To cite this version:

Zein Alabidin Shami. Contrôle des vibrations des structures hydroptères avec des absorbeurs shunt piézoélectriques non linéaires. Mécanique des matériaux [physics.class-ph]. HESAM Université, 2022. Français. NNT : 2022HESAE072 . tel-03863895

HAL Id: tel-03863895
https://pastel.hal.science/tel-03863895

Submitted on 21 Nov 2022

ÉCOLE DOCTORALE SCIENCES ET MÉTIERS DE L'INGÉNIEUR

LISPEN - Campus de Lille

THÈSE

présentée par : M. SHAMI Zein Alabidin
soutenue le : **21 octobre 2022**

pour obtenir le grade de : **Docteur d'HESAM Université**

préparée à : **École Nationale Supérieure d'Arts et Métiers**
Spécialité : **Mécanique**

Vibration Control of Hydrofoil Structures with Nonlinear Piezoelectric Shunt Absorbers

THÈSE co-dirigée par :

M. THOMAS Olivier

et

M. GIRAUD-AUDINE Christophe

Jury		
M. Emmanuel GOURDON	LTDS, ENTPE	Président
M. Pierre-Olivier MATTEI	LMA, CNRS	Rapporteur
M. Elie LEFEUVRE	C2N, Univ. Paris-Saclay	Rapporteur
Mme Marta BERARDENGO	Univ. of Genova, Italy	Examinatrice
M. Olivier THOMAS	LISPEN, Arts et Métiers	Examinateur
M. Christophe GIRAUD-AUDINE	L2EP, Arts et Métiers	Examinateur
M. Boris LOSSOUARN	LMSSC, CNAM	Examinateur
M. Cyril TOUZÉ	IMSIA, ENSTA Paris	Invité

T H È S E

To my parents...

Acknowledgements

> *I seem to have been only like a boy playing on the seashore, and diverting myself in now and then finding a smoother pebble or a prettier shell than ordinary, whilst the great ocean of truth lay all undiscovered before me.*
>
> Isaac Newton, , 1643-1727

Foremost, I would like to thank my supervisors, Prof. Olivier THOMAS and Prof. Christophe GIRAUD-AUDINE, for their continuous support and presence during my Ph.D. Their help, motivation, patience, and guidance were crucial to finish this thesis. I want to thank both of them for pushing me to give my best always to obtain high-quality results. I am very grateful to have such skillful and expert supervisors who taught me a lot. I also want to thank my defense committees for their thoughtful comments and suggestions, which added significant value to this work.

During this thesis, I met wonderful colleagues with whom I shared the same office for three years. I would like to express my deepest gratitude to Eddy ABBOUD for all his support and help from the first day we met until my defense day. His help when I miss or forget some administration stuff (which was quite a lot!!) is really appreciated. I would also like to thank Marielle DEBEURRE for her help and kindness, which always make things easier for me. Many thanks go to Vincent MAHE for all the wonderful after-work nights that were a great relief after the long working days with nonlinearities. I will never forget our discussions, especially with the chocolate beer!! I also want to thank Marguerite DE LA BIGNE for her beautiful spirit and all the German-English mixed words she taught me!! I am also grateful to my colleagues Maxime SELINGUE, Dorian IBERT, Lei WANG, Floriane MAZZONI, Guillaume HAY, and Shuhan LIU.

I am also thankful to the other colleagues I met in the lab: Mathieu COLIN, Arthur GIVOIS, Michel AULELEY, Amélie BEAUVILLE dit EYNAUD, Sebastien RENDON FERNANDEZ, Laurent BIMONT, Martin LEGRY, Muriel HATAB, Laurent BIMONT, François HELENON, and Emre UY-

GUN. Special thanks to Simon BENACCHIO for all his help and advice. I am also grateful to Aurélien GROLET, my supervisor during my Master's degree, for all his brilliant and smart comments and for introducing me to the nonlinear vibration world! I would also like to thank Boris LOSSOUARN for his excellent organization of the "Smart Lifting Surfaces" project, which my thesis was part of, and for his continuous thoughtful suggestions. I am also grateful to Prof. Cyril TOUZÉ for his contribution to this thesis.

I want to thank my childhood and college friends, Mohammad ISSA for all the joy and happiness that he can spread to everyone surrounding him, Ali SBEITY for all the wonderful times and the memories we had together since we were kids, and for helping me the first day I came to France, Adam GHANDOUR for the unforgettable memories I had with him, and Zaher BITAR for his advice, support, and the amazing moments we spent together in Lebanon and France. I also want to thank Prof. Samer ALI, my supervisor during my Master's studies in Lebanon, for his encouragement and support.

Finally, I am very grateful to my parents, to whom this work is dedicated, for all their support, help, and guidance, and for always being on my side to face all the difficulties. Without you, I would not be able to accomplish this. You were and will always be the light of my life that will guide me and shine my way. I also want to deeply thank my brother and sisters for their support and encouragement. All the thankful words are not enough to express my gratitude to you.

> “*Instead of resisting to changes, surrender. Let life be with you, not against you. If you think ‘My life will be upside down’ don’t worry. How do you know down is not better than upside?*”
>
> Shams Tabrizi, , 1185–1248

Contents

Chapter 1

Introduction

Contenu

1.1 Motivation and problem statement

Lifting surfaces became a significant research field due to their numerous applications in the industrial sector. Examples of such applications involve turbojet blades [1], pumps [2], propellers [3], airplane wings [4], and boats hydrofoils [5]. Lifting surfaces mainly refer to thin structures designed in special geometry (e.g., foil or blade geometries) that can lead to a pressure gradient proportional to the velocity field in the fluid medium. The performance of such structures greatly depends on their geometrical and material aspects, which should be optimized to satisfy given specifications.

An important part of enhancing the lifting structures involves the consideration of the flow-induced vibrations [6]–[8] under high excitation levels and certain flow regimes. This can lead to fatigue and erosion and thus reduce the structure's lifetime and possibly leads to failure. Moreover, in aerodynamics and hydrodynamics applications, high vibration levels can substantially reduce the performance and generate high noises level. A famous example in the literature is the flutter phenomenon [9]–[13], which is an unstable, self-excited structural oscillation that can lead to damage in aeronautical applications.

Those problems led to initiate the ”Smart Lifting Surfaces” project in collaboration between the Institut de Recherche de l'École navale (IRENav) in Brest, the Conservatoire National des Arts et Métiers (CNAM) in Paris, Institut Carnot Arts, the Laboratoire d'Ingénierie des Systèmes Physiques et Numériques (LISPEN) in Lille, and Laboratoire d'électrotechnique et d'électronique de puissance (L2EP) in Lille. This project mainly focuses on the hydrofoil structures that are utilized in marine applications. The main aim was to propose novel and practical methods to reduce the vibrations of the hydrofoils, which can be experimentally tested and whose control is simple to implement. The novelty is based on using active materials, such as piezoelectric transducers, that can modify the dynamics in the flow field without substantially changing the structure geometry. Thus, such an approach can reduce the design constraints on the structure geometry to optimize the performance. In addition, it can lead to the implementation of electronic vibration absorbers, which can represent an effective solution since classical mechanical dampers are not feasible for the lightweight lifting bodies in the hydrodynamic regime.

Through this project, two main research paths were followed: the first one focuses on studying the fluid-structure interaction in the water medium to study the vortex sheddings [14], shown in Fig. 1.1, and their consequences on the vibrations of the hydrofoil at different ambient conditions. In addition, the integration of piezoelectric patches and the piezoelectric couplings in the water medium were studied. The second path focuses on designing novel electronic vibration absorbers that can be implemented to the hydrofoil in the hydrodynamics regimes on the one hand and easily controlled in real-life applications on the other hand.

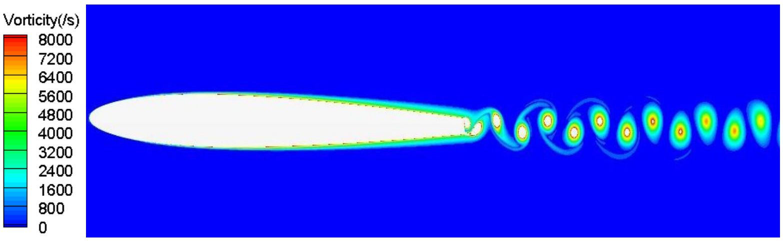

Figure 1.1: Vortex sheddings in the wake of a hydrofoil structure. Retrieved from [15].

This thesis is a part of the second project path. It focuses on proposing different designs of nonlinear electro-mechanical vibration absorbers. These absorbers are composed of an electronic circuit (referred to as a shunt circuit) connected to the hydrofoil through a piezoelectric patch. Such absorbers will be referred to as piezoelectric shunt absorbers. The main goal of this thesis is the intentional use of the nonlinear components in the shunt circuit. Through this thesis, a detailed theoretical study is devoted to analyzing the nonlinear dynamics of the absorbers to deduce the guidelines that can be utilized for practical implementations. In addition, experimental tests are performed on beam and hydrofoil structures to validate the proposed absorbers.

1.2 Hydrofoil structures

Hydrofoils are lift surfaces that operate in water medium and have been used for decades in the marine industry. Using hydrofoils aims to increase the marine, sailing, or surfing boats' efficiency by enhancing the speed to the energy consumption ratio. They are also used in different applications such as surf-boats. The basic idea consists of mounting a foil structure on the boat hull to create a lift force. Consequently, as the boat increases its speed, the boat hull is lifted out of the water, as shown in Fig. 1.2, and the area of contact between the boat and the water is minimized thus reducing the drag force and the wave-induced energy level and as a consequence, reducing the energy consumption.

The idea of using hydrofoils dates back to 1861 when Thomas Moy tested a hull with three lifting surfaces to study the lifting and the drag forces. Also, in 1898, Italian inventor Enrico Forlanini obtained patents in the UK and US for his hydrofoil designs. In 1905, Enrico Forlanini built a hydrofoil and tested it in the Lake Maggiore in Italy, and the hydrofoil enabled an increase of the boat's speed up to 68 kilometers per hour. A lift force was generated and elevated the boat half a meter above the water surface. Those examples proved the validity of the hydrofoils and opened the doors afterward for numerous kinds of research involving optimal studies regarding the design of the hydrofoils in terms of their geometry and material characteristics to overcome many design limitations.

Two important limitations associated with the hydrofoils performance are the ventilation [18], [19] and cavitation [20]–[22] which both cause adverse effects regarding the stability and controllability of the hydrofoils. Ventilation, as shown in Fig. 1.3(a), appears when the subatmospheric pressure causes air to be drawn from above the free surface and forms a semi-stable cavity attached to the foil [23]. Whereas, cavitation is the formation of void or cavities in the liquid when the negative pressure increases on a lifting device [24]. This can appear in different behaviors such as vortex cavitation and bubble cavitation as shown in Fig. 1.3(b) and Fig. 1.3(c), respectively, which can cause errosion that leads to failure, as shown in Fig. 1.3(d) . Both phenomena directly affect the drag and lift coefficients, and they should be taken into account during the design process of the hydrofoil. Moreover, cavitation

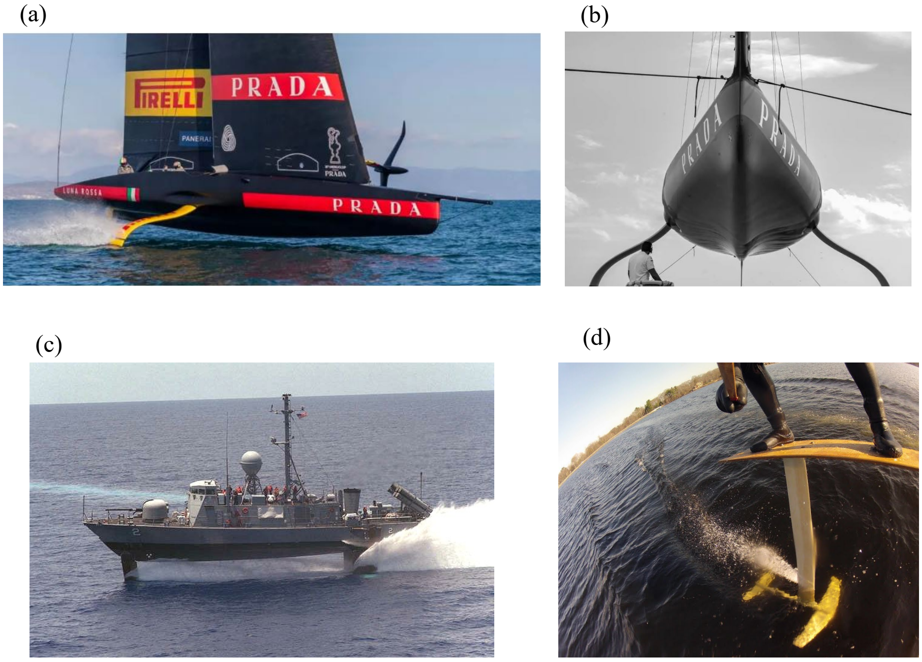

Figure 1.2: (a) and (b) Luna Rossa AC75 sailing boat [16]. (c) USS Hercules (PHM-2) marine boat [17]. (d) Wind surf with a hydrofoil.

can induce high vibration levels [25], [26] that can cause low performance and possible damage of the hydrodynamics structures.

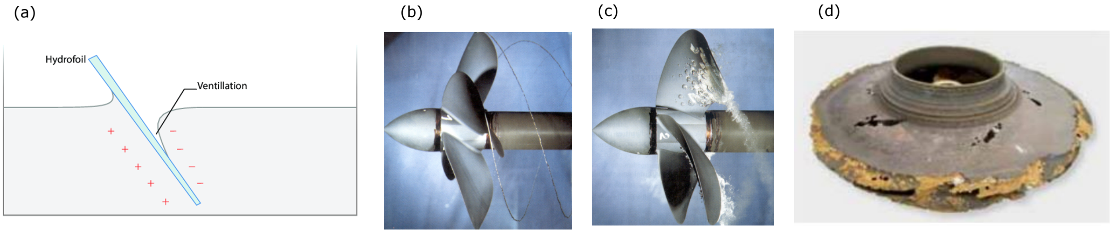

Figure 1.3: (a) Ventilation, (b) Vortex cavitation, (c) Bubble cavitation, and (d) Errosion failure of pump blades due to cavitation. Retrieved from [27]
.

Optimization of the hydrofoil structures involves mainly their geometrical and material characteristics. The geometrical optimization aims to maximize the lift to the drag force ratio [28]–[30] while the material optimization aims to develop lighter and stronger materials that can operate at high speeds [31]–[33]. As the analytical treatment of such problems can be cumbersome, CFD (computational fluid dynamics) numerical tools have been developed to deal with such problems involving fluid-structure interaction (FSI). Examples of such softwares are ABAQUS, ANSYS, OpenFoam, and

STAR-CCM++, in addition to special softwares dedicated to the FSI study of lifting surfaces such as SOPHIA [34] which is developed at Centrale Nantes. Another software to solve FSI problems is developed at IRENav, which involves the coupling between ABAQUS and the open source software CFX [35].

It is also worth mentioning the contributions, through different doctoral theses, developed at IRENav regarding the design and optimization of the hydrofoils, such as the performance study of hydrofoils with isotropic material [36], numerical and experimental FSI investigation of hydrofoils in composites [27], and the effect of the hydrofoil section thickness on the appearance of a twist angle [37].

In addition to the above limitations, the high vibration levels can be a considerable problem, especially when the vortex shedding frequency in the wake of the structure (see Fig. 1.1) becomes close to one of the natural frequencies of the hydrofoils and thus activating resonance [38]–[40]. Consequently, high stress and fatigue levels can be generated in addition to high noise levels. This work attacks this problem using the design of nonlinear electronic absorbers thanks to the ability to integrate smart materials, in particular piezoelectric materials, into the hydrofoil structure.

1.3 Linear vibration suppression

Vibration suppression is a growing research field due to its importance in avoiding the failure of structures that undergo high excitation levels. Different approaches have been proposed for this sake. The most famous linear absorber is the tuned mass damper (TMD) [41], shown in Fig. 1.4(a). TMD represents a secondary attachment to the host structure that can attenuate the vibrations under harmonic excitation (or even random excitation [42]).

The TMD is widely studied in the literature for single and multi modal vibration attenuation [43]–[48] and it is used in wide range of applications in civil engineering [49]–[52], vibration absorption in bladed disks [53], and noise control [54]. The basic idea is to tune the TMD oscillating frequency close to one of the natural frequencies of the primary structure, which is considered linear as shown in Fig. 1.4. This creates an anti-resonance near the tackled natural frequency. The attenuation of the TMD greatly depends on the ratio between the secondary and the primary masses in addition to the damping ratio of the primary oscillator, while the damping ratio of the secondary oscillator can be optimized to reduce the peaks generated across the fundamental resonance (see Fig. 1.4(b)). For a wider review on the TMD and its optimization, one can refer to [55]–[57] and references therein.

Although the TMD proved effective in many applications, it suffers from many limitations, especially in applications involving lightweight structures when the size and mass constraints are presented. In addition, the TMD works in a narrow band near the natural frequency of the structure. Moreover, the TMD is sensitive to any resonance frequency shift in the primary structure, thus substantially

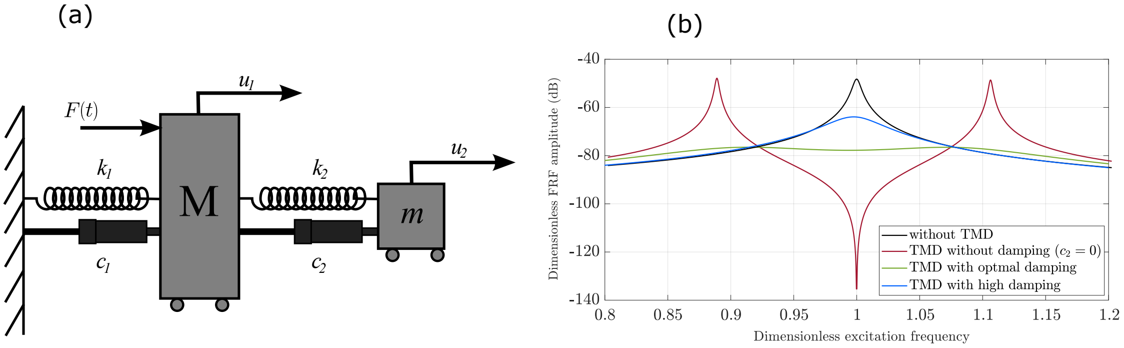

Figure 1.4: (a) Schematic representation of the tuned mass damper applied to a primary system modeled as a single degree of freedom oscillator. u_1, M, k_1, and c_1 are the displacement, mass, stiffness, and damping coefficient of the primary oscillator. u_2, m, k_2, and c_2 are the displacement, mass, stiffness, and damping coefficient of the TMD attachment. $F(t)$ is the excitation force. (b) Typical frequency response function (FRF) of the primary oscillator with a TMD under harmonic forcing for different damping coefficient c_2.

losing its performance [58].

1.4 Nonlinear vibration suppression

1.4.1 Main features

Nonlinear theory and its applications related to mechanical vibrations took a wide range of interest since it can describe a wide range of phenomena that linear theory lacks to identify. In structural mechanics, the linear theory is shown to be applicable for small deformations where the linear version of Hook's law is valid. However, for high deformations, a nonlinear correction should be considered [59], [60]. Analysis tools for solving linear problems such as the modal superposition, time domain, and frequency domain analysis are well developed [61], [62]. However, in the modern industry, where lighter weight structures are demanded, large deformations are expected, and thus the analysis should be extended to the nonlinear domain.

Sources of nonlinearities can be geometrical (e.g. pendulums [63] and large deformations of beams [64], [65] and plates and shells [66]), contact (e.g. nonlinear boundary conditions [67]), and material nonlinearities (e.g. nonlinear elasticity [68] and thus nonlinear stress-strain relation). In those applications, the linear spring model requires correction through an additional nonlinear stiffness (which can be a combination of quadratic, cubic, and nonsmooth terms) that should be introduced to the equations of motion. In addition, nonlinearities can appear in the damping terms such as the problems involving nonsmooth and nonlinear friction [69], [70] or drag force [71] in aeronautics applications. Indeed, nonlinear analysis is harder since it involves the consideration of features that do not have a counterpart in the linear theory. In addition, the principle of superposition does not extend to the nonlinear theory. Examples of those features involve [72], [73]:

- rich response in which multiple steady-state solutions (periodic, quasi-periodic, and chaotic) can be observed for harmonic excitation,
- sensitive dependence on the initial conditions and possible chaos responses,
- jump phenomenon and bifurcations in addition to the appearance of stable and unstable responses,
- the dependence of the resonance frequency on the oscillation amplitude,
- modal interaction and energy transfer through internal resonances and the response of the sub-harmonics or the super-harmonics with mono-harmonic excitation.

Some of the above features can even appear for a simple nonlinear model such as the Duffing equation [74] in which a weak nonlinear term is added to the linear oscillator. This equation is very essential in nonlinear vibration theory as it covers many simplified single degree of freedom (DOF) models such as nonlinear cables [75], nonlinear circuits [76], cantilever beams motion [65], beam buckling [77] and pendulum under harmonic excitation [78]. The Duffing equation reads in terms of the unknown $x(t)$:

$$\ddot{x} + \mu\dot{x} + \omega_0^2 x + \gamma x^3 = F\cos\Omega t, \tag{1.1}$$

where μ, ω_0, γ, F, Ω, and t denote the damping factor, resonance frequency, nonlinear coefficient, forcing, excitation frequency, and time, respectively. To emphasize some features of this equation, the frequency responses of the first and third harmonics amplitudes of $x(t)$, computed numerically with MANLAB software (see Sec. 1.6.1.3 for more details), are plotted in Fig.1.5(a) and Fig. 1.5(b), respectively, for different excitation levels. It is observed in Fig. 1.5(a) that for small excitation, the response undergoes linear behavior. However, as the excitation increases, a hardening behavior is observed (the curve shape bends to the right), with unstable branches detected. In addition, Fig. 1.5(b) shows the response of the third harmonics with an appearance of hardening behavior and the response of the third order super-harmonic at $\Omega = \omega_0/3$. The black dashed lines are the so-called "backbone curves" that represent the dependence of the excitation frequency on the oscillation amplitude [79]–[81]. They also represent the free conservative periodic solution of Eq. (1.1). In a physical sense, backbone curves satisfy the phase resonance condition when the dissipation energy cancels the injected energy to the system [82]–[84]. Geometrically, they determine the skeleton of the forced response [85], as can be seen in Fig. 1.5. When considering higher number of DOFs, these backbone curves define a family

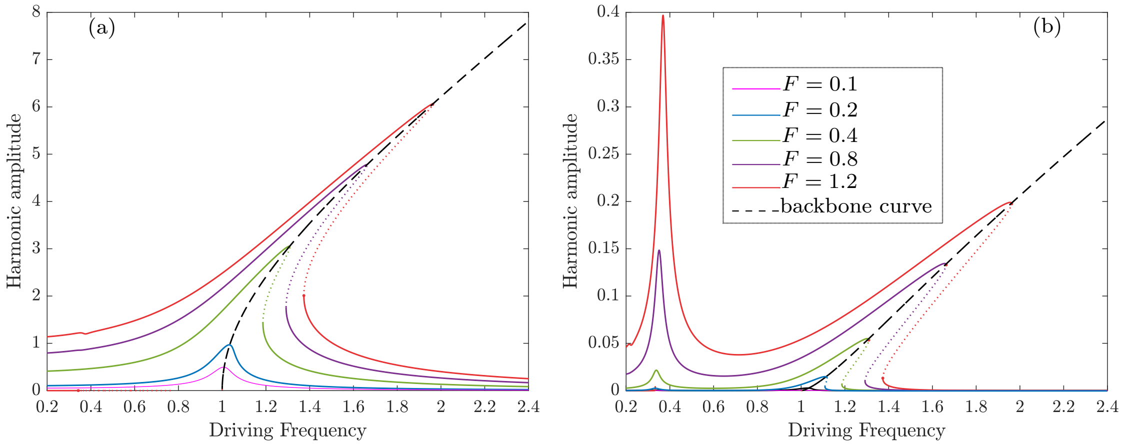

Figure 1.5: Frequency response of the Duffing oscillator in Eq. (1.1) for different forcing levels. (a) first harmonic, (b) third harmonic. The dashed line denotes the backbone curve for the free conservative case ($F = \mu = 0$). Solid and dotted lines denote the stable and unstable solution of the forced response, respectively. The numerical values are $\gamma = 0.1$, $\mu = 0.1$, and $\omega_0 = 1$.

of periodic solutions on two-dimensional invariant manifolds (i.e., orbits that start out in the manifold remain in it for all time) in the phase space, called the nonlinear normal modes [86]–[88]. The nonlinear normal modes can be considered as the extension of the classical linear normal modes [89]–[91] which represent a very useful tool to analyze complicated nonlinear modal dynamics problems. Examples of such problems include the analysis of nonlinear absorbers [92], parametrically excited cantilever beam [93], nonlinear MEMS [94], nonlinear finite element modeling [95], model order reduction [96], [97], nonlinear dynamics of cables [98], and beam buckling [99]. One can also refer to the following review articles for more applications [100]–[102].

1.4.2 Nonlinear absorbers: state of the art

Nonlinear absorbers are proposed to enhance the efficiency of the linear absorbers in terms of attenuation reduction, robustness, design feasibility, and broadband frequency range. Thanks to the features mentioned in the previous section, new concepts and ideas can be exploited to achieve the enhancement goal. The basic idea is that instead of avoiding the nonlinearities, they are *intentionally added to the absorber* and tuned in a particular way to generate different nonlinear phenomena. Like linear absorbers, the nonlinear ones can be passive or active depending on the application. In the following, an illustration of some families of nonlinear absorbers and their main advantages are emphasized.

Nonlinear energy sink (NES) is a family of nonlinear absorbers introduced in [103] with a huge contribution afterward (e.g. [104]–[107]) due to its ability to create high attenuation with a high broadband frequency range. The main idea consists of adding a secondary attachment to the primary structure with light mass, strong nonlinear stiffness, and a damping element [108]. The NES then has a non constant natural frequency leading to a transient resonance capture in a 1:1 resonance manifold [109], [110]. Consequently, a fast irreversible energy pumping from the primary structure to the NES occurs, which is denoted by ”targeted energy transfer” [103], [111], [112], and then the energy is dissipated in the damping element. In particular, the NES can extract energy from virtually any mode of the primary structure [113]. Comparisons between the NES and TMD performance [114], [115] showed that the former leads to a wider frequency band of attenuation and is less sensitive to the shifts in the natural frequency of the primary structure. In addition, a lighter mass is required for the NES, giving it the advantage when mass constraints are presented. Applications of NES are numerous including seismic mitigation [116], sound mitigation [117], aeronautics [118], [119] and industrial machines [120]. Vibro-impact NES were also introduced to act as shock isolators by including a nonsmooth piecewise stiffness term [121]–[124]. For a wider overview of the NES one can refer also to the following review articles [125]–[127].

More adaptive nonlinear absorbers are also proposed, such as the nonlinear tuned vibration absorber (NLTVA), which is introduced in [128] to damp the vibration of structures with nonlinearities. It utilizes the same concept as the NES in terms of adding a nonlinear stiffness in the secondary attachment. However, the main difference is that the added nonlinearity is tuned according to the nonlinear restoring forces in the primary structure. Such tuning ensures the robustness of the absorber for higher oscillation amplitudes that can lead to the change of the resonance frequencies of the host structure. Applications with mechanical absorbers and tuning guidelines can be found in [129].

Other types of nonlinear absorbers are also proposed in the literature such as those involving nonlinear damping attachments [130], [131] and centrifugal pendulum vibration absorbers [132]–[135].

1.4.3 Two to one (2:1) internal resonance and saturation phenomenon

Internal resonance is a nonlinear feature that occurs through modal interaction when two or more modal frequencies are commensurable [136]. For example, if two modal frequencies ω_i and ω_j satisfy $p\omega_i = q\omega_j$, with $p, q \in \mathbb{N}^*$, a strong coupling between the two corresponding modes occur, leading to an energy transfer between the modes and the internal resonance is denoted by a p-to-q (or $p : q$) internal resonance. Such phenomenon can occur at small amplitudes with geometries involving symmetries such as 1:1 internal resonance in beams [137] and cylindrical shells [97], [138] or by intentional tuning of mechanical systems such as the 2:1 internal resonance in gongs [139] and combination of 1:1 and 1:2 internal resonance (i.e., 1:1:2 internal resonance) as in spherical shells [140], [141]. The internal resonance can also occur at high amplitudes due to the variation of the resonance frequencies with the oscillation amplitude so that a commensurable relation is obtained at a certain amplitude [90]. One can note that the type of internal resonance depends on the nonlinearities in the system. For example, 1:1 or 1:3 internal resonance [142] (or combination of both) are associated with cubic nonlinearities, while other types, such as 2:1 internal resonance, are associated with quadratic nonlinearities. A two-to-one (2:1 or 1:2) internal resonance occurs when two modal frequencies satisfy $\omega_2 = 2\omega_1$, in the presence of quadratic nonlinear coupling. Two cases can be considered [72], [143] for this particular type of internal resonance; if the energy is injected into the mode oscillating near ω_2 (i.e., the excitation frequency Ω near ω_2), the energy is transferred to the mode oscillating at half the driving frequency near $\omega_1 = \Omega/2$. Conversely, if the energy is injected to the mode oscillating near ω_1 (i.e., Ω near ω_1), the energy is transferred to the mode oscillating at twice the driving frequency near $\omega_2 = 2\Omega$. It was firstly discovered in [144] that the former case exhibits an exciting feature denoted by the "saturation phenomenon". In addition, it is illustrated in [145], [146] that both cases can exhibit Hopf bifurcations.

To examine the saturation feature, let's consider the following two degrees of freedom nonlinear system in terms of $x_1(t)$ and $x_2(t)$:

$$\ddot{x}_1 + 2\mu_1\dot{x}_1 + \omega_1^2 x_1 + \alpha_1 x_1 x_2 = 0, \tag{1.2a}$$

$$\ddot{x}_2 + 2\mu_2\dot{x}_2 + \omega_2^2 x_2 + \alpha_2 x_1^2 = f\cos\Omega t. \tag{1.2b}$$

System (1.2a, b) is the canonical form to examine the 2:1 internal resonance and its dynamics. It considers two quadratic resonant terms $\alpha_1 x_1 x_2$ and $\alpha_2 x_1^2$ (refer to Appendix A in Sec. 5.2 for illustration about the resonant and non-resonant terms). If $\omega_2 = 2\omega_1$ and we drive the system near ω_2 (i.e. Ω near ω_2), the first order multiple scales solution (see Sec. 1.6.1.1) of x_1 and x_2 reads:

$$x_1(t) = a_1\cos\left(\frac{\Omega}{2}t - \frac{\gamma_1+\gamma_2}{2}\right), \quad x_2(t) = a_2\cos\left(\Omega t - \gamma_2\right), \tag{1.3}$$

where (a_1, a_2) are the amplitudes and (γ_1, γ_2) are phase angles. Their closed form are given in Sec. 2.2. To examine the system dynamics, the typical frequency response of a_1 and a_2 is shown in Fig. 1.6(a) as function of $\sigma_1 = \Omega - \omega_2$. Realize that if we assume a linear case, only a_2 should respond (the black curve). However, above a threshold excitation, the primary resonance enters an instability region in which an energy transfer occurs to the subharmonic of x_1 leading a_1 to respond (the blue curves). Consequently, the primary resonance of a_2 is replaced by an antiresonance at $\Omega = \omega_2$ with an amplitude independent of the excitation level, as shown in Fig. 1.6(c) where the amplitudes at $\Omega = \omega_2$ (a_1^* and a_2^*) are plotted versus the excitation level. The phase response is shown in Fig. 1.6(b) suggesting a monotonic behavior of γ_1 with a lockage at $3\pi/2$ at $\Omega = \omega_2$.

By defining the attenuation as the amplitude reduction with respect to the linear resonance amplitude corresponding the response of $x_2(t)$ with $\alpha_1 = \alpha_2 = 0$ (i.e., the amplitude difference between the green and black curves in Fig. 1.6(c)), one can conclude that the saturation phenomenon leads to an increasing attenuation as the forcing increases beyond a given threshold value. Thus, the attenuation can be considered amplitude dependent. This conclusion led to the design of auto-parametric absorbers that exploit the saturation feature by intentionally adding quadratic nonlinearities. The idea of utilizing the 2:1 internal resonance is proposed in many contributions, mainly with an electro-mechanical control systems with feedbacks [147]–[149] or with piezoelectric actuators [150], [151] for active vibration control strategy. In some other application, the 2:1 internal resonance proved to be efficient for energy harvesting [152]–[154].

Contrary to the mentioned works where the saturation feature is realized with an active control strategy, we aim to exploit this feature in a passive way through a nonlinear piezoelectric shunt absorber. Such an absorber will be realized through an electronic circuit (referred to as a shunt circuit) with a nonlinear voltage component, intentionally introduced. The electronic circuit will be connected to the host structure through a piezoelectric transducer. The main concepts of the piezoelectric shunt absorbers are introduced in the next section.

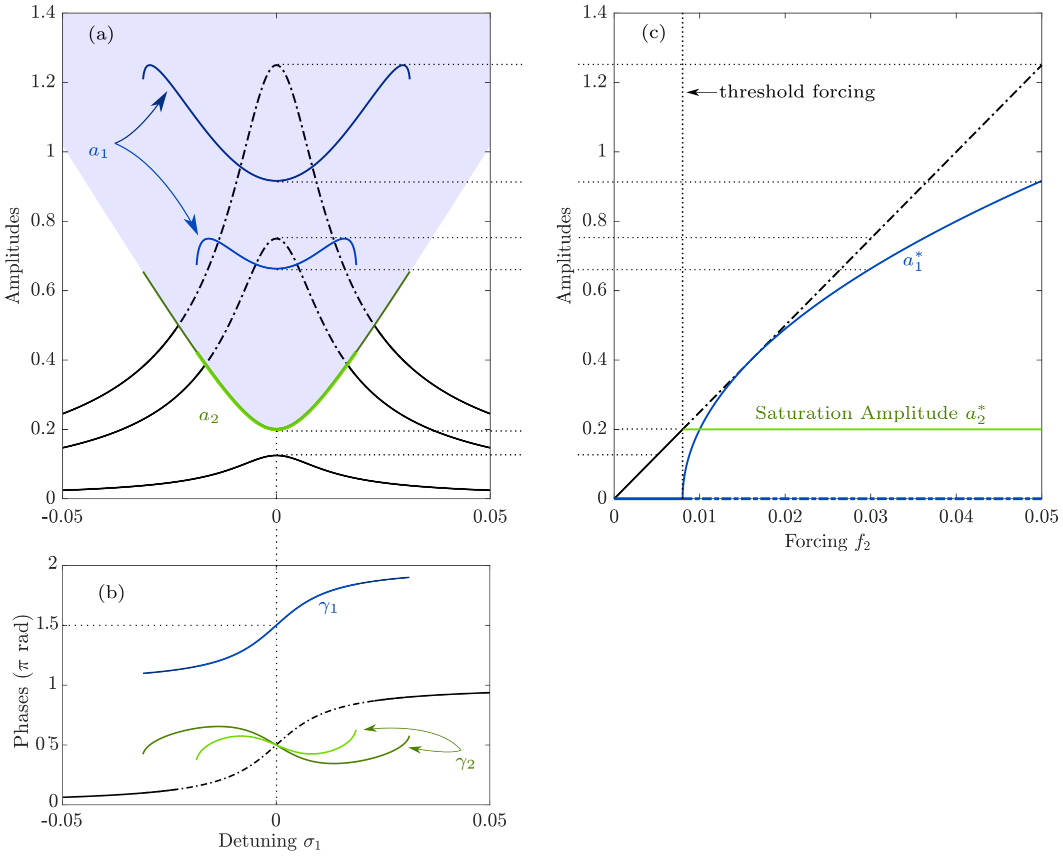

Figure 1.6: Typical response of the amplitudes a_1 and a_2 and the phases γ_1 and γ_2 by solving (1.2a,b) for $\omega_2 = 2\omega_1$. The numerical values are $\alpha_1 = \alpha_2 = 0.1$, $\mu_1 = 0.005$, $\mu_2 = 0.01$. (a) and (b) show respectively the amplitude and phase response with respect to the detuning $\sigma_1 = \Omega - \omega_2$ for values of the forcing f ($f \in \{0.005; 0.03; 0.05\}$). (c) amplitude response at the resonance frequency ($\sigma_1 = 0$) with respect to the excitation level f. In the plots, the linear responses of a_2 and γ_2 are plotted in black. The solid and the dashed-dotted lines denote respectively the stable and the unstable solutions.

1.5 Piezoelectric shunt absorbers

1.5.1 General aspects of piezoelectric materials

Piezoelectric materials are the most studied smart material for practical implementations. This is due to the numerous advantages such as low cost, large frequency bandwidth, and the easiness of implementation. Thank to the piezoelectric direct effect [155] (i.e., applied mechanical strain generates electric charge) and the inverse effect [156] (i.e., applied electric potential generates mechanical stress), the piezoelectric materials can be used for sensing and actuating in wide range of applications such as active control of vibration [157]–[159], noise [160], energy harvesting [161], [162], and structural health monitoring [163].

There exist a lot of types of piezoelectric materials [164], [165] such as single crystalline material such as quartz (Fig. 1.7(a)), piezoceramics (Fig. 1.7(b)) such as lead zirconate titanate (PZTs), polymer (such as polyvinylidene fluoride, PVDF), piezoelectric composites, such as macro-fiber composite (MCF) [166] (Figs. 1.7(c), (d)), and glass ceramics (such as Li2Si2O5 and Ba2TiSiO6). Those types have their own pros and cons depending on the application. Nevertheless, PZT materials are still the most widely used in many applications due to their high piezoelectric coupling. Their main drawback is that they are limited to small deformations due to their brittle characteristic.

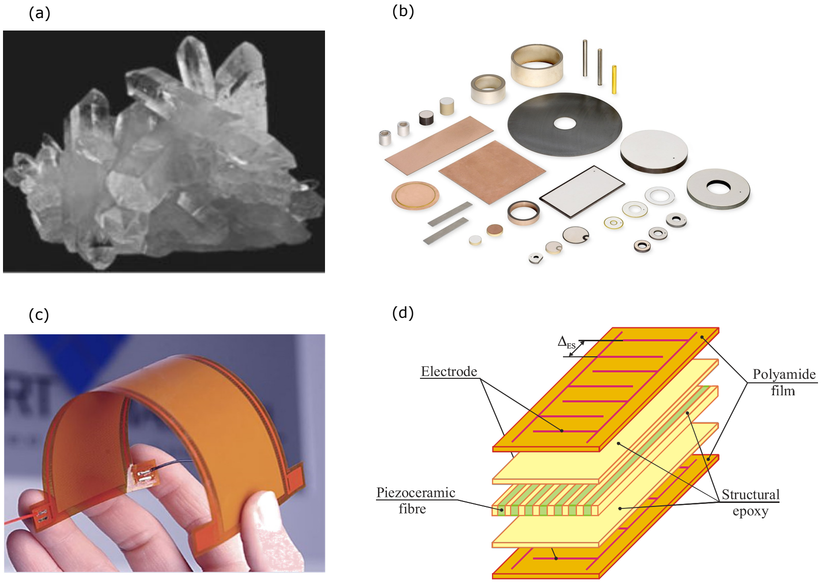

Figure 1.7: (a) natural piezoelectric crystal materials: Quartz (SiO2). (b) Different shapes and sizes of PZT ceramics. (c) MCF patch layout. (d) MCF structural arrangement [167].

The mathematical formulation of the direct and inverse piezoelectric effects is denoted by the piezoelectric constitutive equations, which are expressed in the tensor form as [168]:

$$S_{ij} = s^E_{ijkl} T_{kl} + d_{kij} E_k, \tag{1.4a}$$

$$D_i = d_{ikl} T_{kl} + \varepsilon^T_{ik} E_k, \tag{1.4b}$$

where S_{ij} is the mechanical strain, D_i is the electric displacement, T_{kl} is the mechanical stress, E_k is the electric field, s^E_{ijkl} is the mechanical compliance (reciprocal of the elastic modulus) measured at zero electric field, d_{ikl} is the piezoelectric strain coefficient, and ε^T_{ik} is the dielectric permittivity measured at zero mechanical stress. Note that the constitutive equations can be written in other three forms by arranging differently the state variables $\mathbf{S}$, $\boldsymbol{D}$, $\boldsymbol{E}$, and $\boldsymbol{T}$. Note also that those equations neglect the nonlinearities that can be presented for high deformations [169].

Three possible coupling methods of the piezoelectric materials denoted by 31, 33, and 15 modes are shown in Fig. 1.8. The coupling is distinguished by the direction of the applied loading or the imposed electric field with respect to the poling direction in which the latter is usually considered in the 3-direction (see the back arrows in Fig. 1.8). Namely, the coupling is associated with the 31 mode if the imposed electric field direction is perpendicular to the polar direction and one considers the deformation in the same direction. Whereas, if the directions of the imposed electric field and the poling are parallel, then the coupling is associated with the 33 mode and the deformation is in the two orthogonal directions (i.e., 1and 2). Finally, the 15 mode is associated with the shearing of the piezoelectric material which considers an imposed electric field orthogonal to the polarity direction. One can refer to [170] for a further illustration about the piezoelectric coupling methods and their characteristics.

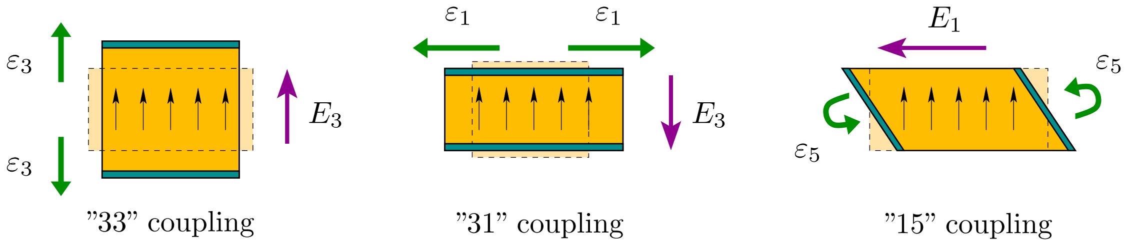

Figure 1.8: Piezoelectric coupling modes. Retrieved from [171].

1.5.2 Piezoelectric shunt absorber: Basic concept and linear configurations

Piezoelectric shunt absorbers are firstly introduced in [172] as an electro-mechanical extension of the mechanical dampers in which a dedicated electronic circuit (referred to as a shunt circuit) is connected to an elastic structure through a piezoelectric transducer bonded to the host structure. Thanks to the piezoelectric effects, the mechanical energy injected into the host structure can be transformed into electrical form and then dissipated or counteracted in the shunt circuit. The main advantages of those absorbers are the easiness of set and control compared to the mechanical dampers. They are also more efficient for lightweight structures where size and weight represent design constraints.

The two simplest architectures of the linear piezoelectric shunts are resistive and resonant shunts, denoted respectively by the R-shunt and RL-shunt, as shown in Fig. 1.9. R-shunt enables the dissipation of the energy into Joule's heat. Regarding the RL-shunt, since the piezoelectric patch can be electrically modeled as a capacitor, an RLC circuit oscillator is then formed, which can be tuned to behave analogously to a TMD in which the structure mode is replaced by two damped modes [173]. Those shunts architectures are passive and collocated as the sensing and actuation are served simultaneously by the piezoelectric patch, giving them the control stability advantage over active control strategies [174].

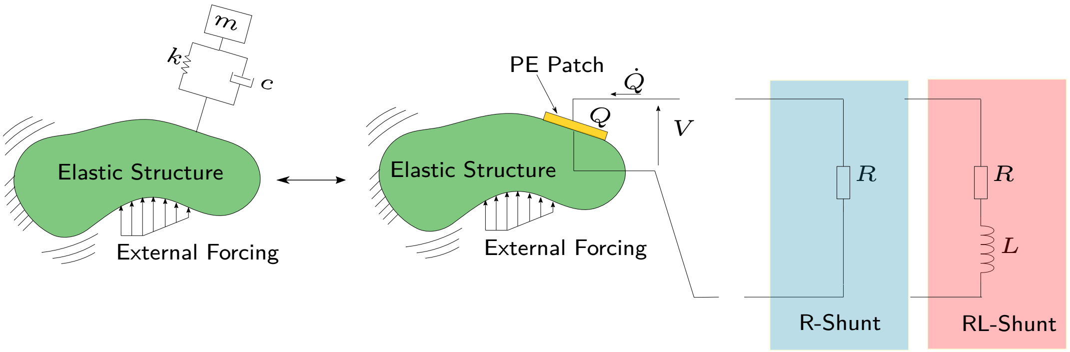

Figure 1.9: R-shunt and RL-shunt schematics. PE patch refers to a piezoelectric patch. Q, $\dot{Q}$, and V are the charge in the piezoelectric electrode, the time derivative of the charge (i.e., the current), and the voltage across the PE patch.

Optimizing the R-shunt and RL-shunt in terms of attenuation ability has been studied widely in the literature. For example, [175] enhanced the R-shunt performance by means of negative capacitance. In [176], detailed theoretical and experimental studies of the performance of the R-shunts and RL-shunts in the case of free and forced vibrations and closed-form expressions of the optimal attenuation are derived. In [177], an optimal study of the RL-shunt to damp the first vibration mode of a beam with a circular cross-section and three collocated resonantly shunted stack transducers is established. In [178], an optimal study regarding the placement and the dimensions of the piezoelectric shunt is performed. In addition, [179] presented an exact closed-form solution to the H_∞ optimization of an R-shunt.

An important result in [176] showed that the critical parameter for an optimal attenuation of the RL-shunt, for a given mechanical damping ratio, is the piezoelectric coupling factor. It is equivalent to a stiffness ratio, contrary to the mechanical TMD, where the critical parameter is the mass ratio between the secondary and primary systems. This piezoelectric coupling can be represented as a dimensionless quantity denoted by k_i (with subscript i being the $i-$th mode of the structure) and characterizes the energy ratio transformed by the PE patch. Following [180], it is defined as:

$$k_i^2 = \frac{\hat{\omega}_i^2 - \breve{\omega}_i^2}{\hat{\omega}_i^2}, \tag{1.5}$$

with $\hat{\omega}_i$ and $\breve{\omega}_i$ are the resonance frequencies of the $i-th$ mode measured by setting the piezoelectric patch in open and short circuit configuration, respectively.

Similar to the mechanical dampers, the R-shunt and RL-shunt act near a single modal frequency of the structure. However, an extension to multi-modal damping using parallel or series arrays of RL-shunts is also proposed. For example, [181] proposed a method for designing and adapting multi-modal piezoelectric resonant shunts with a lower required number of electrical components. Moreover, a periodic array of shunted patches is discussed in [182]. It is also worth mentioning the technique of self-adaptive RL-shunt proposed in [183] where the inductance is designed to tune the mechanical resonance. Some industrial applications of the piezoelectric shunts involved the optimization of machining performance in a boring of aluminum to increase cutting stability [184], the sound attenuation in a duct [185], mistuned bladed disks [186], and vibration suppression of a hard disk driver [187].

1.5.3 Nonlinear piezoelectric shunt absorbers

Nonlinear piezoelectric shunts are an extension of the linear configuration that aims to exploit the nonlinear features presented in the dynamical response. The basic idea consists of intentionally adding a nonlinear voltage source V_{nl} to an RL-shunt circuit, as shown in Fig. 1.10.

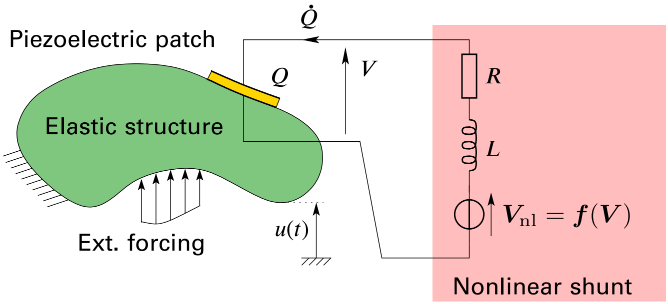

Figure 1.10: Nonlinear shunt circuit schematic with a nonlinear voltage source component V_{nl}.

The idea of utilizing nonlinearities with piezoelectric shunt methodology has few applications in the literature thus far. Namely, the applications extended the mentioned families of nonlinear absorbers in section 1.4.2 to be realized with piezoelectric devices in an active or passive way. For example, the nonlinear energy sink is extended theoretically in [186], [188] to be realized with a piezoelectric shunt to overcome the challenges associated with the implementation of the mechanical NES. In addition, [189] experimentally tested an essentially nonlinear circuit with piezoelectric NES to attenuate the vibrations of mistuned bladed disks. The piezoelectric NES in [189] is realized with a semi-passive nonlinear shunt circuit to damp the vibrations of a cantilever beam. The shunt circuit is composed of a collection of operational amplifiers (OA) and a negative capacitance to cancel the piezoelectric capacitance. In addition, the nonlinearity introduced in the circuit is proportional to the cubic of the charge in the piezoelectric electrode and realized through two analog multipliers, as shown in Fig. 1.11. The results suggested high attenuation with robustness with respect to the misturning in the system.

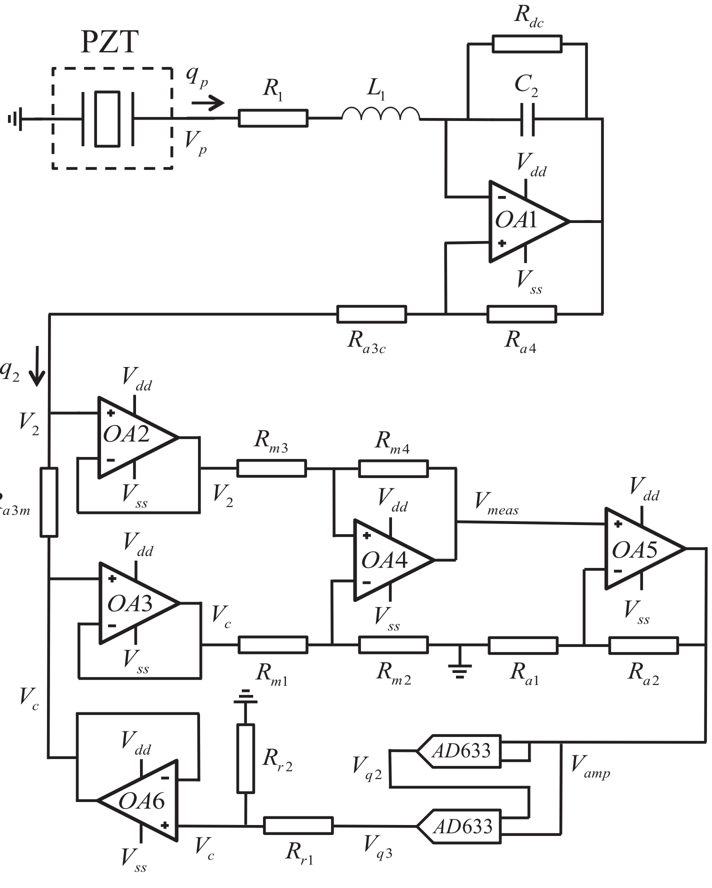

Figure 1.11: Nonlinear shunt circuit to realize the nonlinear energy sink. Retrieved from [189].

In addition to the NES, the NLTVA is also realized theoretically in [190] with piezoelectric shunt methodology and validated experimentally on a cantilever beam in [191] through a digital controller composed of a microprocessor and a current source.

The realization of the NES and the NLTVA with piezoelectric shunt methodology involved the usage of nonlinearities of polynomial type (i.e., quadratic or/and cubic) that appear explicitly in the shunt circuit. Thus, the electro-mechanical system functions in a smooth behavior. Nonsmooth behavior was also exploited with the piezoelectric shunt absorbers with the so-called synchronized switch damping (SSD) technique, which was proposed in [192]. The nonsmooth behavior is presented since the SSD technique consists of continuously switching, through an introduced switch component, the electric impedance of the shunt circuit in a synchronous manner with the structure oscillation. Although no explicit nonlinearities are involved with this technique, it is considered in the nonlinear piezoelectric shunts family since the nonsmooth behavior can generate strong implicit nonlinearities. It is also worth mentioning that the synchronized switch technique was used also for applications involving energy harvesting [193], [194].

As explained in [195], switching synchronization is crucial for SSD technique performance. Namely, the switch is left open most of the time and is closed every time the structure reaches a maximum amplitude. Thus, an opposition of the voltage is obtained, which is imposed on the piezoelectric element. The obtained voltage has the equivalent effect to a force imposed on the structure that changes its sign at oscillation and thus opposes the motion of the structure. Three types of the SSD technique were proposed: the synchronized switch damping on a short circuit (SSDS) such that the shunt includes only a resistive element [192], the synchronized switch damping on inductor (SSDI) where an inductor is additionally added [196], and the synchronized switch damping on voltage (SSDV) where a constant voltage source is added [197], [198]. The SSDS and the SSDI techniques, shown in Fig. 1.12, are semi-passive, contrary to the SSDV, in which their optimal design can lead to higher performance compared to the linear resonant shunt when considering a one DOF structure [195]. Namely, because of the synchronization of the electric circuit to the structural oscillations, no precise tuning of the electric parameters on the mechanical frequency characteristics is required. Thus, the attenuation is very robust to any change in the mechanical structure.

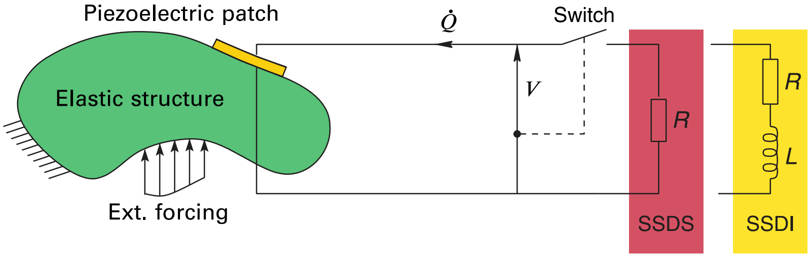

Figure 1.12: SSDS and SSDI piezoelectric shunts schematics. Retrieved from [195].

Following the above contributions, this work proposes designing three different semi-passive nonlinear piezoelectric shunt absorbers, depending on the nonlinear voltage V_{nl}, intentionally introduced to an RL-shunt (see Fig. 1.10). The first design, discussed in chapters 2 and 3, includes solely a quadratic nonlinearity proportional to the square of the piezoelectric voltage V such that $V_{\mathrm{nl}} = \beta V^2$

where β is a controlled gain. The main idea is to activate the two-one-internal resonance (discussed in Sec. 1.4.3) and thus exploit the saturation phenomenon. The second design includes quadratic and cubic nonlinear voltage components such that $V_{\mathrm{nl}} = \beta_q V^2 + \beta_c V^3$ where β_q and β_c are respectively the gains of the quadratic and the cubic nonlinearities. The idea behind adding the cubic nonlinearities, as discussed in chapters 4 and 5, is to correct the saturation phenomenon violated due to the presence of unavoidable quadratic nonresonant terms. The final design, discussed in chapter 6 includes a nonsmooth behavior such that $V_{\mathrm{nl}} = \beta(V + |V|)$, realized by a diode in the shunt circuit.

1.5.4 Problem of high inductance

In the applications involving the usage of an RL-shunt, the optimal attenuation requires that the electrical resonance frequency to be close to the mechanical one corresponding to the structure mode to be attenuated [176]. Thus, when tackling low frequency modes, the low capacitance characteristic of the piezoelectric transducer (usually to the order of nano-Farads) demands a high inductance in the shunt circuit, which can represent a practical limit. For example, if one aims to design an RL-shunt to damp a mode at a frequency close to $\omega = 30 \times (2\pi)$rad/s with a piezoelectric capacitance around $C_p = 30$nF, an inductance value close to $L = 1/(\omega^2 C_p) = 940$H is necessary to obtain an optimal attenuation. Such inductance value is very high to be achieved through the classical passive inductor. To overcome this issue, synthetic inductors have been proposed, which are mainly composed of electrical components such as resistors, capacitors, and operational amplifiers.

Synthetic inductors are based on a generalized impedance converter (GIC), which is known as a gyrator. The most frequently used synthetic inductors in the piezoelectric shunt applications are the Antoniou [199] and Riordan [200] since they are easy to implement and tune. A schematic of both synthetic inductors is shown in Fig. 1.13.

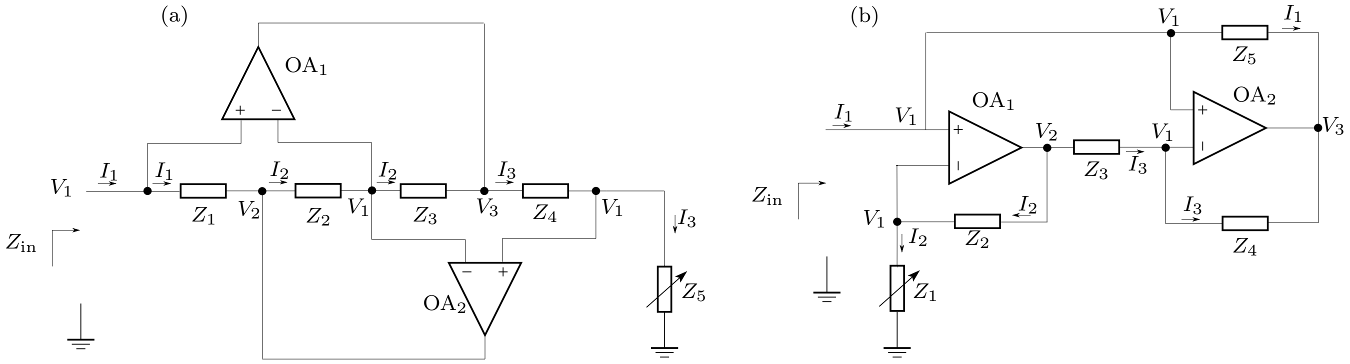

Figure 1.13: (a) Antoniou synthetic inductor and (b) Riordan synthetic inductor.

Assuming ideal operational amplifiers and zero losses, the input impedance Z_{in} of both inductors is the same and can be estimated as:

$$Z_{\text{in}} = \frac{Z_1 Z_3 Z_5}{Z_2 Z_4}. \tag{1.6}$$

To arrive to an expression of Z_{in} admitting an inductance impedance, Z_1 Z_3, and Z_5 are set as resistive impedances (i.e. $Z_1 = R_1$, $Z_2 = R_2$, and $Z_3 = R_3$) . Regarding Z_2 and Z_4, two options can be used, either setting Z_2 with a resistive impedance and Z_4 with a capacitive impedance (i.e., $Z_2 = R_2$ and $Z_4 = 1/(j\omega C)$), or vise versa. With both options, the input impedance can be expressed as:

$$Z_{\text{in}} = j\omega L, \tag{1.7}$$

with L being the synthetic inductor that can be tuned by the variable resistors shown in Fig. 1.13. Its numerical value can be estimated as:

$$L = \frac{R_1 R_3 R_5 C}{R_2}. \tag{1.8}$$

The behavior of the synthetic inductor is proved to be identical to a real inductor only in a specific frequency range [201]. However, two main issues have been addressed. Since the RL-shunt is sensitive to any mistuning in the structure resonance frequency, the synthetic inductor should be adaptive, which can be practically hard for the classic configurations in Fig. 1.13. A solution to this issue is addressed in [202] using a voltage-controlled synthetic inductor in which an analog multiplier is required in the circuit.

The second issue is the parasitic resistance, which is addressed in some experimental applications as in [201], [203] and in our experiments (see chapter 3 and chapter 5), is not predicted theoretically in Eq. (1.7). It can be noted that there is no mathematical formulation in the literature to explain this parasitic resistance theoretically. However, experimentally, it is proven to increase linearly with the inductance value. This can be an issue in the applications of the RL-shunt, especially if the parasitic resistance is higher than the optimal resistance required. Two possible solutions were proposed to overcome this issue. The first solution is to add a capacitance in parallel to the piezoelectric capacitance [204], which leads to the reduction of the optimal inductance required and thus reduces the parasitic resistance. However, the main drawback is the attenuation reduction since the piezoelectric coupling factor will be lowered. The other solution is to use a negative resistance in series with the inductance or to use the proposed modified Antoniou synthetic inductor in [176], [205] where a negative resistance can be generated by adding a resistor between the inverting inputs of the two operational amplifiers shown in Fig. 1.13(a). The drawback of the second solution is the limitation of the negative resistance due to the stability limit.

One can note that the usage of synthetic inductors requires an external energy source to supply the operational amplifiers. Thus, careful attention should be given to the voltage and current limits at their input and output ports. Due to this energy source, the RL-shunts are transformed from fully passive to semi-passive absorbers. In this context, it is worth mentioning the successful attempt to design a passive inductor with high values that led to preserving the passive feature of the shunt circuit [206], [207]. Note that in most applications of the RL-shunt, the Antoniou inductor is used instead of the Riordan one. In our experimental tests, as shown in chapters 3, 5, and 6, we adopted this choice. In addition, the ability of adding a negative resistance [176] to oppose the parasitic resistance is an advantage for the Antonio inductor.

1.6 Nonlinear system analysis and solution methodologies

1.6.1 Theoretical methods

Contrary to the linear systems where exact solutions can be easily obtained, this can be a very hard task in the models exhibiting nonlinear behavior due to their rich and complex dynamics. In many branches of physics and engineering, mechanical oscillations are modeled as nonlinear differential equations. Thus, numerous analytical and numerical techniques have been established to retrieve the essential dynamics of these equations enabling a parametric study of the system, stability and bifurcation analysis, and obtaining the rich response of different harmonics. Consequently, the theoretical analysis of the nonlinear systems is crucial to obtain different design aspects and constraints for real-life engineering problems.

In this work, the nonlinear dynamics of the designed absorber is analyzed theoretically using two analytical approaches, the multiple scales method and the normal form. In addition, a numerical continuation software "MANLAB" is used for numerical analysis. In what follows, those tools will be introduced.

1.6.1.1 Multiple scales method

Perturbation methods represent efficient analytical tools to analyze nonlinear vibration problems. They can be used to obtain closed-form solutions of different simplified nonlinear models. In the literature, different perturbation techniques have been proposed [208], [209] such as straightforward expansion, Lindstedt-Poincaré method, method of renormalization, method of averaging, and method of multiple scales.

The basic idea of the perturbation methods is to perform an asymptotic expansion of the solution with respect to a small perturbation parameter (usually denoted by ε). Such perturbation parameter can have a physical meaning in the system or can be introduced as a scaling parameter (or a bookkeeping parameter) to scale the nonlinearities present in the system in addition to the damping and the forcing at different orders. The main advantage of the perturbation techniques is their ability to give accurate results at small oscillation amplitudes. However, at higher amplitudes (or low amplitudes with strong nonlinearities), achieving accurate results requires higher orders of expansion which can be a cumbersome process. In this context, one can refer to [210] where a Python code is developed to obtain high-order solutions with MSM.

The multiple scales method (MSM) proved to be very efficient in terms of easier derivations and accuracy in many applications compared to the other methods. Examples of those applications involve different nonlinear problems in structural dynamics (e..g reduced order models of beams [211], [212], shells [140], [213], rings [214]), problems with internal resonance [145], [215], nonlinear vibration absorbers [216], buckling dynamics [217], and MEMS (micro electro-mechanical systems) cantilever resonators [88].

In our analysis of the nonlinear absorber behavior, the MSM is used for the analytical treatment. To emphasize the steps of this method, we consider a simple case by applying this method to the Duffing oscillator presented in Eq. (1.1). As a first step, Eq. (1.1) is rescaled with respect to an introduced small book-keeping parameter ε as follows:

$$\ddot{x} + \varepsilon\mu\dot{x} + \omega_0^2 x + \varepsilon\gamma x^3 = \varepsilon F \cos\Omega t. \tag{1.9}$$

Note that here the highest order of expansion is to the order of ε. However, if quadratic nonlinearities are additionally presented, a higher order of expansion (i.e., order of ε^2) is required so that the effect of quadratic nonlinearities is considered at order ε and the cubic ones at ε^2. In addition, it is common to consider the forcing and damping scaling at the highest order considered in the problem [209], nevertheless, this choice is not unique.

The MSM requires the definition of different time scales as:

$$T_k = \varepsilon^k t, \tag{1.10}$$

where $k \in \mathbb{N}$ represents the order of expansion. Since we consider the expansion to the order of ε, we consider only the times scales T_0 and T_1. Using the chain rule, the first and second derivatives of $x(t)$ can be expressed as:

$$\frac{d}{dt} = D_0 + \varepsilon D_1 + O(\varepsilon^2), \tag{1.11a}$$

$$\frac{d^2}{dt^2} = D_0^2 + 2\varepsilon D_0 D_1 + O(\varepsilon^2), \tag{1.11b}$$

where $D_k = \frac{d}{dT_k}$. To simplify the derivation and to obtain a closed form expression of the backbone curves, we consider the free conservative case (i.e., $F = \mu = 0$). Then, by substituting Eqs. (1.11a, b) in Eq. (1.9), one obtains:

$$D_0^2 x + \omega_0^2 x + \varepsilon(2D_0 D_1 x + \gamma x^3) + O(\varepsilon^2) = 0. \tag{1.12}$$

We seek an approximation of $x(t)$ by expanding with respect to ε as:

$$x(t;\varepsilon) = x_0 + \varepsilon x_1 + O(\varepsilon^2). \tag{1.13}$$

Then by substituting Eq. (1.13) in Eq. (1.12) and by equating the coefficient of $\varepsilon^0 = 1$ and ε, one obtains:

$$D_0^2 x_0 + \omega_0^2 x_0 = 0, \tag{1.14a}$$

$$D_0^2 x_1 + \omega_0^2 x_1 = -2 D_0 D_1 x_0 - \gamma x_0^3. \tag{1.14b}$$

The obtained differential equations in (1.14a, b) are solved successively. The solution of the first equation can be easily obtained as:

$$x_0 = A(T1) e^{i\omega_0 T_0} + \text{c.c}, \tag{1.15}$$

where $A(T1)$ is the unknown amplitude that depends solely on T_1, i is the imaginary number, and c.c denotes the complex conjugate. Then by substituting Eq. (1.15) in Eq. (1.14b), one obtains:

$$D_0^2 x_1 + \omega_0^2 x_1 = (-2i\omega_0 D_1 A - 3\gamma A^2 \bar{A}) e^{i\omega_0 T_0} - \gamma A^3 e^{3i\omega_0 T_0} + \text{c.c.} \tag{1.16}$$

The most important step in the MSM derivation is to identify and then eliminate the so-called secular terms in Eq. (1.16), which are the terms that express oscillations at the resonance frequency. Precisely, they are the terms multiplying $e^{i\omega_0 T_0}$. Eliminating those terms is essential since they force the system at its resonance causing unbounded oscillations. Equating those terms to zero demands:

$$D_1 A = \frac{3i\gamma}{2\omega_0} A^2 \bar{A}. \tag{1.17}$$

In addition, upon eliminating the secular terms from Eq. (1.16), one can obtain x_1 as :

$$x_1 = \frac{\gamma}{9\omega_0^2 - 1} A^3 e^{3i\omega_0 T_0} + \text{cc}. \tag{1.18}$$

At this step, it is convenient to use the polar form of $A(T1)$ defined as:

$$A(T1) = \frac{1}{2} a(T1) e^{i\theta(T1)}, \tag{1.19}$$

where $a(T1)$ and $\theta(T1)$ are respectively the amplitude and the phase. Note that one can also use the Cartesian form instead. Then by substituting the polar form in Eq. (1.15) and Eq. (1.18), $x(t)$ can be recovered from Eq. (1.13) as :

$$x(t;\varepsilon) = a\cos(\omega_0 t + \theta) + \frac{\gamma}{4(9\omega_0^2 - 1)} a^3 \cos(3\omega_0 t + 3\theta) + O(\varepsilon^2). \tag{1.20}$$

To obtain θ and a, the polar form is introduced in the secular condition presented in Eq. (1.17) . By equating the real and imaginary parts, one arrives to the following modulation equations:

$$D_1 a = 0, \tag{1.21a}$$

$$a D_1 \theta = \frac{3\gamma}{8\omega_0} a^3, \tag{1.21b}$$

Eq. (1.21a) suggest that $a = a_0 =$ constant while θ can be found by integrating Eq. (1.21b) to obtain for $a \neq 0$:

$$\theta = \frac{3\gamma}{8\omega_0} a^2 T_1 + \theta_0. \tag{1.22}$$

Then, by substituting Eq. (1.22) in Eq. (1.20), the free solution to the first order of ε is expressed as:

$$x(t;\varepsilon) = a_0 \cos(\omega_{\mathrm{nl}} t + \theta_0) + \frac{\gamma}{4(9\omega_0^2 - 1)} a_0^3 \cos(3\omega_{\mathrm{nl}} t + 3\theta_0) + O(\varepsilon^2), \tag{1.23}$$

where ω_{nl} defines the backbone curve near the primary resonance as:

$$\omega_{\mathrm{nl}} = \omega_0 + \varepsilon \frac{3\gamma}{8\omega_0} a^2. \tag{1.24}$$

One can realize that Eq. (7.14) predicts that if $\gamma > 0$, ω_{nl} increases with the oscillation amplitude and thus hardening behavior occurs, as predicted numerically in Fig. 1.5. However, if $\gamma < 0$, the opposite occurs, and thus a softening behavior occurs. In addition, Eq. (1.23) suggests a contribution of the third harmonic in the dynamics.

For the case of forced damped response, one can follow the same derivation steps to derive the frequency responses of the steady-state amplitude a and phase angle θ of the first harmonic, which are expressed as [72]:

$$\Omega = \omega_0 + \varepsilon \left[\frac{3\gamma}{8\omega_0} a^2 \pm \frac{1}{2} \sqrt{\frac{F^2}{a^2\omega_0^2} - \mu^2} \right], \tag{1.25a}$$

$$\tan\theta = \frac{1}{2} \frac{\mu}{\Omega - \omega_0 - \frac{3\gamma}{8\omega_0} a^2}. \tag{1.25b}$$

One can realize that the expression of the backbone curve presented in Eq. (7.14) can be obtained by setting $F = \mu = 0$ in the amplitude forced response in Eq. (1.25a) and by replacing Ω by ω_{nl}. Moreover, the same equation of the backbone curve can be obtained from the phase expression in Eq. (1.25b) by setting the denominator to zero to obtain the phase resonance condition (i.e., $\theta = \pi/2$). This suggests that the backbone curve intersects the forced damped response at the phase resonance. Note that this conclusion is very important for the detection of the backbones experimentally, but it cannot be generalized since, for some cases (for example, in the free solution with 2:1 internal resonance as suggested in chapter 4), the free and forced response do not intersect. In addition, stability analysis can be established by identifying the eigen-values of the Jacobian matrix. In conclusion, the MSM method is able to predict the main dynamics features of the free and forced solutions, with relatively easy derivation, showing its ability to analyze weakly nonlinear systems. Note also that the steps shown can be applied exactly in the same manner for more complicated problems such as analyzing the features of the internal resonance suggested in our designed absorber.

1.6.1.2 Normal form method

Normal form method is an approach that aims to analyze the nonlinear systems and their bifurcation topology by expressing their dynamics in the simplest form possible. It was introduced by Poincaré [218] and Poincaré-Dulac [219] and reviewed through many introduction textbooks since then [220], [221]. The normal form requires a nonlinear change of coordinates through a power series expansion near a hyperbolic fixed point [222]–[225]. Then, the expansion coefficients can be freely chosen, thanks to the method of free function [224], to cancel as much as possible the nonlinear terms, specifically the nonresonant terms, to achieve a simplified system in the normal form basis [226]–[228]. Three types of normal form exist in the literature, the complex normal form [101], the real normal form [229], and the fully real normal form [225]. The latter is the most suitable for oscillation problems, and thus it is used in our analysis (see chapter 4). In this context, two important theorems govern the derivation of the normal that focus on the existence of an internal resonance condition, which is important for the nonlinear analysis of the absorber dynamics illustrated in this work.

To present the two theorems, a general nonlinear system is considered and expressed as:

$$\dot{\boldsymbol{X}} = \boldsymbol{L}\boldsymbol{X} + \sum_{k=2}^{N} \boldsymbol{G}_k(\boldsymbol{X}), \tag{1.26}$$

where $\boldsymbol{X} \in \mathbb{R}^N$ is the state vector. The term $\boldsymbol{L}\boldsymbol{X}$ represents the linear part where $\boldsymbol{L} = \text{diag}(\lambda_N)$ is an $N \times N$ matrix and λ_N is the eigen-value. $\boldsymbol{G}_k$ represents the nonlinear part with k denoting the order of expansion (e.g., $k = 2$ denotes the quadratic nonlinearities and $k = 3$ denotes the cubic ones), and N is the maximum order retained. The internal resonance condition can then be expressed as:

$$\lambda_i = \sum_j p_j \lambda_j \quad \text{with} \quad p_j \in \mathbb{N}^* \quad \text{and} \quad \sum_j p_j = N. \tag{1.27}$$

The first theorem (Poinacré theorem) states that in case there is no internal resonance presented in the system, one can find a nonlinear transformation $\boldsymbol{Y} = \boldsymbol{X} + \boldsymbol{H}(\boldsymbol{Y})$ that *linearize the system* in Eq. (1.26) so that $\dot{\boldsymbol{Y}} = \boldsymbol{L}\boldsymbol{Y}$ is obtained (i.e., all the nonlinear contributions of $\boldsymbol{G}_k$ are canceled). On the other hand, the second theorem (Poincaré Dulac theorem) states that in the case of the internal resonance, the linearization is not possible and the *resonant nonlinear terms should be retained in the normal form system*. Thus, the cancellation is only possible for the nonresonant terms, leading to simplify the initial system in Eq. (1.26). The latter theorem plays an important role in our analysis (see chapter 4) of the nonlinear absorber exhibiting the 2:1 internal resonance.

In addition to its ability to simplify the dynamics, normal form has a strong relation with the nonlinear normal modes since the introduced nonlinear transformation spans the dynamics on curved *invariant manifolds* in the phase space that are tangent to the linear flat manifolds near the hyperbolic fixed point [226], [227], [230]. Those two features (i.e., dynamics simplification and definition of the nonlinear normal modes) led the researchers to utilize this method to build efficient reduced order models of the nonlinear systems through the finite element method with a lower number of modes retained in the system to arrive for accurate results [231]–[233].

1.6.1.3 MANLAB

MANLAB is an interactive path-following and bifurcation analysis software implemented in a MATLAB environment to compute the periodic solutions of the nonlinear dynamical system through a numerical continuation. The continuation relies on the so-called Asymptotic Numerical Method (ANM) combined with Fourier series expansion, known as the Harmonic Balance Method (HBM). MANLAB is an open source code in which different versions are developed by several theses [234]–[236] and available to download on the "Laboratoire de Mécanique et d'Acoustique de Marseille" website [237]. This software is the main numerical tool that has been used in this work, and thus its basics will be introduced in this section. Note that in what follows, all the explanations are a summary of the detailed works in [238]–[242].

We start by explaining the ANM, which is the basic method for the numerical continuation in MANLAB. It is first introduced in [243], [244] as a continuation technique based on a high-order Taylor series expansion of the unknowns with respect to a path parameter. The main aim of ANM is to find a solution for the following N-dimensional algebraic system:

$$\boldsymbol{R}(\boldsymbol{U}, \lambda) = \boldsymbol{0}, \tag{1.28}$$

where $\boldsymbol{U} \in \mathbb{R}^N$, $\lambda \in \mathbb{R}$ is the continuation parameter, and $\boldsymbol{R} : \mathbb{R}^N \times \mathbb{R} \longrightarrow \mathbb{R}^N$ is a real analytic function of its arguments which can be expressed as a combination of rotational and elementary transcendental functions such as polynomials, exponential, trigonometric, log, etc... The analytic function assumption means that the arguments of $\boldsymbol{R}$ should be smooth, otherwise a regularization procedure should be introduced [245](refer to Appendix B in Sec. 6.2). Thanks to the implicit function theorem which states that if $\boldsymbol{R}$ is continuously differentiable with respect to $\boldsymbol{U}$ and λ, and if the Jacobian $\boldsymbol{J} = \frac{\partial \boldsymbol{R}}{\partial \boldsymbol{U}}$ is invertible, there exist a differentiable function $\boldsymbol{g}$ such that:

$$g : \left| \begin{array}{ccc} \mathbb{R} & \longrightarrow & \mathbb{R}^N \\ \lambda & \longmapsto & \boldsymbol{g}(\lambda) = \boldsymbol{U} \end{array} \right. \tag{1.29}$$

Thus, the unknown $\boldsymbol{U}$ can be expressed as a function of the continuation parameter λ. However, some issues can be presented with this representation, especially when the curve of $\boldsymbol{U}$ crosses a vertical tangent with respect to λ. Classical example can be observed during the bifurcation analysis when a saddle-node bifurcation occurs in the bifurcation diagram of $\boldsymbol{U}$ with λ considered as the bifurcation parameter as shown in Fig. 1.14. To overcome this issue, a path parametrization procedure can be

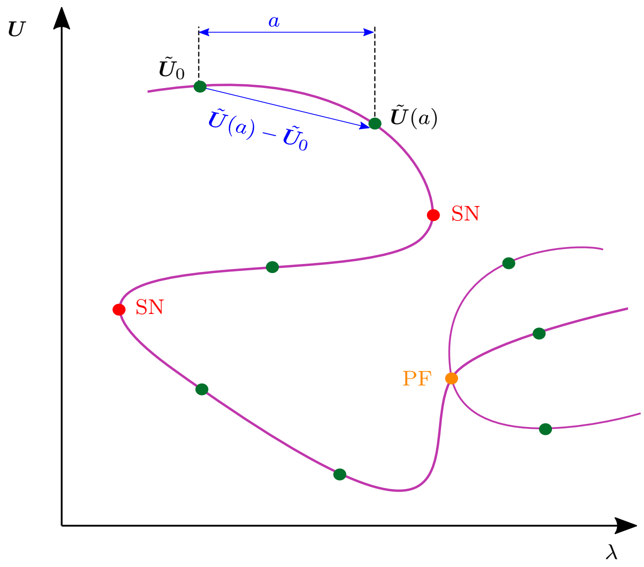

Figure 1.14: Bifurcation diagram of $\boldsymbol{U}$ with respect to λ. The green dots denote the computations steps boundary according to a. The red and orange dots denote respectively the saddle-node bifurcations (SN) and Pitchfork bifurcations (PF).

introduced with respect to a scalar quantity a such that:

$$\begin{cases} \boldsymbol{U} = \boldsymbol{U}(a) \\ \lambda = \lambda(a) \\ f(\boldsymbol{U}, \lambda(a)) = 0 \end{cases} \implies \begin{cases} \boldsymbol{R}(\boldsymbol{U}(a), \lambda(a)) = 0 \\ f(\boldsymbol{U}, \lambda(a)) = 0 \end{cases} \tag{1.30}$$

Thus, new algebraic equations of size $\mathbb{R}^{N+1}$ are defined, which are not singular with respect to a. In MANLAB, the pseudo-arclength parametrization is used, which leads to the definition of a as:

$$f(\boldsymbol{U}, \lambda(a)) = 0 \quad \implies \quad a = \left(\tilde{\boldsymbol{U}}(a) - \tilde{\boldsymbol{U}}_0\right)^{\mathrm{T}} \tilde{\boldsymbol{U}}_1, \tag{1.31}$$

where $\tilde{\boldsymbol{U}} = \left[\boldsymbol{U}^{\mathrm{T}} \quad \lambda\right]^{\mathrm{T}}, \tilde{\boldsymbol{U}}_0 = \tilde{\boldsymbol{U}}(a=0)$, $\tilde{\boldsymbol{U}}_1 = \left.\frac{\partial \tilde{\boldsymbol{U}}}{\partial a}\right|_{a=0}$, and the superscript "T" denotes transpose. Upon defining the parametrization technique and thanks to the implicit function theorem assumptions, $\tilde{\boldsymbol{U}}$ can then be expanded as a power series with respect to a. According to the definition of $\tilde{\boldsymbol{U}}$, one obtains:

$$\boldsymbol{U}(a) = \sum_{k=0}^{P} a^k \boldsymbol{U}_k, \tag{1.32a}$$

$$\lambda(a) = \sum_{k=0}^{P} a^k \lambda_k. \tag{1.32b}$$

In practice, the power series is truncated to a given order P, which is commonly taken equal to 20. The approach implemented in MANLAB to compute the unknowns $\boldsymbol{U}_k$ relies on *quadratic recasting* of Eq. (1.28) through the definition of auxiliary variables $\boldsymbol{U}_a \in \mathbb{R}^{N_a}$:

$$\boldsymbol{R}\left(\tilde{\boldsymbol{U}}, \boldsymbol{U}_a\right) = \boldsymbol{R}\left(\tilde{\boldsymbol{W}}\right) = \boldsymbol{C} + \boldsymbol{L}\left(\tilde{\boldsymbol{W}}\right) + \boldsymbol{Q}\left(\tilde{\boldsymbol{W}}, \tilde{\boldsymbol{W}}\right) = \boldsymbol{0}, \tag{1.33}$$

where $\tilde{\boldsymbol{W}} = \left[\tilde{\boldsymbol{U}}, \boldsymbol{U}_a\right]^{\mathrm{T}} \in \mathbb{R}^{N_f}$, with $N_f = N + N_a + 1$, is the new unknown vector which is composed of the initial vector $\tilde{\boldsymbol{U}}$ and the auxiliary vector $\boldsymbol{U}_a$ so that the system will solely include nonlinearities of quadratic type. $\boldsymbol{C}$, $\boldsymbol{L}$, and $\boldsymbol{Q}$ are, respectively, constant, linear and quadratic operators with values in $\mathbb{R}^{N_f}$. Note that $\boldsymbol{U}_a$ is expanded as Taylor series with respect to a in a similar manner to $\boldsymbol{U}$ in Eq. (1.32a). Upon substituting the expansions of $\tilde{\boldsymbol{U}}$ and $\boldsymbol{U}_a$ in Eq. (1.33) then balancing the coefficients of a^k for each order $k \in [0, P]$ and using the definition of a in Eq. (1.31), *one arrives at a nonlinear initial system at order a^0 and P-linear equations at higher orders of a* as follows:

$$\begin{aligned}
&\text{Order } a^0: && \boldsymbol{R}(\tilde{\boldsymbol{W}}_0) = \boldsymbol{0} \\
&\text{Order } a^1: && \begin{cases} \boldsymbol{J}_0 \tilde{\boldsymbol{W}}_1 = \boldsymbol{0} \\ \tilde{\boldsymbol{W}}_1^{\mathrm{T}} \tilde{\boldsymbol{W}}_1 = 1 \end{cases} \\
&\text{Order } a^2: && \begin{cases} \boldsymbol{J}_0 \tilde{\boldsymbol{W}}_2 = -\boldsymbol{Q}\left(\tilde{\boldsymbol{W}}_1, \tilde{\boldsymbol{W}}_1\right) \\ \tilde{\boldsymbol{W}}_1^{\mathrm{T}} \tilde{\boldsymbol{W}}_2 = 0 \end{cases} \\
&\text{Order } a^3: && \begin{cases} \boldsymbol{J}_0 \tilde{\boldsymbol{W}}_3 = -\left[\boldsymbol{Q}\left(\tilde{\boldsymbol{W}}_1, \tilde{\boldsymbol{W}}_1\right) + \boldsymbol{Q}\left(\tilde{\boldsymbol{W}}_2, \tilde{\boldsymbol{W}}_2\right) + \boldsymbol{Q}\left(\tilde{\boldsymbol{W}}_3, \tilde{\boldsymbol{W}}_3\right)\right] \\ \tilde{\boldsymbol{W}}_1^{\mathrm{T}} \tilde{\boldsymbol{W}}_3 = 0 \end{cases} \\
&\quad\vdots && \quad\vdots \\
&\text{Order } a^P: && \begin{cases} \boldsymbol{J}_0 \tilde{\boldsymbol{W}}_P = -\sum_{i=1}^{P-1} \boldsymbol{Q}\left(\tilde{\boldsymbol{W}}_i, \tilde{\boldsymbol{W}}_{P-i}\right) \\ \tilde{\boldsymbol{W}}_1^{\mathrm{T}} \tilde{\boldsymbol{W}}_P = 0 \end{cases}
\end{aligned} \tag{1.34}$$

The terms $\left(\tilde{\boldsymbol{W}}_0, \tilde{\boldsymbol{W}}_1, \tilde{\boldsymbol{W}}_2, \tilde{\boldsymbol{W}}_3, ..., \tilde{\boldsymbol{W}}_P\right)$ are the Taylor series coefficients of $\tilde{\boldsymbol{W}}$ to be determined. $\boldsymbol{J}_0 = \frac{\partial \boldsymbol{R}}{\partial \tilde{\boldsymbol{W}}}\Big|_{\tilde{\boldsymbol{W}}_0}$ is denoted by the stiffness matrix which appears in the all P linear systems at orders of a higher than zero. Thus, computing the initial vector $\tilde{\boldsymbol{W}}_0$ and the matrix $\boldsymbol{J}_0$ is necessary to obtain the Taylor coefficients at higher orders. In MANLAB, this is established through an initialization procedure using the Newton-Raphson method [246], which can be modified at each solution branch. One must also note that the defined power series with respect to a admits a radius of convergence that defines the range of utility of the series by a maximum value of a, denoted by $a_{\max}$, defined by:

$$\forall a \in [0 \; a_{\max}], \qquad \|\boldsymbol{R}\left(\tilde{\boldsymbol{W}}(a)\right)\| \leq \varepsilon, \tag{1.35}$$

where ε is a tolerance parameter defined by the user which remains constant at each computation step of the solution branches while $a_{\max}$ is automatically computed. Note also that the complete branch of solutions (i.e., each local branch bounded by two green points in Fig. 1.14) is obtained by successive power series, meaning that the series is initiated such that its first point equals the last point of the previous one. With this process, the zeroth order $\boldsymbol{R}(\tilde{\boldsymbol{W}}_0) = \boldsymbol{0}$ is always satisfied, up to the chosen tolerance ε.

In this work, we are interested in using MANLAB to estimate the periodic responses of nonlinear oscillatory problems so that the nonlinear dynamics of our designed absorbers (i.e. nonlinear forced frequency response, stabilities, bifurcations, backbone curves etc...) can be determined. To explain the implementation of such a problems in MANLAB, we consider a simple example which is the simple Duffing oscillator in Eq. 1.9. The main preliminary step is to expand the unknown $x(t)$ (assumed periodic with period $2\pi/\omega$ with ω the angular frequency) in the form of a truncated Fourier series up to harmonic $H \in \mathbb{N}$ as:

$$x(t) = x_0 + \sum_{k=1}^{H} \left(x_k^c \cos k\omega t + x_k^s \sin k\omega t \right), \tag{1.36}$$

where x_0, x^c, and x^s are the Fourier coefficients of $x(t)$. Then by substituting $x(t)$ in Eq. (1.9) and balancing the $2H + 1$ harmonic terms (i.e., use the harmonic balance method (HBM)), one arrives at an algebraic system of the form:

$$\boldsymbol{R}(\boldsymbol{X}, \omega, \lambda) = \boldsymbol{0}, \tag{1.37}$$

where $\boldsymbol{X} \in \mathbb{R}^{N_t}$ is a vector containing all the Fourier coefficients. $N_t = N_{\text{dof}}(2H + 1)$ with N_{dof} is the number of degrees of freedom which is one in our simple case. $\boldsymbol{R} : \mathbb{R}^{N_t} \times \mathbb{R}^2 \longrightarrow \mathbb{R}^{N_t}$ is a real analytic function that defines the residual of the HBM. Thus, one can realize that we arrived at an algebraic system similar to that in Eq. 1.28 which can be solved by ANM by the same steps discussed above. In other words, *the role of the* HBM *is to transform the nonlinear differential system into an algebraic system that is suitable to be solved with* ANM *using* MANLAB. The main difference is the appearance of an additional unknown ω, and thus an additional equation is required.

To determine this additional equation, we consider two different cases, the forced response and the free response, where the latter is used to determine the backbone curves. In the former case, the computation is straightforward by setting $\omega = \Omega = \lambda$ as the new equation (i.e., Ω is the bifurcation parameter, and thus the frequency response can be directly determined). However, for the free response it can be more complicated since in this case, Ω is not defined and the system is autonomous and conservative. The autonomous nature of the system then requires defining a phase condition which is necessary to achieve a unique solution for the periodic orbit [247]. Note that for the forced response case, one can consider the bifurcation parameter to be the excitation amplitude (i.e., $\lambda = F$) or the nonlinear coefficient (i.e., $\lambda = \gamma$) by fixing Ω at a certain excitation frequency in either case.

Implementing the nonlinear differential equations in MANLAB should be done in the first order

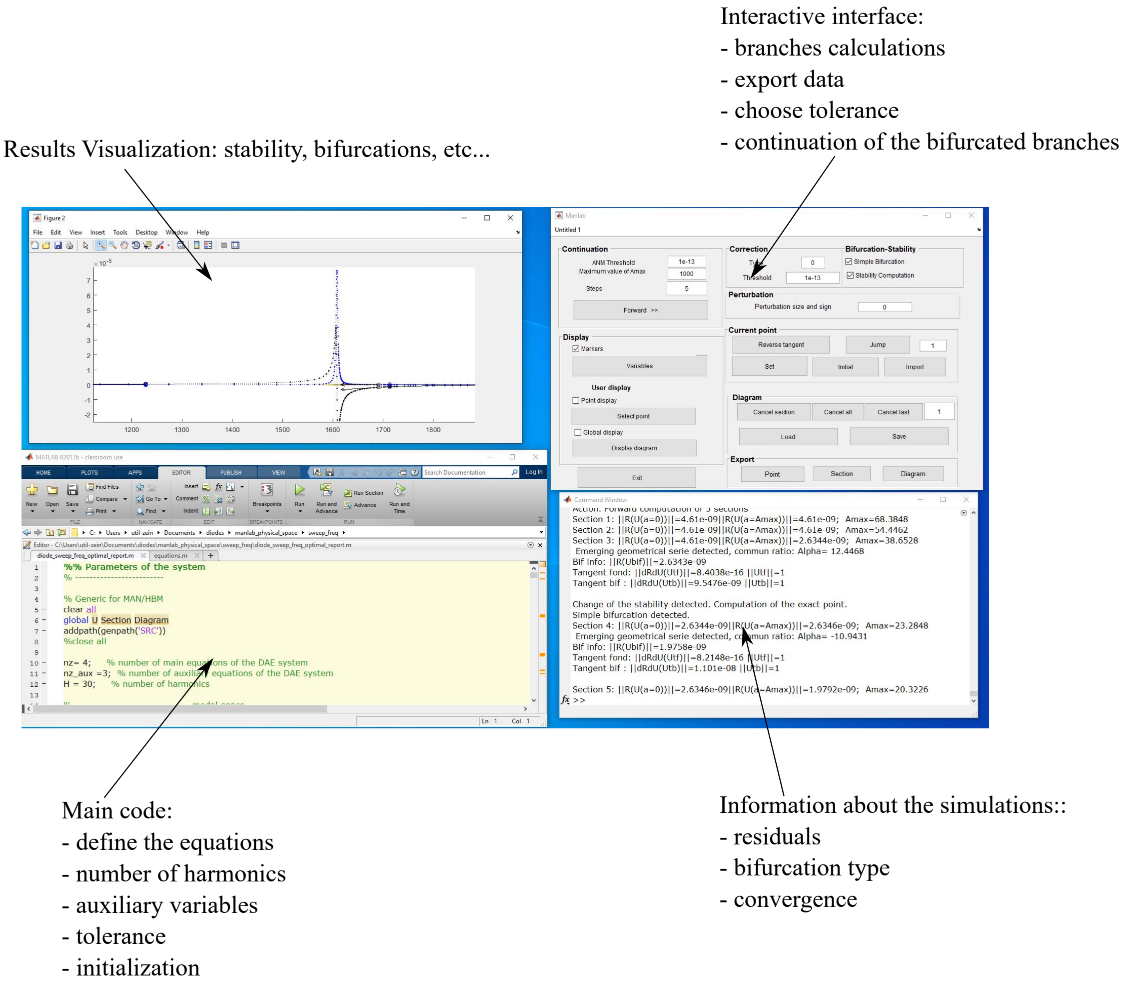

Interactive interface:
- branches calculations
- export data
- choose tolerance
- continuation of the bifurcated branches

Results Visualization: stability, bifurcations, etc...

Main code:
- define the equations
- number of harmonics
- auxiliary variables
- tolerance
- initialization

Information about the simulations::
- residuals
- bifurcation type
- convergence

Continuation
ANM Threshold 1e-13
Maximum value of Amax 1000
Steps 5

Correction
Type 0
Threshold 1e-13

Bifurcation-Stability
☑ Simple Bifurcation
☑ Stability Computation

Perturbation
Perturbation size and sign 0

Display
☑ Markers

User display
☐ Point display
☐ Global display

Current point
Jump 1

Diagram
Cancel last 1

Editor - C:\Users\util-zein\Documents\diodes\manlab_physical_space\sweep_freq\diode_sweep_freq_optimal_report.m

```
%% Parameters of the system
% ------------------------

% Generic for MAN/HBM
clear all
global U Section Diagram
addpath(genpath('SRC'))
%close all

nz= 4;     % number of main equations of the DAE system
nz_aux =3;  % number of auxiliary equations of the DAE system
H = 30;     % number of harmonics
```

```
Action: Forward computation of 5 sections
Section 1: ||R(U(a=0))||=4.61e-09||R(U(a=Amax))||=4.61e-09;  Amax=68.3848
Section 2: ||R(U(a=0))||=4.61e-09||R(U(a=Amax))||=4.61e-09;  Amax=54.4462
Section 3: ||R(U(a=0))||=4.61e-09||R(U(a=Amax))||=2.6344e-09;  Amax=38.6528
 Emerging geometrical serie detected, commun ratio: Alpha= 12.4468
Bif info: ||R(Ubif)||=2.6343e-09
Tangent fond: ||dRdU(Utf)||=8.4038e-16 ||Utf||=1
Tangent bif : ||dRdU(Utb)||=9.5476e-09 ||Utb||=1

Change of the stability detected. Computation of the exact point.
Simple bifurcation detected.
Section 4: ||R(U(a=0))||=2.6344e-09||R(U(a=Amax))||=2.6346e-09;  Amax=23.2848
 Emerging geometrical serie detected, commun ratio: Alpha= -10.9431
Bif info: ||R(Ubif)||=1.9758e-09
Tangent fond: ||dRdU(Utf)||=8.2148e-16 ||Utf||=1
Tangent bif : ||dRdU(Utb)||=1.101e-08 ||Utb||=1

Section 5: ||R(U(a=0))||=2.6346e-09||R(U(a=Amax))||=1.9792e-09;  Amax=20.3226
>>
```

Figure 1.15: MANLAB interface.

after performing the quadratic recast in the form of the algebraic system presented in Eq. (1.33). In the older versions of MANLAB, the operators $\boldsymbol{C}$, $\boldsymbol{L}$, and $\boldsymbol{Q}$ should be defined explicitly; however, for the recent version used in this work, it is enough to only define the first order form of the nonlinear system with the auxiliary condition with non-explicit definition of the operators. For example, the forced Duffing oscillator in Eq.(1.33) is implemented by including three variable (x, v, w) such that:

$$
\begin{cases}
\dot{x} = v, & (1.38a)\\
\dot{v} = F\cos\Omega t - \omega_0^2 x - 2\xi\omega_0 v - \gamma x w, & (1.38b)\\
0 = w - x^2 & (1.38c)
\end{cases}
$$

where $\lambda = \Omega$ and w defines the auxiliary variable introduced for the quadratic recast.

For the free solution case, the implementation can be done as follows:

$$\begin{cases} \dot{x} = v, & (1.39\text{a}) \\ \dot{v} = -\omega_0^2 x - \lambda v - \gamma x w, & (1.39\text{b}) \\ 0 = w - x^2 & (1.39\text{c}) \end{cases}$$

Note that the term λv is kept in the equation to avoid an overdetermined system with the phase resonance condition because the latter condition is implicit in MANLAB [247], [248]. Thus λ can be considered as a fictitious bifurcation parameter with $\lambda \simeq 0$ to consider an undamped case. Examples of the free and forced response of the Duffing equation solved with MANLAB can be found in Fig. 1.5. One can also refer to Fig. 1.15 that shows the MANLAB interface. Regarding the stability computation with MANLAB, it is based on the computation of the Floquet exponents in the frequency domain with a Hill eigenvalue problem. The stability analysis is beyond the scope of this brief introduction, but one can refer to [249] for further explanation.

1.6.2 Experimental methods

Experimental vibration analysis is widely studied in the literature in terms of measurement procedures, signal processing, vibration noise, and data post-processing. An essential tool in experimental vibrations is the experimental modal analysis which is a technique used to estimate the modal model of the linear time-invariant systems [250]. The main tool used for the modal analysis is the frequency response function (FRF) which is defined as the ratio between the output signal (i.e., the measured signal such as the displacement or the velocity) to the input signal (i.e., the excitation), expressed in the Fourier domain. Experimental FRFs can be estimated by measuring the desired output through various methods such as shock excitation or continuous chirp signal excitation [251]. The input and output data are usually transferred to data acquisition systems that use dedicated algorithms such as fast Fourier transformation (FFT). Upon estimating the FRFs, the natural frequencies and the modal damping ratios can be directly extracted for the oscillation modes in a certain frequency spectrum. In addition, the FRF characterizes the whole dynamical behavior of the linear system (i.e., when the nonlinearities are not involved).

When nonlinearities are involved in the vibration system, the classical methods to identify the FRFs can not be utilized since the superposition principle does not extend to the nonlinear theory. Indeed, those methods lack the ability to identify the dynamics behavior, such as the ones depicted in the nonlinear frequency response shown in Fig. 1.5, which undergoes bifurcation and change of stability. The experimental determination of the nonlinear frequency response, which is the linear extension of the linear FRF, can be categorized into two families, which are the open and close loop methods.

Open loop methods are the simplest methods that do not require any feedback to the input. Measuring the frequency response with such methods is point-wise, meaning that a single excitation frequency should be identified at each step in a certain frequency spectrum, keeping the excitation level fixed throughout the measurement. Example of such method is the stepped sine method (SSM) [142] which is the one used in the experimental validations in this work (see chapters 3, 5, and 6). The main procedure involves exciting the system at different excitation frequencies and constant forcing levels. At each excitation frequency, the time histories of the output signals are measured and post-processed to compute the amplitude and the phase angles frequency responses. Since the possible appearance of multi-harmonic response due to the nonlinearities, the frequency response should be measured for each harmonic separately. This can be performed through a homodyne detection [252] (or demodulation technique). Two main limitations of the SSM can be summarized as: i) the SSM is usually slow, especially for large transient states with very small damping. ii) SSM cannot identify the unstable responses since the basin of attraction near a bifurcation point shrinks, leading to a jump phenomenon to a stable periodic orbit [73].

Closed loop methods are introduced to achieve faster experiments and identify the unstable periodic orbits and the backbone curves. Examples of such method are the phase lock loop (PLL) [253], [254], control-based continuation (CBC) [255], and response-controlled stepped-sine testing (RCT) [256]. The common feature between those methods is that they use a control strategy through feedback to the input signal. For example, the PLL enables the measurements of the backbone curves by sweeping the excitation amplitude and prescribing the phase resonance condition, and the error between the measured and prescribed phase is feedbacked to an integral controller. In the same manner, the stable and unstable forced responses are obtained by sweeping the phase lag between the measured and the input signals, keeping the excitation amplitude constant.

1.7 Research aims and challenges

The main research idea is about designing piezoelectric shunt absorbers that exploit nonlinear features, in particular the saturation phenomenon, to enhance the vibration attenuation of the hydrofoils. In this context, there are two main aims of this research summarized as follows:

- Propose different design strategies of the nonlinear piezoelectric shunt absorbers that enable to exploit the nonlinear features efficiently to enhance the attenuation. Two types of nonlinearities will be realized, namely smooth nonlinearities (cubic and quadratic) and nonsmooth ones (realized with a diode). Theoretical analysis and a parametric study are performed to conclude a guideline for a practical implementation that includes the main advantages, constraints, and limitations.

- The second aim is to validate experimentally the designed absorber on a real hydrofoil structure, in a laboratory setup. The experimental validation includes experimental modal analysis of the electro-mechanical modal system, the design of the nonlinear shunt circuit, and nonlinear frequency response estimation.

- The saturation phenomenon represents the core idea of our proposed absorbers. This thesis aims to design electro-mechanical nonlinear absorbers with piezoelectric transduction that exploits this feature but in a passive or semi-passive methodology. Namely, instead of following the control strategies as in [147]–[151] that involved displacement or velocity feedbacks with active controllers. The main challenge in our design is to be able to sustain the passive feature of the shunt design, thanks to the piezoelectric ability of intrinsic sensing and actuating. Indeed, the necessary nonlinearities that should be introduced to the system will involve the electric quantities, such as the voltage across the piezoelectric patch. Although it is easier to be measured in practice, it can generate more complicated dynamics. Thus, we aim to obtain shunt circuits that are capable of sustaining high voltage and current limits and tuned to overcome different issues that can be a result of preserving the passive feature of the absorber.

1.8 Dissertation Overview

This dissertation is a collection of articles accepted/submitted to peer-reviewed journal articles. Each article represents a chapter on its own. An overview of the dissertation content is summarized as follows:

- Chapter 2 is devoted to presenting the theoretical model of a semi-passive nonlinear piezoelectric shunt absorber exhibiting a saturation phenomenon through a 2:1 internal resonance tuning. Two possible implementations of the quadratic nonlinearities are proposed, and the main governing equations for each case are presented and analyzed through an electro-mechanical modal expansion. An analytical and numerical analysis has been established to study the effect of the design parameters on the response. An antiresonance correction is also proposed to correct the saturation that is violated due to the complex dynamics suggested by the nonresonant quadratic terms. Such nonresonant terms appear as a consequence of the piezoelectric coupling which admit high value compared to the resonant terms in (1.2a,b) and thus breaking the symmetry of the typical response in Fig. 1.6. In the end, the absorber is numerically applied to a beam structure, and a guideline for the absorber design is then illustrated.

- Chapter 3 shows the experimental validation of the results suggested in chapter 2 by applying the absorber to damp the first vibration mode of a cantilever beam. The experimental measurement protocol and the experimental electro-mechanical modal analysis are illustrated. In addition, the design of the nonlinear shunt circuit is shown. The measured frequency response is compared with the numerical ones. The suggested antiresonance correction in chapter 2 is tested experimentally thanks to a locking property of the phase angle between the two mechanical and electrical oscillators. Thanks to the saturation phenomenon, shown in Fig. 1.6, higher attenuation is achieved compared to that of an optimized linear absorber but less efficient for broadband attenuation due to the existence of an additional peak near the primary resonance.

- Since the nonresonant quadratic terms lead to a symmetry breaking and lack of performance of the absorber, chapter 4 shows the analysis of a two degree of freedom system that considers quadratic and cubic nonlinearities using the normal form method. This method enables the appearance of the quadratic nonresonant terms as cubic terms in the normal form basis that perturbates the symmetrical behavior of the dynamics. The dynamics is analyzed analytically and numerically, and closed-form expressions of the backbone curves are presented. In addition, the relation between the free and forced solutions is presented, and the representation of the dynamics with 2 :1 internal resonance on the invariant manifolds is illustrated. Finally and most importantly, a saturation correction is presented by properly tuning the cubic nonlinearities to cancel the effects of the quadratic nonresonant terms.

- Chapter 5 uses the cubic tuning suggested in chapter 4 to estimate the cubic nonlinear gain to be added to the shunt circuit. This technique is tested experimentally on a hydrofoil structure to damp its first bending mode. Through this study, the experimental protocol is detailed in addition to the design of the nonlinear shunt circuit. The measured frequency response is compared with the numerical ones validating the proposed technique in preserving the saturation up to high excitation levels, and thus enhancing the attenuation.

- Chapter 6 illustrates the theoretical design of the nonlinear shunt absorber with a nonsmooth component. The nonsmooth component is set to be proportional to the superposition of the piezoelectric voltage and its absolute value function. The main idea is to utilize the nonsmooth gain to tune the electrical frequency. In addition, introducing a nonsmooth term can create even harmonics if it is not symmetric in the same way as quadratic nonlinearities. The idea is therefore to introduce in series with the piezoelectric, a semi-rectified voltage driven by its own voltage, and modulated by a gain to weight its effects. The nonsmooth component can be realized in practice in a passive manner using a diode or a transistor. Two possible tunings, namely 1:1 and 1:2 tunings between the electrical and the mechanical resonance frequencies, are considered, showing a similar behavior compared to a linear resonant shunt. The main advantage is the ability to set a much lower inductance required for the optimal tuning, and richer dynamics is observed including strong nonlinear coupling between the electrical and the mechanical modes through a 2:1 internal resonance associated with the 2:1 tuning case. We also present the experimental validation of the proposed absorber in which both tunings are considered. The shunt circuit is illustrated in which the nonsmooth component is realized with a half-wave rectifier circuit that includes a diode. The absorber is applied to damp the first twisting mode of the hydrofoil, and the experimental frequency response curves are shown to validate the numerical predictions.

Chapter 2

Theoretical modeling of the nonlinear shunt absorber with quadratic nonlinearity

Contenu

2.1 Article presentation

The present chapter solely constitutes of the text of the article entitled by ”A nonlinear piezoelectric shunt absorber with a 2:1 internal resonance: Theory” published in ”Mechanical system and system processing (MSSP)” journal. The article illustrates the theoretical analysis of a semi-passive nonlinear piezoelectric shunt absorber to attenuate the vibrations of an elastic structure under external excitation. The absorber consists of a resonant circuit with a nonlinear quadratic component intentionally added to activate the two-to-one (2:1) internal resonance. Such a particular type of internal resonance additionally requires tuning the electrical resonance frequency close to half of the mechanical frequency of the structure mode to be attenuated. The main feature that we aim to exploit is the resulting saturation phenomenon in which the mechanical displacement becomes independent of the excitation level, above a threshold forcing, leading to a high vibration reduction.

The main governing equations of the electro-mechanical system are obtained by truncating the displacement on the mode to be attenuated, leading to a two degrees of freedom system where the unknowns are the displacement and the charge in the piezoelectric electrode. Two design architectures regarding the nonlinear component were then studied. The first requires a nonlinearity proportional to the square of the charge in the piezoelectric electrode ($V_{\mathrm{nl}} = \beta Q^2$), while the other is designed such that the nonlinearity is proportional to the square of the voltage across the piezoelectric patch

($V_{\rm nl} = \beta V^2$). The two choices are examined by expanding the equations on an electro-mechanical basis characterizing the mechanical and the electrical behaviors. The expansion led to a two degree of freedom system exhibiting nonlinear coupling with two resonant quadratic terms (similar to that studied in Sec. 1.4.3) and four nonresonant terms. The nonresonant terms are unavoidable due to the piezoelectric coupling and the passive nature of the absorber.

The multiple scales method is then adopted to obtain a closed form expression by neglecting the effect of the nonresonant terms. The obtained expressions described the *appearance of an antiresonance that replaces the primary resonance of the excited mode associated with a saturation phenomenon.* In addition, the results suggested the energy transfer to the subharmonic of the electrical mode.

A parametric study is then established to study the effect of the design parameters, namely the electrical damping ratio ξ_e, the nonlinear gain β, and the tuning between the electrical and mechanical frequencies, on the performance. The results showed the attenuation is proportional to $k_i\beta/\xi_e$ where k_i is the electro-mechanical modal coupling factor of the i-th mode of the structure. Thus, for a constant piezoelectric coupling, the attenuation can be enhanced by increasing the nonlinear gain and setting a lower electrical damping ratio.

The physical system is solved numerically, showing a more complicated response and loss of saturation due to a shift of the antiresonance as the excitation increases. In addition, the response curve symmetry observed for the simplified system with the quadratic resonant terms is broken leading to a kind of softening behavior. This is due to the *influence of one of the nonresonant terms that admit high value.* Nevertheless, two features are preserved, the shifted antiresonance amplitude remains the same and the the phase between the electrical and the mechanical modes is locked at $3\pi/2$ at the antiresonance frequency.

The absorber is then numerically applied to a beam structure, and the results showed that choosing the nonlinearity to be proportional to the square of the voltage across the piezoelectric patch is more practical. Taking into account this choice and using the proposed antiresonance correction, the preserved saturation suggested a high vibration reduction, compared to the linear response. This is because the saturation feature suggests a displacement amplitude independent of the excitation level. In the end, a design guideline is illustrated to state the optimal selection of the design parameters.

2.2 A nonlinear piezoelectric shunt absorber with a 2:1 internal resonance: Theory

Mechanical Systems and Signal Processing 170 (2022) 108768

Contents lists available at ScienceDirect

Mechanical Systems and Signal Processing

journal homepage: www.elsevier.com/locate/ymssp

A nonlinear piezoelectric shunt absorber with a 2:1 internal resonance: Theory

Zein A. Shami [a,*], Christophe Giraud-Audine [b], Olivier Thomas [a]

[a] Arts et Metiers Institute of Technology, LISPEN, HESAM Université, F-59000 Lille, France
[b] Arts et Metiers Institute of Technology, L2EP, HESAM Université, University Lille, Centrale Lille, HEI, F-59000 Lille, France

ARTICLE INFO

Communicated by J.E. Mottershead

Keywords:
Piezoelectric shunt circuit
2:1 internal resonance
Energy transfer
Nonlinear oscillations

ABSTRACT

In this paper, a semi-passive nonlinear piezoelectric shunt absorber is presented, aiming at attenuating the vibration of a resonant elastic structure under external excitation. This is done by connecting the elastic structure to a nonlinear shunt circuit via a piezoelectric patch. The nonlinear shunt circuit consists of resonant circuit that includes a quadratic non-linearity. A particular tuning of the natural frequency of the shunt enables to create a two to one internal resonance. This generates a strong coupling between the mechanical mode and the electrical mode, leading to replace the mechanical resonance with a nonlinear antiresonance associated with an amplitude saturation, thus leading to an efficient vibration reduction. In this paper, we first propose a theoretical model that is expanded onto a suitable electromechanical modal basis and reduced to the two modes of interest, nonlinearly coupled by quadratic terms. Then, analytical solutions are obtained by the multiple scale method and compared to a reference numerical solutions stemming from the harmonic balance method. This enables to investigate the performance of the system in term of vibration absorption as well as giving design rules to tune the nonlinear shunt and to choose the free parameters of the system.

1. Introduction

Vibration reduction is an important research field in many engineering applications, especially in the industrial machine design and in the sectors where lightweight structures can be used. One of the efficient strategies that took a wide range of interest the past 20 years is the electrical shunt damping family of techniques, due to its efficient vibration attenuation properties and to its ease of set and control. It consists in using an electromechanical transducer to convert the vibratory energy of the host structure into electrical energy in a dedicated electronic circuit, designed to dissipate it and/or to counteract the structure's vibrations. Depending on the physics of the transducer, piezoelectric or electromagnetic, shunts have been proposed in the pioneering works [1,2] and have been addressed in a huge number of contribution since (see [3,4] and reference therein). Contrary to active control for which independent sensors and actuator are connected in closed loop, the shunt principle consists in using a single transducer, that serves as sensor and actuator at the same time when connected to a suitable electronic circuit. In most shunt architectures, the system is unconditionally stable, contrary to active control strategies.

A large majority of shunts are linear, the simplest architecture being the electromechanical analogs of mechanical dynamical dampers such as Frahm (also called dynamic vibration absorber, DVA) or Lanchester dampers [5,6], also called respectively resonant and resistive shunts [7]. In the case of a piezoelectric transducer, equivalent to a capacitor C, the resonant shunt consists in using a

---

* Corresponding author.

E-mail addresses: zein_alabidin.shami@ensam.eu (Z.A. Shami), christophe.giraud-audine@ensam.eu (C. Giraud-Audine), olivier.thomas@ensam.eu (O. Thomas).

https://doi.org/10.1016/j.ymssp.2021.108768
Received 6 April 2021; Received in revised form 25 November 2021; Accepted 19 December 2021

simple inductor L as electronic circuit (and eventually an additional resistor R) to obtain a resonant RC (RLC) circuit coupled to a given mode of the primary mechanical structure [7,8]. More complex architectures can include a negative impedance to improve the performances [9] or be based on periodic piezoelectric transducers architectures for multimode damping [10].

However, it might be interesting to benefit from special dynamical phenomenon related to nonlinearities, examples of which are given in the recent reviews [11,12]. In the field of nonlinear absorbers, several families of strategies have been proposed in the past, firstly using mechanical devices and then being sometimes transposed to electromechanical analogs. The first family of absorbers, currently known as "nonlinear energy sinks" (NES) and using the so-called principle of "targeted energy transfer", was originally proposed in 2001 [13]. In the original concept, it consisted in attaching to a primary linear structure an essentially nonlinear oscillator into which the vibratory energy is transferred and localized. Because of the essentially nonlinear properties of the absorber, its free oscillation frequency strongly depends on the amplitude of the motion and there is always an amplitude for which the two oscillators lock in frequency, leading to an irreversible energy transfer (precisely through a one to one internal resonance). Since then, a huge amount of works emerged (more than one hundred selected publication are mentioned in the recent review [14]). We cite here some of them, relevant to us because they explain the design rules and propose several types of nonlinearities: [15] for cubic spring smooth stiffness, [16] for polynomial magnetic stiffness, [17] for a bistable stiffness and [18] for vibro-impact nonlinearities. The extension of the mechanical NES to piezoelectric devices has been theoretically proposed in [19] and recently realized, for the first time, with an analog circuitry (using multipliers) in [20]. It was also recently proposed in [21] in an active control philosophy, using force feedback.

A second family is the one of the so-called "nonlinear tuned vibration absorbers" (NLTVA), introduced in [22], that are a generalization of the classical DVA adapted for primary structures which have nonlinearities. Indeed, those nonlinearities, in most cases, lead to a dependence of the characteristic frequencies (free oscillations, resonance, antiresonance…) upon the amplitude of the motion. Consequently, a DVA, which has to be tuned to a particular fixed frequency, will correctly work on a limited range of amplitude. In contrary, the NLTVA is designed to present nonlinearities similar to those of the primary system. It is then naturally able to adapt itself to the dynamics of the primary structure for a large amplitude range. Since the pioneering work [22], the principle has been investigated in several studies using mechanical absorbers (see [23] and reference therein). The extension of NLTVA to piezoelectric shunts has been theoretically proposed in [24] and experimentally demonstrated in [25] with passive only electronic components and in [26] with a digital signal processor connected to the piezoelectric patches by analog electronic interfaces made of operational amplifiers.

The third family of nonlinear absorbers is composed of the synchronized switch damping (SSD) strategies. They consist in switching the electromechanical transducer on two distinct shunt impedances, synchronously with the oscillations of the host structure. This idea was initially proposed in [27,28] for piezoelectric transduction and developed in numerous contributions since then (see [29] for a recent review). Those SSD techniques are adaptive, intrinsically stable, require low power but their effect can be viewed as a resonance peak reduction, proportional to the excitation amplitude, similarly to traditional resistive or resonant shunts, with higher performance for one degree of freedom host structure [30].

The fourth family of nonlinear absorbers is based on the use of internal resonances. In a nonlinear system, if the ratio of two modal frequencies ω_i and ω_j is a rational number, namely $q\omega_i \simeq p\omega_j$ with $p, q \in \mathbb{N}^*$, a strong coupling between the two corresponding modes can occur, leading to particular exchanges of energy between the modes. This is called a p:q internal resonance and (ω_i, ω_j) can be the (linear) natural frequencies of the modes as well as there nonlinear extension (the frequencies of the nonlinear modes, that depend on the amplitude of the motion). On the first case, the internal resonance is observed at low amplitude and is often a consequence of a particular geometry, obtained with symmetries (1:1 internal resonance are encountered in beams/strings of symmetric cross section [31], in circular/square plates [32,33], in cylindrical shells [34] and spherical caps [35]) or by intentional tuning, in musical instruments (1:2, 1:2:4 and 1:2:2:4:4:8 internal resonances are encountered in gongs and steel-pans [36,37]) or in micro-systems applications [38–40]. In the second case of an internal resonance with the nonlinear free oscillation frequencies, the coupling appear at larger amplitude, when the change of frequencies due to the amplitude of the motion is compatible with the frequency relationship (see e.g. [41,42]).

When two modes of a system with quadratic nonlinearities fulfills a 1:2 internal resonance ($\omega_2 \simeq 2\omega_1$), the modal coupling leads to energy exchanges that occur at different frequencies (if the energy is injected to the second mode resonance near ω_2, it is transferred to the first mode at half the driving frequency. On the contrary if the first mode is resonantly driven near ω_1, the energy is transferred to the second mode at twice the driving frequency, near $\omega_2 \simeq 2\omega_1$. To signify the energy transfer, those two cases a sometimes called 2:1 and 1:2 internal resonances, respectively) and that leads to a significant reduction of the amplitude of the driven mode. Moreover, a saturation phenomenon is theoretically predicted in the first case, for which the amplitude of the driven mode becomes independent of the forcing amplitude above a threshold, whereas in the second case, a quasi-periodic regime is obtained at resonance [43]. This leads to the idea of intentionally designing a resonant absorber with quadratic nonlinearities tuned to half the frequency of one mode of the primary structure, to beneficiate of the saturation phenomenon. In mechanical systems, this leads to the concept of autoparametric vibration absorbers, firstly proposed in [44] and addressed in many contributions since then (see [45,46] and references therein). The use of a 2:1 internal resonance to design an electromechanical control system has been proposed in many works. A first family of works proposes the vibration reduction of an elastic beam by the active control of the rotation of a direct current (DC) motor (see [47,48] in which the controller is an analog electronic circuit made of multipliers). Then, this technique has been extended to piezoelectric actuators in [49] with also an analog circuit with multipliers. Then, the same concept has been applied with a real time digital controller to several structures (a beam and a truss in [50] and a triangular panel in [51]), with design guidelines exposed in [52]. The same authors also tried a 1:2:4 internal resonance in [53].

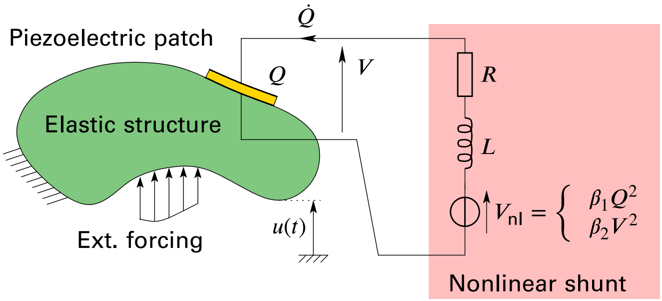

Fig. 1. Nonlinear shunt circuit.

All the above internal resonance based contributions can be related to active control. Indeed, they rely on the use of separate sensor and actuator linked with a controller (analog or digital), in which the nonlinearities and the additional degree of freedom are implemented and tuned. To our knowledge, no attempt on implementing a 2:1 internal resonance with a piezoelectric shunt has been published and this article aims at filling this gap. It is worth citing that other internal resonances have been tested: a 1:1 internal resonance in [54] as well as in the already considered NES contribution [20]. A 1:3 internal resonance between two modes of a PZT cantilever beam has been investigated in [55]. It is also worth citing [56,57], which propose strategies to implement electrical circuits analog to particular nonlinear oscillators, using multipliers.

In this paper, we propose a new semi-passive vibration attenuation approach based on a nonlinear piezoelectric shunt. Indeed, we test the simple idea of connecting, thanks to a piezoelectric transducer, a linear vibrating structure to a resonant electronic circuit in which a quadratic nonlinearity is intentionally introduced. We then add a new vibration mode in the system, that can be tuned to obtain a 2:1 internal resonance. We target creating a nonlinear antiresonance in place of the resonance of the mechanical mode as well as a saturation phenomenon. We also test two type of quadratic nonlinearities: one which is equivalent to a nonlinear capacitor, for which the electric charge is proportional to the square of the voltage, and a second one which is simply a voltage source proportional to the square of the voltage at the terminals of the piezoelectric element. In this paper, we restrict ourselves to the theory, the experimental proof of concept being postponed to an incoming article.

The outline of this paper follows. In Section 2, a model of the mechanical structure coupled to the nonlinear electric circuit is proposed, leading to a reduced model composed of two electromechanical modes coupled by quadratic terms. In Section 3, closed form approximated expressions for the amplitude and the phases of the two modes are obtained with the method of multiple scales (MMS) and the effect of several design parameters is studied. In Section 4, those results are compared to a reference solution obtained by a numerical continuation method to analyze the effect of the non-resonant nonlinear terms of the system. In Section 5, the results are applied to design a test case of a nonlinear piezoelectric absorber coupled to the first bending mode of a cantilever beam with piezoelectric patches. Some general guidelines are given in the last two sections.

2. Governing equations

We consider an arbitrary elastic structure subjected to a mechanical harmonic excitation and connected to a nonlinear resonant shunt circuit through a piezoelectric element, as shown in Fig. 1. If we discretize the displacement field of the elastic structure in a finite-element context, the equations of motions can be written [58]:

$$\boldsymbol{M}\ddot{\boldsymbol{u}} + \boldsymbol{K}\boldsymbol{u} + \boldsymbol{K}_c V = \boldsymbol{F}\cos\Omega t, \tag{1a}$$

$$C_{\rm p} V - Q - \boldsymbol{K}_c^{\rm T}\boldsymbol{u} = 0, \tag{1b}$$

$$V + L\ddot{Q} + R\dot{Q} + V_{\rm nl} = 0, \tag{1c}$$

where $\boldsymbol{u}(t)$ is the mechanical displacement vector of size $N \in \mathbb{N}$ at time t, $V(t)$ is the voltage at the terminals of the piezoelectric element, $Q(t)$ is the charge in one of its electrodes, $\boldsymbol{M}$ and $\boldsymbol{K}$ are the mass and stiffness matrices, of size $N \times N$, $\boldsymbol{K}_c$ is the electromechanical coupling vector, of size N, $\boldsymbol{F}$ is the external excitation vector, of size N, Ω is the driving frequency, $C_{\rm p}$ is the blocked capacitance of the piezoelectric patch, L and R are the inductance and the resistance in the shunt circuit and $V_{\rm nl}(t)$ represents the nonlinear voltage added to the shunt circuit.

We propose in this text to investigate the following two choices for $V_{\rm nl}$:

$$\begin{cases} \beta_1 Q^2, & \text{(a)} \\ \beta_2 V^2, & \text{(b)} \end{cases} \tag{2}$$

where β_i $(i = 1, 2)$ are constant parameters. The first case, Eq. (2)a, can be viewed as a nonlinear capacitor for which the inverse of its capacitance $C_{\rm nl}$ depends linearly on the amplitude of the charge: $V_{\rm nl} = Q/C_{\rm nl}$ with $C_{\rm nl} = 1/(\beta_1 Q)$. The unit of β_1 is $\mathrm{V/C^2}$. This choice is driven by the mechanical nonlinear absorbers, for which their stiffness is nonlinear. The second case, Eq. (2)b, is simply a voltage source that is proportional to the square of the voltage $V(t)$ at the terminals of the piezoelectric patch, since in practice this voltage is easily monitored. The units of β_2 is $\mathrm{V^{-1}}$. Those kind of nonlinearities can be obtained in practice by analog circuits with multipliers [20] or with a digital real time controller [26]. In the following, to simplify the mathematical expressions, β will be written with no index when not necessary.

2.1. Modal expansion

We consider the natural modes $(\breve{\omega}_i, \boldsymbol{\Phi}_i)$, $i = 1, \dots, N$, of the mechanical structure with the piezoelectric element in short circuit ($V = 0$), solutions of:

$$\left(\boldsymbol{K} - \breve{\omega}_i^2 \boldsymbol{M}\right) \boldsymbol{\Phi}_i = \boldsymbol{0}. \tag{3}$$

We expand the mechanical displacement vector on this modal basis, truncated to the ith mode only:

$$\boldsymbol{u}(t) = \boldsymbol{\Phi}_i q_i(t), \tag{4}$$

where $q_i(t)$ is the ith modal coordinate. This one mode assumption is valid as long as the other modes natural frequencies are far enough from $\breve{\omega}_i$ and from internal resonance relations with $\breve{\omega}_i$. The initial problem (1)a,b is then equivalent to, for all $i = 1, \dots, N$:

$$\ddot{q}_i + \breve{\omega}_i^2 q_i + \frac{\theta_i}{m_i} V = \frac{F_i}{m_i} \cos \Omega t, \tag{5a}$$

$$C_{\mathrm{p}i} V - Q - \theta_i q_i = 0 \tag{5b}$$

where $m_i = \boldsymbol{\Phi}_i^{\mathrm{T}} \boldsymbol{M} \boldsymbol{\Phi}_i$ is the ith modal mass, $F_i = \boldsymbol{\Phi}_i^{\mathrm{T}} \boldsymbol{F}$ is the ith modal forcing and $\theta_i = \boldsymbol{\Phi}_i^{\mathrm{T}} \boldsymbol{K}_c$ is the ith modal piezoelectric coupling coefficient. As explained in [59], $C_{\mathrm{p}i}$ is the effective capacitance of the piezoelectric patch in the vicinity of the ith resonance, which takes into account the static effect of all the other modes than the ith one. The above one degree of freedom model is then valid for a resonant motion of the system around its ith mode, namely by forcing around its natural frequency ($\Omega \simeq \omega_i$).

Using Eq. (5)b to eliminate the piezoelectric voltage V in Eqs. (5)a and (1)c, one obtains a problem in term of (q_i, Q) as unknowns:

$$\ddot{q}_i + 2\xi_i \hat{\omega}_i \dot{q}_i + \hat{\omega}_i^2 q_i + \frac{\theta_i}{m_i C_{\mathrm{p}i}} Q = \frac{F_i}{m_i} \cos \Omega t, \tag{6a}$$

$$\ddot{Q} + 2\xi_e \omega_e \dot{Q} + \omega_e^2 Q + \frac{\theta_i}{L C_{\mathrm{p}i}} q_i + \frac{V_{nl}}{L} = 0, \tag{6b}$$

where $\hat{\omega}_i^2 = \omega_i^2 + \theta_i^2/(C_{\mathrm{p}i} m_i)$ is an approximation (because of the one mode expansion) of the ith open circuit natural frequency. A mechanical modal viscous damping term of factor ξ_i has been added. In addition, the electrical natural frequency and damping factor are defined by:

$$\omega_e = \frac{1}{\sqrt{L C_{\mathrm{p}i}}}, \quad \xi_e = \frac{R}{2} \sqrt{\frac{C_{\mathrm{p}i}}{L}} \tag{7}$$

We also define the dimensionless electromechanical modal coupling factor (EMMCF) of the ith mode as:

$$k_i^2 = \frac{\hat{\omega}_i^2 - \breve{\omega}_i^2}{\hat{\omega}_i^2} = \frac{\theta_i^2}{\hat{\omega}_i^2 C_{\mathrm{p}i} m_i}. \tag{8}$$

Notice that its denominator is the open circuit natural frequency, following the IEEE standard [60] and because it simplifies the upcoming calculations. This is a different choice than in [58], where the short-circuit natural frequency was chosen, which gives a slightly different value of the EMMCF.

To simplify the writing of the governing equations (6)a,b, we define the following parameters:

$$\tau = \hat{\omega}_i t, \quad \bar{q}_i = \sqrt{m_i} q_i, \quad \bar{Q} = \sqrt{L} Q, \quad r_i = \frac{\omega_e}{\hat{\omega}_i}, \tag{9a}$$

$$\bar{F}_i = \frac{F_i}{\hat{\omega}_i^2 \sqrt{m_i}} \quad \bar{V}_{\mathrm{nl}} = \frac{V_{\mathrm{nl}}}{\hat{\omega}_i^2 \sqrt{L}} \quad \bar{\Omega} = \frac{\Omega}{\hat{\omega}_i} \tag{9b}$$

in order to obtain:

$$\ddot{\bar{q}}_i + 2\xi_i \dot{\bar{q}}_i + \bar{q}_i + k_i r_i \bar{Q} = \bar{F}_i \cos \bar{\Omega} \tau, \tag{10a}$$

$$\ddot{\bar{Q}} + 2\xi_e r_i \dot{\bar{Q}} + r_i^2 \bar{Q} + k_i r_i \bar{q}_i + \bar{V}_{\mathrm{nl}} = 0, \tag{10b}$$

where the derivatives in Eq. (10) are with respect to the dimensionless time τ. The time has been rescaled by the open circuit natural frequency $\hat{\omega}_i$ and we use a special scaling of the unknowns, so that $(\bar{q}_i, \bar{Q})$ share the same dimension ($\mathrm{m\,kg}^{1/2}$), to obtain the same coupling parameter $k_i r_i$ in both equations, with r_i the ratio of the electrical and mechanical natural frequencies. To prove that $(\bar{q}_i, \bar{Q})$ share the same dimension, remember that energy units can be equivalently J, N m or C V. Since the time τ is dimensionless, the units of $\bar{F}_i$ and $\bar{V}_{nl}$ are the same as $(\bar{q}_i, \bar{Q})$: $\mathrm{m\,kg}^{1/2}$.

2.2. Electro-mechanical modal expansion

The two degrees of freedom $(\bar{q}_i, \bar{Q})$ of Eq. (10)a,b are linearly coupled because of the piezoelectric coupling k_i. It is then possible to obtain a new system with diagonal linear part by expanding the unknowns onto the electromechanical modal basis $(\omega_k, \boldsymbol{\Psi}_k)$ of

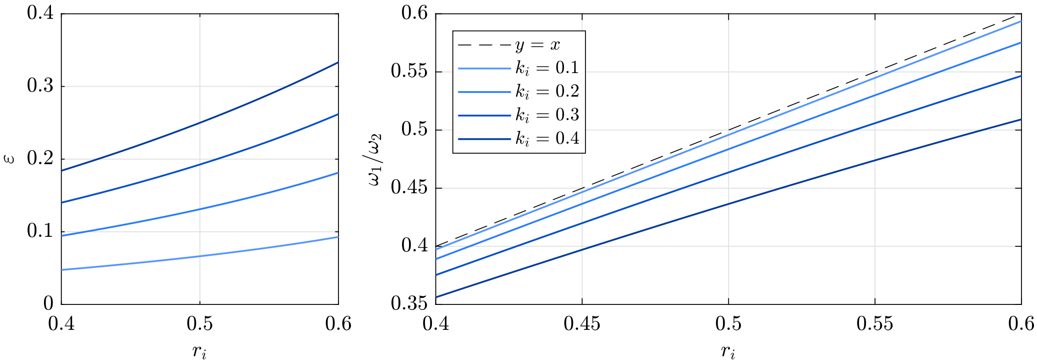

Fig. 2. (left) Mode shape parameter ε (from Eq. (14)) and (right) electromechanical natural frequency ratio ω_1/ω_2 (from Eqs. (12)) as a function of the frequency ratio r_i, for various values of the EMMCF k_i, as specified.

the problem, solution of:

$$\left(\bar{\boldsymbol{K}} - \omega_k^2 \boldsymbol{I}\right)\boldsymbol{\Psi}_k = \boldsymbol{0}, \quad k = 1, 2, \quad \bar{\boldsymbol{K}} = \begin{pmatrix} 1 & k_i r_i \\ k_i r_i & r_i^2 \end{pmatrix}. \tag{11}$$

Solving this eigenproblem, one obtains:

$$\omega_1^2 = \frac{1 + r_i^2 - \sqrt{\Delta}}{2}, \quad \omega_2^2 = \frac{1 + r_i^2 + \sqrt{\Delta}}{2} \tag{12}$$

with $\Delta = (1 - r_i^2)^2 + 4k_i^2 r_i^2$ and

$$\boldsymbol{\Psi}_1 = \begin{pmatrix} -\varepsilon \\ 1 \end{pmatrix}, \quad \boldsymbol{\Psi}_2 = \begin{pmatrix} 1 \\ \varepsilon \end{pmatrix}, \tag{13}$$

with

$$\varepsilon = \frac{2k_i r_i}{1 - r_i^2 + \sqrt{\Delta}}. \tag{14}$$

Then, following the modal expansion:

$$\begin{pmatrix} \bar{q}_i(\tau) \\ \bar{Q}(\tau) \end{pmatrix} = \sum_{k=1}^{2} \boldsymbol{\Psi}_k x_k(\tau), \tag{15}$$

one obtains the following change of variables:

$$\bar{q}_i(\tau) = -\varepsilon x_1(\tau) + x_2(\tau), \tag{16a}$$

$$\bar{Q}(\tau) = x_1(\tau) + \varepsilon x_2(\tau). \tag{16b}$$

Since the coupling factor k_i is small compared to 1, ε is also small compared to 1, which is illustrated in Fig. 2(left). For instance, for $r_i = 0.5$ and $k_i = 0.1$, $\varepsilon = 0.07$. Eq. (16) then shows that the dominant effect of x_1 and x_2 will be respectively on $\bar{Q}$ and $\bar{q}$. Based on that, $\boldsymbol{\Psi}_1$ and $\boldsymbol{\Psi}_2$ will be designated as the electrical and mechanical modes respectively.

As for the frequencies, ω_1 is close to the dimensionless electrical frequency $\omega_e/\hat{\omega}_i = r_i$ and ω_2 is close to the dimensionless mechanical frequency $\hat{\omega}_i/\hat{\omega}_i = 1$. In particular, if the EMMCF k_i is zero, there is no electromechanical coupling, the system (10)a,b is uncoupled and $\varepsilon = 0$, $\omega_1 = r_i$ and $\omega_2 = 1$. To quantify the effect of k_i on the electromechanical eigenmodes shift with respect to purely electrical and mechanical modes, Fig. 2(right) shows the natural frequency ratio ω_1/ω_2 as a function of r_i for various values of k_i. One can see that k_i imposes a detuning between the electromechanical natural frequency ratio ω_1/ω_2 with respect to r_i. In particular, to obtain a specified tuning ω_1/ω_2 (for instance 0.5 to obtain a 2:1 internal resonance), r_i has to be slightly overtuned ($r_i > \omega_1/\omega_2$).

Regarding the nonlinear voltage V_{nl}, considering Eq. (5)b, we write it in the following form:

$$V_{nl} = \beta(\kappa_1 Q + \kappa_2 q_i)^2, \tag{17}$$

where $(\kappa_1, \kappa_2) = (1, 0)$ to verify Eq. (2)a and $(\kappa_1, \kappa_2) = (1, \theta_i)/C_{pi}$ to verify Eq. (2)b.

By substituting Eq. (15) in Eqs. (10), multiplying by $\boldsymbol{\Psi}_k^T$, using the orthogonality properties of the electromechanical eigenmodes and the form of V_{nl} defined in Eq. (17), and by considering that the modal mass is $1 + \varepsilon^2 \simeq 1$ because $\varepsilon \ll 1$, the following can be written:

$$\ddot{x}_1 + 2\mu_1\dot{x}_1 + 2\mu_{12}\dot{x}_2 + \omega_1^2 x_1 + \Lambda_1 x_1^2 + \Lambda_2 x_1 x_2 + \Lambda_3 x_2^2 = f_1 \cos\bar{\Omega}\tau, \tag{18a}$$

$$\ddot{x}_2 + 2\mu_{12}\dot{x}_1 + 2\mu_2\dot{x}_2 + \omega_2^2 x_2 + \Lambda_4 x_1^2 + \Lambda_5 x_1 x_2 + \Lambda_6 x_2^2 = f_2 \cos \bar{\Omega}\tau. \tag{18b}$$

In the above system, the new (dimensionless) damping terms are defined as:

$$\begin{aligned} &\mu_1 = \xi_e r_i - \xi_i \varepsilon^2, \quad \mu_{12} = (\xi_e r_i - \xi_i)\varepsilon, \\ &\mu_2 = \xi_i + \xi_e r_i \varepsilon^2 \end{aligned} \tag{19}$$

and the forcing terms are:

$$f_1 = -\varepsilon \bar{F}_i, \quad f_2 = \bar{F}_i, \tag{20}$$

with units $\mathrm{m\,kg}^{1/2}$. The nonlinear coefficients of Eq. (18) write:

$$\begin{aligned} \Lambda_1 &= \lambda_1 - \lambda_2\varepsilon + \lambda_3\varepsilon^2 & \Lambda_4 &= \varepsilon\Lambda_1 \\ \Lambda_2 &= 2\lambda_1\varepsilon + \lambda_2(1-\varepsilon^2) - 2\lambda_3\varepsilon & \Lambda_5 &= \varepsilon\Lambda_2 \\ \Lambda_3 &= \lambda_1\varepsilon^2 + \lambda_2\varepsilon + \lambda_3 & \Lambda_6 &= \varepsilon\Lambda_3 \end{aligned} \tag{21}$$

where

$$\lambda_1 = \beta\kappa_1^2 r_i^3 \hat{\omega}_i C_{\mathrm{p}i}^{3/2}, \quad \lambda_2 = \frac{2\beta\kappa_1\kappa_2 r_i^2 C_{\mathrm{p}i}}{\sqrt{m_i}}, \tag{22a}$$

$$\lambda_3 = \frac{\beta\kappa_2^2 r_i \sqrt{C_{\mathrm{p}i}}}{m_i \hat{\omega}_i}. \tag{22b}$$

The common units of all those coefficients are $\mathrm{m}^{-1}\,\mathrm{kg}^{-1/2}$.

Then, for the choice of Eq. (2)a, $(\kappa_1, \kappa_2) = (1, 0)$ and the λ_i write:

$$\lambda_1 = \beta_1 r_i^3 \hat{\omega}_i C_{\mathrm{p}i}^{3/2}, \quad \lambda_2 = \lambda_3 = 0. \tag{23}$$

For the choice of Eq. (2)b, $(\kappa_1, \kappa_2) = (1, \theta_i)/C_{\mathrm{p}i}$ and:

$$(\lambda_1, \lambda_2, \lambda_3) = (r_i^3, 2r_i^2 k_i, r_i k_i^2)\lambda_0, \quad \lambda_0 = \frac{\beta_2 \hat{\omega}_i}{\sqrt{C_{\mathrm{p}i}}}. \tag{24}$$

3. Analytical results

3.1. Multiple scale solution

In this section, closed form expressions governing the response of the electromechanical modal system of Eqs. (18)a,b is given. This is done in order to study the performance of the vibration absorber and the effect of the design parameters, given later in this section, that could be controlled to enhance the vibration absorber performance.

We restrict ourselves to the case of a 2:1 internal resonance with $\omega_2 \simeq 2\omega_1$. This leads to neglect in Eqs. (18)a,b the effect of the non-resonant terms of coefficients Λ_1, Λ_3, Λ_5, and Λ_6 on the dynamics. This is motivated by the normal form theory, which proves that only the resonant terms (of coefficients Λ_2 and Λ_4) have an effect at first order (see [61,62]). We are also interested in the case for which the energy is injected mainly to the mechanical (2nd. mode) and transferred to the electrical (1st. mode) because of the nonlinear term. We then consider a pure forcing of the second (mechanical, high frequency) oscillator and neglect εf_1 with respect to f_2, since $\varepsilon \ll 1$. Finally, the damping coupling terms of coefficient μ_{12} are neglected. This is motivated because $\varepsilon \ll 1$ and also because the damping is considered small: $\mu_1, \mu_2 \ll 1$. In this case, it can be shown that the non diagonal terms have a negligible effect on the dynamics [63].

Consequently, for the analytical results, we consider the following system:

$$\ddot{x}_1 + 2\epsilon\mu_1\dot{x}_1 + \omega_1^2 x_1 + \epsilon\Lambda_2 x_1 x_2 = 0 \tag{25a}$$

$$\ddot{x}_2 + 2\epsilon\mu_2\dot{x}_2 + \omega_2^2 x_2 + \epsilon\Lambda_4 x_1^2 = f_2 \cos \bar{\Omega}\tau \tag{25b}$$

where a bookkeeping parameter ϵ has been added to scale the terms of the equation before applying the perturbation method. Following the multiple scales method, as fully described in [64], the two modal coordinates $x_1(\tau)$ and $x_2(\tau)$ are approximated at first order by:

$$x_1 = a_1 \cos\left(\frac{\bar{\Omega}}{2}\tau - \frac{\gamma_1 + \gamma_2}{2}\right), \tag{26a}$$

$$x_2 = a_2 \cos(\bar{\Omega}\tau - \gamma_2). \tag{26b}$$

where the amplitudes a_1 and a_2 and the phase angles γ_1 and γ_2 are the solutions of the following modulation equations:

$$a_1' = -\mu_1 a_1 - \frac{\Lambda_2 a_1 a_2}{4\omega_1}\sin\gamma_1, \tag{27a}$$

$$\frac{1}{2}(\gamma_1' + \gamma_2')a_1 = \frac{\sigma_1 + \sigma_2}{2}a_1 - \frac{\Lambda_2 a_1 a_2}{4\omega_1}\cos\gamma_1, \tag{27b}$$

$$a_2' = -\mu_2 a_2 + \frac{\Lambda_4 a_1^2}{4\omega_2}\sin\gamma_1 + \frac{f_2}{2\omega_2}\sin\gamma_2, \tag{27c}$$

$$\gamma_2' a_2 = \sigma_1 a_2 - \frac{\Lambda_4 a_1^2}{4\omega_2}\cos\gamma_1 + \frac{f_2}{2\omega_2}\cos\gamma_2, \tag{27d}$$

where $\circ' = \partial\circ/(\partial\epsilon\tau)$ is the derivative with respect to the slow time scale and

$$\epsilon\sigma_1 = \bar{\Omega} - \omega_2, \quad \epsilon\sigma_2 = \omega_2 - 2\omega_1, \tag{28}$$

are the two detuning parameters, which express respectively the nearness of the driving frequency to the mechanical resonance $\bar{\Omega} \simeq \omega_2$ and the detuning of the two natural frequency with respect to the exact internal resonance, which would be $\omega_2 = 2\omega_1$.

The response amplitudes a_1 and a_2 and the phase angles γ_1 and γ_2 are estimated using the fixed-point solution of the above dynamical system, i.e with $a_1' = a_2' = \gamma_1' = \gamma_2' = 0$. It leads to two kinds of solutions (see e.g. [64,65] for details):

- An *uncoupled (U) solution*, for which only the directly excited mode responds ($a_2 \neq 0, a_1 = 0$). This is the trivial linear solution, which writes:

$$a_2^U = \frac{f_2}{2\omega_2\sqrt{\sigma_1^2 + \mu_2^2}}, \quad \gamma_2^U = \arctan\frac{\mu_2}{-\sigma_1}, \tag{29a}$$

$$a_1^U = 0. \tag{29b}$$

- A *coupled (C) solutions*, for which the energy is transferred from the second (directly excited) oscillator to the first one thanks to the nonlinear terms. In this case, $a_1 \neq 0$ and $a_2 \neq 0$ are obtained by:

$$a_2^C = \frac{2\omega_1}{|\Lambda_2|}\sqrt{4\mu_1^2 + (\sigma_1 + \sigma_2)^2}, \tag{30a}$$

$$a_1^C = 2\sqrt{-\Gamma_1 \pm \sqrt{\frac{f_2^2}{4\Lambda_4^2} - \Gamma_2^2}}, \tag{30b}$$

$$\gamma_1^C = \arctan\frac{-2\mu_1}{\sigma_1 + \sigma_2}\,[2\pi], \tag{30c}$$

$$\gamma_2^C = \arctan\frac{2(\Lambda_4\mu_1\omega_1 a_1^2 + \Lambda_2\mu_2\omega_2 a_2^2)}{(\sigma_1 + \sigma_2)\Lambda_4\omega_1 a_1^2 - 2\sigma_1\Lambda_2\omega_2 a_2^2}\,[2\pi], \tag{30d}$$

where $[2\pi]$ means modulo 2π and with

$$\Gamma_1 = \frac{2\omega_1\omega_2}{\Lambda_2\Lambda_4}\left[2\mu_1\mu_2 - \sigma_1(\sigma_1 + \sigma_2)\right], \tag{31a}$$

$$\Gamma_2 = \frac{2\omega_1\omega_2}{\Lambda_2\Lambda_4}\left[2\sigma_1\mu_1 + \mu_2(\sigma_1 + \sigma_2)\right]. \tag{31b}$$

In all the above expressions, the phases γ_1 and γ_2 are strictly defined since their sine and cosine are given in the dynamical system (27). The formula including $\arctan(b/a)$ must be understood as the angle of the complex number $a+ib$, computed numerically with the function $\mathrm{atan2}(b, a)$ in most numerical languages.

3.2. Typical response

A stability analysis of the fixed points of the slow scale dynamical system (27) shows that there exists an instability region in the plane (σ_1, a_2) in which the U-solution is unstable [65]. Namely, it is the case as long as:

$$a_2 \geq \mathcal{L}(\sigma_1), \quad \mathcal{L}(\sigma_1) = \frac{2\omega_1}{|\Lambda_2|}\sqrt{4\mu_1^2 + (\sigma_1 + \sigma_2)^2}. \tag{32}$$

The analytical expression of $\mathcal{L}(\sigma_1)$ is exactly the same than $a_2^C(\sigma_1)$ which means that the boundary of the instability region coincides with the C-solution for the directly excited mode a_2.

Fig. 3 shows the typical frequency response of the system when driven at constant f_2 and sweeping around the second oscillator resonance $\bar{\Omega} \simeq \omega_2$ ($\sigma_1 \simeq 0$). At the crossing points between the amplitude of the U-solution and the instability region, two subcritical pitchfork bifurcations (points "PF" in Fig. 3) give rise to an unstable C-solution, which becomes stable after saddle–node bifurcations (points "SN"). This stable C-solution is characterized by a non-zero response of the low-frequency (electrical) mode, which oscillates at the subharmonic $\bar{\Omega}/2$ (see Eq. (26)a). In the frequency band between the two pitchfork bifurcations, the resonance of the driven (mechanical) mode is replaced by a low amplitude response, *which shows a minimum at exactly* $\bar{\Omega} = 2\omega_1$ (Point A of Fig. 3, $\sigma_1 = -\sigma_2$, see Eq. (30)a), that can be viewed as a *nonlinear antiresonance*. The phase γ_1 is exactly $3\pi/2\,[2\pi]$ at this point (see Eq. (30)c). The main idea of the article is to take advantage of this nonlinear antiresonance to reduce de vibrations of a given resonance.

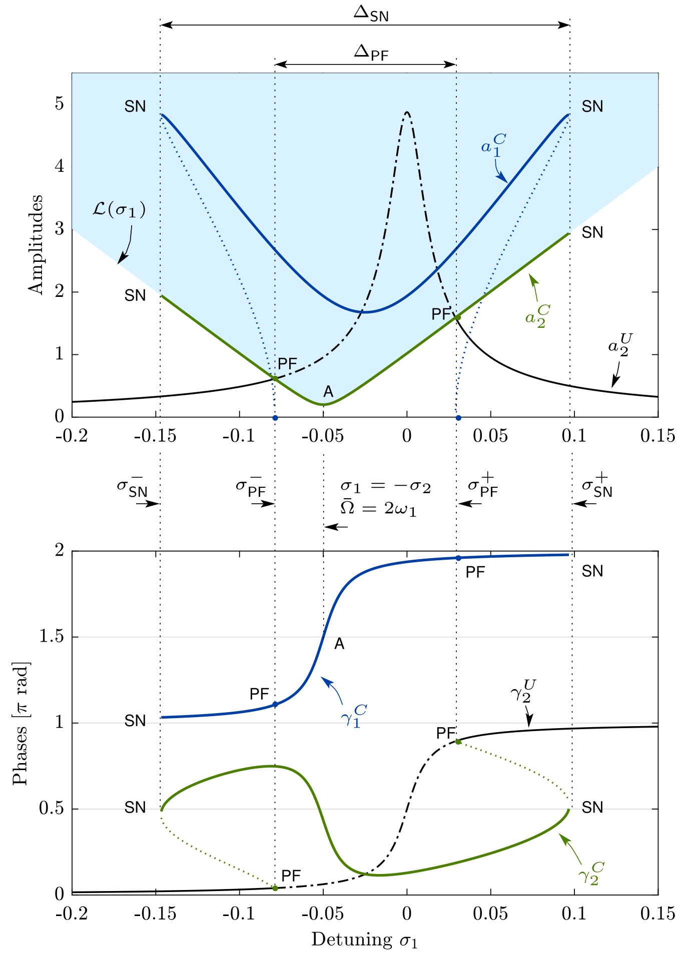

Fig. 3. Typical frequency response of Eqs. (25) obtained with the MS method: amplitude a_1, a_2 and phases γ_1, γ_2 as a function of the detuning σ_1 for a constant forcing f_2. The parameters are $\Lambda_2 = \Lambda_4 = 0.1$, $\mu_1 = 0.005$, $\mu_2 = 0.01$, $f_2 = 0.2$, $\sigma_2 = 0.05$. "PF"means pitchfork bifurcation; "SN"means saddle–node bifurcation; superscript U refers to the uncoupled solution (in black) whereas superscript C refers to the coupled solution (in blue for (a_1, γ_1) and in green for (a_2, γ_2)). The blue shaded area depicts the instability region for a_2^U. Dotted and dash-dotted lines depict unstable branches.

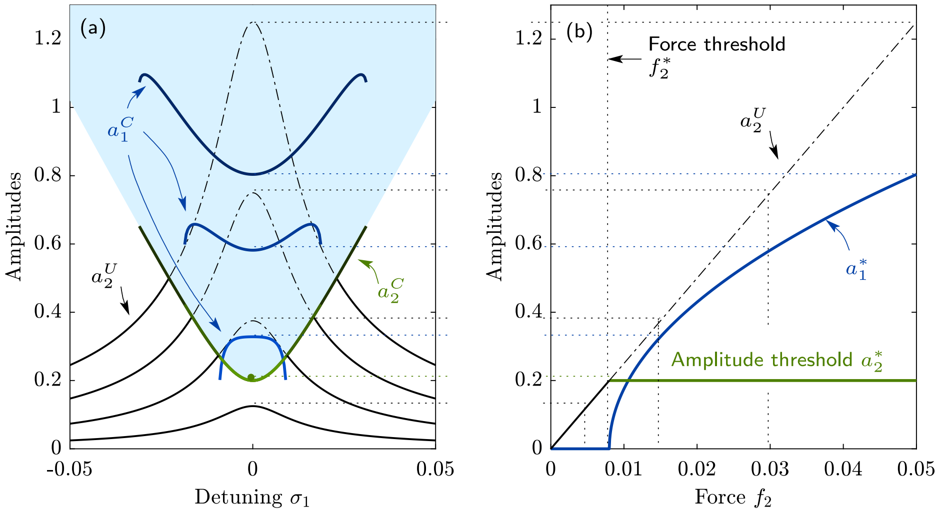

Fig. 4. Typical response of Eqs. (25) obtained with the MS method for a perfect tuning $\sigma_2 = 0$ ($\omega_2 = 2\omega_1$). (a) amplitudes a_1 and a_2 as a function of the detuning σ_1 for several values of the forcing f_2 ($f_2 \in \{0.005; 0.015; 0.03; 0.05\}$); (b) amplitudes a_1 and a_2 for a forcing at the antiresonance ($\sigma_1 = 0$, $\bar{\Omega} = \omega_2$, as a function of the forcing f_2. The numerical values are $\Lambda_2 = \Lambda_4 = 0.1$, $\mu_1 = 0.005$, $\mu_2 = 0.01$. Superscript U refers to the uncoupled solution (in black) whereas superscript C refers to the coupled solution (in blue for a_1 and in green for a_2). The blue shaded area depicts the instability region for a_2^U.

By tuning the electrical mode eigenfrequency exactly to half the one of the mechanical mode, $\omega_1 = \omega_2/2$ ($\sigma_2 = 0$), it is then possible to replace the linear resonance of the mechanical mode by the nonlinear antiresonance. Since the energy transfer to the electrical mode is nonlinear, the performances are dependent on the excitation level. This is illustrated in Fig. 4 in which several response curves are shown for increasing forcing levels f_2. For low values of f_2, the linear resonance (the U-solution) is below the instability region and no energy transfer occurs. For the perfect tuning, $\sigma_2 = 0$, the minimum value f_2^* of the force necessary to create the energy transfer is obtained by equating a_2 between Eqs. (29)a and (30)a with $\sigma_1 = \sigma_2 = 0$:

$$f_2^* = \frac{8\omega_1\omega_2\mu_1\mu_2}{|\Lambda_2|} = \frac{4\omega_2^2\mu_1\mu_2}{|\Lambda_2|}. \tag{33}$$

Above this threshold ($f_2 > f_2^*$), the coupled regime occurs and an interesting result is that the amplitude a_2^C of the driven mode is independent of the forcing level f_2 instead of being proportional to it, which is observed before the threshold. This leads to a *saturation phenomenon* for a_2^C, shown in Fig. 4(b), with the constant amplitude:

$$a_2^* = \frac{f_2^*}{2\omega_2\mu_2} = \frac{4\omega_1\mu_1}{|\Lambda_2|} = \frac{2\omega_2\mu_1}{|\Lambda_2|}, \tag{34}$$

equal to the one at the antiresonance.

On the contrary, the amplitude of the electrical mode increases with a square root dependence on the forcing amplitude at the antiresonance, also shown in Fig. 4(b). It can be written:

$$a_1^* = \sqrt{\frac{2}{|\Lambda_4|}(f_2 - f_2^*)}, \tag{35}$$

obtained by setting $\sigma_1 = \sigma_2 = 0$ in Eqs. (31) and (30)b.

Still in the special case of perfect tuning ($\sigma_2 = 0$), the values of the pitchfork bifurcation frequencies can be obtained by equating a_2 between Eqs. (29)a and (30)a with $\sigma_2 = 0 \Rightarrow \omega_1 = \omega_2/2$ (or equivalently by enforcing $a_1^C = 0$ in Eq. (30)b), as:

$$\sigma_{\text{PF}}^+ = \sqrt{\frac{\sqrt{(4\mu_1^2 - \mu_2^2)^2 + \dfrac{f_2^2\Lambda_2^2}{\omega_2^4}} - 4\mu_1^2 - \mu_2^2}{2}}, \tag{36a}$$

$$\sigma_{\text{PF}}^- = -\sigma_{\text{PF}}^+, \quad \Delta_{\text{PF}} = 2\sigma_{\text{PF}}^+. \tag{36b}$$

where Δ_{PF} characterizes the instability bandwidth (see Fig. 3). Moreover, the values of the saddle–node bifurcations frequencies are obtained by enforcing to zero the radicand of the inner square root of a_1^C in Eq. (30)b:

$$\sigma_{\text{SN}}^+ = \frac{f_2|\Lambda_2|}{\omega_2^2(2\mu_1 + \mu_2)}, \quad \sigma_{\text{SN}}^- = -\sigma_{\text{SN}}^+, \quad \Delta_{\text{SN}} = 2\sigma_{\text{SN}}^+, \tag{37}$$

where Δ_{SN} characterizes the full bandwidth of the response (see Fig. 3).

One idea could be to use Δ_{SN} and Δ_{PF} as design parameters: one could think of adjusting the shunt parameters μ_1 and Λ_2 to obtain a vibration reduction bandwidth Δ_{PF} as large as possible while minimizing the amplitude of the two lateral "wings" of the frequency response by decreasing Δ_{SN} as much as possible. However, it should not be forgotten that the response of the system is nonlinear and forcing amplitude dependent. In particular, Δ_{SN} and Δ_{PF} are increasing functions of the forcing f_2. Consequently, by looking at Fig. 4, it is clear that tailoring Δ_{PF} and Δ_{SN} is possible at a given forcing amplitude, but that the particular shape of the frequency response will by lost for higher forcing amplitudes.

3.3. Effect of the parameters

In order to propose guidelines for the design of the nonlinear shunt, this section addresses the effect of the parameters of the system: the detuning $\sigma_2 = \omega_2 - 2\omega_1$ (from now on, we drop the bookkeeping parameter ϵ in the equations, meaning that the small parameters μ_1, μ_2, Λ_2, Λ_4, σ_1, σ_2 are now considered with there nominal values, assumed small, to guarantee the validity of the multiple scale developments), the excitation level f_2, the damping parameters (μ_1, μ_2) and the coefficients of the quadratic terms (Λ_2, Λ_4). In all this section, we assume that $\omega_1 = 1$, with no loss of generality since one can rescale the time in Eqs. (25) and show that the topology of the response curves does not depend on ω_1. The effect of f_2 has been investigated in the previous section and we consider here the other parameters.

The effect of the detuning parameter σ_2 is to shift the antiresonance frequency ($\sigma_2 > 0$ (resp. $\sigma_2 < 0$) shifts it to the lower (resp. upper) frequencies) and to desymmetrize the shape of the frequency response. In particular, a perfect tuning ($\sigma_2 = 0$, $\omega_2 = 2\omega_1$) gives symmetrical curves with respect to the vertical axis $\sigma_1 = 0$ ($\bar{\Omega} = \omega_2$). This can be inferred by comparing Fig. 3 (obtained with $\sigma_2 = 0.05$) and Fig. 4(a) (with a perfect tuning, $\sigma_2 = 0$). In practice, a perfect tuning appears to be optimal since it guarantees the tuning of the antiresonance in place of the linear resonance. This case is solely investigated in the remaining of the section.

By observing Eqs. (32)–(37), one can conclude that Λ_2 and μ_1 have a crucial effect on the system's response, since they appear in all those equations. The first effect of (Λ_2, μ_1) is on the shape of the instability region boundary $\mathcal{L}$. Following Eq. (32), if $\mu_1 = 0$, $\mathcal{L} = 2\omega_1|\sigma_1|/|\Lambda_2|$ and thus reduces to a triangle bounded by straight lines of slope $\pm 2\omega_1/|\Lambda_2|$. Consequently, increasing Λ_2 decreases

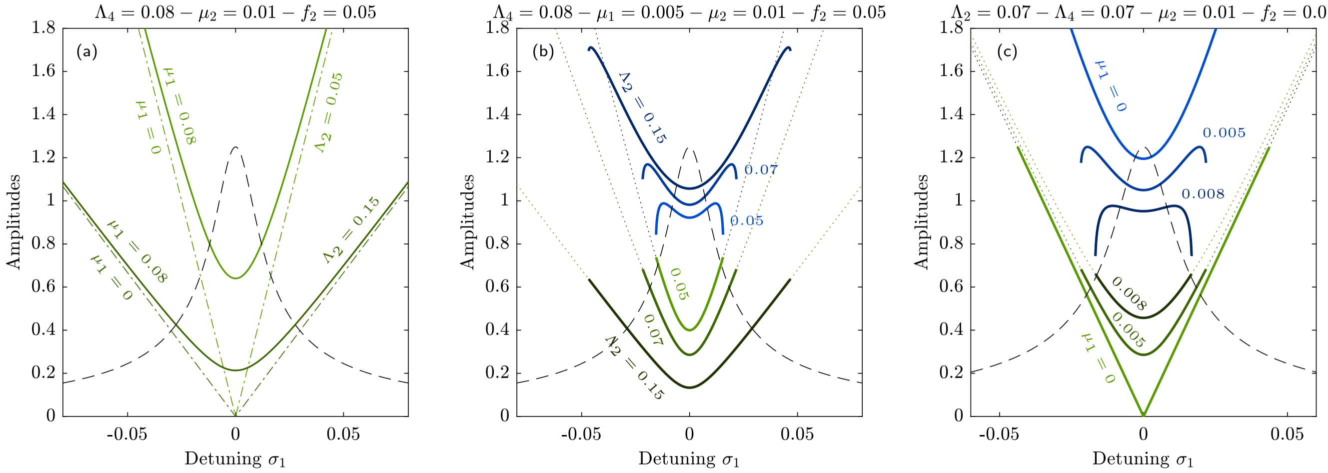

Fig. 5. Effect of variation of parameters Λ_2 and μ_1 on the system's frequency response, obtained with the MS method for a perfect tuning $\sigma_2 = 0$ ($\omega_2 = 2\omega_1$). (a) Effect of the variation of Λ_2, with $\mu_1 = 0$ and $\mu_1 \neq 0$, on the instability region $\mathcal{L}(\sigma_1)$; (b) Effect of the variation of Λ_2 on the response curves amplitudes (a_1, a_2); (c) Effect of the variation of μ_1 on the response curves amplitudes (a_1, a_2). The uncoupled solution a_2^U is in black and the coupled solutions (a_1^C, a_2^C) are respectively in blue and green.

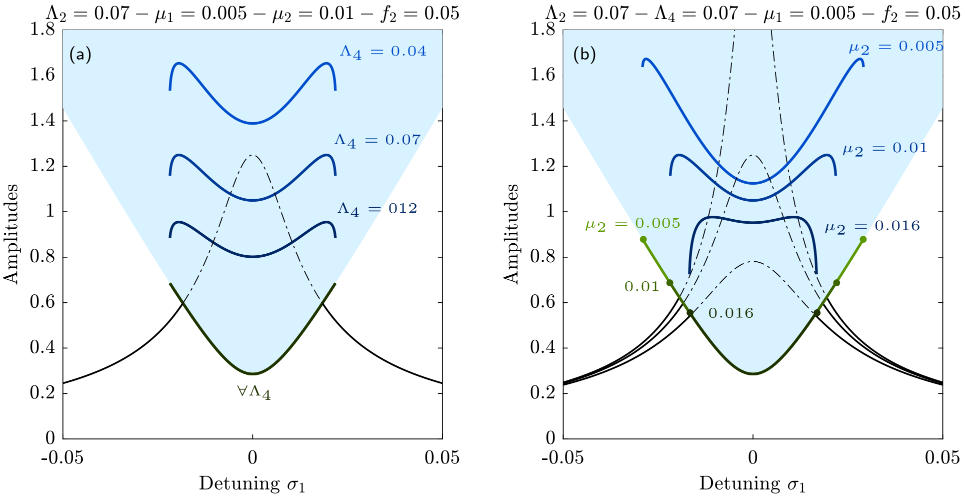

Fig. 6. Effect of variation of parameters Λ_4 and μ_2 on the system's frequency response, obtained with the MS method for a perfect tuning $\sigma_2 = 0$ ($\omega_2 = 2\omega_1$). (a) Effect of the variation of Λ_4 on the response curves amplitudes (a_1, a_2); (b) Effect of the variation of μ_2 on the response curves amplitudes (a_1, a_2). The uncoupled solution a_2^U is in black and the coupled solutions (a_1^C, a_2^C) are respectively in blue and green.

these slopes and thus widens the instability region, as illustrated in Fig. 5(a). The effect of increasing μ_1 from zero is to round the shape of the instability region at its lower end and thus to decrease its area. Since the amplitude a_2^C of the driven mode coincides with $\mathcal{L}$, the same conclusions can be drawn, as shown in Figs. 5(b, c). In particular, the parameter $|\Lambda_2|/\mu_1$ seems crucial: increasing it leads to reduce the threshold amplitude of the energy transfer (see Eqs. (33) and (34) and Fig. 5(a–c)). A zero value of (f_2^*, a_2^*) can even theoretically be obtained with a zero electrical damping ($\mu_1 = 0$). In addition, Figs. 5(b, c) illustrate the effect of (Λ_2, μ_1) on the amplitude a_1^C of the electrical mode: increasing Λ_2 and/or decreasing μ_1 increases a_1^C. As a conclusion, it is clear that increasing $|\Lambda_2|/\mu_1$ leads to improve the performances of the absorber.

On the contrary, Λ_4 appears only in the amplitude a_1 of the electrical mode. Consequently, increasing it leads to decrease a_1^C and thus to improve the absorber performance, as shown in Fig. 6(a). Finally, Fig. 6(b) illustrates the effect of the mechanical mode damping μ_2 on the system's response. Decreasing μ_2 leads to increase the amplitude of the linear resonance, but has no effect on the instability boundary $\mathcal{L}$ and the saturation amplitude a_2^*. Consequently, the less the mechanical mode is damped, the less the forcing threshold f_2^* is and the better performance the absorber has.

4. Validity of the analytical solution and design of the nonlinear absorber

In Section 3, an analytical solution of the dynamical system (18) is investigated, by canceling the non diagonal damping terms and the non-resonant terms (of coefficients Λ_i, $i = 1, 3, 5, 6$). This section is devoted to the validity of this analytical solution, by comparing it to reference numerical simulations. They are obtained with the software Manlab, that enables the numerical continuation of

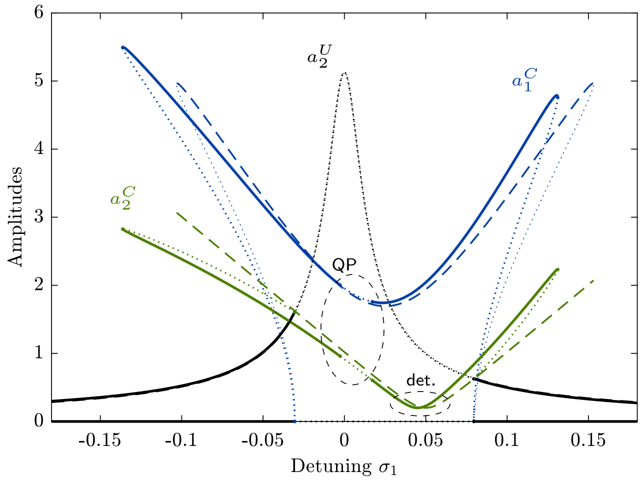

Fig. 7. Frequency response of Eqs. (25): comparison of the analytical MS solution (thin '- -') to a reference Manlab solution (thick '—') of the same system. Amplitude a_1, a_2 the detuning σ_1. The parameters are $\Lambda_2 = \Lambda_4 = 0.1$, $\mu_1 = 0.005$, $\mu_2 = 0.01$, $f_2 = 0.2$, $\sigma_2 = -0.05$. "QP" means quasi-periodic response; "det." means "detuning". The uncoupled solution a_2^U is in black and the coupled solutions (a_1^C, a_2^C) are respectively in blue and green. $H = 20$ harmonics have been considered for the Manlab HBM computations.

periodic solutions of the dynamical system. It is based on the harmonic balance method (HBM) and the asymptotic numerical method [66,67], with a special strategy to compute the branching points and the stability of the branches [42,68].

4.1. Validity of the analytical solution without the non-resonant terms

We first investigate the validity of the analytical MS solution of Eqs. (27) of the simplified dynamical system (25) in 2:1 internal resonance ($\omega_2 \simeq 2\omega_1$), by comparing it to the Manlab solution. Fig. 7 shows its frequency response with typical parameters. We can observe that the reference Manlab solution is more asymmetrical with respect to the MS solution. One interesting effect is that the frequency of the nonlinear antiresonance is slightly shifted to the low frequencies and does not appear exactly at $\bar{\Omega} = 2\omega_1$ ($\sigma_1 = -\sigma_2$). By changing the tuning of the two modes, it has been verified that this shift always appears toward the low frequencies, for any positive or negative small detuning σ_2, and that it increases with the excitation level f_2. It has also been numerically verified that the phase of the electrical mode is precisely $\gamma_1^C = 3\pi/2\,[2\pi]$ at the numerical antiresonance frequency, as predicted by the MS solution.

Another feature is the appearance of a small frequency band in which the periodic response is unstable due to Neimark–Sacker bifurcations, which leads to a quasi-periodic response. This quasi-periodic response does not appear for any values of the parameters and tends to be more prominent for large values of f_2. These Neimark–Sacker bifurcations can be predicted with the MS solution, but no close form expression is at hand since they depend on the solution of an order four polynomial [69]. We consequently decided not to show them on the MS solution plots.

4.2. Effect of non-resonant terms

We investigate in this section the effect of the non-resonant terms on the dynamics. To estimate their order of magnitude in a practical piezoelectric shunt example, we consider, as explained in Section 2, that the coupling factor k_i, and thus ε, are small compared to 1. Then, for the case of $V_{\text{nl}} = \beta_1 Q^2$ (Eqs. (2)a, (23)), one has with Eqs. (21):

$$\Lambda_1 = \lambda_1, \quad \Lambda_2 = 2\varepsilon\lambda_1, \quad \Lambda_4 = \varepsilon\lambda_1 \tag{38}$$

$$\Lambda_3 = \varepsilon^2\lambda_1, \quad \Lambda_5 = 2\varepsilon^2\lambda_1, \quad \Lambda_6 = \varepsilon^3\lambda_1. \tag{39}$$

In the other case of $V_{\text{nl}} = \beta_2 V^2$ (Eqs. (2)b, (24)), keeping the leading order in ε in Eqs. (21) conducts to $\Lambda_k \simeq \lambda_k$ for all $k = 1, 2, 3$. Then, to set the ideas, we consider numerical values: $r_i = 0.5$ and $k_i = 0.1$ leads to $\varepsilon = 0.07$ (Fig. 2). One then obtains:

$$\Lambda_1 = 0.13\lambda_0, \quad \Lambda_2 = 0.05\lambda_0, \quad \Lambda_4 = 0.009\lambda_0 \tag{40}$$

$$\Lambda_3 = 0.005\lambda_0, \quad \Lambda_5 = 0.004\lambda_0, \quad \Lambda_6 = 0.0004\lambda_0. \tag{41}$$

In both cases for the choice of V_{nl}, Λ_1 is larger than the two coefficients (Λ_2, Λ_4) of the resonant terms, with the other coefficient $(\Lambda_3, \Lambda_5, \Lambda_6)$ negligible. It is then assumed in the remaining of the section that Λ_1 is the dominant non-resonant term and we analyze its effect on the frequency response of the system, with $\Lambda_3 = \Lambda_5 = \Lambda_6 = 0$. We thus consider Eqs. (25) with an additional nonlinear term $\Lambda_1 x_1^2$ in Eq. (25)a.

As a first step, the effect of Λ_1 on the response is investigated in Fig. 8 for the perfect tuning case ($\sigma_2 = 0 \Leftrightarrow \omega_2 = 2\omega_1$). One can see that increasing Λ_1 from zero to positive values of the order of magnitude of the resonant term coefficients Λ_2 and Λ_4 leads

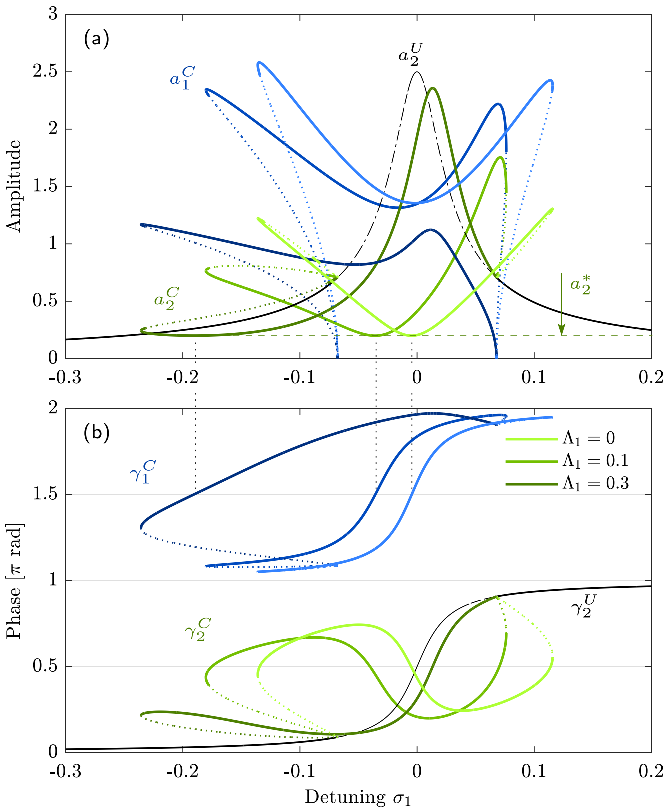

Fig. 8. Effect of variation of parameter Λ_1 on the frequency response of the complete system (18), obtained with Manlab, for a perfect tuning $\sigma_2 = 0$ ($\omega_2 = 2\omega_1$). The parameters are $\Lambda_1 \in \{0; 0.2; 0.3\}$, $\Lambda_2 = \Lambda_4 = 0.1$, $\Lambda_3 = \Lambda_5 = \Lambda_6 = 0$, $\mu_1 = 0.005$, $\mu_2 = 0.01$, $f_2 = 0.1$. The uncoupled solution (a_2^U, γ_2^U) is in black and the coupled solutions (a_1^C, γ_1^C), (a_2^C, γ_2^C) are respectively in blue and green, with a darker color as Λ_1 increases.

to a qualitative change of the shape of the response curves. Their symmetry with respect to the axis $\sigma_1 = 0$ is lost, with a kind of overall "bending" of the curves to the low frequencies and with a decreasing of the amplitude of a_1^C (blue curves). This bending seems qualitatively analogous to a softening behavior of the resonance of a Duffing oscillator. The main result is that *increasing* Λ_1 *shifts the antiresonance frequency of* a_2^C *to the low frequencies* (see the minimum of the green curves in Fig. 8(a)). It then shows that the simple tuning property of the simplified model (see Section 3.2, the antiresonance depends only on the eigenmode tuning since it is obtained exactly at $\sigma_1 = -\sigma_2$ ($\bar{\Omega} = 2\omega_1$)) is lost with a non-zero Λ_1. One can also observe that the asymmetry of the response curves due to high values of Λ_1 also increases the amplitude of the high frequency peak of the mechanical mode response a_2^C.

However, two interesting properties are kept with a non-zero Λ_1. First, the amplitude of the antiresonance seems independent of Λ_1 and thus keeps the analytical value a_2^* of Eq. (34). Secondly, the property of phase locking of $\gamma_1^C = 3\pi/2[2\pi]$ at the antiresonance seems perfectly kept. Those results have only been verified numerically by observing the minimum of a_2^C and the crossing of $\gamma_1^C = f(\sigma_1)$ curve with the horizontal $3\pi/2$ line, as seen in Fig. 8.

We now investigate the effect on the frequency response of the other parameters of the system, namely f_2, σ_2 and μ_1, with a nonzero value of the non-resonant term coefficient, chosen equal to the ones of the resonant terms ($\Lambda_1 = \Lambda_2 = \Lambda_4 = 0.1$). Figs. 9(a, b) show that increasing f_2 or decreasing μ_1 naturally increase the amplitude of the responses but also amplifies the negative effect of a non-zero Λ_1 described above, by increases the shift the antiresonance to the low frequencies. However, as seen in Fig. 9(c), it is still possible to adjust the value of the antiresonance frequency by changing the eigenmode detuning σ_2: decreasing (increasing) σ_2 from zero shifts it to the high-frequencies (low-frequencies). Moreover, one can observe in the insets of Figs. 9(a, c) that the antiresonance amplitude is still independent of f_2 and σ_2 and equal to a_2^*. Another remark is that a quasi-periodic response can also be observed for low (negative) values of σ_2, a feature already observed with $\Lambda_1 = 0$ in Fig. 7. Moreover, one can observe in Fig. 9(b) that the amplitude of a_1^C at the antiresonance seems independent of μ_1. This effect is here a particular case, a consequence of the choice of the parameters, different from the one used in Fig. 5, and not of the presence of Λ_1.

4.3. Correction of the antiresonance detuning

As seen in the previous sections and contrary to what predicted by the MS solution of the simplified model, the frequency of the antiresonance of a_2^C is clearly affected by the parameters and this effect is amplified by a non-zero value of the non-resonant term coefficient Λ_1. On the contrary, the amplitude of this antiresonance keeps its analytical value a_2^* (Eq. (34)), independent of the forcing f_2. In the purpose of the vibration control of the mechanical mode, it then seems possible to keep the saturation phenomenon

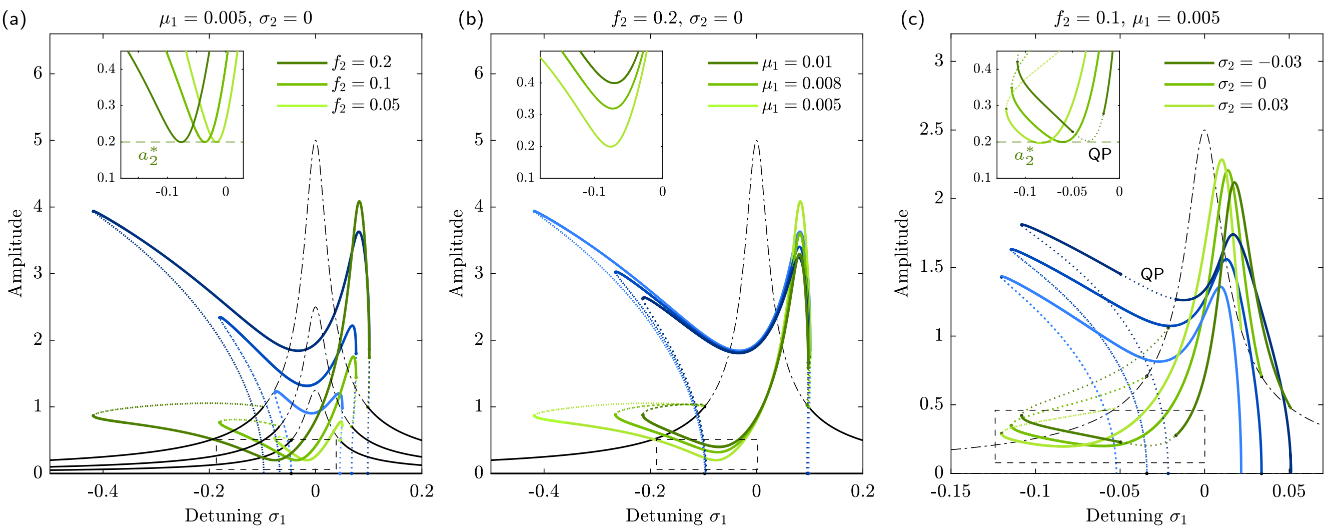

Fig. 9. Effect of variation of parameters f_2, σ_2 and μ_1 on the frequency response of the complete system (18), obtained with Manlab. (a) Variation of forcing f_2. (b) Variation of the damping μ_1. (c) Variation of the detuning σ_2 ($\omega_2 = 2\omega_1 + \sigma_2$). The common parameters are $\Lambda_1 = \Lambda_2 = \Lambda_4 = 0.1$, $\Lambda_3 = \Lambda_5 = \Lambda_6 = 0$, $\mu_2 = 0.01$, the others are specified on the plots. The uncoupled solution (a_2^U, γ_2^U) is in black and the coupled solutions (a_1^C, γ_1^C), (a_2^C, γ_2^C) are respectively in blue and green, with a darker color as the varied parameter increases. The insets show a zoom of the nonlinear antiresonance region. "QP" means quasi-periodic response.

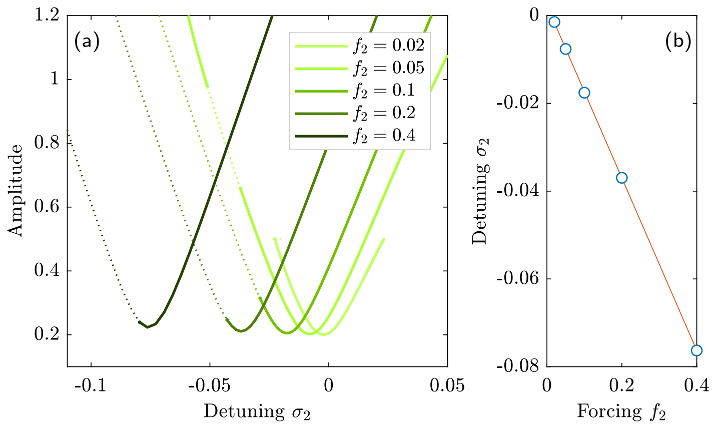

Fig. 10. (a) Amplitude of a_2^C at $\sigma_1 = 0$ as a function of the detuning σ_2 ($\omega_2 = 2\omega_1 + \sigma_2$), for several values of the forcing f_2 ($f_2 \in \{0.02; 0.05; 0.1; 0.2; 0.4\}$), obtained with Manlab with the complete system (18); (b) 'o': values of σ_2 for each minima of the curves of Fig. (a), as a function of f_2, and '—': linear fit. The parameters are: $\Lambda_1 = \Lambda_2 = \Lambda_4 = 0.1$, $\Lambda_3 = \Lambda_5 = \Lambda_6 = 0$, $\mu_1 = 0.005$, $\mu_2 = 0.01$.

of a_2^C at a fixed frequency, by adjusting the eigenmode detuning σ_2 ($\omega_2 = 2\omega_1 + \sigma_2$) as a function of f_2, in order to counterbalance the detuning of the antiresonance as a function of f_2.

To investigate this idea, Fig. 10(a) shows the amplitude a_2^C at the mechanical mode resonance $\sigma_1 = 0$ ($\bar{\Omega} = \omega_1$) as a function of the eigenmode detuning σ_2, for several values of the forcing f_2, all the other parameters being chosen constant. This was numerically obtained with Manlab, by performing a continuation in σ_2, with $\sigma_1 = 0$ and f_2 constant. This plot shows that the $a_2^C = f(\sigma_2)$ curves show a minimum, which corresponds to the value σ_2^* of σ_2 necessary to place the antiresonance of a_2^C exactly at the resonance $\sigma_1 = 0 \Leftrightarrow \bar{\Omega} = \omega_2$. Then, Fig. 10(b) shows those optimal values σ_2^* as a function of the forcing f_2. A linear fit is also plotted, showing that a linear relation

$$\sigma_2^* = -\alpha f_2, \quad \alpha \in \mathbb{R}^+, \tag{42}$$

is at hand. The slope is negative, in agreement with that can be observed in Figs. 9(a, c), in which one has to reduce the detuning σ_2 to shift the antiresonance to the high frequencies to counterbalance an increase of f_2.

The $\sigma_2^* = -\alpha f_2$ curve of Fig. 11(b) has been tested, to verify that the antiresonance of a_2^C can be placed at the resonance frequency ω_2 regardless of the excitation level. Several resonance curves for different excitation levels f_2 are shown in Fig. 11(a), with, for each response, the value of the detuning σ_2 adjusted to verify Eq. (42). One can observe in the inset that the antiresonance frequency is perfectly kept at $\sigma_1 = 0$, allowing for a perfect autotuning. Then, using Manlab, we performed a continuation with f_2 left free, $\sigma_1 = 0$ and σ_2 function of f_2 with Eq. (42). We obtained Fig. 11(b), that shows that using the autotuning relation (42) enables to recover the saturation phenomenon, since the amplitude $a_2^C(\sigma_1 = 0)$ at the antiresonance is independent of f_2. Fig. 11(b) also

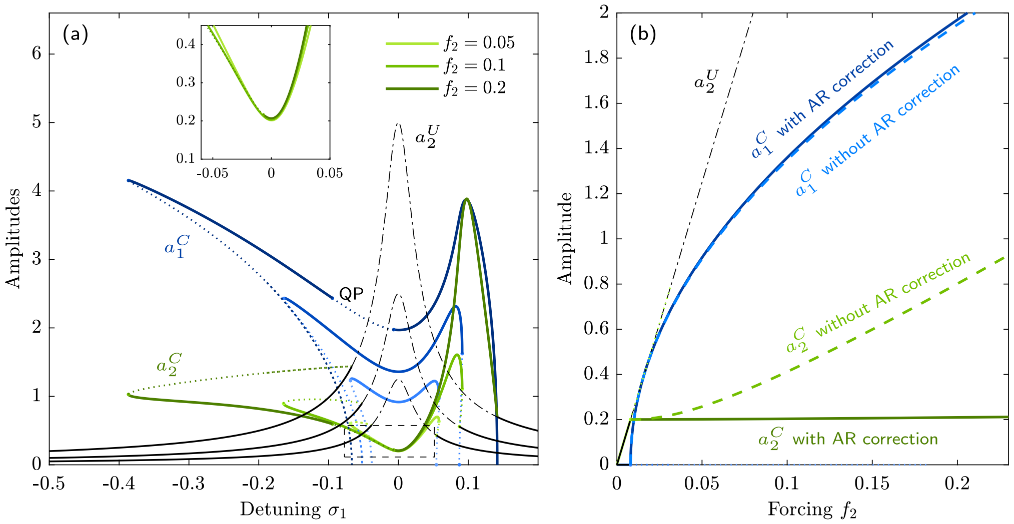

Fig. 11. Typical response of the complete system (18) obtained with Manlab, with the value of the detuning σ_2 adjusted as a function of the forcing f_2 according to Fig. 10(b) to place the nonlinear antiresonance (AR correction) at $\sigma_1 = 0$. (a) frequency response: amplitudes a_1 and a_2 as a function of the detuning σ_1 for several values of the forcing f_2 ($f_2 \in \{0.05; 0.1; 0.2\}$), with a darker color as f_2 increases. The inset shows a zoom of the nonlinear antiresonance region. "QP" means quasi-periodic response; (b) Force response: amplitudes a_1 and a_2 at $\sigma_1 = 0$ as a function of the forcing f_2 with ('—') and without ('- -') the AR correction. The parameters are: $\Lambda_1 = \Lambda_2 = \Lambda_4 = 0.1$, $\Lambda_3 = \Lambda_5 = \Lambda_6 = 0$, $\mu_1 = 0.005$, $\mu_2 = 0.01$.

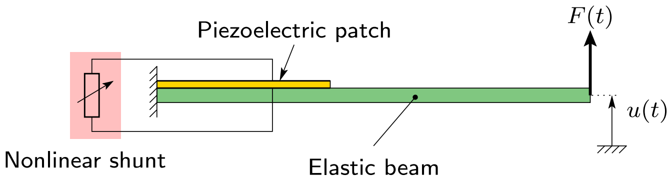

Fig. 12. Beam with a piezoelectric patch and a nonlinear shunt.

shows the response of the system without the autotuning (with $\sigma_2 = 0$), showing that the saturation phenomenon is lost but that a vibration reduction at the resonance of a_2 is however achieved, since the green dashed curved (a_2^C without AR correction) is below the black dash-dotted curve (a_2^U). One can also observe that the amplitude of the electrical mode a_1^C is almost left unchanged, at the antiresonance, by the non-zero value of Λ_1, since the two blue solid and dashed curves are almost merged.

4.4. Conclusions

The comparison between the responses of the complete system (18) and the MS analytical solution (27) of the simplified system (without the non-resonant terms) seen in the previous sections leads to the following conclusions, regarding the design of the vibration absorber. We studied only the effect of the leading resonant-term, of coefficient Λ_1. The complete system (18) shows a more complicated frequency response in comparison to that of the simplified one, due to the non-resonant term, that appeared to have a significant effect on the response. First, a kind of softening behavior is observed, since the curves show an overall bending to the low frequencies. It is responsible of a shift of the antiresonance frequency of the mechanical mode, that is now a function of the forcing and the damping. Secondly, we showed that the amplitude of this antiresonance remains independent of the forcing amplitude, with a phase γ_1^C also locked at $3\pi/2$. Thirdly, in order to correct this antiresonance shift, we showed that it is possible to continuously adjust the frequency ω_1 of the electrical mode as a function of the forcing amplitude f_2 (with the linear relation of Eq. (42) and $\sigma_2 = \omega_2 - 2\omega_1 \Rightarrow \omega_1 = (\omega_2 + \alpha f_2)/2$), to keep the antiresonance frequency independent of f_2 and then to obtain a perfect saturation phenomenon of the mechanical mode amplitude a_2^C at the antiresonance. Qualitatively, since $\alpha > 0$, one has to overtune ω_1 with respect to the perfect tuning $\omega_1 = \omega_2/2$. A last comment is that the proportionality coefficient α depends on the other parameters of the system and in particular on the nonlinearity coefficient β. This will be investigated in Section 5.7.

5. Application to a real structure

We investigate in the section the application of the proposed nonlinear shunt absorber to an arbitrary elastic structure with piezoelectric patches (as depicted in Fig. 1) and we give an example considering a beam structure (Fig. 12).

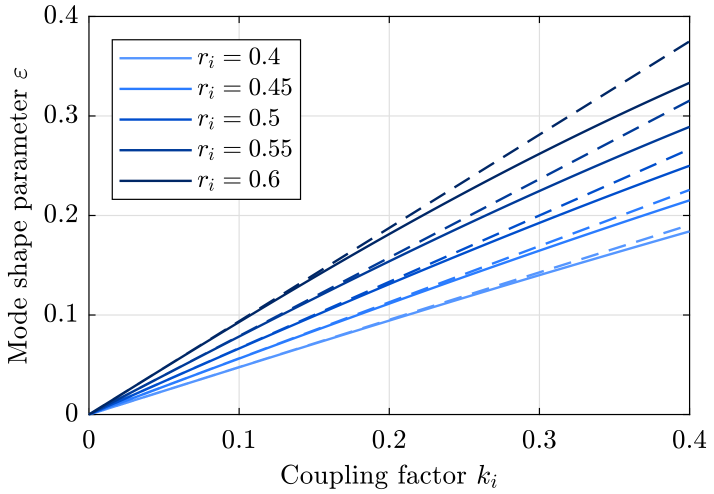

Fig. 13. Mode shape parameter ε as a function of the electromechanical coupling factor k_i for different values of the frequency ratio r_i, as specified. '—': exact value from Eq. (14); '- -': linear approximation, Eq. (46).

5.1. *Effect of electromechanical modal expansion*

The simplified model of Section 3 aimed at raising simple design guidelines, which were extended to a more realistic model in Section 4. However, both models are valid within the electromechanical modal expansion of Eqs. (15) and (16). The effect of this latter is investigated in this section.

First, the electromechanical modal analysis of Section 2.2 shows that the two dimensionless natural frequencies of the system are ω_1 and ω_2. Analyzing Eq. (12) shows that ω_1 is slightly smaller than r_i and ω_2 is slightly above 1. This shows that the two corresponding dimensioned natural frequencies of the system, denoted $\tilde{\omega}_e = \omega_1\hat{\omega}_i$ and $\tilde{\omega}_i = \omega_2\hat{\omega}_i$, are such that $\tilde{\omega}_e \lesssim \omega_e$ and $\tilde{\omega}_i \gtrsim \hat{\omega}_i$: they are located apart from the two uncoupled frequencies ω_e and $\hat{\omega}_i$, because of the piezoelectric coupling. This means that all the frequency responses shown in Sections 3 and 4, and consequently the frequency band of vibration reduction, are *in the vicinity of the* $\tilde{\omega}_i$ *resonance*, slightly above the open circuit resonance at $\hat{\omega}_i$, obtained with $Q = 0$ in Eqs. (6). This will be illustrated in Fig. 16.

Then, following the modal expansion (4), the displacement of the point of the structure can be written $\boldsymbol{u}(t) = \boldsymbol{\Phi}_i q_i(t) = \boldsymbol{\Phi}_i \bar{q}_i(t)/\sqrt{m_i}$, where the scaling of Eq. (9) has been used. We consider that the external forcing is harmonic, of angular frequency Ω. Then, the first order solutions for the displacement and charge electromechanical modal coordinates $(x_1(t), x_2(t))$ seen in Sections 3 and 4, Eqs. (26)a,b, and the electromechanical modal change of variables (16)a enable writing the displacement as:

$$\boldsymbol{u}(t) = \frac{\boldsymbol{\Phi}_i}{\sqrt{m_i}}\Big[\underbrace{-\varepsilon\, a_1 \cos\left(\frac{\Omega}{2}t - \frac{\gamma_1+\gamma_2}{2}\right)}_{x_1(t)} + \underbrace{a_2\cos\left(\Omega t - \gamma_2\right)}_{x_2(t)}\Big], \tag{43}$$

As a first result, because the leading harmonics of $x_1(t)$ is $\Omega/2$ (H1/2) and the one of $x_2(t)$ is Ω (H1), there is a frequency splitting between $x_1(t)$ and $x_2(t)$. Consequently, the *saturation phenomenon* (see Fig. 11) that has been exhibited on $x_2(t)$ in Sections 3 and 4 is equally *observed on the mechanical displacement* $\boldsymbol{u}(t)$ of any point of the structure, at the driving frequency Ω. In addition, the electromechanical modal change of variables (16)a creates a subharmonic component (H1/2) in $\boldsymbol{u}(t)$, proportional to $x_1(t)$, a priori of a smaller amplitude because of the ε factor.

In the same manner, Eqs. (9), (16)b give, for the electrical charge:

$$Q(t) = \frac{1}{\sqrt{L}}\Big[\underbrace{a_1\cos\left(\frac{\Omega}{2}t - \frac{\gamma_1+\gamma_2}{2}\right)}_{x_1(t)} + \varepsilon\,\underbrace{a_2\cos\left(\Omega t - \gamma_2\right)}_{x_2(t)}\Big]. \tag{44}$$

Here, the leading harmonics is H1/2, with a H1 harmonics of smaller amplitude, because of the ε factor.

5.2. *Saturation amplitude and design*

To evaluate the relevant parameters for the design of the nonlinear shunt, we base ourselves on the amplitude a_2^* of the mechanical mode saturation given by Eq. (34). Inserting this equation into Eq. (43), the Ω (H1) harmonics amplitude of the displacement vector then reads:

$$\boldsymbol{u}^*_{\mathrm{H1}} = \frac{a_2^*\boldsymbol{\Phi}_i}{\sqrt{m_i}} = u^*_{\mathrm{H1}}\boldsymbol{\Phi}_i, \quad \text{with} \quad u^*_{\mathrm{H1}} = \frac{2\omega_2\mu_1}{\Lambda_2\sqrt{m_i}} \tag{45}$$

Table 1
Typical values of capacitance $C_{\mathrm{p}i}$ and β_1/β_2 for a thickness/length ratio $h_p/l_p = 0.01$, a frequency ratio $r_i = 0.5$, a typical dielectric permittivity $\epsilon_{33} = 2000\epsilon_0 \simeq 2 \cdot 10^{-8}$ F/m ($\epsilon_0 = 8.82 \cdot 10^{-12}$ F/m is the vacuum permittivity) for a PZT like piezoelectric material [58], as a function of width b.

b_p [m]	1e−6	1e−3	1e−2	1e−1
$C_{\mathrm{p}i}$	2 pF	2 nF	20 nF	200 nF
$\beta_1/\beta_2 = 1/(C_{\mathrm{p}i}^2 r_i^2)$	10^{24}	10^{18}	10^{16}	10^{14}

We can verify that the above amplitude is logically independent of the scaling of the mode shape $\boldsymbol{\Phi}_i$ since the modal mass is $m_i = \boldsymbol{\Phi}_i^{\mathrm{T}} \boldsymbol{M} \boldsymbol{\Phi}_i$ (see Eqs. (5)).

To go further, we consider practical values of the parameters. As explained in Section 2.2, the parameter ε is small and depends on the electromechanical coupling factor k_i and the tuning of the electrical resonance r_i. To easily analyze the mathematical results, we neglect in Δ the term $4r_i^2k_i^2$ and Eqs. (14) and (12) give:

$$\varepsilon \simeq \frac{k_i r_i}{1 - r_i^2}, \quad \omega_2 \simeq 1. \tag{46}$$

Fig. 13 shows that the above linear approximation of ε as a function of k_i is valid on a large range of k_i values, below $k_i = 0.2$. Then, because ε is small, we approximate μ_1 and μ_2 in Eq. (19) by:

$$\mu_1 \simeq \xi_e r_i, \quad \mu_2 \simeq \xi_i. \tag{47}$$

Finally, $\boldsymbol{u}_{\mathrm{H1}}$ depends on Λ_2, which depends on the choice of the nonlinear shunt in Eq. (2).

Considering the first case of nonlinear shunt for which the voltage is proportional to the squared electrical charge (Eq. (2)a)), one obtains, with Eqs. (21) and (23), $\Lambda_2 = 2\varepsilon\beta_1 r_i^3 \hat{\omega}_i C_{\mathrm{p}i}^{3/2}$, which gives:

$$\boldsymbol{u}_{\mathrm{H1}}^{*(1)} = \frac{\xi_e}{k_i\beta_1} \frac{1 - r_i^2}{r_i^3 C_{\mathrm{p}i}^{3/2}} \frac{\boldsymbol{\Phi}_i}{\hat{\omega}_i\sqrt{m_i}} \tag{48}$$

In the second case for which the voltage is proportional to the squared piezoelectric voltage (Eq. (2)b), one obtains, with Eqs. (21) and (24),

$$\Lambda_2 \simeq 2\lambda_1\varepsilon + \lambda_2 - 2\lambda_3\varepsilon = \frac{2r_i^2 k_i(1 - k_i^2)}{1 - r_i^2} \frac{\beta_2\hat{\omega}_i}{\sqrt{C_{\mathrm{p}i}}},$$

which gives, with $1 - k_i^2 \simeq 1$:

$$\boldsymbol{u}_{\mathrm{H1}}^{*(2)} = \frac{\xi_e}{k_i\beta_2} \frac{(1 - r_i^2)\sqrt{C_{\mathrm{p}i}}}{r_i} \frac{\boldsymbol{\Phi}_i}{\hat{\omega}_i\sqrt{m_i}} \tag{49}$$

Eqs. (48) and (49) share similarities. If one wants to minimize the saturation vibration amplitude of the structure $\boldsymbol{u}_{\mathrm{H1}}^*$, one has to consider the factor $\eta = \xi_e/(k_i\beta)$ as low as possible, *i.e.* with a low electrical shunt damping ratio ξ_e and high piezoelectric coupling factor k_i and nonlinearity coefficient β. Since the values of ξ_e and k_i are in practice limited by the material constants of the components, one can imagine increasing β as much as possible, with a suitable electronic circuit, to efficiently improve the shunt performance, and/or balance a too high ξ_e or a two low k_i.

5.3. Order of magnitude of coefficient β

Following the previous section and considering the two choices for the nonlinear shunt design in Eq. (2), if we consider a given targeted saturation amplitude $\boldsymbol{u}_{\mathrm{H1}}^*$, the ratio between $u_{\mathrm{H1}}^{*(1)}$ and $u_{\mathrm{H1}}^{*(2)}$ gives the order of magnitude of β_1/β_2 of the two choices:

$$\frac{u_{\mathrm{H1}}^{*(1)}}{u_{\mathrm{H1}}^{*(2)}} = 1 = \frac{\beta_2}{\beta_1 C_{\mathrm{p}i}^2 r_i^2} \quad \Rightarrow \quad \frac{\beta_1}{\beta_2} = \frac{1}{C_{\mathrm{p}i}^2 r_i^2}. \tag{50}$$

Remember that the units of β_1 and β_2 are not the same. One observes that β_1/β_2 depends only on the piezoelectric patch capacitance $C_{\mathrm{p}i}$ and the frequency ratio r_i. In most practical cases, $C_{\mathrm{p}i}$ takes a very small value in Farads. This is illustrated in Table 1 in which the capacitance of a rectangular piezoelectric patch of length l_p, thickness h_p and width b_p is indicated, computed with:

$$C_{\mathrm{p}i} = \frac{\epsilon_{33} l_p b_p}{h_p}, \tag{51}$$

where ϵ_{33} is the permittivity of the material. Typically, if the patch is thin ($L/h = 100$) and of centimetric dimensions, $C_{\mathrm{p}i} \simeq 20$nF, which leads to a very large ratio β_1/β_2, of the order of 10^{16} F^2. This huge ratio can be explained because piezoelectric transducers typically exhibit small charges and high voltages. More insights on practical values of the gains β_k are investigated in the next section on a practical example, of centimetric size.

5.4. Electric charge order of magnitude

We evaluate here the effect of the design parameters on the value of the electric charge at the antiresonance. We consider its leading harmonics H1/2, which, considering Eqs. (44) and (35), (9), (20), reads:

$$Q^*_{\mathrm{H1/2}} = \frac{a_1^*}{\sqrt{L}} = \sqrt{\frac{2}{L\Lambda_4}}\sqrt{\frac{F-F^*}{\hat{\omega}_i^2\sqrt{m_i}}}. \tag{52}$$

In the above equation, $F^* = \boldsymbol{\Phi}_i^{\mathrm{T}}\boldsymbol{F}^*$ is the value of the forcing amplitude $F = \boldsymbol{\Phi}_i^{\mathrm{T}}\boldsymbol{F}$ at the nonlinear coupling threshold. Considering Eq. (34) and the scaling (9), one shows that:

$$F^* = 2\xi_i\hat{\omega}_i^2 m_i u^*_{\mathrm{H1}}. \tag{53}$$

In the same manner than in the previous sections, we consider successively the two shunt designs. For the first case (Eq. (2)a), one obtains, with Eqs. (21) and (23), $\Lambda_4 = \varepsilon\beta_1 r_i^3\hat{\omega}_i C_{\mathrm{p}i}^{3/2}$ which gives:

$$Q^{*(1)}_{\mathrm{H1/2}} = \sqrt{\frac{2(1-r_i^2)}{k_i\beta_1 r_i^2\hat{\omega}_i\sqrt{m_iC_{\mathrm{p}i}}}}\sqrt{F-F^*}, \quad F^* = \frac{2\xi_i\xi_e(1-r_i^2)\hat{\omega}_i\sqrt{m_i}}{k_i\beta_1 r_i^3 C_{\mathrm{p}i}^{3/2}}. \tag{54}$$

In the above equation, the relation (7) between L and ω_e as well as the approximation (46) for ε have been used.

For the second case (Eq. (2)b), one obtains, with Eqs. (21), (24), (46),

$$\Lambda_4 = \varepsilon(\lambda_1 - \lambda_2\varepsilon + \lambda_3\varepsilon^2) = \frac{r_i^4 k_i}{1-r_i^2}\left(1 - o(k_i^2)\right)\frac{\beta_2\hat{\omega}_i}{\sqrt{C_{\mathrm{p}i}}},$$

where $o(k_i^2)$, of the order of k_i^2, will be neglected in the following. One then obtains:

$$Q^{*(2)}_{\mathrm{H1/2}} = \sqrt{\frac{2(1-r_i^2)C_{\mathrm{p}i}^{3/2}}{r_i^2 k_i\beta_2\hat{\omega}_i\sqrt{m_i}}}\sqrt{F-F^*}, \quad F^* = \frac{2\xi_i\xi_e(1-r_i^2)\hat{\omega}_i\sqrt{m_iC_{\mathrm{p}i}}}{k_i\beta_1 r_i} \tag{55}$$

As considered in the previous Section 5.3, by considering a given targeted threshold amplitude $\boldsymbol{u}^*_{\mathrm{H1}}$, the ratio between the two charge expressions in the two cases of shunt design gives:

$$\frac{Q^{*(1)}_{\mathrm{H1/2}}}{Q^{*(2)}_{\mathrm{H1/2}}} = \frac{\beta_2}{\beta_1 C_{\mathrm{p}i}^2} = r_i^2 \simeq 1/4, \tag{56}$$

where the last equality comes from Eq. (50) and $r_i \simeq 0.5$.

Two comments can be raised. The first one is that, considering a given threshold amplitude $\boldsymbol{u}^*_{\mathrm{H1}}$, the electric charge amplitudes estimated for the two shunt designs (Eq. (2)a or (2)b) are of the same order of magnitude, since the ratio is $\simeq 1/4$. Then, the other major parameter which influences the amplitude of the electric charge is the force threshold F^*: the smaller it is, the higher $Q^*_{\mathrm{H1/2}}$ is for a given excitation amplitude F. This is illustrated in Figs. 4(b) or 11(b), where decreasing F^* (or f_2^*) would translate the a_1^C curve to the left and thus increase the value of its amplitude for a given forcing f_2. Finally, another important parameter is $k_i\beta$ which appears in the denominator of $Q^*_{\mathrm{H1/2}}$ and in F^*. We can write $Q^*_{\mathrm{H1/2}} = \sqrt{(ax-b)/x^2}$ with $x = k_i\beta$ and a, b functions of the other parameters. One can remark that this function is increasing as a function of x, showing that *an increase of* $k_i\beta$ *also leads to an increase of the electric charge*. This was already observed in Figs. 5(b) and 6(a) where a_1^C increases as a function of Λ_2 and Λ_4, both proportional to $k_i\beta$.

5.5. Subharmonic of the displacement

As shown in Eq. (43), the electromechanical coupling is responsible of a parasitic subharmonic H1/2 in the displacement $\boldsymbol{u}(t)$. To estimate its relative amplitude, we compute the ratio of harmonics H1/2 and H1 at the antiresonance:

$$\frac{u^*_{\mathrm{H1/2}}}{u^*_{\mathrm{H1}}} = \frac{\varepsilon a_1^*}{a_2^*} = \varepsilon\sqrt{\frac{2(F-F^*)}{\Lambda_4\hat{\omega}_i^2\sqrt{m_i}}\frac{\Lambda_2^2}{4\omega_2^2\mu_1^2}}. \tag{57}$$

With the same reasoning as in the previous sections, for the first case of $V_{\mathrm{nl}} = \beta_1 Q^2$, one obtains $\Lambda_4 = \Lambda_2/2$ and:

$$\frac{u^{*(1)}_{\mathrm{H1/2}}}{u^{*(1)}_{\mathrm{H1}}} = \sqrt{\frac{k_i^3\beta_1}{\xi_e^2}\frac{2r_i^4 C_{\mathrm{p}i}^{3/2}(F-F^*)}{(1-r_i^2)^3\hat{\omega}_i\sqrt{m_i}}}. \tag{58}$$

For the second case of $V_{\mathrm{nl}} = \beta_2 V^2$, $\Lambda_4 = r_i^2\Lambda_2/2$ and:

$$\frac{u^{*(2)}_{\mathrm{H1/2}}}{u^{*(2)}_{\mathrm{H1}}} = \sqrt{\frac{k_i^3\beta_2}{\xi_e^2}\frac{2(F-F^*)}{(1-r_i^2)^3\hat{\omega}_i\sqrt{m_iC_{\mathrm{p}i}}}}. \tag{59}$$

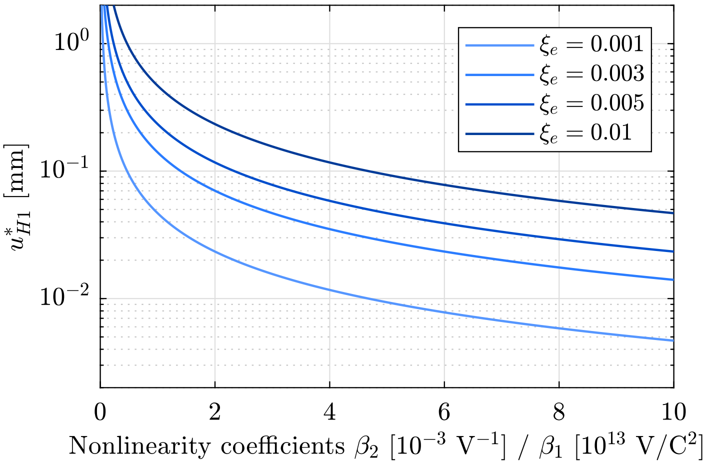

Fig. 14. Saturation amplitude $u^{*(k)}_{\mathrm{H1}}$, $k = 1, 2$ as a function of β_k, from Eqs. (61) and (62), for various values of the electrical damping ratio ξ_e, as specified. The plot is related to the first mode of a beam ($\zeta_i = \zeta_1 = 1.875$) in steel ($E = 200$ GPa), with a thickness/length ratio $h/L = 0.01$, a frequency ratio $r_i = 0.5$, a dielectric permittivity $\epsilon_{33} = 2000\epsilon_0 \simeq 2 \cdot 10^{-8}$F/m ($\epsilon_0 = 8.82 \cdot 10^{-12}$F/m is the vacuum permittivity) and a coupling factor $k_i = 0.2$. In the first case, $k = 1$, the beam thickness is $b = 10$ mm.

Considering the above result, two conclusions can be drawn. First, since the subharmonic is proportional to a_1^* (similarly to the electric charge $Q^*_{\mathrm{H1/2}}$), it is also proportional to the factor $\sqrt{F - F^*}$. Secondly, it is proportional to the factor $\sqrt{k_i^3 \beta / \xi_e^2}$, a fact that will be analyzed in Section 6.

5.6. An arbitrary thin piezoelectric beam

All the previous investigations can be applied to an arbitrary structure. To precise the design, we particularize the geometry and we consider a beam with a piezoelectric patch, as depicted in Fig. 12. To obtain the order of magnitude of the several parameters, we neglect the mechanical inertia and stiffness of the piezoelectric patch and consider in the model only those of the elastic layer (see for instance [58,70] for more refined models). We denote by (E, ρ) the Young's modulus and density of the elastic layer and we consider a rectangular cross section of width b and thickness h. l is the length of the beam. An analytical model is thus at hand and gives, for this beam (with a classical Euler–Bernoulli kinematics [71]):

$$\breve{\omega}_i \simeq \hat{\omega}_i = \frac{\zeta_i^2 h}{l^2}\sqrt{\frac{E}{12\rho}}, \quad m_i = \rho b h l/4, \quad \Phi_i(l) = 1, \tag{60}$$

with $\zeta_1 = 1.875$, $\zeta_2 = 4.694$, $\zeta_3 = 7.855\ldots$ and $\Phi_i(l)$ the value of the ith mode shape at the tip of the beam. To obtain a consistent order of magnitude of the electric capacitance of the piezoelectric patch, we use Eq. (51), by considering a piezoelectric patch of equivalent size to that of the elastic layer.

Introducing the above parameters in Eqs. (48) and (49) leads to:

$$u^{*(1)}_{\mathrm{H1}} = \frac{4\sqrt{3}\xi_e}{k_i \zeta_i^2 \sqrt{E}} \frac{1 - r_i^2}{r_i^3} \frac{1}{\beta_1 \epsilon_{33}^{3/2} b^2}, \tag{61}$$

$$u^{*(2)}_{\mathrm{H1}} = \frac{4\sqrt{3}\xi_e}{k_i \zeta_i^2 \sqrt{E}} \frac{1 - r_i^2}{r_i} \frac{\sqrt{\epsilon_{33}} L^2}{\beta_2 h^2}, \tag{62}$$

where $u^{*(k)}_{\mathrm{H1}}$, $k = 1, 2$, are the beam tip displacement amplitudes for the two shunt design choices. One observes that those two equations are independent of the density of the material ρ. They are composed of three factors. The first one is common two both equations; the second one depends on the piezoelectric shunt tuning $r_i = \omega_e/\hat{\omega}_i \simeq 0.5$. The third one differs in the two equations, because of the different physical nature of β_1 (of unit V/C^2) and β_2 (of units V^{-1}), stemming from the two choices for the nonlinear shunt.

In the case of the second choice ($V_{nl} = \beta_2 V_p^2$), Eq. (62) shows that the saturation value $u^{*(2)}_{\mathrm{H1}}$ of the tip amplitude of the beam, expressed in [m], does not depend on the size of the structure but only of its slenderness ratio h/l. On the contrary, $u^{*(1)}_{\mathrm{H1}}$ for the first choice ($V_{nl} = \beta_1 Q^2$) is inversely proportional to the squared size of the structure, through its squared width b^2. The dependence on the other parameters is the same for both cases. To set the ideas of the order of magnitude of β_1 or β_2 in a practical case, Fig. 14 gives the saturation amplitude $u^{*(k)}_{\mathrm{H1}}$ of the beam's tip as a function of β_k. In the case of a centimetric thin beam ($h/l = 0.01$) in steel, with a PZT piezoelectric patch, a saturation amplitude of 0.05 mm is obtained for $\beta_2 \simeq 0.005$ V^{-1}, whereas $\beta_1 \simeq 5 \cdot 10^{13}$ V/C^2, in agreement with Table 1. In a practical case, since analog nonlinear capacitors with the required level of nonlinearity are scarce in common electronic components, one would probably rely on analog multipliers or a synthetic digital shunt to realize the electronics. In those cases, huge values of β_1, naturally explained by the small electric charge generated by the piezoelectric transducers, would probably

Table 2
Parameters of the first mode of the beam used for the frequency response of Fig. 16.

$\hat{\omega}_1/(2\pi)$	ξ_1	m_1	$C_{\mathrm{p}1}$	θ_1	k_1	$\Phi_1(l)$
37.51 Hz	0.005	8.9 g	32.45 nF	0.88 mN/V	0.22	1

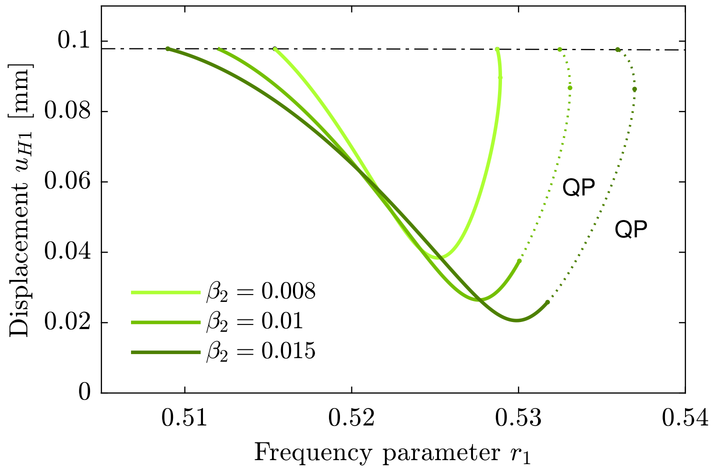

Fig. 15. Amplitude $u_{\mathrm{H}1}$ at the open circuit natural frequency $\Omega = \hat{\omega}_1$ of the beam tip of the beam as a function of the frequency parameter $r_1 = \omega_e/\hat{\omega}_1$, for several values of the nonlinearity coefficient β_2 ($\beta_2 \in \{0.008; 0.01; 0.015\}$ V^{-1}), as specified, and for a given value of the forcing $F = 0.53$ mN. Those curves were obtained by numerical continuation of Eqs. (6) with Manlab. The parameters are those of Table 2 and the electrical damping ratio is $\xi_e = 0.0053$.

be realized in practice using dedicated charge amplifiers, with possible complex electronic implementations. On the contrary, the second design choice of $V_{nl} = \beta_2 V_p^2$ appears more straightforward, with smaller values of β_2, and would probably lead to simpler electronic circuit designs, which motivates the practical example of the next section.

5.7. A practical example

In this section, we give an example of design of the nonlinear piezoelectric shunt on a particular structure. We choose the piezoelectric beam already used in [59]. It is a stainless steel cantilever beam (with a length of 178.8 mm, a width of 30.5 mm and a thickness of 1.1 mm) with two Physik Instrumente PIC 151 piezoelectric patches (with a length of 70 mm each, 0.5 mm thick and with wrapped electrodes) bonded on each side of the beam and electrically connected in series. An experimental modal analysis gave us the modal parameters of Table 2, for the first mode of the beam ($i = 1$). In the following, we consider that the beam is driven at its tip, with a point force $F(t) = F\cos\Omega t$.

We choose to design a shunt based on the second possible case, namely with $V_{\mathrm{nl}} = \beta_2 V^2$. Looking at Fig. 1 shows that three parameters have to be chosen to design the shunt: its inductance L, resistance R and nonlinearity coefficient β_2. The inductance L influences the electrical frequency ω_e (Eq. (7)), that has to be tuned properly to obtain the 2:1 internal resonance. In theory, it is obtained with $\omega_2/\omega_1 = \tilde{\omega}_i/\tilde{\omega}_e = 0.5$. Following Fig. 2, ω_e has to be overtuned with respect to $\hat{\omega}_i/2$ and with the present electromechanical coupling factor of $k_i = 0.22$, an estimation of the tuning is $r_i \simeq 0.525$.

Moreover, to lock the antiresonance at a given frequency, this tuning slightly depends on the amplitude of the motion and other parameters, as explained in Section 4. We then use a numerical continuation of the modal reduced order model (6) as a function of the electrical frequency ω_e to precisely determine it. It is obtained in practice with Manlab, by leaving ω_e free whereas the driving frequency Ω and forcing F are prescribed. Since we are targeting an antiresonance in the middle of the frequency band of vibration reduction, we choose here $\Omega = \tilde{\omega}_i$: the resonance of the coupled electromechanical system, corresponding to $\bar{\Omega} = \omega_2$ or $\sigma_1 = 0$ in Sections 3 and 4. As explained in Section 5.1, $\tilde{\omega}_i$ is slightly above the open circuit resonance of the system at $\Omega \simeq \hat{\omega}_i$. With Eq. (12), it is clear that $\tilde{\omega}_i = \omega_2\hat{\omega}_i$ depends on k_i and r_i. Consequently, we choose our initial guess $r_i = 0.525$, which leads to $\tilde{\omega}_1 = 37.85$ Hz with Eq. (12).

Fig. 15 (analogous to Fig. 10(a) in the case of the modal model Eqs. (18)) is obtained. It shows that the amplitude $u_{\mathrm{H}1}^{(2)}$ of the first harmonics of the beam tip has a minimum for a certain value r_i^* of the frequency ratio r_i that correspond to place the antiresonance of $u_{\mathrm{H}1}^{(2)} = f(\Omega)$ exactly at $\Omega = \tilde{\omega}_1$. This plot is also valuable since it enables to visualize the value of β_2 necessary to obtain a certain amplitude threshold $u_{\mathrm{H}1}^{*(2)}$. For instance, the dark green curve shows that $\beta_2 = 0.015$ V^{-1} leads to an amplitude threshold of $u_{\mathrm{H}1}^{*(2)} = 0.02$ mm and that a tuning $r_i = 0.5309$ is necessary for the AR correction at this forcing ($F = 0.53$ mN). The obtained tunings for the three values of β_2 shown in Fig. 15 are, as expected, slightly above our initial guess of $r_i = 0.525$.

Using the values of r_i^* taken from Fig. 15, Fig. 16 shows the frequency response of the first harmonics of the beam tip $u_{\mathrm{H}1}^{(2)} = f(\Omega)$ and the subharmonics of the electric charge $Q_{\mathrm{H}1/2} = f(\Omega)$. Instead of plotting this frequency response for several values of the forcing F, which would give a plot similar to Fig. 11, we show here the frequency response for several values of the nonlinearity coefficient β_2 for a given value of the external forcing F. This plot confirms that the AR correction obtained by adjusting r_i according to the

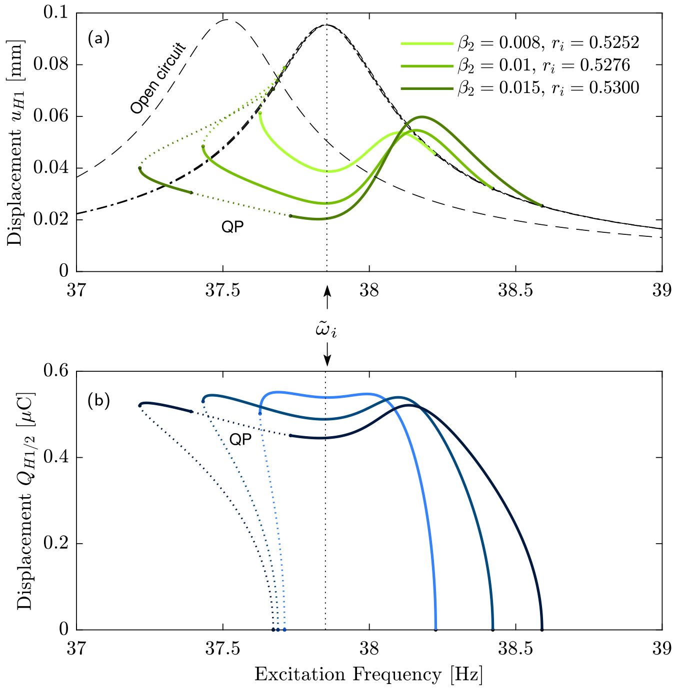

Fig. 16. Resonant response around the first resonance of the beam for several values of the nonlinearity coefficient β_2 ($\beta_2 \in \{0.008; 0.01; 0.015\}$ V^{-1}) and the nonlinear shunt tuned to obtain the nonlinear antiresonance at $\Omega = \hat{\omega}_1$, according to the minima of the curves in Fig. 15 ($r_1 = \omega_e/\hat{\omega}_1 \in \{0.5252; 0.5276; 0.5300\}$). (a) amplitude of the first harmonics of the beam's tip displacement u_{H1} and (b) amplitude of the subharmonic of the electrical charge $Q_{\mathrm{H1/2}}$ obtained by numerical continuation of Eqs. (6) with Manlab, with a darker blue as β_2 increases. The parameters are those of Table 2, with $F = 0.53$ mN and $\xi_e = 0.0053$.

minima of Fig. 15 works since the nonlinear antiresonance is perfectly located at $\Omega = \tilde{\omega}_1$, the resonance of the coupled system. This plot also shows the linear resonances of the system, in the vicinity of $\Omega = \tilde{\omega}_i \simeq 37.85$ Hz. The slight dependence of $\Omega = \tilde{\omega}_i$ upon r_i is also visible in Fig. 16(a), since three linear resonances are obtained in dashed–dotted lines. The open circuit resonance around $\hat{\omega}_i = 37.51$ Hz is also shown in dashed lines. An interesting point is that increasing the value of β_2 slightly decreases the value of the electrical charge in Fig. 16(b).

Moreover, as already observed in Section 4, some quasiperiodic (QP) responses are obtained in Fig. 16. They can be close to the antiresonance point and seems to approach it as β_2 or F are increased. Those QP responses are also obtained in Fig. 15. Some examples of QP response as a function of time are shown in Figs. 17(d, e). There amplitude is of the same order of magnitude than the one of the periodic response at the antiresonance point (Figs. 17(b, c)), leading to think that this QP responses are not an issue for the vibration reduction. On the contrary, it can be observed that there is a unexpected strong effect of the subharmonic H1/2 on the total response in displacement, since its amplitude is of the same order of magnitude than the leading harmonics H1. This is the joint consequence of the large coupling factor $k_1 = 0.22$ used in the simulations as well as the fact that at the antiresonance point, the H1 harmonics is small because of the saturation phenomenon, leading to H1/2 harmonics of the same order of magnitude.

6. Design guidelines and parameter optimization for high vibration attenuation

As highlighted in the previous section, the design parameters that have to be chosen and controlled in a given application of the nonlinear shunt are the electrical frequency tuning $r_i = \omega_e/\hat{\omega}_i$, the nonlinearity coefficient β, the electrical damping factor ξ_e and the piezoelectric coupling factor k_i. Here is a set of guidelines that can be considered when selecting each parameter.

Firstly, one has to remark that the response of the nonlinear shunt is amplitude dependent, as shown for instance in Fig. 11. It means that, contrary to a fully linear system, the shape of the frequency response depends on the amplitude F of the forcing. On the contrary, the major property of the shunt is the saturation phenomenon, that depends on the vibration amplitude threshold u^*_{H1}, which is the minimum vibration amplitude above which it is independent of the forcing. This occurs at a particular driving frequency, close to twice the electrical frequency ω_e, that has to be tuned close to half the targeted resonance, such that $r_i = \omega_e/\hat{\omega}_i \simeq 0.5$ in order to activate the energy transfer thanks to the 2:1 internal resonance.

The main design criterion is thus the amplitude threshold u^*_{H1}, that we want to be as small as possible. In addition, the amplitude of the electric charge $Q^*_{\mathrm{H1/2}}$ during the energy transfer has also to be considered for the design of the electrical components of the circuit. Finally, the electromechanical coupling creates a subharmonic H1/2 in the displacement signal that can have a non negligible amplitude with respect to the H1 harmonics, and thus decreases the damping performance (see Fig. 17). The harmonics ratio $u^*_{\mathrm{H1/2}}/u^*_{\mathrm{H1}}$, to be minimized, is thus also a design criterion.

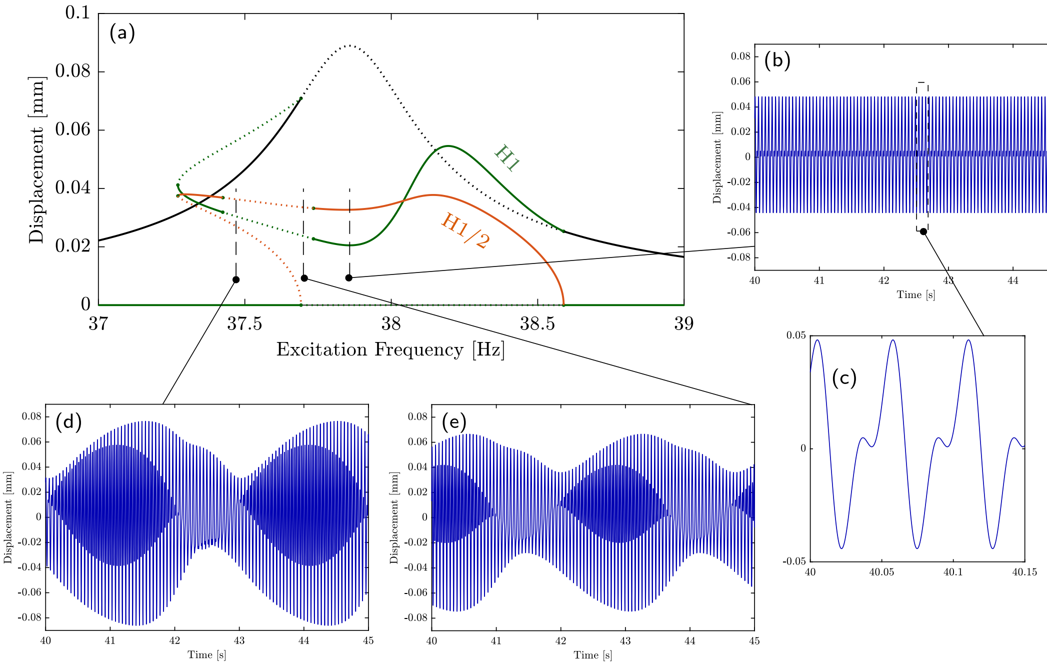

Fig. 17. (a) Resonant response around the first resonance of the beam with both the leading harmonics H1 and the subharmonic H1/2 of the beam's tip displacement (same case as Fig. 15 for $\beta_2 = 0.015\ \mathrm{V}^{-1}$); (b, c): periodic response at the antiresonance point; (d, e): examples of quasi-periodic responses, obtained by time integration. The parameters are those of Table 2, with $F = 0.53$ mN and $\xi_e = 0.0053$.

As shown in Sections 5.2 and 5.5:

$$u^*_{\mathrm{H1}} \propto \frac{\xi_e}{k_i\beta} = \eta, \qquad \frac{u^*_{\mathrm{H1/2}}}{u^*_{\mathrm{H1}}} \propto \sqrt{\frac{k_i^3\beta}{\xi_e^2}} = \frac{1}{\eta}\sqrt{\frac{k_i}{\beta}}, \tag{63}$$

where $\propto$ means "proportional to". Consequently, to minimize the saturation amplitude u^*_{H1}, one has to choose η as small as possible. However, decreasing η leads to an increase of the subharmonic $u^*_{\mathrm{H1/2}}$... Considering the criterion "minimize u^*_{H1} *and* $u^*_{\mathrm{H1/2}}$", one can first choose the *electrical damping factor ξ_e as small as possible*. It is linked to the electrical resistance of the electronic circuit built for the shunt. Decreasing it is often limited in practice by the inherent resistance of the wires. Using an active negative capacitance synthetic circuit could be an alternative to artificially decrease ξ_e (see *e.g.* [4]). Then, one can remark that the piezoelectric coupling factor k_i and the nonlinearity parameter β play the same role and that their product $k_i\beta$ has to be as large as possible to minimize η and thus u^*_{H1}. On the contrary, the subharmonic amplitude $u^*_{\mathrm{H1/2}}$ is directly linked to the piezoelectric coupling. Then, a correct design should be with *a low (but non-zero) piezoelectric coupling factor k_i* to minimize $u^*_{\mathrm{H1/2}}$, which can be counterbalanced by *a high nonlinearity coefficient β*. In particular, if a given u^*_{H1} is targeted, one can think of minimizing $u^*_{\mathrm{H1/2}}$ by decreasing k_i while increasing β in the same proportion, to keep $k_i\beta$ (and u^*_{H1}) constant.

In most applications (linear shunt damping, energy harvesting), the piezoelectric coupling factor k_i has to be as high as possible, which also leads to a good performance here by minimizing the saturation amplitude u^*_{H1}. This is achieved by selecting a quality piezoelectric material as well as with suitable optimization of the geometry and placement of the piezoelectric patch on the structure (see [70,72]). It can be also improved by adding a negative capacitance in the shunt circuit, since it is equivalent to artificially increase the coupling factor [59]. On the contrary, for our present application, a not too high k_i is preferable to minimize the subharmonic amplitude, and the opposite reasoning has to be followed, allowing piezoelectric materials with lower coupling constants and non optimal geometry/placement of the patches.

As shown in Section 5.4, the amplitude $Q^*_{\mathrm{H1/2}}$ of the electric charge is an increasing function of $k_i\beta$. It is also proportional to $\sqrt{F - F^*}$, with F^* being proportional to u^*_{H1} (see Eq. (53)). It then means that optimizing the parameters to decrease u^*_{H1} also leads to an increase of $Q^*_{\mathrm{H1/2}}$. Moreover, increasing $k_i\beta$ or decreasing ξ_e has also the negative effect to widen the bistability region of the response curve in which a potential high amplitude response of the system can be reached, on the sides of the antiresonance (see Fig. 5, since Λ_2 is proportional $k_i\beta$ and μ_1 is proportional to ξ_e). Consequently, the benefit gained by decreasing the amplitude threshold u^*_{H1} has a direct effect on increasing the electrical charge in the circuit and widening the side bistable regions.

In addition, the parameter r_i must be chosen so that the coupled solution appears and must be slightly corrected as a function of the values of β and F, as illustrated in Sections 4.3 and 5.7. It has been shown in Fig. 10 that the correct tuning r_i^* is a linear function of the forcing F, with a coefficient that depends on the other parameters. Consequently, a performant shunt design should include a tuning correction of the electrical mode, using the proportionality relation (42). In practice, since the antiresonance occurs for a phase locking $\gamma_1 = 3\pi/2$, this property could be used to estimate the α proportionality coefficient.

7. Conclusion

In this paper, a passive nonlinear vibration absorber has been designed by utilizing a nonlinear piezoelectric electric shunt circuit with quadratic non-linearity. The quadratic non-linearity has been chosen to create a 2:1 internal resonance between a given resonant (mechanical) mode of the primary structure and a resonant electric circuit tuned at the order two subharmonic. The main feature to exploit from the 2:1 internal resonance is the saturation phenomenon, which leaves the mechanical amplitude independent of the forcing amplitude above a threshold. It is linked to a nonlinear energy transfer from the mechanical mode to the electric mode, leading to an efficient vibration attenuation near the resonance frequency.

Since the coupling of the mechanical mode and the electric mode through the piezoelectric patch breaks the invariance of those linear modes, the $2:1$ internal resonance properties are directly linked to the electromechanical modal coordinates, that are linear combination of the electrical and mechanical modes. However, because the energy is transferred from the excitation frequency harmonic to the subharmonic, we proved that this does not break the pure saturation phenomenon that is created on the mechanical amplitude of the structure at the driving frequency. However, this invariance break is also responsible of an unwanted subharmonic component in the displacement.

The choice of the nonlinear shunt parameters (piezoelectric coupling factor k_i, inductance L, resistance R and nonlinearity parameter β) has also been thoroughly addressed. It was shown that improving the performance of the shunt, by lowering as much as possible the mechanical amplitude coupling threshold u^*_{H1}, relies on decreasing as much as possible the factor $\eta = \xi_e/(k_i\beta)$, with ξ_e the dimensionless damping ratio proportional to R. Consequently, the electric circuit of the shunt must be designed as less resistive as possible, and, contrary to more classical shunt applications, the piezoelectric coupling factor k_i must be chosen not so high to minimize the subharmonic component creation. The main design parameter is thus the nonlinearity parameter β, that has to be chosen as high as possible.

The second design parameter set is the electrical tuning of the shunt, linked to the inductance L. The electrical frequency ω_e has to be chosen close to half the short circuit natural frequency of the targeted mechanical mode: $\omega_e \simeq \hat{\omega}_i/2$ to activate the $2:1$ internal resonance. The fine tuning depends on the piezoelectric coupling factor k_i (because of the invariance break considered above) in a constant fashion, but also slightly on the forcing amplitude. This unexpected effect is directly related to the high value of the non resonant term of coefficient Λ_1 in the electromechanical modal system. This high value of Λ_1 cannot be avoided with the architecture of our shunt. However, it was proven that the relation between the fine tuning of ω_e as a function of the forcing amplitude is linear, which gives a simple manner to correct this effect in a practical electronic circuit implementation.

Two shunt designs have also been tested (see Eqs. (2)). In theory, no difference of performance has been shown between both designs in the shunt performance and in the shape of the frequency response. The only notable difference is in the numerical value of the nonlinearity coefficient β, that has to be chosen very high in the first design ($V_{\mathrm{nl}} = \beta Q^2$, $\beta \simeq 5 \cdot 10^{13}\mathrm{V/C^2}$) and small for the other one ($V_{\mathrm{nl}} = \beta V^2$, $\beta \simeq 5 \cdot 10^{-3}\mathrm{V^{-1}}$). This huge difference in the orders of magnitudes has to be considered in a practical implementation of the electronic circuit. If electronic multiplier components are used like in [20], the second design has probably to be preferred.

Some quasi-periodic (QP) solutions have also been observed in our simulations, close to the antiresonance point. Those QP solutions are responsible for beatings superimposed to the classical periodic solutions, that could slightly decrease the vibration control performance, depending on the beating amplitude. The appearance of those QP responses is also probably linked to the increase of the performance factor $k_i\beta/\xi_e$, in a non trivial manner. A way of investigation should be the tracking of the Neimark–Sacker bifurcations, using numerical continuation, as proposed for instance in [73]. The study of those QP solutions is left for further studies.

Finally, one must bear in mind that this kind of nonlinear shunt is forcing amplitude dependent. The first consequence is that the amplitude reduction appears above an amplitude threshold. So, below this amplitude, a classical linear absorber (like a resonant shunt for instance [7]) has better performance. However, above the threshold, since the amplitude at the antiresonance saturates, the present nonlinear shunt behaves better and better as long as the forcing amplitude increases. It is thus well suited to cases for which the force is harmonics (like in rotating machines [74]), with a frequency in the vicinity of the mechanical resonance. In other cases of a force with a large band frequency content, the side resonance created by the non-resonant term Λ_1 on the right of the antiresonance, as seen in Fig. 11 or 16, could be an issue.

Declaration of competing interest

The authors declare that they have no known competing financial interests or personal relationships that could have appeared to influence the work reported in this paper.

Acknowledgments

The *Région Hauts de France* and the *Carnot ARTS Institute*, France are warmly thanked for the PhD grant of the first author.

References

[1] N.W. Hagood, A. Von Flotow, Damping of structural vibrations with piezoelectric materials and passive electrical networks, J. Sound Vib. 146 (2) (1991) 243–268.

[2] S. Behrens, A.J. Fleming, S.O.R. Moheimani, Electromagnetic shunt damping, in: Proceedings of the 2003 IEEE/ASME International Conference on Advanced Intelligent Mechatronics (AIM 2003), 2003, pp. 1145–1150.

[3] J.A.B. Gripp, D.A. Rade, Vibration and noise control using shunted piezoelectric transducers: A review, Mech. Syst. Signal Process. 112 (2018) 259–383.

[4] M. Auleley, O. Thomas, C. Giraud-Audine, H. Mahé, Enhancement of a dynamic vibration absorber by means of an electromagnetic shunt, J. Intell. Mater. Syst. Struct. 32 (3) (2020) 331–354, http://dx.doi.org/10.1177/1045389X20957097.

[5] S. Krenk, Frequency analysis of the tuned mass damper, J. Appl. Mech. 72 (2005) 936–942.

[6] M. Vakilinejad, A. Grolet, O. Thomas, A comparison of robustness and performance of linear and nonlinear lanchester dampers, Nonlinear Dynam. 100 (2020) 269–287, http://dx.doi.org/10.1007/s11071-020-05512-x.

[7] O. Thomas, J. Ducarne, J.-F. Deü, Performance of piezoelectric shunts for vibration reduction, Smart Mater. Struct. 21 (1) (2012) 015008, http://dx.doi.org/10.1088/0964-1726/21/1/015008.

[8] G. Caruso, A critical analysis of electric shunt circuits employed in piezoelectric passive vibration damping, Smart Mater. Struct. 10 (2001) 1059–1068.

[9] M. Berardengo, S. Manzoni, O. Thomas, M. Vanali, Piezoelectric resonant shunt enhancement by negative capacitances: Optimisation, performance and resonance cancellation, J. Intell. Mater. Syst. Struct. 29 (12) (2019) 2581–2606.

[10] R. Darleux, B. Lossouarn, J.-F. Deü, Broadband vibration damping of nonperiodic plates by piezoelectric coupling to their electrical analogues, Smart Mater. Struct. 29 (2020) 054001.

[11] G. Gatti, M. Brennan, B. Tang, Some diverse examples of exploiting the beneficial effects of geometric stiffness nonlinearity, Mech. Syst. Signal Process. 125 (2019) 4–20.

[12] D.F. Ledezma-Ramirez, P.E. Tapia-González, N. Ferguson, M.J. Brennan, B. Tang, Recent advances in shock vibration isolation: An overview and future possibilities, Appl. Mech. Rev. 71 (2019) 060802.

[13] A.F. Vakakis, O. Gendelman, Energy pumping in nonlinear mechanical oscillators: Part II - Resonance capture, J. Appl. Mech. 68 (2001) 42–48.

[14] Z. Lu, Z. Wang, Y. Zhou, X. Lu, Nonlinear dissipative devices in structural vibration control: A review, J. Sound Vib. 423 (2018) 18–49.

[15] B. Vaurigaud, A.T. Savadkoohi, C.-H. Lamarque, Targeted energy transfer with parallel nonlinear energy sinks. Part I: Design theory and numerical results, Nonlinear Dynam. 66 (2011) 763–780.

[16] S. Benacchio, A. Malher, J. Boisson, C. Touzé, Design of a magnetic vibration absorber with tunable stiffnesses, Nonlinear Dynam. 85 (2016) 893–911.

[17] V. Iurasov, P.-O. Mattei, Bistable nonlinear damper based on a buckled beam configuration, Nonlinear Dynam. 99 (2020) 1801–1822.

[18] D. Qiu, S. Seguy, M. Paredes, Design criteria for optimally tuned vibro-impact nonlinear energy sink, J. Sound Vib. 442 (2019) 497–513.

[19] B. Zhou, F. Thouverez, D. Lenoir, Essentially nonlinear piezoelectric shunt circuits applied to mistuned bladed disks, J. Sound Vib. 333 (2014) 2520–2542.

[20] T.M.P. Silva, M.A. Clementino, C.D.M. Jr., A. Erturk, An experimentally validated piezoelectric nonlinear energy sink for wideband vibration attenuation, J. Sound Vib. 437 (2018) 68–78.

[21] G. Zhao, G. Raze, A. Paknejad, A. Deraemaeker, G. Kerschen, C. Collette, Active nonlinear energy sink using force feedback under transient regime, Nonlinear Dynam. 102 (2020) 1319–1336.

[22] G. Habib, T. Detroux, R. Viguié, G. Kerschen, Nonlinear generalization of Den Hartog's equal-peak method, Mech. Syst. Signal Process. 52–53 (2015) 17–28.

[23] G. Raze, G. Kerschen, Multimodal vibration damping of nonlinear structures using multiple nonlinear absorbers, Int. J. Non-Linear Mech. 119 (2020) 103308.

[24] P. Soltani, G. Kerschen, The nonlinear piezoelectric tuned vibration absorber, Smart Mater. Struct. 24 (2015) 075015.

[25] B. Lossouarn, J.-F. Deü, G. Kerschen, A fully passive nonlinear piezoelectric vibration absorber, Phil. Trans. R. Soc. A 376 (2018) 20170142.

[26] G. Raze, A. Jadoul, S. Guichaux, V. Broun, G. Kerschen, A digital nonlinear piezoelectric tuned vibration absorber, Smart Mater. Struct. 29 (2020) 015007.

[27] C. Richard, D. Guyomar, D. Audigier, G. Ching, Semi-passive damping using continuous switching of a piezoelectric device, in: Proc. of SPIE Smart Structures and Materials Conference: Passive Damping and Isolation, Vol. 3672, 1999, pp. 104–111.

[28] W.W. Clark, Vibration control with state-switching piezoelectric material, J. Intell. Mater. Syst. Struct. 11 (2000) 263–271.

[29] P. Shivashankar, S. Gopalakrishnan, Review on the use of piezoelectric materials for active vibration, noise, and flow control, Smart Mater. Struct. 29 (2020) 053001.

[30] J. Ducarne, O. Thomas, J.-F. Deü, Structural vibration reduction by switch shunting of piezoelectric elements: modelling and optimization, J. Intell. Mater. Syst. Struct. 21 (8) (2010) 797–816, http://dx.doi.org/10.1177/1045389X10367835.

[31] O. Thomas, A. Lazarus, C. Touzé, A harmonic-based method for computing the stability of periodic oscillations of non-linear structural systems, in: Proceedings of the ASME 2010 International Design Engineering Technical Conferences & Computers and Information in Engineering Conference, IDETC/CIE 2010, Montreal, Canada, 2010.

[32] A. Givois, J.-J. Tan, C. Touzé, O. Thomas, Backbone curves of coupled cubic oscillators in one-to-one internal resonance: bifurcation scenario, measurements and parameter identification, Meccanica 55 (2020) http://dx.doi.org/10.1007/s11012-020-01132-2, 581–503.

[33] S.I. Chang, A.K. Bajaj, C.M. Krousgrill, Non-linear vibrations and chaos in harmonically excited rectangular plates with one-to-one internal resonance, Nonlinear Dynam. 4 (1993) 433–460.

[34] C. Touzé, M. Amabili, Non-linear normal modes for damped geometrically non-linear systems: application to reduced-order modeling of harmonically forced structures, J. Sound Vib. 298 (4–5) (2006) 958–981.

[35] O. Thomas, C. Touzé, Luminais, Non-linear vibrations of free-edge thin spherical shells: experiments on a 1:1:2 internal resonance, Nonlinear Dynam. 49 (1–2) (2007) 259–284, http://dx.doi.org/10.1016/j.ijsolstr.2004.10.028.

[36] A. Chaigne, C. Touzé, O. Thomas, Nonlinear vibrations and chaos in gongs and cymbals, Acoust. Sci. Technol. 26 (5) (2005) 403–409, http://dx.doi.org/10.1250/ast.26.403.

[37] M. Monteil, O. Thomas, C. Touzé, Identification of mode couplings in nonlinear vibrations of the steelpan, Appl. Acoust. 89 (2015) 1–15, http://dx.doi.org/10.1016/j.apacoust.2014.08.008.

[38] K.R. Qalandar, B.S. Strachan, B. Gibson, M. Sharma, A. Ma, S.W. Shaw, K.L. Turner, Frequency division using a micromechanical resonance cascade, Appl. Phys. Lett. 105 (2014) 244103.

[39] J. Yu, K. Asadi, H. Brahmi, H. Cho, S. Nezmi, S. Lee, Frequency stabilization in a MEMS oscillator with 1:2 internal resonance, in: 2019 IEEE International Symposium on Inertial Sensors and Systems (INERTIAL), 2019, pp. 1–4, http://dx.doi.org/10.1109/ISISS.2019.8739695.

[40] D.A. Czaplewski, S. Strachan, O. Shoshani, S.W. Shaw, D. López, Bifurcation diagram and dynamic response of a MEMS resonator with a 1:3 internal resonance, Appl. Phys. Lett. 114 (2019) 254104.

[41] G. Kerschen, M. Peeters, J.C. Golinval, A. F.Vakakis, Nonlinear normal modes, Part I : A useful framework for the structural dynamicist, Mech. Syst. Signal Process. 23 (2009) 170–194.

[42] L. Guillot, A. Lazarus, O. Thomas, C. Vergez, B. Cochelin, A purely frequency based floquet-hill formulation for the efficient stability computation of periodic solutions of ordinary differential systems, J. Comput. Phys. 416 (2020) 109477, http://dx.doi.org/10.1016/j.jcp.2020.109477.

[43] A.G. Haddow, A.D.S. Barr, D.T. Mook, Theoretical and experimental study of modal interaction in a two-degree-of-freedom structure, J. Sound Vib. 97 (3) (1984) 451–473.

[44] R.S. Haxton, A.D.S. Barr, The autoparametric vibration absorber, J. Eng. Ind. 94 (1) (1972) 119–125.

[45] A. Vyas, A.K. Bajaj, A. Raman, Dynamics of structures with wideband autoparametric vibration absorbers: theory, Proc. R. Soc. Lond. A 460 (2004) 1547–1581.

[46] S. Mahmoudkhani, H.S. Meymand, Effects of nonlinear interactions of flexural modes on the performance of a beam autoparametric vibration absorber, J. Vib. Control 26 (7–8) (2019) 459–474.

[47] S.S. Oueini, M.F. Golnaraghi, Experimental implementation of the internal resonance control strategy, J. Sound Vib. 191 (3) (1996) 377–396.

[48] S.S. Oueini, A.H. Nayfeh, M.F. Golnaraghi, A theoretical and experimental implementation of a control method based on saturation, Nonlinear Dynam. 13 (1997) 189–202.

[49] S.S. Oueini, A.H. Nayfeh, J.R. Pratt, A nonlinear vibration absorber for flexible structures, Nonlinear Dynam. 15 (1998) 259–282.

[50] P.F. Pai, B. Wen, A.S. Naser, M.J. Schultz, Structural vibration control using PZT patches and non-linear phenomena, J. Sound Vib. 215 (2) (1998) 273–296.

[51] P.F. Pai, B. Rommel, M.J. Schultz, Dynamics regulation of a skew cantilever plate using PZT patches and saturation phenomenon, J. Intell. Mater. Syst. Struct. 11 (2000) 642–655.

[52] P.F. Pai, M.J. Schultz, A refined nonlinear vibration absorber, Int. J. Mech. Sci. 42 (2000) 537–560.

[53] P.F. Pai, B. Rommel, M.J. Schultz, Non-linear vibration absorbers using higher order internal resonances, J. Sound Vib. 234 (5) (2000) 799–817.

[54] G.S. Agnes, D.J. Inman, Nonlinear piezoelectric vibration absorbers, Smart Mater. Struct. 5 (1996) 704–714.

[55] V. Guillot, A. Givois, M. Colin, O. Thomas, A.T. Savadkoohi, C.-H. Lamarque, Theoretical and experimental investigation of a 1:3 internal resonance in a beam with piezoelectric patches, J. Vib. Control 26 (13–14) (2020) 1119–1132, http://dx.doi.org/10.1177/1077546320910536.

[56] J. Kengne, J.C. Chedjou, G. Kenne, K. Kyamakya, G.H. Kom, Analog circuit implementation and synchronization of a system consisting of a van der Pol oscillator linearly coupled to a duffing oscillator, Nonlinear Dynam. 70 (2012) 2163–2173.

[57] T.M.P. Silva, M.A. Clementino, A. Erturk, C. De Marqui, Equivalent electrical circuit framework for nonlinear and high quality factor piezoelectric structures, Mechatronics 54 (2018) 133–143.

[58] O. Thomas, J.-F. Deü, J. Ducarne, Vibration of an elastic structure with shunted piezoelectric patches: efficient finite-element formulation and electromechanical coupling coefficients, Int. J. Numer. Methods Eng. 80 (2) (2009) 235–268, http://dx.doi.org/10.1002/nme.2632.

[59] M. Berardengo, O. Thomas, C. Giraud-Audine, S. Manzoni, Improved resistive shunt by means of negative capacitance: new circuit, performances and multi-mode control, Smart Mater. Struct. 25 (7) (2016) 075033, http://dx.doi.org/10.1088/0964-1726/25/7/075033.

[60] ANSI/IEEE Std 176-1987, IEEE Standard on Piezoelectricity, The Institute of Electrical and Electronics Engineers, Inc., 1988.

[61] C. Touzé, O. Thomas, A. Chaigne, Hardening/softening behaviour in non-linear oscillations of structural systems using non-linear normal modes, J. Sound Vib. 273 (1–2) (2004) 77–101, http://dx.doi.org/10.1016/j.jsv.2003.04.005.

[62] V. Denis, M. Jossic, C. Giraud-Audine, B. Chomette, A. Renault, O. Thomas, Identification of nonlinear modes using phase-locked-loop experimental continuation and normal form, Mech. Syst. Signal Process. 106 (2018) 430–452, http://dx.doi.org/10.1016/j.ymssp.2018.01.014.

[63] M. Géradin, D. Rixen, Mechanical Vibrations: Theory and Applications to Structural Dynamics, 3rd, J. Wiley & Sons, 2015.

[64] A.H. Nayfeh, D.T. Mook, Nonlinear Oscillations, John Wiley & sons, inc., New-York, 1979.

[65] O. Thomas, C. Touzé, A. Chaigne, Non-linear vibrations of free-edge thin spherical shells: modal interaction rules and 1:1:2 internal resonance, Int. J. Solids Struct. 42 (11–12) (2005) 3339–3373, http://dx.doi.org/10.1016/j.ijsolstr.2004.10.028.

[66] L. Guillot, B. Cochelin, C. Vergez, A taylor series-based continuation method for solutions of dynamical systems, Nonlinear Dynam. 98 (2019) 2827–2845.

[67] L. Guillot, B. Cochelin, C. Vergez, A generic and efficient taylor series-based continuation method using a quadratic recast of smooth nonlinear systems, Int. J. Numer. Methods Eng. 119 (2019) 261–280.

[68] B. Cochelin, M. Medale, Power series analysis as a major breakthrough to improve the efficiency of asymptotic numerical method in the vicinity of bifurcations, J. Comput. Phys. 236 (2013) 594–607.

[69] A.H. Nayfeh, R.A. Raouf, Non-linear oscillations of circular cylindrical shells, Int. J. Solids Struct. 23 (12) (1987) 1625–1638.

[70] J. Ducarne, O. Thomas, J.-F. Deü, Placement and dimension optimization of shunted piezoelectric patches for vibration reduction, J. Sound Vib. 331 (14) (2012) 3286–3303, http://dx.doi.org/10.1016/j.jsv.2012.03.002.

[71] D. Saya, D. Dezest, A.J. Welsh, F. Mathieu, O. Thomas, T. Leïchlé, S. Trolier-McKinstry, L. Nicu, Piezoelectric nanoelectromechanical systems integrating microcontact printed lead zirconate titanate films, J. Micromech. Microeng. 30 (2020) 035004, http://dx.doi.org/10.1088/1361-6439/ab60bf.

[72] A. Sénéchal, O. Thomas, J.-F. Deü, Optimization of shunted piezoelectric patches for vibration reduction of complex structures - Application to a turbojet fan blade, in: Proceedings of the ASME 2010 International Design Engineering Technical Conferences & Computers and Information in Engineering Conference, IDETC/CIE 2010, Montreal, Canada, 2010.

[73] G. Gobat, L. Guillot, A. Frangi, B. Cochelin, C. Touzé, Backbone curves, Neimark-Sacker boundaries and appearance of quasi-periodicity in nonlinear oscillators: Application to 1:2 internal resonance and frequency combs in MEMS, Meccanica 56 (8) (2021) 1937–1969.

[74] A. Renault, O. Thomas, H. Mahé, Numerical antiresonance continuation of structural systems, Mech. Syst. Signal Process. 116 (2019) 963–984, http://dx.doi.org/10.1016/j.ymssp.2018.07.005.

Chapter 3

Experimental investigation of the nonlinear shunt absorber with quadratic nonlinearity

Contenu

3.1 Article presentation

The present chapter solely constitutes of the text of the article entitled by ”A nonlinear piezoelectric shunt absorber with a 2:1 internal resonance: experimental proof of concept” published in ”Smart Materials and Structures (SMS)” journal. The article illustrates the experimental investigation of the absorber presented in chapter 2 to damp the first bending mode of a cantilever beam structure. The article starts with a review of the main results suggested in chapter 2 focusing on the loss of saturation, the antiresonance correction strategy, and the preserved phase locking feature.

Experimental modal analysis is also presented to identify the electro-mechanical modal parameters of the first bending modes necessary to design the circuit. Those parameters are the modal mass, resonance frequency, mechanical damping ratio, piezoelectric coupling factor, and piezoelectric capacitance. The modal analysis relies on the piezoelectric coupling characteristic in which different experimental frequency response functions are measured and fitted with their equivalent ones to determine the unknown parameters.

The nonlinear shunt circuit and its main components are discussed with the nonlinearity generated through an analog multiplier. The electrical parameters used are presented with a focus on the behavior of the synthetic inductor. In addition, the measurement protocol is illustrated, showing the main signals measured throughout the experiment, namely the beam tip velocity and piezoelectric voltage. To validate the energy transfer, the nonlinear frequency responses of the first harmonic of the velocity and the subharmonic of the voltage are obtained using the sine step method with a demodulation procedure both for the amplitudes and the phase angles.

A comparison between the numerical and experimental results is performed with an excellent fitting validating the antiresonance shifting with a constant amplitude and the lockage of the phase γ_1 between the electrical and the mechanical modes at the antiresonance frequency. In addition, the effect of increasing the excitation is illustrated, validating the antiresonance shifting with constant amplitude. The effect of increasing the nonlinear gain is also measured, showing a reduction in the antiresonance amplitude with a shifting similar to the effect of increasing the excitation level. The antiresonance correction proposed in chapter 2 is then tested thanks to the preserved lockage of the relative phase angle γ_1, leading to experimentally preserving the saturation and to a high attenuation level.

The performance of the designed absorber is then compared with that of an optimized linear resonant shunt showing a higher attenuation near the resonance frequency. The main drawback is the limitation of broadband attenuation due to the additional peak presented near the primary resonance. In addition, a quasiperiodic response is observed with the nonlinear absorber near the antiresonance frequency which can be an issue.

3.2 A nonlinear piezoelectric shunt absorber with 2:1 internal resonance: experimental proof of concept

IOP Publishing | Smart Materials and Structures
Smart Mater. Struct. 31 (2022) 035006 (18pp) | https://doi.org/10.1088/1361-665X/ac4ab5

A nonlinear piezoelectric shunt absorber with 2:1 internal resonance: experimental proof of concept

Zein Alabidin Shami[1], **Christophe Giraud-Audine**[2] and **Olivier Thomas**[1],*

[1] Arts et Metiers Institute of Technology, LISPEN, HESAM Université, F-59000 Lille, France
[2] Arts et Metiers Institute of Technology, L2EP, HESAM Université, Univ. Lille, Centrale Lille, HEI, F-59000 Lille, France

E-mail: olivier.thomas@ensam.eu

Received 25 September 2021, revised 20 December 2021
Accepted for publication 10 January 2022
Published 28 January 2022

Abstract

An experimental proof of concept of a new semi-passive nonlinear piezoelectric shunt absorber, introduced theoretically in a companion article, is presented in this work. This absorber is obtained by connecting, through a piezoelectric transducer, an elastic structure to a resonant circuit that includes a quadratic nonlinearity. This nonlinearity is obtained by including in the circuit a voltage source proportional to the square of the voltage across the piezoelectric transducer, thanks to an analog multiplier circuit. Then, by tuning the electric resonance of the circuit to half the value of one of the resonances of the elastic structure, a two-to-one internal resonance is at hand. As a result, a strong energy transfer occurs from the mechanical mode to be attenuated to the electrical mode of the shunt, leading to two essential features: a nonlinear antiresonance in place of the mechanical resonance and an amplitude saturation. Namely, the amplitude of the elastic structure oscillations at the antiresonance becomes, above a given threshold, independent of the forcing level, contrary to a classical linear resonant shunt. This paper presents the experimental setup, the designed nonlinear shunt circuit and the main experimental results.

Keywords: nonlinear piezoelectric shunt, vibration attenuation, 2:1 internal resonance, energy transfer, saturation phenomenon

(Some figures may appear in colour only in the online journal)

1. Introduction

Mechanical structures used in industrial applications are often submitted to high levels of vibration. This could lead to large amounts of stress, fatigue, and noise, especially for lightweight structures, reducing their life cycle and the comfort of their users. This article proposes the experimental proof of concept of an original nonlinear piezoelectric shunt vibration absorber, theoretically introduced in [1], and based on an intentional two-to-one internal resonance between a mode of the mechanical structure and a nonlinear electrical oscillator.

Passive dynamical vibrations absorbers were the first to be designed, such as Lanchester [2] or Frahm dampers [3]. They consist of adding inertial, damping, and stiffness components to the primary structure, organized so that their vibrations counteract or dissipate those of the primary structure. Though still well used in many applications, researchers began developing in the early 1990s electromechanical analogs of those mechanical dampers. The principle is to couple the structure vibrations to an electrical circuit thanks to an electromechanical transducer. The circuit, usually called a shunt, can be designed passive, active, or semi-passive in the case

---

[*] Author to whom any correspondence should be addressed.

of supplied electronic components such as operational amplifiers. Since piezoelectric transduction was first proposed in the pioneering work [4], electromagnetic transduction has also been investigated (see [5] and reference therein).

Most of the shunts strategies published until now are linear, which means that the electronic circuit is a combination of inductances, resistances, and capacitances, the electric analogs of mechanical inertia, viscous damper, and stiffness. They can be devoted to the resonance reduction of a single mode, with an analog of Frahm and Lanchester dampers (see e.g. [6]), possibly enhanced by negative capacitances [7, 8]. They can also be used to create a frequency adaptive antiresonance to filter a monoharmonic excitation signal [9]. Among others, one can design a shunt with an electronic network as an electromechanical analog of the mechanical structure, to achieve broadband vibration damping (see e.g. [10]). Many other designs have been proposed, the interested reader being redirected to recent review papers on the subject [11, 12].

On the contrary to the above cited linear shunts, nonlinearities can be introduced intentionally in the vibration control device to benefit from particular dynamical phenomena without counterparts in the linear theory. Examples of the use of geometrically nonlinear stiffnesses are reviewed in [13, 14]. Then, in the field of nonlinear absorbers, several strategies have been proposed, that can be gathered in four main families. For each family, the present text considers solutions based on piezoelectric control with experiments, the interested reader being redirected to [1] for a broader literature review. The first family is related to nonlinear energy sinks (NES), which take the benefit of an absorber with strong nonlinearities, into which the energy is transferred and trapped. To our knowledge, only two experimental studies propose a NES that includes a piezoelectric transduction: [15], with an analog electronics that includes multipliers and [16], in an active control philosophy with force feedback. The second family is related to nonlinear tuned vibration absorber (NLTVA), introduced in [17]. They are designed with nonlinearities in the absorber mirroring those of the primary system, leading to self-adaptation to the host structure's dynamics amplitude, contrary to the linear tuned absorbers. Such nonlinear vibration absorbers were extended to piezoelectric shunt circuits theoretically in [18] and experimentally validated in [19–21] with passive electronic components. The third family is related to the so called synchronized switch damping techniques, proposed in [22, 23], that was addressed in many theoretical and experimental studies since (see the recent review [12]).

A fourth family, directly related to our present work, is based on the intentional use of internal resonances. In a nonlinear system, if the ratio of two modal frequencies ω_k and ω_l is a rational number (i.e. $\omega_\mathrm{k}/\omega_\mathrm{l} \simeq n/m$ with $n, m \in \mathbb{N}^*$), a strong coupling between the two corresponding modes is likely to occur, enabling to transfer energy from one mode to the other. As explained in [1], the present article focus on the intentional use of a 2:1 internal resonance, that is activated by the presence of quadratic nonlinearities in the system, leading to an energy transfer from the driven mode (of natural frequency ω_2), to a mode tuned at half this frequency (of natural frequency $\omega_1 \simeq \omega_2/2$). This leads to two important features: (a) a significant amplitude reduction of the resonance of the driven mode, which is replaced by a nonlinear antiresonance, and (b) a saturation phenomenon, that leads to an amplitude of the driven mode independent of the excitation level. Using the features of a 2:1 internal resonance for vibration reduction purposes has been illustrated in some works in the past, and we focus here only on experimental studies. For example, an analog electronic circuit made of multipliers was proposed in [24, 25] to damp the vibration of a plant composed of a beam connected to the shaft of a DC motor, by tuning the natural frequency of the controller to half that of the beam. In [26], the same technique was used, but with piezoelectric actuators. Moreover, the same method has been applied on different structures like a truss in [27] and triangular panels [28] using a real-time digital controller coupled to the elastic structure with quadratic nonlinearities and tuned to have the saturation phenomenon.

The main originality of our work is to use the particular features of a 2:1 internal resonance in a semi-passive way using a piezoelectric shunt circuit. We proposed a complete theoretical analysis to design such an absorber in a previous work [1], in which a detailed guideline for the absorber design has been given. In this work, an experimental analysis based on the previous theoretical results is proposed, by applying the vibration absorber to a cantilever beam structure to damp its first bending mode. The outline of this paper is as follows: in section 2, a brief theoretical analysis, emphasizing the main features of the designed absorber, is given. In section 3, the experimental setup and protocol, in addition to the nonlinear shunt circuit design, are shown. Finally, section 4 is devoted to experimental results and the absorber's performance.

2. Theory

2.1. Governing equations

In this section, a summary of the main equations that govern the electromechanical system is illustrated. The full theoretical model with numerical and analytical results is outlined in our previous paper [1], and only the main points are recalled here. We consider an arbitrary elastic structure subjected to an external excitation and connected to a nonlinear shunt circuit via a piezoelectric (PE) patch as shown in figure 1. The displacement vector $\boldsymbol{u}(\boldsymbol{x},t)$ at any point $\boldsymbol{x}$ of the structure at date t is expanded on a given linear modes $\phi_i(\boldsymbol{x})$ of the structure in short circuit. One obtains:

$$\boldsymbol{u}(\boldsymbol{x},t) = \phi_i(\boldsymbol{x}) q_i(t), \tag{1}$$

where $q_i(t)$ is the ith modal coordinate, that verifies [1]:

$$\ddot{q}_i + 2\xi_i\hat{\omega}_i\dot{q}_i + \hat{\omega}_i^2 q_i + \frac{\theta_i}{m_i C_\mathrm{pi}} Q = \frac{F_i}{m_i}\cos\Omega t, \tag{2a}$$

$$\ddot{Q} + 2\xi_e\omega_e\dot{Q} + \omega_e^2 Q + \frac{\theta_i}{L C_\mathrm{pi}} q_i + \frac{V_\mathrm{nl}}{L} = 0. \tag{2b}$$

In the above equations, $Q(t)$ is the electric charge in one of the electrodes of the PE patch and (m_i, ξ_i, $\hat{\omega}_i$, F_i, θ_i) are

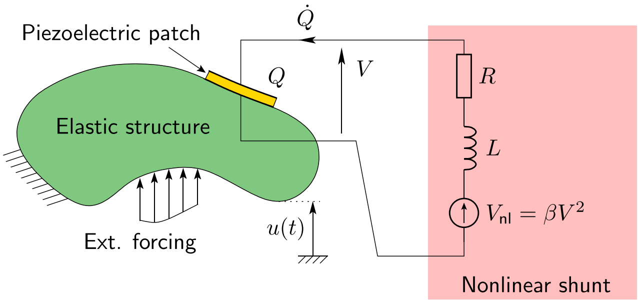

Figure 1. Nonlinear shunt principle.

respectively the modal mass, damping, natural frequency in open circuit ($Q = 0$), forcing and piezoelectric coupling coefficient of the ith mode. $C_{\mathrm{p}i}$ is the effective capacitance of the piezoelectric patch [7], and the electrical natural frequency and damping factor are defined by:

$$\omega_{\mathrm{e}} = \frac{1}{\sqrt{LC_{\mathrm{p}i}}}, \quad \xi_e = \frac{R}{2}\sqrt{\frac{C_{\mathrm{p}i}}{L}}, \tag{3}$$

where (R,L) are respectively the resistance and the inductance of the electric circuit. $V_{\mathrm{nl}}(t)$ represents the nonlinear voltage source added to the shunt circuit, that is chosen to include quadratic nonlinearities to activate the 2:1 internal resonance. In this study, $V_{\mathrm{nl}}(t)$ is taken to be proportional to the square of the voltage $V(t)$ across the piezoelectric patch, by a constant gain β, as shown in figure 1. Another choice could be a nonlinear voltage proportional to the square of the electric charge in the PE patch electrode (i.e. $V_{\mathrm{nl}} = \beta Q^2$). As shown in [1], this latter choice would lead to a huge value of β (of the order of 10^{15} V/C^2) to achieve the absorber's design conditions, unrealistic in practice. One has thus:

$$V_{\mathrm{nl}} = \beta V^2, \quad V = \frac{1}{C_{\mathrm{p}i}}\left(Q + \theta_i q_i\right), \tag{4}$$

where the second equation is the classical constitutive law of the PE patch [1]. We also define the dimensionless electromechanical modal coupling factor (EMMCF) of the ith mode as [29]:

$$k_i^2 = \frac{\hat{\omega}_i^2 - \check{\omega}_i^2}{\hat{\omega}_i^2} = \frac{\theta_i^2}{\hat{\omega}_i^2 C_{\mathrm{p}i} m_i}, \tag{5}$$

with $\check{\omega}_i$ the natural frequency in short circuit ($V = 0$).

To simplify the writing of the governing equations (2*a*) and (2*b*), we define the following parameters:

$$\tau = \hat{\omega}_i t, \quad \bar{q}_i = \sqrt{m_i} q_i, \quad \bar{Q} = \sqrt{L} Q, \quad r_i = \frac{\omega_e}{\hat{\omega}_i}, \% \quad \delta_i = k_i r_i, \tag{6a}$$

$$\bar{F}_i = \frac{F_i}{\hat{\omega}_i^2 \sqrt{m_i}} \quad \bar{V}_{\mathrm{nl}} = \frac{V_{\mathrm{nl}}}{\hat{\omega}_i^2 \sqrt{L}} \quad \bar{\Omega} = \frac{\Omega}{\hat{\omega}_i} \tag{6b}$$

to obtain a system in term of $\hat{q}_i$ and $\hat{Q}$ with symmetric coupling terms:

$$\ddot{\bar{q}}_i + 2\xi_i \dot{\bar{q}}_i + \bar{q}_i + k_i r_i \bar{Q} = \bar{F}_i \cos \bar{\Omega}\tau, \tag{7a}$$

$$\ddot{\bar{Q}} + 2\xi_e r_i \dot{\bar{Q}} + r_i^2 \bar{Q} + k_i r_i \bar{q}_i + \bar{V}_{\mathrm{nl}} = 0, \tag{7b}$$

where the derivatives in equation (7) are with respect to the dimensionless time τ. Note that the unknowns $(\bar{q}_i, \bar{Q})$ share the same unit ($\mathrm{m\,kg}^{1/2}$). Moreover, an important parameter is r_i, the ratio between the electrical natural frequency (linked to the resonant electric circuit) and the mechanical natural frequency, that will be chosen close to 0.5 to achieve the $2:1$ internal resonance.

Since equations (2*a*), (2*b*) or (7*a*), (7*b*) are linearly coupled because of the piezoelectric coupling, this latter system is diagonalized by further expanding the unknowns $(\bar{q}_i, \bar{Q})$ on the electromechanical modal basis, constituted of two modes $\mathbf{\Psi}_k$, $k = 1, 2$ such that:

$$\mathbf{\Psi}_1 = \begin{pmatrix} -\varepsilon \\ 1 \end{pmatrix}, \quad \mathbf{\Psi}_2 = \begin{pmatrix} 1 \\ \varepsilon \end{pmatrix}, \tag{8}$$

with

$$\varepsilon = \frac{2k_i r_i}{1 - r_i^2 + \sqrt{\Delta}}, \tag{9}$$

and the associated eigenfrequencies:

$$\omega_1^2 = \frac{1 + r_i^2 - \sqrt{\Delta}}{2}, \quad \omega_2^2 = \frac{1 + r_i^2 + \sqrt{\Delta}}{2}, \tag{10}$$

with $\Delta = (1 - r_i^2)^2 + 4k_i^2 r_i^2$. The modal expansion reads:

$$\begin{pmatrix} \bar{q}_i(\tau) \\ \bar{Q}(\tau) \end{pmatrix} = \sum_{k=1}^{2} \mathbf{\Psi}_k x_k(\tau) = \begin{pmatrix} -\varepsilon x_1(\tau) + x_2(\tau) \\ x_1(\tau) + \varepsilon x_2(\tau) \end{pmatrix}. \tag{11}$$

Because the electromechanical coupling is often small ($k_i < 0.2$), ε is also small (of the same order of magnitude) and the two electromechanical modes are very close to a purely electrical mode for $\mathbf{\Psi}_1$ ($x_1 \simeq \bar{Q}$) and a purely mechanical mode for $\mathbf{\Psi}_2$ ($x_2 \simeq \bar{q}_i$). The same rule applies to the eigenfrequencies ω_1 and ω_2, which are close to the dimensionless uncoupled natural frequencies $\omega_e/\hat{\omega}_i = r_i$ and $\hat{\omega}_i/\hat{\omega}_i = 1$. Precisely, because of the small positive term $4k_i^2 r_i^2$ in Δ, (ω_1, ω_2) are slightly out of the frequency band $[r_i, 1]$ ($\omega_1 \lesssim r_i$; $\omega_2 \gtrsim 1$). Consequently, the mechanical resonance of the system appears at a dimensioned frequency $\tilde{\omega}_i = \omega_2 \hat{\omega}_i$, which is slightly above the open circuit frequency $\hat{\omega}_i$. Moreover, the tuning of the electrical mode at almost half the frequency of the mechanical mode to achieve the 2:1 internal resonance, must be prescribed on the electromechanical natural frequency ratio ω_1/ω_2, which is slightly lower than $r_i = \omega_e/\hat{\omega}_i$. This is quantitatively illustrated in figure 2, which shows that for a targeted value of ω_1/ω_2, r_i must be chosen slightly larger (for instance, $r_i = 0.543$ for $\omega_1/\omega_2 = 0.5$ and $k_i = 0.2$).

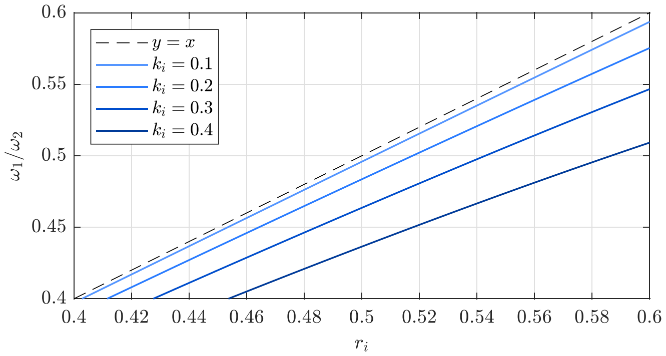

Figure 2. Electromechanical natural frequency ratio ω_1/ω_2 (from equations (10)) as a function of the frequency ratio r_i, for various values of the EMMCF k_i, as specified.

After modal expansion and using the definition (4) of V_{nl}, one obtains [1]:

$$\ddot{x}_1 + 2\mu_1\dot{x}_1 + \omega_1^2 x_1 + \Lambda_1 x_1^2 + \Lambda_2 x_1 x_2 + \Lambda_3 x_2^2 = f_1 \cos\bar{\Omega}\tau, \tag{12a}$$

$$\ddot{x}_2 + 2\mu_2\dot{x}_2 + \omega_2^2 x_2 + \Lambda_4 x_1^2 + \Lambda_5 x_1 x_2 + \Lambda_6 x_2^2 = f_2 \cos\bar{\Omega}\tau. \tag{12b}$$

In the above system, we assume that the modal mass is such that $1+\varepsilon^2 \approx 1$ since $\varepsilon \ll 1$ and that the non-diagonal damping terms are neglected since they are small and have thus a negligible effect on the dynamics [30]. The expressions of the damping terms μ_1 and μ_2, the nonlinear coefficients Λ_k, and the modal forcing terms f_1 and f_2 are given in [1]. This last system (12*a*) and (12*b*) is at the basis of the theoretical analysis of [1] since it is the canonical system to study the 2:1 internal resonance and its dynamical effects (nonlinear antiresonance and saturation phenomenon), as recalled in the following.

2.2. Typical response and saturation phenomenon

To illustrate the main features of the 2:1 internal resonance used for our absorber design, a first order solution of system (12*a*) and (12*b*), in the case of the 2:1 internal resonance ($\omega_2 \approx 2\omega_1$), can be written [1, 31]:

$$x_1(\tau) = a_1 \cos\left(\frac{\bar{\Omega}}{2}\tau - \frac{\gamma_1+\gamma_2}{2}\right), x_2(\tau) = a_2\cos\left(\bar{\Omega}\tau - \gamma_2\right), \tag{13}$$

where a_1 and a_2 are the amplitudes, γ_2 is the phase angle of $x_2(\tau)$, and γ_1 represents the relative phase angle between $x_1(\tau)$ and $x_2(\tau)$. The closed-form expressions of the amplitudes and phase angles (obtained with a first order multiple scale, MSM), in addition to a detailed theoretical study, can be found in [1]. A typical example is illustrated in figure 3. It shows the response of amplitudes a_1 and a_2 with respect to the detuning $\sigma_1 = \bar{\Omega} - \omega_2$ for different excitation levels. Two main features are visible:

- there exists a threshold force for the excitation f_2 above which the linear response enters an instability region (shaded in blue). In this region, the energy transfer from the high to low-frequency modes occurs, and the linear response loses its stability. This activates the response of a_1, which increases with the excitation, while a_2 tends to have a *kind of antiresonance* in place of the linear resonance frequency (see figure 3(a));
- focusing on the amplitudes at the resonance frequency (a_1^* and a_2^*), it can be observed in figure 3(b) that a_2^* becomes independent of the excitation level, a feature called a *saturation phenomenon*, whereas a_1^* keeps increasing. Note that the same analysis could be drawn at any other frequency that lies in the frequency range of the instability region since the a_2 curve is independent of f_2.

Another major feature of this system is related to phase γ_1. The analytical results suggest that γ_1 is monotonic as a function of the excitation frequency Ω, independent of the excitation level f_2, and *always locked at a value of* $3\pi/2\,[2\pi]$ at the antiresonance frequency ($[2\pi]$ means modulo 2π).

2.3. Response in the physical space

Figure 3 and equations (12*a*) and (12*b*) are related to the electromechanical coordinates $x_1(\tau)$ and $x_2(\tau)$. To go back to the physical coordinates (the mechanical displacement and the electric charge), the modal transform of equation (11) is used to write:

$$\boldsymbol{u}(t) = \frac{\boldsymbol{\Phi}_i}{\sqrt{m_i}}\left[-\varepsilon\,\underbrace{a_1\cos\left(\frac{\Omega}{2}t - \frac{\gamma_1+\gamma_2}{2}\right)}_{x_1(t)} + \underbrace{a_2\cos\left(\Omega t - \gamma_2\right)}_{x_2(t)}\right], \tag{14a}$$

$$Q(t) = \frac{1}{\sqrt{L}}\left[\underbrace{a_1\cos\left(\frac{\Omega}{2}t - \frac{\gamma_1+\gamma_2}{2}\right)}_{x_1(t)} + \varepsilon\,\underbrace{a_2\cos\left(\Omega t - \gamma_2\right)}_{x_2(t)}\right]. \tag{14b}$$

Consequently, $\boldsymbol{u}(t)$ and $Q(t)$ are mainly composed of two harmonics, at $\Omega/2$ (harmonic H1/2) and at Ω (harmonic H1). Because of the small value of ε, the leading harmonics in the response of $\boldsymbol{u}(t)$ and $Q(t)$ are, respectively, H1 and H1/2, so that, at the antiresonance, the energy is transferred from the mechanical mode to the electrical mode and from the frequency Ω to its subharmonic $\Omega/2$.

2.4. Effect of nonresonant terms

The first order analytical solution that leads to figure 3 (using the multiple scale method, MSM) naturally neglects the nonresonant nonlinear terms of system (12*a*) and (12*b*), namely the terms of coefficients Λ_1, Λ_3, Λ_5, Λ_6. Indeed, the skeleton of the dynamics under 1:2 internal resonance is constituted by the resonant terms (of coefs. Λ_2 and Λ_4) which are responsible

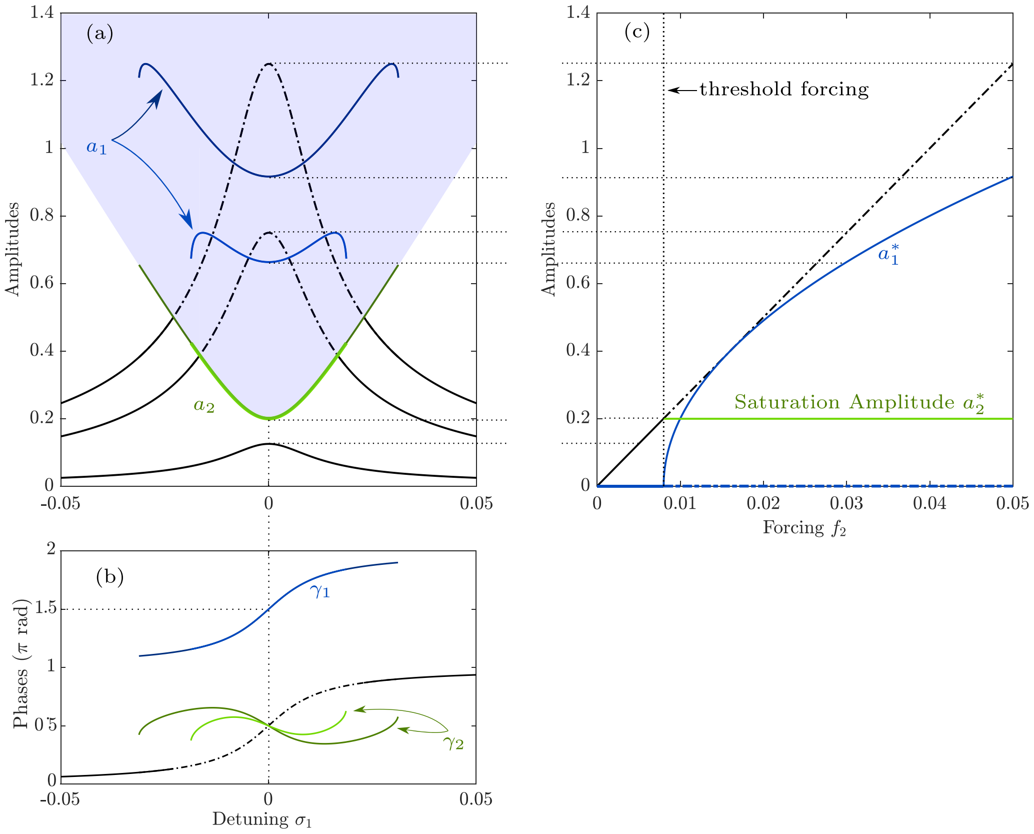

Figure 3. Typical response of the amplitudes a_1 and a_2 and the phases γ_1 and γ_2, stemming from the first order multiple scale solution of system (12*a*) and (12*b*), for $\omega_2 = 2\,\omega_1$ and by neglecting the nonresonant terms, from [1]. The numerical values are $\Lambda_2 = \Lambda_4 = 0.1$, $\mu_1 = 0.005$, $\mu_1 = 0.01$. (a) and (b) show respectively the amplitude and phase response with respect to the detuning σ_1 for values of the forcing f_2 ($f_2 \in \{0.005; 0.03; 0.05\}$). (c) amplitude response at the resonance frequency ($\sigma_1 = 0$) with respect to the excitation level f_2. In the plots, the linear responses of a_2 and γ_2 are plotted in black. The solid and the dashed-dotted lines denote respectively the stable and the unstable solutions.

for the strong coupling between the modes (see [1, 31, 32] for the analytical solution and [33, 34] for details about resonant terms). However, it is shown in [1] that in the present case of a nonlinear shunt, the order of magnitude of Λ_1 is larger than the one of Λ_2 and Λ_4, leading to an unusual and major effect of the corresponding non-resonant term, which quantitatively modifies the ideal response of figure 3.

This is illustrated in figure 4 in which a numerical solution of equations (2*a*) and (2*b*) (obtained with the continuation software Manlab [35, 36]) is shown. To be more precise, we considered the case of the first bending mode of the cantilever beam structure shown in figure 6, with the displacement $u(t)$ considered at the beam tip ($u(t) = q_i(t)$ with a mode shape scaled to 1). The modal parameters used in the numerical simulations are the ones found experimentally and gathered in table.

By observing the physical response of the amplitudes corresponding to the H1 and H1/2 harmonics of the displacement and charge (u_{H1} and $Q_{H/12}$), shown in figure 4, and by comparison with the typical response illustrated in figure 3, the effect of the non-resonant terms can be inferred [1]:

- the antiresonance shifts to the low frequencies with increasing excitation level, violating the saturation phenomenon;
- although the antiresonance is shifting, its amplitude remains constant at a saturation amplitude u_{H1}^*, which is the same as a_2^* analytically obtained with the MSM;
- the phase angle γ_1 is kept locked at $3\pi/2$ at the antiresonance point;
- a break in the response symmetry is observed, leading to another peak to the right of the resonance peak and the appearance of a softening behavior, as it can be seen in the charge response.

The main aim of this work is to exploit the saturation phenomenon, which is broken because of the non-resonant terms intrinsically related to the nonlinear shunt. To correct this, we proposed an antiresonance correction (AR correction) technique, that consists in locking the antiresonance by choosing the proper value of the ratio r_i for each excitation level *to counter-balance* the shifting observed in figure 4. As shown in detail in [1], this can be simulated by a numerical continuation of the system (2*a*) and (2*b*) using Manlab, to obtain the amplitude of u_{H1} as a function of r_i for a certain excitation level and with a prescribed driving frequency equal to the resonance frequency shown in figure 4 ($\tilde{\omega}_1 = 37.7$ Hz). Then, the value of r_i where u_{H1} achieves its minimum value is the required value to lock the antiresonance at the resonance frequency.

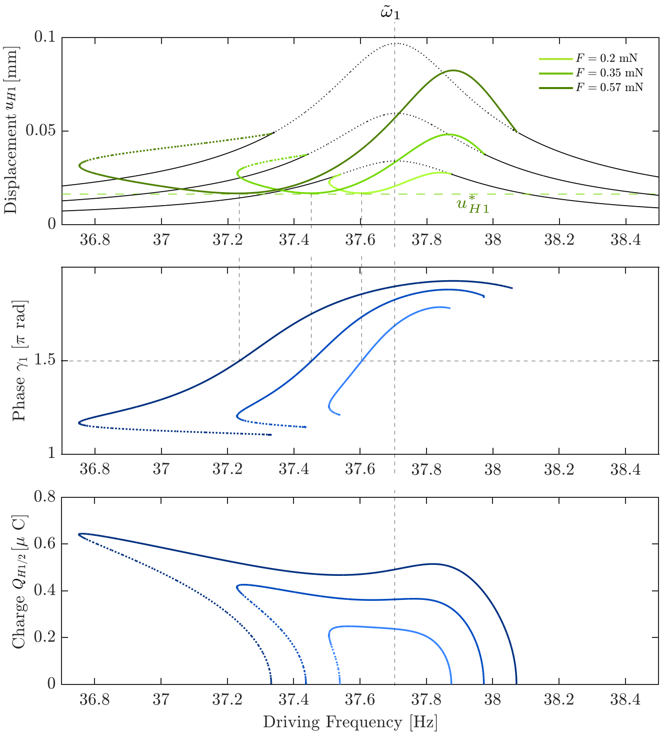

Figure 4. Frequency response of the beam tip displacement first harmonic u_{H1} amplitude, the charge $Q_{\mathrm{H1/2}}$ subharmonic and the phase γ_1, obtained by solving system (2*a*) and (2*b*) using Manlab for several excitation levels. The numerical values are $\beta = 0.012$, $r_i = 0.52$, $\xi_e = 0.002$, and the mechanical damping coefficient is $\xi_1 = 0.005$. The displacement linear response is plotted in black. The solid and dotted lines denote, respectively, the stable and the unstable solutions.

Following the AR correction, the response of u_{H1} shown in figure 4 is replaced by the one shown in figure 5(a) where it clearly shows that the antiresonance is locked at $\tilde{\omega}_1$. One can note the appearance of a quasi-periodic solution (QP) for $F = 0.57$ mN. Also, figure 5(b) shows the amplitude of u^*_{H1} with respect to the excitation level where one can observe that the proposed AR correction preserves the saturation phenomenon.

Experimentally, the AR correction will be performed analogously, using the preserved feature of $\gamma_1 = 3\pi/2$ at the antiresonance point. Namely, for a certain excitation level and by prescribing the driving frequency at $\tilde{\omega}_i$, the required value of r_i, which is controlled by the inductance in the circuit, is the one that locks γ_1 at $3\,\pi/2$. This will be illustrated in detail in section 4.4.

2.5. Summary on the theoretical results

The main conclusions that can be drawn from the above theoretical analysis in addition to the analysis done in detail in our theoretical paper [1] are as follows:

- Connecting the proposed nonlinear shunt circuit to an arbitrary structure via a PE patch leads to an electromechanical system governed by a fully quadratic nonlinear system (12*a*) and (12*b*). By tuning $\hat{\omega}_i \approx 2\omega_e$, a 2:1 internal resonance occurs, leading to an energy transfer from the mechanical mode to be attenuated to the electrical mode designated by the shunt circuit.
- The saturation phenomenon is violated as seen in figure 4. To preserve this phenomenon, we propose an antiresonance correction by slightly tuning the value of r_i for each excitation level, by locking the phase γ_1 at $3\pi/2$.

3. Experimental details

3.1. Structure under test

The experimental tests were conducted on a cantilever beam with two PIC 151 piezoelectric (PE) patches symmetrically glued on the two faces of a stainless steel beam, as shown in figure 6. The nonlinear shunt circuit is connected to the structure with the PE patches in series and with opposite polarizations to couple the electric shunt circuit to the bending of the beam [37]. A contactless electromagnetic actuator composed of a fixed coil and a magnet attached to the structure tip is used to generate an electromagnetic force by inducing a current in the coil. In [38], a detailed design has been illustrated for such a coil-magnet system and a linear relationship has been found between the current $I(t)$ induced in the coil and the resulting forcing $F(t)$:

$$F(t) = \alpha I(t), \tag{15}$$

where α is a constant.

3.2. Experimental modal analysis

Before conducting the experiments with the nonlinear shunt circuit, an experimental modal analysis was performed to identify the parameters of our model of the electromechanical system under test. The experimental modal analysis shown here consists of utilizing the benefit of the piezoelectric coupling between the mechanical and electrical domains (i.e. the structure and the shunt circuit). Focusing on a particular mechanical mode of the structure (the ith), we normalize its mode shape with its value at the tip x_t of the beam, such that $\phi_i(x_t) = 1$. Considering the transverse displacement $u(t)$ of the beam at its tip and a colocalized point forcing $F(t) = F_0 \cos \Omega t$ (see figure 6), equation (1) shows that $u(t) \equiv q_i(t)$ and $F_i = F_0$ in equation (2*a*). We then consider two sets of experiments:

- a mechanical forcing with the PE patches either in short ($V = 0$) or open ($Q = 0$) circuit, leading to the two frequency response functions (FRFs) (from equations (2*a*), (2*b*) and (4)):

$$H_1(\Omega) = \left.\frac{\overset{\circ}{u}}{\overset{\circ}{I}}\right|_{V=0} = \frac{\gamma_i}{\Omega^2 - \tilde{\omega}_i^2 + 2j\xi_i\tilde{\omega}_i\Omega},$$
$$\hat{H}_1(\Omega) = \left.\frac{\overset{\circ}{u}}{\overset{\circ}{I}}\right|_{Q=0} = \frac{\gamma_i}{\Omega^2 - \hat{\omega}_i^2 + 2j\xi_i\hat{\omega}_i\Omega}. \tag{16}$$

Notice that the difference between H_1 and $\hat{H}_1$ is the short/open natural circuit frequencies $\tilde{\omega}_i$ or $\hat{\omega}_i$.

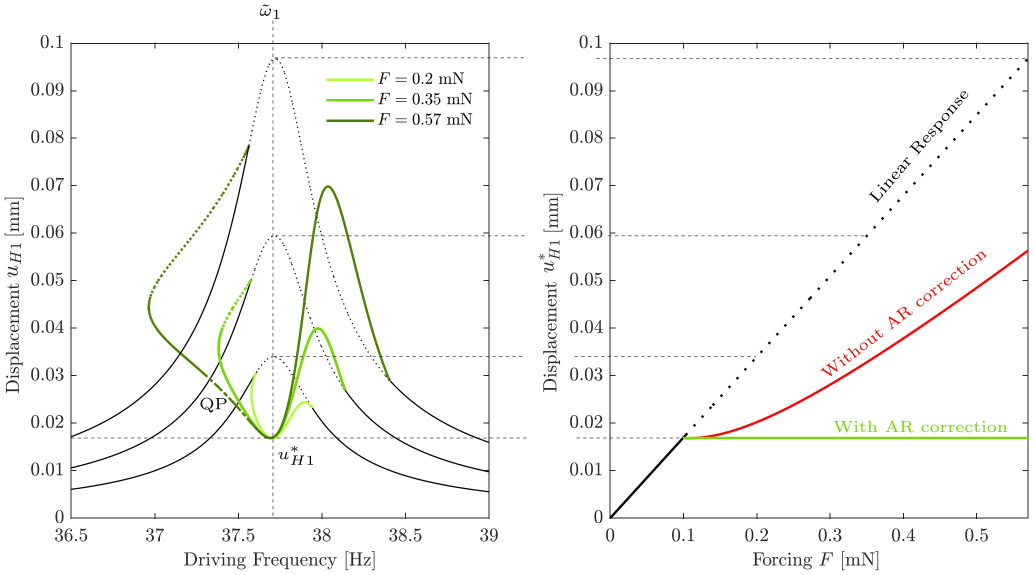

Figure 5. (a) Frequency response of the first harmonic amplitude of the beam tip displacement u_{H1}, estimated by solving system (2*a*) and (2*b*) using Manlab, for several excitation levels and with AR correction. (b) First harmonic amplitude of the beam tip displacement at the resonance frequency u^*_{H1} with respect to the excitation level, with and without AR correction. The numerical values are $\beta = 0.012$ and $\xi_1 = 0.005$. The displacement linear response is plotted in black. The solid and dotted/dashed lines denote, respectively, the stable and unstable solutions. QP refers to a quasi-periodic response, obtained after a loss of stability due to Neimark-Sacker bifurcations.

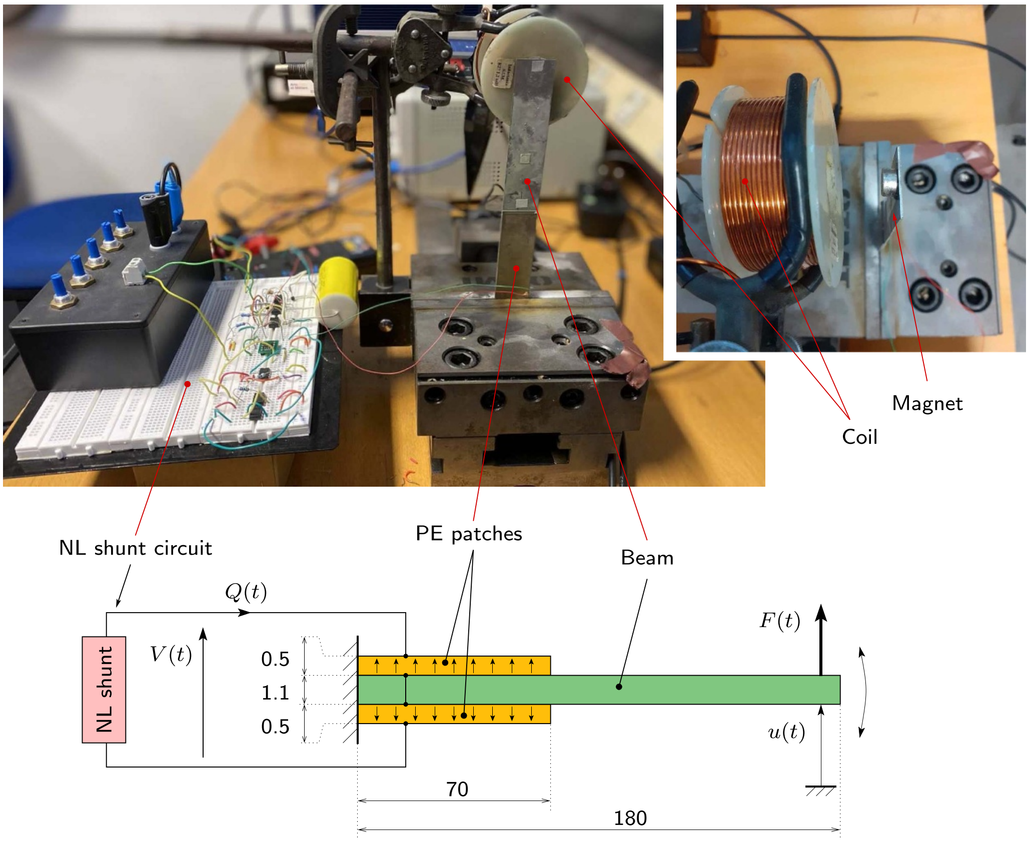

Figure 6. Experimental setup. Dimensions are in mm. The width of the beam and PE patches is 30.5 mm.

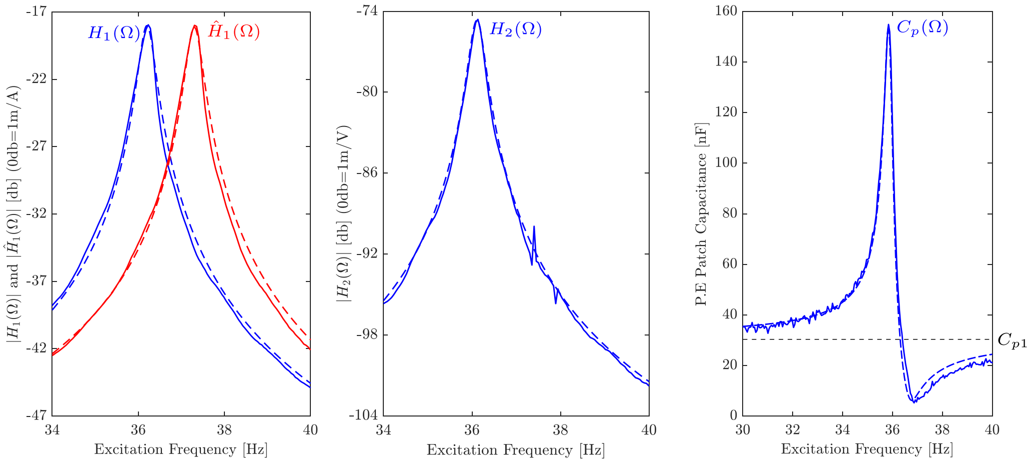

Figure 7. Fitting between experimental and analytical FRFs. The solid and dashed lines depict the experimental and the analytical results, respectively.

Table 1. Electro-mechanical modal parameters of the first bending mode of the cantilever beam (subscript $i = 1$).

Parameters	$\omega_1/(2\pi)$ (Hz)	$\hat{\omega}_1/(2\pi)$ (Hz)	$\xi_1(\%)$	k_1	θ_1(mN V^{-1})	$m_1[g]$	α (N/A)	C_{p1} (nF)
Value	36.6	37.51	0.5	0.20	0.8	8.8	0.6	32.45

- an electrical forcing by prescribing the voltage $V(t)$ without mechanical forcing, that conducts to define:

$$H_2(\Omega) = \left.\frac{\mathring{u}}{\mathring{V}}\right|_{F=0} = -\frac{\lambda_i}{\Omega^2 - \breve{\omega}_i^2 + 2j\xi_i\hat{\omega}_i\Omega},$$
$$C(\Omega) = \left.\frac{\mathring{Q}}{\mathring{V}}\right|_{F=0} = C_{\mathrm{p}i} + \frac{\delta_i}{\Omega^2 - \breve{\omega}_i^2 + 2j\xi_i\hat{\omega}_i\Omega}. \qquad (17)$$

In the above equations, $\mathring{\bullet}(\Omega)$ is the Fourier transform of $\bullet(t)$ and the amplitude constants reads:

$$\gamma_i = \frac{\alpha}{m_i}, \quad \lambda_i = \frac{\theta_i}{m_i}, \quad \delta_i = \frac{\theta_i^2}{m_i}. \qquad (18)$$

By fitting the FRFs of equations (16) and (17) on the experiments, it is possible to estimate the values of the unknown parameters of the ith mode of the structure: $\breve{\omega}_i$, $\hat{\omega}_i$, ξ_i, m_i, θ_i, $C_{\mathrm{p}i}$ and α, as well as the EMMCF k_i with equation (5). Notice that in the first sets of experiments, one could also measure the FRF $\mathring{Q}/\mathring{F}$ (with $\mathring{F} = \alpha\mathring{I}$), which is theoretically equal to H_2 in the second step of experiments (following equations (2*a*) and (2*b*), which is also a consequence of the Maxwell-Betti reciprocity theorem). This could give another set of measurements to improve the parameter estimation because of the redundancy. However, it was not possible to measure Q and I at the same time, since we had only one available current probe in the laboratory.

In practice, we estimated the parameters of the first mode of the experimental beam. We measured the FRFs with a chirp signal as input. For the mechanical forcing, a Brüel & Kjær 2719 power amplifier connected to the coil was used; for the electrical forcing, we used a TREK PZD700A piezoelectric amplifier. In both cases, a Polytec OFV-505 vibrometer measured the velocity at the tip of the beam, and a PHILIPS PM 9355 precision current clamped was used to measure the current intensity, either in the coil ($I(t)$) for the first set of experiments, or in the piezoelectric circuit to obtain the charge $Q(t)$, for the second sets of experiments. The piezoelectric voltage was obtained with the voltage monitor of the TREK amplifier. A M+P international analyzer was used to generate the input signal and compute the FRFs.

Figure 7 shows the experimental FRFs and the obtained fitting, that directly give the open and short circuit frequencies (ω_1 and $\hat{\omega}_1$), the damping coefficient ξ_1 and the effective capacitance $C_{\mathrm{p}1}$. The gains γ_1, λ_1, and δ_1 are also determined directly and used to estimate the other modal parameters: the modal mass m_1, the coupling coefficient θ_1 and the mechanical forcing constant α as follows: $\theta_1 = \delta_1/\lambda_1 \Rightarrow m_1 = \theta_1/\lambda_1 \Rightarrow \alpha = \gamma_1\, m_1$. Finally, the EMMCF is obtained using the second equation (5) ($k_1 = \theta_1/\hat{\omega}_1/\sqrt{m_1 C_{\mathrm{p}1}}$). The deduced modal parameters numerical values are gathered in table 1. Notice that the value of k_1 estimated with the open/short circuit frequencies (the first equation (5)) is slightly larger: $k_1 = 0.22$. The value $k_1 = 0.2$ was however kept since it leads to an excellent match between theory and experiments, seen in figure 7. Moreover, in the process, the velocity and current signals are divided by $j\Omega$ to get the displacement and charge.

3.3. *Nonlinear shunt circuit description*

The nonlinear shunt circuit used in the tests is shown in figure 8. It consists of three sub-circuits to realize (a) a tunable synthetic inductor (outlined in blue in the figure 8). (b) a voltage measurement (orange). (c) a nonlinear voltage generator (light red). Preliminary simulations of the circuit showed that fairly large voltages appear, especially during transients. Hence, the operational amplifiers OA_1 to OA_6 are OPA445 (Texas Instruments) which can operate up to ±40 V input

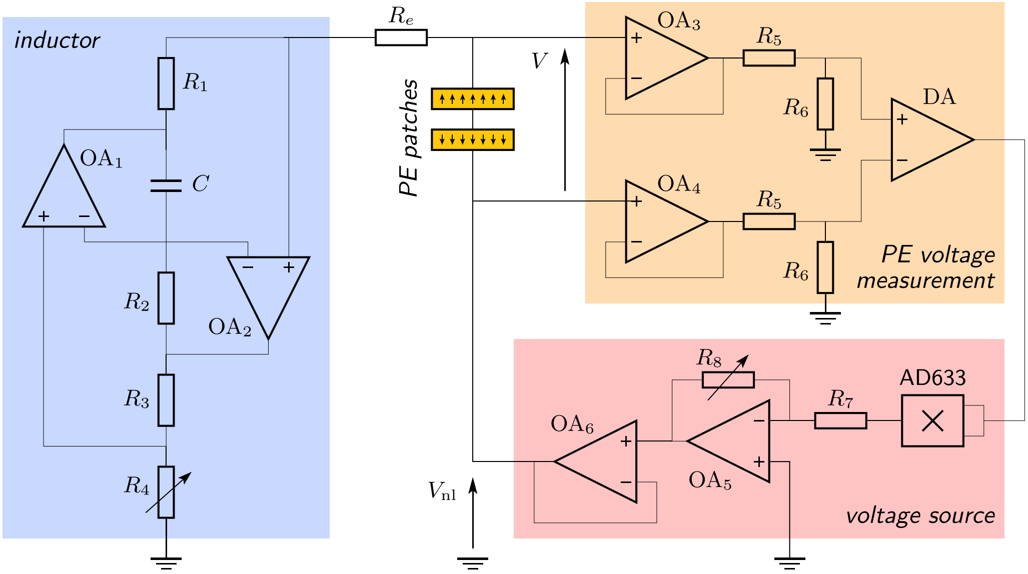

Figure 8. Nonlinear shunt circuit design.

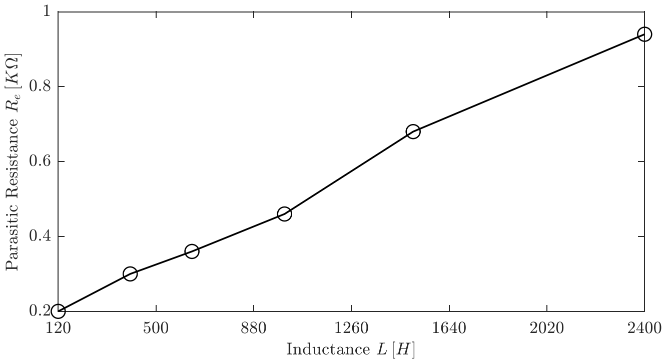

Figure 9. Experimental estimation of the parasitic resistance R_e as function of the inductance L.

Table 2. Fixed component values in the nonlinear shunt circuit.

Component	R_1(kΩ)	R_2(kΩ)	R_3(kΩ)	C(μF)	R_5(kΩ)	R_6($k\Omega$)	R_7(kΩ)
Value	2	1	1	10	82	22	3.8

and output voltage and supply 15 mA to drive the patches. To obtain an electrical resonance frequency close to half the mechanical resonance frequency, an inductance *ca* 2000 H is required for the beam. Therefore, a synthetic inductor is realized using an Antoniou circuit [11, 39], which can achieve large inductor values, given by

$$L = \frac{R_1\, R_2\, R_4\, C}{R_3}. \tag{19}$$

The L value is tuned using the variable resistor R_4. According to the theory, the nonlinear shunt is more effective if the electric damping is null, since it leads to a perfect antiresonance (a zero mechanical mode amplitude, see [1]). In practice, however, it was noticed that this circuit introduces a parasitic resistance as already observed in [40]. The resistance R_e in series with the Antoniou synthetic inductor accounts for this problem in the schematic. The dependence of R_e on L was estimated by testing the Antoniou inductor circuit in series with a 33 nF capacitor to realize a resonant circuit then fit the FRF response. This relationship is shown in figure 9, which was later used during the experiment to assess the results.

The voltage measurement is ensured by two voltage dividers involving the resistor R_5 and R_6, which are decoupled using two voltage followers (OA_3 and OA_4) in order to avoid further introduction of parasitic resistance. The voltage across the patches is thus measured and attenuated to a level compatible with the differential amplifier DA (INA826, Texas Instrument), which ensures noise rejection. Finally, the quadratic non-linearity is realized using a multiplier (AD633, Analog Device) amplified by an inverting amplifier (OA_5) with a tunable gain thanks to R_8 to control β (cf equation (4)) as follows

$$\beta = \frac{R_8}{10\, R_7}\left(\frac{R_6}{R_5 + R_6}\right)^2. \tag{20}$$

The resulting voltage V_{nl} is then supplied to the patches by the follower (OA_6) to ensure a low output impedance. Table 2 gathers the actual values of the components used throughout the experiments presented.

3.4. Nonlinear frequency responses measurements

3.4.1. Measurement of leading harmonics. As discussed in section 2.3, when considering the 2:1 internal resonance, an energy transfer is expected to occur from the driven mechanical mode to an electrical mode at half the driven frequency. To experimentally validate the energy transfer and the nonlinear shunt behavior exhibited by the theoretical results of section 2, we are only interested in the amplitudes and phase angles of the fundamental harmonic (H1) of the structure tip displacement $u(t)$ and the subharmonic (H1/2) of the charge $Q(t)$ in the PE patch electrodes. Following equation (14), we denote them by:

$$u(t) = u_{\mathrm{H1}} \cos(\Omega t - \gamma_2) + \mathrm{oh},$$
$$Q(t) = Q_{\mathrm{H1/2}} \cos\left(\frac{\Omega}{2} t - \frac{\gamma_1 + \gamma_2}{2}\right) + \mathrm{oh}, \qquad (21)$$

with 'oh' meaning 'other harmonics' and u_{H1}, $Q_{\mathrm{H1/2}}$ denoting their amplitudes. In practice, we estimate $u(t)$ and $Q(t)$ by measuring the velocity $v(t)$ of the structure tip with a laser vibrometer (Polytec 0FV 505) and the voltage across the PE patches terminals $V(t)$ with a differential voltage probe (Française d'Instrumentation ST 500-5). Those two signals can be written:

$$v(t) = v_{\mathrm{H1}} \cos(\Omega t - \varphi_v) + \mathrm{oh},$$
$$V(t) = V_{\mathrm{H1/2}} \cos(\Omega/2\, t - \varphi_V) + \mathrm{oh} \qquad (22)$$

with $(v_{\mathrm{H1}}, \varphi_v)$, $(V_{\mathrm{H1/2}}, \varphi_V)$ denoting their amplitude/phase pairs. Taking the time derivative of $u(t)$ in equation (21) leads to:

$$v_{\mathrm{H1}} = \Omega u_{\mathrm{H1}}, \quad \varphi_v = \gamma_2 - \pi/2. \qquad (23)$$

To find the relation between $V(t)$ and $Q(t)$, we rewrite equation (4) as:

$$V(t) = \frac{1}{C_{\mathrm{p}i}} \Big[Q(t) + \theta_1 u(t) \Big], \qquad (24)$$

since $\phi_i(x_t) = 1$ as explained in section 3.2. Then, replacing in equation (24) the H1/2 harmonics of $u(t)$ and $Q(t)$ of equations (14*a*) and (14*b*) and eliminating a_1, one obtains:

$$V_{\mathrm{H1/2}} = \frac{Q_{\mathrm{H1/2}}}{C_{\mathrm{p}i}} \left(1 - \frac{\varepsilon \theta_i \sqrt{L}}{\sqrt{m_i}}\right), \quad \varphi_V = (\gamma_1 + \gamma_2)/2. \qquad (25)$$

The order of magnitude of the second term in the above expression of $V_{\mathrm{H1/2}}$, directly related to the electromechanical coupling, can be evaluated by using the following relations: $\varepsilon \simeq k_i r_i / (1 - r_i^2)$ (obtained by neglecting $4k_i^2 r_i^2$ in Δ in equation (9), see [1]), $\theta_i = k_i \hat{\omega}_i \sqrt{C_{\mathrm{p}i} m_i}$ (equation (5)) and $\sqrt{L} = 1/(\omega_e \sqrt{C_{\mathrm{p}i}})$. After simplifications, one obtains:

$$\frac{\varepsilon \theta_i \sqrt{L}}{\sqrt{m_i}} \simeq \frac{k_i^2}{1 - r_i^2} \simeq \frac{4k_i^2}{3} < 8.3 \cdot 10^{-2}, \qquad (26)$$

for a tuned nonlinear shunt with $r_i \simeq 1/2$ and $k_i < 0.25$. Consequently, even for a high piezoelectric coupling of $k_i = 25\%$, the above term is more than one order of magnitude smaller than one, and can be neglected, leading to:

$$V_{\mathrm{H1/2}} \simeq Q_{\mathrm{H1/2}} / C_{\mathrm{p}i}. \qquad (27)$$

In conclusion, the amplitude and phase of the leading harmonics of the beam tip displacement and the electric charge are directly estimated by the H1 harmonics of the velocity and the H1/2 harmonics of the PE voltage, using equations (23), (25) and (27).

3.4.2. Harmonics amplitude and phase estimation using demodulation.

Since the response of the system is highly nonlinear due to the nonlinear shunt, to validate the theory of figure 4, we prescribe a harmonic force $F(t) = F_0 \cos \Omega t$ at the beam's tip, with the coil/magnet device described in section 3.1, and we perform stepped sine experiments. It consists in choosing a given discrete set of values of Ω around the resonance frequency $\tilde{\omega}_1$ of the structure's first bending mode. For each frequency, the excitation frequency and level (measured by a current clamp) are kept constant until the steady-state is reached, in which several periods of the beam tip velocity $v(t)$ and the PE voltage $V(t)$ are recorded, before stepping to the next discrete frequency. The same measuring devices than in section 3.2 (B&K 2719, PM 9355, OFV 505 & ST 500-5) were used. The input/output signals were synthesized/measured with National Instrument cards (NI-9234, NI-9263) driven by a Matlab program.

At each excitation frequency, the harmonics amplitude and the phase angles are extracted by a demodulation procedure [41] (also known as synchronous or homodyne detection). Each measured signal $s(t)$ is multiplied by sine/cosine signals at the frequency of the leading harmonic, and the result is averaged over a number of periods. Namely, if $s(t)$ is periodic:

$$s(t) = s_0 + \sum_{h=1}^{+\infty} s_h \cos(h\Omega t - \varphi_h), \qquad (28)$$

one obtains for the kth harmonic:

$$I_{\mathrm{c}} = \langle s(t) \cos k\Omega t \rangle_{n_k T_k} = \frac{s_k}{2} \cos \varphi_k,$$
$$I_{\mathrm{s}} = \langle s(t) \sin k\Omega t \rangle_{n_k T_k} = \frac{s_k}{2} \sin \varphi_k, \qquad (29)$$

where

$$\langle \bullet(t) \rangle_{n_k T_k} = \frac{1}{n_k T_k} \int_0^{n_k T_k} \bullet(t) \mathrm{d}t \qquad (30)$$

is the average of the signal $\bullet(t)$ over a duration equal to n_k harmonic periods $T_k = 2\pi/(k\Omega)$. Consequently, the kth harmonic amplitude and phase are obtained by:

$$s_k = 2\sqrt{I_{\mathrm{c}}^2 + I_{\mathrm{s}}^2}, \quad \varphi_k = \arg(I_{\mathrm{c}} + jI_{\mathrm{s}}). \qquad (31)$$

In our case, we used $k = 1$ to estimate the H1 harmonic of $v(t)$ and $k = 1/2$ for the H1/2 harmonic of $V(t)$. In practice, the integral in equation (30) was performed with a trapezoidal numerical integration and the number n_1 of periods used in the averages of equation (29) to estimate the H1 harmonics of $v(t)$ was chosen even to exactly filter the subharmonic part of the

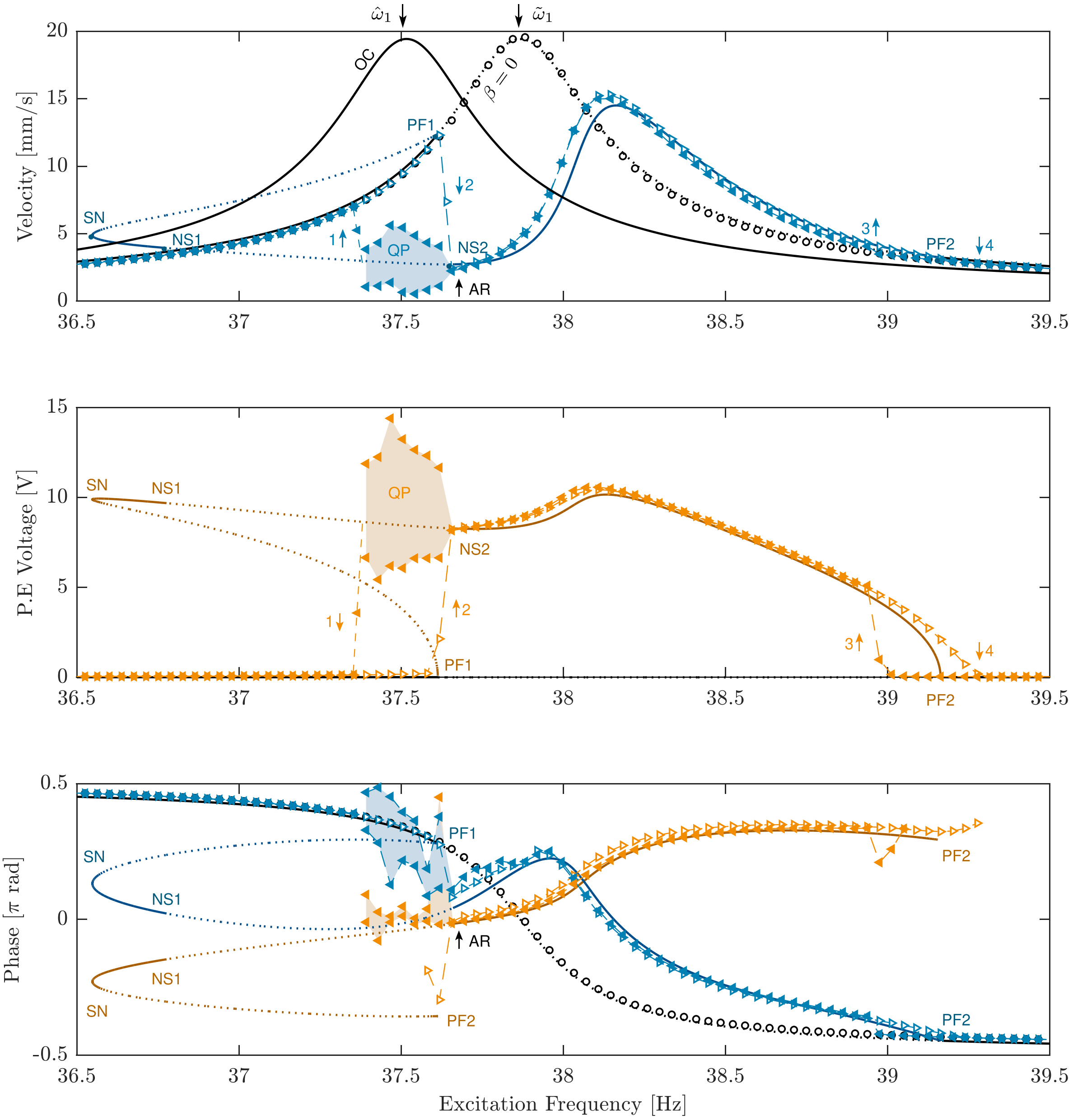

Figure 10. Experimental and numerical results comparison of the amplitudes of v_{H1} and $V_{H1/2}$ and the phase angles ϕ_v and ϕ_V, plotted in blue and orange, respectively. The results are estimated with $F = 0.45$ mN, $\xi_e = 0.002$, $\xi_1 = 0.005$, $\beta = 0.035$, and $r_1 = 0.537$. The numerical data are shown in solid and dotted lines for stable and unstable solutions, respectively, in dark blue and orange, with the uncoupled solution plotted in black. The experimental data are plotted respectively with $- \triangleright -$ and $- \blacktriangleleft -$ for sweeping up and down in the excitation frequency Ω. The experimental uncoupled results are shown in $- \circ -$. The experimental and numerical quasi-periodic regime are shown in the shaded region and the dashed-dotted line, respectively.

signal ($n_1 = n_{1/2} = 12$ in practice). Moreover, at each excitation frequency Ω, the averages of equation (29) were evaluated for ten successive $n_k T_k$ time blocks, to identify quasi-periodic regimes.

This procedure enable to robustly estimate v_{H1}, φ_v, $V_{\mathrm{H1/2}}$ and φ_V, in order to obtain u_{H1}, $Q_{\mathrm{H1/2}}$ and γ_1 using equations (23), (25) and (27):

$$u_{\mathrm{H1}} = v_{\mathrm{H1}}/\Omega, \quad Q_{\mathrm{H1/2}} = C_{\mathrm{p}i} V_{\mathrm{H1/2}}, \quad \gamma_1 = 2\varphi_V - \varphi_v - \frac{\pi}{2}. \tag{32}$$

4. Experimental results

4.1. Experimental validation of the theoretical predictions

As an initial step, we compared the numerical results of the system (2*a*) and (2*b*), integrated with Manlab, to the experimental results. This is shown in figure 10, where the numerical and experimental frequency responses are plotted for the amplitudes of v_{H1} and $V_{H1/2}$, in addition to the phase angles φ_v and φ_V. The measurements were done to catch the whole response features by sweeping up and down the

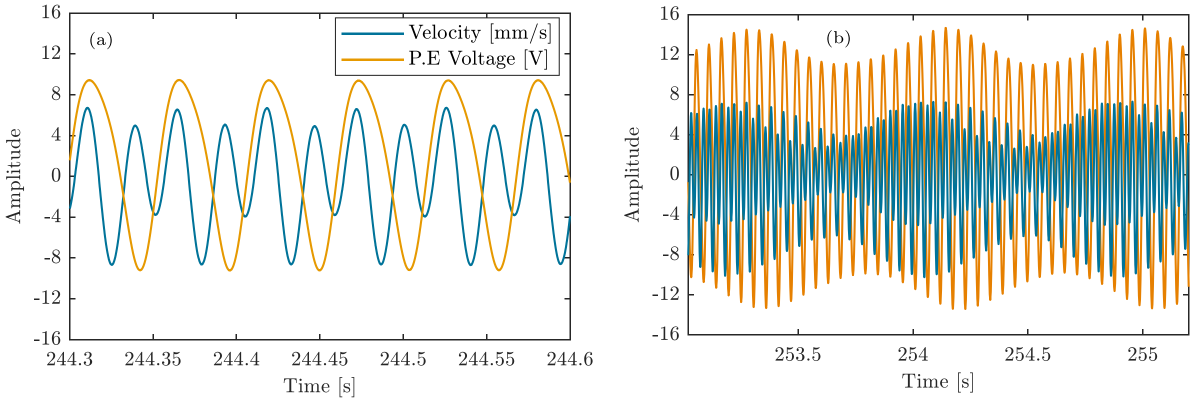

Figure 11. Experimental time signals of $v(t)$ and $V(t)$ for two frequency points in figure 10: (left) the periodic response at $\Omega = 37.75$ Hz and (right) the QP regime at $\Omega = 37.5$ Hz.

excitation frequency. Then, the amplitude and the phases are extracted at each frequency using the demodulation procedure discussed in section 3.4. The comparison between the numerical and experimental results is illustrated as follows.

One can first observe that two linear responses are plotted in black. The first corresponds to the response in the open circuit (OC) case, while the other one corresponds to the linear response when connecting only the R-L version of the full shunt circuit shown in figure 8 (i.e. with $\beta = 0$). The latter case is compared with the experimental results showing an excellent agreement, validating the estimated electromechanical modal parameters of section 3.2. Also, the latter case admits a resonance frequency $\tilde{\omega}_1$ slightly higher than the open circuit frequency $\hat{\omega}_1$ due to the coupling effect, as discussed in section 2.3.

Then the experimental and numerical nonlinear frequency responses of the velocity and voltage show a very good overall agreement. Namely, the energy transfer from the H1 harmonic (at Ω) to the H1/2 harmonic (at $\Omega/2$) due to the 2:1 internal resonance is experimentally observed. The main features obtained theoretically in figure 4 are experimentally validated. Namely, the antiresonance (at point AR, $\Omega/(2\pi) = 37.72$ Hz) is clearly observed, especially in the sweeping-down response. Although the value of r_1 is chosen to have $\omega_2 = 2\omega_1$, the antiresonance is shifted from the resonance frequency (to the lower frequencies), due to the non-resonant terms, as predicted numerically. One can realize that the bifurcation topology of the numerical solution is also validated experimentally, especially for the pitchfork bifurcation PF1, which is predicted at the same frequency as the experimental jump 2. However, a small difference is seen for the other pitchfork bifurcation (PF2), for which the theory suggests that jumps 3 and 4 should appear at the same frequency. The numerically predicted quasi-periodic (QP) solution is also seen experimentally near the antiresonance, only for the sweeping down case. It appears exactly at point NS2, as predicted by the change of stability of the theoretical branch. However, the QP frequency range is smaller in experiments since it stops at jump 1 in the sweep-down response, for which the response jumps back to the uncoupled response. In theory, the end of the QP response is predicted at point NS1 in the low frequencies. This difference could result from an instability in the QP solution (which cannot be predicted by Manlab). A more detailed stability analysis could be necessary to ensure this, which is beyond the scope of this work.

The numerical and experimental responses of the phase angles φ_v and φ_V also show a good agreement. Note that φ_V is only shown in the frequency range where the energy transfer occurs (i.e. between jumps 1 and 4). At the antiresonance (at point AR, $\Omega/(2\pi) = 37.72$ Hz), $\varphi_V = -0.01\ \pi$ rad and $\varphi_v = 0.05\pi$ rad. Thus, using equation (32), γ_1 is estimated to $-0.57\pi \approx 3\ \pi/2$ rad, validating the feature seen theoretically in figure 4.

To extend the above analysis, figure 11 displays two examples of measured time signals. Figure 11(a) shows a periodic response (around $\Omega/(2\pi) = 37.75$ Hz), in which one can clearly observe the H1 and H1/2 harmonics superposition in the time signals, validating equation (14). Moreover, because this periodic response was chosen near the antiresonance, the H1 harmonic amplitude is small and the effect of the H1/2 harmonic, related to the nonlinear shunt, is significantly large. Figure 11(b) shows a QP solution (at $\Omega/(2\pi) = 37.5$ Hz), for which the beatings are clearly visible.

From the above analysis, one can conclude that the agreement between experiments and theory is remarkable and that all theoretical features of the nonlinear shunt are recovered experimentally: the bifurcation scenario, the nonlinear antiresonance, the locking of γ_1 at $3\pi/2$ and the existence of a QP solution.

4.2. *Effect of the nonlinearity gain β*

As illustrated in the theoretical results of [1], the nonlinear gain β has a crucial effect on the absorber performance. We measured the amplitudes v_{H1} and $V_{H1/2}$ for three different values of β, as shown in figure 12, by sweeping up and down in the excitation frequency. Note that the value of β was modified by changing the value of resistance R_8 in the shunt circuit (see equation (20)).

The main advantage of increasing the value of β on the absorber performance is the antiresonance amplitude reduction (at points AR1, AR2, and AR3), which is clearly

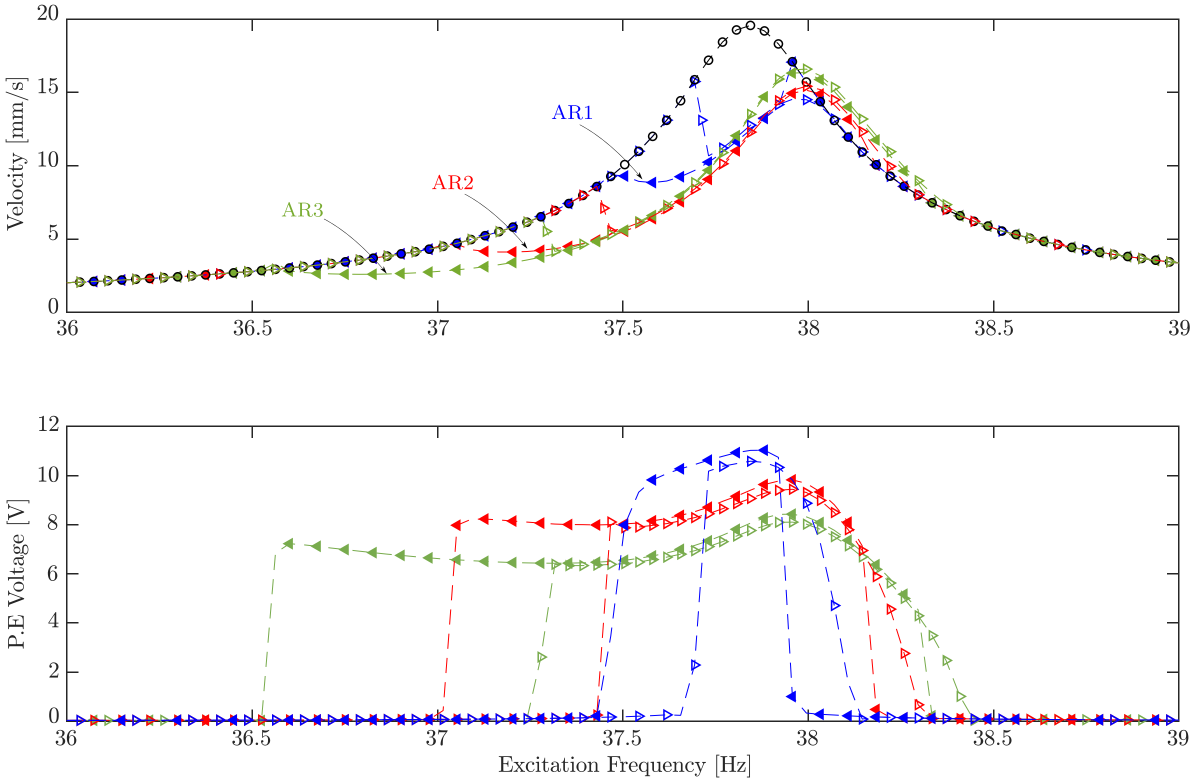

Figure 12. Experimental results for v_{H1} and $V_{H1/2}$ for different values of β. The values of β for the blue, red, and dark green curves are respectively 0.012, 0.023, and 0.035. The tests are done with $F = 0.45$ mN, $\xi_e = 0.002$, $\xi_1 = 0.005$, and $r_1 = 0.524$. The experimental data are plotted respectively with — ▷ — and — ◀ — for sweeping up and down in the excitation frequency Ω. The experimental uncoupled results are shown in — ○ —.

observed. However, it appears in parallel to an antiresonance frequency shift, as predicted by theory. This drawback can be counter-balanced by a detuning of the electrical oscillator, as illustrated in section 4.4.

The other advantage of increasing β is the reduction of the PE voltage amplitude, which could be interesting to remain in the functioning limits of the electrical components of the circuit. Another drawback of increasing β is the amplitude amplification of the peak to the right of the linear resonance, which reduces the usable frequency range of the absorber.

4.3. *Effect of the excitation level*

The effect of the excitation level on the response is illustrated in figure 13, where only downward frequency sweeps are shown. The ratio r_1 is also chosen to have $\omega_1/\omega_2 \simeq 0.5$ and activate the internal resonance, using figure 2 to take into account the effect of the piezoelectric coupling. One can realize that increasing the excitation amplitude while keeping the other design parameters fixed leads to increased velocity and PE patch voltage amplitudes. Also, the peak's amplitude observed to the right of the linear resonance peak in the velocity response increases with the excitation level (analogous to the effect of β). Moreover, a softening behavior can be seen when looking at the voltage response for $F_0 = 2.5$ mN. A QP regime is detected at $F_0 = 0.45$ mN and $F_0 = 1.3$ mN near the antiresonance.

Looking at the antiresonance, one can observe that its amplitude remains almost constant with the increase of the excitation level, but shifts to the lower frequencies as the excitation level increases. This validates the numerical predictions in figure 4, suggesting a violation of the saturation phenomenon at a fixed excitation frequency.

4.4. *Saturation phenomenon with detuning*

Our purpose is to preserve the saturation phenomenon to enhance the absorber's efficiency. Because the antiresonance amplitude remains constant, it is sufficient to lock the antiresonance at the resonance frequency. This is done following the antiresonance (AR) correction described in section 2.4. Namely, a change in the tuning parameter r_1 should be introduced for each excitation level by changing the inductance in the shunt circuit.

The procedure to track the antiresonance and then lock it at a prescribed frequency is established before performing the stepped sine measurements. Namely, a sinusoidal signal of frequency equal to the mechanical resonance frequency $\tilde{\omega}_1/(2\pi) = 37.75$ Hz is amplified to the desired excitation level and then fed to the coil. This resonance frequency is the one measured with $\beta = 0$ as in figure 13. After reaching the steady-state with the nonlinear subharmonic energy transfer, the velocity $v(t)$ and the PE patch voltage $V(t)$ are visualized using an oscilloscope in an XY mode to obtain a Lissajous plot (i.e.

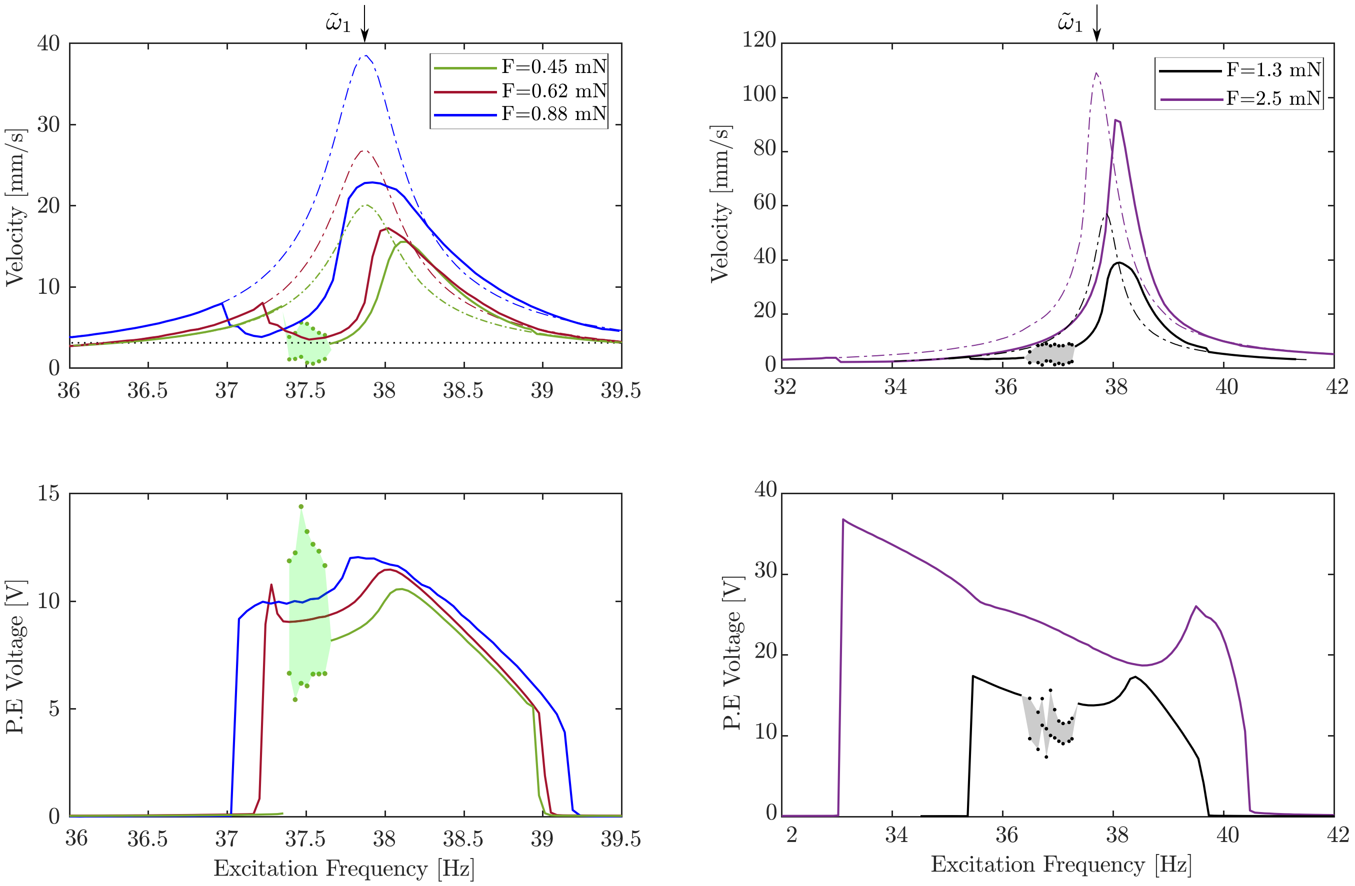

Figure 13. Experimental results of v_{H1} (first row) and $V_{H1/2}$ (second row) for several excitation levels F with unit of mN. Only the data for sweeping down the excitation frequency are shown in solid lines. The measurements are done for $\beta = 0.035$, $\xi_e = 0.002$, $\xi_1 = 0.005$, and $r_1 = 0.537$. The shaded regions depict the detected quasi-periodic regime.

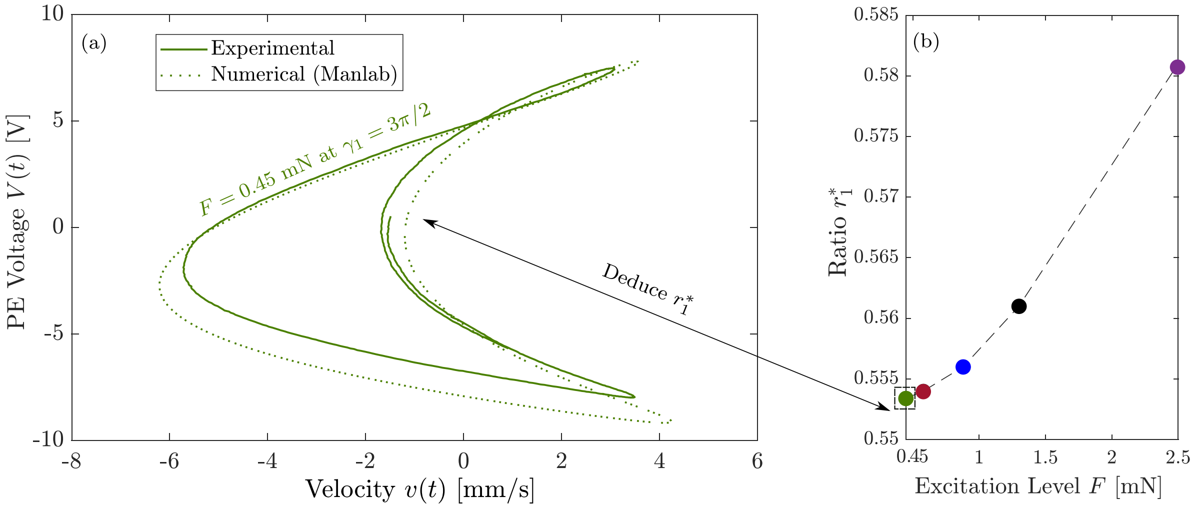

Figure 14. (a) Example of Lissajous plot for $F = 0.45$ mN estimated numerically (with Manlab) and experimentally. (b) Deduced value of r_1^* for different excitation levels. The curves are estimated for $\beta = 0.035$, $\xi_e = 0.002$, and $\xi_1 = 0.005$.

the voltage as a function of the velocity). Because of the fixed value of the phase angle $\gamma_1 = 3\pi/2$, a *unique shape* for the Lissajous plot appears when the antiresonance is shifted to the resonance frequency. In other words, we vary the inductance value until getting the numerically predicted Lissajous plot for $\gamma_1 = 3\pi/2$ as shown in figure 14(a). Thus, the achieved inductance value is the required one to have the proper ratio r_1 (denoted by r_1^*) to lock the antiresonance at the resonance frequency $\tilde{\omega}_1$. The same procedure is repeated for each excitation level, enabling us to have an $r_1^* = f(F_0)$ relation, as

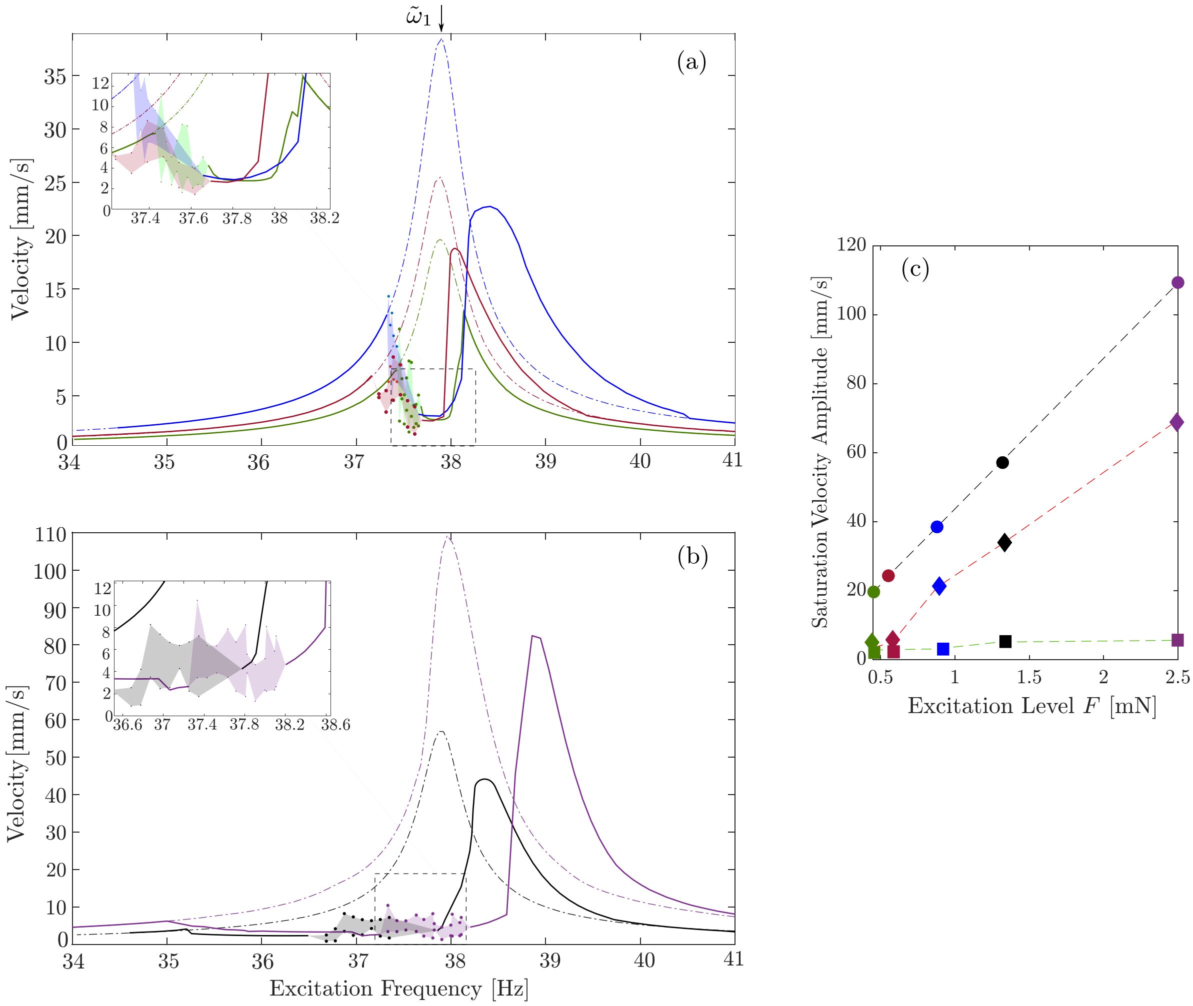

Figure 15. Experimental frequency response of v_{H1} for sweeping down the excitation frequency for several excitation levels with the AR correction. (a) The response for $F = 0.45$ mN (in green), $F = 0.58$ mN (in dark red), and $F = 0.88$ mN (in blue). (b) The response for $F = 1.3$ mN (in black), $F = 2.5$ mN (in purple). (c) Antiresonance saturation amplitude v^*_{H1} at the resonance frequency $\tilde{\omega}_1$ versus the excitation level plotted for three different cases: the linear response, with fixed $r_1 = 0.537$, and with the AR correction in. The curves are estimated for $\beta = 0.035$, $\xi_e = 0.002$, and $\xi_1 = 0.0055$. The shaded regions depict the detected quasi-periodic regime.

plotted in figure 14(b). For example, this relation shows that r^*_1, for $F = 0.45$ mN and $\beta = 0.035$, should be 0.547. Also, this relation suggests that a further decrease in the inductance (i.e. an increase in r_1) should be introduced as the excitation level increases to lock the antiresonance. Note that this relation depends on the other design parameters (i.e. β, k_1).

The frequency response of v_{H1} is experimentally measured by setting the proper value of r_1 using the $r^*_1 = f(F_0)$ relation of figure 14(b). The results are illustrated in figures 15(a) and (b) by sweeping down the excitation frequency for the same excitation levels used in figure 13. One can note that using the suggested AR correction, the antiresonance is locked at the prescribed frequency (i.e. at $\tilde{\omega}_1/(2\pi) = 37.75$ Hz), leading to the preserving of the saturation phenomenon. However, changing the value of r_1 led to the appearance of QP regimes near the antiresonance that were not appearing in figure 13 for constant r_1, for example in the response for $F = 0.88$ mN. Also, one can note a slightly softening behavior on the uncoupled resonance curve in the case of the highest forcing level (in purple), which could be due to the non-negligible effects of the material piezoelectric nonlinearities in the PE patches [42]. In addition, for the highest excitation level, the QP regime being shifted further to the left made the Lissajous plot more complicated to obtain at the resonance frequency 37.75 Hz; we obtained r^*_1 for a slightly higher frequency to have the periodic solution.

Note that the linear responses shown in figures 15(a) and (b) are plotted by setting $\beta = 0$ with values of r_1 equal to r^*_1 which varies for each excitation level (unlike figure 4 where a constant value of r_1 is used). Based on this, the resonance frequency increases slightly above $\tilde{\omega}_1$ as the excitation level increases. This can be observed at the highest excitation that requires the highest value of r^*_1. In this context, the suggested AR correction locks the antiresonance at a unique prescribed frequency that is slightly lower than the resulting linear resonance frequency for higher excitation levels, due to its dependency on r_1.

To further illustrate the saturation phenomenon, the amplitude of v_{H1} at the prescribed frequency $\tilde{\omega}_1$, denoted by v^*_{H1},

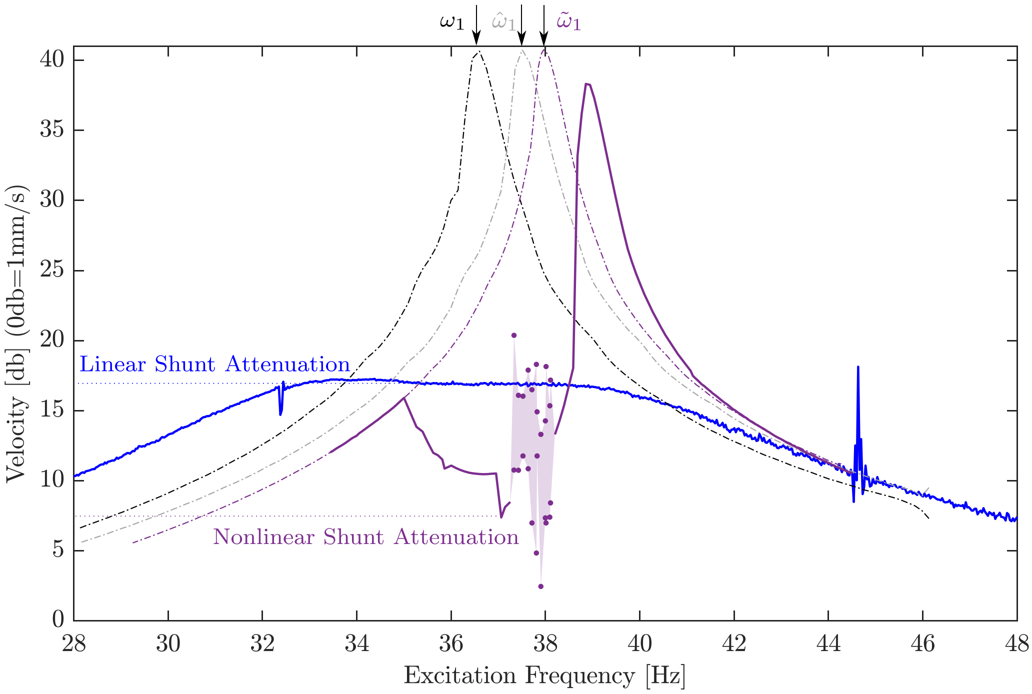

Figure 16. Comparison between the performance of the optimized linear shunt and the designed absorber for $F = 2.5$ mN, $\beta = 0.035$, and $\xi_1 = 0.0055$. The dashed curves depict the linear responses for the short circuit case (black), the open circuit case (brown) and $\beta = 0$ (purple). The solid lines depict the responses for $\beta = 0.035$ (purple) and for the optimized linear shunt (blue).

is plotted versus the excitation level F in figure 15(c) (similar to figure 5(b)). The amplitudes of v_{H1}^* are taken directly from the experimental measurements showing the frequency response of v_{H1}. Three different cases are plotted: the linear case ($\beta = 0$), the case where a constant r_1 is used (see figure 13), and the case when introducing the antiresonance correction (figures 15(a) and (b)). The results suggest a significant attenuation enhancement for the latter case where the saturation phenomenon is *almost* preserved. As a matter of fact, one can observe a slight increase in v_{H1}^* when using the AR correction mainly because of the slight increase of the electrical damping ξ_e due the increasing value of r_1^* for higher excitation levels.

4.5. Performance comparison with optimized linear shunt

To further demonstrate the nonlinear shunt performance, figure 16 shows a comparison of the resonant response of the structure with the nonlinear shunt for the highest excitation level $F = 2.5$ mN (purple curve of figure 15) and with a tuned linear resonant (RL) shunt. For the latter, $\beta = 0$ and the electrical frequency $\omega_e \simeq \hat{\omega}_1$ was tuned with the equal peak method [6] (with $R_e = 35.26$ kΩ and $L = 555.82$ H, with $R_4 = 27.79$ kΩ).

5. Conclusion

In this paper, the experimental validation of a passive nonlinear piezoelectric shunt absorber, introduced theoretically in our previous study [1], was performed. This absorber is designed by intentionally introducing a quadratic nonlinearity proportional to the square of the voltage across the piezoelectric patches (PE patches) in series with a resonant shunt circuit. Doing so creates a 2:1 internal resonance between a given mechanical mode of the primary structure and the shunt circuit tuned at the first subharmonic frequency. Our designed absorber aims to exploit the convenient features of such an internal resonance: a *saturation phenomenon*, in which the amplitude of the mechanical mode becomes independent of the excitation amplitude after a threshold, and a *nonlinear antiresonance* in place of the linear resonance frequency, leading to high vibration attenuation. These two features are linked to the nonlinear energy transfer from the mechanical mode to be attenuated to the electrical mode characterized by the shunt circuit.

We showed a remarkable agreement between our experiments and the theoretical prediction, thus perfectly validating them. In addition, the performances of the shunt were explored, showing an amplitude that is independent of the vibration level at the antiresonance, associated with better performance at high amplitude than a classical linear resonant shunt. One drawback of our architecture, based on a nonlinear voltage proportional to the square of the piezoelectric (PE) voltage, is the unexpected detuning of the shunt as a function of the amplitude, that was manually corrected by a phase-locking of the PE voltage with the mechanical response of the structure. Another drawback is the saturation limit of the analog electronic components, which limits the maximum amplitude of operation of the shunt and constraints the design of the electronic circuit, to finely balance the voltages and avoid noise in the circuit.

Data availability statement

All data that support the findings of this study are included within the article (and any supplementary files).

Aknowledgments

The Région Hauts de France and the Carnot ARTS Institute are warmly thanked for the PhD grant of the first author.

ORCID iDs

Zein Alabidin Shami https://orcid.org/0000-0002-5470-4957
Christophe Giraud-Audine https://orcid.org/0000-0003-3461-0328
Olivier Thomas https://orcid.org/0000-0001-7240-5259

References

[1] Shami Z A, Giraud Audine C and Thomas O 2022 A nonlinear piezoelectric shunt absorber with a 2:1 internal resonance: theory *Mech. Syst. Signal Process.* (https://doi.org/10.1016/j.ymssp.2021.108768) In press

[2] Lanchester F W 1914 Damping torsional vibrations in crank shafts *US Patent* No 1085443

[3] Frahm H 1911 Device for damping vibrations of bodies *US Patent* No 989958

[4] Hagood N and Von Flotow A 1991 Damping of structural vibrations with piezoelectric materials and passive electrical networks *J. Sound Vib.* **146** 243–68

[5] Auleley M, Thomas O, Giraud-Audine C and Mahé H 2021 Enhancement of a dynamic vibration absorber by means of an electromagnetic shunt *J. Intell. Mater. Syst. Struct.* **32** 331–54

[6] Thomas O, Ducarne J and Deü J-F 2012 Performance of piezoelectric shunts for vibration reduction *Smart Mater. Struct.* **21** 015008

[7] Berardengo M, Thomas O, Giraud-Audine C and Manzoni S 2016 Improved resistive shunt by means of negative capacitance: new circuit, performances and multi-mode control *Smart Mater. Struct.* **25** 075033

[8] Berardengo M, Manzoni S, Thomas O and Vanali M 2021 Guidelines for the layout and tuning of piezoelectric resonant shunt with negative capacitances in terms of dynamic compliance, mobility and accelerance *J. Intell. Mater. Syst. Struct.* **32** 2092–107

[9] Auleley M, Giraud-Audine C, Mahé H and Thomas O 2021 Tunable electromagnetic resonant shunt using pulse-width modulation *J. Sound Vib.* **500** 116018

[10] Darleux R, Lossouarn B and Deü J-F 2020 Broadband vibration damping of non-periodic plates by piezoelectric coupling to their electrical analogues *Smart Mater. Struct.* **29** 054001

[11] Gripp J and Rade D 2018 Vibration and noise control using shunted piezoelectric transducers: a review *Mech. Syst. Signal Process.* **112** 359–83

[12] Shivashankar P and Gopalakrishnan S 2020 Review on the use of piezoelectric materials for active vibration, noise and flow control *Smart Mater. Struct.* **29** 053001

[13] Gatti G, Brennan M and Tang B 2019 Some diverse examples of exploiting the beneficial effects of geometric stiffness nonlinearity *Mech. Syst. Signal Process.* **125** 4–20

[14] Ledezma-Ramirez D F, Tapia-González P E, Ferguson N, Brennan M J and Tang B 2019 Recent advances in shock vibration isolation: an overview and future possibilities *Appl. Mech. Rev.* **71** 060802

[15] Silva T M, Clementino M A, De Marqui C and Erturk A 2018 An experimentally validated piezoelectric nonlinear energy sink for wideband vibration attenuation *J. Sound Vib.* **437** 68–78

[16] Zhao G, Raze G, Paknejad A, Deraemaeker A, Kerschen G and Collette C 2020 Active nonlinear energy sink using force feedback under transient regime *Nonlinear Dyn.* **102** 1319–36

[17] Habib G, Detroux T, Viguié R and Kerschen G 2015 Nonlinear generalization of Den Hartog's equal-peak method *Mech. Syst. Signal Process.* **52–53** 17–28

[18] Soltani P and Kerschen G 2015 The nonlinear piezoelectric tuned vibration absorber *Smart Mater. Struct.* **24** 075015

[19] Lossouarn B, Deü J-F and Kerschen G 2018 A fully passive nonlinear piezoelectric vibration absorber *Phil. Trans. R. Soc.* A **376** 20170142

[20] Raze G, Jadoul A, Guichaux S, Broun V and Kerschen G 2019 A digital nonlinear piezoelectric tuned vibration absorber *Smart Mater. Struct.* **29** 015007

[21] Lossouarn B, Kerschen G and Deü J-F 2021 An analogue twin for piezoelectric vibration damping of multiple nonlinear resonances *J. Sound Vib.* **511** 116323

[22] Clark W W 2000 Vibration control with state-switched piezoelectric materials *J. Intell. Mater. Syst. Struct.* **11** 263–71

[23] Richard C, Guyomar D, Audigier D and Ching G 1999 Semi-passive damping using continuous switching of a piezoelectric device *Proc. of SPIE Smart Structures and Conf.: Passive Damping and Isolation* vol 3672 pp 104–11

[24] Oueini S and Golnaraghi M 1996 Experimental implementation of the internal resonance control strategy *J. Sound Vib.* **191** 377–96

[25] Oueini S S, Nayfeh A H and Golnaraghi M F 1997 A theoretical and experimental implementation of a control method based on saturation *Nonlinear Dyn.* **13** 189–202

[26] Oueini S S, Nayfeh A H and Pratt J R 1998 A nonlinear vibration absorber for flexible structures *Nonlinear Dyn.* **15** 259–82

[27] Pai P, Wen B, Naser A and Schulz M 1998 Structural vibration control using pzt patches and non-linear phenomena *J. Sound Vib.* **215** 273–96

[28] Pai P F, Rommel B and Schulz M J 2000 Dynamics regulation of a skew cantilever plate using PZT patches and saturation phenomenon *J. Intell. Mater. Syst. Struct.* **11** 642–55

[29] 1988 IEEE Standard on Piezoelectricity *ANSI/IEEE Std 176-1987* (https://doi.org/10.1109/IEEESTD.1988.79638)

[30] Géradin M and Rixen D 2015 *Mechanical Vibrations* 3rd edn (New York: Wiley)

[31] Nayfeh A H and Mook D T 1979 *Nonlinear Oscillations* (New-York: Wiley)

[32] Monteil M, Touzé C, Thomas O and Benacchio S 2014 Nonlinear forced vibrations of thin structures with tuned eigenfrequencies: the cases of 1:2:4 and 1:2:2 internal resonances *Nonlinear Dyn.* **75** 175–200

[33] Touzé C, Thomas O and Chaigne A 2004 Hardening/softening behaviour in non-linear oscillations of structural systems using non-linear normal modes *J. Sound Vib.* **273** 77–101

[34] Touzé C, Vizzaccaro A and Thomas O 2021 Model order reduction methods for geometrically nonlinear structures: a review of nonlinear techniques *Nonlinear Dyn.* **105** 1141–90

[35] Guillot L, Cochelin B and Vergez C 2019 A Taylor series-based continuation method for solutions of dynamical systems *Nonlinear Dyn.* **98** 2827–45

[36] Guillot L, Lazarus A, Thomas O, Vergez C and Cochelin B 2020 A purely frequency based Floquet-Hill formulation for

the efficient stability computation of periodic solutions of ordinary differential systems *J. Comput. Phys.* **416** 109477

[37] Ducarne J, Thomas O and Deü J-F 2012 Placement and dimension optimization of shunted piezoelectric patches for vibration reduction *J. Sound Vib.* **331** 3286–303

[38] Thomas O, Touzé C and Chaigne A 2003 Asymmetric non-linear forced vibrations of free-edge circular plates, part 2: experiments *J. Sound Vib.* **265** 1075–101

[39] Antoniou A 1969 Realisation of gyrators using operational amplifiers and their use in RC-active-network synthesis *Proc. Inst. Electr. Eng.* **116** 13

[40] Yuce E and Minaei S 2009 On the realization of simulated inductors with reduced parasitic impedance effects *Circuits Syst. Signal Process.* **28** 451–65

[41] Colin M, Thomas O, Grondel S and Cattan E 2020 Very large amplitude vibrations of flexible structures: experimental identification and validation of a quadratic drag damping model *J. Fluids Struct.* **97** 103056

[42] Givois A, Giraud-Audine C, Deü J-F and Thomas O 2020 Experimental analysis of nonlinear resonances in piezoelectric plates with geometric nonlinearities *Nonlinear Dyn.* **102** 1451–62

Chapter 4

Theoretical study of the dynamics of a coupled oscillator with 1:2 internal resonance using normal form

Contenu

4.1 Article presentation

The present chapter solely constitutes of the text of the article entitled by ”Nonlinear dynamics of coupled oscillators in 1:2 internal resonance: effects of the nonresonant quadratic terms and recovery of the saturation effect” published in ”Meccanica” journal. The article aims to understand more rigorously the effect of the nonresonant quadratic terms on the dynamics using the normal form method and propose a procedure to cancel their effect. By doing so, we aim to correct the saturation feature in a more efficient manner and thus increase the performance of the absorber. The choice of utilizing the normal form is based on its ability to simplify the dynamics on the one hand and to represent the nonresonant term as cubic terms that perturbate the dynamics on the other hand. For this sake, a generalized two degree of freedom system considering all the possible quadratic and cubic terms, without restriction on their values, is considered. In addition, the eigen-frequencies are tuned to study the case of 2:1 internal resonance.

The first step was constructing the considered system’s normal form by considering a nonlinear change of coordinates through a third-order Taylor expansion. The obtained normal form system is simplified since a lower number of nonlinear terms are retained. In addition, all the nonresonant quadratic terms are canceled in the second order and appeared as cubic terms in the third order. The main finding which was not illustrated in the previous works considering the normal form derivations is the appearance of cubic terms related to the resonant quadratic terms due to the consideration of the 2:1 internal resonance.

The free conservative version of the normal form system is then considered to obtain closed-form expressions of the backbone curves in the case of the 2:1 internal resonance using the multiple scales method. The obtained results suggested two families of backbone curves depending on the phase angles between the two oscillators. The analytical results are validated by comparing them with the numerical ones showing an excellent fitting. A bifurcation and stability analysis of the backbones curves are also established. In addition, the validation of the normal form system is further discussed by comparing its numerical forced response with that of the initial system showing an excellent fitting, especially at low excitation levels. In addition, the relation between the forced response and backbones is illustrated, showing the ability of the obtained analytical backbones to predict the skeleton of the forced solution for a different set of parameters.

Thanks to the closed-form expression of the backbones, a set of relations between the resonant cubic terms and the nonresonant quadratic terms are estimated to cancel the effect of the latter terms in the normal form basis. This can lead to the recovery of the symmetric behavior and thus the saturation phenomenon. The idea is then tested by estimating the numerical forced response of the initial system with the cubic terms set according to the obtained relations. The results suggested the preservation of the saturation phenomenon up to a high excitation level.

4.2 Nonlinear dynamics of coupled oscillators in 1:2 internal resonance: effects of the nonresonant quadratic terms and recovery of the saturation effect

Meccanica
https://doi.org/10.1007/s11012-022-01566-w

Nonlinear dynamics of coupled oscillators in 1:2 internal resonance: effects of the non-resonant quadratic terms and recovery of the saturation effect

**Zein Alabidin Shami · Yichang Shen ·
Christophe Giraud-Audine · Cyril Touzé ·
Olivier Thomas**

Received: 2 May 2022 / Accepted: 28 July 2022

Abstract This article considers the nonlinear dynamics of coupled oscillators featuring strong coupling in 1:2 internal resonance. In forced oscillations, this particular interaction is the source of energy exchange, leading to a particular shape of the response curves, as well as quasi-periodic responses and a saturation phenomenon. These main features are embedded in the simplest system which considers only the two resonant quadratic monomials conveying the 1:2 internal resonance, since they are the proeminent source allowing one to explain these phenomena. However, it has been shown recently that those features can be substantially modified by the presence of non-resonant quadratic terms. The aim of the present study is thus to explain the effect of the non-resonant quadratic terms on the dynamics. To that purpose, the normal form up to the third order is used, since the effect of the non-resonant quadratic terms will be transferred into the resonant cubic terms. Analytical solutions are detailed using a second-order mutliple scale expansion. A thorough investigation of the backbone curves, their stability and bifurcation, and the link to the forced–damped solutions, is detailed, showing in particular interesting features that had not been addressed in earlier studies. Finally, the saturation effect is investigated, and it is shown how to correct the detuning effect of the cubic terms thanks to a specific tuning of non-resonant quadratic terms and resonant cubic terms. This choice, derived analytically, is shown to extend the validity of the saturation effect to larger amplitudes, which can thus be used in all applications where this effect is needed e.g. for control.

Keywords Nonlinear modes · Backbone curves · Forced response · Invariant manifolds · Quadratic coupling · Normal form · Saturation phenomenon · Second order multiple scale expansion

1 Introduction

The vibratory behaviour of nonlinear systems can be very complex as compared to linear ones, showing,

---

Z. A. Shami (✉) · O. Thomas
Arts et Métiers Institute of Technology, LISPEN, HESAM Université, 59000 Lille, France
e-mail: zein_alabidin.shami@ensam.eu

O. Thomas
e-mail: olivier.thomas@ensam.eu

Y. Shen · C. Touzé
IMSIA, ENSTA Paris, CNRS, EDF, CEA, Institut Polytechnique de Paris, 828 Boulevard des Maréchaux, 91762 Palaiseau Cedex, France
e-mail: yichang.shen@ensta-paris.fr

C. Touzé
e-mail: cyril.touze@ensta-paris.fr

C. Giraud-Audine
Arts et Métiers Institute of Technology, L2EP, HESAM Université, 59000 Lille, France
e-mail: christophe.giraud-audine@ensam.eu

in particular, a dependence of its characteristic frequencies upon the amplitude, bifurcations associated to stable and unstable solutions, periodic response with rich harmonics content as well as more complex quasi-periodic and chaotic responses [1–3]. Those phenomena are often related to strong nonlinear couplings between the degrees of freedom (DOFs) of the system, leading to energy exchanges between them. Important couplings are generally fostered by particular relationships between the characteristic frequencies, leading to the important concept of internal resonance (IR) in vibration theory [4]; but other kind of couplings might also appear for systems with widely spaced frequencies [5].

The specific case of a 1:2 internal resonance is met when two nonlinear oscillators have their eigen-frequencies ω_1 and ω_2 such that $\omega_2 \simeq 2\omega_1$. This case has been the subject of numerous studies in the past, see e.g. [1, 4, 6–9]. In general, the 1:2 case is studied by considering only the quadratic terms and more specifically the two resonant monomials that are responsible of the strong coupling between the two oscillators, see e.g. [1, 10] for the simplified equations (normal form) to use for such case, as well as [11, 12] for general discussion on the normal form and the resonant monomials. The dynamics of such quadratically coupled nonlinear oscillators display a rich behaviour with two families of backbone curves [10, 13], appearance of quasi-periodic behaviour [1], and analytic expression of the locus of Neimark–Sacker bifurcation [10].

A particularly interesting feature of systems with 1:2 internal resonance is the saturation effect that is observed in the forced response, when the external excitation frequency Ω is in the vicinity of the second mode: $\Omega \simeq \omega_2$. As shown for example in [1], once the coupling is effective, then the amplitude of the second mode stays constant for increasing forcing amplitude, while the amplitude of the first mode (not excited by the load) increases, meaning that all the energy, input to the second oscillator, is transferred to the first. This saturation effect is important and can be used with the purpose of controlling the amplitude of the second mode, enforcing its saturation to a maximum amplitude. Successful applications have been reported for example in [14–16].

Recently, it has been shown both theoretically and experimentally in [17, 18] that the non-resonant quadratic terms play an important role in the saturation effect if one goes to moderately large amplitude. Consequently, a fine tuning of a vibration absorber based on the saturation effect needs to properly address not only the resonant quadratic terms, but also the non-resonant ones, in order to obtain a comfortable range of amplitude where the saturation effect is effective. The aim of this paper is to reconsider theoretically the effect of these non-resonant quadratic terms on the dynamics of the system with 1:2 internal resonance, in order to extend the amplitude range of the saturation effect.

Numerous analytical methods have been proposed in the past in order to derive approximate solutions to nonlinear vibration problems thanks to asymptotic expansions. In this realm, the normal form approach is particularly appealing since it conveys very important meaning related to nonlinear resonances [11, 12, 19, 20], derives the simplest form of the dynamics, and expresses its skeleton [21, 22]. It can also be used for model order reduction, see e.g. [23–25], and has a strong relationship with the parametrisation method of invariant manifold, see e.g. [26, 27], such that the normal form dictates the reduced dynamics on an invariant manifold and can be used for building ex-nihilo models [11]. In this contribution, the normal form is used to analyze the dynamics of the system with 1:2 internal resonance. Interestingly, whereas general formulations for deriving real normal forms of coupled oscillators are derived in [11, 23], they are restricted to the case without internal resonance. The computation of the normal form, up to the cubic term, with a 1:2 internal resonance, needs thus a particular development. A first aim of this paper is thus to make this derivation and gives the expression of the normal form with 1:2 resonance up to cubic order.

The second aim of the paper is to analyze the nonlinear dynamics of the system with 1:2 internal resonance up to cubic terms. Recent studies derived important results about the topology of the solutions in the unforced conservative case (nonlinear modes/backbone curves) [10, 13]. These results will be here enlarged to the next order by analyzing the effects of the cubic terms. In the normal form derivation, the non-resonant quadratic coefficients are reported to the cubic order, in the trivially resonant terms. Hence, their effect can be tracked and analyzed. The last aim of the study is thus to show how the non-resonant quadratic terms have important effects on the nonlinear dynamics and more particularly on the saturation effect. At last, it is shown analytically how to tune non-resonant quadratic terms and resonant cubic ones, in order to extend the amplitude validity region where the saturation effect is particularly efficient.

2 Equations of motion, normal form and multiple scales solution

The starting point is a conservative two DOFs system with smooth nonlinearities, in the form of a Taylor expansion up to the third order:

$$\ddot{X}_1 + \omega_1^2 X_1 + g_{11}^1 X_1^2 + g_{12}^1 X_1 X_2 + g_{22}^1 X_2^2 + h_{111}^1 X_1^3 + h_{112}^1 X_1^2 X_2 + h_{122}^1 X_1 X_2^2 + h_{222}^1 X_2^3 = 0, \tag{1a}$$

$$\ddot{X}_2 + \omega_2^2 X_2 + g_{11}^2 X_1^2 + g_{12}^2 X_1 X_2 + g_{22}^2 X_2^2 + h_{111}^2 X_1^3 + h_{112}^2 X_1^2 X_2 + h_{122}^2 X_1 X_2^2 + h_{222}^2 X_2^3 = 0. \tag{1b}$$

In the above system, $(X_1(t), X_2(t))$ are the displacements of the two DOFs at time t, $\dot{\cdot} = \mathrm{d} \cdot /\mathrm{d}t$ is the time derivative, and (g_{ij}^k, h_{ijl}^k), $i, j, l, k = 1, 2$ are the coefficients of the quadratic and cubic terms. This kind of system is encountered in many fields of physics and engineering [2, 4] and especially when reducing the dynamics of curved thin mechanical structures such as shells and arches, the curvature being responsible of the appearance of the quadratic terms [27–29]. Here, all possible quadratic and cubic terms are considered, without restriction on their values. In particular, the case for which Eq. (1) derive from a potential leads to known relationships between some of the coefficients, such that finally, only nine free coefficients remains in this case, which is recalled in "Appendix A", see also e.g. [2, 30]. Note however that this specific case is not considered here for the sake of generality, and also because in some of the targeted applications, the nonlinear terms are artificially created; see e.g. the case of electronic circuits for vibration control applications [17, 31].

2.1 Real normal form up to the third order with a second-order resonance

The aim of this section is to derive the normal form of Eq. (1) up to cubic terms, in the specific case where a 1:2 internal resonance exists between the two eigenfrequencies of the problem, such that the relationship $\omega_2 \approx 2\omega_1$ holds. The theory of normal form has been used for a long time for vibratory problems, in order to simplify as much as possible the dynamical system under study by cancelling all the non-resonant monomials thanks to a nonlinear change of coordinates, see e.g. [19, 21, 32, 33]. It has also been used in the context of model order reduction to underline the link with nonlinear normal modes (NNMs), defined as invariant manifolds in phase space [11, 23, 27]. Importantly, different *styles* of normal form exist due to the non-uniqueness of the solutions of the homological equations, and the freedom of choosing one solution or another leads to the idea of *free functions*, as explained for example in [22, 34].

Focusing on the case of vibratory problems where the eigenspectrum is composed of pairs of complex conjugate eigenvalues, three main different styles of normal forms can be distinguished. The first one is the complex normal form, as first introduced in [19], which is closer to the formulas used in the dynamical system community, see e.g. [21, 33, 35]. The second one is the real normal form introduced in [20, 34, 36], which allows one to retrieve more easily oscillator equations. The third one is a full real normal form, first introduced in [11, 23], where the oscillator form of the equations is strongly enforced throughout the calculation, imposing the variables to stay homogeneous to a displacement and a velocity. Further comments on these different normal forms can also be found in [37], in the context of the parameterisation method for invariant manifolds. In this article, this third normal form will be used to simplify Eq. (1).

A generic calculation, up to cubic order, and including detailed analytical formulas for all the coefficients of the nonlinear mappings and normal form, has already been provided in [11, 38] for conservative problems, and in [12, 23] for assemblies of damped nonlinear oscillators. However, this calculation is led to the case where no internal resonance exists between the eigenfrequencies of the problem. In the case where a second-order internal resonance exist, like the 1:2 resonance considered here, the calculation needs to be adapted. In particular, the cubic terms need to be recomputed to take into account the resonant monomials of second order that are due to the 1:2 resonance. In turn, these resonant terms will modify some coefficients used for the change of coordinates, and some of the cubic terms of the normal form. The aim of this section is thus to enlarge the general results provided in [11] to the case of a 1:2 resonance.

For the sake of conciseness, only the result of this calculation is given here in the main text. The interested reader can find the full demonstration and the complete calculation in "Appendix B". The real normal form of Eq. (1), up to cubic order, with a 1:2 internal resonance between the two eigenfrequencies ($\omega_2 \approx 2\omega_1$), reads:

$$\ddot{R}_1 + \omega_1^2 R_1 + g_{12}^1 R_1 R_2 + (h_{111}^1 + A_{111}^1) R_1^3 + (h_{122}^1 + A_{122}^1) R_1 R_2^2 + B_{111}^1 R_1 \dot{R}_1^2 + B_{122}^1 R_1 \dot{R}_2^2 + B_{212}^1 R_2 \dot{R}_1 \dot{R}_2 = 0, \tag{2a}$$

$$\ddot{R}_2 + \omega_2^2 R_2 + g_{11}^2 R_1^2 + (h_{112}^2 + A_{112}^2 - D_{112}^2) R_1^2 R_2 + (h_{222}^2 + A_{222}^2) R_2^3 + (B_{112}^2 - E_{112}^2) R_1 \dot{R}_1 \dot{R}_2 + B_{211}^2 R_2 \dot{R}_1^2 + B_{222}^2 R_2 \dot{R}_2^2 = 0. \tag{2b}$$

In these equations, (R_1, R_2) are the *normal* coordinates, homogeneous to a displacement. These new coordinates are nonlinearly related to the original ones thanks to an identity-tangent nonlinear mapping. For completeness, the nonlinear change of coordinate needs to consider both the displacements (original displacement with X_p coordinate and normal displacement with R_p, p=1,2) and the velocities, here written as $Y_p = \dot{X}_p$ for the original coordinates, and $S_p = \dot{R}_p$ for the normal ones. The nonlinear mappings read, for p=1,2:

$$X_p = R_p + \sum_{i=1}^{2}\sum_{j\geq i}^{2} a_{ij}^p R_i R_j + \sum_{i=1}^{2}\sum_{j\geq i}^{2} b_{ij}^p S_i S_j + \sum_{i=1}^{2}\sum_{j\geq i}^{2}\sum_{k\geq j}^{2} r_{ijk}^p R_i R_j R_k + \sum_{i=1}^{2}\sum_{j=1}^{2}\sum_{k\geq j}^{2} u_{ijk}^p R_i S_j S_k, \tag{3a}$$

$$Y_p = S_p + \sum_{i=1}^{2}\sum_{j=1}^{2} \gamma_{ij}^p R_i S_j + \sum_{i=1}^{2}\sum_{j\geq i}^{2}\sum_{k\geq j}^{2} \mu_{ijk}^p S_i S_j S_k + \sum_{i=1}^{2}\sum_{j=1}^{2}\sum_{k\geq j}^{2} \nu_{ijk}^p S_i R_j R_k. \tag{3b}$$

The expressions of all the introduced coefficients in Eq. (3) are given in "Appendix B", following the general formulas given in [11]. In Eq. (2), only the resonant monomials are present. Due to the 1:2 internal resonance, only two quadratic monomials are present, instead of the six in the original Eq. (1). Due to the asymptotic nature of the normal form calculation, which eliminates the non-resonant terms order by order, the coefficients of the cubic terms are modified by the appearance of A_{ijk}^p, B_{ijk}^p, D_{ijk}^p and E_{ijk}^p. The first two coefficients A_{ijk}^p and B_{ijk}^p have already been considered in [11], and their expressions read:

$$A_{ijk}^p = \sum_{l\geq i}^{N} g_{il}^p a_{jk}^l + \sum_{l\leq i}^{N} g_{li}^p a_{jk}^l, \tag{4a}$$

$$B_{ijk}^p = \sum_{l\geq i}^{N} g_{il}^p b_{jk}^l + \sum_{l\leq i}^{N} g_{li}^p b_{jk}^l. \tag{4b}$$

One can note in particular that these two coefficients appear due to the elimination of the non-resonant quadratic terms, hence they involve only quadratic original g_{ij}^p coefficients, with the coefficients of the quadratic part of the nonlinear mappings: a_{jk}^p and b_{jk}^p. The last two terms, D_{ijk}^p and E_{ijk}^p, are new as compared to the general results presented in [11], and their presence is only due to the existence of the 1:2 internal resonance and the two resonant quadratic monomials in the normal form. Their expressions write:

$$D_{112}^2 = \gamma_{22}^2 g_{11}^2 - 2b_{22}^2 g_{11}^2 \omega_2^2, \tag{5a}$$

$$E_{112}^2 = 4b_{22}^2 g_{11}^2. \tag{5b}$$

The remainder of the paper consists in analyzing the solutions of the normal form of the system with 1:2 internal resonance and up to cubic terms, Eq. (2). A particular emphasis will be set to understand the effect of the *non-resonant* quadratic monomials on the dynamical characteristics of the system. Note that these non-resonant monomials have been cancelled in Eq. (2). However, the associated coefficients g_{ij}^p intervene in the cubic terms, and will thus have an important effect on backbone curves and frequency response functions. The analysis will be done using a multiple scales solution up to the second-order to take the cubic terms into account.

2.2 Multiple scales solution: modulation equations

In this section, an approximate analytical solution of the normal form system (2), using the multiple scales method (MSM), is proposed. Analytical solutions of 1:2 internally resonant problems have been proposed in many instances, for example, with the MSM for first and second-order developments [1, 39]. They are, however, generally restricted to the case with forcing and damping, and cubic terms are generally not taken into account. Besides, the study of the backbones for free vibration problems has been only recently considered, see e.g. [10, 13], but still without considering the cubic terms. The main aim of the development proposed here is to extend these latter results by including the effect of cubic terms, in the presence of 2:1 internal resonance. For other types of internal resonance, such as 1:1 internal resonance, one can refer to [40], where detailed second-order MSM derivations are established to obtain the free solution of Eq. (1), considering all the quadratic and cubic terms.

Eq. (2) are first rewritten by introducing a small bookkeeping parameter ε in order to scale the different nonlinear terms as:

$$\ddot{R}_1 + \omega_1^2 R_1 = -\varepsilon\beta_1 R_1 R_2 - \varepsilon^2\left[\alpha_1 R_1^3 + \alpha_2 R_1 R_2^2 + \alpha_3 R_1 \dot{R}_1^2 + \alpha_4 R_1 \dot{R}_2^2 + \alpha_5 R_2 \dot{R}_1 \dot{R}_2\right], \tag{6a}$$

$$\ddot{R}_2 + \omega_2^2 R_2 = -\varepsilon\beta_2 R_1^2 - \varepsilon^2\left[\alpha_6 R_1^2 R_2 + \alpha_7 R_2^3 + \alpha_8 R_1 \dot{R}_1 \dot{R}_2 + \alpha_9 R_2 \dot{R}_1^2 + \alpha_{10} R_2 \dot{R}_2^2\right], \tag{6b}$$

where the coefficients $\alpha_k, k = 1, \ldots 10$ have been simply introduced from Eq. (2), see Eq. (50) in "Appendix C" for their detailed expressions.

The second-order expansion using MSM requires the definition of three time scales $T_0 = t, T_1 = \varepsilon t$, and $T_2 = \varepsilon^2 t$. Following the method (see "Appendix C" for details), the free solution is approximated as:

$$R_1(t) = a_1(T_1, T_2)\cos(\omega_1 T_0 + \theta_1(T_1, T_2)) + O(\varepsilon), \tag{7a}$$

$$R_2(t) = a_2(T_1, T_2)\cos(\omega_2 T_0 + \theta_2(T_1, T_2)) + O(\varepsilon), \tag{7b}$$

where a_1, a_2, θ_1 and θ_2 are real functions of the slow time scales only (T_1, T_2). The nearness of the internal resonance condition leads to define the internal detuning parameter σ as:

$$\varepsilon\sigma = 2\omega_1 - \omega_2. \tag{8}$$

The complete derivation is reported in "Appendix C" for the sake of brevity. Solvability conditions are obtained by eliminating resonant terms both at orders ε and ε^2, leading respectively to two sets of equations of the form $D_1 A = \ldots$ and $D_2 A = \ldots$ for each of the slow time scales (where D_1 and D_2 refers to a partial derivative with respect to T_1 and T_2). These two sets of equations can be recombined using the so-called reconstitution method [39, 41], yielding:

$$\dot{A} = \frac{\mathrm{d}A}{\mathrm{d}t} = \varepsilon D_1 A + \varepsilon^2 D_2 A + O(\varepsilon^3), \tag{9}$$

for any complex amplitude $A(T_1, T_2)$. After some algebra, detailed in "Appendix C", one obtains the following slow time scale modulation equations:

$$\dot{a}_1 = \frac{\varepsilon\beta_1 a_1 a_2}{4\omega_1}\left[1 + \frac{\varepsilon\sigma}{2\omega_1}\right]\sin\gamma_p, \tag{10a}$$

$$\dot{a}_2 = -\frac{\varepsilon\beta_2 a_1^2}{4\omega_2}\left[1 - \frac{\varepsilon\sigma}{2\omega_2}\right]\sin\gamma_p, \tag{10b}$$

$$\dot{\theta}_1 = \frac{\varepsilon\beta_1 a_2}{4\omega_1}\left[1 + \frac{\varepsilon\sigma}{2\omega_1}\right]\cos\gamma_p - \varepsilon^2\frac{\Lambda_1 a_2^2 + \Lambda_2 a_1^2}{8\omega_1}, \tag{10c}$$

$$\dot{\theta}_2 = \frac{\varepsilon\beta_2 a_1^2}{4\omega_2 a_2}\left[1 - \frac{\varepsilon\sigma}{2\omega_2}\right]\cos\gamma_p - \varepsilon^2\frac{\Lambda_3 a_1^2 + \Lambda_4 a_2^2}{8\omega_2}, \tag{10d}$$

where

$$\gamma_p = 2\theta_1 - \theta_2 + \sigma T_1. \tag{11}$$

Note that these recombined equations now explicitly depend on both quadratic terms, via the (β_1, β_2) coefficients; and cubic terms, via the newly introduced coefficients $\Lambda_k, k = 1, \ldots 4$, which read:

$$\Lambda_1 = -\beta_1^2\left[\frac{1}{4\omega_1^2} + \frac{1}{\omega_2(2\omega_1 + \omega_2)}\right] - 2\alpha_4\omega_2^2 - 2\alpha_2, \tag{12a}$$

$$\Lambda_2 = \beta_1\beta_2\left[\frac{1}{4\omega_1\omega_2} + \frac{2}{\omega_2^2}\right] - \alpha_3\omega_1^2 - 3\alpha_1, \tag{12b}$$

$$\Lambda_3 = \beta_1\beta_2\left[\frac{1}{2\omega_1\omega_2} - \frac{2}{\omega_2(2\omega_1+\omega_2)}\right] - 2\alpha_6 - 2\alpha_9\omega_1^2, \tag{12c}$$

$$\Lambda_4 = -3\alpha_7 - \alpha_{10}\omega_2^2. \tag{12d}$$

On can remark as a particular feature that the coefficients α_5 and α_8 do not appear in the above Λ_i expressions, even though they are associated to resonant cubic monomials in the real normal form. The MSM expansion shows that their effect is seen from the next order of development. As a matter of fact, real normal form differs from complex normal form, is less symmetric, and produces more resonant monomials. Also, the MSM expansion, using complex notations, implicitly relies on the complex normal form, and expresses the resonant monomials through the solvability condition. Hence it can be concluded that the monomials associated with α_5 and α_8 are resonant for the real normal form, but not for the complex normal form, explaining the fact that they disappear when one writes down the modulation equation with the MSM.

Since γ_p explicitly depends on the slow time scale T_1, the system defined by Eqs. (10a–10d) is not autonomous. Then, it is convenient to combine the phase Eqs. (10c,10d) with (11) to obtain:

$$\begin{aligned}\dot{\gamma}_p =& \varepsilon\sigma + \left(\frac{\varepsilon\beta_1 a_2}{2\omega_1}\left[1+\frac{\varepsilon\sigma}{2\omega_2}\right] - \frac{\varepsilon\beta_2 a_1^2}{4a_2\omega_2}\left[1-\frac{\varepsilon\sigma}{2\omega_2}\right]\right)\cos\gamma_p \\ &+ \varepsilon^2\left(\frac{\Lambda_3 a_1^2+\Lambda_4 a_2^2}{8\omega_2} - \frac{\Lambda_1 a_2^2+\Lambda_2 a_1^2}{4\omega_1}\right),\end{aligned} \tag{13}$$

in which $\mathrm{d}T_1/\mathrm{d}t = \varepsilon$ has been used. Consequently, one obtains two equivalent *autonomous systems*, being, respectively Eqs. (10a, 10b, 10c)–(13) in term of variables $(a_1, a_2, \theta_1, \gamma_p)$ and Eqs. (10a, 10b, 10d)–(13) in term of variables $(a_1, a_2, \theta_2, \gamma_p)$. This generic four-dimensional dynamical system will be reduced to a three-dimensional one in the next section, in the particular case of stationary solutions. One must also remark that Eqs. (10c, 10d) (and consequently Eq. (13)) are valid only if $a_1, a_2 \neq 0$ since they result from Eqs. (62c, 62d) divided respectively by a_1 and a_2.

Now that the modulation equations have been derived, the focus will be on analyzing their solutions. Before proceeding in the next section, it is worth underlining that the quadratic terms in Eq. (62) are the same as those reported in [10], obtained with a first-order MSM solution, hence highlighting how the results presented here will extend earlier derivations. Another important point, discussed in "Appendix C and E", is that these modulation equations are slightly different from those obtained in previous studies, see e.g. Eqs. (175–178) of [39], in which a similar problem is considered through a second-order MSM solution. The discrepancies are the consequence of the different assumptions used in the MSM process. In particular, alternative derivations, as those presented in [39], have been deeply analyzed and compared to the ones presented here, and "Appendix E" is completely devoted to these calculations, which clearly show that the retained assumptions lead to better results as compared to reference numerical solutions, justifying our final choice.

2.3 Branches of stationary solutions

Integrating the modulation Eq. (10) can lead to various free vibration solutions, depending on the four initial conditions $R_1(0)$, $R_2(0)$, $\dot{R}_1(0)$, $\dot{R}_2(0)$. Restricting ourselves to solutions that are stationary in amplitude, *i.e.* such that $\mathrm{d}a_1/\mathrm{d}t = \mathrm{d}a_2/\mathrm{d}t = 0$, imposes a stringent condition on the phase γ_p, since non trivial solutions are obtained when $\sin\gamma_p = 0$, which implies that γ_p *is also stationary*, with value $\gamma_p = k\pi$ with $k \in \mathbb{Z}$ and $\cos\gamma_p = p$ with $p = \pm 1$.

Then, because a_1, a_2 and γ_p are constants, one obtains three conditions. The second member of Eq. (10c, 10d) are constants, which leads to the first two:

$$\dot{\theta}_1 = \tilde{\omega}_1 = \Gamma_1 p\, a_2 + \Gamma_2 a_1^2 + \Gamma_3 a_2^2 \quad\Rightarrow\quad \theta_1(t) = \tilde{\omega}_1 t + \phi_1; \tag{14a}$$

$$\dot{\theta}_2 = \tilde{\omega}_2 = \Gamma_4 p\,\frac{a_1^2}{a_2} + \Gamma_5 a_1^2 + \Gamma_6 a_2^2 \quad\Rightarrow\quad \theta_2(t) = \tilde{\omega}_2 t + \phi_2, \tag{14b}$$

where ϕ_1 and ϕ_2 are integration constants and the coefficients Γ_k, $k = 1, \ldots 6$ are functions of the system's parameters. Their expression naturally appear in the modulation equations in the process of the MSM, see "Appendix C" for details, and their explicit expressions read:

$$\Gamma_1 = \frac{\varepsilon\beta_1}{4\omega_1}\left[1+\frac{\varepsilon\sigma}{2\omega_1}\right], \quad \Gamma_4 = \frac{\varepsilon\beta_2}{4\omega_2}\left[1-\frac{\varepsilon\sigma}{2\omega_2}\right], \tag{15a}$$

$$\Gamma_2 = -\frac{\varepsilon^2\Lambda_2}{8\omega_1}, \quad \Gamma_3 = -\frac{\varepsilon^2\Lambda_1}{8\omega_1}, \quad \Gamma_5 = -\frac{\varepsilon^2\Lambda_3}{8\omega_2}, \quad \Gamma_6 = -\frac{\varepsilon^2\Lambda_4}{8\omega_2}. \tag{15b}$$

Finally, the third condition is the following relationship between a_1 and a_2, obtained with Eqs. (11), (14a, 14b):

$$\dot{\gamma}_p = 2\tilde{\omega}_1 - \tilde{\omega}_2 + \varepsilon\sigma = 0 \quad \Rightarrow \quad a_1^2 = \frac{(2\omega_1-\omega_2)a_2 + 2\Gamma_1 p\, a_2^2 + (2\Gamma_3-\Gamma_6)a_2^3}{\Gamma_4 p + (\Gamma_5 - 2\Gamma_2)a_2}. \tag{16}$$

Then, eliminating (θ_1, θ_2) in Eqs (7a, 7b) with Eqs. (14a–14b), one obtains:

$$R_1(t) = a_1 \cos\left(\omega_{\mathrm{nl1}}t + \phi_1\right) + O(\varepsilon), \tag{17a}$$

$$R_2(t) = a_2 \cos\left(\omega_{\mathrm{nl2}}t + \phi_2\right) + O(\varepsilon), \tag{17b}$$

where the nonlinear frequencies are functions of the amplitudes as follows:

$$\omega_{\mathrm{nl1}} = \omega_1 + \Gamma_1 p\, a_2 + \Gamma_2 a_1^2 + \Gamma_3 a_2^2, \tag{18a}$$

$$\omega_{\mathrm{nl2}} = \omega_2 + \Gamma_4 p\,\frac{a_1^2}{a_2} + \Gamma_5 a_1^2 + \Gamma_6 a_2^2. \tag{18b}$$

One can notice that the obtained solutions are families of periodic orbits, with frequencies ω_{nl1} and ω_{nl2} depending on the amplitudes a_1 and a_2. The frequency dependence upon amplitudes given in Eq. (18) defines the two backbone curves of the coupled solutions of the system. In phase space, the corresponding families of periodic orbits lie on invariant manifolds known as a Lyapunov Subcenter Manifold (LSM) in this conservative case [27]. This LSM is univocally defined as a nonlinear mode (NNM) in vibration theory [11, 12, 27, 42, 43].

Based on the above developments, several solutions can be found:

- The trivial solution $a_1 = a_2 = 0$;
- An uncoupled solution with $(a_1 \neq 0, a_2 = 0)$, denoted as the U1-mode. Eq. (62d) shows that $a_2 = 0 \Rightarrow a_1 = 0$ so that this U1-mode is not admissible[1]. Going back to the initial system (6), this result is natural since a quadratic invariance breaking term $\beta_2 R_1^2$ is present in the second equation. Consequently, the U1-mode does not exist as a possible solution of the system.
- An uncoupled solution with $(a_1 = 0, a_2 \neq 0)$, denoted as the U2-mode. This solution is possible and corresponds to the single mode vibration of the second mode. Since it is dictated by a nonlinear oscillator, on can easily derives the uncoupled backbone curve of the U2-mode from Eq. (18b) as

$$\omega_{\mathrm{nl2}} = \omega_2\left(1 + \frac{\Gamma_6}{\omega_2}a_2^2\right). \tag{19}$$

The backbone curve of the U2-mode, obtained by imposing $R_1 = 0$ in the second equation of the initial system (6b), has thus a hardening/softening behaviour dictated by the sign of Γ_6.

- a coupled solution with $(a_1 \neq 0, a_2 \neq 0)$, denoted as C− mode. In this case, the fact that γ_p is a constant, see Eq. (16), shows that the *oscillations of the two DOFs are locked*, in *frequency and phase*:

$$\omega_{\mathrm{nl1}} = \omega_{\mathrm{nl2}}/2, \quad \phi_1 = (\phi_2 + k\pi)/2, \tag{20}$$

as well as in *amplitude* since a_1 is a function of a_2 thanks to Eq. (16). At this stage, one must remember that two values for $\cos\gamma_p = p = \pm 1$ are admissible, leading to *two distinct coupled modes*: the C+ mode, with $p = 1$, k even and the C− mode, with $p = -1$, k odd. An interesting consequence of the locking is the shape of those C+ and C− modes in the configuration space (R_1, R_2). Using Eq. (20) in Eqs. (17a, 17b), one obtains:

$$R_1(t) = a_1 \cos\left(\frac{\omega_{\mathrm{nl2}}}{2}t + \frac{\phi_2 + k\pi}{2}\right) + O(\varepsilon), \tag{21a}$$

$$R_2(t) = a_2 \cos\left(\omega_{\mathrm{nl2}}t + \phi_2\right) + O(\varepsilon), \tag{21b}$$

from which one easily shows that:

---

[1] One cannot use directly Eq. (14b), since it is valid only if $a_1, a_2 \neq 0$

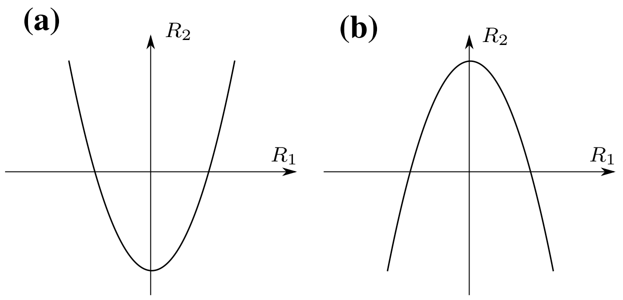

Fig. 1 Parabolic Modes of the coupled solutions in the configuration plane $(R_1(t), R_2(t))$. **a** the C+ mode and **b** the C− mode

$$\text{C+ mode:}\quad \frac{R_2}{a_2} = 2\frac{R_1^2}{a_1^2} - 1; \qquad \text{C − mode:}\quad \frac{R_2}{a_2} = -2\frac{R_1^2}{a_1^2} + 1. \tag{22}$$

The two above equations show that the two modes have the shape of parabolas in the space (R_1, R_2), as shown in Fig. 1, a result that has already been underlined in [10], but using a first-order MSM on a quadratic system. Analogous results on the topology of coupled modes were also obtained in the case of 1:1 internal resonance, where the modes were denoted, depending on their shape in the configuration space, as “normal mode” and “elliptic mode” [44, 45].

The main difference in the results reported here, as compared, for example, to the recent ones on the backbone curves derived in [10], lies in the fact that cubic terms are taken into account thanks to the normal form approach and the second-order MSM. The main consequence is that the backbone curve of the U2-mode has a curvature and is not a straight line anymore, because of the cubic term. In the same context, the coupled backbones of the C+ and C− modes will show a curvature, a feature that was not present in [10].

2.4 Existence conditions and branching of the coupled solution

This section is devoted to the derivation of results on the existing conditions of the C+ and C− modes and their branching to the U2-mode. Only the mathematical derivations are given, illustrative examples being postponed to Sect. 3.1 where a special emphasis on the topology of the bifurcated solutions will be given.

Starting with the uncoupled solution (U2-mode), one easily observes that there are no restriction that might give rise to a condition of existence. The discussion can thus focus on the case of the coupled C+ and C− modes. A simple condition is derived by imposing that the expression of a_1^2 in Eq. (16) must be positive. For the ease of the discussion, let us first consider the simplified case of the first-order MSM solution, already analyzed in [10]. This case is obtained by dropping all ε^2 terms in Eq. (15), leading to $\Gamma_1 = \varepsilon\beta_1/(4\omega_1)$, $\Gamma_4 = \varepsilon\beta_2/(4\omega_2)$ and $\Gamma_2 = \Gamma_3 = \Gamma_5 = \Gamma_6 = 0$. The positive sign of a_1^2 from Eq. (16) depends on the signs of β_1 and β_2, leading to the two following conditions that enforces $a_1^2 \geq 0$:

$$\begin{aligned} &\mathrm{sign}\beta_1 = \mathrm{sign}\beta_2 \Rightarrow a_2 \geq -p\zeta_0; \\ &\mathrm{sign}\beta_1 \neq \mathrm{sign}\beta_2 \Rightarrow a_2 \leq -p\zeta_0, \end{aligned} \tag{23}$$

with

$$\zeta_0 = \frac{2\omega_1 - \omega_2}{2\Gamma_1} = \frac{2\omega_1(2\omega_1 - \omega_2)}{\varepsilon\beta_1} = \frac{2\omega_1\sigma}{\beta_1}. \tag{24}$$

Hence in this simplified case, $-p\zeta_0$ appears as the unique root where a_1^2 vanishes in Eq. (16). Since we can consider $a_2 > 0$ without loss of generality, the coupled backbones exist only if β_1 and β_2 share the same sign, and one of the coupled backbones is defined for $a_2 \geq 0$ whereas the other exists for $a_2 \geq |\zeta_0|$ (reminding that $p = \pm 1$). In this latter case, $a_2 = |\zeta_0|$ leads to $a_1 = 0$ and to $\omega_{\mathrm{nl}2} = \omega_2$, which means that one of the coupled backbones emerges from the uncoupled U2-mode backbone curve (which is in this simplified case the vertical line $\omega_{\mathrm{nl}2} = \omega_2$) at a non zero amplitude $a_2 = |\zeta_0|$. In the special case of $\sigma = 0$, both backbones emerge at a vanishing amplitude, and from the x-axis (referring to the frequency) at the same point as $\omega_2 = 2\omega_1$.

Let us now analyze the more difficult present case of the solutions at second order. In this case, the situation is less straightforward since it depends on all six nonzero Γ_k coefficients. Requiring that a_1^2 is positive in Eq. (16) leads to the following condition:

$$\begin{aligned} L(a_2) \equiv a_2\Big[&(2\omega_1 - \omega_2) + 2\Gamma_1 p\, a_2 \\ &+ (2\Gamma_3 - \Gamma_6)a_2^2\Big]\Big[\Gamma_4 p + (\Gamma_5 - 2\Gamma_2)a_2\Big] \geq 0, \end{aligned} \tag{25}$$

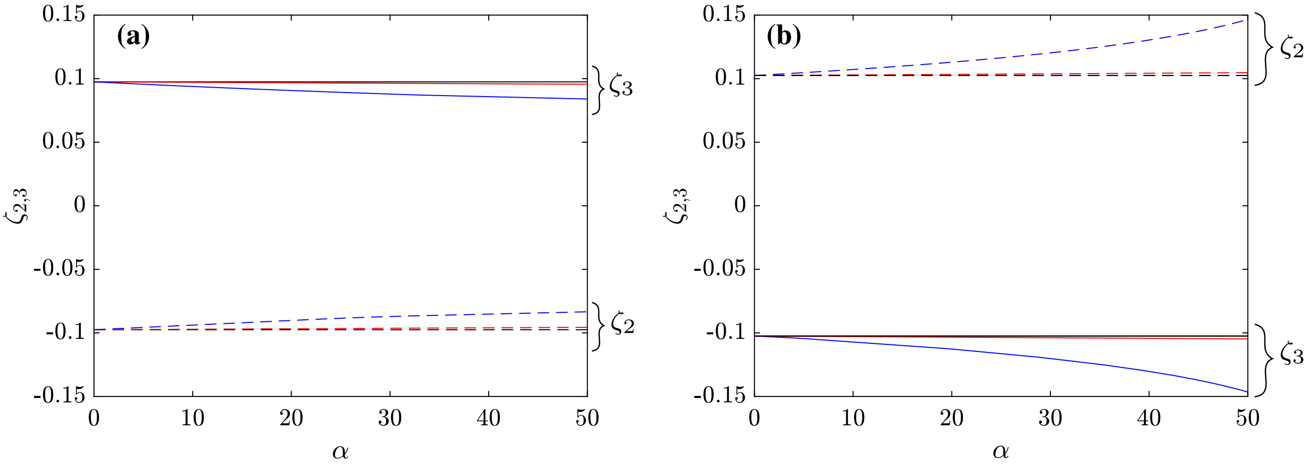

Fig. 2 Behaviour of the roots $\zeta_{2,3}$ as function of the cubic α coefficient taken with equal values for simplicity ($\alpha = \alpha_k\ \forall k$) and with $\beta_1 = \beta_2 = 1$. Solid lines refers to the C+ mode with $p = 1$, while dashed lines refers to the C− mode with $p = -1$. The red and blue lines denote respectively the case with $\varepsilon = 0.001$ and $\varepsilon = 0.01$. The black line denotes $-p\zeta_0$. (**a**) case of a negative detuning with $\omega_2 = 2$ and $\omega_1 = 0.975$, (**b**) case of a positive detuning with $\omega_2 = 2$ and $\omega_1 = 1.025$. (Color figure online)

where $L(a_2)$ is the product of the numerator and denominator of the right-hand side of Eq. (16). The roots of the polynomial $L(a_2)$ are:

$$\zeta_1 = \frac{\Gamma_4 p}{2\Gamma_2 - \Gamma_5},$$
$$\zeta_{2,3} = \frac{1}{\Gamma_6 - 2\Gamma_3}\left[\Gamma_1 p \pm \sqrt{\Gamma_1^2 + (2\omega_1 - \omega_2)(\Gamma_6 - 2\Gamma_3)}\right], \tag{26}$$

in addition to the vanishing solution. The two roots $\zeta_{2,3}$ are important since they come from the numerator of a_1^2, such that they nullify a_1 ($a_2 = \zeta_{2,3} \Rightarrow a_1 = 0$). In comparison to the above considered first-order MSM results, the three roots $\zeta_{1,2,3}$ are obtained instead of the single root $-p\zeta_0$. Note that, as long as ε is small, the second-order MSM solution is a correction to the first-order, and thus should not change the situation drastically. In particular, in the spirit of perturbative reasoning based on the leading orders, one can easily assume that Γ_2, Γ_3, Γ_5, and Γ_6 are small. Consequently, since the denominators $2\Gamma_2 - \Gamma_5$ and $\Gamma_6 - 2\Gamma_3$ are small, one of the two roots, either ζ_2 or ζ_3, should be close to $-p\zeta_0$, whereas the two others, either ζ_2 or ζ_3 in addition to ζ_1, are far from $-p\zeta_0$ in absolute value. As a consequence, we can conjecture by perturbative reasoning that the starting point of the coupled backbone curves in the plane $(\omega_{\mathrm{nl}2}, a_2)$ admits an amplitude of ζ_2 (or ζ_3) and represents a branching point from the uncoupled backbone curves.

To illustrate the above reasoning, we assume an equal value for all cubic coefficients $\alpha_i = \alpha$, $\forall i = 1, \ldots 10$ to control the amount of cubic terms with a single parameter. Then, Fig. 2 shows the evolution of the roots $\zeta_{2,3}$ from Eq. (26), and $-p\zeta_0$, from Eq. (24) as a function of α for two different values of ε and two different values of the detuning. It clearly shows that the new roots $\zeta_{2,3}$ of the second-order analysis emerge from the root $-p\zeta_0$ of the first-order analysis, hence validating the above perturbative reasoning. This will be further illustrated in Figs. 3 and 4 in the next section, showing undoubtedly that the coupled backbone that starts at a non-zero-amplitude branches from the uncoupled U2 mode. With a calculation, this can be verified by substituting a_2 from the numerator of Eq. (16), which defines $\zeta_{2,3}$, in (18a), to obtain Eq. (19).

Note that in the special case of $\sigma = 0$ ($\omega_2 = 2\omega_1$), ζ_1 is given by Eq. (26) and the two roots reads:

$$\zeta_{2,3} = 0 \quad \text{or} \quad \frac{2p\Gamma_1}{\Gamma_6 - 2\Gamma_3}, \tag{27}$$

With the same reasoning, since $\Gamma_6 - 2\Gamma_3$ is small with respect to Γ_1, $\zeta_0 = 0$ is replaced here by $\zeta_{2,3} = 0$, showing that the branching point between the U2-mode and the coupled-mode backbones appears at $a_2 = 0$.

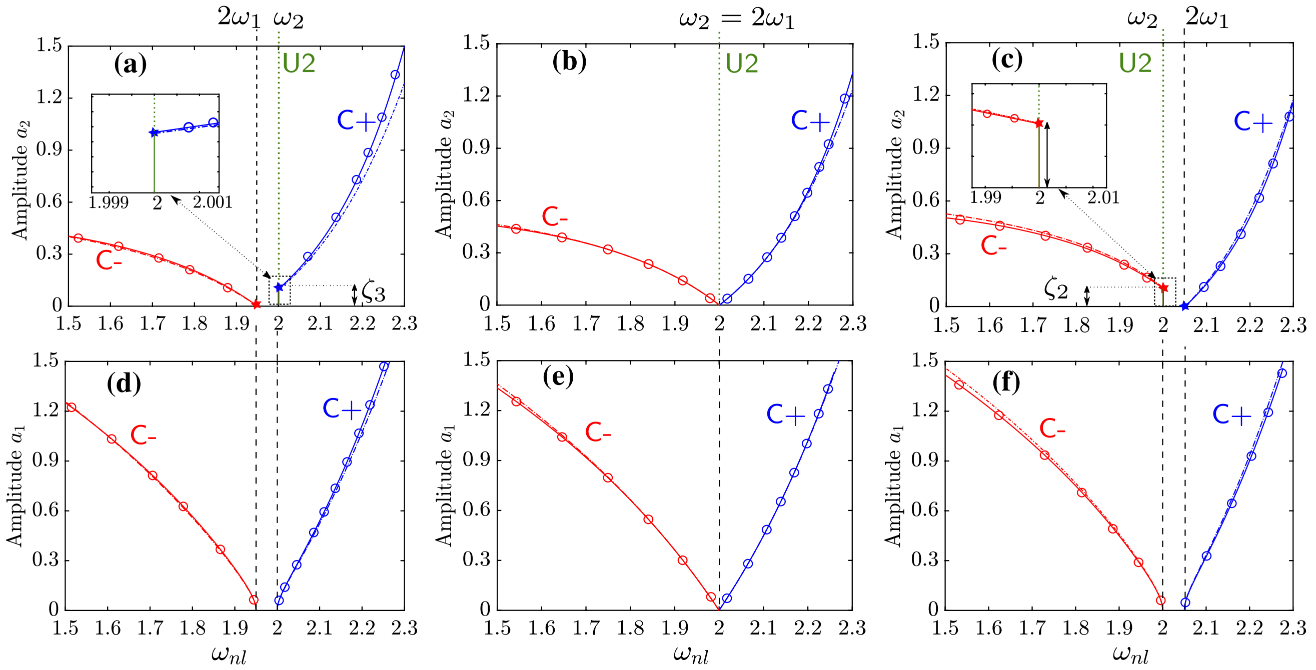

Fig. 3 Backbone curves of the system in the specific case where only the quadratic resonant terms are considered such that $g_{12}^1 = g_{11}^2 = 1$, while the other nonlinear coefficients are zero. Three different detunings are analyzed: $\sigma = -0.05$ (first column), $\sigma = 0$ (second column), and $\sigma = 0.05$ (third column). Comparison between the second-order MSM result (dash-dotted) and the reference numerical solution directly obtained from the normal form (2a–d) (solid line with circle markers). Coupled solutions, C+ mode and C− mode, are plotted in blue and red, respectively. The uncoupled solution (U2 mode) is plotted in green with solid and dotted lines denote the stable and unstable solutions, respectively. (Color figure online)

All these results complement and extend those given in [10]. In particular, the fact that the branch point of the coupled backbones lies on the uncoupled one was not demonstrated in [10]. Moreover, we have shown here that the result extends when considering the cubic terms. The main difference is that under such assumption, the backbone curve of the U2-mode is now curved (thanks to the cubic term). However, the branching point of the C+/C− solution remains on the same uncoupled backbone.

2.5 Stability of the coupled C+ and C− solutions

The stability of the solutions requires computing the eigenvalues of the Jacobian of the modulation equations. For the ease of the solution, it appears more convenient to compute this Jacobian for the underlying three-dimensional autonomous system obtained from the two amplitude Eqs. (10a, 10b), complemented with the angular Eq. (13) (see "Appendix C" for the calculation details). Since there is no damping in the system, the stability is assessed if the eigenvalues are either zero or purely imaginary, leading to a neutrally stable fixed point [4].

In the case of the coupled C+ and C− solutions, the Jacobian is written in "Appendix D" and leads to the eigenvalues:

$$\lambda_1 = 0, \quad \lambda_{2,3} = \pm a_1 \sqrt{\nu a_2 - \Gamma_4^2 \frac{a_1^2}{a_2^2} - 4\Gamma_1\Gamma_4}, \tag{28}$$

with

$$\nu = 2\Gamma_4 p(\Gamma_6 - 2\Gamma_3) + 2\Gamma_1 p(2\Gamma_2 - \Gamma_5). \tag{29}$$

In the most general case of arbitrary coefficients Γ_k, assessing the sign of the radicand is difficult. More simple reasoning can be conducted with a perturbative approach, as in the previous section. Indeed, if ε is small, then $\Gamma_{2,3,5,6}$ are also small with respect to $\Gamma_{1,4}$. Consequently at first-order (thus coinciding with the solution analyzed in [10]), the eigenvalues simplifies to $\lambda_{2,3} \simeq \pm a_1 \sqrt{-\Gamma_4^2 a_1^2 / a_2^2 - 4\Gamma_1\Gamma_4}$. If β_1 and β_2 share the same sign, it is also the case for Γ_1 and Γ_4 and one

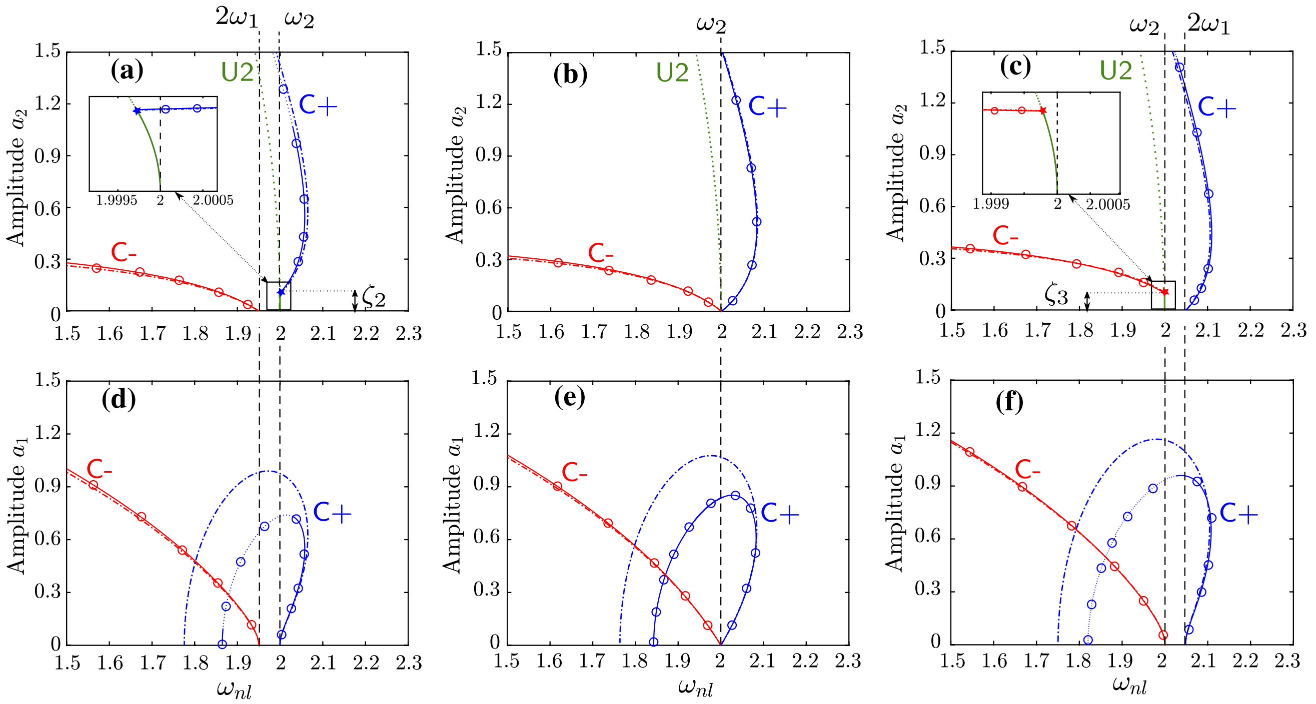

Fig. 4 Backbone curves of the system with quadratic and cubic terms considered: $g^1_{12} = g^2_{11} = 1$, $g^1_{11} = g^1_{22} = g^2_{12} = g^2_{22} = 0.5$, and $h^p_{ijk} = 0.1$ for i, j, k, and $p = 1, 2$. Three different detunings are considered: $\sigma = -0.05$ (first column), $\sigma = 0$ (second column), and $\sigma = 0.05$ (third column). Comparison between the second-order MSM result (dash-dotted) and the reference numerical solution directly obtained from the original Eqs. (2a–d) (solid line for stable solution, dotted line for unstable solution, with circle markers on both types of numerical solutions). Coupled solutions, C+ mode and C− mode, are plotted in blue and red, respectively. The uncoupled solution (U2 mode) is plotted in green with solid and dotted lines denote the stable and unstable solutions, respectively. (Color figure online)

concludes that $\lambda_{2,3}$ are purely imaginary. The coupled solutions C+ and C− are then stable.

Following the same reasoning as in the previous section, the second-order solution can be assessed as a perturbation of the first-order, and one can conclude that for small amplitudes, the coupled backbones will thus be stable. Note that following these branches of the solution to higher amplitudes, then the stability might change, leading to secondary bifurcations and loss of stability of the coupled solutions. This is left for further study and outside the scope of the present analytical development.

2.6 Stability of the uncoupled U2 solution

In the case of the uncoupled U2 solution, the situation is more intricate since the modulation Eqs. (10a, 10b), (13) in the polar form lead to a singular Jacobian. In fact, $a_1 = 0$ for the U2-mode, which means that θ_1 and thus γ_p are not properly defined. One has then to use a Cartesian form of the modulation equations that is written in "Appendix D". In the case of the U2 solution, the eigenvalues of the Jacobian of the modulation equations read (see Eq. (80)):

$$\lambda_1 = 0, \quad \lambda_{2,3} = \pm\sqrt{-N(a_2, 1)N(a_2, -1)}, \tag{30}$$

where $N(a_2, p) = (2\omega_1 - \omega_2)/2 + p\Gamma_1 a_2 + (\Gamma_3 - \Gamma_6/2)a_2^2$. Notice that the zeros of $N(a_2, p)$ in term of a_2 are $\zeta_{2,3}$ introduced in Sect. 2.4 and that $2a_2N(a_2, p)$ is precisely the numerator of a_1^2 in Eq. (16). Consequently, the value $a_2 = \zeta_{2,3}$ makes $\lambda_{2,3} = 0$, which immediately proves that there is a change of stability of the U2-mode at the branching points between the U2-mode and the C+/C− modes, depending on the sign of $2\omega_1 - \omega_2$ and of $p = \pm 1$.

Then, assessing the sign of $N(a_2, p)$ seems difficult in the general case of arbitrary values of $\Gamma_{1,3,6}$ but, as done before, we refer to the first-order MSM solution. In this case, $\Gamma_3 = \Gamma_6 = 0$ and the eigenvalues reads:

$$\lambda_{2,3} = \pm\sqrt{\Gamma_1^2 a_2^2 - \frac{(2\omega_1 - \omega_2)^2}{4}} \tag{31}$$

in which the radicand is negative if $0 < a_2 < |\zeta_0|$ and is positive if $a_2 > |\zeta_0|$, with ζ_0 defined in Eq. (24). Consequently, in the case of the first-order MSM solution, the U2-mode is stable for a_2 below the branching point with the coupled mode, and is unstable above. The branching point between the U2 and the C+/C− modes is consequently a supercritical pitchfork bifurcation. In the general case for which $\Gamma_{3,6}$ are non-zero, one can use the perturbative reasoning, based on the fact that the coefficients of the second-order are small and that we are evaluating locally the loss of stability at the branching point (which is for small amplitudes). Then, one can conclude that the above findings are still valid with ζ_0 replaced by $\zeta_{2,3}$ (see Fig. 2).

In the special case without detuning, $\sigma = 0$ ($\omega_2 = 2\omega_1$), Eq. (30) predicts that

$$\lambda_{2,3} = \pm a_2\sqrt{4\Gamma_1^2 - (2\Gamma_3 - \Gamma_6)^2 a_2^2}/2. \tag{32}$$

Using the same reasoning as in Sect. 2.4, the radicand of the square root is positive, showing that the eigenvalue are real for all $a_2 > 0$. Consequently in this case without detuning, the U2-mode branch is fully unstable, which is in agreement with the location of the branch point at $a_2 = 0$.

3 Backbone curves, frequency response functions and invariant manifolds

3.1 Backbone curves

The aim of this section is to illustrate the previous findings on the topology of the solution branches (backbone curves). A special emphasis is set on showing the changes brought by taking into account the cubic terms in the normal form system (2a-d), as compared to the results given by considering only the quadratic resonant monomials, in order to illustrate the effects of the non-resonant quadratic terms. In all the results shown, the second-order MSM solution is used, either by setting to non-zero values only g_{12}^1 and g_{11}^2, or by considering all the coefficients appearing in (2a–d). The second-order MSM solution is also compared to a reference numerical solution obtained with a continuation procedure. The continuation of periodic orbits is realized thanks to the harmonic balance method (HBM), and the asymptotic numerical method, as implemented in the open code Manlab, which also computes stability [46–48].

The two selected cases are shown respectively in Figs. 3 and 4, depicting the three backbones of the system analyzed in the previous section, for various values of the parameters. The uncoupled, U2-mode, with $a_1 = 0, a_2 \neq 0$ is shown in green, while the two coupled C+ and C− modes are in blue and red.

Figure 3 shows the special case where only the resonant quadratic monomials have been selected ($g_{12}^1 = g_{11}^2 = 1$), while all other coefficients have been set to zero. The system thus reduces to the one studied in [10], with the distinctive feature that a second-order MSM solution is still at hand. Since no cubic terms are present, the uncoupled backbone degenerates to a straight vertical line. The coupled C+ and C− modes share the properties already underlined in [10, 13]. For a negative detuning, the C− mode emerges at zero amplitude for $\omega_{nl} = 2\omega_1$, while the C+ mode emerges at a non-zero a_2 amplitude, at $\omega_{nl} = \omega_2$. The situation is reversed for positive detuning, the C+ mode starting with zero amplitude at $\omega_{nl} = 2\omega_1$ and the C− mode branching from the uncoupled solution with a non-zero amplitude. For a perfectly tuned system, $\sigma = 0$, $\omega_2 = 2\omega_1$ and all branches start at zero amplitude.

The main novelties, as compared to the previous studies, are twofold. First the analysis clearly shows that the non-vanishing branch point is exactly on the uncoupled U2-mode, starting either at amplitude $a_2 = \zeta_3$ for negative detuning, or $a_2 = \zeta_2$ for $\sigma > 0$. Second, since a second-order MSM result is shown here, one can observe that the coupled C+/C− branches show an important curvature in the (ω_{nl}, a_2) plane, which was not the case in the previously shown results using first-order MSM.

Figure 4 shows the more general case where cubic terms are taken into account in the normal form. More specifically, the values have been set to: $g_{12}^1 = g_{11}^2 = 1$, $g_{11}^1 = g_{22}^1 = g_{12}^2 = g_{22}^2 = 0.5$, and $h_{ijk}^p = 0.1$ for i, j, k, and $p = 1, 2$. As a main consequence, the uncoupled U2 backbone is now curved, due to the presence of the non-vanishing Γ_6 coefficient, see Eq. (19). With the selected values, $\Gamma_6 < 0$ and consequently, the U2-mode shows a softening behaviour. Interestingly, and as shown in the previous section, the non-zero branch point of the C+ mode, for a negative detuning, is located at $a_2 = \zeta_3$, exactly on the backbone of the uncoupled solution. The same applies for positive detuning, the C− mode branching from the U2 backbone at amplitude $a_2 = \zeta_2$. Since non-zero cubic terms are now present, the shape of the coupled C+/C− backbones shows a much more important curvature, seen in particular in the plane (ω_{nl}, a_1) where the branches of C+ solution first increases and then decreases.

The comparison between the second-order MSM and the reference numerical solution shows a very good agreement, even in very adverse conditions as the one shown in Fig. 4. Also, the stability analysis led in the previous section is very well recovered by the numerical solution, validating the perturbative reasoning. In particular, U2-mode is seen to lose stability at the supercritical pitchfork bifurcation point as analyzed, where the coupled solution emerges. Also, the stability of the coupled solution is found to be in line with the analytical results, since stable solutions are retrieved for small amplitudes. Interestingly, the numerical solution shows that the coupled branch can lose stability for higher amplitudes, as expected from the analysis following the remarks at the end of Sect. 2.5. Note that in Figs. 3 and 4, the stability of the analytical solution is not addressed at high amplitudes.

As a conclusion to this section, the numerical simulations shown in Figs. 3 and 4 show that the second-order MSM solution presented in Sect. 2.2 is in excellent agreement with a reference numerical solution, both for the quantitative shape of the backbone curves and their stability. Indeed, some discrepancies between the analytical and numerical solutions are observed, especially the response of the C+ backbone in Fig. 4 d,e,f due to the approximate nature of MSM at high amplitudes that can be corrected by taking into account higher expansion orders.

3.2 Forced oscillations: normal form validity and link to the free solutions

This section is devoted to the link between the backbone curves and the forced–damped response of the system, as well as to assess the validity of the normal form transform, Eq. (2), in comparison with the dynamical solutions given by the original equations (1). Since the normal transformation relies on an asymptotic development up to the third order, one needs to assess that the assumption is valid in the range of amplitudes used in the present analysis. In this section, only numerical results will be used, and the second-order MSM solution will not be employed anymore. The numerical solutions are derived thanks to the continuation of periodic orbits with the software Manlab.

The forced–damped frequency response functions will be considered for the original system by adding two linear damping terms $2\xi_1\omega_1\dot{X}_1$ and $2\xi_2\omega_2\dot{X}_2$ to (1a, 1b) where ξ_1 and ξ_2 are the damping coefficients. The forcing will be considered only on the upper-frequency mode, thus a harmonic force $F\cos\Omega t$ is added to Eq. (1b), where F and Ω are, respectively, the forcing amplitude and the driving frequency. For the normal form system, Eqs. (6a, 6b) are used, and damping and forcing are added in the same manner. This constitutes an assumption, which holds as long as small values of damping and forcing are considered, which will be the case here. If too large values of the damping are to be considered, then the normal form calculations need to address the damping within the calculations, as shown for example in [23, 37]. Also, for too large values of the forcing, a non-autonomous version of the normal transform must be derived, see for example [49]. For the range of amplitudes investigated in this contribution, the first-order assumption on the damping and forcing is sufficient, and one might consider high-order terms only if larger amplitudes had to be taken into account.

In order to represent the amplitude of the forced–damped solutions, and by analogy with the first-order MSM solution (see e.g. [17]), $X_1(t)$ and $X_2(t)$ are expressed as:

$$X_1(t) = X_{11/2}\cos\left(\frac{\Omega}{2}t - \frac{\gamma_1+\gamma_2}{2}\right) + \text{OH} \tag{33a}$$

$$X_2(t) = X_{21}\cos(\Omega t - \gamma_2) + \text{OH} \tag{33b}$$

where “OH” means other harmonics of smaller amplitude, γ_1 and γ_2 are the phase angles and $X_{11/2}$ and X_{21} are respectively the amplitudes of the leading harmonics of $X_1(t)$ and $X_2(t)$. In this solution, $X_2(t)$ is the directly excited degree of freedom that oscillates at the driving frequency Ω and $X_1(t)$ gains energy through the internal resonance coupling and oscillates

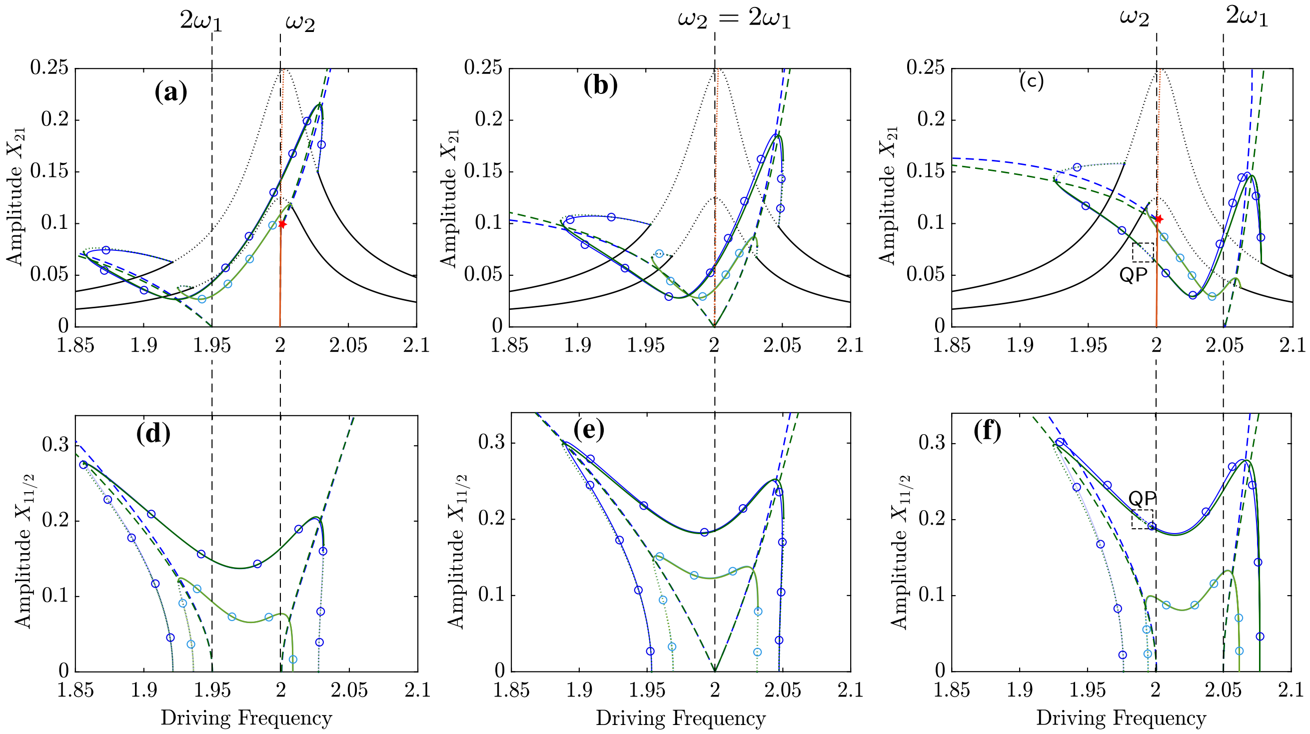

Fig. 5 Frequency response of the fundamental harmonic amplitude X_{21} of $X_2(t)$ (the first row) and the subharmonic amplitude $X_{11/2}$ of $X_1(t)$ (the second row) for $F = 0.01$ (the lighter color) and $F = 0.02$ (the darker color). The plots are done for $g^1_{11} = g^1_{12} = g^2_{11} = 1$, $g^1_{22} = g^2_{12} = g^2_{22} = 0.03$, all the cubic terms $h^p_{ijk} = 0.3$, $\xi_1 = 0.007$, and $\xi_2 = 0.01$. The first, second, and third column are the results for $\sigma = -0.05$, $\sigma = 0$, and $\sigma = 0.05$, respectively. Comparison between numerical solutions obtained from the original system (blue solid lines with circle markers) and the third-order real normal form (green solid lines). Backbone curves are plotted respectively in blue dashed lines (original system) and green dashed lines (normal form). The uncoupled free and forced solutions are plotted in orange and black, respectively (solid line for stable solutions and dotted lines for unstable). The star symbol denotes the bifurcation point from which coupled solution emerges from the U2 backbone. "QP" denotes the quasi-periodic regime that emerges between two Neimark–Sacker bifurcation points. (Color figure online)

at the subharmonic $\Omega/2$. For the solution obtained from the normal form, Eqs. (6a, 6b), $(R_1(t), R_2(t))$ are back transferred to the physical coordinates $(X_1(t), X_2(t))$ with the nonlinear mapping (3a, 3b), and then the amplitude of the first harmonic is selected for representation.

The comparison between the forced responses of both systems is shown in Fig. 5 for positive, negative, and zero values of σ. It is observed that the forced solution develops according to the backbone curves of the C+ and C− modes. Namely, the two peaks appearing in the forced response of X_1 and X_2 lie in the vicinity of the backbone curves. The comparison also shows a very good match between the forced responses of X_1 and X_2, and the two systems (normal form versus initial system) predict a Neimark–Sacker bifurcation along the coupled branch for $\sigma = 0.05$ leading to quasi-periodic solutions. A small mismatch can be observed at larger amplitudes between the two solutions, and it appears to be more salient on the backbone curves than on the forced-damped solutions, meaning that the validity range of the normal form approximation is more limited in this specific case by the third-order truncation than by the assumptions made on damping and forcing.

A last point worth investigation when comparing free and forced-damped solutions, is the point of coincidence of the two solutions, since it has a significant practical application for observing phase resonance in experiments. A phase resonance occurs when, for a particular driving frequency Ω, the forcing term exactly cancels the damping, such that the oscillator behaves as if it was in undamped free oscillations, see e.g. [50] for a discussion of the general case, [51] for application to a single DOF

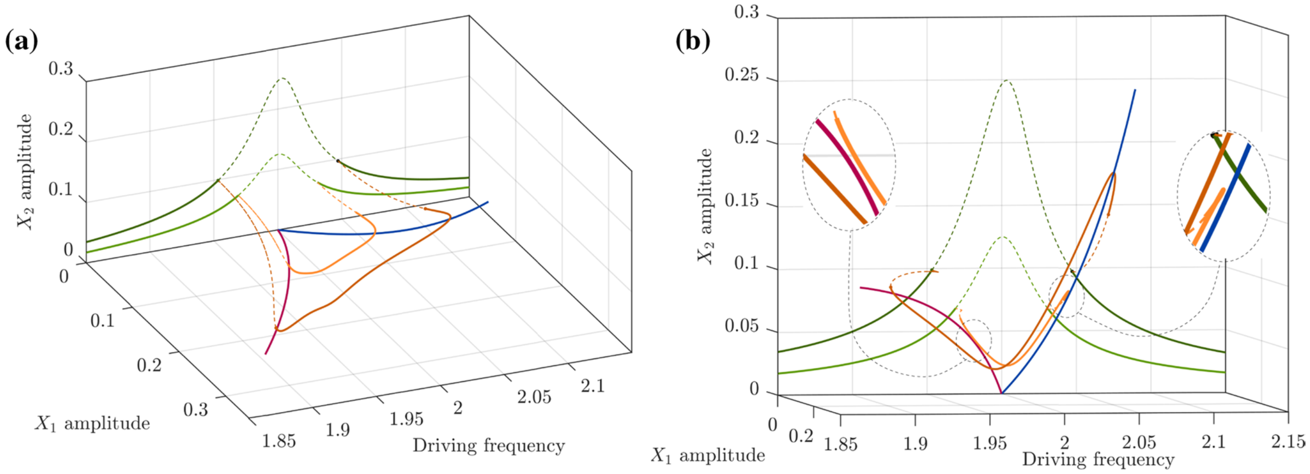

Fig. 6 Three dimensional view, in the space ($\Omega, X_{11/2}, X_{21}$), of the forced response and the backbone curves, analogous to Fig. 5 with $\sigma = 0$. The uncoupled and coupled forced responses are in green and orange, respectively, whereas the C+ and C− backbone curves are in blue and red, respectively. The unstable parts are shown in dashed lines. (**a**) and (**b**) show different view angles of the same plot to clarify the 3D representation. The zooms are selected to highlight that the free and forced solution branches do not cross each other. (Color figure online)

problem, and [45] for two cubic oscillators in 1:1 internal resonance.

In the above simulations, since the forcing term is added only to the second oscillator (Eq. 1b), it can only cancel the damping term $2\xi_2\omega_2\dot{X}_2$ of the second oscillator, and not the one of the first oscillator. We then conclude that a phase resonance is not possible here without adding a forcing term also to the first oscillator (Eq. 1a). This is further illustrated with the three-dimensional views of Fig 6, in which one can see in the insets that the forced response *do not intersect* the backbone curves, since they lie in distinct 3D planes. A limit condition for a phase resonance would be to have no damping in the first oscillator ($\xi_1 = 0$). Those results can be verified by comparing Eqs. (33a, 33b) and (17a, 17b), which shows that the phase resonance can be obtained only with $\gamma_1 = k\pi$, which is possible only if $\xi_1 = 0$ and $\gamma_2 = \pi/2$ (see the first-order MSM solution of [17]), the latter result being consistant with a phase resonance of the second oscillator. These results might have very important practical applications if one is interested in applying phase resonance on an experimental system displaying 1:2 internal resonance.

3.3 Periodic orbits and 3D manifolds

This section is devoted to illustrating the geometry of the nonlinear modes of the system, viewed as periodic orbits and invariant Lyapunov subcenter manifolds in phase space. The validity limit of the normal form is also addressed by highlighting the departure of the computed manifolds, following the presentation shown in [52].

Families of periodic orbits in the undamped case, following the backbone curves, are numerically computed with the continuation method. Fig. 7 shows the obtained results for the initial system, given by Eqs. (1a, 1b). It can be observed that the C+ and C− modes have similar shapes, up to a change $X_2 \mapsto -X_2$, which is consistent with the parabolic shapes of the periodic orbits in the (X_1, X_2) plane, as shown in Fig. 1. Note that the phase space $(X_1, X_2, \dot{X}_1, \dot{X}_2)$ is four-dimensional, while the manifolds are two-dimensional. In order to represent them, two different projections in three-dimensional spaces are given in Fig. 7a, b, for the perfectly tuned case with $\sigma = 0$. As shown in Sect. 3.1, if $\sigma = 0$, the backbone curves of both C+ and C− modes emerge from zero $X_1 = X_2 = 0$ amplitude, a result consistent with the birth of the manifold at the origin of the phase space in this case. On the other hand, if $\sigma \neq 0$, one of the modes branches from the U2-mode with a pitchfork bifurcation, which corresponds to the black orbit shown in Fig. 7c.

About this branching, a remark is worth to be raised: since the pitchfork is supercritical (see Sects. 2.5 and 2.6), after the bifurcation, two stable

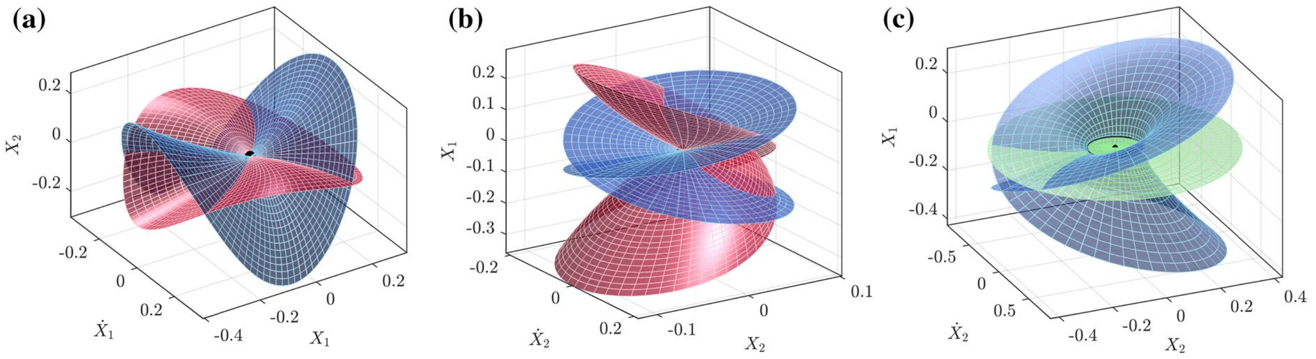

Fig. 7 Three-dimensional phase space representation of the invariant manifolds (LSM, families of periodic orbits/nonlinear modes) of the initial system given by Eqs. (1a, 1b), computed by numerical continuation. Parameter values selected as in Fig. 5a, b C+ and C− modes, respectively in blue and red, for the perfectly tuned case with $\sigma = 0$ such that $\omega_2 = 2\omega_1$. (**a**) Representation in $(X_1, \dot{X}_1, X_2)$ space, (**b**) in $(X_2, \dot{X}_2, X_1)$ space. (**c**) case with a negative detuning, $\sigma = -0.05$. The manifold in green is the U2-mode (uncoupled solution), which shows a branch point with the C+ mode (in blue). The orbit for which branching is occuring at the pitchfork bifurcation is highlighted in black. A black point shows the origin of the phase space. (Color figure online)

coupled branches are observed. In fact, those two solutions correspond to the two possible values of k for each C+ or C− coupled mode in Eq. (21a). For the C+ mode (resp. the C− mode), k must be even (resp. odd) and $k = 0$ and $k = 2$ (resp. $k = 1$ and $k = 3$) give two different periodic orbits that have the same shape in the phase space (so as the corresponding manifolds), but differ because of a π phase shift in $X_1(t)$.

The validity limit of the third-order real normal form approximation can also be ascertained graphically by comparing the invariant manifolds of the initial system, Eq. (1a, 1b), with those obtained with the normal form, as given in Eq. (2). Fig. 8 shows the invariant manifolds of the C+ and C− nonlinear modes computed by numerical continuation with Manlab. On the one hand, the periodic orbits $(X_1(t), X_2(t))$ of the initial system (1a, 1b) are shown in orange color. On the other hand, the third-order normal form of Eq. (2) is used to compute the periodic orbits $(R_1(t), R_2(t))$, which are transformed back to the initial coordinates using the nonlinear mapping (3a, 3b), shown in green. One can observe that the third-order solution suggests an excellent approximation of the reference solution for small amplitudes, consistent with the backbones curves shown in Fig. 5. At higher amplitudes, the third-order manifold departs from the reference solution, in which qualitative changes in the solution are observed. One can note in particular, for the case considered, that the folding of the original manifold shown in Fig. 8d is missed by the third-order approximation. Higher-orders are then needed to recover the folding, as shown for example in [37].

4 Recovering the saturation phenomenon

A well-known feature of a system presenting 1:2 resonance is the saturation phenomenon, as recalled in the introduction. This saturation effect is very well described for coupled oscillators including only the resonant quadratic monomials, *i.e.* the terms with coefficients g^1_{12} and g^2_{11} in the initial system (1a, 1b), and gave rise to numerous descriptions and applications in the past, see e.g. [1, 14–16] and references therein. The saturation effect exists when the system is forced in the vicinity of the high-frequency mode ω_2. After a threshold corresponding to the loss of stability of the uncoupled U2-mode, the coupled solution appears, and is characterized by a constant amplitude for X_2 when the amplitude of the forcing is increased, meaning that all the energy is transferred to the first oscillator. In terms of the frequency-response functions, this corresponds to the fact that the coupled branch shows a minimum in the vicinity of $\Omega \simeq \omega_2$, which can be interpreted as an anti-resonance. This case is illustrated in Figs. 9a and 10, for the resonant excitation considered in Sect. 3.2, for which the amplitude X_{21} of the H1 harmonics of $X_2(t)$

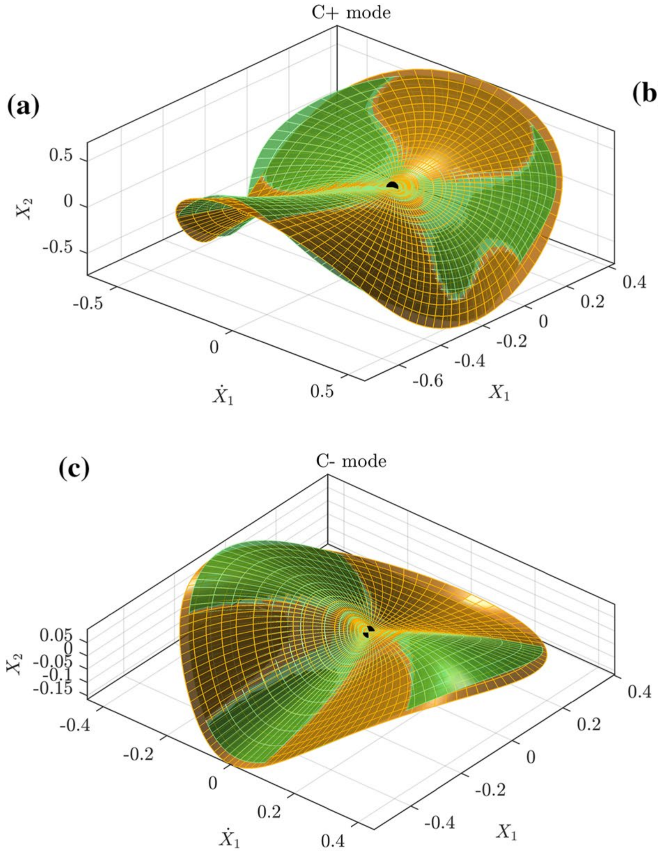

Fig. 8 Invariant manifolds corresponding to the C+ and C− nonlinear modes of the system, with the parameters of Fig. 5, in the case $\sigma = 0 \Leftrightarrow \omega_2 = 2\omega_1$. Comparison between the numerical solution of the initial system (1a, 1b) (orange, periodic orbits computed with numerical continuation) and the one from the third order normal form of Eq. (2) (green, periodic orbits computed with numerical continuation and back transformed with the nonlinear mapping (3a, 3b)). First row: C+ mode, second row: C− mode. First column, space (X_1, $\dot{X}_1$, X_2); second column, space (X_2, $\dot{X}_2$, X_1). The parameters are: $g^1_{11} = g^1_{12} = g^2_{11} = 1$, $g^1_{22} = g^2_{12} = g^2_{22} = 0.03$, and all the cubic terms $h^p_{ijk} = 0.1$. The view angle is different in the first and second row for clarity reason. A black point shows the origin of the phase space. (Color figure online)

shows a valley-like shape, with a minimum around $\Omega = \omega_2 = 2$, whose amplitude is almost independent of the forcing (F is multiplied by a factor 3 in the plot). Consequently, locking the frequency of the excitation around the minimum of X_{21} and increasing the amplitude F leads to no increase of X_{21} and thus its saturation.

However, if non-resonant quadratic terms are present in (1a, 1b), it has been observed in [17, 18] that this saturation phenomenon is much less efficient, mainly because the anti-resonance is shifted as the excitation increases. Consequently, if one locks the driving frequency at a given value, then X_{21} at this particular frequency will depend on the driving amplitude F, thus severely mitigating the saturation phenomenon. The effect of the non-resonant terms is illustrated in Figs. 9b and 10, with a shift of the anti-resonance toward the low frequencies and a symmetry breaking of the shape of the response curves.

Considering, as explained in Sect. 3.1, that the main effect of both the quadratic non-resonant terms and the cubic ones is to bend the response curves, one could think of using intentionally some cubic terms to *cancel the bending of the response curves* brought by the quadratic terms, using the analytical free solution of the normal form of Sect. 2.2. This idea shares some common points with the one developed in [53], where the nonlinearity is also intentionally tuned in order to create a nonlinear vibration absorber that extends the so-called den Hartog's equal peak method.

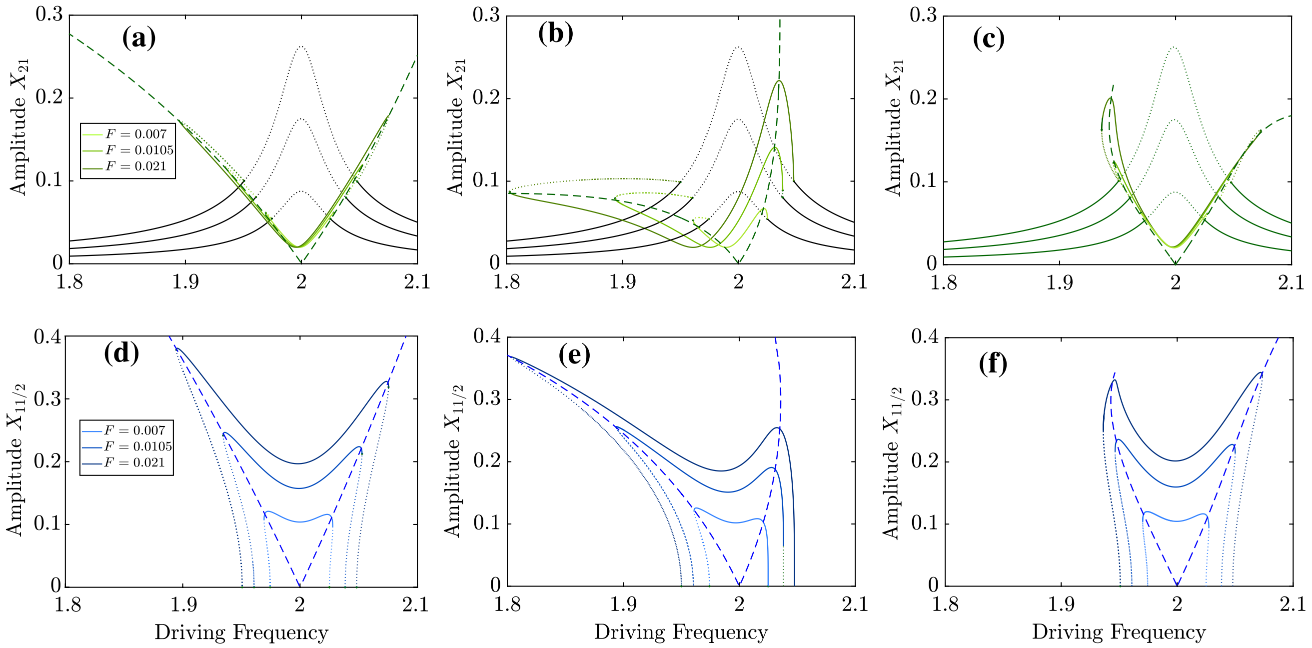

Fig. 9 Frequency response of the fundamental harmonic amplitude X_{21} of $X_2(t)$ (the first row) and the subharmonic amplitude $X_{11/2}$ of $X_1(t)$ (the second row) for several excitation levels, computed numerically with Manlab in the case $\sigma = 0$ (i.e. $\omega_2 = 2\omega_1$). The first column: only the quadratic resonant terms are considered ($g^1_{12} = g^2_{11} = 1$). The second column: all the quadratic terms are considered with null cubic terms ($g^1_{11} = g^1_{12} = g^2_{11} = 1$, $g^1_{22} = g^2_{12} = g^2_{22} = 0.1$). Third column: all the quadratic terms are considered with the cubic terms are set based on (34a–34d). The damping coefficients are $\xi_1 = 0.007$ and $\xi_2 = 0.01$. The uncoupled forced solution is plotted in black and the coupled solutions are plotted in green and blue. The dotted and solid lines denote the stable and unstable solutions, respectively. The dashed lines denotes the coupled free solution. (Color figure online)

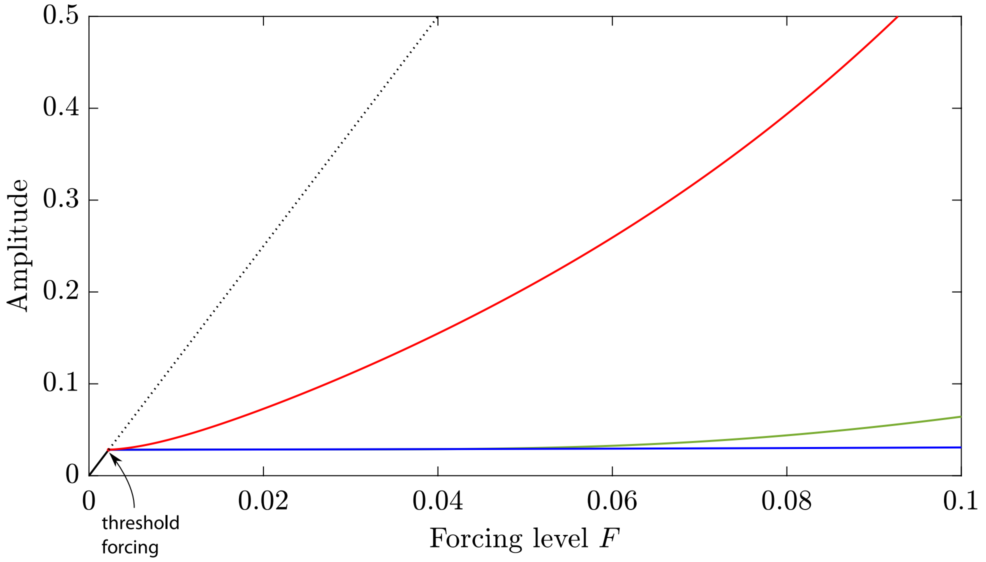

Fig. 10 Fundamental harmonic amplitude X_{21} of $X_2(t)$ as a function of the excitation level F, computed numerically with a continuation method, in the perfectly tuned case $\sigma = 0$ (i.e. $\omega_2 = 2\omega_1$), and for an external excitation frequency $\Omega = \omega_2$, corresponding to the cases of Fig. 9. Black line: linear response with all nonlinear terms cancelled; blue line: only the quadratic resonant terms are considered (Fig. 9a); red line: all the quadratic terms are considered with null cubic terms (Fig. 9b); green line: same quadratic terms with the tuned cubic terms of Eqs. (34a–34d) (Fig. 9c). The solid and dotted lines denote the stable and unstable solutions, respectively. (Color figure online)

In order to do so, the idea is to select the values of the cubic coefficients h^p_{ijk} in order to cancel the effect of the quadratic non resonant terms g^1_{11}, g^1_{22}, g^2_{12}, g^2_{22} in the coefficients $\Gamma_{2,3,5,6}$, such that the backbone curve of Eqs. (18a, 18b) degenerate to those obtained if only the quadratic resonant terms were present. Using the complete expressions of the Γ coefficients as reported in the "Appendix C", Eqs. (67b, 67c, 67e, 67f), the following tuning rule expresses the cubic nonlinear coefficients as function of the quadratic non-resonant ones, as:

$$h^1_{111} = \frac{10}{9\omega_1^2}\left(g^1_{11}\right)^2 \tag{34a}$$

$$h^1_{122} = \frac{1}{\omega_2^2} g^1_{12} g^2_{22} - \frac{8\omega_2^2 - 2\omega_1^2}{\omega_1^2(\omega_1^2 - 4\omega_2^2)} g^1_{11} g^1_{22} - \frac{2}{\omega_1^2 - 4\omega_2^2} g^2_{22} g^2_{12} \tag{34b}$$

$$h^2_{112} = \frac{2}{3\omega_2^2} g^2_{11} g^2_{22} + \frac{1}{\omega_1^2} g^1_{11} g^2_{12} - \frac{1}{\omega_1^2 - 4\omega_2^2}\left(g^2_{12}\right)^2 \tag{34c}$$

$$h^2_{222} = \frac{10}{9\omega_2^2}\left(g^2_{22}\right)^2 - \frac{2\omega_2^2 - \omega_1^2}{\omega_1^2(\omega_1^2 - 4\omega_2^2)} g^1_{22} g^2_{12} \tag{34d}$$

Note that only the resonant cubic terms are the parameters to be controlled. The other cubic terms are not considered since they are eliminated in the normal form derivation process, in which it is assumed that such terms have a negligible effect at the third order. To catch the effect of such terms, one has to continue the derivation up to the fourth order, which is not considered in this study.

To validate the proposed technique, Fig. 9c considers the resonant excitation of Sect. 3.2 with the cubic coefficients set as suggested in Eqs. (34a–34d). One observes that this leads first to a lock of the anti-resonance point as the excitation level increases and secondly to response curves with a more symmetric shape, as compared to Fig. 9b where the cubic correction terms are not included. In addition, one can see that for the first two excitation levels, the frequency response is almost identical to that of Fig. 9a, which shows the simplified version of (1a, 1b) where only the quadratic resonant terms are considered. Differences are finally observed when going up to very large amplitudes, which are due to higher-order effects (quintic, ..) that are not taken into account in the analytics. As a final result, Fig. 10 shows that the present tuning of the cubic terms perfectly cancels the effect of the non-resonant quadratic terms, obtaining a perfect saturation phenomenon, up to comfortable amplitudes for an experimental application, and that significantly enhanced the saturation effect obtained by considering only the resonant quadratic terms. In the numerical example considered here, the green and the blue curves almost perfectly match up to an amplitude 23 times the threshold forcing level.

5 Conclusion

In this article, the second-order effect of the quadratic non-resonant terms, and the cubic terms, of two oscillators featuring 1:2 internal resonance has been investigated. A special emphasis has been put on the topology of the solution branches for free vibrations (backbone curves) and forced–damped response. The conjugated effect of the non-resonant quadratic terms and the cubic terms, appearing in the same order of expansion in the normal form approach, has been analyzed with a second-order multiple scales expansion. The overall topology in terms of instabilities, bifurcation, and branching is not deeply modified as compared to a first-order analysis; since the most important features of the 1:2 internal resonance are driven by the resonant quadratic terms. However, important quantitative features have been deeply analyzed, complementing already published results on the same problem, which were limited to a first-order development [10, 13].

In the course of the development, numerous interesting results have been derived. The complete analytical derivation of the real normal form for a problem featuring 1:2 internal resonance, and up to the third order, has been shown, complementing the results given in [11, 38] where the assumptions of no internal resonance were retained. The topology of the invariant manifolds linked to the backbone curves/nonlinear modes of the system with 1:2 internal resonance has also been investigated. In particular, the fact that the branch point of the coupled solution is along the uncoupled U2-mode, hence complementing the bifurcation portrait of the conservative problem, has been highlighted. The validity domain of the normal form transform, in both free and forced vibrations, is also assessed by comparisons to numerical solutions. Finally, the connection between the free and the forced responses of the system has been analyzed, with possible future applications in phase resonance testing of structures with internal resonances [45, 51].

The main application of the analysis presented herein is the improvement of the saturation effect, typical of systems featuring 1:2 internal resonance, and that has already attracted attention in the past in order to design an effective method for passive vibration control. In particular, the simulations show that when the vibration amplitudes increase, cubic nonlinearities cannot be neglected anymore, resulting in numerous effects that have been analyzed with the present developments, in particular the bending of all backbone curves (uncoupled and coupled). Due to the combined effects of quadratic non-resonant and cubic terms, the overall symmetry of the response is broken, the shape of the frequency response curves is importantly modified, and the minimum of the coupled branch, denoted as a sort of anti-resonance, depends strongly on the amplitude, thus destroying the perfectness of the saturation effect. A tuning methodology, involving quadratic non-resonant terms and cubic terms, has thus been proposed in order to recover this saturation effect and enlarge its range of validity, by giving back a more symmetric shape to the frequency response functions.

Acknowledgements The Région Hauts de France and the Carnot ARTS Institute, France, are warmly thanked for the PhD grant of the first author.

Declarations

Conflict of interest The authors declare that they have no conflict of interest.

A Relationships between nonlinear coefficients

This appendix details the known relationships existing between the coefficients of the monomials given in Eq. (1) when the internal force is assumed to derive from a potential. In such case, the potential energy is a quartic function whose general expression reads:

$$\begin{aligned}\mathcal{V} = {} & \frac{1}{2}(\omega_1^2 X_1^2 + \omega_2^2 X_2^2) + \frac{1}{3}(g_{11}^1 X_1^3 + g_{22}^2 X_2^3) + g_{11}^2 X_1^2 X_2 \\ & + g_{22}^1 X_1 X_2^2 + \frac{1}{4}(h_{111}^1 X_1^4 + h_{222}^2 X_2^4) + \frac{1}{2} h_{112}^2 X_1^2 X_2^2 \\ & + h_{111}^2 X_1 X_2^3 + h_{222}^1 X_1^3 X_2.\end{aligned} \tag{35}$$

The internal forces are found by deriving this expression with respect to X_1 and X_2, which leads to the following relationships between the coefficients:

$$g_{12}^1 = 2g_{11}^2, \tag{36a}$$

$$g_{12}^2 = 2g_{22}^1, \tag{36b}$$

$$h_{122}^1 = h_{112}^2, \tag{36c}$$

$$h_{122}^2 = 3h_{222}^1, \tag{36d}$$

$$h_{112}^1 = 3h_{111}^2. \tag{36e}$$

B Detailed calculation of the normal form

This appendix is devoted to the complete presentation of the calculations needed to arrive at the normal form given in Eq. (2), starting from the original set of two coupled nonlinear oscillators, Eq. (1). The calculation follows the general guidelines given in [11, 38], and is adapted here to take into account the additional condition given by the presence of a 1:2 internal resonance between the two eigenfrequencies of the system. This resonance condition being on the second-order terms will have consequences on the calculation of the cubic terms, which needs to be properly tracked. Since the normal form calculation is sequential in nature, the first step consists in processing the quadratic terms. To that purpose, let us truncate Eq. (1) at the second-order of the nonlinearity, and rewrite them as a first-order problem in time, in order to make clearly appear the contributions due to the two independent variables displacement and velocity:

$$\dot{X}_1 = Y_1, \tag{37a}$$

$$\dot{Y}_1 = -\omega_1^2 X_1 - g_{11}^1 X_1^2 - g_{12}^1 X_1 X_2 - g_{22}^1 X_2^2, \tag{37b}$$

$$\dot{X}_2 = Y_2, \tag{37c}$$

$$\dot{Y}_2 = -\omega_2^2 X_2 - g_{11}^2 X_1^2 - g_{12}^2 X_1 X_2 - g_{22}^2 X_2^2. \tag{37d}$$

A quadratic, indentity-tangent, nonlinear change of coordinates, is first introduced in order to cancel as much as possible the nonlinear terms in Eq. (37). New variables (U_i, V_i) are introduced as:

$$X_1 = U_1 + a_{11}^1 U_1^2 + a_{12}^1 U_1 U_2 + a_{22}^1 U_2^2 + b_{11}^1 V_1^2 + b_{12}^1 V_1 V_2 + b_{22}^1 V_2^2, \tag{38a}$$

$$Y_1 = V_1 + \gamma_{11}^1 U_1 V_1 + \gamma_{12}^1 U_1 V_2 + \gamma_{21}^1 U_2 V_1 + \gamma_{22}^1 U_2 V_2, \tag{38b}$$

$$X_2 = U_2 + a_{11}^2 U_1^2 + a_{12}^2 U_1 U_2 + a_{22}^2 U_2^2 + b_{11}^2 V_1^2 + b_{12}^2 V_1 V_2 + b_{22}^2 V_2^2, \tag{38c}$$

$$Y_2 = V_2 + \gamma_{11}^2 U_1 V_1 + \gamma_{12}^2 U_1 V_2 + \gamma_{21}^2 U_2 V_1 + \gamma_{22}^2 U_2 V_2. \tag{38d}$$

In these equations, the introduced coefficients a_{ij}^p, b_{ij}^p, and γ_{ij}^p, for i, j, p=1, 2; are unknowns and will be set according to the idea of canceling non-resonant monomials in the equations of motion. To that purpose, Eq. (38) are differentiated with respect to time and introduced in (37). Identification of the same monomials leads to the values of the coefficients that can be used. Let us first recall the general solution reported in [11, 38] for the case where no internal resonance exists between ω_1 and ω_2. One obtains:

$$\begin{aligned}
&a_{11}^1 = \frac{-g_{11}^1}{3\omega_1^2}, \quad b_{11}^1 = \frac{-2g_{11}^1}{3\omega_1^4}, \quad \gamma_{11}^1 = \frac{2g_{11}^1}{3\omega_1^2}, \quad \gamma_{21}^1 = \frac{g_{12}^1}{4\omega_1^2 - \omega_2^2},\\
&a_{12}^1 = \frac{g_{12}^1}{\omega_2^2 - 4\omega_1^2}, \quad b_{12}^1 = \frac{2g_{12}^2}{\omega_2^2(\omega_2^2 - 4\omega_1^2)}, \quad \gamma_{12}^1 = \frac{g_{12}^1(2\omega_1^2 - \omega_2^2)}{\omega_2^2(4\omega_1^2 - \omega_2^2)}, \quad \gamma_{21}^2 = \frac{g_{12}^2(\omega_1^2 - 2\omega_2^2)}{\omega_1^2(\omega_1^2 - 4\omega_2^2)},\\
&a_{22}^1 = \frac{g_{22}^1(2\omega_2^2 - \omega_1^2)}{\omega_1^2(\omega_1^2 - 4\omega_2^2)}, \quad b_{22}^1 = \frac{2g_{22}^1}{\omega_1^2(\omega_1^2 - 4\omega_2^2)}, \quad \gamma_{22}^1 = \frac{2g_{22}^1}{4\omega_2^2 - \omega_1^2},\\
&a_{11}^2 = \frac{g_{11}^2(\omega_2^2 - 2\omega_1^2)}{\omega_2^2(4\omega_1^2 - \omega_2^2)}, \quad b_{11}^2 = \frac{2g_{11}^2}{\omega_2^2(\omega_2^2 - 4\omega_1^2)}, \quad \gamma_{11}^2 = \frac{2g_{11}^2}{4\omega_1^2 - \omega_2^2},\\
&a_{12}^2 = \frac{g_{12}^2}{\omega_1^2 - 4\omega_2^2}, \quad b_{12}^2 = \frac{2g_{12}^2}{\omega_1^2(\omega_1^2 - 4\omega_2^2)}, \quad \gamma_{12}^2 = \frac{g_{12}^2}{4\omega_2^2 - \omega_1^2},\\
&a_{22}^2 = \frac{-g_{22}^2}{3\omega_2^2}, \quad b_{22}^2 = \frac{-2g_{22}^2}{3\omega_2^4}, \quad \gamma_{22}^2 = \frac{2g_{22}^2}{3\omega_2^2}.
\end{aligned} \tag{39}$$

In the case of the 1:2 internal resonance condition (i.e., $\omega_2 \approx 2\omega_1$), it appears that the coefficients a_{12}^1, b_{12}^1, γ_{12}^1, γ_{21}^1, a_{11}^2, b_{11}^2, and γ_{11}^2 are singular since their denominators contains the term $(\omega_2 - 2\omega_1)$. In such case, the remedy is to set all these coefficients to zero. The coefficients used in Eq. (3) in the main text are thus those given in Eq. (39), except for the singular ones that are replaced by:

$$a_{12}^1 = b_{12}^1 = \gamma_{12}^1 = \gamma_{21}^1 = a_{11}^2 = b_{11}^2 = \gamma_{11}^2 = 0. \tag{40}$$

As a consequence, the associated resonant second-order monomials, which are here $g_{12}^1 X_1 X_2$ and $g_{11}^2 X_1^2$, cannot be eliminated from the normal form, in contrary to the other four quadratic terms. After this first step, one is thus able to write the normal form of the problem with 1:2 resonance, up to the quadratic terms, as:

$$\dot{U}_1 = V_1 + O(U_i^3, V_i^3), \tag{41a}$$

$$\dot{V}_1 = -\omega_1^2 U_1 - g_{12}^1 U_1 U_2 + O(U_i^3, V_i^3), \tag{41b}$$

$$\dot{U}_2 = V_2 + O(U_i^3, V_i^3), \tag{41c}$$

$$\dot{V}_2 = -\omega_2^2 U_2 - g_{11}^2 U_1^2 + O(U_i^3, V_i^3). \tag{41d}$$

The next step of the calculation is to rewrite Eq (41) up to the cubic terms. Besides the original cubic terms with coefficients h_{ijk}^p, present in Eq (1), new cubic terms will appear due to the nonlinear nature of the change of coordinates, where products involving linear and quadratic terms will produce new cubic terms. Let us first focus on the processing of these new terms. In the calculation, the derivatives of Eq. (38) with respect to time need to be computed. The derivative of quadratic terms (e.g. V_1^2) makes appear products involving the time derivative ($2V_1\dot{V}_1$ in this case). To eliminate time, one can simply use Eq. (41), such that, up to order four, one can write for the monomial considered as an example: $V_1\dot{V}_1 = -\omega_1^2 U_1 V_1 - g_{12}^1 U_1 U_2 V_1 + O(U_i^4, V_i^4)$, hence making appear the new expected cubic terms. Repeating this procedure for the four equations, and using Eq. (40) to simplify the expressions, one easily arrives at:

$$\dot{U}_1 = V_1 + 2b_{11}^1 g_{12}^1 U_1 U_2 V_1 + 2b_{22}^1 g_{11}^2 U_1^2 V_2, \tag{42a}$$

$$\dot{V}_1 = -\omega_1^2 U_1 - g_{12}^1 U_1 U_2 + \gamma_{11}^1 g_{12}^1 U_1^2 U_2 + \gamma_{22}^1 g_{11}^2 U_1^2 U_2, \tag{42b}$$

$$\dot{U}_2 = V_2 + b_{12}^2 g_{12}^1 U_1 U_2 V_2 + b_{12}^2 g_{11}^2 V_1 U_1^2 + 2b_{22}^2 g_{11}^2 U_1^2 V_2, \tag{42c}$$

$$\dot{V}_2 = -\omega_2^2 U_2 - g_{11}^2 U_1^2 + \gamma_{12}^2 g_{11}^2 U_1^3 + \gamma_{21}^2 g_{12}^1 U_1 U_2^2 + \gamma_{22}^2 g_{11}^2 U_1^2 U_2. \tag{42d}$$

Note that the obtained cubic terms in (42) are solely due to the presence of the 1:2 internal resonance condition. Importantly, those terms were not present in the previous calculations shown in [11, 38], led under the specific assumption of no internal resonance. This means that the general guidelines provided in [11, 38] to derive the normal form can be followed, provided the changes underlined here to take correctly into account a 1:2 resonance.

At this stage, one can observe that the first and third lines, Eqs. (42a)–(42c), are not as simple as they were at the starting point, see e.g. Eq. (37), underlining a simple link between displacement and velocity. To recover this and obtain a more convenient expression of (42a)-(42c), one can define W_1 and W_2 as:

$$W_1 = V_1 + 2b_{11}^1 g_{12}^1 U_1 U_2 V_1 + 2b_{22}^1 g_{11}^2 U_1^2 V_2, \tag{43a}$$

$$W_2 = V_2 + b_{12}^2 g_{12}^1 U_1 U_2 V_2 + b_{12}^2 g_{11}^2 V_1 U_1^2 + 2b_{22}^2 g_{11}^2 U_1^2 V_2, \tag{43b}$$

such that the system (42) can be rewritten as:

$$\dot{U}_1 = W_1, \tag{44a}$$

$$\begin{aligned}\dot{W}_1 = &-\omega_1^2 U_1 - g_{12}^1 U_1 U_2 + \gamma_{11}^1 g_{12}^1 U_1^2 U_2 \\ &+ \gamma_{22}^1 g_{11}^2 U_1^2 U_2 + 2b_{11}^1 g_{12}^1 (W_1^2 U_2 \\ &+ U_1 W_2 W_1 - U_1^2 U_2 \omega_1^2) + 2b_{22}^1 g_{11}^2 (2U_1 W_1 W_2 - U_1^2 U_2 \omega_2^2) \\ &+ O(U_i^4, W_i^4),\end{aligned} \tag{44b}$$

$$\dot{U}_2 = W_2, \tag{44c}$$

$$\begin{aligned}\dot{W}_2 = &-\omega_2^2 U_2 - g_{11}^2 U_1^2 + \gamma_{12}^2 g_{11}^2 U_1^3 \\ &+ \gamma_{21}^2 g_{12}^1 U_1 U_2^2 + \gamma_{22}^2 g_{11}^2 U_1^2 U_2 \\ &+ b_{12}^2 g_{12}^1 (W_1 U_2 W_2 + U_1 W_2^2 - U_1 U_2^2 \omega_2^2) \\ &+ b_{12}^2 g_{11}^2 (-\omega_1^2 U_1^3 + 2U_1 W_1^2) \\ &+ 2b_{22}^2 g_{11}^2 (2U_1 W_1 W_2 - U_1^2 U_2 \omega_2^2) + O(U_i^4, W_i^4).\end{aligned} \tag{44d}$$

As mentioned earlier, Eq. (44) refer to the problem up to cubic nonlinearity where only the terms added by the presence of the 1:2 resonance have been tracked. We are now in the position of rewriting the complete system up to the third order, on which the next step of the normal transform could be applied by vanishing the non-resonant cubic monomials thanks to a third-order nonlinear change of coordinates. To that purpose, one simply needs to track the cubic terms coming from the original system with h_{ijk}^p coefficients, and those created by the quadratic nonlinear change of coordinate and appearing without the second-order internal resonance. This leads to the following equations:

$$\dot{U}_1 = W_1, \tag{45a}$$

$$\begin{aligned}\dot{W}_1 = &-\omega_1^2 U_1 - g_{12}^1 U_1 U_2 - (h_{111}^1 + A_{111}^1) U_1^3 \\ &- (h_{112}^1 + A_{112}^1 - D_{112}^1) U_1^2 U_2 - (h_{122}^1 + A_{122}^1) U_1 U_2^2 \\ &- (h_{222}^1 + A_{222}^1) U_2^3 - B_{111}^1 U_1 W_1^2 - B_{122}^1 U_1 W_2^2 \\ &- (B_{112}^1 - E_{112}^1) U_1 W_1 W_2 - (B_{211}^1 - E_{211}^1) U_2 W_1^2 \\ &- B_{212}^1 U_2 W_1 W_2 - B_{222}^1 U_2 W_2^2 + O(U_i^4, W_i^4),\end{aligned} \tag{45b}$$

$$\dot{U}_2 = W_2, \tag{45c}$$

$$\begin{aligned}\dot{W}_2 = &-\omega_2^2 U_2 - g_{11}^2 U_1^2 - (h_{111}^2 + A_{111}^2 - D_{111}^2)U_1^3 \\ &- (h_{112}^2 + A_{112}^2 - D_{112}^2)U_1^2 U_2 - (h_{122}^2 + A_{122}^2 - D_{122}^2)U_1 U_2^2 \\ &- (h_{222}^2 + A_{222}^2)U_2^3 - (B_{111}^2 - E_{111}^2)U_1 W_1^2 \\ &- (B_{122}^2 - E_{122}^2)U_1 W_2^2 - (B_{112}^2 - E_{112}^2)U_1 W_1 W_2 \\ &- B_{211}^2 U_2 W_1^2 - (B_{212}^2 - E_{212}^2)U_2 W_1 W_2 \\ &- B_{222}^2 U_2 W_2^2 + O(U_i^4, W_i^4).\end{aligned} \tag{45d}$$

In these equations, the coefficients A_{ijk}^p and B_{ijk}^p, with $i, j, k, p = 1, 2$; are the same as those already reported in [11, 38], meaning that they arise from the computation of the non internally resonant case. Their general expressions are the same as reported in [11, 38] and read:

$$A_{ijk}^p = \sum_{l \geq i}^{N} g_{il}^p a_{jk}^l + \sum_{l \leq i}^{N} g_{li}^p a_{jk}^l, \tag{46a}$$

$$B_{ijk}^p = \sum_{l \geq i}^{N} g_{il}^p b_{jk}^l + \sum_{l \leq i}^{N} g_{li}^p b_{jk}^l. \tag{46b}$$

As compared to the case without internal resonance, one can note that the general expression is exactly similar, but one has just to take care that due to the 1:2 resonance, some of the a_{ij}^p, b_{ij}^p, γ_{ij}^p coefficients vanish following Eq. (40).

On the other hand, the coefficients D_{ijk}^p and E_{ijk}^p, with $i, j, k, p = 1, 2$, comes from Eq. (45), and are only due to the presence of the 1:2 internal resonance. They read:

$$\begin{aligned}D_{112}^1 &= \gamma_{11}^1 g_{12}^1 + \gamma_{22}^1 g_{11}^2 - 2b_{11}^1 g_{12}^1 \omega_1^2 - 2b_{22}^1 g_{11}^2 \omega_2^2, \\ D_{111}^2 &= \gamma_{12}^2 g_{11}^2 - b_{12}^2 g_{11}^2 \omega_1^2, \\ D_{112}^2 &= \gamma_{22}^2 g_{11}^2 - 2b_{22}^2 g_{11}^2 \omega_2^2, \\ D_{122}^2 &= \gamma_{21}^2 g_{12}^1 - b_{12}^2 g_{12}^1 \omega_2^2, \\ E_{112}^1 &= 2b_{11}^1 g_{12}^1 + 4b_{22}^1 g_{11}^2, \\ E_{211}^1 &= 2b_{11}^1 g_{12}^1, \\ E_{111}^2 &= 2b_{12}^2 g_{11}^2, \\ E_{122}^2 &= b_{12}^2 g_{12}^1, \\ E_{112}^2 &= 4b_{22}^2 g_{11}^2, \\ E_{212}^2 &= b_{12}^2 g_{12}^1.\end{aligned} \tag{47}$$

The last step of the computation of the real normal form up to cubic terms consists of applying a third-order nonlinear change of coordinates in order to cancel all non-resonant cubic monomials in (45). As already noted, for example, in [11, 12, 38], the main difference with second-order is the presence of trivial resonances at the cubic order. Due to the fact that the eigenspectrum is composed of pairs of purely imaginary complex conjugate numbers, trivial resonances are always fulfilled at third order so that numerous monomials cannot be cancelled whatever the values of the eigenvalues. This is in contrast to quadratic terms where, in case of no second-order internal resonance, all the terms can be cancelled by the change of coordinate. Here the procedure simply follows the general guidelines given in [11, 12, 38]. The nonlinear change of coordinates is introduced as:

$$U_p = R_p + \sum_{i=1}^{N} \sum_{j \geq i}^{N} \sum_{k \geq j}^{N} r_{ijk}^p R_i R_j R_k + \sum_{i=1}^{N} \sum_{j=1}^{N} \sum_{k \geq j}^{N} u_{ijk}^p R_i S_j S_k, \tag{48a}$$

$$W_p = \dot{U}_p = S_p + \sum_{i=1}^{N} \sum_{j \geq i}^{N} \sum_{k \geq j}^{N} \mu_{ijk}^p S_i S_j S_k + \sum_{i=1}^{N} \sum_{j=1}^{N} \sum_{k \geq j}^{N} \nu_{ijk}^p S_i R_j R_k. \tag{48b}$$

To derive the expressions of the unknown coefficients r_{ijk}^p, u_{ijk}^p, μ_{ijk}^p, and ν_{ijk}^p, with $i, j, k, p = 1, \dots, 2$; introduced in Eq. (48), one has to differentiate (48) with respect to time and report in the equations of motion, Eq. (45). Identifying the monomials term-by-term leads to explicit expressions for the unknowns, some of them being set directly to zero because of the trivial resonances. Interestingly, this step of the calculation exactly follows the guidelines already provided in [11, 12, 38]. Hence the general formula can be simply used without changes.

After this calculation, most of the cubic monomials present in Eq. (45) can be cancelled by the nonlinear change of coordinates, the only remaining being linked to trivial resonances. Finally, the normal form, up to the third order, and with the 1:2 internal resonance taken into account, reads:

$$\dot{R}_1 = S_1, \tag{49a}$$

$$\begin{aligned}\dot{S}_1 = &-\omega_1^2 R_1 - g_{12}^1 R_1 R_2 - (h_{111}^1 + A_{111}^1)R_1^3 - (h_{122}^1 + A_{122}^1)R_1 R_2^2 \\ &- B_{111}^1 R_1 S_1^2 - B_{122}^1 R_1 S_2^2 - B_{212}^1 R_2 S_1 S_2,\end{aligned} \tag{49b}$$

$$\dot{R}_2 = S_2, \tag{49c}$$

$$\begin{aligned}\dot{S}_2 = &-\omega_2^2 R_2 - g_{11}^2 R_1^2 - (h_{112}^2 + A_{112}^2 - D_{112}^2) R_1^2 R_2 \\ &- (h_{222}^2 + A_{222}^2) R_2^3 - (B_{112}^2 - E_{112}^2) R_1 S_1 S_2 \\ &- B_{211}^2 R_2 S_1^2 - B_{222}^2 R_2 S_2^2.\end{aligned} \tag{49d}$$

One can note that the normal form is equivalent to that obtained in [11], except for the additional terms E_{112}^2 and D_{112}^2, which comes as a direct consequence of keeping the resonant quadratic terms due to the 1:2 internal resonance.

C Detailed calculation of the Multiple scales solution

In this section, we develop the application of the second-order MSM to Eq. (2). The starting point is the system given by Eq. (6), that makes appear the scaled following coefficients:

$$g_{12}^1 = \varepsilon\beta_1, \quad g_{11}^2 = \varepsilon\beta_2, \tag{50a}$$

$$\begin{aligned}h_{111}^1 + A_{111}^1 = \varepsilon^2\alpha_1, \quad & h_{122}^1 + A_{122}^1 = \varepsilon^2\alpha_2, \\ B_{111}^1 = \varepsilon^2\alpha_3, \quad B_{122}^1 &= \varepsilon^2\alpha_4, \quad B_{212}^1 = \varepsilon^2\alpha_5,\end{aligned} \tag{50b}$$

$$\begin{aligned}h_{112}^2 + A_{112}^2 - D_{112}^2 = \varepsilon^2\alpha_6, \quad & h_{222}^2 + A_{222}^2 = \varepsilon^2\alpha_7, \\ B_{112}^2 - E_{112}^2 = \varepsilon^2\alpha_8,&\end{aligned} \tag{50c}$$

$$B_{211}^2 = \varepsilon^2\alpha_9, \quad B_{222}^2 = \varepsilon^2\alpha_{10}. \tag{50d}$$

The unknowns $R_1(t)$ and $R_2(t)$ of Eq. (6) are expanded in powers of ε as:

$$\begin{aligned}R_1(t;\varepsilon) = &\, r_{10}(T_0, T_1, T_2) + \varepsilon r_{11}(T_0, T_1, T_2) \\ &+ \varepsilon^2 r_{12}(T_0, T_1, T_2) + O(\varepsilon^3),\end{aligned} \tag{51a}$$

$$\begin{aligned}R_2(t;\varepsilon) = &\, r_{20}(T_0, T_1, T_2) + \varepsilon r_{21}(T_0, T_1, T_2) \\ &+ \varepsilon^2 r_{22}(T_0, T_1, T_2) + O(\varepsilon^3).\end{aligned} \tag{51b}$$

In addition, the first and second derivatives with respect to the initial time t are expressed as:

$$\frac{d}{dt} = D_0 + \varepsilon D_1 + \varepsilon^2 D_2 + O(\varepsilon^3), \tag{52a}$$

$$\frac{d^2}{dt^2} = D_0^2 + 2\varepsilon D_0 D_1 + \varepsilon^2 (D_1^2 + 2D_0 D_2) + O(\varepsilon^3), \tag{52b}$$

where $D_n \equiv \partial/\partial T_n$. Substituting Eq. (51) in (6), using (52) and equating the coefficients of like powers of ε yields:

- At order ε^0:

$$D_0^2 r_{10} + \omega_1^2 r_{10} = 0, \tag{53a}$$

$$D_0^2 r_{20} + \omega_2^2 r_{20} = 0. \tag{53b}$$

- At order ε:

$$D_0^2 r_{11} + \omega_1^2 r_{11} = -2D_0 D_1 r_{10} - \beta_1 r_{10} r_{20}, \tag{54a}$$

$$D_0^2 r_{21} + \omega_2^2 r_{21} = -2D_0 D_1 r_{20} - \beta_2 r_{10}^2. \tag{54b}$$

- At order ε^2:

$$\begin{aligned}D_0^2 r_{12} + \omega_1^2 r_{12} = &-2D_0 D_1 r_{11} - 2D_0 D_2 r_{10} - D_1^2 r_{10} \\ &- \beta_1 r_{10} r_{21} - \beta_2 r_{11} r_{20} - \alpha_1 r_{10}^3 - \alpha_2 r_{10} r_{20}^2 \\ &- \alpha_3 r_{10} (D_0 r_{10})^2 - \alpha_4 r_{10} (D_0 r_{20})^2 \\ &- \alpha_5 r_{20} D_0 r_{10} D_0 r_{20},\end{aligned} \tag{55a}$$

$$\begin{aligned}D_0^2 r_{22} + \omega_2^2 r_{22} = &-2D_0 D_1 r_{21} - 2D_0 D_2 r_{20} - D_1^2 r_{20} \\ &- 2\beta_2 r_{10} r_{11} - \alpha_6 r_{10}^2 r_{20} - \alpha_7 r_{20}^3 \\ &- \alpha_8 r_{10} D_0 r_{10} D_0 r_{20} - \alpha_9 r_{20} (D_0 r_{10})^2 \\ &- \alpha_{10} r_{20} (D_0 r_{20})^2.\end{aligned} \tag{55b}$$

The solutions of (53a, 53b) are expressed as:

$$r_{10} = A_1(T_1, T_2) e^{i\omega_1 T_0} + cc, \tag{56a}$$

$$r_{20} = A_2(T_1, T_2) e^{i\omega_2 T_0} + cc, \tag{56b}$$

where cc stands for the complex conjugate. Upon substituting (56) in (54), the elimination of the resonant terms yield the following solvability condition:

$$D_1 A_1 = \frac{i\beta_1 \bar{A}_1 A_2}{2\omega_1} e^{-i\sigma T_1}, \tag{57a}$$

$$D_1 A_2 = \frac{i\beta_2 A_1^2}{2\omega_2} e^{i\sigma T_1}, \tag{57b}$$

where the internal detuning is $\varepsilon\sigma = 2\omega_1 - \omega_2$, already introduced by Eq. (8) in the main text to quantify the nearness of ω_2 to $2\omega_1$. With the elimination of the resonant terms, Eq. (54) are rewritten as:

$$D_0^2 r_{11} + \omega_1^2 r_{11} = -\beta_1 A_1 A_2 e^{i(\omega_1+\omega_2)T_0} + cc, \tag{58a}$$

$$D_0^2 r_{21} + \omega_2^2 r_{21} = -2\beta_2 A_1 \bar{A}_1. \tag{58b}$$

The solutions of Eq. (58) can be expressed as:

$$r_{11} = B_1 e^{i\omega_1 T_0} + \frac{\beta_1 A_1 A_2}{\omega_2(2\omega_1 + \omega_2)} e^{i(\omega_1+\omega_2)t} + cc, \tag{59a}$$

$$r_{21} = B_2 e^{i\omega_2 T_0} - \frac{\beta_2 A_1 \bar{A}_1}{\omega_2^2} + cc. \tag{59b}$$

Note that in the latter equations, both homogeneous and particular solutions have been taken into account, hence explaining that two terms are present. Indeed, homogeneous solutions to (58) leads to the first terms with coefficients $B_i(T_1, T_2)$, $i = 1, 2$; while the particular solutions give rise to the other two terms.

The modulation equations at order ε^2 can now be constructed by substituting Eqs. (59), (57) and (56) in (55). By canceling the resonant terms, one obtains the solvability condition at this order as:

$$\begin{aligned}2i\omega_1 D_2 A_1 = {} & \Lambda_1 A_1 A_2 \bar{A}_2 + \Lambda_2 A_1^2 \bar{A}_1 - \sigma \frac{\beta_1 \bar{A}_1 A_2}{2\omega_1} e^{-i\sigma T_1} \\ & - \left[2i\omega_1 D_1 B_1 + (\beta_1 \bar{A}_1 B_2 + \beta_2 A_2 \bar{B}_1) e^{-i\sigma T_1} \right],\end{aligned} \tag{60a}$$

$$\begin{aligned}2i\omega_2 D_2 A_2 = {} & \Lambda_3 A_1 A_2 \bar{A}_1 + \Lambda_4 A_2^2 \bar{A}_2 + \sigma \frac{\beta_2 A_1^2}{2\omega_2} e^{i\sigma T_1} \\ & - \left[2i\omega_1 D_1 B_2 + 2\beta_2 A_1 B_1 e^{i\sigma T_1} \right],\end{aligned} \tag{60b}$$

with the coefficients Λ_k defined in the main text by Eq. (12a–12d).

The present second-order MSM has the peculiarity of the treatment of the homogeneous solution introduced at order ε (terms of coefficients B_i in Eq. (59)). To derive a solution, one has to find the complex amplitudes (A_1, A_2, B_1, B_2), requiring eight real numbers, whereas the system has two DOFs and thus only four initial conditions. As a consequence, one has to find four real additional relationships to close the problem. In [54, §4.1] and [1, §2.3.1], considering a free Duffing equation, it is shown with a straightforward expansion that it is equivalent to: (i) consider the homogeneous solution of the order ε system and compute its redundant complex amplitude at the end of the process by considering the initial conditions; and (ii) simply discard the homogeneous solution. In [55, §6.2.1], the MSM, up to second-order, is applied to a Duffing equation using method (ii), since much less algebra is involved. This issue is precisely the subject of [39], in which second-order MSM is applied to several forced one DOFs examples and the free vibration of the 2-DOFs system considered here, Eq. (6), but without cubic terms. It is shown that better solutions, as compared to those obtained by other perturbation methods, are obtained by considering a non-zero homogeneous solution and by computing it using conditions based on physical considerations. In particular, the system (6) is assumed to derive from a potential energy (with the relations on quadratic and cubic coefficients given in "Appendix A") and the B_i complex amplitudes are selected as functions of A_i, such that the modulation equations (60) also derives from a potential. This method is tested in "Appendix E" for our system. However, it seems to us that this approach is not consistent in our case since our initial system (6) does not necessarily derive from a potential. Consequently, as done for the free Duffing equation in [55, §6.2.1], we propose here to simply cancel the homogeneous solution $(B_1 = B_2 = 0)$. It is shown in "Appendix E" that the obtained solution is more accurate at large amplitude, compared to a numerical reference simulation. It must also be noted that in [39], a solution with $B_1 = B_2 = 0$ *and* $D_1^2 A_i = 0$ (which leads to cancel also the terms in the second members of Eq. (60) proportional to σ) is proposed, as well as in [8, 56, 57] for the same system in forced vibrations. Our solution is slightly different as we only enforce $B_1 = B_2 = 0$ and we compute $D_1^2 A_i$ with Eq. (57).

Another issue is the treatment of the two time scales T_1 and T_2 since our initial ordinary differential equations (ODEs) (6) have been replaced by partial differential equations (57),(60) as functions of the two time scales (T_1, T_2). For simple systems like a free Duffing oscillator, it is possible to exactly integrate them (see [55, §6.2.1]). However, we prefer here recombining them in a single ODE using the chain rule (52a) (also called the reconstitution method [39, 41]), as given by Eq. (9).

The complex-valued amplitudes $A_1(T_1, T_2)$, $A_2(T_1, T_2)$ are expressed in polar form as follows:

$$A_k(T_1, T_2) = \frac{1}{2} a_k(T_1, T_2) e^{i\theta_k(T_1, T_2)}, \quad k = 1, 2. \tag{61}$$

Then, by substituting those equations in Eqs. (57), (60) and by using Eq. (9), the separation of the real and imaginary parts yields to:

$$\dot{a}_1 = \frac{\varepsilon \beta_1 a_1 a_2}{4\omega_1} \left[1 + \frac{\varepsilon\sigma}{2\omega_1}\right] \sin(2\theta_1 - \theta_2 + \sigma T_1), \tag{62a}$$

$$\dot{a}_2 = -\frac{\varepsilon \beta_2 a_1^2}{4\omega_2} \left[1 - \frac{\varepsilon\sigma}{2\omega_2}\right] \sin(2\theta_1 - \theta_2 + \sigma T_1), \tag{62b}$$

$$\begin{aligned} a_1 \dot{\theta}_1 = & \frac{\varepsilon \beta_1 a_1 a_2}{4\omega_1} \left[1 + \frac{\varepsilon\sigma}{2\omega_1}\right] \cos(2\theta_1 - \theta_2 + \sigma T_1) \\ & - \varepsilon^2 \frac{\Lambda_1 a_1 a_2^2 + \Lambda_2 a_1^3}{8\omega_1}, \end{aligned} \tag{62c}$$

$$\begin{aligned} a_2 \dot{\theta}_2 = & \frac{\varepsilon \beta_2 a_1^2}{4\omega_2} \left[1 - \frac{\varepsilon\sigma}{2\omega_2}\right] \cos(2\theta_1 - \theta_2 + \sigma T_1) \\ & - \varepsilon^2 \frac{\Lambda_3 a_1^2 a_2 + \Lambda_4 a_2^3}{8\omega_2}. \end{aligned} \tag{62d}$$

It is convenient to rewrite the above equations as:

$$\dot{a}_1 = \Gamma_1 a_1 a_2 \sin\gamma_p, \tag{63a}$$

$$\dot{a}_2 = -\Gamma_4 a_1^2 \sin\gamma_p, \tag{63b}$$

$$a_1 \dot{\theta}_1 = \Gamma_1 a_1 a_2 \cos\gamma_p + \Gamma_2 a_1^3 + \Gamma_3 a_1 a_2^2, \tag{63c}$$

$$a_2 \dot{\theta}_2 = \Gamma_4 a_1^2 \cos\gamma_p + \Gamma_5 a_1^2 a_2 + \Gamma_6 a_2^3. \tag{63d}$$

where

$$\gamma_p = 2\theta_1 - \theta_2 + \sigma T_1, \tag{64}$$

and

$$\Gamma_1 = \frac{\varepsilon\beta_1}{4\omega_1}\left[1 + \frac{\varepsilon\sigma}{2\omega_1}\right], \quad \Gamma_4 = \frac{\varepsilon\beta_2}{4\omega_2}\left[1 - \frac{\varepsilon\sigma}{2\omega_2}\right], \tag{65}$$

$$\Gamma_2 = -\frac{\varepsilon^2\Lambda_2}{8\omega_1}, \quad \Gamma_3 = -\frac{\varepsilon^2\Lambda_1}{8\omega_1}, \quad \Gamma_5 = -\frac{\varepsilon^2\Lambda_3}{8\omega_2}, \quad \Gamma_6 = -\frac{\varepsilon^2\Lambda_4}{8\omega_2}. \tag{66}$$

Those coefficients can be rewritten as function of the initial parameters of the system as

$$\Gamma_1 = \frac{g_{12}^1 (4\omega_1 - \omega_2)}{8\omega_1^2}, \tag{67a}$$

$$\Gamma_2 = \frac{1}{8\omega_1}\left[3h_{111}^1 - \left(\frac{2}{\omega_2^2} + \frac{1}{4\omega_1\omega_2}\right) g_{12}^1 g_{11}^2 - \frac{10\left(g_{11}^1\right)^2}{3\omega_1^2}\right], \tag{67b}$$

$$\begin{aligned} \Gamma_3 = & \frac{1}{8\omega_1}\left[2h_{122}^1 + \frac{16\omega_2^2 - 4\omega_1^2}{\omega_1^2(\omega_1^2 - 4\omega_2^2)} g_{11}^1 g_{22}^1 - \frac{2g_{12}^1 g_{22}^2}{\omega_2^2}\right. \\ & \left. + \left(\frac{1}{4\omega_1^2} + \frac{1}{\omega_2(2\omega_1 + \omega_2)}\right)\left(g_{12}^1\right)^2 + \frac{4g_{22}^1 g_{12}^2}{\omega_1^2 - 4\omega_2^2}\right], \end{aligned} \tag{67c}$$

$$\Gamma_4 = \frac{g_{11}^2 (3\omega_2 - 2\omega_1)}{8\omega_2^2}, \tag{67d}$$

$$\begin{aligned} \Gamma_5 = & \frac{1}{8\omega_2}\left[2h_{112}^2 + \frac{2}{\omega_1^2 - 4\omega_2^2}\left(g_{12}^2\right)^2 - \frac{4g_{11}^2 g_{22}^2}{3\omega_2^2}\right. \\ & \left. + \left(\frac{2}{\omega_2(2\omega_1 + \omega_2)} - \frac{1}{2\omega_1\omega_2}\right) g_{12}^1 g_{11}^2 - \frac{2g_{11}^1 g_{12}^2}{\omega_1^2}\right], \end{aligned} \tag{67e}$$

$$\Gamma_6 = \frac{1}{8\omega_2}\left[3h_{222}^2 + \frac{8\omega_2^2 - 3\omega_1^2}{\omega_1^2(\omega_1^2 - 4\omega_2^2)} g_{22}^1 g_{12}^2 - \frac{10\left(g_{22}^2\right)^2}{3\omega_2^2}\right], \tag{67f}$$

Using Eq. (64) with (63c,d) to eliminate θ_1 or θ_2, one has:

$$\begin{aligned} \dot{\gamma}_p = & 2\omega_1 - \omega_2 + \left(2\Gamma_1 a_2 - \Gamma_4 \frac{a_1^2}{a_2}\right)\cos\gamma_p \\ & + (2\Gamma_2 - \Gamma_5) a_1^2 + (2\Gamma_3 - \Gamma_6) a_2^2 \end{aligned} \tag{68}$$

D Stability details

The Jacobian of the modulation equations in polar coordinates (63a, 63b),(68) reads:

$$\boldsymbol{J}=\begin{pmatrix}\Gamma_1 a_2\sin\gamma_p & \Gamma_1 a_1\sin\gamma_p & \Gamma_1 a_1 a_2\cos\gamma_p\\ -2\Gamma_4 a_1\sin\gamma_p & 0 & -\Gamma_4 a_1^2\cos\gamma_p\\ J_{31} & J_{32} & J_{33}\end{pmatrix} \quad (69)$$

with

$$J_{31}=-2\Gamma_4\frac{a_1}{a_2}\cos\gamma_p+2(2\Gamma_2-\Gamma_5)a_1, \quad (70)$$

$$J_{32}=\left(2\Gamma_1+\frac{\Gamma_4 a_1^2}{a_2^2}\right)\cos\gamma_p+2(2\Gamma_3-\Gamma_6)a_2, \quad (71)$$

$$J_{33}=-\left(2\Gamma_1 a_2-\frac{\Gamma_4 a_1^2}{a_2}\right)\sin\gamma_p. \quad (72)$$

For the coupled solutions C+ or C−, $\sin\gamma_p=0$ and $\cos\gamma_p=p$, which leads to:

$$\boldsymbol{J}=\begin{pmatrix}0 & 0 & J_{13}\\ 0 & 0 & J_{23}\\ J_{31} & J_{32} & 0\end{pmatrix} \quad (73)$$

with

$$\begin{aligned}J_{13}&=\Gamma_1 p a_1 a_2,\\ J_{23}&=-\Gamma_4 p a_1^2,\\ J_{31}&=-2\Gamma_4 p\frac{a_1}{a_2}+2(2\Gamma_2-\Gamma_5)a_1,\\ J_{32}&=2\Gamma_1 p+\frac{\Gamma_4 a_1^2}{a_2^2}p+2(2\Gamma_3-\Gamma_6)a_2.\end{aligned} \quad (74)$$

To assess the stability of the uncoupled U2 solution, the modulation equations must be rewritten under a Cartesian form. To do so, according to [4, 31], we define:

$$p_1=a_1\cos\left(\gamma_p/2\right),\qquad q_1=a_1\sin\left(\gamma_p/2\right),\qquad p_2=a_2. \quad (75)$$

Differentiating p_1, q_1 and p_2 with respect to t, one obtains:

$$\begin{aligned}\dot p_1&=\dot a_1\cos(\gamma_p/2)-a_1\dot\gamma_p/2\sin(\gamma_p/2),\\ \dot q_1&=\dot a_1\sin(\gamma_p/2)+a_1\dot\gamma_p/2\cos(\gamma_p/2),\\ \dot p_2&=\dot a_2.\end{aligned} \quad (76)$$

Then, replacing in the above equations $\dot a_1$, $\dot a_2$ and $\dot\gamma_p$ by their values in the polar modulation equations (63) and (68), using basic trigonometric identities and the definitions (75) of p_1, q_1 and p_2, one replaces the modulation equations (63) and (68) by:

$$\begin{aligned}\dot p_1&=\Gamma_1 p_2 q_1+\frac{\Gamma_4}{2}\frac{q_1}{p_2}(p_1^2-q_1^2)-\left(\Gamma_3-\frac{\Gamma_6}{2}\right)p_2^2 q_1\\ &\quad-\left(\Gamma_2-\frac{\Gamma_5}{2}\right)q_1(p_1^2+q_1^2)-\frac{1}{2}(2\omega_1-\omega_2)q_1,\end{aligned} \quad (77a)$$

$$\begin{aligned}\dot q_1&=\Gamma_1 p_1 p_2-\frac{\Gamma_4}{2}\frac{p_1}{p_2}(p_1^2-q_1^2)+\left(\Gamma_3-\frac{\Gamma_6}{2}\right)p_1 p_2^2\\ &\quad+\left(\Gamma_2-\frac{\Gamma_5}{2}\right)p_1(p_1^2+q_1^2)+\frac{1}{2}(2\omega_1-\omega_2)p_1,\end{aligned} \quad (77b)$$

$$\dot p_2=-2\Gamma_4 p_1 q_1. \quad (77c)$$

Computing the Jacobian $\boldsymbol{J}$ of the above modulation equations and imposing $a_1=0\Rightarrow p_1=q_1=0$ for the uncoupled U2 solution, one obtains:

$$\boldsymbol{J}=\begin{pmatrix}0 & J_{12} & 0\\ J_{21} & 0 & 0\\ 0 & 0 & 0\end{pmatrix} \quad (78)$$

with

$$\begin{aligned}J_{12}&=-(2\omega_1-\omega_2)/2+\Gamma_1 a_2-(\Gamma_3-\Gamma_6/2)a_2^2,\\ J_{21}&=(2\omega_1-\omega_2)/2+\Gamma_1 a_2+(\Gamma_3-\Gamma_6/2)a_2^2,\end{aligned} \quad (79)$$

where $a_2=p_2$ by definition. Its eigenvalues are thus:

$$\lambda_1=0,\qquad \lambda_{2,3}=\pm\sqrt{J_{12}J_{21}} \quad (80)$$

E MSM with homogeneous solution and enforced Lagrangian

We consider here the approach of [39] that considers the homogeneous solutions in Eq. (59) and enforces the modulation Eq. (60) to derive from a potential. This is obtained by enforcing:

$$2i\omega_1 D_1 B_1+D_1^2 A_1=0,\quad 2i\omega_1 D_1 B_2+D_1^2 A_2=0, \quad (81)$$

or

$$B_1=\frac{-\beta_1}{4\omega_1^2}A_2\bar A_1 e^{-i\sigma T_1}+cc, \quad (82a)$$

$$B_2 = \frac{-\beta_2}{4\omega_2^2} A_1^2 e^{i\sigma T_1} + cc. \tag{82b}$$

One can note that upon substituting (82) in (60), all the terms related to B_1 and B_2 in addition to the terms multiplied by σ will be eliminated. We arrive at the following modulation equations:

$$2i\omega_1 D_2 A_1 = \Lambda'_1 A_1 A_2 \bar{A}_2 + \Lambda'_2 A_1^2 \bar{A}_1, \tag{83a}$$

$$2i\omega_2 D_2 A_2 = \Lambda'_3 A_1 A_2 \bar{A}_1 + \Lambda'_4 A_2^2 \bar{A}_2, \tag{83b}$$

with

$$\Lambda'_1 = \beta_1^2 \left[\frac{1}{4\omega_1^2} - \frac{1}{\omega_2(2\omega_1 + \omega_2)} \right] - 2\alpha_4 \omega_2^2 - 2\alpha_2, \tag{84a}$$

$$\Lambda'_2 = \frac{9\beta_1\beta_2}{4\omega_2^2} - \alpha_3\omega_1^2 - 3\alpha_1, \tag{84b}$$

$$\Lambda'_3 = 2\beta_1\beta_2 \left[\frac{1}{4\omega_1^2} - \frac{1}{\omega_2(2\omega_1 + \omega_2)} \right] - 2\alpha_6 - 2\alpha_9\omega_1^2, \tag{84c}$$

$$\Lambda'_4 = -3\alpha_7 - \alpha_{10}\omega_2^2. \tag{84d}$$

Note that coefficients Λ'_k are different than the Λ_k in Eq. (60). In addition, one can note that the modulation equations in (83a, b) don't derive from a potential since $\Lambda'_1 \neq \Lambda'_3$ even if it is the case for the initial system (i.e., by setting $g_{12}^1 = 2g_{11}^2$, $g_{12}^2 = 2g_{22}^1$, $h_{122}^1 = h_{112}^2$, $h_{122}^2 = 3h_{222}^1$ and $h_{112}^1 = 3h_{111}^2$). This can be analyzed by realizing that if one considers the initial system (1a, 1b) to derivee from a potential, it is not necessarily the case for the normal form system (2a, 2b) which relies on a truncation from an asymptotic development. In particular, if one neglects all the cubic terms from ((2a, 2b), one obtains the same results as in [39] where the Lagrangian is enforced.

Following the same procedure in Sect. 2.2, the modulation equations are expressed in the polar form as:

$$\frac{\mathrm{d}a_1}{\mathrm{d}t} = \frac{\varepsilon\beta_1 a_1 a_2}{4\omega_1} \sin\gamma_p, \tag{85a}$$

$$\frac{\mathrm{d}a_2}{\mathrm{d}t} = -\frac{\varepsilon\beta_2 a_1^2}{4\omega_2} \sin\gamma_p, \tag{85b}$$

$$\frac{\mathrm{d}\theta_1}{\mathrm{d}t} = \frac{\varepsilon\beta_1 a_2}{4\omega_1} \cos\gamma_p - \varepsilon^2 \frac{\Lambda'_1 a_2^2 + \Lambda'_2 a_1^2}{8\omega_1}, \tag{85c}$$

$$\frac{\mathrm{d}\theta_2}{\mathrm{d}t} = \frac{\varepsilon\beta_2 a_1^2}{4\omega_2 a_2} \cos\gamma_p - \varepsilon^2 \frac{\Lambda'_3 a_1^2 + \Lambda'_4 a_2^2}{8\omega_2}, \tag{85d}$$

and the autonomous version is obtained by combining (85c, 85d) with Eq. (11), yielding:

$$\begin{aligned} \frac{\mathrm{d}\gamma_p}{\mathrm{d}t} =& \varepsilon\sigma + \varepsilon \left(\frac{\beta_1 a_2}{2\omega_1} - \frac{\beta_2 a_1^2}{4a_2\omega_2} \right) \cos\gamma_p \\ &+ \varepsilon^2 \left(\frac{\Lambda'_3 a_1^2 + \Lambda'_4 a_2^2}{8\omega_2} - \frac{\Lambda'_1 a_2^2 + \Lambda'_2 a_1^2}{4\omega_1} \right). \end{aligned} \tag{86}$$

Using the same procedure in Sect. 2.2, we can find the expressions governing the relation between a_1 and a_2 in addition to the expressions of the nonlinear modes ω_{nl1} and ω_{nl2}, as:

$$a_1^2 = \frac{(2\omega_1 - \omega_2)a_2 + 2\Gamma'_1 a_2^2 + (2\Gamma'_3 - \Gamma'_6)a_2^3}{\Gamma'_4 + (\Gamma'_5 - 2\Gamma'_2)a_2}, \tag{87a}$$

$$\omega_{\text{nl1}} = \omega_1 + \Gamma'_1 a_2 + \Gamma'_2 a_1^2 + \Gamma'_3 a_2^2, \tag{87b}$$

$$\omega_{\text{nl2}} = \omega_2 + \Gamma'_4 \frac{a_1^2}{a_2} + \Gamma'_5 a_1^2 + \Gamma'_6 a_2^2, \tag{87c}$$

where

$$\Gamma'_1 = p\,\frac{g_{12}^1}{4\omega_1}, \tag{88a}$$

$$\Gamma'_2 = \frac{1}{8\omega_1} \left[3h_{111}^1 - \frac{9}{4\omega_2^2} g_{12}^1 g_{11}^2 - \frac{10}{3\omega_1^2} \left(g_{11}^1 \right)^2 \right], \tag{88b}$$

$$\begin{aligned} \Gamma'_3 = \frac{1}{8\omega_1} \Bigg[& 2h_{122}^1 + \left(\frac{16\omega_2^2 - 4\omega_1^2}{\omega_1^2(\omega_1^2 - 4\omega_2^2)} \right) g_{11}^1 g_{22}^1 - \frac{2g_{12}^1 g_{22}^2}{\omega_2^2} \\ & + \left(\frac{1}{\omega_2(2\omega_1 + \omega_2)} - \frac{1}{4\omega_1^2} \right) \left(g_{12}^1 \right)^2 + \frac{4g_{22}^1 g_{12}^2}{\omega_1^2 - 4\omega_2^2} \Bigg], \end{aligned} \tag{88c}$$

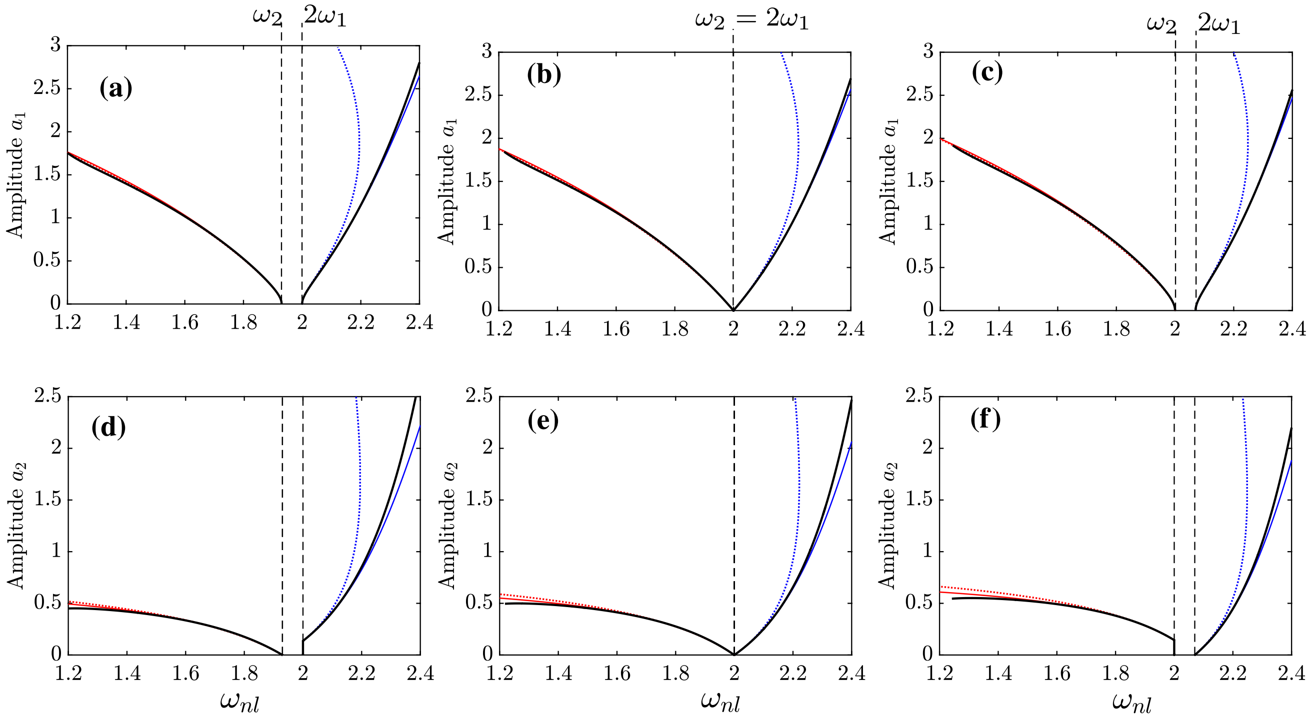

Fig. 11 Comparison between the analytical results of the two approaches presented in (18a, b) and (87a, b) with the numerical results computed with Manlab. Only the quadratic resonant terms are considered such that $g^1_{12} = g^2_{11} = 1$ with the other nonlinear coefficients are set to zero. The backbones are plotted in the planes $(a_1, \omega_{\mathrm{nl2}})$ and $(a_2, \omega_{\mathrm{nl2}})$ in the first and second row, respectively. The first, second, and third column are the results for $\sigma = -0.07$, $\sigma = 0$, $\sigma = 0.07$, respectively. The analytical results for the C+ and C− modes are plotted in blue and red, respectively. The dotted and solid lines are results of (87) and (18), respectively. The Manlab results are shown in black for the C+ and C− modes. (Color figure online)

$$\Gamma'_4 = p\,\frac{g^2_{11}}{4\omega_2}, \tag{88d}$$

$$\Gamma'_5 = \frac{1}{8\omega_2}\Bigg[2h^2_{112} + \left(\frac{2}{\omega_1^2 - 4\omega_2^2}\right)\left(g^2_{12}\right)^2 - \frac{4g^2_{11}g^2_{22}}{3\omega_2^2} + \left(\frac{2}{\omega_2(2\omega_1 - \omega_2)} - \frac{1}{4\omega_1^2}\right)g^1_{12}g^2_{11} - \frac{2g^1_{11}g^2_{12}}{\omega_1^2}\Bigg], \tag{88e}$$

$$\Gamma'_6 = \frac{1}{8\omega_2}\left[3h^2_{222} + \left(\frac{8\omega_2^2 - 3\omega_1^2}{\omega_1^2(\omega_1^2 - 4\omega_2^2)}\right)g^1_{22}g^2_{12} - \frac{10\left(g^2_{22}\right)^2}{3\omega_2^2}\right], \tag{88f}$$

Note that the relation $\omega_{\mathrm{nl2}} = 2\omega_{\mathrm{nl1}}$ is still satisfied. In addition, the solution of $R_1(t)$ and $R_2(t)$ illustrates the same locking properties in the amplitudes and phase angles illustrated in Section 2.2.

A comparison is shown in Fig. 11 between the analytical results governing the backbone curves of both approaches presented in (18a, 18b) and (87b, 87c), with the numerical solution computed with the continuation method implemented in Manlab, which is considered as our reference solution. The plots are done for positive, negative, and zero values of σ to underline the effect of the additional term appearing in (60a, 60b). Both results match with the numerical solution at low amplitudes. However, at higher amplitudes, the first approach used in Sect. 2.2 suggests more accurate results as compared to the numerical ones, especially for the C+ mode. Namely, the second approach that leads to the results in (87b, 87c) shows a kind of softening behavior associated with the response of the C+ mode at high amplitudes.

References

1. Nayfeh A, Mook D (1979) Nonlinear Oscillations, In: Pure and applied mathematics. A Wiley Series of Texts, Monographs and Tracts, Wiley

2. Thomsen JJ (2003) Vibrations and stability. Advanced theory, analysis and tools, 2nd edn. Springer, Berlin, Heidelberg
3. Strogatz S (2014) Nonlinear dynamics and chaos, with applications to physics, biology, chemistry and engineering, 2nd edn. Westview Press, New-York
4. Nayfeh AH (2000) Nonlinear interactions: analytical, computational, and experimental methods. Wiley
5. Nayfeh SA, Nayfeh AH (1993) Nonlinear intercations between two widely spaced modes: external excitation. Int J Bifurc Chaos 3(2):417–427
6. Nayfeh AH, Mook DT, Marshall LR (1973) Nonlinear coupling of pitch and roll modes in ship motions. J Hydronaut 7(4):145–152
7. Miles JW (1984) Resonantly forced motion of two quadratically coupled oscillators. Phys D 13:247–260
8. Lee CL, Perkins NC (1992) Nonlinear oscillations of suspended cables containing a two-to-one internal resonance. Nonlinear Dyn 3:465–490
9. Tien WM, Namachchivaya NS, Bajaj AK (1994) Nonlinear dynamics of a shallow arch under periodic excitation, I : 1:2 internal resonance. Int J Non-linear Mech 29(3):349–366
10. Gobat G, Guillot L, Frangi A, Cochelin B, Touzé C (2021) Backbone curves, Neimark–Sacker boundaries and appearance of quasi-periodicity in nonlinear oscillators: application to 1:2 internal resonance and frequency combs in MEMS. Meccanica 56:1937–1969
11. Touzé C, Thomas O, Chaigne A (2004) Hardening/softening behaviour in non-linear oscillations of structural systems using non-linear normal modes. J Sound Vib 273(1–2):77–101
12. Touzé C (2014) Normal form theory and nonlinear normal modes: theoretical settings and applications. In: Kerschen G (ed) Modal analysis of nonlinear mechanical systems, vol 555. Springer Series CISM courses and lectures, New York, pp 75–160
13. Lenci S, Clementi F, Kloda L, Warminski J, Rega G (2021) Longitudinal-transversal internal resonances in Timoshenko beams with an axial elastic boundary condition. Nonlinear Dyn 103:3489–3513
14. Oueini SS, Nayfeh AH, Pratt JR (1998) A nonlinear vibration absorber for flexible structures. Nonlinear Dyn 15:259–282
15. Pai PF, Rommel B, Schulz MJ (2000) Dynamics regulation of a Skew cantilever plate Using PZT Patches and Saturation Phenomenon. J Intell Mater Syst Struct 11:642–655
16. Wood HG, Roman A, Hanna JA (2018) The saturation bifurcation in coupled oscillators. Phys Lett A 382:1968–1972
17. Shami ZA, Giraud-Audine C, Thomas O (2022) A nonlinear piezoelectric shunt absorber with a 2:1 internal resonance: Theory. Mech Syst Sig Process 170:108768
18. Shami ZA, Giraud-Audine C, Thomas O (2022) A nonlinear piezoelectric shunt absorber with 2:1 internal resonance: experimental proof of concept. Smart Materials and Structures. online
19. Jézéquel L, Lamarque CH (1991) Analysis of non-linear dynamical systems by the normal form theory. J Sound Vib 149(3):429–459
20. Neild SA, Champneys AR, Wagg DJ, Hill TL, Cammarano A (2015) The use of normal forms for analysing nonlinear mechanical vibrations. Proc R Soc A 373:20140404
21. Murdock J (2003) Normal forms and unfoldings for local dynamical systems. Springer Monographs in Mathematics, New-York
22. Kahn PB, Zarmi Y (2014) Nonlinear dynamics: exploration through normal forms. Over Books on Physics
23. Touzé C, Amabili M (2006) Nonlinear normal modes for damped geometrically nonlinear systems: application to reduced-order modelling of harmonically forced structures. J Sound Vib 298:958–981
24. Vizzaccaro A, Shen Y, Salles L, Blahoš J, Touzé C (2021) Direct computation of nonlinear mapping via normal form for reduced-order models of finite element nonlinear structures. Comput Methods Appl Mech Eng 384:113957
25. Opreni A, Vizzaccaro A, Frangi A, Touzé C (2021) Model order reduction based on direct normal form: application to large finite element MEMS structures featuring internal resonance. Nonlinear Dyn 105:1237–1272
26. Haro A, Canadell M, Figueras J-L, Luque A, Mondelo J-M (2016) The parameterization method for invariant manifolds. Springer, From rigorous results to effective computations. Switzerland
27. Touzé C, Vizzaccaro A, Thomas O (2021) Model order reduction methods for geometrically nonlinear structures: a review of nonlinear techniques. Nonlinear Dyn 105:1141–1190
28. Amabili M (2008) Nonlinear vibrations and stability of shells and plates. Cambridge University Press
29. Thomas O, Touzé C, Chaigne A (2005) Non-linear vibrations of free-edge thin spherical shells: modal interaction rules and 1:1:2 internal resonance. Int J Solids Struct 42(11–12):3339–3373
30. Muravyov AA, Rizzi SA (2003) Determination of nonlinear stiffness with application to random vibration of geometrically nonlinear structures. Comput Struct 81(15):1513–1523
31. Pai PF, Wen B, Naser AS, Schultz MJ (1998) Structural vibration control using PZT patches and non-linear phenomena. J Sound Vib 215(2):273–296
32. Leung A, Zhang Q (1998) Complex normal form for strongly non-linear vibration system exemplified by Duffing: van der Pol equation. J Sound Vib 213(5):907–914
33. Elphick C, Iooss G, Tirapegui E (1987) Normal form reduction for time-periodically driven differential equations. Phys Lett A 120(9):459–463
34. Wagg DJ (2022) Normal form transformations for structural dynamics: an introduction for linear and nonlinear systems. J Struct Dyn 1
35. Iooss G, Adelmayer M (1998) Topics in bifurcation theory. World Scientific
36. Neild SA, wagg DJ (2011) Applying the method of normal forms to second-order nonlinear vibration problems. Proc R Soc A 467:1141–1163
37. Vizzaccaro A, Opreni A, Salles L, Frangi A, Touzé C (2021) High order direct parametrisation of invariant manifolds for model order reduction of finite element structures: application to large amplitude vibrations and uncovering of a folding point. Nonlinear Dynamics. submitted

38. Touzé C (2003) A normal form approach for non-linear normal modes, tech. rep., Publications du LMA, numéro 156, (ISSN: 1159-0947, ISBN: 2-909669-20-3)
39. Nayfeh AH (2005) Resolving controversies in the application of the method of multiple scales and the generalized method of averaging. Nonlinear Dyn 40:61–102
40. Clementi F, Lenci S, Rega G (2020) 1:1 internal resonance in a two d.o.f. complete system: A comprehensive analysis and its possible exploitation for design. Meccanica 55:1309–1332
41. Luongo A, Paolone A (1999) On the reconstitution problem in the multiple time-scale method. Nonlinear Dyn 19:133–156
42. Rosenberg RM (1962) The normal modes of nonlinear n-degree-of-freedom systems. J Appl Mech 29:7–14
43. Kerschen G, Peeters M, Golinval JC, Vakakis AF (2009) Non-linear normal modes, part I: a useful framework for the structural dynamicist. Mech Syst Sign rocess 23(1):170–194
44. Manevitch AI, Manevitch LI (2003) Free oscillations in conservative and dissipative symmetric cubic two-degree-of-freedom systems with closed natural frequencies. Meccanica 38(3):335–348
45. Givois A, Tan JJ, Touzé C, Thomas O (2020) Backbone curves of coupled cubic oscillators in one-to-one internal resonance: bifurcation scenario, measurements and parameter identification. Meccanica 55:481–503
46. Guillot L, Lazarus A, Thomas O, Vergez C, Cochelin B (2018) Manlab 4.0: an interactive path-following and bifurcation analysis software. tech. rep., Laboratoire de Mécanique et d'Acoustique, CNRS, http://manlab.lma.cnrs-mrs.fr
47. Guillot L, Cochelin B, Vergez C (2019) A Taylor series-based continuation method for solutions of dynamical systems. Nonlinear Dyn 98:2827–2845
48. Guillot L, Lazarus A, Thomas O, Vergez C, Cochelin B (2020) A purely frequency based Floquet-Hill formulation for the efficient stability computation of periodic solutions of ordinary differential systems. J Comput Phys 416:109477
49. Opreni A, Vizzaccaro A, Touzé C, Frangi A (2022) High order direct parametrisation of invariant manifolds for model order reduction of finite element structures: application to generic forcing terms and parametrically excited systems. Nonlinear Dynamics, submitted
50. Peeters M, Kerschen G, Golinval JC (2011) Dynamic testing of nonlinear vibrating structures using nonlinear normal modes. J Sound Vib 220(3):486–509
51. Denis V, Jossic M, Giraud-Audine C, Chomette B, Renault A, Thomas O (2018) Identification of nonlinear modes using phase-locked-loop experimental continuation and normal form. Mech Syst Sign Process 106:430–452
52. Lamarque C-H, Touzé C, Thomas O (2012) An upper bound for validity limits of asymptotic analytical approaches based on normal form theory. Nonlinear Dyn 70:1931–1949
53. Habib G, Detroux T, Viguié R, Kerschen G (2015) Nonlinear generalization of den Hartog's equal-peak method. Mech Syst Sign Process 52–53:17–28
54. Nayfeh AH (1993) Introduction to perturbation techniques, 1st edn. Wiley Classics Library, Wiley-VCH
55. Nayfeh AH (1973) Perturbation methods. Wiley
56. Benedettini F, Rega G, Alaggio R (1995) Non-linear oscillations of a four-degree-of-freedom model of a suspended cable under multiple internal resonance conditions. J Sound Vib 182(5):775–798
57. Pan R, Davies HG (1996) Responses of a non-linearly coupled pitch-roll ship model under harmonic excitation. Nonlinear Dyn 9:349–368

Chapter 5

Experimental validation of the Saturation Correction with cubic nonlinearity

Contenu

5.1 Article presentation

The present chapter solely constitutes of the text of the article entitled by ”Saturation correction for a piezoelectric shunt absorber based on 2:1 internal resonance using a cubic nonlinearity” submitted to ”Smart Materials and Structures (SMS)” journal and currently, it is under review. The article addresses the experimental validation of the proposed procedure in chapter 4 which consists of designing a shunt absorber that includes both quadratic ($\beta_q V^2$) and cubic ($\beta_c V^3$) with V is the voltage across the piezoelectric patch, and β_q and β_c are the quadratic and cubic nonlinear gains, respectively. The main idea is to properly tune the cubic nonlinearity according to the results in chapter 4. The experimental tests are performed to attenuate the first bending mode of a hydrofoil structure.

The article starts by reviewing the main results presented in chapter 2 and chapter 3 and the results regarding the tuning of the cubic nonlinearities suggested from the normal form method in chapter 4 are also recalled. The main governing equations are presented, and the electro-mechanical expansion, used in chapter 2 is adopted to estimate the cubic and quadratic nonlinearities, in the modal basis, as a function of the cubic nonlinear gain β_c and the quadratic gain β_q, respectively.

As suggested in chapter 4, four conditions on the cubic nonlinearities should be taken into account. However, due to experimental limitations, only one condition can be satisfied. The condition selection criteria is based on identifying the nonresonant quadratic term with the highest value of the nonresonant quadratic terms (and thus the strongest influence on the dynamics). Upon identifying this term, a simple tuning of the cubic gain β_c is estimated, which appeared to depend only on the chosen quadratic gain β_q such that $\beta_c = 10/9\beta_q^2$. With this tuning of β_c, the numerical results showed the recovery of the saturation up to a certain amplitude where the non-tuned cubic nonlinearities start to admit significant mistuning.

The experiment protocol and the experimental modal analysis are discussed. In addition, the measurement procedure of the frequency response is shown that relies on the sine step method with the demodulation procedure to determine the amplitude and phase angles of the first harmonic of velocity and the subharmonic of the voltage. The nonlinear shunt circuit is also presented, which includes two analog multipliers to generate the quadratic and the cubic nonlinearities.

A comparison between the numerical and the experimental frequency response suggested an excellent fitting. The ability to shift back the antiresonance to the resonance frequency and to symmetrize the response by setting the obtained tuning of β_c is also validated. The saturation recovery is also validated up to high excitation amplitudes by measuring the amplitude-frequency response of the velocity for different excitation levels. To extend the saturation limit, a sensitivity analysis regarding the value of β_c is performed, showing that at high excitation amplitudes, a small correction of the estimated analytical tuning should be performed. Indeed, this technique has an amplitude limitation that should be considered when choosing the main design parameters (i.e., β_q and the electrical damping ratio ξ_e).

5.2 Saturation correction for a piezoelectric shunt absorber based on 2:1 internal resonance using a cubic nonlinearity

Saturation correction for a piezoelectric shunt absorber based on 2:1 internal resonance using a cubic nonlinearity

Zein Alabidin SHAMI[a,*], Christophe GIRAUD-AUDINE[b], Olivier THOMAS[a]

[a] *Arts et Métiers Institute of Technology, LISPEN, HESAM Université, F-59000 Lille, France*
[b] *Arts et Métiers Institute of Technology, L2EP, HESAM Université, Univ. Lille, Centrale Lille, JUNIA, F-59000 Lille, France*

Abstract

In this study, we present a theoretical and experimental analysis of an antiresonance detuning correction for a nonlinear piezoelectric shunt absorber based on a two-to-one internal resonance. Thanks to this purely nonlinear feature, the oscillations of the primary system become independent of the forcing at a particular antiresonance frequency, thus creating an efficient reduction of the vibration. Past works of the literature present the design of the piezoelectric shunt and show that it is subjected to a softening behavior that detunes the antiresonance frequency as a function of the amplitude and thus degrades the performance. It is also shown that this softening behavior is caused by some non-resonant terms present in the equations, linked to the piezoelectric coupling. To counteract this undesired effect, we propose in this work to add a cubic nonlinearity in the shunt circuit, in addition to the quadratic one already present. Its tuning is based on a normal form analysis already published, which shows how cubic nonlinearities can cancel the effect of quadratic non-resonant terms. The present article focuses on the experimental proof of concept of this antiresonance detuning correction as well as the analysis of its range of validity. It is applied to the damping of the first bending mode of a hydrodynamic foil

---

[*] Corresponding author
Email address: `zein_alabidin.shami@ensam.eu` (Zein Alabidin SHAMI)

Preprint submitted to Journal of LaTeX Templates *November 9, 2022*

structure.

Keywords: Piezoelectric shunt absorbers, 2:1 Internal Resonance, Normal Form, Saturation phenomenon, Nonlinear Vibrations

---

1. Introduction

In the domain of vibration attenuation, passive absorbers are used in many industrial applications due to their simplicity and well-established tuning rules. Two famous classical examples are the Lanchester [1] and Frahm [2] mechanical dampers, which consist in adding inertia, stiffness, and damping components to the primary structure to mitigate its vibration. This principle has been extended by proposing electromechanical analogs. To do so, the primary structure is coupled to a dedicated electrical circuit, referred to as a shunt, through an electromechanical transducer. Depending on its nature, the so-called piezoelectric shunts or electromechanical shunts were proposed in the pioneering works [3, 4] and were addressed in a huge number of contributions since then (see [5, 6, 7] and reference therein). Shunt circuits can be passive or semi-passive when electronic components which require a power supply are used, like operational amplifiers. In either case, shunt circuits consist in resistive or/and reactive dipoles (i.e., a capacitor or an inductor) in order to modify and/or create resonances and antiresonances in the vibratory behavior of the structure. Many studies investigated the enhancement of the basic resistive or resonant shunts [8, 7], among others, in terms of broadband / multimodal attenuation [9, 10, 11], artificial increasing of coupling factor using negative capacitances [12, 13], adaptivity using pulse width modulation [14] and experimental concept for high voltage in the shunt [15].

Whereas all the above cited works rely on purely linear behaviors, nonlinear components can be added intentionally to the shunt circuit to benefit from particular features to enhance the absorber's performance. Several contributions have already been proposed in the literature, being ,in most of the cases, the electromechanical implementation of an earlier purely mechanical concept. They can be gathered into four families, and we consider here only a few relevant references dedicated to piezoelectric shunts, since broader literature reviews are available elsewhere, for instance in [16, 17]. The first concept is known as nonlinear energy sinks (NES), for which strong nonlinear components are used in order to transfer and trap the vibratory energy in the absorber, the idea being to improve the properties of traditional tuned vibration absorbers, in particular in term of robustness to a detuning. This concept was introduced in [18] and extended to piezoelectric shunts in [19] for the theory and in [20] for an experimental proof of concept using analog multipliers. The second concept, so-called nonlinear tuned vibration absorbers, is intentionally adapted to a primary nonlinear structure. It was introduced in [21], extended to piezoelectric shunts in [22] for a single resonance attenuation and for multi-mode control in [23]. In this case, the nonlinear behavior of the shunt is chosen as a mirror to the one of the primary structure, such that the damping performance is independent of the amplitude. The third family gathers the synchronized switch damping techniques, addressed in many contributions since the pioneering works [24, 25] for vibration damping and energy harvesting (see the review [6]).

The fourth concept, which interests us here, is based on the intentional use of internal resonance between two vibration modes. Namely, if two modal frequencies ω_p and ω_k are commensurable (i.e. $\omega_p/\omega_k = n/m$ with $n, m \in \mathbb{N}^*$) and if the system has some particular nonlinearities, a strong energy transfer can occur between the corresponding modes. In particular, in the presence of quadratic nonlinearities in the shunt circuit, a special case can be realized by tuning two natural frequencies of the system such that $\omega_2 = 2\omega_1$, a so-called two-to-one (2:1) internal resonance. As a result, an energy transfer occurs from the driven mode (at ω_2) to the other mode tuned at ω_1 [26]. This particular nonlinear interaction can be used to reduce the vibration amplitude of the driven mode since it creates an antiresonance in the frequency response, which is associated with an amplitude saturation [16]. Namely, if the system is driven at the antiresonance frequency, the amplitude of the driven mode is reduced and independent of the driving amplitude thanks to an energy transfer to the other mode. This principle was exploited for vibration attenuation using mechanical systems (see [27, 28, 29] and reference therein) or within an active control context in [30, 31, 32, 33, 34]. One can also refer to [35], where the saturation phenomenon is theoretically studied considering cubic nonlinearities.

In the context of piezoelectric shunts, the use of a 2:1 internal resonance was proposed by the authors in [16]. The principle is to couple an electrical oscillator to the primary structure that includes quadratic nonlinear terms and to tune its natural frequency ω_1 close to half ω_2, one of the natural frequencies of the primary structure. An experimental proof of concept was proposed in [17] using an analog shunt circuit including a multiplier to create quadratic nonlinearities. It was shown that because of the linear piezoelectric coupling (which is mandatory), some unwanted nonlinear terms appear in the equations, which are responsible for a deterioration of the nonlinear interaction. Indeed, those terms bring a softening behavior to the system, which detunes the antiresonance frequency as a function of the amplitude of driving, thus killing the saturation phenomenon. In [16], the saturation phenomenon was artificially recovered by manually detuning the electrical resonator as a function of the amplitude.

The effect of the unwanted nonlinear quadratic coupling terms was recently investigated in theory in [36]. It was proven using the normal form theory that they are equivalent to cubic nonlinearities and that their effect is equivalent to the hardening/softening effect brought by the cubic nonlinear term of a classical Duffing oscillator. As a consequence, it was proposed to add cubic nonlinearities in the shunt circuit, specifically tuned to cancel the effect of the unwanted quadratic terms, thus recovering the antiresonance frequency stability and the saturation phenomenon. The present article is specifically devoted to the experimental proof of concept of this idea. We first recall in section 2 the main ideas of the underlying theory, already exposed in detail in [16, 36]. Then, section 3 is devoted to the experimental proof of concept. We target the first bending mode of a hydrodynamic foil with embedded piezoelectric patches, which are connected to a shunt circuit including two analog multipliers to create cubic nonlinearities in addition to the quadratic ones. Finally, section 4 investigates the limits of our saturation correction and the practical tuning of the cubic nonlinearity in the shunt circuit.

2. Theoretical Model

2.1. Governing Equations

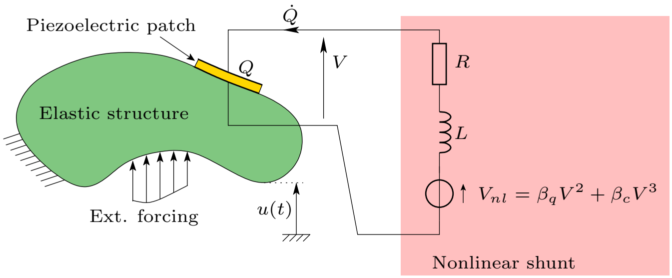

Figure 1: Nonlinear shunt circuit

This section briefly describes the model of an electromechanical system coupled to a nonlinear shunt as sketched in Fig. 1. For a full theoretical analysis, one can refer to [16]. We consider an elastic structure subjected to external forcing and connected to a nonlinear shunt circuit via a piezoelectric patch (PE patch). The displacement $\boldsymbol{u}(\boldsymbol{x}, t)$ at a position $\boldsymbol{x}$ of the structure and at time t is expanded on the basis of the linear modes. Considering that the frequency of the external forcing is close to the resonant frequency of a weakly damped mode i ($i \in \mathbb{N}^*$), its modal shape $\boldsymbol{\phi}_i(\boldsymbol{x})$ dominates, hence:

$$\boldsymbol{u}(\boldsymbol{x}, t) \simeq \boldsymbol{\phi}_i(\boldsymbol{x}) q_i(t), \tag{1}$$

where $q_i(t)$ is the i-th modal displacement. Due to the piezoelectric effect, the modal displacement is coupled to the electric charge $Q(t)$ in one of the electrodes as follows [8, 16]:

$$\ddot{q}_i + 2\xi_i \hat{\omega}_i \dot{q}_i + \hat{\omega}_i^2 q_i + \frac{\theta_i}{m_i C_{\mathrm{pi}}} Q = \frac{F_i}{m_i} \cos \Omega t \tag{2a}$$

$$\ddot{Q} + 2\xi_e \omega_e \dot{Q} + \omega_e^2 Q + \frac{\theta_i}{L C_{\mathrm{pi}}} q_i + \frac{V_{\mathrm{nl}}}{L} = 0 \tag{2b}$$

where m_i, ξ_i, $\hat{\omega}_i$, and F_i are respectively the modal mass, the modal damping coefficient, the natural frequency in open circuit condition (i.e., $Q = 0$), and the forcing. θ_i is the piezoelectric coupling coefficient and $C_{\mathrm{p}i}$ is the effective capacitance of the piezoelectric patch [12]. Considering the schematic in Fig. 1, the shunt circuit includes an inductance L in series with a resistor R and a voltage source $V_{\mathrm{nl}}(t)$. The electric natural frequency and damping factor are then:

$$\omega_e = \frac{1}{\sqrt{LC_{\mathrm{p}i}}}, \quad \xi_e = \frac{R}{2}\sqrt{\frac{C_{\mathrm{p}i}}{L}}. \tag{3}$$

In this study, the nonlinear voltage component $V_{\mathrm{nl}}(t)$ is composed of two terms, respectively proportional to the square and the cube of the PE voltage $V(t)$, given by:

$$V_{\mathrm{nl}} = \beta_q V^2 + \beta_c V^3, \tag{4}$$

where β_q and β_c are two tuning constants, of units V^{-1} and V^{-2}, respectively. The piezoelectric law [8, 16] relates the PE patch voltage $V(t)$ to $q_i(t)$ and $Q(t)$ as:

$$V = \frac{1}{C_{pi}}(Q + \theta_i q_i). \tag{5}$$

Another important quantity, that characterize the energy transfer from a mode i to the shunt circuit, is the dimensionless electromechanical modal coupling factor (EMMCF) of the i-th mode, defined as [37, 8, 16]:

$$k_i^2 = \frac{\hat{\omega}_i^2 - \breve{\omega}_i^2}{\hat{\omega}_i^2} = \frac{\theta_i^2}{\hat{\omega}_i^2 C_{\mathrm{p}i} m_i}, \tag{6}$$

with $\breve{\omega}_i$ the natural frequency in short circuit conditions (i.e $V = 0$).

The dynamical system (2) is then expanded on the electromechanical basis to diagonalize its linear part as follows [16]:

$$\begin{pmatrix} q_i(t) \\ Q(t) \end{pmatrix} = \begin{pmatrix} [-\varepsilon x_1(t) + x_2(t)]/\sqrt{m} \\ [x_1(t) + \varepsilon x_2(t)]/\sqrt{L} \end{pmatrix}, \tag{7}$$

where (x_1, x_2) are the two electromechanical modal coordinates and

$$\varepsilon = \frac{2k_i r_i}{1 - r_i^2 + \sqrt{\Delta}}, \tag{8}$$

with

$$r_i = \omega_e/\hat{\omega}_i \quad \text{and} \quad \Delta = (1 - r_i^2)^2 + 4k_i^2 r_i^2. \tag{9}$$

In the sequel, the ratio between the electrical resonance frequency and the open circuit frequency r_i is chosen close to 0.5 to activate the 2:1 internal resonance. Moreover, because k_i is often small, it is also the case for ε, meaning that $x_1(t) \simeq Q(t)$ and $x_2(t) \simeq q_i(t)$: the two electromechanical modal coordinates are close to a mainly electrical mode for $x_1(t)$ and a mainly mechanical mode for $x_2(t)$.

Using the change of variables (7) in the governing equations (2a,b) as well as the following time scaling:

$$\bar{t} = \hat{\omega}_i t, \quad \bar{\Omega} = \Omega/\hat{\omega}_i, \tag{10}$$

and by droping the overbars in the result, one obtains:

$$\begin{aligned} &\ddot{x}_1 + 2\mu_1\dot{x}_1 + \omega_1^2 x_1 + g_{11}^1 x_1^2 + g_{12}^1 x_1 x_2 + g_{22}^1 x_2^2 \\ &\qquad + h_{111}^1 x_1^3 + h_{112}^1 x_1^2 x_2 + h_{122}^1 x_1 x_2^2 + h_{222}^1 x_2^3 = f_1 \cos\Omega t, \quad \text{(11a)} \\ &\ddot{x}_2 + 2\mu_2\dot{x}_2 + \omega_2^2 x_2 + g_{11}^2 x_1^2 + g_{12}^2 x_1 x_2 + g_{22}^2 x_2^2 \\ &\qquad + h_{111}^2 x_1^3 + h_{112}^2 x_1^2 x_2 + h_{122}^2 x_1 x_2^2 + h_{222}^2 x_2^3 = f_2 \cos\Omega t. \quad \text{(11b)} \end{aligned}$$

For this new system, the new modal frequencies ω_k and the damping terms μ_k are related to the original ones by:

$$\mu_1 = \xi_e r_i - \xi_i \varepsilon^2, \quad \mu_2 = \xi_i + \xi_e r_i \varepsilon^2, \tag{12a}$$

$$\omega_1^2 = \frac{1 + r_i^2 - \sqrt{\Delta}}{2}, \quad \omega_2^2 = \frac{1 + r_i^2 + \sqrt{\Delta}}{2}, \tag{12b}$$

and the forcing terms become

$$f_2 = \frac{F_i}{\hat{\omega}_i^2 \sqrt{m_i}}, \quad f_1 = -\varepsilon f_2. \tag{13}$$

Notice that ω_1 and ω_2 are scaled thanks to Eq. (10), such that, if $r_i = 0.5$, $\omega_1 \simeq 0.5$ and $\omega_2 \simeq 1$. The system (2) thus admits a mechanical resonance frequency $\tilde{\omega}_i = \omega_2 \hat{\omega}_i$ slightly higher than the open circuit frequency $\hat{\omega}_i$ due to the coupling with the shunt circuit [16, 17].

The quadratic nonlinear coefficients g_{ij}^p(for i, j, and $p = 1, 2$) are expressed as:

$$\begin{aligned}
g_{11}^1 &= \lambda_1 - \lambda_2\varepsilon + \lambda_3\varepsilon^2 & g_{11}^2 &= \varepsilon g_{11}^1 \\
g_{12}^1 &= 2\lambda_1\varepsilon + \lambda_2(1-\varepsilon^2) - 2\lambda_3\varepsilon & g_{12}^2 &= \varepsilon g_{12}^1 \\
g_{22}^1 &= \lambda_1\varepsilon^2 + \lambda_2\varepsilon + \lambda_3 & g_{22}^2 &= \varepsilon g_{22}^1
\end{aligned} \tag{14}$$

where the coefficients λ_k are:

$$(\lambda_1, \lambda_2, \lambda_3) = (r_i^3, 2r_i^2 k_i, r_i k_i^2)\lambda_0, \quad \lambda_0 = \frac{\beta_q \hat{\omega}_i}{\sqrt{C_{\mathrm{p}i}}}. \tag{15}$$

Finally, the cubic coefficients h_{ijk}^p (for i, j, k, and $p = 1, 2$) are given by:

$$\begin{aligned}
h_{111}^1 &= \gamma_1 - \gamma_2\varepsilon + \gamma_3\varepsilon^2 - \gamma_4\varepsilon^3 & h_{111}^2 &= \varepsilon h_{111}^1 \\
h_{112}^1 &= \gamma_2 + (3\gamma_1 - 2\gamma_3)\varepsilon + (\gamma_4 - 2\gamma_2)\varepsilon^2 + \gamma_3\varepsilon^3 & h_{112}^2 &= \varepsilon h_{112}^1 \\
h_{122}^1 &= \gamma_3 + (2\gamma_2 - \gamma_4)\varepsilon + (3\gamma_1 - 2\gamma_3)\varepsilon^2 - \gamma_2\varepsilon^3 & h_{122}^1 &= \varepsilon h_{122}^1 \\
h_{222}^1 &= \gamma_4 + \gamma_3\varepsilon + \gamma_2\varepsilon^2 + \gamma_1\varepsilon^3 & h_{222}^2 &= \varepsilon h_{222}^1
\end{aligned} \tag{16}$$

where the coefficients γ_k are:

$$(\gamma_1, \gamma_2, \gamma_3, \gamma_4) = (r_i^4, 3k_i r_i^3, 3k_i^2 r_i^2, k_i^3 r_i)\gamma_0, \quad \gamma_0 = \frac{\beta_c \hat{\omega}_i^2}{C_{\mathrm{p}i}}. \tag{17}$$

2.2. The case of purely quadratic nonlinearities

First, system (11) is studied considering only the quadratic nonlinearities, to recall the main results exposed in [16, 17, 36]. The six quadratic nonlinear terms can be gathered into two families since they don't have the same effect on the dynamics. The two terms of coefficients g_{12}^1 and g_{11}^2 are called resonant terms since, because $\omega_2 \simeq 2\omega_1$, they drive the two oscillators close to their resonance. They are responsible for the skeleton of the nonlinear dynamics since they condition the energy transfers and the appearance of the bifurcations. The four other terms (of coefficients g_{11}^1, g_{22}^1, g_{12}^2, and g_{22}^2) are non-resonant: they drive the oscillators far from their resonances and have, for this reason, a second-order effect in most classical systems (see Appendix A for more details). However, because the value of some of the coefficients can be large in our present application, it was shown that they introduce a non-negligible softening behavior in the system that breaks the symmetry of its frequency response, degrading the saturation property and thus reducing the absorber's efficiency. We briefly recall in the remaining of this section the main characteristics of the dynamics of system (11) with quadratic terms only before explaining in the next section how cubic terms can correct it.

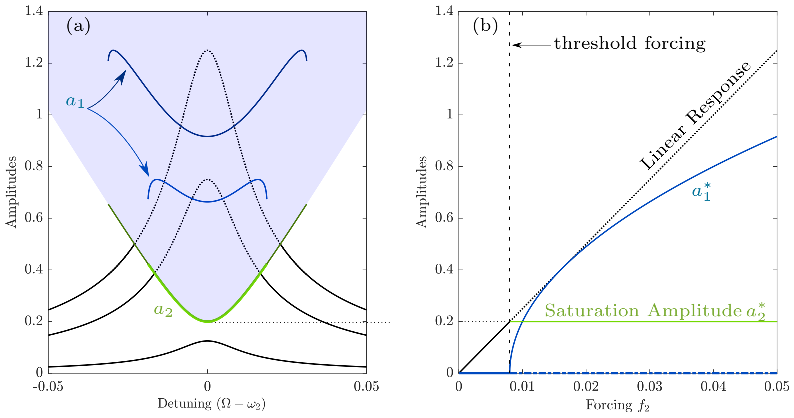

Figure 2: Typical response of the amplitudes a_1 and a_2, stemming from the first order multiple scale solution of system (11a, b), for $\omega_2 = 2\omega_1$ and by neglecting the non-resonant terms. The numerical values are $g^1_{12} = g^2_{11} = 0.1$, $\mu_1 = 0.005$, $\mu_2 = 0.01$. (a) amplitude response with respect to the detuning σ_1 for values of the forcing f_2 ($f_2 \in \{0.005; 0.03; 0.05\}$). (b) amplitude response at the resonance frequency ($\sigma_1 = 0$) with respect to the excitation level f_2. In the plots, the linear responses of a_2 are plotted in black. The solid and dotted lines denote, respectively, the stable and the unstable solutions.

Excluding the *non-resonant* quadratic terms, that is keeping only g^1_{12} and g^2_{11} in Eqs. (11), the system is reduced to its canonical form to study the 2:1 internal resonance and its dynamical effects. Using the multiple scale method (MSM), the first order solution for the tuning $\omega_2 \approx 2\omega_1$ can be expressed as [38]:

$$x_1(t) = a_1 \cos\left(\frac{\Omega}{2}t - \frac{\gamma_1+\gamma_2}{2}\right), \quad x_2(t) = a_2 \cos\left(\Omega t - \gamma_2\right), \tag{18}$$

where (a_1, a_2) are the amplitudes of the electromechanical variables and (γ_1, γ_2) are phase differences. Their closed form are given in [16].

Figure 2(a) shows a_1 and a_2 as functions of the frequency of excitation (precisely the detuning parameter $\sigma_1 = \Omega - \omega_2$), for different values of f_2 and with $f_1 = 0$ ($f_1 \neq 0$ and large would account for an independent electrical excitation, which is out of the scope of the paper). The main feature is that when the amplitude of x_2 reaches the instability region outlined in light blue, it remains on its border regardless of the excitation level, as the energy is transferred to x_1 at the subharmonic $\Omega/2$. This energy exchange leads to a minimum of a_2 for $\Omega = \omega_2$, called "antiresonance" for simplicity from now on. Plotting $a_2^* = a_2(\Omega = \omega_2)$, the amplitude of x_2 at the antiresonance, against the forcing level reveals the so-called saturation of the amplitude a_2 (Fig.2(b)).

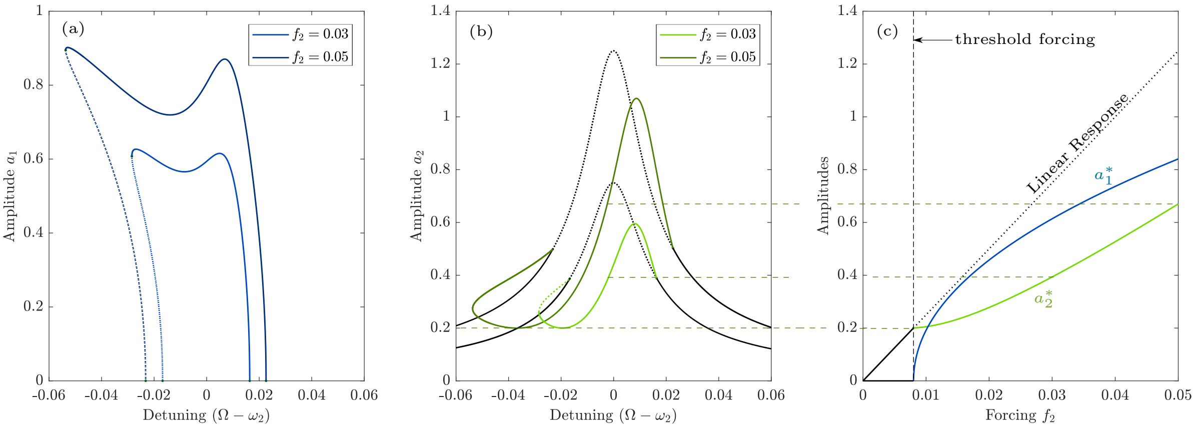

Figure 3: Numerical response of the amplitudes a_1 and a_2 obtained by solving (11a, b) using MANLAB, for $\omega_2 = 2\omega_1$. The numerical values are $g_{11}^1 = 0.25$, $g_{12}^1 = g_{11}^2 = 0.1$, $g_{22}^1 = g_{12}^2 = g_{22}^2 = 0.005$, $\mu_1 = 0.005$, and $\mu_2 = 0.01$. (a) and (b) show respectively the amplitude response of a_1 and a_2 with respect to the detuning σ_1 for two forcing levels. (c) amplitude response at the resonance frequency ($\sigma_1 = 0$) with respect to the excitation level f_2. In the plots, the linear responses of a_2 are plotted in black. The solid and dotted lines denote, respectively, the stable and the unstable solutions.

If all quadratic terms are considered in Eq. (11a, b), a second order MSM would be required to calculate closed-form expressions for the amplitude and the phase, as shown in [36]. In this study, we rely on numerical solutions using MANLAB [39, 40]. In Fig. 3, the frequency response of both electromechanical variables are depicted independently for comparison with Fig. 2(a,b). First, because of the non-resonant terms, the curves lose their symmetry with respect to the origin, bending downward as the amplitude increases in a way similar to a softening Duffing oscillator. Second, and more critically, the antiresonance shifts to the left (note that the minimum of the antiresonance is not affected) while the resonance reappears and increases. Plotting a_2^* (the value of a_2 at $\sigma = 0$) versus the excitation amplitude in Fig. 3(c) shows that the saturation property disappears. This behavior has been experimentally reproduced on a cantilever beam structure equipped with a PE patch connected to a nonlinear shunt circuit similar to the one used in section 3 without cubic nonlinearities (the one of Fig. 8 with $\beta_c = 0$) [17].

2.3. Correction of the antiresonance with cubic nonlinearities

It has been shown in [36] with the normal form theory that the non-resonant quadratic terms are equivalent to cubic terms. Therefore, we propose to additionally add a cubic nonlinear component in the nonlinear voltage presented in the shunt circuit to create cubic terms in the dynamics, tuned in order to cancel the effect of the quadratic non-resonant terms. To fully understand this process, we consider the free response (canceling damping and forcing) of system (11), including the cubic nonlinear terms (h_{ijk}^p). Using a normal form transform and applying a second order MSM, the two electromechanical variables read [36]:

$$x_1(t) \simeq R_1(t) = a_1 \cos\big(\omega_{\mathrm{nl1}} t + \phi_1\big) + O(\epsilon), \tag{19a}$$

$$x_2(t) \simeq R_2(t) = a_2 \cos\big(\omega_{\mathrm{nl2}} t + \phi_2\big) + O(\epsilon), \tag{19b}$$

where ϵ is a small parameter, (R_1, R_2) are so-called normal coordinates and $(a_1, a_2, \phi_1, \phi_2)$ are the amplitude and phase of the free solution. The nonlinear frequencies ω_{nl1} and ω_{nl2} are functions of the amplitudes as follows:

$$\omega_{\mathrm{nl1}} = \omega_1 + \Gamma_1\, p\, a_2 + \Gamma_2 a_1^2 + \Gamma_3 a_2^2, \tag{20a}$$

$$\omega_{\mathrm{nl2}} = \omega_2 + \Gamma_4\, p\, \frac{a_1^2}{a_2} + \Gamma_5 a_1^2 + \Gamma_6 a_2^2, \tag{20b}$$

where the coefficients Γ_k are expressed as:

$$\Gamma_1 = p\,\frac{g^1_{12}(4\omega_1 - \omega_2)}{8\omega_1^2}, \tag{21a}$$

$$\Gamma_2 = \frac{1}{8\omega_1}\left[\zeta_1 - \left(\frac{2}{\omega_2^2} + \frac{1}{4\omega_1\omega_2}\right) g^1_{12} g^2_{11}\right], \tag{21b}$$

$$\Gamma_3 = \frac{1}{8\omega_1}\left[\zeta_2 + \left(\frac{1}{4\omega_1^2} + \frac{1}{\omega_2(2\omega_1 + \omega_2)}\right)\left(g^1_{12}\right)^2\right], \tag{21c}$$

$$\Gamma_4 = p\,\frac{g^2_{11}(3\omega_2 - 2\omega_1)}{8\omega_2^2}, \tag{21d}$$

$$\Gamma_5 = \frac{1}{8\omega_2}\left[\zeta_3 + \left(\frac{2}{\omega_2(2\omega_1 + \omega_2)} - \frac{1}{2\omega_1\omega_2}\right) g^1_{12} g^2_{11}\right], \tag{21e}$$

$$\Gamma_6 = \frac{\zeta_4}{8\omega_2}, \tag{21f}$$

in which the parameter $p = \pm 1$ defines two sets of solutions, respectively denoted p^+ and p^- modes. The coefficients ζ_k depend only on the cubic and the non-resonant quadratic terms, as follows:

$$\zeta_1 = 3h^1_{111} - \frac{10}{3\omega_1^2}\left(g^1_{11}\right)^2, \tag{22a}$$

$$\zeta_2 = 2h^1_{122} - \left(\frac{16\omega_2^2 - 4\omega_1^2}{\omega_1^2(4\omega_2^2 - \omega_1^2)}\right) g^1_{11} g^1_{22} - \frac{2g^1_{12} g^2_{22}}{\omega_2^2} - \frac{4g^1_{22} g^2_{12}}{4\omega_2^2 - \omega_1^2}, \tag{22b}$$

$$\zeta_3 = 2h^2_{112} - \left(\frac{2}{4\omega_2^2 - \omega_1^2}\right)\left(g^2_{12}\right)^2 - \frac{4g^2_{11} g^2_{22}}{3\omega_2^2} - \frac{2g^1_{11} g^2_{12}}{\omega_1^2}, \tag{22c}$$

$$\zeta_4 = 3h^2_{222} - \left(\frac{8\omega_2^2 - 3\omega_1^2}{\omega_1^2(4\omega_2^2 - \omega_1^2)}\right) g^1_{22} g^2_{12} - \frac{10\left(g^2_{22}\right)^2}{3\omega_2^2}. \tag{22d}$$

For details about the above results, the reader is routed to [36].

The curves $(\omega_{nl1}, \omega_{nl2}) = f(a_1, a_2)$ defines the backbone curves of the system. They are plotted in Fig. 4 for different sets of parameters, and one can observe that they are very close to the resonance points of the forced responses and that their overall bending as a function of the amplitudes (a_1, a_2) controls the one of the frequency response and especially its symmetry. Eqs. (20) shows that the bending of the backbone curves is controlled by the value of the coefficients Γ_k, that depends first on the resonant quadratic coefficients (g^1_{12}, g^2_{11}), but also on the non-resonant quadratic terms and the cubic terms h^l_{ijk}. This

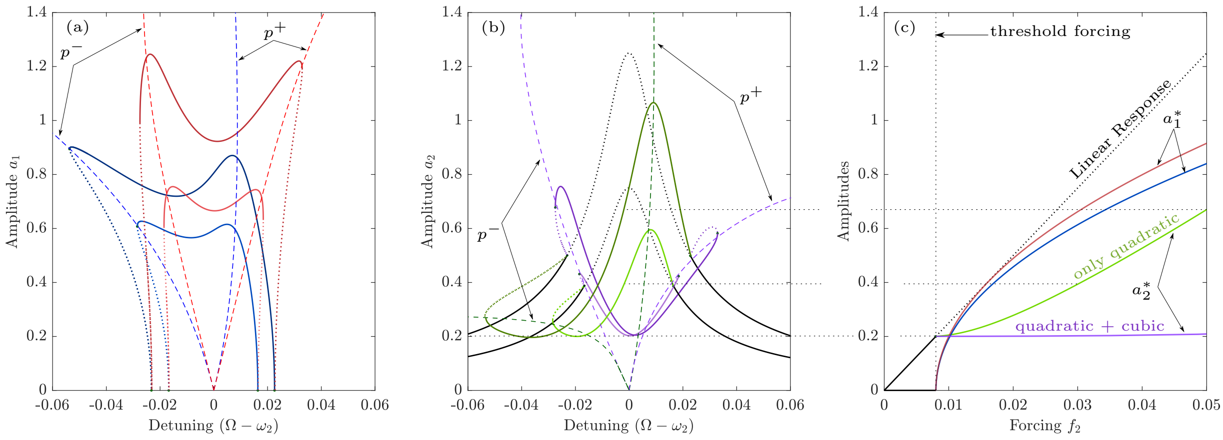

Figure 4: (a) and (b) show respectively the comparison between the responses of a_1 and a_2 by considering only the quadratic terms (in green for a_2 and in blue for a_1) and by additionally considering the cubic terms as illustrated in (23a, d) (in purple for a_2 and in red for a_1). The plots are done for $f_2 = 0.03$ (the light colors) and $f_2 = 0.05$ (the darker colors) with $\omega_2 = 2\omega_1$. The numerical values are $g^1_{11} = 0.25$, $g^1_{12} = g^2_{11} = 0.1$, $g^1_{22} = g^2_{12} = g^2_{22} = 0.005$, $\mu_1 = 0.005$, and $\mu_2 = 0.01$. The solid and dotted lines denote the stable and unstable forced solutions, respectively, and the dashed lines denote the free solution. (c) shows the amplitude response at the resonance frequency ($\sigma_1 = 0$) with respect to the excitation level f_2. In the plots, the linear responses of a_2 are plotted in black.

dependence on the two latter terms is gathered into coefficients ζ_k of Eqs. (22). Consequently, *we propose to tune the values of the cubic coefficients* h^k_{ijl} *to nullify coefficients* ζ_k*, in order to cancel the effect of the non-resonant quadratic terms.* It leads to the following values for the cubic coefficients:

$$h^1_{111} = \frac{10}{9\omega_1^2}\left(g^1_{11}\right)^2 \tag{23a}$$

$$h^1_{122} = \left(\frac{8\omega_2^2 - 2\omega_1^2}{\omega_1^2(\omega_1^2 - 4\omega_2^2)}\right) g^1_{11} g^1_{22} - \frac{g^1_{12} g^2_{22}}{\omega_2^2} + \frac{2g^1_{22} g^2_{12}}{\omega_1^2 - 4\omega_2^2}, \tag{23b}$$

$$h^2_{112} = \left(\frac{1}{\omega_1^2 - 4\omega_2^2}\right)\left(g^2_{12}\right)^2 - \frac{2g^2_{11} g^2_{22}}{3\omega_2^2} - \frac{g^1_{11} g^2_{12}}{\omega_1^2}, \tag{23c}$$

$$h^2_{222} = \left(\frac{8\omega_2^2 - 3\omega_1^2}{3\omega_1^2(\omega_1^2 - 4\omega_2^2)}\right) g^1_{22} g^2_{12} - \frac{10\left(g^2_{22}\right)^2}{9\omega_2^2} \tag{23d}$$

190 Notice that only four of the cubic terms are concerned with the previous process.

It is logical since they are resonant and all the other cubic terms are non-resonant and have thus no influence at this (cubic) order of the nonlinearities of the system. Their effect would appear at least in a fourth-order normal form, out of the scope of the present study.

For comparison, the forced response with and without the compensation based on Eqs. (23a-d) are depicted in Fig. 4 for different excitation levels. The two backbone curves corresponding to the p^+ and p^- modes are also represented. As expected, the compensation proposed permits to restore ,to a fair extent, the desirable properties visible in Fig. 2. First, the symmetry is recovered at least for low to medium forcing (cf. Fig. 4(a)). Second, the antiresonance is mostly decoupled from the excitation level, that is, its frequency is almost fixed, as visible in Fig. 4(b), and the nearby resonant peaks and pseudo periodic regimes vanish. Finally, this clearly restores the saturation of the amplitude a_2^* as illustrated in Fig. 4(c).

Apart from the present saturation correction, it is interesting to investigate if the bending effect of the quadratic non-resonant terms on the frequency response of the system is hardening or softening. First, considering the leading term in the expressions of the g_{ij}^k as a function of $\varepsilon \ll 1$ shows that all g_{ij}^k are positive. Moreover, the expressions of the Γ_k coefficients (21) shows that the quadratic non-resonant terms appear only within coefficients ζ_k, given by Eqs. (22). Those equations show that because $\omega_2 \simeq 2\omega_1$, the contribution in the ζ_k of the quadratic non-resonant terms is always *negative*. Considering the backbone curve equations (20), it proves that the effect of the quadratic non-resonant terms is *always softening*.

2.4. Application to our piezoelectric shunt

The previous section showed how to tune four of the cubic nonlinear terms in (11) to cancel the softening effect of the quadratic non-resonant terms. However, in the practical implementation of our shunt circuit, the cubic term are created with the term $\beta_c V^3$ in the voltage source $V_{\mathrm{nl}}(t)$ (see Eqs. (4), (16), (17)). Consequently, there is only one parameter to be tuned, the coefficient β_c. We must then adapt the strategy of the previous section considering this constraint.

To do so, we consider the magnitude of the four non-resonant quadratic terms g^1_{11}, g^1_{22}, g^2_{12}, g^2_{22} given by Eqs. (14). Since $\varepsilon \ll 1$ (the piezoelectric coupling factor k_i is small), and keeping the leading order in ε, we can assume that $g^1_{11} \simeq \lambda_1 = r_i^3\lambda_0$, $g^1_{22} \simeq \lambda_3 = r_i k_i^2 \lambda_0$, $g^2_{12} \simeq \varepsilon\lambda_2 = 2r_i^2 k_i \varepsilon\lambda_0$, $g^2_{22} \simeq \varepsilon\lambda_3 = \varepsilon r_i k_i^2 \lambda_0$, meaning that g^1_{11} is the largest, almost one order of magnitude larger than the three others. This is confirmed by a numerical example: if we choose $r_i = 0.5$, $k_i = 0.15$, this leads to $\varepsilon = 0.1$, $g^1_{11} = 0.125\lambda_0$, $g^1_{22} = 0.0112\lambda_0$, $g^2_{12} = 0.0075\lambda_0$ and $g^2_{22} = 0.001125\lambda_0$. Consequently, our strategy is *to tune* β_c *to cancel the effect of* g^1_{11} *only, such that* $\zeta_1 = 0$.

Thus, β_c is deduced by substituting Eq. (16) and (14) into Eq. (23a) to get:

$$\beta_c = \frac{10}{9}\frac{r_i}{\omega_1^2}(r_i - \varepsilon k_i)\beta_q^2 = \frac{10}{9}\beta_q^2, \tag{24}$$

since one has $r_i(r_i - \varepsilon k_i)/\omega_1^2 = 1$ for any value of r_i by substituting the expressions of ω_1^2 from Eq. (12b) and ε from Eq. (8). Notice that Eq. (24) respects the units of β_q and β_c, which are respectively V^{-1} and V^{-2}.

Two important remarks follow from Eq. (24):

- The required value of β_c is independent of the electromechanical modal parameters of the structure. It is set based on the value of β_q only, which is a free parameter set thanks to the shunt circuit.

- Contrary to β_q, β_c always admits a positive value. Note that changing the sign of β_q does not affect the amplitude response, but modifies the phase [16].

To validate the proposed technique, we solve numerically the physical system in (2) using the modal parameters of the first bending mode of the experimental foil that will be tested in section 3, gathered in Table. 1, and by enforcing β_c to satisfy Eq. (24) with $r_1 = \omega_e/\hat{\omega}_1 = 0.5051$ to ensure the 2:1 resonance condition $\omega_2 = 2\omega_1$. The frequency response of the first harmonic amplitude of the displacement u_{H1} is shown in Fig. 5 for several excitation levels, and two cases are illustrated. The first case considers only the quadratic voltage source

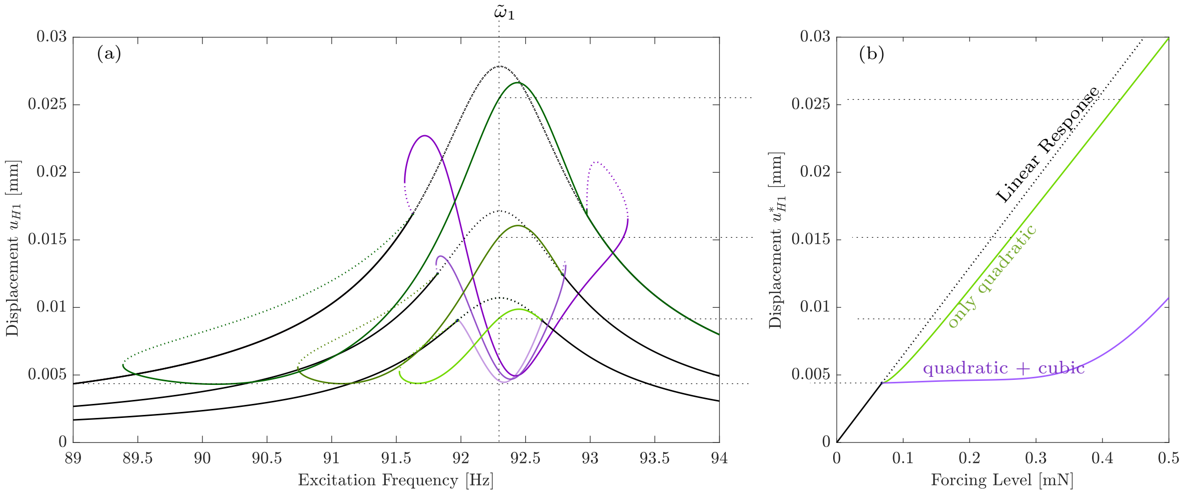

Figure 5: (a) Numerical frequency response of the first harmonic of the displacement u_{H1}, obtained by numerical continuation of (2a, b) using MANLAB, considering only quadratic nonlinear term (in green) and by considering additionally a cubic term (in purple) such that β_c verifies Eq. (24). The excitation level $F \in [0.42, 0.26, 0.16]$ mN with darker color as F increases. The numerical values are $\beta_q = 0.03$ V^{-1}, $\beta_c = 0.001$ V^{-2} , $\xi_e = 0.002$, and $r_1 = 0.5055$. The modal parameters used are the ones gathered in Table 1. (b) Amplitude of u_{H1} at the resonance frequency ($\Omega = \tilde{\omega}_1$), denoted by u^*_{H1}, with respect to the excitation level. In the plots, the solid and dotted lines denote the stable and unstable solutions, respectively. The linear responses (i.e., $\beta_q = \beta_c = 0$) are plotted in black.

(i.e., $V_{\mathrm{nl}} = \beta_q V^2$) while the other case considers additionally a cubic voltage source (i.e., $V_{\mathrm{nl}} = \beta_q V^2 + \beta_c V^3$), such that β_c verifies Eq. (24).

Comparing Fig. 5 with Fig. 4, the following remarks about the efficiency of our control strategy can be formulated:

- even if only ζ_1 is used for the compensation, the cubic term $\beta_c V^3$ in the shunt voltage clearly counterbalances the shift of the antiresonance toward the low-frequencies and pins it near the mechanical resonance frequency $\tilde{\omega}_1$ (Fig. 5(a)). As a consequence, the saturation of the amplitude at $\Omega = \tilde{\omega}_1$ is recovered for an interesting range of forcing below 0.3 N (Fig. 5(a)). There are also no quasi-periodic parts in the frequency response curves, as would be the case with a tuning using r_i instead of β_c, as proposed in [17].

- above 0.3 N, the amplitude saturation disappears, and our compensation with $\beta_c V^3$ ceases to be efficient. This is probably because of the three resonant cubic terms h^1_{122}, h^2_{112} and h^2_{222}, created by the non-resonant quadratic terms, whose effects in the response are not compensated by β_c.
- it should also be noted a slight shift of the antiresonance to the right as well as a slight increase of its amplitude as a function of the forcing in Fig. 5(a). This creates a very slight positive slope in the saturation plateau below 0.3 N in Fig. 5(b), of negligible importance at first sight. This is probably due to the presence of the non-resonant cubic terms, since the coefficients h^1_{112}, h^1_{222}, h^2_{122} and h^2_{111} are non-zero because the voltage term $\beta_c V^3$ (see Eqs. (16)). In comparison, if $\beta_c = 0$, those terms are strictly null, leading to a shift in the antiresonance frequency, but with constant amplitude (see the green curves in Fig. 5(a))

2.5. Tuning the saturation region

The free parameters of our absorber are the nonlinear voltage coefficients (β_q, β_c) and the electrical damping ξ_e. The electrical frequency ω_e (or equivalently the ratio $r_i = \omega_e/\hat{\omega}_i$) is fixed by the shunt tuning in 1:2 internal resonance, such that $\omega_2 = 2\omega_1$, using Eq. (12b). In this section, we study the effect of ξ_e and β_q, while β_c verifies Eq. (24). The effect of β_c on the response is addressed in section 4.

The effect of ξ_e and β_q on the saturation region are depicted respectively in Fig. 6(a) and Fig. 6(b) where u^*_{H1}, the first harmonic amplitude measured at the resonance frequency, is represented as a function of the forcing level for different values of ξ_e and β_q. It is observed that they have an adverse effect on the range where the amplitude saturation is effective. Moreover, as mentioned earlier, the amplitude at $\sigma = 0$ is directly linked to the ratio $\xi_e/k_i\beta_q$, that is: widening

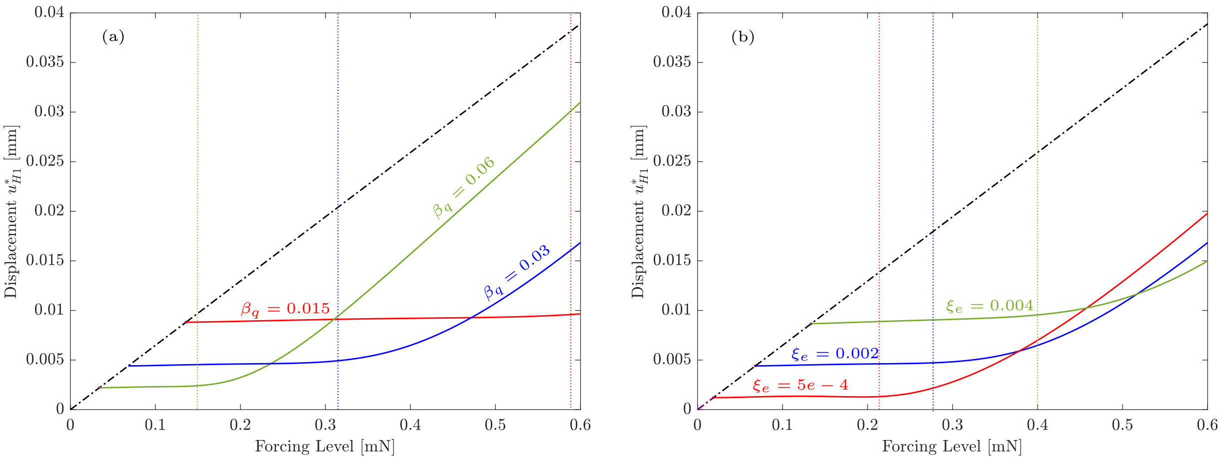

Figure 6: Displacement at the resonance frequency u^*_{H1} as function of the excitation level by considering the cubic component with β_c verifies Eq. (24) and $r_1 = 0.5055$. (a) for different values of β_q and (b) for different values of ξ_e. The modal parameters used are gathered in Table. 1. The dotted lines denote the maximum excitation level where the saturation is valid. The black dashed-dotted line denotes the linear response.

the saturation range also reduces the attenuation at resonance. Therefore, in the experimental proof of concept shown in the next section, we will choose $\xi_e = 0.002$ and $\beta_q = 0.03$ (corresponding to the blue curves in Fig. 6) as a trade-off between having a lower antiresonance on the one hand and a wider saturation region on the other hand.

3. Experimental proof of concept

3.1. Experimental Setup

Parameters	$\tilde{\omega}_1/(2\pi)$ [Hz]	$\hat{\omega}_1/(2\pi)$ [Hz]	$\xi_1(\%)$	k_1	θ_1[mN/V]	$m_1[g]$	α [N/A]	C_{p1} [nF]
Value	91.5	92.1	0.54	0.11	0.78	4.1	0.6	38

Table 1: Electro-mechanical modal parameters of the first bending mode of the foil (subscript $i = 1$) with relation to PE patch 2.

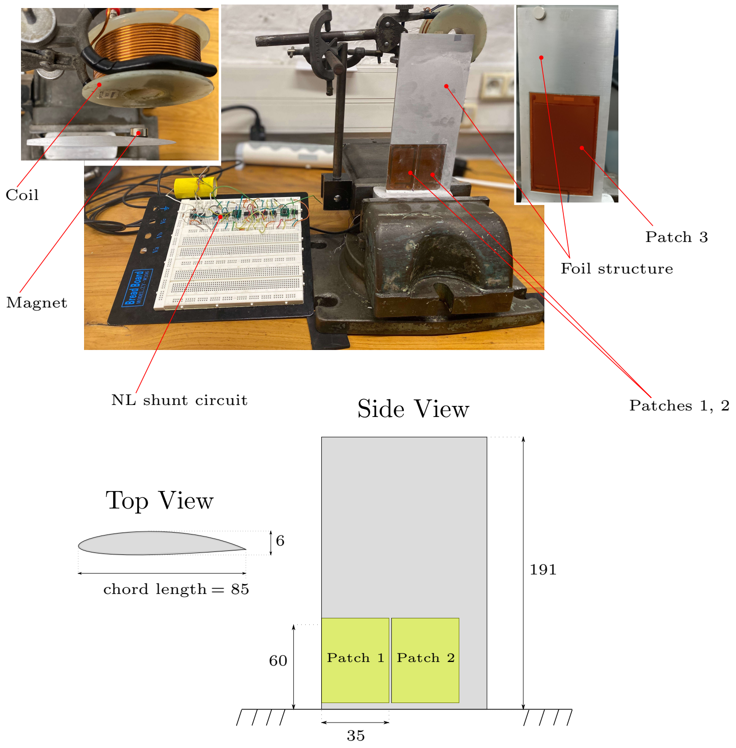

Figure 7: Experimental Setup. Dimensions are in mm. The thickness of the PE patches is 1mm.

The experimental tests were conducted on a clamped-free foil structure fixed at its base in a vice, as shown in Fig. 7. This structure is similar to the one used in [41]. Three PE patches are glued on cavities machined on the surfaces of the foil: on one face (denoted patches 1, 2), two P-876.A15 DuraAct polymer coated multi-layer piezoelectric patches are used for transduction with the first bending mode, whereas a macro-fiber composite M8557-F1 with 45° fiber orientation is used on the other face (denoted patch 3) for a coupling with the first torsion mode. In all the tests of this article, only patch 2 is used since we focus on the first bending mode. Consequently, patch 2 is connected to the shunt circuit, and patch 1 and 3 are short-circuited. The three PE patches are from the PI Ceramic manufacturer.

The mechanical excitation is realized by a coil interacting with a magnet fixed on the foil. The applied force is proportional to the current in the coil i.e $F(t) = \alpha I(t)$, where $\alpha = 0.6\ \mathrm{N \cdot A^{-1}}$ [17], with very low distortion [42]. A Brüel & Kjær 2719 power amplifier, connected to the coil, is used for all mechanical excitations. The foil vibrations are measured with a Polytec OFV-505 vibrometer, that provides the velocity of a point colocalized with the magnet location, close to the tip of the foil. Electrical measurements are performed using a PHILIPS PM 9355 precision current probe in the piezoelectric circuit to obtain the charge $Q(t)$ and a *Française d'Instrumentation* ST 500-5 differential voltage probe to measure the PE patch voltage $V(t)$.

A first set of experiments is performed to obtain the modal characteristics of the first bending mode of the foil, which are gathered in Table. 1. All details of this set of measurements are provided in Appendix B.

3.2. Nonlinear shunt circuit description

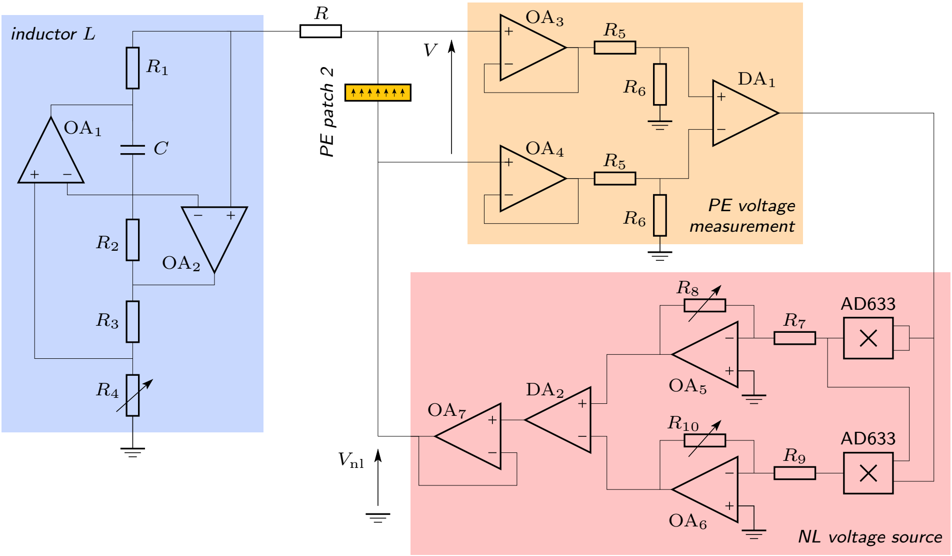

Figure 8: Nonlinear shunt circuit design.

Component	R_1 [kΩ]	R_2 [kΩ]	R_3 [kΩ]	C [μF]	R_5 [kΩ]	R_6 [kΩ]	R_7 [kΩ]	R_9 [kΩ]
Value	2	1	1	10	82	22	10	10

Table 2: Component values in the nonlinear shunt circuit of Fig. 8

The nonlinear shunt circuit used for the tests is shown in Fig. 8. It consists of three interconnected sub-circuits to realize (i) a tunable synthetic inductor (outlined in blue); (ii) a voltage measurement (outlined in orange), and (iii) a nonlinear voltage generator (outlined in light red). To handle the large voltage levels that can appear, especially during transients, the operational amplifiers OA_1 to OA_7 are OPA445 (Texas Instrument) which can operate up to ±40V and supply 15mA to drive the patches. The synthetic inductor is a so-called Antoniou circuit [43] to achieve the high inductance value needed to obtain an electrical resonance frequency close to half of the mechanical resonance frequency. The inductance value is given by

$$L = \frac{R_1 R_2 R_4 C}{R_3} \tag{25}$$

Here L is tuned using the variable resistance R_4.

In this study, we fix the value of the frequency ratio to $r_1 = 0.5055$ (notice the subscript $i = 1$ for the first bending mode of the foil structure under test) to verify the 2:1 internal resonance condition between the electromechanical natural frequencies $\omega_2 = 2\omega_1$. Therefore, considering the values of Table. 2, $R_4 = 15.3\,\mathrm{k}\Omega$ to obtained the required value $L = 307.5\,\mathrm{H}$. The resistor R models the parasitic resistance generated by the Antoniou circuit and a physical resistance added to tune the electrical damping. Based on the observations in [17], the parasitic resistance of the Antoniou circuit is proportional to the inductance value L set in the circuit. In the current set-up, we measured a parasitic resistance of 260Ω, estimated with a frequency-to-bandwidth ratio of the electrical resonance, close to $\Omega = \omega_e$, in linear operation, with $\beta_q = \beta_c = 0$. Then, to achieve an electrical damping ratio of $\xi_e = 0.002$, corresponding to the setting discussed in Section 2.5, a resistor of value $100\,\Omega$ is added, such that

$R = 260 + 100 = 360\,\Omega$.

The PE voltage measurement is established through two voltage dividers composed of R_5 and R_6 and two voltage followers OA_3 to OA_4 (OPA445, Texas Instrument) to ensure a large input impedance. The voltage dividers are used to attenuate the voltage to values compatible with the multipliers used afterward. Since the PE patch is not grounded, these voltages are first fed to the differential amplifier DA_1 (INA826, Texas Instrument). The quadratic and cubic nonlinearities are generated using two multipliers (AD633, Analog Device). The output voltages of the multipliers are amplified through two inverting amplifiers involving OA_5 and OA_6 and fed to the differential amplifier DA_2 (INA826, Texas Instrument) to eliminate common mode noises that were observed at the output of the multipliers. The follower OA_7 minimizes the output impedance while protecting the AD633 and the INA826 from excessive current. The nonlinear coefficients β_q and β_c are controlled respectively by the variable resistance R_8 and R_{10}, and they are given by

$$\beta_q = \frac{R_8}{10R_7}\left(\frac{R_6}{R_5+R_6}\right)^2, \qquad \beta_c = \frac{R_{10}}{100R_9}\left(\frac{R_6}{R_5+R_6}\right)^3 \tag{26}$$

To satisfy the value of β_c, realized by Eq. 24, R_{10} should be set as

$$R_{10} = \frac{10R_9}{9}\frac{R_6}{R_5+R_6}\left(\frac{R_8}{R_7}\right)^2. \tag{27}$$

3.3. Measurement protocol

To validate experimentally the energy transfer during the 2:1 internal resonance and the nonlinear shunt behavior, the amplitudes and phase angles of the fundamental harmonic (H1) of the structure tip displacement $u(t)$ and the subharmonic (H1/2) of the charge $Q(t)$ in the PE patch electrodes are considered. Since the mode shape is scaled to verify $\boldsymbol{\phi}_1(\boldsymbol{x}_m) = 1$ (see Appendix B), $u(t)$ and $Q(t)$ can be recovered by substituting Eq. (18) in Eq. (7) to have:

$$u(t) = u_{\mathrm{H1}}\cos(\Omega t - \gamma_2) + u_{\mathrm{H1/2}}\cos\left(\frac{\Omega}{2}t - \frac{\gamma_1+\gamma_2}{2}\right), \tag{28a}$$

$$Q(t) = Q_{\mathrm{H1}}\cos(\Omega t - \gamma_2) + Q_{\mathrm{H1/2}}\cos\left(\frac{\Omega}{2}t - \frac{\gamma_1+\gamma_2}{2}\right). \tag{28b}$$

In practice, $u(t)$ and $Q(t)$ can be obtained by measuring the foil tip velocity $v(t)$ with the laser vibrometer and the voltage across the PE patch terminals $V(t)$ using the differential voltage probe. The latter two signals can be expressed as:

$$v(t) = v_{\mathrm{H1}} \cos(\Omega t - \varphi_v) + \mathrm{oh}, \quad V(t) = V_{\mathrm{H1/2}} \cos(\Omega/2t - \varphi_V) + \mathrm{oh}. \tag{29}$$

with "oh" meaning "other harmonics" and $(v_{\mathrm{H1}}, \varphi_v)$, $(V_{\mathrm{H1/2}}, \varphi_V)$ denote the experimentally measured amplitude/phase pairs. To recover the amplitude u_{H1} and γ_2, we differentiate Eq. (28a) with respect to time to have:

$$u_{\mathrm{H1}} = v_{\mathrm{H1}}/\Omega, \quad \gamma_2 = \varphi_v + \pi/2, \tag{30}$$

and to estimate $Q_{H/2}$ and the relative phase angle γ_1, we substitute Eq. (28a, b) in Eq. (5) resulting in:

$$Q_{\mathrm{H1/2}} \approx V_{\mathrm{H1/2}}\, C_{\mathrm{p}i}, \quad \gamma_1 = 2\varphi_V - \varphi_v - \pi/2. \tag{31}$$

Note that the relation between $Q_{\mathrm{H1/2}}$ and $V_{\mathrm{H1/2}}$ is an approximation where the contribution of the mechanical displacement in Eq. (5) is neglected based on the previous observations related in [17]. Thus, one can use Eq. (31) to relate the subharmonic amplitudes of the charge and the voltage. Note also that the charge can be obtained by measuring the current through the current probe. However, in practice, the measured time signals with the current probe appeared to be more noisy compared to that with a differential voltage probe. In addition, it is useful to obtain the order of magnitude of the PE voltage $V(t)$ to ensure that it does not exceed the operating limits of the operational and differential amplifiers. For those reasons, we preferred to measure the PE voltage $V(t)$ instead of $Q(t)$. Thus, in the following sections, we will show the frequency response of $V_{\mathrm{H1/2}}$ instead of $Q_{\mathrm{H1/2}}$.

To establish the amplitude and phase frequency responses, a sine current with fixed intensity is fed to the coil/magnet device to generate a harmonic force $F = F_0 \cos \Omega t$. Then, the excitation frequency Ω is increased (or decreased) by steps, keeping the intensity fixed, sweeping a domain close to the resonance frequency $\tilde{\omega}_1$ of the first bending mode of the foil. For each frequency, v_{H1}, $V_{\mathrm{H1/2}}$,

φ_v, and φ_V are extracted in the steady state using the demodulation technique explained in [17]. The input/output signals were synthesized/measured with National Instrument cards (NI-9234, NI-9263) driven by a Matlab program.

3.4. Experimental validation of the theoretical results

For comparison, Fig. 9 presents experimental results and numerical simulations of system (2) with MANLAB. The experimental frequency responses of v_{H1}, $V_{H1/2}$, φ_v, and γ_1 were obtained by sweeping up and down the excitation frequency. γ_1 was not directly measured but deduced from the measured phases φ_v and φ_V using Eq. (31). To experimentally validate the effects of the additional cubic component, seen in Fig. 5, Figure 9 presents both the result considering only the quadratic nonlinearity (i.e., $V_{\mathrm{nl}} = \beta_q V^2$) as well as those with the cubic compensation, namely $V_{\mathrm{nl}} = \beta_q V^2 + \beta_c V^3$. Only the sweep-down response is plotted in the first case, while in the latter case, the sweep-up and down responses are shown.

For completeness, the linear responses with the PE patch 2 of the foil in open circuit (OC) as well as the one with patch 2 connected to the RL circuit (i.e for $\beta_q = \beta_c = 0$) are also depicted in Fig. 9. The latter response admits a resonance frequency $\tilde{\omega}_1$ slightly higher than the open frequency $\hat{\omega}_1$ due to the piezoelectric coupling, as mentioned in Section 2.1. In addition, one can observe an excellent fitting between the numerical and the experimental results of the linear response.

Regarding the nonlinear frequency response, the experimental and numerical results of the velocity, voltage amplitudes, and phase angles are overall in excellent agreement with the theory. The energy transfer from the H1 harmonic to the H1/2 harmonic, typical for the 2:1 internal resonance, is thus experimentally validated and the response behavior with the additional cubic term as seen in Fig. 5 is well reproduced. In particular, the effect of setting β_c and r_1 as discussed is demonstrated. Clearly, the resonance is replaced by the antiresonance AR2, as opposed to the $\beta_c = 0$ case, where the antiresonance is moved to AR1 (cf Fig. 5). In addition, the experimental results confirm the recovery

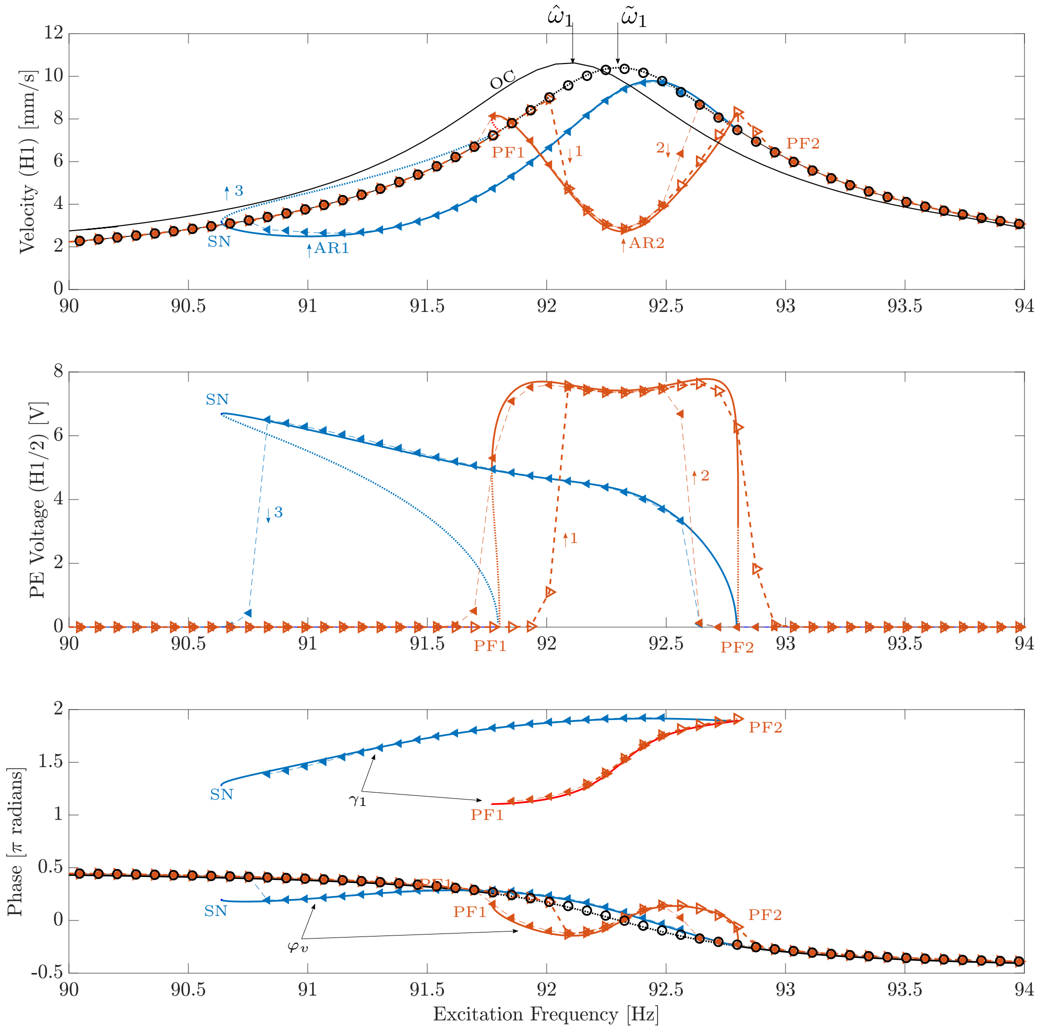

Figure 9: Experimental and numerical results comparison of the amplitudes of v_{H1} and $V_{H1/2}$ and the phase angles ϕ_v and γ_1, considering only quadratic nonlinear term (in blue) and by considering additionally a cubic term (in orange) such that β_c verifies Eq. (24). The results are estimated with $F = 0.27$mN, $\xi_e = 0.002$, $\xi_1 = 0.0052$, $\beta = 0.03$, and $r_1 = 0.5055$. The numerical data are shown in solid and dotted lines for stable and unstable solutions, respectively. The experimental data are plotted respectively with $- \triangleright -$ and $- \blacktriangleleft -$ for sweeping up and down in the excitation frequency Ω. The experimental uncoupled results are shown in $- \circ -$.

of the response symmetry with the usage of the cubic component. Concerning the antiresonance amplitude, a slight increase is detected with the usage of the cubic component, validating the numerical prediction in Fig. 5.

The bifurcation topology of the numerical solution is experimentally reproduced since near the frequencies corresponding to the pitchfork-bifurcations (PF1 and PF2), jump 1 and jump 2 are detected, and near the saddle-node bifurcation (SN), jump 3 to the linear solution is observed. Furthermore, the small discrepancy between the jumps and the numerical bifurcation point was also observed in [17]. Regarding the response of the phase angles, the experimental results suggest that the locking of γ_1 at the antiresonance frequency with a value $3\pi/2$ is not altered by the presence of the cubic component.

Figure 10 shows the time signals of the foil tip velocity $v(t)$ and the PE voltage $V(t)$ measured for the case for the two nonlinear configurations. The signals are recorded for their respective antiresonance, i.e., $\Omega/(2\pi) = 91.07\,\mathrm{Hz}$ for the quadratic case (AR1), and $\Omega/(2\pi) = 92.3\,\mathrm{Hz}$ for the quadratic and cubic case (AR2). The addition of the cubic compensation modifies the phases with respect to the excitation (all curves in Fig. 10 are synchronized with the currents, which are not represented here for clarity). However, one should note that the relative phase between the harmonics H1 and H1/2 remains equal to $3\pi/2$ for all configurations of the nonlinearity (cf. Fig. 9). One can also notice the presence of a subharmonic component in the velocity signal. This is due to the PE coupling (the term $\varepsilon x_1(t)$ in $q_i(t)$ in Eq. (7)) and this can represent a drawback since it increases the peak-to-peak amplitude of the mechanical vibration. This issue is discussed in [16] in terms of minimizing the effect of the subharmonic, by acting on β_q and ξ_e.

3.5. Effect of the excitation level and recovery of the saturation

Experimental tests have been conducted for different excitation levels, keeping the other parameters fixed, to validate the antiresonance correction. Fig.11(a) and Fig. 11(b) depict the measured frequency responses of the first harmonic amplitude of the foil tip velocity v_{H1} and the first subharmonic amplitude of

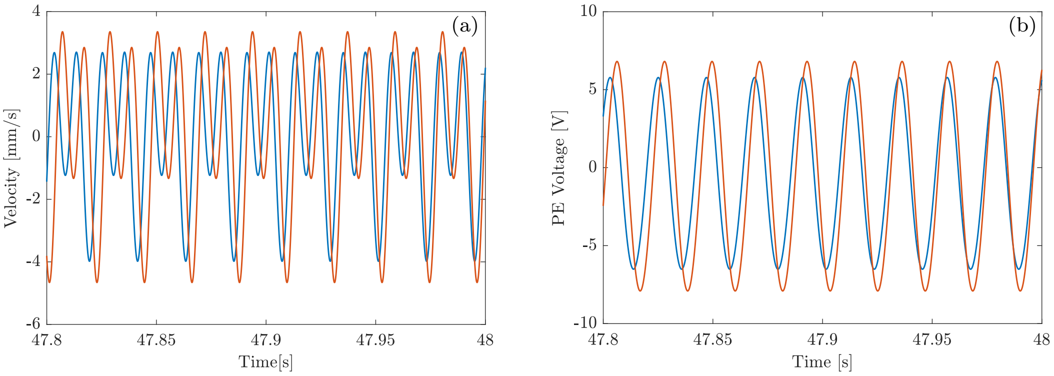

Figure 10: (a) and (b) show respectively the time signals of the foil tip velocity and the PE voltage at the antiresonance points of Fig. 9. The blue and orange lines denote respectively the measured signals at $\Omega/(2\pi) = 91.07\,\mathrm{Hz}$ (point AR1) and at $\Omega/(2\pi) = 92.3\,\mathrm{Hz}$ (point AR2) when considering only the quadratic component and when considering both the quadratic and the cubic components.

the PE voltage $V_{H1/2}$ respectively.

In the case where only the quadratic component is considered, the frequency response, estimated by sweeping down the excitation frequency, is shown. Whereas only the sweeping-up response is shown when considering the cubic component. The predicted features are confirmed by the experiment. First, the addition of the cubic term β_c pins the antiresonance to a certain extent, as opposed to the purely quadratic case where the antiresonance is obviously displaced. This observation holds up to some excitation level where the shift of the antiresonance starts toward higher frequencies. Simultaneously, one can notice the progressive increase of the response at the upper limit of the 2:1 resonance. To further confirm the interest of the additional cubic term, Fig. 5(c) gathers the amplitudes at the resonance and antiresonance for the linear and nonlinear cases, respectively. By comparing with Fig. 4(c), the experiment shows a good agreement with the theory, and supports the claim that this strategy enhances the energy transfer between the foil and the electronic circuit.

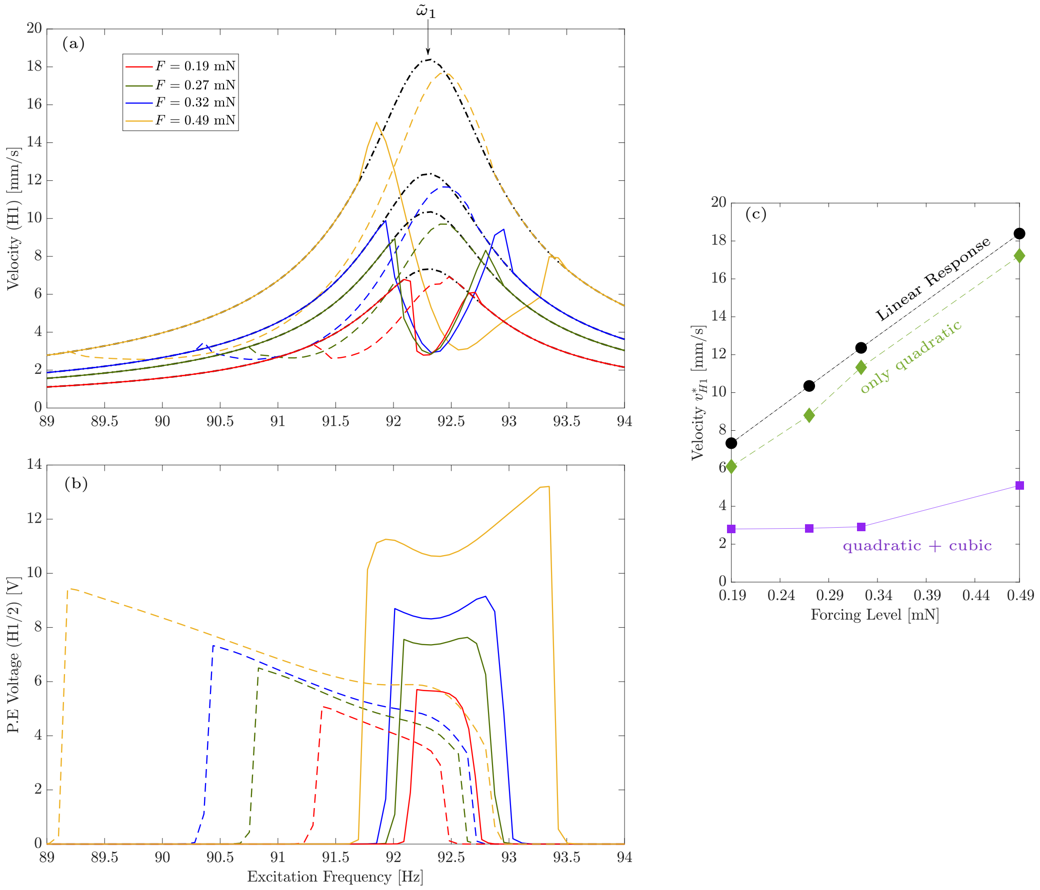

Figure 11: (a) and (b) show respectively the experimentally measured frequency responses of the amplitudes of v_{H1} and $V_{H1/2}$ for different excitation levels, considering only quadratic nonlinear term (dashed lines) and by considering additionally a cubic term (solid lines) such that β_c verifies Eq. (24). The results are estimated with $\xi_e = 0.002$, $\xi_1 = 0.0052$, $\beta_q = 0.03$, $\beta_c = 0.001$, and $r_1 = 0.5055$. The black dashed-dotted line denote the experimentally measured linear response of v_{H1} (i.e., $\beta_q = \beta_c = 0$). (c) Amplitude of v_{H1} measured at the resonance frequency, denoted by v_{H1}^*, as function of the excitation level.

4. Sensitivity to the Value of β_c

As discussed in section 2.5, the saturation region is restored by the addition of a cubic component in the shunt circuit, and its width can be enlarged by decreasing the nonlinear quadratic coefficient β_q and/or increasing the electri-

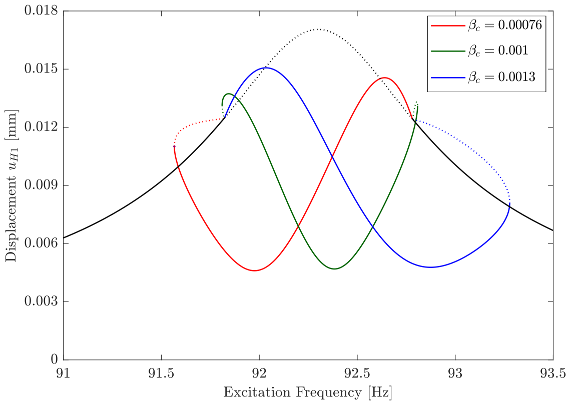

Figure 12: Numerical frequency response of the first harmonic of the displacement u_{H1}, obtained by numerical continuation of (2a, b) using MANLAB, for three different values of β_c. One of those values satisfies Eq. (24) (in green) with two other lower and higher values (respectively in red and blue). The dotted and solid lines denote the stable and unstable solutions, respectively. The results are estimated for $F = 0.26$mN, $\xi_e = 0.002$, $\beta_q = 0.03$, and $r_1 = 0.5055$. The modal parameters used are the ones gathered in Table 1. The black lines denote the linear response (with $\beta_q = \beta_c = 0$).

cal damping coefficient ξ_e. However, this benefit is counterbalanced by a lower attenuation. Nonetheless, this could be improved by considering β_c as a tuning parameter that depends on the amplitude of the forcing. The numerical simulations depicted in Fig. 12 demonstrate the idea: here, different frequency responses of the first harmonic of the displacement u_{H1} are plotted for various values of β_c resulting in different locations of the antiresonance. In this respect, β_c has a similar effect as the tuning parameter $r_1 = \omega_e/\hat{\omega}_1$ which is used to correct the antiresonance in [17], but with the interesting benefit of creating no quasi-periodic zones and keeping the overall symmetry of the frequency response.

Based on the free solution, Eq. (24) suggests that β_c is simply proportional to β_q, and it can indeed be used for low excitation levels. However, this is only true if the non-compensated quadratic components are small, and generally, β_c depends on the excitation level. Since no closed-form expressions are at hand for the forced solution, we estimate numerically β_c required to set the antiresonance at a given frequency by studying the first harmonic amplitude of the displacement measured at the resonance frequency u^*_{H1} as a function of β_c for fixed values of the excitation in terms of amplitude and frequency. Such simulations are depicted in Fig. 13(a). Based on such simulation, the required tuning of β_c estimated in Eq.(24) (i.e., $\beta_c = 0.001$) is validated for low excitation levels since it enables minimizing the amplitude. However, as the excitation increases, a correction through lowering the required value of β_c should be prescribed ($\beta_c = 0.00093$ for $F = 0.49$mN).

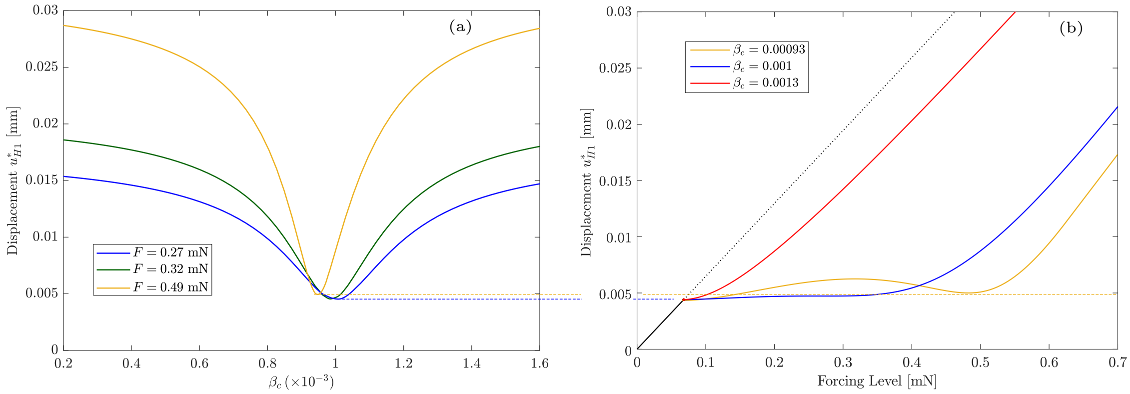

Figure 13: First harmonic amplitude of the foil tip displacement evaluated at the resonance frequency $\tilde{\omega}_1$, denoted by u^*_{H1}, as function of β_c for three different excitation levels, plotted in (a), and as function of F for three different values of β_c, plotted in (b) . The plots are obtained by numerical continuation of (2a, b), keeping β_c and F free in (a) and (b), respectively and by prescribing the excitation frequency Ω at $\tilde{\omega}_1$ in both plots. The plots are estimated for $\beta_q = 0.03$, $\xi_e = 0.002$, $r_1 = 0.5055$. The modal parameters used are the ones gathered in Table. 1. The linear response ($\beta_q = \beta_c = 0$) in (b) is shown in black, with the stable and unstable responses depicted in solid and dotted lines, respectively.

The effect of β_c on the saturation is shown in Fig. 13(b) by studying the amplitude of u^*_{H1} as a function of the forcing level, estimated at the resonance frequency. The results suggest that if β_c is set according to Eq. (24), a saturation region appears up to a certain excitation, as studied in Fig. 6(a,b). If a higher value of β_c is chosen, the saturation phenomenon is not presented. For a lower value of β_c, in particular $\beta_c = 0.00093$, the saturation phenomenon is not presented also, but the response curve shows three different phases. The first phase suggests an amplitude increasing up to a certain amplitude which can be explained by the low value of β_c that lacks to correct the antiresonance shifting. The second phase suggests an amplitude decreasing until reaching a minimum at $F = 0.49$mN, compatible with the result in Fig. 13(a). The third face suggests a further increase in the amplitude due to the high effects of the uncompensated nonresonant quadratic terms.

To validate the antiresonance correction by a suitable tuning of β_c, we performed the same experimental tests shown in Section. 3.5 but considering only the highest excitation level ($F = 0.49$mN) and by setting $\beta_c = 0.00093$, as suggested from Fig. 13a. The experimental frequency response of u^*_{H1} suggests a correction of the antiresonance in which, with the numerical predicted value of β_c , the antiresonance AR1 is replaced by AR2 at the first bending mode resonance frequency $\tilde{\omega}_1$. In Fig. 14, we give an experimental validation of the

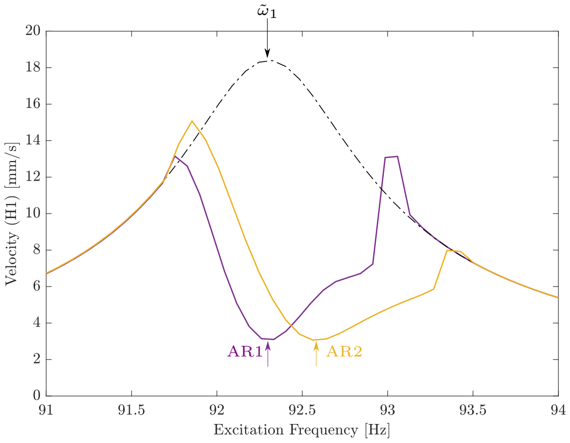

Figure 14: Experimentally measured frequency response of v_{H1} for two different cases. The first case corresponds to $\beta_c = 0.001$ to satisfy Eq. (24), plotted in yellow. The other case corresponds to $\beta_c = 0.00093$ as predicted in Fig. 13 for $F = 0.49$mN, plotted in purple. The results are estimated for $\beta_q = 0.03$, $\xi_e = 0.002$, $r_1 = 0.5055$, and $F = 0.49$mN. The black dashed-dotted line denotes the linear response (with $\beta_q = \beta_c = 0$).

antiresonance correction procedure at higher forcing levels. Actually, the proposed antiresonance correction can be repeated for higher excitations to have a wider stability region. Moreover, here we rely on the numerical value of the suitable β_c suggested from Fig. 13, but for a more practical estimation of the suitable value, one can use the property verified the phase between H1 and H1/2 at antiresonance where $\gamma_1 = 3\pi/2$ (cf. Fig. 9).

5. Conclusions

This study addressed theoretically and experimentally a solution to handle the detuning of a quadratic nonlinear piezoelectric shunt absorber. This type of vibration absorber aims at exploiting the saturation of the vibration of the primary system that occurs during a 2:1 internal resonance. This feature is hindered by unwanted side effects when the nonlinearity is implemented using a measurement of the PE patch voltage. When doing so, nonresonant quadratic terms appear, and we showed that they introduce undesirable softening behavior of the free response. Based on the normal form theory, quadratic nonresonant terms are equivalent to cubic terms, and we showed that an added cubic nonlinearity in the shunt can compensate the largest nonresonant quadratic coupling. It is found that the gain governing the cubic term β_c is simply proportional to the quadratic gain for small excitation levels. This was validated experimentally, but this correction has a limited effect: as the excitation level increases, this approach is less effective. Thus, for a given excitation level, β_c was modified based on the prediction of the model, and the experiments confirmed that the antiresonance could be restored. Future work will explore the possibility of automatically adjusting β_c based on the antiresonance condition $\gamma_1 = 3\pi/2$.

Appendix A. Resonant and non-resonant terms

This section gives a basic explanation of the resonant and nonresonant terms. More rigorous definitions are given in texts related to the normal form theory, see [44, 45]. Considering Eqs. (11) with quadratic nonlinear terms only and in free vibrations, one obtains:

$$\ddot{x}_1 + \omega_1^2 x_1 = -g_{11}^1 x_1^2 - g_{12}^1 x_1 x_2 - g_{22}^1 x_2^2, \tag{A.1a}$$

$$\ddot{x}_2 + \omega_2^2 x_2 = -g_{11}^2 x_1^2 - g_{12}^2 x_1 x_2 - g_{22}^2 x_2^2. \tag{A.1b}$$

Then, at first order, one can consider that $x_1(t) \simeq a_1 \cos(\omega_1 t + \varphi_1)$ and $x_2(t) \simeq a_2 \cos(\omega_2 t + \varphi_2)$, with $(a_1, a_2, \varphi_1, \varphi_2)$ being the amplitudes and phases. Then, using basic trigonometric identities, one shows that the nonlinear term $x_1^2(t)$ contains a constant and an harmonic at $2\omega_1$, $x_2^2(t)$ contains a constant and an harmonic at $2\omega_2$ and $x_1(t)x_2(t)$ contains two harmonics, at $\omega_1 + \omega_2$ and $|\omega_1 - \omega_2|$. Then, if $\omega_2 \simeq 2\omega_1$, the frequency content of the nonlinear terms can be summarized as:

$$x_1^2(t) \qquad \rightsquigarrow \; 2\omega_1 \simeq \omega_2, \tag{A.2}$$

$$x_2^2(t) \qquad \rightsquigarrow \; 2\omega_2 \simeq 4\omega_1, \tag{A.3}$$

$$x_1(t)x_2(t) \qquad \rightsquigarrow \; \omega_1 + \omega_2 \simeq 3\omega_1, \quad |\omega_1 - \omega_2| \simeq \omega_1, \tag{A.4}$$

which shows that $x_1^2(t)$ (resp. $x_1(t)x_2(t)$) can be considered as a forcing term that drives the second (resp. the first) oscillator close to its resonance frequency, at ω_2 (resp. ω_1). All the other terms have a frequency content away from the two resonance of the oscillators. This is a physical explanation of the resonant or nonresonant role of the different nonlinear terms in the equations.

Appendix B. Linear Modal Analysis

Before conducting the experiments with the nonlinear shunt circuit, a linear modal analysis was performed to estimate the electromechanical modal parameters necessary to design the shunt circuit properly. The modal analysis procedure is similar to that of [17]. It consists in fitting the analytical frequency response functions (FRFs) with the experimental ones.

Focusing on a particular mode of the foil (i-th mode), the FRFs are measured with two different sets of experiments depending on the forcing type:

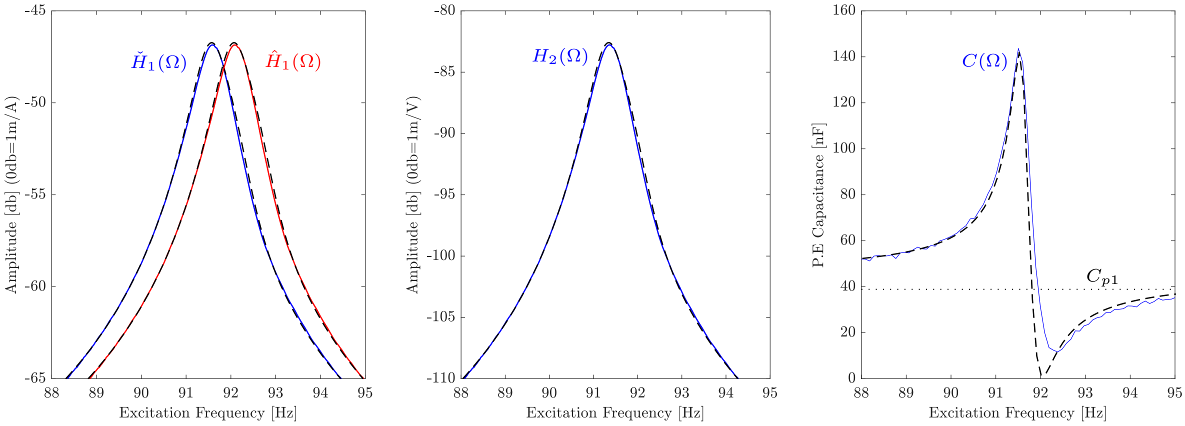

Figure B.15: Fitting between the experimental (solid lines) and analytical FRFs (dashed lines).

- We consider a mechanical forcing using the coil-magnet system, and we measure the velocity $v(t)$ of the foil with the laser vibrometer at the measurement point, collocated with the magnet location $\boldsymbol{x}_m$. We perform these operations in two successive conditions: with patch 2 in short-circuit ($V = 0$) and in open-circuit ($Q = 0$), all the other patches being short-circuited. We then obtain the following FRFs, the displacement spectrum at the tip of the foil being obtained by dividing the spectrum of $v(t)$ by $j\Omega$. Considering that the coil/magnet system is equivalent to a point forcing and that the mode shape is normalized such that $\boldsymbol{\phi}_1(\boldsymbol{x}_m) = 1$, one has $q_1(t) = u(t)$ and, following Eqs. (2):

$$\check{H}_1(\Omega) = \left.\frac{\mathring{u}}{\mathring{I}}\right|_{V=0} = \frac{\gamma_i}{\Omega^2 - \check{\omega}_i^2 + 2j\xi_i\hat{\omega}_i\Omega}, \tag{B.1a}$$

$$\hat{H}_1(\Omega) = \left.\frac{\mathring{u}}{\mathring{I}}\right|_{Q=0} = \frac{\gamma_i}{\Omega^2 - \hat{\omega}_i^2 + 2j\xi_i\hat{\omega}_i\Omega}, \tag{B.1b}$$

where $\check{H}_1(\Omega)$ and $\hat{H}_1(\Omega)$ are the FRFs in the short and open circuit case, respectively.

- We consider an electrical forcing by prescribing a voltage $V(t)$ to patch 2 with a TREK PZD700A piezoelectric amplifier, with the other patches short-circuited. Then we obtain:

$$H_2(\Omega) = \left.\frac{\mathring{u}}{\mathring{V}}\right|_{F=0} = -\frac{\lambda_i}{\Omega^2 - \breve{\omega}_i^2 + 2j\xi_i\hat{\omega}_i\Omega}, \tag{B.2a}$$

$$C(\Omega) = \left.\frac{\mathring{Q}}{\mathring{V}}\right|_{F=0} = C_{\mathrm{p}i} + \frac{\delta_i}{\Omega^2 - \breve{\omega}_i^2 + 2j\xi_i\hat{\omega}_i\Omega}. \tag{B.2b}$$

In the above equations, $\mathring{\bullet}(\Omega)$ is the Fourier transform of $\bullet(t)$ and the amplitude constants read:

$$\gamma_i = \frac{\alpha}{m_i}, \quad \lambda_i = \frac{\theta_i}{m_i}, \quad \delta_i = \frac{\theta_i^2}{m_i}. \tag{B.3}$$

The fitting near the resonance frequency of the first bending mode is shown in Fig. B.15. This fitting allows to estimate γ_1, λ_1, and δ_1 (subscript $i = 1$ stands for the first bending mode) and thus deduce the modal mass m_1, the coupling coefficient $\theta_1 = \delta_1/\lambda_1$ and $m_1 = \theta_1/\lambda_1$. The open and short circuit frequencies (resp. $\breve{\omega}_1$ and $\hat{\omega}_1$), the mechanical damping coefficient ξ_1, and the effective PE capacitance C_{p1} can be directly obtained by the fitting. In addition, the EMMCF k_1 can be obtained using Eq. 6. $\alpha = \gamma_1 m_1$ is obtained in [17]. All the electromechanical modal parameters of the first bending mode of the foil are gathered in Table. 1.

References

[1] F. W. Lanchester, “Damping torsional vibrations in crank shafts,” Jan. 1914. U.S. Patent No. 1085443.

[2] H. Frahm, “Device for damping vibrations of bodies,” Apr. 1911. U.S. Patent No. 989958.

[3] N. Hagood and A. Von Flotow, “Damping of structural vibrations with piezoelectric materials and passive electrical networks,” *Journal of Sound and Vibration*, vol. 146, pp. 243–268, Apr. 1991.

[4] S. Behrens, A. Fleming, and S. Reza Moheimani, “Electromagnetic shunt damping,” in *Proceedings 2003 IEEE/ASME International Conference on*

Advanced Intelligent Mechatronics (AIM 2003), vol. 2, (Kobe, Japan), pp. 1145–1150, IEEE, 2003.

[5] J. Gripp and D. Rade, "Vibration and noise control using shunted piezoelectric transducers: A review," *Mechanical Systems and Signal Processing*, vol. 112, pp. 359–383, Nov. 2018.

[6] P. Shivashankar and S. Gopalakrishnan, "Review on the use of piezoelectric materials for active vibration, noise, and flow control," *Smart Materials and Structures*, vol. 29, p. 053001, 2020.

[7] M. Auleley, O. Thomas, C. Giraud-Audine, and H. Mahé, "Enhancement of a dynamic vibration absorber by means of an electromagnetic shunt," *Journal of Intelligent Material Systems and Structures*, vol. 32, pp. 331–354, Feb. 2021.

[8] O. Thomas, J. Ducarne, and J.-F. Deü, "Performance of piezoelectric shunts for vibration reduction," *Smart Materials and Structures*, vol. 21, p. 015008, Jan. 2012.

[9] R. Darleux, B. Lossouarn, and J.-F. Deü, "Broadband vibration damping of non-periodic plates by piezoelectric coupling to their electrical analogues," *Smart Materials and Structures,*, vol. 29, no. 5, p. 054001, 2020.

[10] B. Lossouarn, L. Rouleau, R. Darleux, and J.-F. Deü, "Comparison of passive damping treatments based on constrained viscoelastic layers and multi-resonant piezoelectric networks," *Journal of Structural Dynamics*, 2021.

[11] J. F. Toftekær and J. Høgsberg, "Multi-mode piezoelectric shunt damping with residual mode correction by evaluation of modal charge and voltage," *Journal of Intelligent Material Systems and Structures*, vol. 31, no. 4, pp. 570–586, 2020.

[12] M. Berardengo, O. Thomas, C. Giraud-Audine, and S. Manzoni, "Improved resistive shunt by means of negative capacitance: New circuit, perfor-

mances and multi-mode control," *Smart Materials and Structures*, vol. 25, p. 075033, July 2016.

[13] M. Berardengo, S. Manzoni, O. Thomas, and M. Vanali, "Guidelines for the layout and tuning of piezoelectric resonant shunt with negative capacitances in terms of dynamic compliance, mobility and accelerance," *Journal of Intelligent Material Systems and Structures*, 2021.

[14] M. Auleley, C. Giraud-Audine, H. Mahé, and O. Thomas, "Tunable electromagnetic resonant shunt using pulse-width modulation," *Journal of Sound and Vibration*, vol. 500, p. 116018, 2021.

[15] K. Dekemele, P. V. Torre, and M. Locufier, "High-voltage synthetic inductor for vibration damping in resonant piezoelectric shunt," *Journal of Vibration and Control*, vol. 27, no. 17-18, pp. 2047–2057, 2020.

[16] Z. A. Shami, C. Giraud-Audine, and O. Thomas, "A nonlinear piezoelectric shunt absorber with a 2:1 internal resonance: Theory," *Mechanical Systems and Signal Processing*, vol. 170, 2022.

[17] Z. A. Shami, C. Giraud-Audine, and O. Thomas, "A nonlinear piezoelectric shunt absorber with 2:1 internal resonance: experimental proof of concept," *Smart Materials and Structures*, vol. 31, no. 3, 2022.

[18] A. F. Vakakis and O. Gendelman, "Energy pumping in nonlinear mechanical oscillators: Part ii - resonance capture," *Journal of Applied Mechanics*, vol. 68, pp. 42–48, 2001.

[19] B. Zhou, F.Thouverez, and D. Lenoir, "Essentially nonlinear piezoelectric shunt circuits applied to mistuned bladed disks," *Journal of Sound and Vibration*, vol. 333, pp. 2520–2542, 2014.

[20] T. M. Silva, M. A. Clementino, C. De Marqui, and A. Erturk, "An experimentally validated piezoelectric nonlinear energy sink for wideband vibration attenuation," *Journal of Sound and Vibration*, vol. 437, pp. 68–78, Dec. 2018.

[21] G. Habib, T. Detroux, R. Viguié, and G. Kerschen, “Nonlinear generalization of Den Hartog’s equal-peak method,” *Mechanical Systems and Signal Processing*, vol. 52-53, pp. 17–28, Feb. 2015.

[22] B. Lossouarn, J.-F. Deü, and G. Kerschen, “A fully passive nonlinear piezoelectric vibration absorber,” *Philosophical Transactions of the Royal Society A: Mathematical, Physical and Engineering Sciences*, vol. 376, p. 20170142, Aug. 2018.

[23] B. Lossouarn, G. Kerschen, and J.-F. Deü, “An analogue twin for piezoelectric vibration damping of multiple nonlinear resonances,” *Journal of Sound and Vibration*, vol. 511, p. 116323, 2021.

[24] W. W. Clark, “Vibration Control with State-Switched Piezoelectric Materials,” *Journal of Intelligent Material Systems and Structures*, vol. 11, pp. 263–271, Apr. 2000.

[25] C. Richard, D. Guyomar, D. Audigier, and G. Ching, “Semi-passive damping using continuous switching of a piezoelectric device,” in *Proc. of SPIE Smart Structures and Materials Conference: Passive Damping and Isolation*, vol. 3672, pp. 104–111, 1999.

[26] A. H. Nayfeh and D. T. Mook, *Nonlinear Oscillations.* New-York: John Wiley & Sons, inc., 1979.

[27] A. Vyas, A. K. Bajaj, and A. Raman, “Dynamics of structures with wideband autoparametric vibration absorbers: theory,” *Proceedings of the Royal Society of London A*, vol. 460, pp. 1547–1581, 2004.

[28] S. Mahmoudkhani and H. S. Meymand, “Effects of nonlinear interactions of flexural modes on the performance of a beam autoparametric vibration absorber,” *Journal of Vibration and Control*, vol. 26, no. 7-8, pp. 459–474, 2019.

[29] V. Mahé, A. Renault, A. Grolet, H. Mahé, and O. Thomas, "Subharmonic pendulum vibration absorbers allowing a rotational mobility," *Mechanical Systems and Signal Processing*, vol. 177, p. 109125, 2021.

[30] S. Oueini and M. Golnaraghi, "Experimental Implementation Of The Internal Resonance Control Strategy," *Journal of Sound and Vibration*, vol. 191, pp. 377–396, Apr. 1996.

[31] S. S. Oueini, A. H. Nayfeh, and M. F. Golnaraghi, "A theoretical and experimental implementation of a control method based on saturation," *Nonlinear Dynamics*, vol. 13, pp. 189–202, 1997.

[32] S. S. Oueini, A. H. Nayfeh, and J. R. Pratt, "A Nonlinear Vibration Absorber for Flexible Structures," *Nonlinear Dynamics*, vol. 15, pp. 259–282, 1998.

[33] P. Pai, B. Wen, A. Naser, and M. Schulz, "Structural vibration control using pzt patches and non-linear phenomena," *Journal of Sound and Vibration*, vol. 215, pp. 273–296, Aug. 1998.

[34] P. F. Pai, B. Rommel, and M. J. Schulz, "Dynamics regulation of a skew cantilever plate using pzt patches and saturation phenomenon," *Journal of Intelligent Material Systems and Structures*, vol. 11, pp. 642–655, Aug. 2000.

[35] S. S. Oueini, C.-M. Chin, and A. H. Nayfeh, "Dynamics of a cubic nonlinear vibration absorber," *Nonlinear dynamics*, vol. 20, no. 3, pp. 283–295, 1999.

[36] Z. A. Shami, Y. Shen, C. Giraud-Audine, C. Touzé, and O. Thomas, "Nonlinear dynamics of coupled oscillators in 1:2 internal resonance: effects of the non-resonant quadratic terms and recovery of the saturation effect," *Meccanica*, 2021.

[37] ANSI/IEEE Std 176-1987, *IEEE Standard on Piezoelectricity.* The Institute of Electrical and Electronics Engineers, Inc., 1988.

[38] A. Nayfeh and D. Mook, *Nonlinear Oscillations.* Pure and Applied Mathematics: A Wiley Series of Texts, Monographs and Tracts, Wiley, 1979.

[39] L. Guillot, B. Cochelin, and C. Vergez, "A generic and efficient Taylor series–based continuation method using a quadratic recast of smooth nonlinear systems," *International Journal for Numerical Methods in Engineering*, vol. 119, pp. 261–280, July 2019.

[40] L. Guillot, A. Lazarus, O. Thomas, C. Vergez, and B. Cochelin, "A purely frequency based Floquet-Hill formulation for the efficient stability computation of periodic solutions of ordinary differential systems," *Journal of Computational Physics*, vol. 416, p. 109477, Sept. 2020.

[41] L. Pernod, B. Lossouarn, J.-A. Astolfi, and J.-F. Deü, "Vibration damping of marine lifting surfaces with resonant piezoelectric shunts," *Journal of Sound and Vibration*, vol. 496, p. 115921, 2021.

[42] O. Thomas, C. Touzé, and A. Chaigne, "Asymmetric non-linear forced vibrations of free-edge circular plates, part 2: experiments," *Journal of Sound and Vibration*, vol. 265, no. 5, pp. 1075–1101, 2003.

[43] M. Vatavu, V. Nastasescu, F. Turcu, and I. Burda, "Voltage-controlled synthetic inductors for resonant piezoelectric shunt damping: A comparative analysis," *Applied Sciences*, vol. 9, no. 22, 2019.

[44] C. Touzé, *Modal Analysis of Nonlinear Mechanical Systems*, vol. CISM, volume 555, ch. Normal form theory and nonlinear normal modes: Theoretical settings and applications, pp. 75—-160. Springer, 2014.

[45] C. Touzé, A. Vizzaccaro, and O. Thomas, "Model order reduction methods for geometrically nonlinear structures: a review of nonlinear techniques," *Nonlinear Dynamics*, vol. 105, pp. 1141–1190, 2021.

Chapter 6

Theoretical modeling and experimental analysis of nonlinear piezoelectric shunt absorber with a nonsmooth component

Contenu

6.1 Article presentation

The present chapter solely constitutes of the text of the article entitled by ”A nonlinear tunable piezoelectric resonant shunt using a bilinear component: theory and experiment” submitted to ”Nonlinear Dynamics” journal. The article addresses the design of a tunable resonant piezoelectric shunt with a nonsmooth component. The nonsmooth component is chosen to be proportional to the superposition of the voltage across the piezoelectric patch and its absolute value function, leading to a bilinear form. The obtained nonsmooth component is not symmetric and thus generate even harmonics similar to quadratic nonlinearities. Such nonsmooth component can be analyzed by a simple electric component such as a diode or a transistor in practice. In addition, the nonsmooth component leads to switch the electric resonance frequency between two distinct values depending on the sign of the voltage. The main feature that we aim to study is the ability to tune the electric shunt resonance frequency with the nonsmooth component by setting lower inductance in the shunt circuit. In addition, we aim to examine the possibility of obtaining nonlinear modal coupling between the electrical and mechanical modes, thanks to the implicit nonlinearities generated by the nonsmooth component.

As a first step, the effect of the nonsmooth component is studied by considering one degree of freedom oscillator with a nonsmooth term. Then, the free and forced solutions are examined. The free solution is proved to be periodic but not harmonic with a modified resonance frequency $\bar{\omega}_e$ that depends on the nonsmooth gain β and is independent of the oscillation amplitude. The forced solution is analyzed numerically by examining the multi-harmonic response generated by the nonsmooth component. Namely, the frequency response of each harmonic is studied in which the results suggest that each harmonic admits a frequency response equivalent to a linear oscillator with a resonance frequency equals to the estimated resonance frequency $\bar{\omega}_e$. This led us to propose an approximation of dominant harmonics, namely the zeroth, the first, and the second harmonics, by a linear oscillator. To establish the approximation, a gain ϕ_p, corresponding to the p-th harmonic, is introduced to quantify the energy distribution to each harmonic. Interestingly, a strong nonlinear behavior of the harmonic appeared at the superharmonic resonances motivating the ability to activate internal resonance.

The approximation is then extended to the full system by considering two tuning cases of the nonsmooth component. The first one considers a one-to-one tuning (1:1 tuning) such that the modified electric resonance frequency $\bar{\omega}_e$ is tuned equal to the mechanical resonance frequency $\hat{\omega}$ of the structure mode to be attenuated. The second one considers a two-to-one tuning (2:1 tuning) such that $\bar{\omega}_e = 1/2\hat{\omega}$. The tuning is solely performed through the nonsmooth component, considering the inductance to be free parameter in the circuit (i.e., no condition is imposed on the inductance value).

Thanks to the obtained approximation, an analytical approximation of the frequency responses were obtained by introducing a new piezoelectric coupling factor modified by a factor of $\sqrt{\phi_1}$ and $\sqrt{\phi_2}$ for the 1:1 tuning and 2:1 tuning, respectively. Both tuning cases suggested that the behavior of the first harmonic response is equivalent to a linear resonant shunt with the activation of the 2:1 internal resonance for the latter case. Thus, an optimization study is established to determine the optimal tuning of β and the electric damping ratio ξ_e to achieve an optimal attenuation with low inductance compared to the linear resonant shunt. In particular, the effect of the inductance on the optimal attenuation is studied for each tuning case as it appears explicitly in the attenuation expressions, contrary to the linear resonant shunt in which the inductance should satisfy a tuning condition. It is shown that the optimal attenuation for the 1:1 tuning case reduced by 1dB, compared to that of a linear resonant shunt, for a reduction of the inductance by a factor of 100. Interestingly, for the 2:1 tuning case, the attenuation increases with the decrease of the inductance up to a limit where it stays almost constant. The results are then verified numerically by applying the absorber to attenuate the first twisting mode of a hydrofoil structure.

An experimental proof of concept is also established considering also the first twisting mode of the hydrofoil structure in which the nonsmooth behavior is realized in a passive way with a half-wave rectifier circuit that includes a diode. The measurement protocol to estimate the experimental frequency response for each case is discussed in addition to the shunt circuit used in the experiments. The theoretical predictions regarding the optimal parameters are experimentally validated through a comparison between the numerical and the experimental frequency responses, considering the first harmonics of the displacement and the piezoelectric voltage for the 1:1 tuning case. For the 2:1 tuning case, the first harmonic of the displacement with the subharmonic of the voltage were considered to validate the energy transfer and thus the activation of the 2:1 internal resonance. Then, a sensitivity analysis regarding the values of β and ξ_e on the response for both tuning cases is performed, showing tuning characteristics similar to that of a linear resonant shunt. A discussion is finally illustrated regarding the experimental tests which validates the dependence of the optimal attenuation on the inductance in the shunt circuit regarding the 1:1 and 2:1 tuning cases.

6.2 A nonlinear tunable piezoelectric resonant shunt using a bilinear component: theory and experiment

Noname manuscript No.
(will be inserted by the editor)

A nonlinear tunable piezoelectric resonant shunt using a bilinear component: theory and experiment

Zein A. Shami · Christophe Giraud-Audine · Olivier Thomas

Received: date / Accepted: date

Abstract In this article, we propose a new concept for tuning a resonant piezoelectric shunt absorber thanks to the use of a nonsmooth electronic component. It consists in adding in the resonant shunt circuit a voltage source which is a bilinear function of the voltage across the piezoelectric patch. The main advantage is the ability to change the electrical resonance frequency with the bilinear component gain, enabling a tuning as well as a possible reduction of the required inductance value. Because of the intrinsic nonlinear nature of the bilinear component, a multi-harmonic response is at hand, leading to a nonlinear coupling between the mechanical and electrical modes. Two particular tunings between the electrical and the mechanical resonance frequencies are tested. The first one is one-to-one, for which the electrical resonance is tuned close to the mechanical one. It is proved to be similar to a classical linear resonant shunt, with the additional tuning ability. The second case consists in tuning the electrical circuit at half the mechanical resonance, leading to a two-to-one (2:1) internal resonance. The obtained response is also found to be similar to a classical resonant shunt near the main resonance. In either case, the shunt performances are analytically and numerically studied, leading to optimal values of the design parameters as well as an estimation of the amplitude reduction provided by the shunt. Finally, experimental validation is proposed, targeting the damping of the twisting mode of a hydrofoil structure, in which the bilinear component is realized with a diode.

Keywords Piezoelectric shunt absorber, Nonsmooth component, bilinear absorber, 2:1 internal resonance, Nonlinear Oscillations, Diode

1 Introduction

Piezoelectric shunt absorbers represent an efficient way to attenuate the vibrations of structures under external excitation, especially when the size and weight constraints are presented. Those absorbers were proposed in [1] as an extension to the mechanical absorbers by utilizing a piezoelectric (PE) transducer connected to a dedicated electronic circuit.

Z.A. Shami, O. Thomas
Arts et Métiers Institute of Technology, LISPEN, HESAM Université, F-59000 Lille, France
E-mail: zein_alabidin.shami@ensam.eu,olivier.thomas@ensam.eu

C. Giraud-Audine
Arts et Métiers Institute of Technology, L2EP, HESAM Université, F-59000 Lille, France
E-mail: christophe.giraud-audine@ensam.eu

The simplest architectures of those shunt circuits are the resistive shunt (R-shunt, including a simple resistor) and the resonant shunt (RL-shunt, composed of a resistor and an inductor L), which are passive absorbers with a linear behavior. While the R-shunt dissipates the energy in heat form, the RL-shunt consists in coupling an electrical resonator (an RLC circuit, with C being the intrinsic capacitance of PE patch) to the host structure. It is thus an electrical analogue of a tuned mass damper (TMD) which can be tuned in a similar manner to achieve an optimal attenuation. In this context, it has been shown through the optimal study of the RL-shunt in [2] that for a given mechanical damping ratio, the optimal attenuation depends only on the PE coupling factor. Thus, enhancing the absorber performance can be done by increasing the PE coupling using, for example, a negative capacitance [3] or by optimizing the placement of the PE patch on the host structure [4]. Two main issues are encountered with the PE shunts: i) their sensitivity to any change in the resonance frequency of the structure [5], ii) for some applications targeting low-frequency modes, a very high inductance is required, which can be a practical issue [6, 7]. In addition, the R and RL-shunts act near a single structure mode, but they can be extended for multi-modal attenuation through multiple attachments [8–10]. One can refer further to the following reviews [11, 12] for a wider illustration regarding the optimization and different applications of the PE shunts.

PE shunts properties can be enhanced by intentionally introducing a nonlinear component in the shunt circuit to exploit some purely nonlinear features. An example of such applications is the so-called nonlinear energy sink ”NES”, introduced in [13], and realized theoretically and experimentally with piezoelectric shunt methodology in [14] and [15], respectively, by adding cubic nonlinear component in the shunt circuit. Another example is the so-called nonlinear tuned vibration absorber ”NLTVA” introduced in [16] and realized with PE shunt theoretically [17] and experimentally [18]. Recently, a new semi-passive absorber, introduced in [19] and realized experimentally in [20], exploited a two-to-one (2:1) internal resonance and a saturation phenomenon by adding a quadratic nonlinear component in a classical RL-shunt. This concept was improved to correct an unwanted detuning by adding a cubic component, as shown theoretically in [21] and experimentally in [22].

In many applications, the nonlinearities can be presented (or approximated) in a polynomial form (i.e., quadratic or/and cubic). In essence, polynomial nonlinearities naturally appear in a wide range of nonlinear models involving geometric and material nonlinearities such as thin beam and plate models [23, 24]. The free and forced response of systems involving such types of nonlinearities can be analyzed analytically (up to a certain order) using several methods such as perturbation techniques [25], elliptic functions [26], and normal form [27]. However, in some other applications involving clearance [28], vibro-impacts [29] or dry friction [30, 31], nonsmooth piece-wise functions naturally appear in the model, leading to strong nonlinear effects.

Utilizing nonsmooth nonlinear components for vibration reduction is firstly introduced in [32] to enhance the design of the NES to act as shock isolators. A lot of studies were then conducted to analyze the energy transfer between linear and nonsmooth NES attachments. For example, the targeted energy transfer between a single degree of freedom linear system and nonsmooth NES is studied in [33]. Also, the dynamics of a NES of non-polynomial piece-wise potential is investigated in [34]. In addition, introducing a nonsmooth component led to the design of vibro-impact NES where detailed design rules were given in [35]. A recent theoretical and experimental study [36] proposed an enhanced NES by using a cubic spring in addition to a piece-wise linear spring.

To the authors’ knowledge, the only attempt to use a nonsmooth component in a PE shunt methodology involved the synchronized switch damping (SSD) technique. The latter idea is proposed in [37] for piezoelectric transduction that is switched between two distinct shunt impedances, in synchronicity with the oscillations of the host structure [38]. The principle is the following: when the system is moving away from equilibrium, a voltage is applied such that the piezoelectric force resulting tends to restore the system to its equilibrium point. Various topologies have been proposed regarding the circuit connected in series with the patch via the switch: a simple resistor [37], a resistor and an inductor to increase the voltage inversion [39] or the same circuit with an added static voltage source [40, 41]. In the latter case, the voltage may have to be controlled as well to avoid instabilities [42]. This technique proved to be efficient in terms of vibration reduction, but it can become complicated to tune in practice due to the imperfection of synchronization time required [38] as well as to the creation of higher harmonics and noise [43].

The main originality of this work is to present the design of a tunable PE resonant shunt with a nonsmooth voltage component, without any required synchronization. In practice, the nonsmooth voltage component can be realized in a passive way with a half-wave rectifier circuit that includes a diode, so that the bilinear function of the voltage across the piezoelectric transducer is obtained. In addition, the proposed design of the nonsmooth component allows us to tune the resonance frequency of the shunt circuit without changing the inductance. Thus, a lower inductance can be set for the optimum design, which is an advantage when considering low-frequency modes. This paper focuses on the theoretical bases of the absorber and its experimental proof of concept, by targeting the mitigation of the first twisting resonance of a hydrofoil structure.

This paper is organized as follows: in section 2, the theoretical study is illustrated, showing the main governing equations with the nonsmooth term in addition to their approximation. We also show the optimal study for one-to-one and two-to-one tuning cases of the electric resonance frequency. The obtained optimal parameters, in addition to the optimal attenuation, are then numerically verified. In section. 4 we show the experimental proof of concept where the nonlinear shunt circuit and the measurement protocol are illustrated. In addition, we show the experimental frequency responses for both tuning cases to validate the theoretical estimations.

2 Theoretical Analysis

2.1 Governing Equations

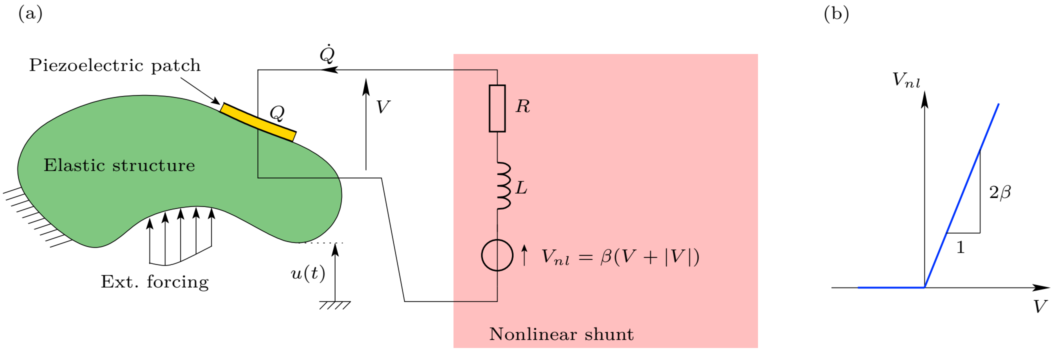

Fig. 1: (a) Elastic structure coupled to the nonlinear shunt circuit; (b) graph of the function $V \rightarrow V_{nl} = \beta(V + |V|)$.

We consider an arbitrary elastic structure subjected to an external excitation and connected to a shunt circuit via a piezoelectric patch, as shown in Fig. 1(a). Following [2, 19, 20], the displacement $u(\boldsymbol{x}, t)$ at position $\boldsymbol{x}$ in the structure and time t is truncated on one linear mode such that:

$$u(\boldsymbol{x}, t) = \psi(\boldsymbol{x}) q(t), \tag{1}$$

where $\psi(\boldsymbol{x})$ is the mode shape and $q_i(t)$ is the i-th modal displacement. Then, $(Q(t),\ q(t))$ are the solutions of the following system:

$$\ddot{q}_i + 2\xi_i\hat{\omega}_i\dot{q}_i + \hat{\omega}_i^2 q_i + \frac{\theta_i}{m_i C_{\mathrm{p}i}} Q = \frac{F_i}{m_i}\cos\Omega t, \tag{2a}$$

$$\ddot{Q} + 2\xi_e\omega_e\dot{Q} + \omega_e^2 Q + \frac{\theta_i}{LC_{\mathrm{p}i}} q_i - \frac{V_{\mathrm{nl}}}{L} = 0. \tag{2b}$$

In the above equations, m_i, ξ_i, $\hat{\omega}_i$, θ_i, and F_i are, respectively, the modal mass, the mechanical damping ratio, the natural frequency in open circuit condition ($Q = 0$), the piezoelectric coupling coefficient, and the forcing, all corresponding to the i-th mode. $C_{\mathrm{p}i}$ is the effective capacitance of the piezoelectric patch for the i-th mode [3]. The electrical natural frequency ω_e and electric damping ratio ξ_e are defined as:

$$\omega_e = \frac{1}{\sqrt{LC_{\mathrm{p}i}}}, \quad \xi_e = \frac{R}{2}\sqrt{\frac{C_{\mathrm{p}i}}{L}}, \tag{3}$$

where R and L are the resistance and the inductance in the shunt circuit, respectively.

The PE patch voltage $V(t)$ can be defined as a function of $q_i(t)$ and $Q(t)$ using [2]:

$$V = \frac{1}{C_{pi}}(Q + \theta_i q_i). \tag{4}$$

We also define the dimensionless electromechanical modal coupling factor (EMMCF) of the i-th mode as:

$$k_i^2 = \frac{\hat{\omega}_i^2 - \check{\omega}_i^2}{\hat{\omega}_i^2} = \frac{\theta_i^2}{\hat{\omega}_i^2 C_{\mathrm{p}i} m_i}, \tag{5}$$

with $\check{\omega}_i$ the natural frequency in short circuit ($V = 0$).

In this study, we consider the nonlinear voltage component $V_{nl}(t)$ to be bilinear in terms of $V(t)$, as shown in Fig. 1(b), and expressed as:

$$V_{nl} = \beta(V + |V|), \tag{6}$$

where β is a dimensionless gain. The goal of introducing a nonsmooth nonlinearity in the form presented in Eq. (6) is first to generate even harmonics in the system, because it is not a symmetrical function of V, to possibly activate a 2:1 internal resonance, and second to use simple electrical components such as a diode or a transistor to practically realize it.

By substituting Eq. (6) in Eq. (2b) and eliminating V using Eq. (4), we obtain:

$$\ddot{q}_i + 2\xi_i\hat{\omega}_i\dot{q}_i + \hat{\omega}_i^2 q_i + \frac{\theta_i}{m_i C_{\mathrm{p}i}} Q = \frac{F_i}{m_i}\cos\Omega t, \tag{7a}$$

$$\ddot{Q} + 2\xi_e\omega_e\dot{Q} + \omega_e^2 Q + \omega_e^2\theta_i q_i - \beta\omega_e^2\left(Q + \theta_i q_i + |Q + \theta_i q_i|\right) = 0. \tag{7b}$$

Two important conclusions can then be drawn at this stage: (i) the governing equations in (7a,b) are indeed non-linear because of the non-smooth term ($|V| \implies |Q + \theta_i q_i|$) which only appears in Eq. (7b) and creates a harmonic distortion. (ii) although nonlinearities are present, (7a,b) *are in fact fully linear in amplitude.* For example, replacing F by $2F$ in Eq. (7a) leads to obtain $(2q_i,\ 2Q)$ instead of $(q_i,\ Q)$ (see also Fig. 10) since the absolute value function is linear in amplitude (i.e., $|2x| = 2|x|$ for $x \in \mathbb{R}$). However, it is not always additive or superposable, since $|x_1 + x_2| \neq |x_1| + |x_2|$ if $x_1 x_2 < 0$ for $x_1, x_2 \in \mathbb{R}$.

2.2 1DOF system with the nonsmooth term

To give a first analysis of the behavior of the coupled system (7a,b), we consider here only Eq. (7b), we exclude the piezoelectric coupling (i.e., setting $\theta_i = 0$), and we add a direct forcing term, leading to:

$$\ddot{Q} + 2\xi_e\omega_e\dot{Q} + \omega_e^2 Q - \beta\omega_e^2\left(Q + |Q|\right) = P\cos\Omega t, \tag{8}$$

where P is the forcing amplitude.

2.2.1 Free solution

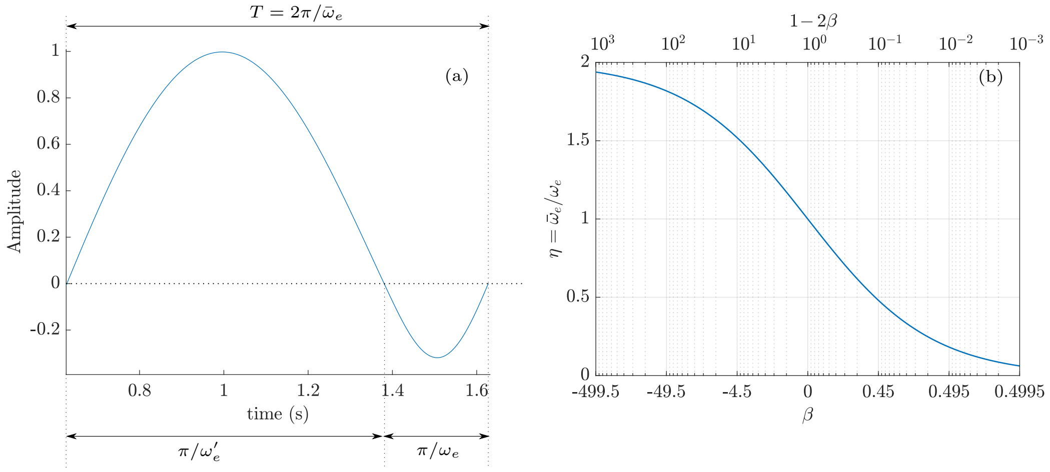

Fig. 2: (a) Example of the free response of Eq. (8) over one period. (b) Ratio $\eta = \bar{\omega}_e/\omega_e$ as a function of β.

To analyze the free response, we set $P = 0$, and we rewrite Eq. (8) as:

$$\ddot{Q} + 2\xi_e\omega_e\dot{Q} + \omega_e^2 Q = 0 \quad \text{if} \quad Q \leq 0, \tag{9a}$$

$$\ddot{Q} + 2\xi_e\omega_e\dot{Q} + \omega_e'^2 Q = 0 \quad \text{if} \quad Q \geq 0, \tag{9b}$$

where $\omega'_e = \omega_e\sqrt{1-2\beta}$. In the conservative case ($\xi_e = 0$), Eqs. (9) suggest that the free response is a succession of one half period of sine of period ω_e and one half period of sine of frequency ω'_e, as illustrated Fig. 2(a) . Then, the oscillation period can be expressed as:

$$T = \frac{2\pi}{\bar{\omega}_e} = \frac{\pi}{\omega_e} + \frac{\pi}{\omega'_e}, \tag{10}$$

where $\bar{\omega}_e$ is the modified angular frequency of the free response due to the nonsmooth term, which reads:

$$\bar{\omega}_e = \underbrace{\frac{2\sqrt{1-2\beta}}{1+\sqrt{1-2\beta}}}_{\eta}\omega_e = \frac{2\sqrt{1-2\beta}}{1+\sqrt{1-2\beta}}\frac{1}{\sqrt{LC_p}}, \qquad \eta = \frac{\bar{\omega}_e}{\omega_e}, \tag{11}$$

where η represents the ratio between the modified ($\bar{\omega}_e$) and unmodified (ω_e) natural frequencies. Eq. (11) proves that *even if the behaviour is nonlinear, the free oscillation frequency of Eq. (7b) does not depend on the amplitude.* Indeed, the oscillations are periodic but not harmonic since they are the succession of two half sine functions of different periods: the more β is large, the more the two periods are different, and higher the harmonics content is expected.

Moreover, Eq. (11) suggests that given an electrical resonance frequency ω_e (i.e., given an inductance), the modified electrical oscillation frequency $\bar{\omega}_e$ can be adjusted according to the value of β. However, *the value of* β *should be less than 1/2* to avoid unstable response (if $\beta > 0.5$, ω_e' admits imaginary part). This feature is the main advantage of this nonlinear shunt circuit: by adjusting the nonlinear parameter β, one can tune the electrical circuit frequency at a particular value while fixing the inductance at a low value, which is an advantage for practical implementation. Fig. 2(b) shows the ratio η as a function of β, illustrating that it can be lowered to zero (at $\beta = 0.5$) and increased up to a factor of 2 (for $\beta \to -\infty$).

2.2.2 Forced Solution

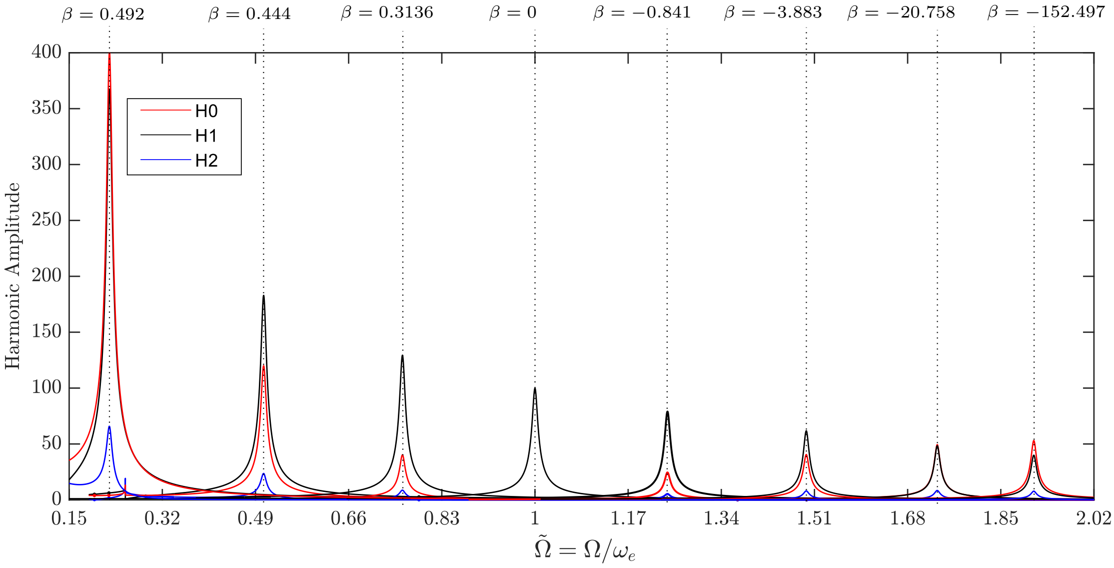

Fig. 3: Harmonics H0, H1 and H2 of the periodic solutions of Eq. (8) in the vicinity of the primary resonance, as a function of $\tilde{\Omega} = \Omega/\omega_e$ for $\xi_e = 0.005$. The harmonics' amplitude is normalized with respect to the excitation level. The vertical dotted black lines show the value $\bar{\omega}_e(\beta)$.

To analyze the forced response, we rewrite Eq. (8) in a dimensionless form by introducing the following parameters:

$$\tilde{t} = \omega_e t, \quad \tilde{Q} = Q\frac{\omega_e^2}{P}, \quad \tilde{\Omega} = \Omega/\omega_e. \tag{12}$$

Using the dimensionless parameters in Eq. (12), one obtains:

$$\ddot{\tilde{Q}} + 2\xi_e\dot{\tilde{Q}} + \tilde{Q} - \beta\left(\tilde{Q} + |\tilde{Q}|\right) = \cos\tilde{\Omega}\tilde{t}. \tag{13}$$

One can realize that the solution of Eq. (13) depends only on the damping ratio ξ_e and the gain β. As a consequence, *the shape of the resonance curve of Eq. (13) is independent of the excitation level* P and can be obtained for any value of P and ω_e using the scaling defined in (12).

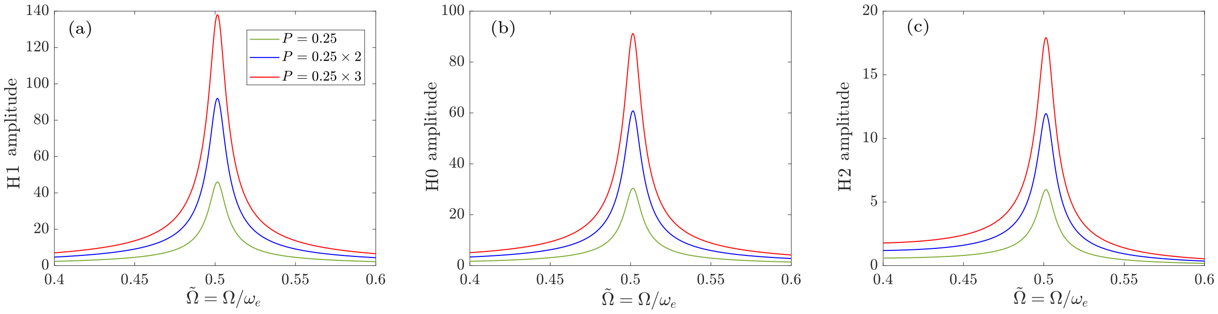

Fig. 4: Harmonics H1 (a), H0 (b) and H2 (c) of the periodic solutions of Eq. (8) in the vicinity of the primary resonance, as a function of $\tilde{\Omega} = \Omega/\omega_e$ for $\xi_e = 0.005$ and different excitation levels P. The numerical values used in the simulations are $\xi_e = 0.005$ and $\beta = 0.444$.

Eq. (13) is solved numerically with the continuation software MANLAB [44, 45] since there is no analytical solution at hand. MANLAB is based on a Harmonic Balance method to compute the periodic solutions. It requires a regularization of the nonsmooth term, which is discussed in Appendix B. Note that in all the numerical simulations with MANLAB, 40 harmonics were considered. Fig. 3 shows the dimensionless frequency response, normalized with respect to the excitation level, of the zeroth (H0), first (H1), and second (H2) harmonics of the periodic solutions of Eq. (8) for different values of β. Note that only H0, H1, and H2 harmonics are considered since they represent the dominant harmonics observed in the numerical simulations, and they will be relevant in the upcoming analysis. Indeed, other harmonics with lower amplitudes are present such as the third and fourth harmonics.

Two important conclusions can be drawn from the response shown in Fig.3. First, the nonlinear term creates a full harmonic content, with H0 being dominant in amplitude, H2 being significant but with lower amplitude, and the higher harmonics being negligible. Second, the relative amplitude of the harmonics with respect to the fundamental H1 increases with the absolute value of the nonlinear coefficient $|\beta|$: with $\beta = 0$, the response is fully linear with no harmonics, except H1. However, if β is close to 0.5 or tends to $-\infty$, the harmonic content increases significantly. Interestingly, the amplitude of H0 exceeds that of H1 for extreme values of β (e.g., for $\beta = 0.492$ and $\beta = -152.497$).

The most important observation is that the shape of each harmonic, considered separately, seems close to the frequency response of a linear oscillator near its resonance frequency, which is obtained here in the vicinity of the free oscillations frequency, for $\Omega = \bar{\omega}_e$. Such property is conserved even for higher excitation, as shown in Fig. 4, in which the linearity property with respect to the excitation level is clearly observed.

On the contrary to the quasi-linear behavior described above, the nonlinear nonsmooth term can generate a strongly nonlinear superharmonic response near $\Omega = \bar{\omega}_e/2$. This is emphasized in Fig. 5, which shows the superharmonic responses for different values of β, of the H0, H1, and H2 harmonics. The results suggest that the superharmonic response appears to be nonlinear (hardening effect with unstable branches), and the nonlinear effect increases with $|\beta|$. This suggests that introducing the nonsmooth term can represent an option for the application involving internal resonance (as will be discussed in section 3.2).

2.2.3 Forced response approximation with a linear oscillator

As discussed in the previous section, the nonlinear frequency response of the harmonics seems similar to the frequency response function (FRF) of a linear oscillator near the primary resonance. Thus, we

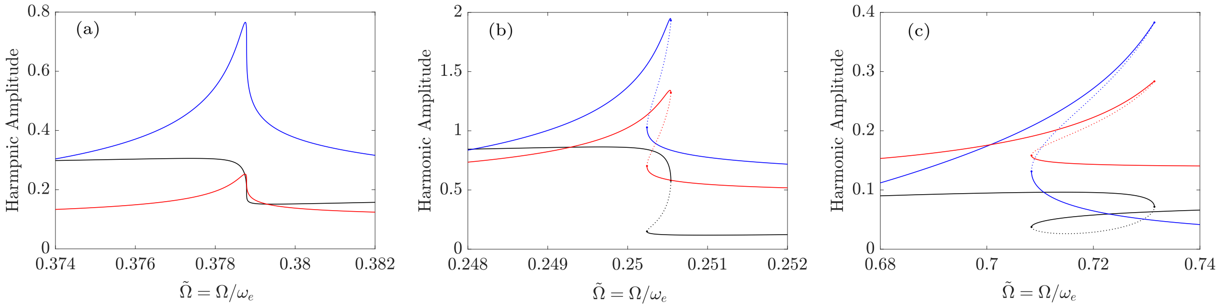

Fig. 5: Harmonics H0 (in red), H1 (in black), and H2 (in blue) of the periodic solutions of Eq. (8) in the vicinity of the superharmonic resonance of order two. (a) $\beta = 0.3136$, (b) $\beta = 0.444$, and (c) $\beta = -3.883$. The numerical values are $\xi_e = 0.005$ and $P = 0.1$. The solid and dotted lines denote the stable and unstable responses, respectively.

seek an approximation of Eq. (8) that is defined by the following linear oscillator, for $p = 0, 1, 2$:

$$\ddot{Q}_p + 2\bar{\xi}_e\bar{\omega}_e\dot{Q}_p + \bar{\omega}_e^2 Q_p = \phi_p P \cos \varOmega t, \tag{14}$$

where Q_p is the approximated response of the p-th harmonic of $Q(t)$, $\bar{\xi}_e$ is the modified damping ratio due to the nonsmooth term, and ϕ_p is an unknown gain, corresponding to the p-th harmonic, introduced to quantify the difference between the analytical and numerical solutions and to be determined by fitting the analytical frequency response of Q_p with the numerical frequency response of the p-th harmonic. From a physical point of view, the gain ϕ_p enables quantifying the energy distribution at each harmonic due to the presence of the nonsmooth component.

To determine the modified damping ratio $\bar{\xi}_e$, we assume (and we will verify hereafter) that the nonsmooth term has no effect on the damping coefficient (i.e., the term multiplying $\dot{Q}$), and thus:

$$\bar{\xi}_e\bar{\omega}_e = \xi_e\omega_e \quad \Rightarrow \quad \bar{\xi}_e = \xi_e/\eta. \tag{15}$$

Then, the FRF of Q_p is expressed as:

$$Z_p(\varOmega) = \frac{\mathring{Q}_p}{P} = \frac{\phi_p}{\bar{\omega}_e^2 - \varOmega^2 + 2j\bar{\xi}_e\bar{\omega}_e\varOmega}. \tag{16}$$

where $\mathring{Q}_p$ denotes the Fourier transform of $Q_p(t)$ and $j = \sqrt{-1}$. To validate the estimated damping ratio and to determine the gain ϕ_p, we set $\bar{\xi}_e$ according to Eq. (15) and we only vary the value of ϕ_p to fit the numerical FRFs, shown in Fig. 3, for each harmonic with their equivalent analytical ones, defined in Eq. (16). Examples of those fittings for different values of β are shown in Fig. 6 near the primary resonance. Notice the appearance of superharmonic responses, clearly observed in the H2 response in Fig. 6(c), not taken into account in our equivalent linear model.

Considering this numerical fitting, we can draw two conclusions. The first one is that the equivalent damping ratio $\bar{\xi}_e$, defined in Eq. (15), is the perfect one since the fitted equivalent linear FRFs match exactly the shape of the numerical (nonlinear) ones, by varying only the value of $\phi_{H_{\mathrm{p}}}$ to reach the perfect fit.

The second conclusion is that by fitting the analytical and numerical frequency responses for H0, H1, and H2 for different values of β, the gain ϕ_p for each of those harmonics can be estimated as a function of β (it is shown by markers in Fig. 7). Note that the estimated values of ϕ_p are firstly plotted with respect to $\log_{10}(1 - 2\beta)$ and then mapped to the values of β. Additionally, the results prove that increasing $|\beta|$ leads to more distribution of energy to the other harmonics as both ϕ_0 and ϕ_2 increase.

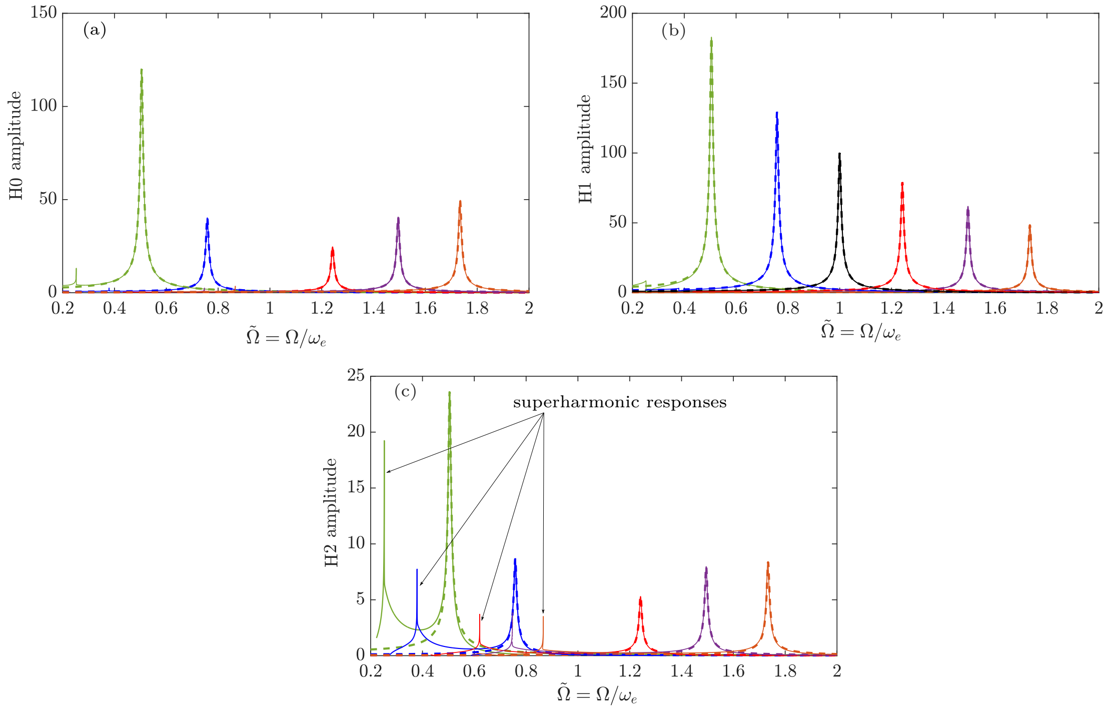

Fig. 6: Examples of the fitting between the numerical and analytical frequency responses, normalized with respect to the excitation level, of the harmonics H0 (a), H1 (b), and H2 (c). The numerical results, estimated by solving Eq. (13) with MANLAB, are depicted in solid lines and the analytical results, according to Eq. (16), are depicted in dashed lines. The fittings are performed near the primary resonance for $\beta \in \{0.444, 0.313, 0, -0.841, -5.1, -20.758\}$ and $\xi_e = 0.005$.

Compatible with the results in Fig. 3, H2 harmonic has a lower influence compared to H0 even for high values of $|\beta|$. More precisely, it appeared that the amplitude of H2 tends to a constant value as $|\beta|$ increases. On the contrary, H0 harmonic admits larger influence in which ϕ_0 suggests higher value compared to ϕ_1 for extreme values of $|\beta|$.

Table 1: Polynomial coefficients a_m of $\phi_p(\beta)$ for $\beta > 0$.

	a_0	a_1	a_2	a_3	a_4	a_5	a_6
ϕ_1	1	0.0065	-0.1432	0.0610	-0.0078	0	0
ϕ_0	0	0.7354	0.002	-0.1528	0.0547	-0.0061	0
ϕ_2	0	0.1628	0.0066	-0.0825	0.0455	-0.0102	0.0008

Interestingly, those last results suggest that ϕ_p *admits a symmetric behavior with respect to* $\log_{10}(1-2\beta)$. Thus, to obtain a closed-form approximation of ϕ_p, which will be used in the further analysis, we seek a polynomial expression of ϕ_p as:

$$\phi_p(y) = \sum_{m=0}^{N} a_m y^m, \qquad y(\beta) = -\log_{10}(1-2\beta) = -2\log_{10}\left(\frac{\eta}{2-\eta}\right), \tag{17}$$

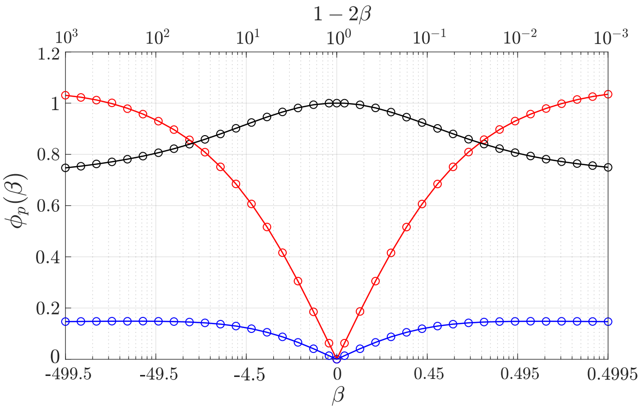

Fig. 7: ϕ_p as a function of β corresponding to harmonics H0 (red), H1 (black), and H2 (blue). The circles denote the values estimated by fitting the analytical and the numerical responses for each value of β, and the solid lines denote the closed form approximated polynomial curves.

where $N \in \mathbb{N}$ is the polynomial order and $a_m \in \mathbb{R}$ are the polynomial coefficients. Thanks to the symmetric property, the relation $\phi_p(y) = -\phi_p(y)$ can be used to estimate the coefficients a_m only for $y > 0$ (i.e., $\beta > 0$) and then directly obtain the coefficients for $y < 0$ (i.e., $\beta < 0$) by changing the sign of the coefficients a_m of the odd monomials (i.e. a_m with m odd). In addition, to take into account the fact that only H1 will respond for $y = 1$ (i.e., $\beta = 0$), we enforce constraints on a_0 for each harmonic such that $a_0 = 1$ for H1 and $a_0 = 0$ for H0 and H2. With the constraint enforcement on a_0, a good fitting between the polynomial expressions (solid lines in Fig. 7) and the obtained data (circle markers) required $N = 4$ for ϕ_1, $N = 5$ for ϕ_0, and $N = 6$ for ϕ_2. The estimated coefficients a_m for each harmonic are gathered in Table. 1 only for $\beta > 0$.

3 Response of the full system according to the tuning of the nonsmooth component

In this section, we study the response of the full system (7a,b) with two particular tunings of the nonsmooth term. Based on the analysis in section 2.2, two main points can be emphasized. First, it was shown that each harmonic of the response of the electrical oscillator could be considered separately and approximated by an equivalent linear system. This suggests using the first harmonic as an oscillator that can be tuned on one resonance of the host mechanical system to act as an RL-shunt, with the additional interest of tuning it using the nonsmooth gain β. This is investigated in section 3.1, by tuning the electrical oscillator on the i-th vibration mode, such that $\bar{\omega}_e \simeq \hat{\omega}_i$. Secondly, a nonlinear behavior was observed with the appearance of H0 and H2 harmonics and of a 1:2 superharmonic response of the electrical oscillator. This behaviour is a characteristic of a non-symmetric nonlinearity (see the curve $V_{\text{nl}} = f(V)$ in Fig. 1(b)) and suggests to investigate a 2:1 internal resonance, by tuning the electric oscillator at half the mechanical frequency ($\bar{\omega}_e \simeq \hat{\omega}_i/2$) and testing a transfer of energy from the mechanical oscillator to the electrical one, as already done using quadratic nonlinear terms in [19, 20, 22]. This is investigated in section 3.2.

3.1 One-to-one tuning of the nonlinear shunt ($\bar{\omega}_e = \hat{\omega}_i$)

3.1.1 FRF approximation

As analyzed in the previous sections, the nonlinear electrical oscillator (Eq. (7b)) oscillates with a fundamental harmonic (H1) that responds linearly around its primary resonance $\Omega \simeq \bar{\omega}_e$, suggesting that it can serve as a linear attachment similar to a standard RL-shunt. Thus, we consider here a tuning of β to have $\bar{\omega}_e = \hat{\omega}_i$: the modified electrical frequency is tuned to the open circuit natural frequency of the host structure, as a classical linear resonant shunt, expecting similar behavior.

For this tuning case, we are interested in the first harmonic response behavior. Then, we replace Eq. (7b) by its linear approximation (14). Since the external forcing is only applied on Eq. (7a), the PE coupling term $\theta/(LC_{\mathrm{p}i})q_i$ in Eq. (7b) is considered as a forcing term, thus a multiplication by ϕ_1 will be enforced based on the linear approximation in section 2.2.3. In addition, $\omega_e = 1/(\sqrt{LC_{\mathrm{p}i}})$ is replaced by the modified frequency $\bar{\omega}_e$. Thus, we arrive at the following approximation:

$$\ddot{q}_i + 2\xi_i\hat{\omega}_i\dot{q}_i + \hat{\omega}_i^2 q_i + \frac{\theta_i}{m_i C_{\mathrm{p}i}}Q = \frac{F_i}{m_i}\cos\Omega t, \tag{18a}$$

$$\ddot{Q} + 2\bar{\xi}_e\bar{\omega}_e\dot{Q} + \bar{\omega}_e^2 Q + \bar{\omega}_e^2\phi_1\theta_i q_i = 0. \tag{18b}$$

To simplify the writing of (18a,b), we define the following change of variables:

$$\tilde{t} = \hat{\omega}_i t, \quad \tilde{\Omega} = \frac{\Omega}{\hat{\omega}_i}, \quad \tilde{q}_i = \sqrt{m_i}q_i, \quad \tilde{Q} = \frac{1}{\bar{\omega}_e\sqrt{\phi_1 C_{pi}}}Q = \frac{\sqrt{L}}{\eta\sqrt{\phi_1}}Q, \quad f_i = \frac{F_i}{\hat{\omega}_i^2\sqrt{m_i}}, \tag{19}$$

where the dimensionless time $\tilde{t}$ and frequency $\tilde{\Omega}$ are different than those of section 2.2.2. The two following frequency ratios are also defined:

$$r_i = \frac{\omega_e}{\hat{\omega}_i}, \quad \bar{r}_i(\beta) = \frac{\bar{\omega}_e(\beta)}{\hat{\omega}_i}, \tag{20}$$

r_i being related to the electrical frequency ω_e and $\bar{r}_i$ its modified version due to the detuning brought by the nonsmooth term. One arrives at the following system:

$$\ddot{\tilde{q}}_i + 2\xi_i\dot{\tilde{q}}_i + \tilde{q}_i + \bar{k}_i\bar{r}_i\tilde{Q} = f_i\cos\tilde{\Omega}\tilde{t}, \tag{21a}$$

$$\ddot{\tilde{Q}} + 2\bar{\xi}_e\bar{r}_i\dot{\tilde{Q}} + \bar{r}_i^2\tilde{Q} + \bar{k}_i\bar{r}_i\tilde{q}_i = 0, \tag{21b}$$

where the derivatives are with respect to the dimensionless time τ. $\bar{k}_i$ is the modified dimensionless electromechanical modal coupling factor due to the presence of the nonsmooth term defined as:

$$\bar{k}_i(\beta) = k_i\sqrt{\phi_1(\beta)}. \tag{22}$$

Note that $\bar{k}_i$ depends on β, as suggested by the expression of ϕ_p in Eq. (17). More importantly, $\bar{k}_i$ is *smaller than the unmodified coupling factor k_i* since $\phi_1 < 1$ for for any nonzero value of β, as illustrated in Fig. 7. The physical meaning of this observation is that the nonsmooth term leads to a distribution of the energy to different harmonics, contrary to the linear case, where all the energy is transferred to the fundamental harmonic. Thus, a reduction of energy in the H1 harmonic is observed and quantified by the gain ϕ_1.

The FRFs of Eqs. (18a,b) reads:

$$H_q(\Omega) = \frac{\mathring{q}}{F} = \frac{1}{m_i}\frac{\bar{\omega}_e^2 - \Omega^2 + 2j\bar{\xi}_e\bar{\omega}_e\Omega}{D(\Omega)}, \quad H_Q(\Omega) = \frac{\mathring{Q}}{F} = \frac{-\bar{\omega}_e^2\phi_1\theta_i}{m_i}\frac{1}{D(\Omega)}, \tag{23}$$

with $D(\Omega) = (\hat{\omega}_i^2 - \Omega^2 + 2j\xi_i\hat{\omega}_i\Omega)(\bar{\omega}_e^2 - \Omega^2 + 2j\bar{\xi}_e\bar{\omega}_e\Omega) - \bar{k}_i^2\bar{\omega}_e^2\hat{\omega}_i^2$ and where $\mathring{q}$ and $\mathring{Q}$ are the Fourier transform of $q(t)$ and $Q(t)$, respectively.

3.1.2 Optimal tuning

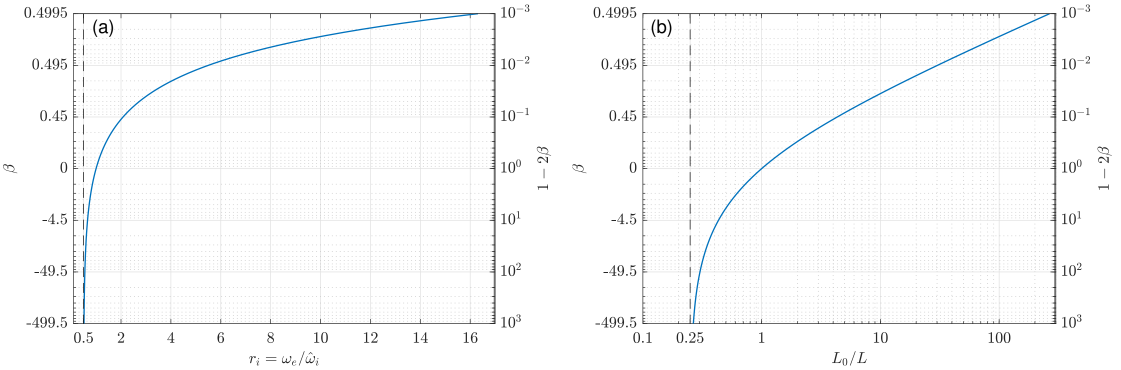

Fig. 8: Optimal value β^{op} of β to tune the RL-shunt as a function of (a) $r_i = \omega_e/\hat{\omega}_i$ and (b) as a function of the reduction ratio of the shunt inductance with respect to its optimal value for a linear RL-shunt L_0/L.

To obtain the optimal response of our modified RL-shunt, we follow the same optimization procedure as the one used for classical RL-shunts [2], as recalled in Appendix A. Comparing Eqs. (21) and (A.1), one observes that $(\bar{\omega}_e, \bar{k}_i, \bar{\xi}_e)$ replace (ω_e, k_i, ξ_e). Considering first the frequency tuning, the optimal value for the modified electrical frequency, denoted by $\bar{\omega}_e^{\mathrm{op}}$, should satisfy:

$$\bar{\omega}_e^{\mathrm{op}} = \hat{\omega}_i \quad \Rightarrow \quad \bar{r}_i^{\mathrm{op}} = 1. \tag{24}$$

Then, by substituting $\bar{\omega}_e$ from Eq. (11) in Eqs. (24), one arrives to the following optimal value of β, denoted by β^{op}, as a function of the unmodified electrical tuning ratio $r_i = \omega_e/\hat{\omega}_i$:

$$\eta^{\mathrm{op}} = \frac{\bar{\omega}_e^{\mathrm{op}}}{\omega_e} = \frac{\hat{\omega}_i}{\omega_e} = \frac{1}{r_i} \quad \Rightarrow \quad \beta^{\mathrm{op}} = \frac{1}{2}\left[1 - \frac{1}{(2r_i-1)^2}\right]. \tag{25}$$

Notice that (see Fig. 2(b)):

$$r_i \in [1, +\infty] \quad \Leftrightarrow \quad \eta \in [0,1] \quad \Leftrightarrow \quad \beta \in [0, 0.5], \tag{26a}$$

$$r_i \in [0.5, 1] \quad \Leftrightarrow \quad \eta \in [1,2] \quad \Leftrightarrow \quad \beta \in [-\infty, 0], \tag{26b}$$

such that r_i is necessary larger than 0.5.

The above equations show that the nonsmooth component brings a new degree of freedom in the tuning of the resonant shunt. In practice, one can adjust the value of the nonlinear gain such that $\beta = \beta^{\mathrm{op}}$ (Eq. (25)), bringing the modified electrical frequency close to the mechanical one, such that $\bar{\omega}_e = \hat{\omega}_i$ ($\bar{r}_i = 1$). In practice, a standard RL-shunt is tuned using the value L of the inductance, such that the electrical frequency is equal to the open-circuit mechanical one: $\omega_e = 1/\sqrt{LC_{\mathrm{pi}}} = \hat{\omega}_i$. Here, adjusting the value of β is an additional degree of freedom to tune the RL-shunt. The range of tuning can be such that $\omega_e > \hat{\omega}_i$ ($r_i > 1$): in this case $\beta^{\mathrm{op}} > 0$; on the contrary, one can have $\hat{\omega}_i/2 < \omega_e < \hat{\omega}_i$, leading to $\beta^{\mathrm{op}} < 0$. This is illustrated in Fig. 8(a), which shows the evolution of β^{op} as a function of r_i.

This new degree of freedom can be used in practice to finely adjust the tuning of an RL-shunt that has a nonoptimal value of the inductance L. It can also be used intentionally in the case of a low-frequency mechanical mode that would require a high value of L, often difficult to achieve in practice.

In this case, one chooses a smaller L than the optimal one and corrects the tuning by adjusting β. To clarify the reduction in L, we compare it with the required inductance for the optimal condition of the linear RL-shunt (see Appendix A), denoted by L_0. Considering that $\omega_e = 1/\sqrt{LC_{\mathrm{pi}}}$, one has:

$$\frac{L}{L_0} = \left(\frac{\bar{\omega}_e}{\omega_e}\right)^2 = \frac{1}{r_i^2} \quad \Rightarrow \quad L = \frac{L_0}{r_i^2}. \tag{27}$$

Thus, the inductance can be reduced by a factor of r_i^2 compared to that of the linear RL-shunt. This quadratic law can be very advantageous in practice: for instance, a value of $r_i = 10$ leads to a reduction in the inductance of a factor $L_0/L = 100$. This is illustrated in Fig. 8(b), which shows β^{op} as a function of L_0/L.

In addition to the frequency tuning, the electrical damping must also be tuned. The optimal value of the electrical damping ratio ξ_e and thus of the resistor R are obtained by:

$$\bar{\xi}_e^{\mathrm{op}} = \frac{\sqrt{6}\bar{k}_i}{4} \quad \Rightarrow \quad \xi_e^{\mathrm{op}} = \eta^{\mathrm{op}}\bar{\xi}_e^{\mathrm{op}} = \frac{\sqrt{6}}{4r_i}\bar{k}_i = \frac{\sqrt{6}}{4r_i}k_i\sqrt{\phi_1^{\mathrm{op}}} \quad \Rightarrow \quad R^{\mathrm{op}} = \frac{\sqrt{6}}{2C_{\mathrm{pi}}r_i^2\hat{\omega}_i}k_i\sqrt{\phi_1^{\mathrm{op}}}, \tag{28}$$

where $\phi_1^{op} = \phi_1(\beta = \beta^{\mathrm{op}})$ as defined by Eq. (17). Contrary to the linear RL-shunt, the optimal damping ratio ξ_e^{op} do not depend only on the coupling factor k_i, but also on the linear tuning $r_i = \omega_e/\hat{\omega}_i$ of the shunt, since ϕ_1^{op} depends on r_i through β^{op} (Eq. (25)):

$$\phi_1^{\mathrm{op}} = \sum_{m=0}^{4} a_m \left[2\log_{10}(2r_i - 1)\right]^m, \tag{29}$$

where a_m are defined in Table 1 for the first harmonic and for $\beta > 0$ ($r_i > 1$). For $\beta < 0$ ($0.5 < r_i < 1$), one must change the sign of a_m for m even, as explained in section 2.2.3.

3.1.3 Performance

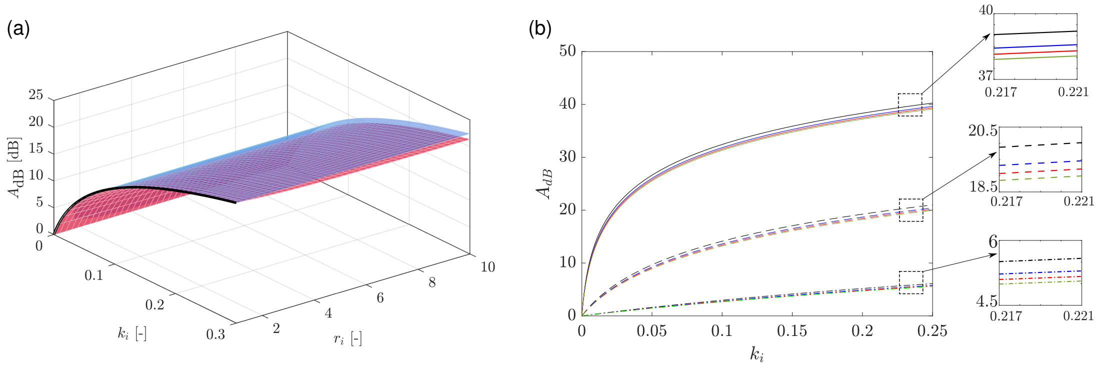

Fig. 9: Optimal attenuation A_{dB} as a function of r_i and k_i. (a) 3D plot for a linear RL-shunt (blue surface, $\beta = 0$) and for the 1:1 tuning case with the nonsmooth component (red surface), for $\xi_i = 0.01$. The black line denotes the intersection between the two surfaces at $r_i = 1$; (b) A_{dB} as function of k_i for $\xi_i = 0.001$ (solid lines), $\xi_i = 0.01$ (dashed lines), and $\xi_i = 0.1$ (dashed-dotted lines) and for each value of ξ_i, for three different values of r_i: $r_i = 10$ (in green), $r_i = 5$ (in red), $r_i = 2$ (in blue), and $r_i = 1$ (in black). The case for $r_i = 1$ denotes also the linear resonant shunt since $\beta = 0$.

The optimal attenuation A_{dB} of the nonlinear RL-shunt, in dB scale, can be obtained using the procedure of Appendix A by replacing k_i by its modified value $\bar{k}_i$. It reads:

$$A_{\mathrm{dB}} = 20\log_{10}\frac{H_q|_{\bar{k}_i=0}(\tilde{\Omega}=1)}{H_q|_{\bar{\xi}_e=\bar{\xi}_e^{\mathrm{op}}\bar{r}_i=1}(\tilde{\Omega}=1)} = 20\log_{10}\left(1+\frac{\bar{k}_i}{\xi_i\sqrt{6}}\right) = 20\log_{10}\left(1+\frac{k_i\sqrt{\phi_1^{\mathrm{op}}}}{\xi_i\sqrt{6}}\right). \qquad (30)$$

By substituting Eq. (29) in Eq. (30), we can conclude that in contrary to the linear resonant shunt case where only k_i and ξ_i are involved, the optimal attenuation depends also on the ratio r_i (and thus on the inductance). In addition, one can expect a reduction of A_{dB} as β increases due to the reduction of k_i by a factor of $\sqrt{\phi_1}$.

The dependence of A_{dB} on (k_i, ξ_i, r_i) is examined in Fig. 9. Classically, one observe that A_{dB} increases as a function of the coupling factor k_i and when the mechanical damping ratio ξ_i is decreased, in the same way than for a linear RL-shunt (see Fig. 24 in Appendix A and [2]). On the contrary, the effect of the nonsmooth term on A_{dB} appears through its dependence on the tuning ratio r_i through $\phi_1^{\mathrm{op}} = \phi_1(\beta^{\mathrm{op}})$. Fig. 9 clearly show that this dependence on r_i is very weak since A_{dB} is only slightly reduced with respect to the linear RL-shunt (with $\beta = 0 \Leftrightarrow r_i = 1$). This is an excellent result since the huge benefit of being able to decrease a lot the inductance L ($r_i = 10 \Leftrightarrow L = L_0/100$) is not counterbalanced by a significant decrease of the performance, of the order of 1 dB.

3.1.4 Numerical validation

In this section, we numerically validate the frequency response and the optimal parameters of our modified RL-shunt by considering the first twisting mode of the hydrofoil structure that will be tested experimentally in section 4 (see Fig. 17). The modal parameters corresponding to this mode are gathered in Table. 3. The numerical results are obtained by solving Eq. (7a,b) with MANLAB, considering 40 harmonics in the simulations. Then, the frequency responses of the first harmonic amplitude of the displacement u_{H1}, the charge Q_{H1}, and the PE voltage V_{H1} are obtained. Note that in what follows, the modal parameters correspond to this particular mode, and thus *the subscript i associated with the modal parameters notations is omitted in the remaining of this section.* Note also that the modal parameters are gathered in Table. 3 follow the normalization of the mode shape such that $\psi = 1$ at the point of the structure where the displacement is studied and thus according to Eq. (1), we have $u(t) = q(t)$.

As a first step, we choose the inductance L such that $\omega_e = 2\hat{\omega}$ (*i.e.* $r = 2$ and $L = 0.737$ H), meaning that the linear RL-shunt is overtuned by a factor 2. We correct this overtuning by adjusting the other parameters at their optimal value: $\beta = \beta^{\mathrm{op}} = 0.444$ (Eq. (25)) and $\xi_e = \xi_e^{\mathrm{op}}$ (Eq. (28)). The first harmonics of $u(t)$ and $Q(t)$ in the periodic steady state are shown in Figs. 10(a,b) as a function of the driving frequency Ω, for three values of the forcing F. Then, in Figs. 10(c,d), the same curves are plotted normalized by the forcing level F and superimposed to the FRFs $H_q(\Omega)$ and $H_Q(\Omega)$ (Eqs. (23)) of the linear equivalent system (18a,b). One observes a perfect match, proving first that the linearity of the response with respect to the excitation level is perfect, as well as the agreement between the full nonlinear system (7a,b) and its linear approximation (18a,b).

Fig. 11 is analogous to Fig. 10(c,d) and shows how the frequency responses are changed when the parameters β and ξ_e are changed around their optimal values β^{op} and ξ_e^{op}. Note that we chose to plot V_{H1} instead of Q_{H1} since obtaining the order of magnitudes of the voltage will be useful for the practical realization of the shunt circuit. Those plots are similar to the response of a linear RL-shunt when ω_e and ξ_e are varied around their optimal value, showing again the equivalence of our modified RL-shunt to a classical linear RL-shunt.

To validate numerically the dependence of the optimal attenuation on the frequency ratio r and, thus the inductance, as suggested in Figs. 9(a,b), Fig. 12(a) shows the numerical frequency response of u_{H1} normalized with respect to the forcing level for different values of r in which the optimal

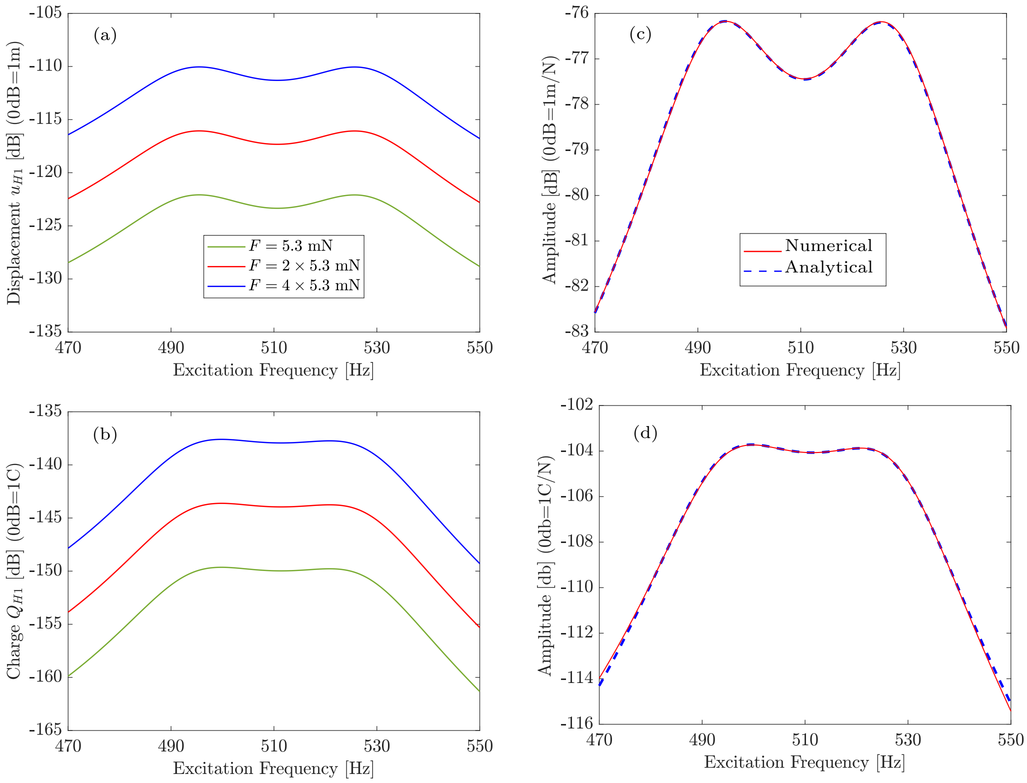

Fig. 10: (a,b): Numerical frequency response of the first harmonics u_{H1} and Q_{H1} of $u(t)$ and $Q(t)$ for increasing excitation levels; (c,d) superposition of analytical ($H_q(\mathit{\Omega})$ and $H_Q(\mathit{\Omega})$ from (23a,b) in dashed blue line) and numerical (u_{H1}/F and Q_{H1}/F in solid red line) frequency responses normalized with respect to the forcing. In the plots, optimal values are used such that $\beta = \beta^{\mathrm{op}} = 0.444$ $R = R^{\mathrm{op}} = 237.58\Omega$, estimated from Eq. (25) and Eq. (28), respectively. The modal parameters used are the ones gathered in Table. 3 and $L = 0.737\mathrm{H} \Leftrightarrow r = \omega_e/\hat{\omega} = 2$.

conditions are always satisfied (i.e., for each value of r we set $R = R^{\mathrm{op}}$, $\beta = \beta^{\mathrm{op}} \Rightarrow \bar{\omega}_e = \hat{\omega}$). Similar to Fig. 11, we consider the first twisting mode of the hydrofoil structure shown in Fig. 17. The results validate that tuning r to higher values, and thus lower inductance, reduces the optimal attenuation with respect to that of the RL-shunt while preserving the response shape. In addition, Fig. 12(b) shows the optimal attenuation A_{dB} as function of r for the RL-shunt with $\beta = 0$ (Eq. (A.4)) and for the shunt with the nonsmooth term Eq. (30). Compatible with the results in Figs. 9(a,b), the results clearly show that for higher values of r (lower values of inductance), the optimal attenuation is slightly decreased, compared to the linear RL-shunt, by $\simeq$ 1dB for a reduction of the inductance by a factor of 100 for $r = 10$, compatible with results in Figs. 9(a,b). One can note that the attenuation predicted in Eq. (30) is numerically validated by a comparison with that obtained numerically, where an excellent fitting is obtained for different values of r. Note that the numerical attenuation, shown in circle markers in Fig. (12b), is directly deduced from Fig. 12(a) by the amplitude difference in dB scale between the open circuit frequency and the optimal response at $\mathit{\Omega} = \bar{\omega}_e$.

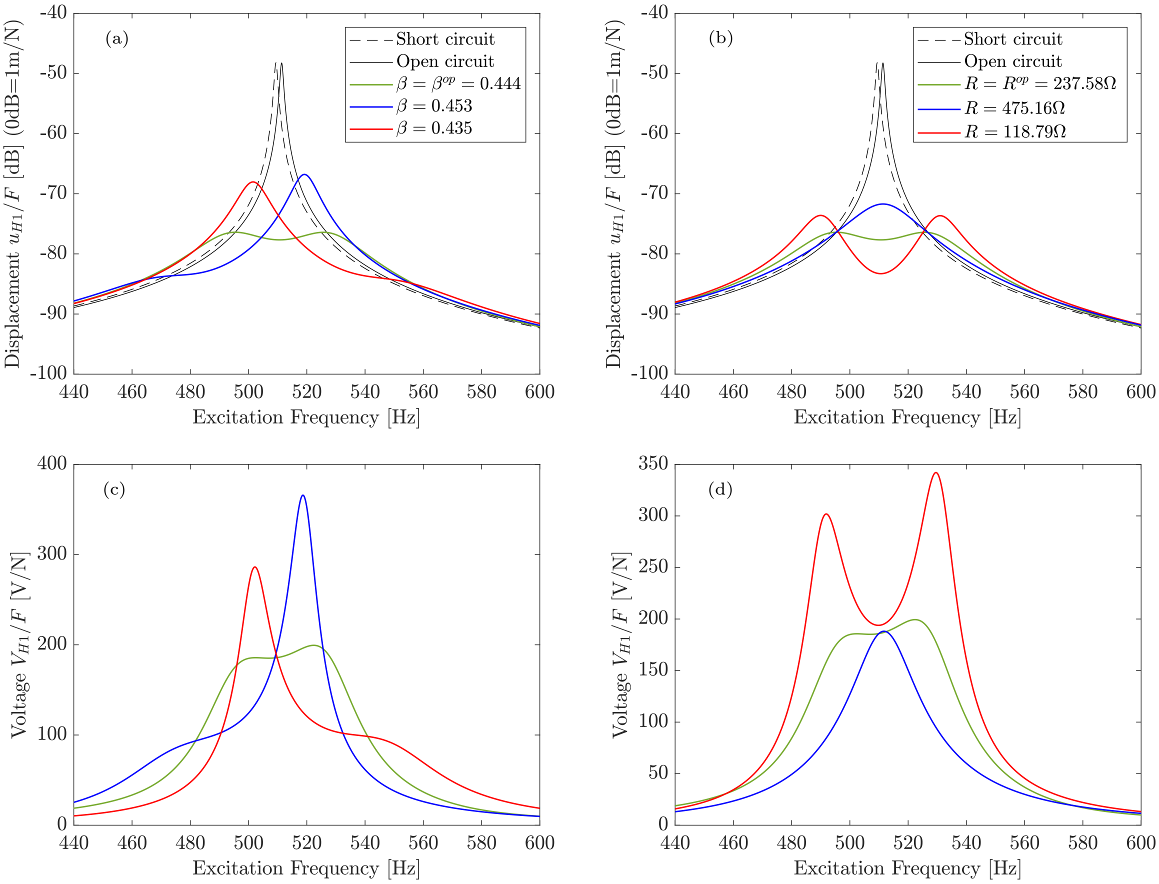

Fig. 11: Numerical frequency response of the first harmonics of u_{H1} (a,b) and V_{H1} (c,d) of $u(t)$ and $V(t)$, both normalized by the excitation level F. The response is shown for different values of β with $R = R^{\mathrm{op}} = 237.58\Omega$ (a,c) and different values of R with $\beta = \beta^{\mathrm{op}} = 0.444$ (b,d). The modal parameters used are the ones gathered in Table. 3 and $L = 0.737\mathrm{H} \Leftrightarrow r = \omega_e/\hat{\omega} = 2$.

3.2 One-to-two tuning of the nonlinear shunt ($\bar{\omega}_e = 1/2\hat{\omega}_i$)

In this section, we examine another possible tuning denoted by two-to-one (2:1) tuning such that $\bar{\omega}_e = \hat{\omega}_i/2$. Due to the nonlinearities generated by the nonsmooth term, this tuning is expected to activate a nonlinear modal coupling through a 2:1 internal resonance. As discussed in [19, 20], if quadratic nonlinear terms are present in $V_{\mathrm{nl}}(t)$, the 2:1 internal resonance leads to create an antiresonance at which the amplitude of the host structure becomes independent of the forcing level, a so-called saturation phenomenon. In this section, we investigate the behavior of our system (which includes a nonsmooth nonlinearity and not a quadratic one) in the same internal resonance condition.

3.2.1 Validation of the occurrence of the 2:1 internal resonance

To validate the energy transfer through the 2:1 internal resonance, we focus on the first harmonic response of the displacement amplitude u_{H1} and the first subharmonic response of the charge $Q_{\mathrm{H1/2}}$. We consider them dominant in the Fourier series like in a classical 2:1 internal resonance energy

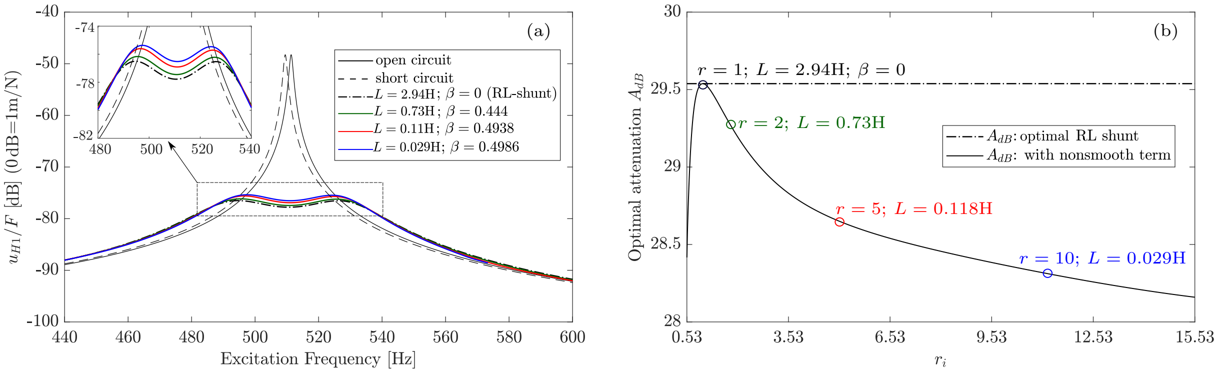

Fig. 12: (a) Numerical frequency response of the first harmonic u_{H1} of the displacement $u(t)$, normalized with respect to the forcing level F, for different values of the ratio r and by satisfying the optimal conditions in Eq. (25) and Eq. (28). (b) Optimal attenuation for the case of RL-shunt (Eq. (A.4)) and the case with the nonsmooth component with one to one tuning (Eq. (30)). The circle markers are the attenuation obtained numerical frequency responses for each value of r. The modal parameters used are the ones gathered in Table. (3).

transfer (see [19]) and we express $u(t)$ and $Q(t)$ as:

$$u(t) = u_{\mathrm{H1}} \cos\left(\Omega t - \gamma_2\right) + \mathrm{oh}, \tag{31a}$$

$$Q(t) = Q_{\mathrm{H1/2}} \cos\left(\frac{\Omega}{2}t - \frac{\gamma_1 + \gamma_2}{2}\right) + \mathrm{oh}, \tag{31b}$$

where “oh” denotes other harmonics, including the contribution of the H0 and H2 harmonics due to the presence of the nonsmooth term. γ_2 is the phase angle of the first harmonic of the displacement with respect to the forcing, and γ_1 can be considered as the relative phase angle between the two oscillators, which is proved to be locked at $3\pi/2$ at the antiresonance frequency in the case of 2:1 internal resonance [19].

Similar to the 1:1 tuning case in section 3.1, the electrical frequency is tuned according to the nonsmooth gain β with no condition on the inductance value. Thus, the 2:1 tuning condition requires tuning β as:

$$\bar{\omega}_e = \frac{1}{2}\hat{\omega} \quad \Rightarrow \quad \beta = \frac{1}{2}\left[1 - \left(\frac{1}{4r_i - 1}\right)^2\right] \tag{32}$$

To test the ability of activating the 2:1 internal resonance, we solve numerically the system (2a,b) by setting β according to Eq. (32) with an arbitrary low electrical damping ratio and using the modal parameters in Table. 3. In addition, the inductance $L = 2.948$ H is chosen to have $r = \omega_e/\hat{\omega} = 1$. The results are shown in Fig. 13, which clearly shows that a nonlinear energy transfer occurs from the first harmonics H1 of $u(t)$ to the subharmonic H1/2 of $Q(t)$. This energy transfer occurs after pitchfork bifurcation “PF” (or period-doubling bifurcation), in a frequency band centered around the mechanical resonance, at $\Omega \simeq \hat{\omega}_i$.

However, contrary to a classical 2:1 internal resonance produced by quadratic nonlinear terms (as in [19]), the topology of the coupled response curve is completely different and *does not show any saturation phenomenon.* They appear with a shape very close to the response of a linear RL-shunt. This suggests to consider the second harmonic of $Q(t)$ (which is H1 here) as *an equivalent linear oscillator that can be optimized as a classical RL-shunt to mitigate the resonance of the i-th mode of the host structure.* Following this idea, as seen in Fig. 13(a), the tuning of β according to Eq. (32)

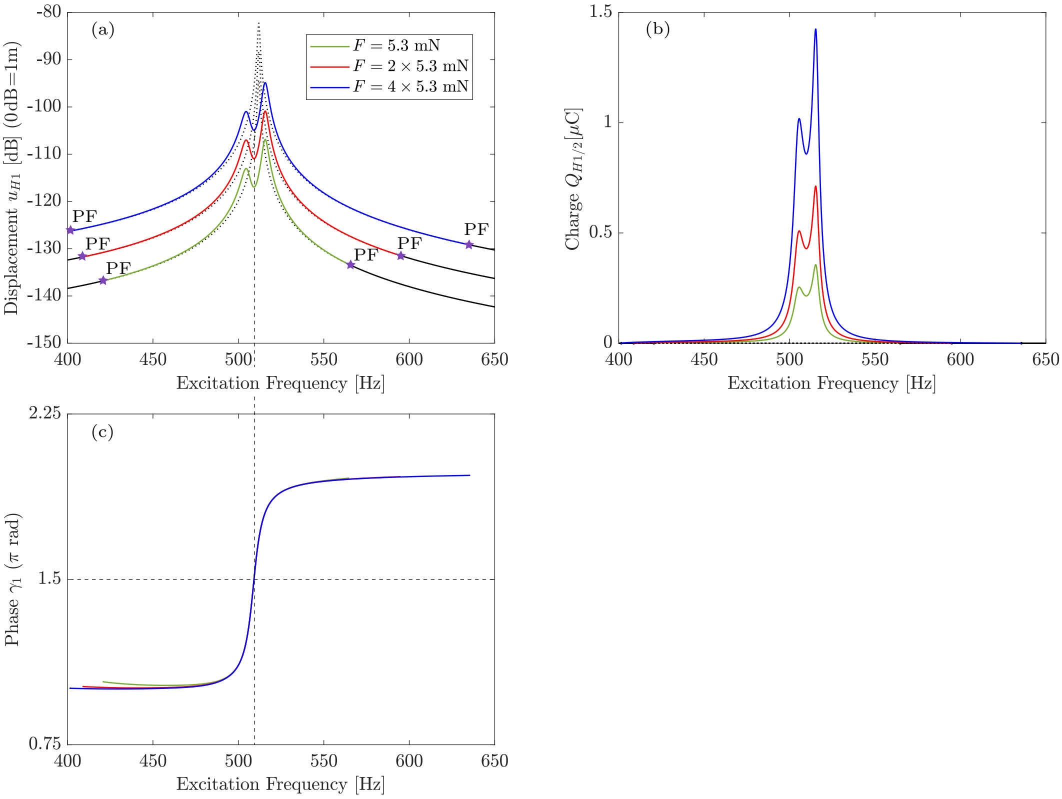

Fig. 13: (a) and (b) show respectively the numerical frequency response of u_{H1} and $Q_{\mathrm{H1/2}}$ for increasing excitation levels. (c) shows the relative phase γ_1 between the two oscillators. The linear response is plotted in black. The stable and unstable responses are depicted in solid and dotted lines, respectively. The purple star denotes the pitchfork bifurcation (PF). The numerical values used are $\beta = 0.444$, $R = 36\Omega$, $L = 2.948$H. The modal parameters used are the ones gathered in Table. 3.

and the chosen ξ_e do not lead to an optimal response, that would be characterized by a symmetric shape and minimal peaks, as observed in Fig. 11 for the 1:1 tuning case. Thus, an optimization study is necessary to obtain the optimal values of β and ξ_e to achieve an optimal attenuation similar to that of a linear RL-shunt.

Another important feature concerns the relative phase γ_1 that locks at $3\pi/2$ at the antiresonance frequency, independent from the excitation level. This feature was proved analytically and numerically in [19] with the addition of quadratic nonlinearities in the shunt circuit. As seen in Fig 13c, the same phase lockage is equally preserved, which can be exploited for tuning the system in practical implementation, similar to the experimental study in [20].

3.2.2 Optimization study

Similar to the case with 1:1 tuning, the optimization is established through the nonsmooth gain β to tune the electrical resonance frequency and the electrical damping ratio ξ_e (thus the resistance R), to obtain a mechanical frequency response as low and flat as possible. Two points are considered for this optimization: (i) we are looking for an optimal value of β that symmetrizes the frequency response, as for a classical RL-shunt; (ii) the coupled response is obtained through a 2:1 internal resonance, as observed in the previous section.

As shown in [19], the symmetric response with a 2:1 internal resonance requires a ratio between the electrical frequency $\bar{\omega}_e$ and the mechanical one $\hat{\omega}_i$ to be slightly higher than half (i.e., contrary to the tuning in (Eq. (32)). The exact value of this ratio, denoted by r_i^*, can be estimated by setting $\omega_2 = 2\omega_1$ where ω_2 and ω_1 are the natural frequencies in the electro-mechanical basis (see Appendix C and [19]). The obtained r_i^* depends only on the piezoelectric coupling factor k_i as follows:

$$r_i^* = \sqrt{\frac{1}{8}\left(17 - 25k_i^2 - 5\sqrt{25k_i^4 - 34k_i^2 + 9}\right)}. \tag{33}$$

Given the value of r_i^*, the optimal value of β is then estimated as:

$$\bar{\omega}_e^{\mathrm{op}} = r_i^* \hat{\omega}_i \quad \Rightarrow \quad \eta^{op} = \frac{r_i^*}{r_i} \quad \Rightarrow \quad \beta^{\mathrm{op}} = \frac{1}{2}\left[1 - \left(\frac{r_i^*}{2r_i - r_i^*}\right)^2\right] \tag{34}$$

Since it is the second harmonics of the charge $Q(t)$ that is coupled to the primary (mechanical) oscillator, we consider for the optimization its equivalent linear oscillator, as defined by Eq. (14) in section 2.2.3 with $p = 2$. Thus, the key point is to modify the piezoelectric coupling through the gain ϕ_2. Following the same reasoning as in section 3.1.1, the modified PE coupling factor for the two-to-one tuning case can be expressed as:

$$\bar{k_i}^* = k_i \sqrt{\phi_2(\beta)}. \tag{35}$$

We then express the optimal value of ξ_e (and the resistance R) as follows:

$$\bar{\xi}_e^{\mathrm{op}} = \frac{\sqrt{6}}{4}\bar{k}_i^*, \quad \Rightarrow \quad \xi_e^{\mathrm{op}} = \frac{\sqrt{6} r_i^* \bar{k}_i^*}{4 r_i} = \frac{\sqrt{6} r_i^* k_i \sqrt{\phi_2^{\mathrm{op}}}}{4 r_i} \quad \Rightarrow \quad R^{\mathrm{op}} = \frac{\sqrt{6} r_i^*}{2 C_{\mathrm{p}_i} r_i^2 \hat{\omega}_i} k_i \sqrt{\phi_2^{\mathrm{op}}}, \tag{36}$$

where $\phi_2^{op} = \phi_2(\beta = \beta^{\mathrm{op}})$ to satisfy the optimal conditions. Considering Eq. (17) and (34), on has:

$$\phi_2^{\mathrm{op}} = \sum_{m=0}^{6} a_m \left[2 \log_{10}\left(\frac{2r_i - r_i^*}{r_i^*}\right)\right]^m, \tag{37}$$

where a_m are defined in Table 1 for the second harmonic. The optimal attenuation can then be expressed as:

$$A_{\mathrm{dB}} = 20 \log_{10}\left(1 + \frac{\bar{k_i}^*}{\xi_i \sqrt{6}}\right) = 20 \log_{10}\left(1 + \frac{k_i \sqrt{\phi_2^{\mathrm{op}}}}{\xi_i \sqrt{6}}\right). \tag{38}$$

Similar to 1:1 tuning case, the optimal attenuation depends explicitly on r_i (thus the inductance) but with a reduction of the piezoelectric coupling factor by $\sqrt{\phi_2}$. Thus, a further reduction of the attenuation compared to that of the linear resonant shunt is expected since ϕ_2 admits an order of magnitude lower than that of ϕ_1, as suggested in Fig. 7. This is further illustrated in Fig. 14 by comparing A_{dB} of the 2:1 tuning case and that of a linear RL-shunt.

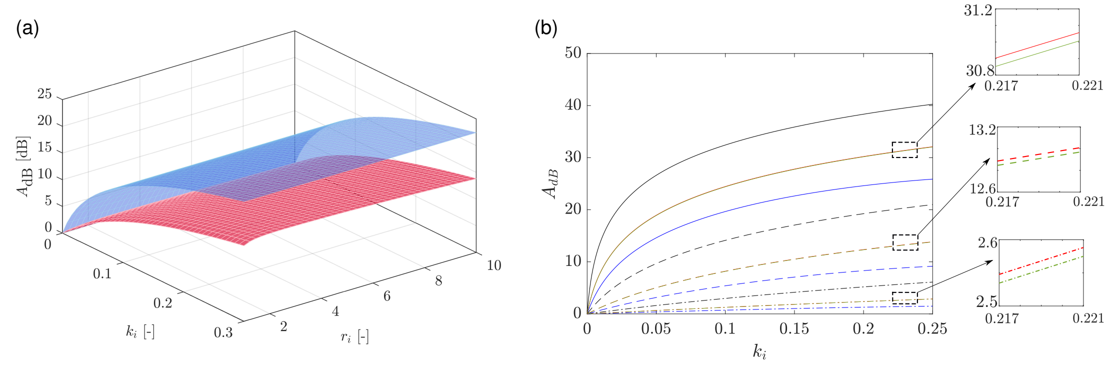

Fig. 14: Optimal attenuation A_{dB} as a function of r_i and k_i. (a) 3D plot for a linear RL-shunt (blue surface, $\beta = 0$) and for the 2:1 tuning case with the nonsmooth component (red surface), for $\xi_i = 0.01$; (b) A_{dB} as function of k_i for $\xi_i = 0.001$ (solid lines), $\xi_i = 0.01$ (dashed lines), and $\xi_i = 0.1$ (dashed-dotted lines) and for each value of ξ_i, for three different values of r_i: $r_i = 10$ (in green), $r_i = 5$ (in red), $r_i = 2$ (in blue), and $r_i = 1$ (in black). The case for $r_i = 1$ denotes also the linear resonant shunt since $\beta = 0$.

3.2.3 Numerical validation

In order to validate the results suggested from the optimal analysis, we solve numerically the system (7a,b) to obtain the frequency responses of u_{H1} and $V_{\mathrm{H1/2}}$ for different values of β and R (thus ξ_e) including the optimal conditions in Eq. (34) and Eq. (36), respectively. This is shown in Fig. 15 in which we choose the inductance such that $r = 1 \Leftrightarrow L = 2.948$ H.

Similar to the plots in section 3.1.4, we consider the first twisting mode of the foil shown in Fig. 17. The results clearly suggest that setting R and β according to the obtained optimal conditions enables the recovery of the symmetric behavior and the minimization of the peaks near the resonance frequency. It is worth mentioning that the response is very sensitive to any small perturbation of the optimal value of β (observe the very close values of β used in Figs. 15(a,c)).

Regarding the optimal attenuation, one can realize that Eq. (38) shares similar behavior compared to that of the 1:1 tuning case in Eq. (30) in which the attenuation depends on the inductance. However, as observed in Fig. 7 and contrary to the behavior of ϕ_1, the value of ϕ_2 increases with β then tends to admit a constant value as β increases. This suggests that *decreasing the inductance and thus the optimal value of β leads to enhancing the optimal attenuation*, contrary to the one-to-one tuning case. To validate this result, we perform a similar analysis to that in section 3.1.4 (in Fig. 12) by studying the frequency response of u_{H1} at the optimal condition with different values of the inductance. The numerical results in Fig. 16(a) clearly validate the increase of the attenuation as the inductance decreases, which can also be seen in Fig. 16(b), where the optimal attenuation is plotted versus the inductance value. In addition, it is realized that the attenuation increases up to a certain level where it remains almost constant as the inductance decreases. This behavior is explained by the presence of ϕ_2 in the optimal attenuation expression, which admits the same trend versus β as shown in Fig. 7. Moreover, comparing the numerical attenuation obtained numerically and analytically shows an excellent fitting, validating the attenuation expression in Eq. (38). It is also worth mentioning that the attenuation in this tuning case is reduced compared to the optimized RL-shunt with a narrower bandwidth due to the substantial reduction of the coupling factor suggested in Eq. (35) since ϕ_2 admits a very low amplitude.

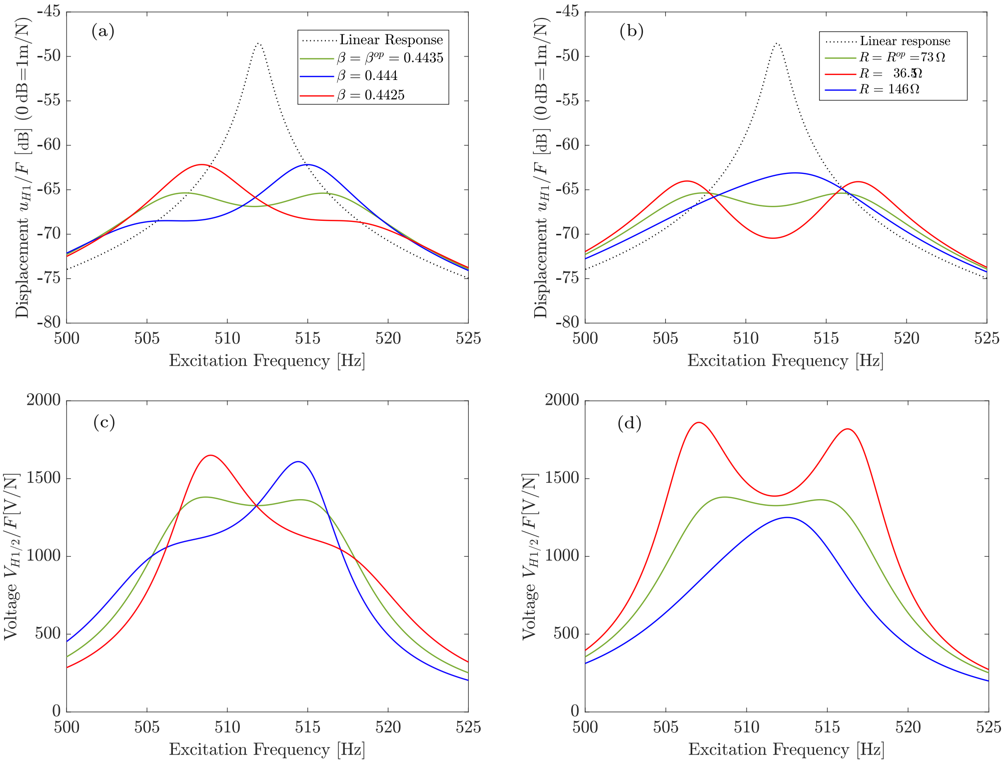

Fig. 15: Numerical frequency response of the first harmonic of the velocity u_{H1} (first row) and the PE voltage $V_{\mathrm{H1/2}}$ (second row), both normalized with respect to the excitation level. The response is shown for different values of β with $R = R^{\mathrm{op}} = 73\Omega$ (first column) and different values of R with $\beta = \beta^{\mathrm{op}} = 0.4435$ (second column). The inductance value used in the simulations is $L = 2.94\mathrm{H} \implies r = \omega_e/\hat{\omega} = 1$. The stable and unstable responses are depicted in solid and dotted lines, respectively. The displacement and voltage responses are plotted in dB and linear scales, respectively.

3.3 Summary

The introduced nonsmooth term enables tuning the electric resonance frequency of the shunt circuit while setting a low inductance in the circuit. In addition, it suggests a multi-harmonic response dominated by the zeroth, first, and second harmonics that appeared to be similar to that of a linear oscillator. In addition, strong nonlinearities appeared in the superharmonic response. A 1:1 and 2:1 tuning cases has been studied through the approximation of the main system (7a, b) to an approximated system in (18a,b) by modifying (and reducing) the piezoelectric coupling factor by $\sqrt{\phi_1}$ and $\sqrt{\phi_2}$ for the 1:1 and 2:1 tuning, respectively. In either case, closed-form expressions of the optimal values of β and R in addition to optimal attenuation are determined and gathered in Table. 2. Contrary to the linear resonant shunt, the frequency ratio r_i (thus the inductance) appears explicitly in the attenuation expression. The 1:1 tuning case shows an important feature in which one can reduce the required inductance by a factor of 100 for an attenuation reduction around 1dB compared to that of a linear resonant shunt. While for the 2:1 tuning case, a substantial reduction of the attenuation is observed but with an interesting feature in which the attenuation increases with the reduction of the inductance up to a certain level where it stays almost constant. The analytical results were then validated numerically by applying the absorber to attenuate the first twisting mode of a hydrofoil

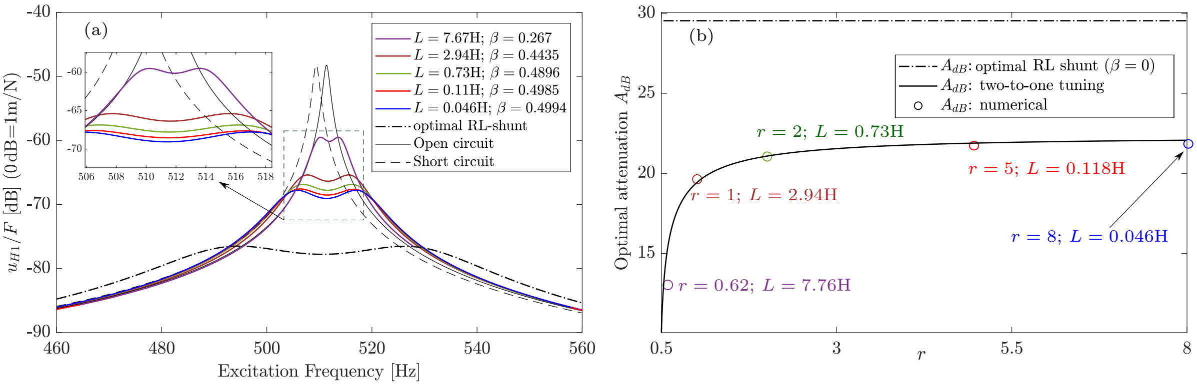

Fig. 16: (a) Frequency response of the first harmonic of the displacement, normalized with respect to the forcing level, for different values of the ratio r and by satisfying the optimal conditions in Eq. (34) and Eq. (36). (b) Optimal attenuation for the case of RL-shunt (Eq. (A.4)) and the case with the nonsmooth component with two to one tuning (Eq. (38)). The circle markers are the attenuation obtained numerical frequency responses for each value of r. The modal parameters used are the ones gathered in Table. (3).

structure. Considering also the first twisting mode of the hydrofoil, an experimental validation will be shown in the next section.

Table 2: Optimal parameters and optimal attenuation for the 1:1 and 2:1 tuning cases.

Case	Optimal β	Optimal R	Optimal attenuation [dB]
1:1 tuning	$\beta^{\mathrm{op}} = \frac{1}{2}\left[1 - \left(\frac{1}{2r_i - 1}\right)^2\right]$	$R^{\mathrm{op}} = \frac{\sqrt{6}}{2C_{\mathrm{pi}} r_i^2 \hat{\omega}_i} k_i \sqrt{\phi_1^{\mathrm{op}}}$	$A_{\mathrm{dB}} = 20\log_{10}\left(1 + \frac{k_i}{\xi_i\sqrt{6}}\sqrt{\phi_1^{\mathrm{op}}}\right)$
2:1 tuning	$\beta^{\mathrm{op}} = \frac{1}{2}\left[1 - \left(\frac{r_i^*}{2r_i - r_i^*}\right)^2\right]$	$R^{\mathrm{op}} = \frac{\sqrt{6}r_i^*}{2C_{\mathrm{p}_i} r_i^2 \hat{\omega}_i} k_i \sqrt{\phi_2^{\mathrm{op}}}$	$A_{\mathrm{dB}} = 20\log_{10}\left(1 + \frac{k_i}{\xi_i\sqrt{6}}\sqrt{\phi_2^{\mathrm{op}}}\right)$

4 Experimental Validation

4.1 Experimental setup

The experimental tests were conducted on a clamped-free foil structure fixed at its base in a vice, as shown in Fig. 17. This structure is similar to the one used in [22, 46]. Three PE patches are glued on cavities machined on the surfaces of the foil: on one face (denoted patches 1, 2), two P-876.A15 DuraAct polymer coated multi-layer piezoelectric patches are used for transduction with the first bending mode, whereas a macro-fiber composite M8557-F1 with 45° fiber orientation is used on the other face (denoted patch 3) for coupling with the first twisting mode. In all the tests of this article, only patch 3 is used since we focus on the first twisting mode. Consequently, patch 3 is connected to the shunt circuit, and patch 1 and 2 are short-circuited. The three PE patches are from the PI Ceramic manufacturer.

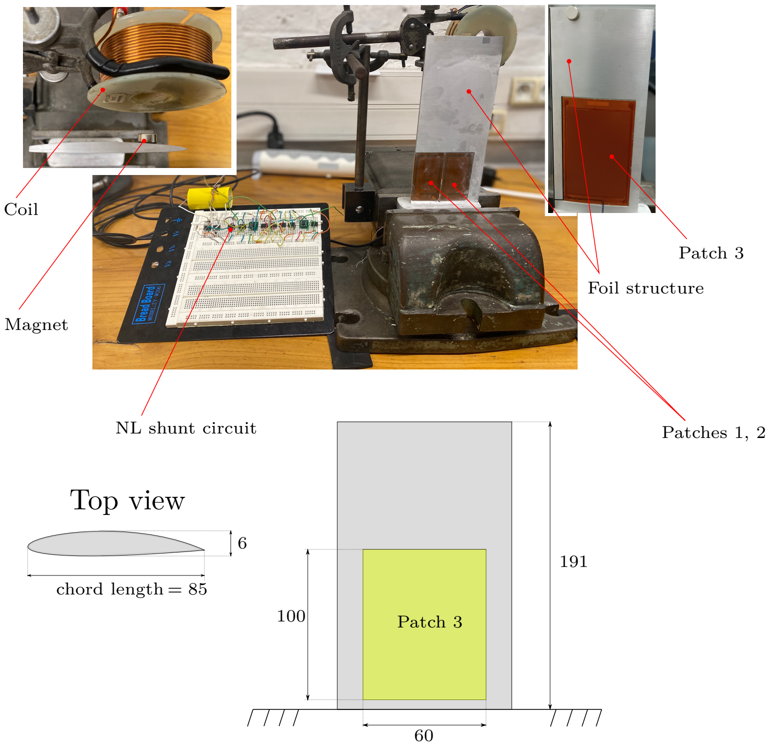

Fig. 17: Experimental Setup. Dimensions are in mm. The thickness of the PE patches is 1mm.

The mechanical excitation is realized by a coil interacting with a magnet fixed on the foil. The applied force is proportional to the current in the coil i.e $F(t) = \alpha I(t)$, where $\alpha = 0.6\ \mathrm{N\,A^{-1}}$ [20], with very low distortion [47]. A Brüel & Kjær 2719 power amplifier, connected to the coil, is used for all mechanical excitations. The foil vibrations are measured with a Polytec OFV-505 vibrometer, that provides the velocity of a point colocalized with the magnet location, close to the tip of the foil. Electrical measurements are performed using a PHILIPS PM 9355 precision current probe in the piezoelectric circuit to obtain the charge $Q(t)$ and a *Française d'Instrumentation* ST 500-5 differential voltage probe to measure the PE patch voltage $V(t)$.

To properly design the nonlinear shunt, we firstly performed an experimental modal analysis, equivalent to that in [20, 22], to obtain the modal characteristics of the first twisting mode of the foil, which are gathered in Table. 3. Note that since we tackle only the twisting mode, the subscript i will be omitted in what follows.

Table 3: Electro-mechanical modal parameters.

Parameter	$\breve{\omega}/(2\pi)$	$\hat{\omega}/(2\pi)$	ξ	m	C_p	θ	k	$\psi(\boldsymbol{x}_m)$
Value	509.4 Hz	511.36 Hz	0.0012	10.42 g	32.8 nF	5.2 mN/V	0.0875	1

Note that $\psi(\boldsymbol{x}_m) = 1$ means that the modal parameters are estimated by scaling the mode shape at the measurement point of the structure $\boldsymbol{x}_m$ to be unity, thus according to Eq. 1, $u(t) = q(t)$ (i.e., the same scaling of the mode shape considered in the previous section).

4.2 Nonsmooth shunt circuit

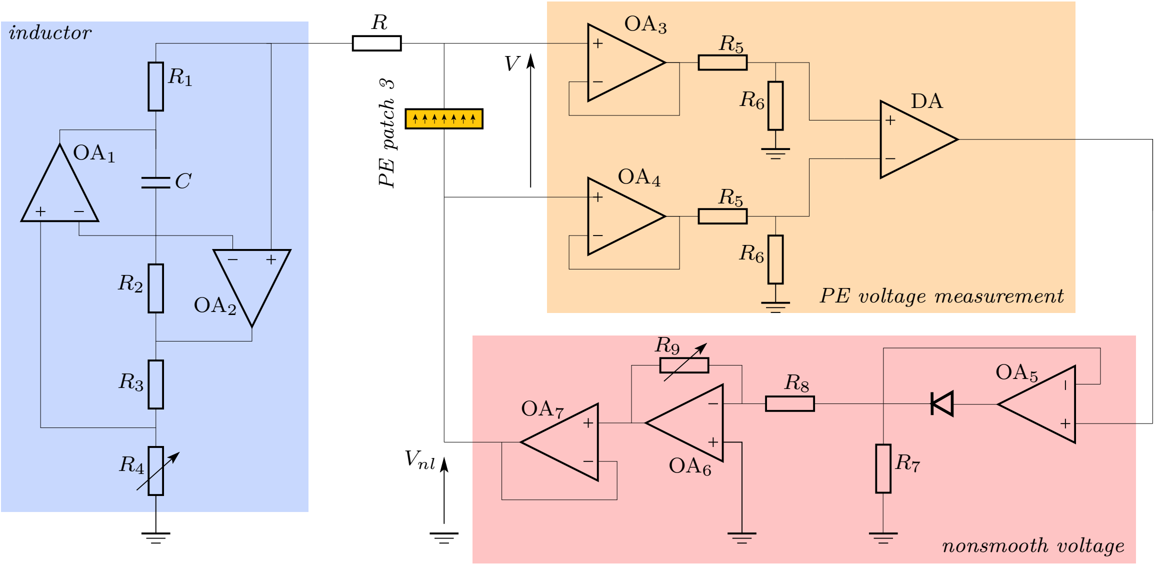

Fig. 18: Shunt circuit schematic.

Table 4: Component values in the nonlinear shunt circuit of Fig. 18

Component	R_1 [kΩ]	R_2 [kΩ]	R_3 [kΩ]	C [μF]	R_5 [kΩ]	R_6 [kΩ]	R_7 [kΩ]	R_8 [kΩ]
Value	2	1	1	10	82	22	10	10

The nonlinear shunt circuit used for the tests is shown in Fig. 18. It consists of three interconnected sub-circuits to realize (i) a tunable synthetic inductor (outlined in blue); (ii) a voltage measurement (outlined in orange), and (iii) a nonlinear voltage generator (outlined in light red). To handle the large voltage levels that can appear, especially during transients, the operational amplifiers OA$_1$ to OA$_7$ are OPA445 (Texas Instrument) which can operate up to ±40V and supply 15mA to drive the patches. The synthetic inductor is a so-called Antoniou circuit [48] to achieve the high inductance value needed to obtain an electrical resonance frequency close to half of the mechanical resonance frequency. The inductance value is given by

$$L = \frac{R_1 R_2 R_4 C}{R_3}, \tag{39}$$

where L is tuned using the variable resistance R_4.

As discussed in section 3, the *electric resonance frequency is controlled solely with the nonsmooth gain β according to a free choice of the inductance L*. In all the experimental tests in this study, and for different tunings of the shunt circuit, the value of L is always chosen to be less than 3 H. For such values, the parasitic resistance generated by the Antoniou inductor, observed in [20], is to the order of 0.1Ω and will be neglected here. Thus, the resistor R in the shunt models corresponds to a physical resistance added to tune the electrical damping. Note that the parasitic resistance is estimated with a frequency-to-bandwidth ratio of the electrical resonance, close to $\Omega = \omega_e$, in linear operation, with $\beta = 0$.

The PE voltage measurement is established through two voltage dividers composed of R_5 and R_6 and two voltage followers OA_3 to OA_4 (OPA445, Texas Instrument) to ensure a large input impedance. The voltage dividers are used to attenuate the voltage to values compatible with the differential amplifier DA (INA826, Texas Instrument). Since the PE patch is not grounded, these voltages are first fed to the differential amplifier DA. The nonsmooth voltage with the absolute function, as in Eq. (6), is generated through a half-wave rectifier circuit composed of OA_5, a diode (1N4002), and a resistor R_7 connected to the ground. The output voltage of the half-wave rectifier circuit is fed to an inverting amplifier, realized with OA_6, to respect the assumed sign convention of the nonsmooth voltage in (2a,b) and to control the nonsmooth gain β. The follower OA_7 is used to minimize the output impedance while protecting the INA826 from excessive current. The nonsmooth gain β is controlled according to the variable resistor R_9 as:

$$\beta = \frac{1}{2}\left(\frac{R_6}{R_5 + R_6}\right)\frac{R_9}{R_8}. \tag{40}$$

Note that changing the sign of the nonsmooth voltage can be done by flipping the polarity of the diode without using the inverting amplifier. However, for such a case, the nonsmooth gain will be controlled either by a voltage divider composed of R_5 and R_6 or by adding a new voltage divider instead of the inverting amplifier. In the first case, and for certain values of β, one might risk achieving a voltage at the input of the DA higher than the operating levels. In the second case, a restriction on the value of β is presented. Thus, we prefer to use the inverting amplifier so that the sign convention is respected with easy controllability of the nonsmooth gain.

4.3 Measurement protocol

The experimental tests aim to verify the results suggested theoretically in section 3, and thus we consider the same tuning cases, namely, the 1:1 and 2:1 tuning. It is proved that the former case leads to a fully linear response near the resonance frequency while the latter activates the 2:1 internal resonance and thus leads to the response of the subharmonic of the charge. Since the mode shape is scaled to verify $\psi(\boldsymbol{x}_m) = 1$, we express the time signals of the displacement $u(t)$ and the charge $Q(t)$ for the 1:1 tuning as:

$$u(t) = u_{\mathrm{H1}}\cos(\Omega t - \delta_1) + \mathrm{oh}, \tag{41a}$$

$$Q(t) = Q_{\mathrm{H1}}\cos(\Omega t - \delta_2) + \mathrm{oh}, \tag{41b}$$

and for the 2:1 tuning case, we include the subharmonic response such that [19]:

$$u(t) = u_{\mathrm{H1}}\cos(\Omega t - \gamma_2) + u_{\mathrm{H1/2}}\cos\left(\frac{\Omega}{2}t - \frac{\gamma_1 + \gamma_2}{2}\right) + \mathrm{oh}, \tag{42a}$$

$$Q(t) = Q_{\mathrm{H1}}\cos(\Omega t - \gamma_2) + Q_{\mathrm{H1/2}}\cos\left(\frac{\Omega}{2}t - \frac{\gamma_1 + \gamma_2}{2}\right) + \mathrm{oh}, \tag{42b}$$

where u_{H1} and $u_{\mathrm{H1/2}}$ are respectively the amplitude of the first and subharmonic of the displacement and Q_{H1} and $Q_{\mathrm{H1/2}}$ are respectively the amplitude of the first and subharmonic of the charge. δ_1 and δ_2 are the phase angles of first harmonic of $u(t)$ and $Q(t)$ for 1:1 tuning case. γ_2 is the phase angle of the first harmonic of $u(t)$ for the 2:1 tuning case. Note that δ_1, δ_2, and γ_2 are measured with respect to the forcing. γ_1 is the relative phase angle between the first and the subharmonic, which is estimated to be locked at $3\pi/2$ at the antiresonance frequency associated with the 2:1 internal resonance [19, 20]. "oh" denotes the other harmonics, in particular, the zeroth and the second harmonics, generated due to the nonsmooth component.

In practice, the amplitude and phase angles of the harmonics of $u(t)$ and $Q(t)$ can be obtained by measuring the foil tip velocity $v(t)$ with the laser vibrometer and the voltage across the PE patch terminals $V(t)$ using the differential voltage probe (see the procedure in [20]). In what follows, we chose to show the experimental frequency response of u_{H1}, instead of v_{H1}, in both tuning cases because it will be more convenient to validate the optimization results suggested theoretically (see Table. 2). In addition, we chose to show V_{H1} and $V_{\mathrm{H1/2}}$ in the 1:1 and 2:1 tuning cases, respectively, instead of Q_{H1} and $Q_{\mathrm{H1/2}}$, since it will be useful to obtain the voltage level to ensure that it does not exceed the operating limits of the operational and differential amplifiers in the shunt circuit (see Fig. 18). Indeed, the subharmonic response is measured for the 2:1 tuning case to validate the energy transfer and, thus, the activation of the 2:1 internal resonance.

Note that in either tuning case, the frequency responses will be shown normalized with respect to the forcing, following the results in section 3, which suggest that the response curves are linear with respect to the excitation. To estimate the forcing F in [N], the current I in the coil is measured using a PHILIPS PM 9355 precision current probe, then the relation $F = \alpha I$ is used.

To establish the amplitude and phase frequency responses, we consider two different procedures for the 1:1 and 2:1 tuning cases. In the former case, the frequency response is directly estimated by exciting the foil with a chirp signal of time-varied excitation frequency using the coil/magnet system. This method can be extended to realize the frequency response for the 1:1 tuning case since it is proved in section 3.1 that the response is fully linear near the resonance frequency (i.e., no bifurcations or change of stability). In addition, we consider the first harmonics to be dominant in comparison with the zeroth and second harmonics for the range of β used in this study. Thus, the multi-harmonic nature of the response at the steady state will not lead to a significant effect on the measured frequency response. In the 2:1 tuning case, the chirp signal method is not suitable due to the bifurcation and change of stability associated with the response. Thus the sine-stepped method is used instead, similar to that in [20]. Namely, a sine current with fixed intensity is fed to the coil/magnet device to generate a harmonic force $F = F_0 \cos \mathit{\Omega} t$. Then, the excitation frequency $\mathit{\Omega}$ is increased (or decreased) by steps, keeping the intensity fixed, sweeping a domain close to the resonance frequency of the first twisting mode of the foil. For each frequency, the harmonics amplitude and phases of the velocity (thus the displacement) and the PE voltage are extracted in the steady state using the demodulation technique explained in [20]. The input/output signals were synthesized/measured with National Instrument cards (NI-9234, NI-9263) driven by a Matlab program.

5 Experimental Results

5.1 Experimental validation of the theoretical results

In order to validate the numerical predictions in section 3 and, in particular, the estimated optimal parameters, a comparison between the numerical and experimental results is presented in Fig. 19 for the 1:1 and 2:1 tuning cases. In the former case, the frequency responses of u_{H1} and V_{H1} in addition to δ_1 are shown. In the latter case, u_{H1} and $V_{\mathrm{H1/2}}$ in addition to the phase γ_1 and γ_2 are presented. Moreover, in the 1:1 tuning case, the inductance $L = 0.73$H is chosen such that $r = \omega_e/\hat{\omega} = 2$ while for the 2:1 tuning case, $L = 2.94$H is chosen such that $r = \omega_e/\hat{\omega} = 1$. In either case, the values of β and R are set according to their optimal conditions gathered in Table 2.

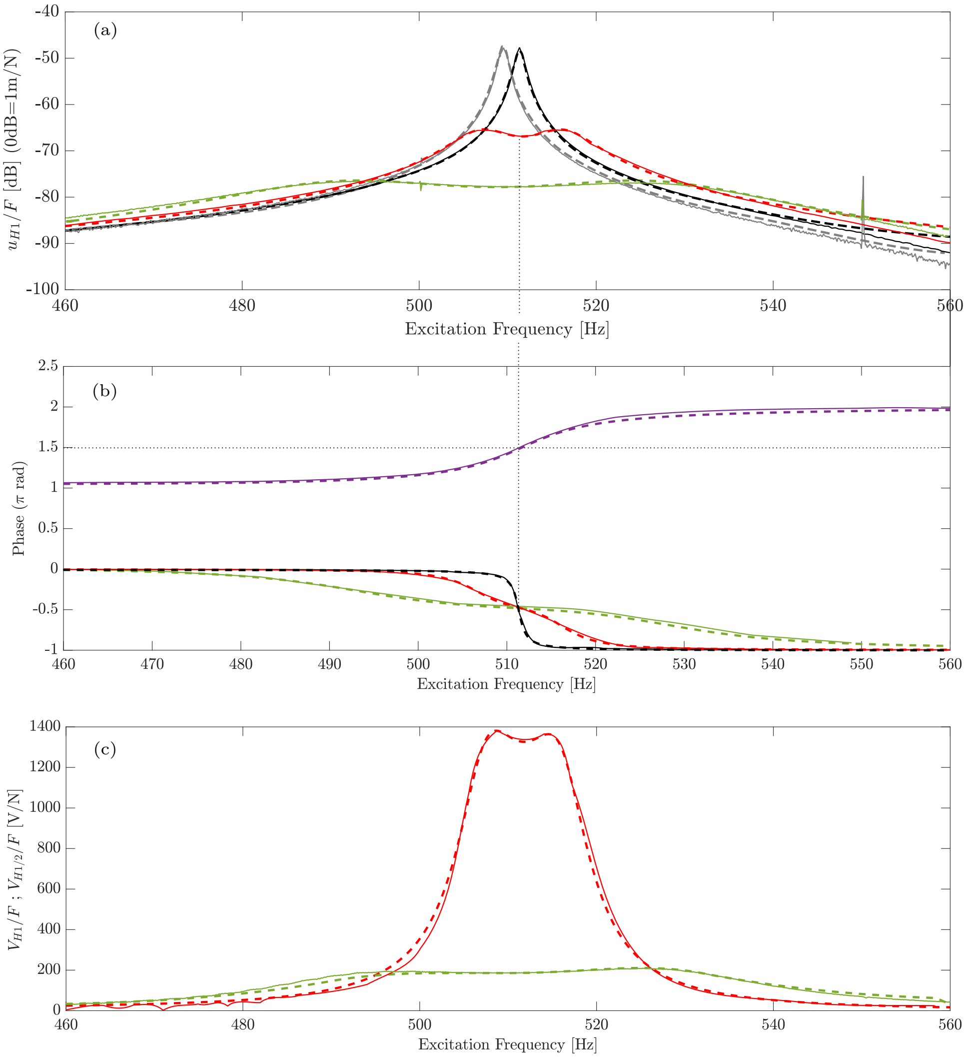

Fig. 19: Comparison between the numerical (dashed lines) and experimental (solid lines) frequency responses. In (a), the response of u_{H1} is shown for the 1:1 tuning (in green) and 2:1 tuning (in red), respectively. The short and open circuit responses are shown in gray and black lines, respectively. In (b), the phase δ_1 is shown for the linear case (in black) and for the 1:1 tuning (in green) in addition to γ_2 (in red) and γ_1 (in purple) for the 2:1 tuning. In (c), the responses of V_{H1} and $V_{\mathrm{H1/2}}$ are shown for the 1:1 tuning (in green) and 2:1 tuning (in red), respectively. For the 1:1 tuning case, we set $L = 0.73\mathrm{H}, \beta = \beta^{\mathrm{op}} = 0.444$, and $R = R^{\mathrm{op}} = 237.5\Omega$. For the 2:1 tuning case, we set $L = 2.94\mathrm{H}, \beta = \beta^{\mathrm{op}} = 0.4435$, and $R = R^{\mathrm{op}} = 73\Omega$. The modal parameters used in the numerical simulations are gathered in Table 3.

For completeness and comparison purposes, both the linear and the nonlinear frequency responses are depicted. The linear ones are estimated with the PE patch 3 in open and short circuit configurations. Comparing the numerical and the experimental results of the linear responses shows an excellent fitting validating the modal parameters estimated in Table 2 and the inductance tuning with the Antoniou inductor.

Regarding the nonlinear responses (i.e., with the nonsmooth component included in the shunt), the numerical and experimental frequency responses of the displacement, PE voltage, and phase angles suggest an excellent agreement for the 1:1 and 2:1 tuning cases. The following major points, suggested numerically in section 3, are validated: i) the response of u_{H1} for both tuning cases suggests a curve shape similar to that of the resonant shunt. ii) the estimated optimal parameters of β and R_e lead to the optimal response for both tuning cases since the response curves of u_{H1} show a symmetric behavior with respect to the resonance frequency with the amplitude of the two peaks around primary resonance is minimized. iii) Although an equivalent response shape compared to the RL-shunt is observed, the amplitude of u_{H1} in the 1:1 tuning case admits slightly higher amplitude while a substantial increase in the amplitude is observed for 2:1 tuning case. This suggests different attenuation abilities for the two tuning cases, which is further discussed in section 5.3. vi) the response of the voltage subharmonic for the 2:1 tuning validates the energy transfer and the activation of the 2:1 internal resonance. It can be realized the substantial increase in the order of magnitude of $V_{\mathrm{H1/2}}$ compared to V_{H1} of the 1:1 tuning case. v) the last major point concerns the phase angles. It appeared that in the optimal condition, the first harmonic phase angle of the displacement for both tuning cases (i.e., δ_1 and γ_2) are equal at the resonance frequency. Thus, if the first harmonic is dominant, the displacement signals corresponding to the two tuning cases will be in phase (see Fig. 20(a)). In addition, the relative phase angle γ_1, only defined for the 2:1 tuning case, admits a value of $3\pi/2$ at the antiresonance frequency, equivalent to the results obtained in [19, 20] when quadratic nonlinearities are introduced in the shunt.

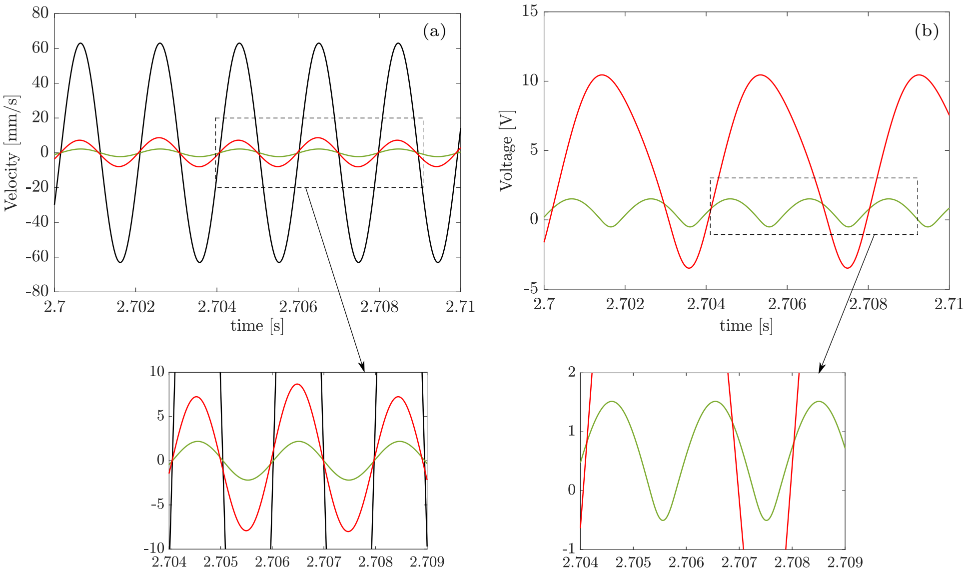

Fig. 20: (a) and (b) show respectively the measured time signals of the velocity and the PE voltage for the 1:1 tuning (in green) and 2:1 tuning (in red) at $\Omega = \hat{\omega} = 511.3 \times (2\pi)$ rad/s with excitation level $F = 5.2$ mN. For the 1:1 tuning case, we set $L = 0.73$H, $\beta = \beta^{\mathrm{op}} = 0.444$, and $R = R^{\mathrm{op}} = 237.5\Omega$. For the 1:1 tuning case, we set $L = 2.94$H,$\beta = \beta^{\mathrm{op}} = 0.4435$, and $R = R^{\mathrm{op}} = 73\Omega$.

The time signals of the velocity $v(t)$ and the PE voltage $V(t)$ are shown in Fig. 20 for the tuning cases in addition to the linear response in the open circuit configuration. The signals are recorded at the open circuit frequency (i.e., $\Omega = \hat{\omega} = 511.3 \times (2\pi)$ rad/s). The signals clearly show that for the 1:1 tuning case, the switching effect between two resonance frequencies (i.e., ω_e and ω_e' in Eq. (9)) appears clearly in PE voltage signals with a slight effect in the velocity signal. In addition, one can realize that the velocity signals of the 1:1 tuning and 2:1 tuning in Fig. 20(a) are in phase at the resonance frequency, as suggested in Fig. 19(b). Also, one can clearly observe the presence of the subharmonic in the voltage and velocity signal in the 2:1 tuning case in Fig. 20(b), following the expressions in (42a,b).

5.2 Effect of the design parameters

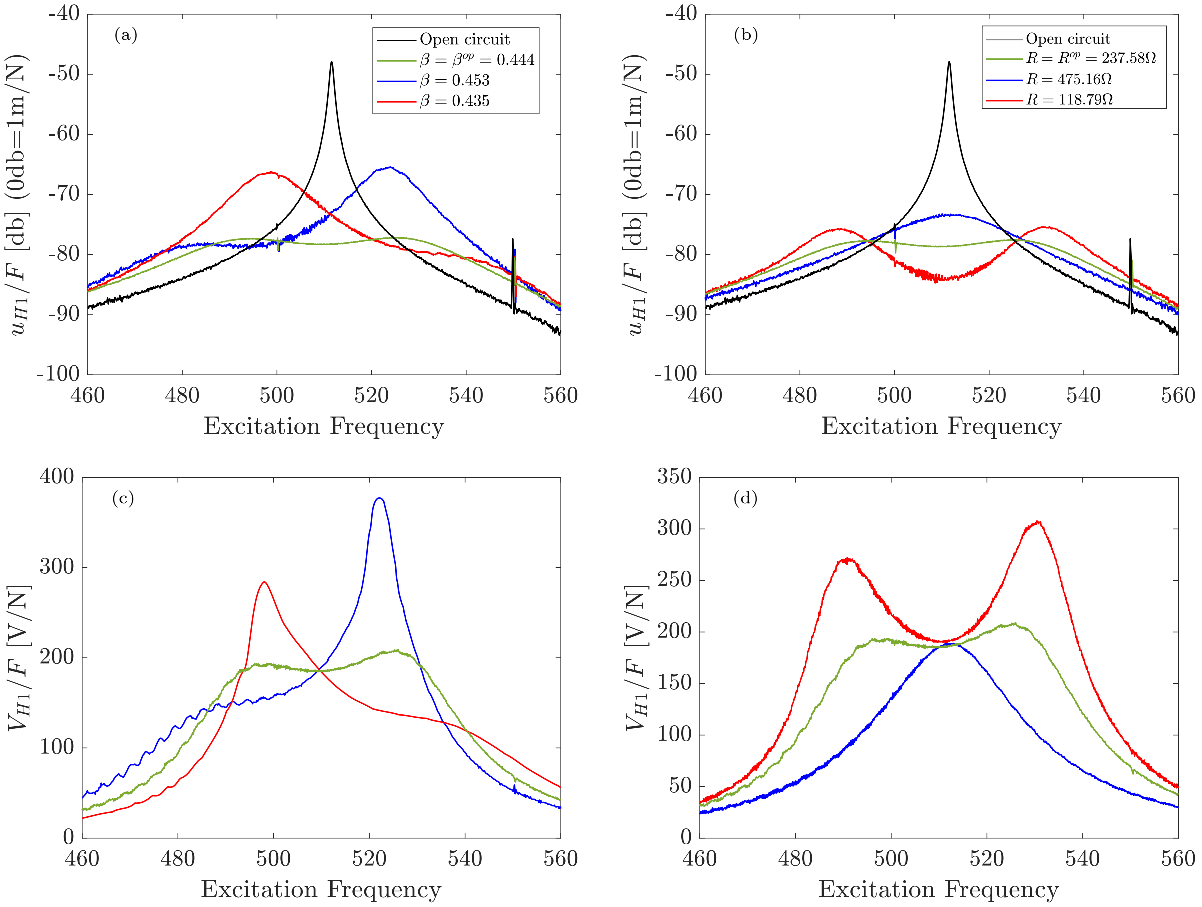

Fig. 21: Experimental frequency response of the first harmonic of the velocity u_{H1} (first row) and the PE voltage V_{H1} (second row), both normalized with respect to the excitation level, for the 1:1 tuning case. The response is shown for different values of β with $R = R^{\mathrm{op}} = 237.58\Omega$ (first column) and different values of R with $\beta = \beta^{\mathrm{op}} = 0.444$ (second column). The inductance value used in the simulations is $L = 0.737\mathrm{H} \implies r = \omega_e/\hat{\omega} = 2$. The displacement and voltage responses are plotted in dB and linear scales, respectively.

This section is devoted to show the tuning effect of the design parameters, namely the resistor in the shunt R (thus ξ_e) and the nonsmooth β. Thus, we performed two sets of experiments. In the first set, we considered three different values of β, including its optimal value, and we fixed the R at the optimum value. Similarly, in the second set, we considered three different values of R, including its optimal value, and we fixed β at its optimum value. We show in Fig. 21 the frequency responses of

u_{H1} and V_{H1} for the 1:1 tuning case and in Fig. 22, we show the frequency responses of u_{H1} and $V_{\mathrm{H1/2}}$ for the 2:1 tuning case. Regarding the value of the inductance, we consider the same setting as in Fig. 19 for both tuning cases.

One can realize from Figs. 21(a),(c) and Figs. 22(a),(c) that the response is very sensitive to β since it appears that any small perturbation of the optimal value of β in both tuning cases can break the response symmetry (i.e., the two peaks around the primary resonance admit different amplitudes) and thus shift the antiresonance from the resonance frequency. As β is varied with the resistance R_9 in the shunt circuit (see. Fig. 18), the value of this resistance should be set in a precise manner. The results in Figs. 21(b),(d) and Figs. 22(b),(d) show that setting a resistance lower than the optimal value in the shunt leads to an increase in the peaks' amplitude around the primary resonance with a decrease in the amplitude of the antiresonance. However, setting a higher value leads to the appearance of one peak near the resonance frequency in which no antiresonance is detected. The experimental results clearly validate the numerical ones in Fig. 11 and Fig. 15 for the 1:1 and 2:1 tuning cases, respectively. In addition, it is validated that the behavior with respect to β and R is equivalent to that of the linear RL-shunt but with the main difference that the tuning parameter in our case is β instead of the inductance (see Appendix A).

5.3 Discussion about the optimal attenuation

The main advantage suggested by the absorber is the ability to choose the inductance to be lower compared to that required by the RL-shunt, in which the electric resonance frequency is tuned with the nonsmooth gain β. Thus, it is necessary to experimentally validate the effect of the inductance value on the optimum attenuation suggested with the nonsmooth component. The analytical expressions of the optimal attenuation in Table 2 show that the inductance appears explicitly through the gain ϕ_1 and ϕ_2 for the 1:1 and 2:1 tuning cases, respectively. To validate those results, we measure the frequency response of u_{H1} considering the two tuning cases for different values of the inductance. The results are shown in Fig 23(a) and (b) for the 1:1 and 2:1 tuning, respectively. For each value of the inductance, we correct β and the value of R to respect the optimal condition. The 1:1 tuning suggests that the attenuation decreases as the chosen inductance in the circuit is reduced. On the contrary, the 2:1 tuning case suggests an increase of the attenuation, accompanied by a narrower bandwidth, as the inductance is reduced up to a certain level where the attenuation appears to stay constant around 22dB. Indeed, the optimal attenuation for both tuning always admits a value lower than that of the linear RL-shunt.

This attenuation behavior for both tunings is predicted through the expressions in Table. 2 as shown in Fig. 23(c) (see the solid and dashed lines). For clarity, the optimal attenuation is plotted versus the frequency ratio r instead of the inductance. Those two quantities are related by $r = \omega_e/\hat{\omega} = 1/(\hat{\omega} L C_{\mathrm{p}})$. As the results in Figs 23(a) and (b) are shown in the dB scale, the optimal attenuation, measured experimentally, is obtained by subtracting the amplitude of the linear response from that corresponding to the nonsmooth response, both measured at the resonance frequency (similar to the plots in Fig. 12 and Fig. 16). This is repeated for different values of inductance, in which the results are then plotted in Fig. 23(c) (with circle and diamond markers). Clearly, for both tunings, the experimental results follow the same pattern suggested analytically with a small discrepancy, especially for the 2:1 tuning. Realize also that we were able to reach an inductance reduction by a factor of 64 compared to that required by the linear resonant shunt with a reduction in the attenuation around 0.8dB for the 1:1 tuning case. A further reduction in the inductance was hard to be achieved in practice since it requires a value β more closer to 0.5, which can lead to unstable response.

It is worth mentioning that not only the attenuation depends on the tuning of β but indeed the whole dynamics. For example, if we consider the case with the inductance $L = 0.11$H (red curve in Fig. 23(a),(b)), the transition between the 1:1 tuning (i.e., fully linear behavior near the resonance

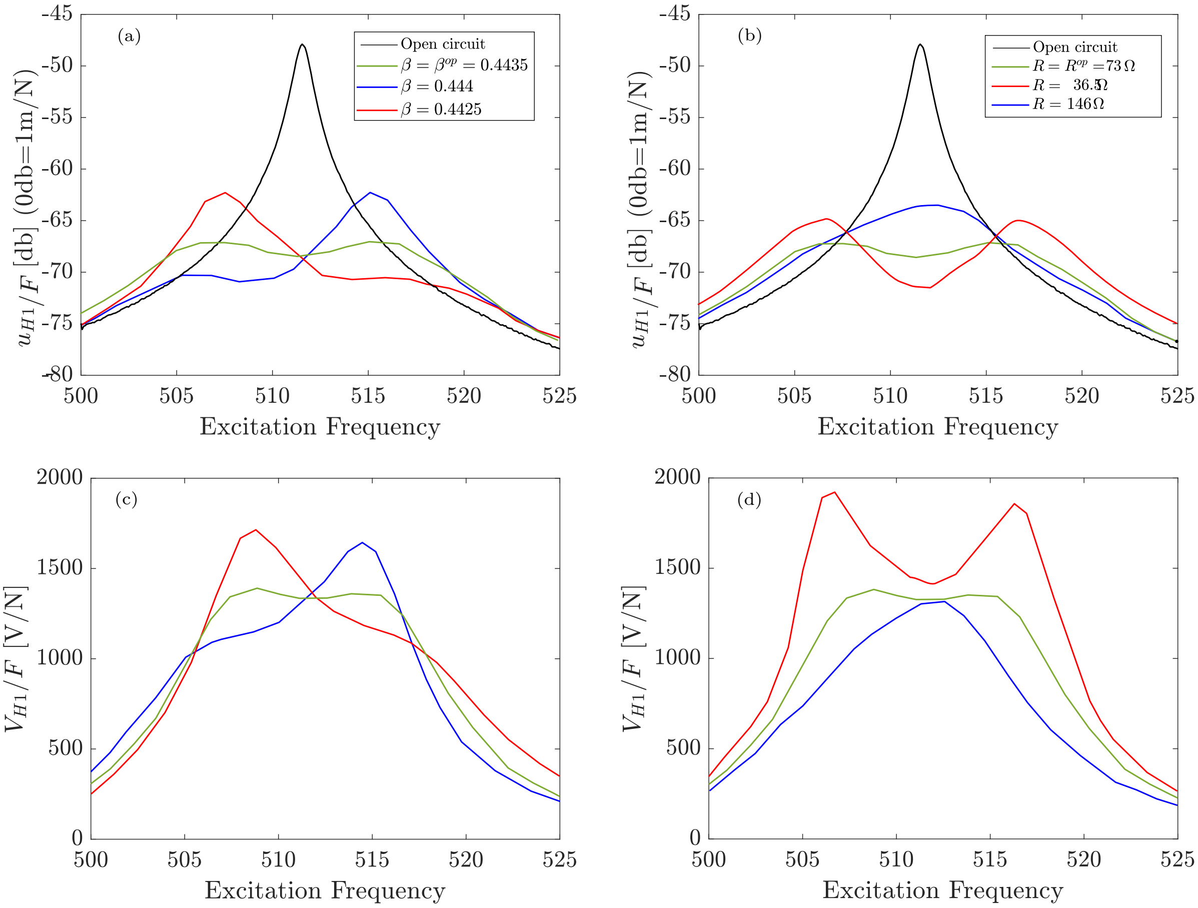

Fig. 22: Experimental frequency response of the first harmonic of the velocity u_{H1} (first row) and the PE voltage $V_{\mathrm{H1/2}}$ (second row), both normalized with respect to the excitation level, for the 2:1 tuning case. The response is shown for different values of β with $R = R^{\mathrm{op}} = 73\Omega$ (first column) and different values of R with $\beta = \beta^{\mathrm{op}} = 0.4435$ (second column). The inductance value used in the simulations is $L = 2.94\mathrm{H} \implies r = \omega_e/\hat{\omega} = 1$. The displacement and voltage responses are plotted in dB and linear scales, respectively.

frequency) to the 2:1 tuning (i.e., activation of the 2:1 internal resonance) required a change of β by around 1%. Thus, a high precision in the value of β is required to obtain the required behavior associated with each tuning case which is challenging in practice.

6 Conclusion

In this article, a new nonlinear piezoelectric shunt was proposed, based on the intentional use of a bilinear component in the electrical circuit. This nonlinear component has three important properties. The first one is to create an apparent electrical oscillation frequency $\bar{\omega}_e$ with a value that can be adjusted with the gain β, thus creating a *tunable oscillator*. The second property is that its response *is fully linear in amplitude*: despite its nonsmooth nature, no strong nonlinear behavior was observed. The nonlinearity appears through the creation of harmonics in the response of the system, mainly of

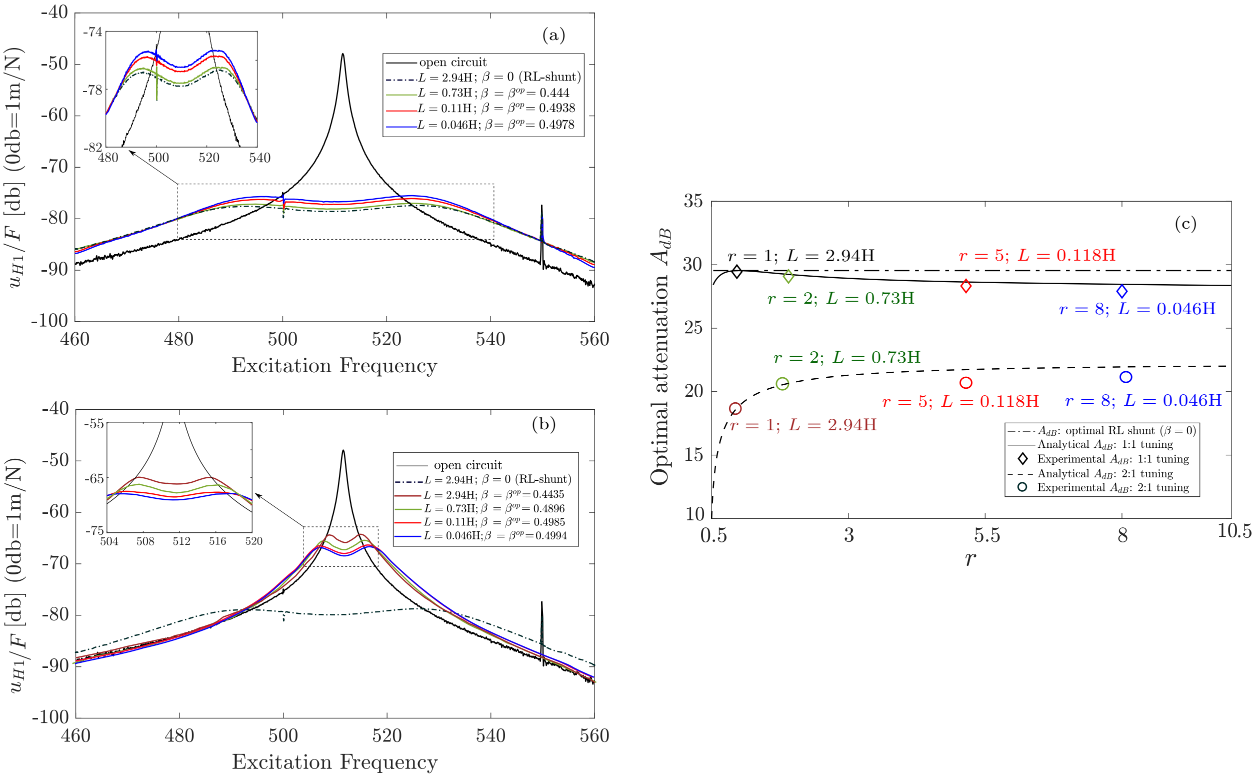

Fig. 23: (a) and (b) show the experimental frequency response of the first harmonic of the velocity u_{H1} for different values of the inductance for the 1:1 and 2:1 tuning, respectively. (c) Comparison between the optimal analytical attenuation and that measured experimentally for both tuning cases.

even order, because of its non-symmetric characteristic. The third property is that the behavior of the harmonics can be *approximated by independent linear oscillators*. Mixing those three properties, it was shown that the behavior of our shunt is (i) *equivalent to a standard RL-shunt* with (ii) the noteworthy property of being *tunable* using the gain β.

We investigated two possible tuning of the shunt. The first (classical) one is a 1:1 tuning, for which the apparent electrical frequency is tuned equal to the mechanical resonance frequency to mitigate ($\bar{\omega}_e = \hat{\omega}_i$). In this case, it was shown that it is possible to detune the RL-shunt by a factor $r_i = \omega_e/\hat{\omega}_i$ between 0.5 and 10 (in theory up to $+\infty$) without changing the amplitude reduction performance significantly: only a 1 dB decrease was observed. This tuning ability can be a considerable advantage in practice since it substantially decreases the inductance L of the shunt by a factor r_i^2, *i.e., up to a factor 100 if* $r_i = 10$.

The second tuning case, relying on a 2:1 internal resonance (the apparent electrical frequency is tuned equal to half the mechanical resonance frequency to mitigate, $\bar{\omega}_e \simeq \hat{\omega}_i/2$), shows a similar RL-shunt behavior though relying on a purely nonlinear process of energy transfer between two frequency bands, from the driving frequency Ω to its subharmonic $\Omega/2$. However, the performances are decreased since they rely on the energy transfer between the oscillators, which is weaker in the case of a 2:1 tuning with respect to the 1:1.

Even if strongly nonlinear behavior were not at hand, this nonsmooth component could pave the way for future studies involving energy harvesting and the possibility of adding quadratic and cubic nonlinearities with the nonsmooth component in the shunt circuit to possibly obtain a response similar to an RL-shunt but associated with a saturation phenomenon. In addition, due to the multi-harmonic response generated by the nonsmooth component, and also the possible design of other nonsmooth laws for the component, the tuning cases shown in this study are not unique. One can test the possibility of other types of nonlinear modal coupling through a 1:3 internal resonance (i.e., $\bar{\omega}_e = 1/3\hat{\omega}$) or 1:2 internal resonance (i.e., $\bar{\omega}_e = 2\hat{\omega}$). The analysis of other types of internal resonance with the nonsmooth component is left for future studies.

References

1. N. Hagood and A. von Flotow, “Damping of structural vibrations with piezoelectric materials and passive electrical networks,” *Journal of Sound and Vibration*, vol. 146, pp. 243–268, Apr. 1991.
2. O. Thomas, J. Ducarne, and J.-F. Deü, “Performance of piezoelectric shunts for vibration reduction,” *Smart Materials and Structures*, vol. 21, p. 015008, Jan. 2012.
3. M. Berardengo, O. Thomas, C. Giraud-Audine, and S. Manzoni, “Improved resistive shunt by means of negative capacitance: new circuit, performances and multi-mode control,” *Smart Materials and Structures*, vol. 25, jun 2016.
4. L. P. da Silva, W. Larbi, and J.-F. Deü, “Topology optimization of shunted piezoelectric elements for structural vibration reduction,” *Journal of Intelligent Material Systems and Structures*, vol. 26, no. 10, pp. 1219–1235, 2015.
5. J.-W. Park and J.-H. Han, “Sensitivity analysis of damping performances for passive shunted piezoelectrics,” *Aerospace Science and Technology*, vol. 33, no. 1, pp. 16–25, 2014.
6. A. J. Fleming, S. Behrens, and S. O. R. Moheimani, “Reducing the inductance requirements of piezoelectric shunt damping systems,” *Smart Materials and Structures*, vol. 12, pp. 57–64, jan 2003.
7. B. Lossouarn, M. Aucejo, J.-F. Deü, and B. Multon, “Design of inductors with high inductance values for resonant piezoelectric damping,” *Sensors and Actuators A: Physical* , vol. 259, pp. 68–76, 2017.
8. J. J. Hollkamp, “Multimodal passive vibration suppression with piezoelectric materials and resonant shunts,” *Journal of intelligent material systems and structures*, vol. 5, no. 1, pp. 49–57, 1994.
9. S. Livet, M. Collet, M. Berthillier, P. Jean, and J. Cote, “Structural multi-modal damping by optimizing shunted piezoelectric transducers,” *Revue Européenne de Mécanique Numérique/European Journal of Computational Mechanics*, vol. 20, no. 1-4, pp. 73–102, 2011.
10. B. Lossouarn, J.-F. Deü, and M. Aucejo, “Multimodal vibration damping of a beam with a periodic array of piezoelectric patches connected to a passive electrical network,” *Smart Materials and Structures*, vol. 24, no. 11, 2015.
11. K. Marakakis, G. Tairidis, P. Koutsianitis, and G. Stavroulakis, “Shunt piezoelectric systems for noise and vibration control: A review,” *Frontiers in Built Environment*, vol. 5, p. 64, 05 2019.
12. J. Gripp and D. Rade, “Vibration and noise control using shunted piezoelectric transducers: A review,” *Mechanical Systems and Signal Processing*, vol. 112, p. 359, 11 2018.
13. A. F. Vakakis and O. Gendelman, “Energy Pumping in Nonlinear Mechanical Oscillators: Part II—Resonance Capture,” *Journal of Applied Mechanics*, vol. 68, pp. 42–48, Jan. 2001.

14. B. Zhou, F. Thouverez, and D. Lenoir, “Essentially nonlinear piezoelectric shunt circuits applied to mistuned bladed disks,” *Journal of Sound and Vibration*, vol. 333, pp. 2520–2542, Apr. 2014.

15. T. M. Silva, M. A. Clementino, C. De Marqui, and A. Erturk, “An experimentally validated piezoelectric nonlinear energy sink for wideband vibration attenuation,” *Journal of Sound and Vibration*, vol. 437, pp. 68–78, Dec. 2018.

16. G. Habib, T. Detroux, R. Viguié, and G. Kerschen, “Nonlinear generalization of den hartog’s equal-peak method,” *Mechanical Systems and Signal Processing*, vol. 52–53, pp. 17–28, 2015.

17. P. Soltani and G. Kerschen, “The nonlinear piezoelectric tuned vibration absorber,” *Smart Materials and Structures*, vol. 24, p. 075015, July 2015.

18. G. Raze, A. Jadoul, S. Guichaux, V. Broun, and G. Kerschen, “A digital nonlinear piezoelectric tuned vibration absorber,” *Smart Materials and Structures*, vol. 29, p. 015007, Jan. 2020.

19. Z. A. Shami, C. Giraud-Audine, and O. Thomas, “A nonlinear piezoelectric shunt absorber with a 2:1 internal resonance: Theory,” *Mechanical Systems and Signal Processing*, vol. 170, p. 108768, May 2022.

20. Z. A. Shami, C. Giraud-Audine, and O. Thomas, “A nonlinear piezoelectric shunt absorber with 2:1 internal resonance: Experimental proof of concept,” *Smart Materials and Structures*, vol. 31, p. 035006, Mar. 2022.

21. Z. Shami, Y. Shen, C. Giraud-Audine, C. Touzé, and O. Thomas, “Nonlinear dynamics of coupled oscillators in 1:2 internal resonance: effects of the non-resonant quadratic terms and recovery of the saturation effect,” *Meccanica*, 2022.

22. Z. A. Shami, C. Giraud-Audine, and O. Thomas, “Antiresonance detuning correction for a piezoelectric shunt absorber based on 2:1 internal resonance using a cubic nonlinearity,” *Smart Materials and Structures.* Under review.

23. C. Touzé, O. Thomas, and A. Chaigne, “Asymmetric non-linear forced vibrations of free-edge circular plates. part 1: Theory,” *Journal of Sound and Vibration*, vol. 258, pp. 649–676, Dec. 2002.

24. A. Givois, A. Grolet, O. Thomas, and J.-F. Deü, “On the frequency response computation of geometrically nonlinear flat structures using reduced-order finite element models,” *Nonlinear Dynamics*, vol. 97, pp. 1747–1781, July 2019.

25. A. H. Nayfeh, *Perturbation Methods.* Wiley Classics Library, New York: John Wiley & Sons, wiley classics library ed., 2000.

26. I. Kovacic, L. Cveticanin, M. Zukovic, and Z. Rakaric, “Jacobi elliptic functions: A review of nonlinear oscillatory application problems,” *Journal of Sound and Vibration*, vol. 380, pp. 1–36, Oct. 2016.

27. C. Touzé, “Normal form theory and nonlinear normal modes: Theoretical settings and applications,” in *Modal Analysis of Nonlinear Mechanical Systems* (G. Kerschen, ed.), vol. 555, pp. 75–160, Vienna: Springer Vienna, 2014.

28. A. Darabi and M. J. Leamy, “Clearance-type nonlinear energy sinks for enhancing performance in electroacoustic wave energy harvesting,” *Nonlinear Dynamics*, vol. 87, pp. 2127–2146, Mar. 2017.

29. Y. S. Lee, F. Nucera, A. F. Vakakis, D. M. McFarland, and L. A. Bergman, “Periodic orbits, damped transitions and targeted energy transfers in oscillators with vibro-impact attachments,” *Physica D: Nonlinear Phenomena*, vol. 238, pp. 1868–1896, Sept. 2009.

30. M. Vakilinejad, A. Grolet, and O. Thomas, “A comparison of robustness and performance of linear and nonlinear lanchester dampers,” *Nonlinear dynamics*, vol. 100, pp. 269–287, 2020.

31. S. Benacchio, C. Giraud-Audine, and O. Thomas, “Effect of dry friction on a parametric nonlinear oscillator,” *Nonlinear Dynamics*, vol. 108, pp. 1005–1026, Apr. 2022.

32. F. Georgiadis, A. F. Vakakis, D. M. McFarland, and L. Bergman, “Shock Isolation Through Passive Energy Pumping in a System With Piecewise Linear Stiffnesses,” in *Volume 5: 19th Biennial Conference on Mechanical Vibration and Noise, Parts A, B, and C*, (Chicago, Illinois, USA), pp. 1569–1574, ASMEDC, Jan. 2003.

33. C.-H. Lamarque, O. V. Gendelman, A. Ture Savadkoohi, and E. Etcheverria, “Targeted energy transfer in mechanical systems by means of non-smooth nonlinear energy sink,” *Acta Mechanica*, vol. 221, pp. 175–200, Sept. 2011.

34. C.-H. Lamarque, A. Ture Savadkoohi, and Z. Dimitrijevic, “Dynamics of a linear system with time-dependent mass and a coupled light mass with non-smooth potential,” *Meccanica*, vol. 49, pp. 135–145, Jan. 2014.

35. B. Youssef and R. I. Leine, “A complete set of design rules for a vibro-impact NES based on a multiple scales approximation of a nonlinear mode,” *Journal of Sound and Vibration*, vol. 501, p. 116043, June 2021.

36. X.-F. Geng and H. Ding, “Theoretical and experimental study of an enhanced nonlinear energy sink,” *Nonlinear Dynamics*, vol. 104, pp. 3269–3291, June 2021.

37. C. Richard, D. Guyomar, D. Audigier, and G. Ching, “Semi-passive damping using continuous switching of a piezoelectric device,” in *SPIE Smart Structures and Materials Conference*, vol. 3672, pp. 104–111, 1999.

38. J. Ducarne, O. Thomas, and J.-F. Deü, “Structural Vibration Reduction by Switch Shunting of Piezoelectric Elements: Modeling and Optimization,” *Journal of Intelligent Material Systems and Structures*, vol. 21, pp. 797–816, 2010.

39. C. Richard, D. Guyomar, D. Audigier, and H. Bassaler, “Enhanced Semi-passive Damping Using Continuous Switching of a Piezoelectric Device on an Inductor,” in *Proceedings of SPIE Smart Structures and Materials Conference: Passive Damping and Isolation*, vol. 3989, pp. 288–299, 2000.

40. L. Petit, E. Lefeuvre, C. Richard, and D. Guyomar, “A Broadband Semi Passive Piezoelectric Technique for Structural Damping,” in *Proceedings of SPIE Smart Structures and Materials Conference: Passive Damping and Isolation*, vol. 5386, pp. 414–425, 2004.

41. E. Lefeuvre, A. Badel, L. Petit, C. Richard, and D. Guyomar, “Semi-passive Piezoelectric Structural Damping by Synchronized Switching on Voltage Sources,” *Journal of Intelligent Material Systems and Structures*, vol. 17, pp. 653–660, 2006.

42. A. Badel, G. Sebald, D. Guyomar, M. Lallart, E. Lefeuvre, C. Richard, and J. Qiu, “Piezoelectric vibration control by synchronized switching on adaptive voltage sources: Towards wideband semi-active damping,” *The Journal of the Acoustical Society of America*, vol. 119, pp. 2815–2825, 2006.

43. J. Ducarne, O. Thomas, and J. Deü, “Vibration reduction by switch shunting of piezoelectric elements: nonlinear energy transfers between modes and optimization,” in *Proc. of the 19th. International Conference on Adaptative Structures and Technologies*, (Ascona, Switzerland), Oct. 2008.

44. L. Guillot, B. Cochelin, and C. Vergez, “A taylor series-based continuation method for solutions of dynamical systems,” *Nonlinear Dynamics*, vol. 98, pp. 2827–2845, 2019.

45. L. Guillot, A. Lazarus, O. Thomas, C. Vergez, and B. Cochelin, “A purely frequency based floquet-hill formulation for the efficient stability computation of periodic solutions of ordinary differential systems,” *Journal of Computational Physics*, vol. 416, p. 109477, 2020.

46. L. Pernod, B. Lossouarn, J.-A. Astolfi, and J.-F. Deü, “Vibration damping of marine lifting surfaces with resonant piezoelectric shunts,” *Journal of Sound and Vibration*, vol. 496, p. 115921, 2021.

47. O. Thomas, C. Touzé, and A. Chaigne, “Asymmetric non-linear forced vibrations of free-edge circular plates, part 2: experiments,” *Journal of Sound and Vibration*, vol. 265, no. 5, pp. 1075–1101, 2003.

48. M. Vatavu, V. Nastasescu, F. Turcu, and I. Burda, “Voltage-controlled synthetic inductors for resonant piezoelectric shunt damping: A comparative analysis,” *Applied Sciences*, vol. 9, no. 22, 2019.

Statements & Declarations

The authors declare that they have no known competing financial interests or personal relationships that could have appeared to influence the work reported in this paper.
The Région Hauts de France and the Carnot ARTS Institute, France are warmly thanked for the PhD grant of the first author.

Data Availability

The datasets generated during and/or analysed during the current study are not publicly available but are available from the corresponding author on reasonable request.

Appendix A: RL-shunt response and optimization: reference solution

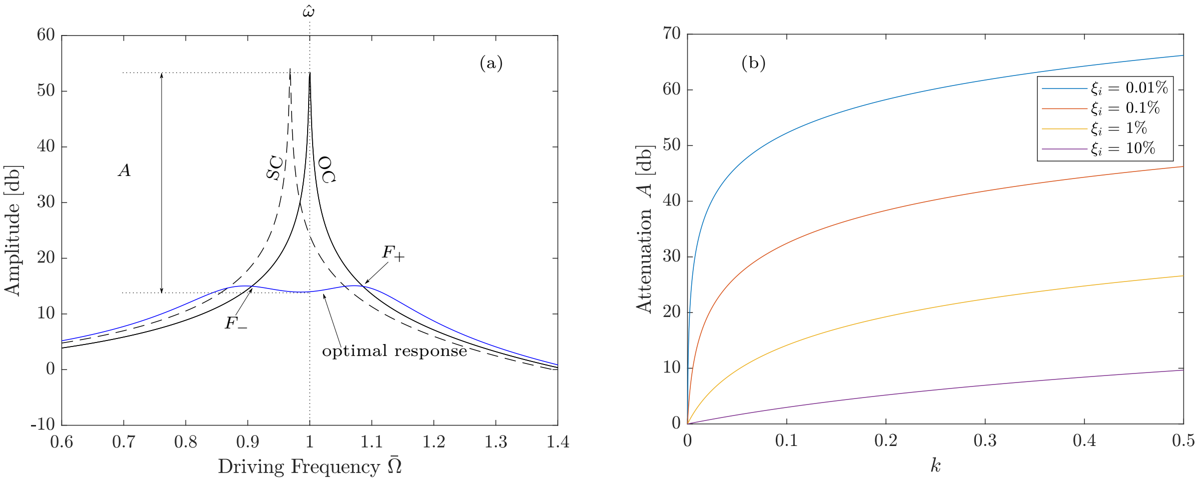

Fig. 24: (a) Typical FRF of the RL-shunt in the optimal case. (b) Attenuation A as function of k for different mechanical damping factor ξ_i.

In this section, we recall the response of a mechanical system coupled to a RL-shunt. We thus consider Eqs. (21a,b) without the nonsmooth term (i.e., $\beta = 0 \Rightarrow \bar{r}_i = r_i, \bar{k}_i = k_i$), which reads:

$$\ddot{\tilde{q}}_i + 2\xi_i\dot{\tilde{q}}_i + \tilde{q}_i + k_i r_i \tilde{Q} = f_i \cos \tilde{\Omega}\tilde{t}, \tag{A.1a}$$

$$\ddot{\tilde{Q}} + 2\xi_e r_i \dot{\tilde{Q}} + r_i^2 \tilde{Q} + k_i r_i \tilde{q}_i = 0. \tag{A.1b}$$

The mechanical FRF is thus:

$$H_q(\tilde{\Omega}) = \hat{\omega}_i^2 m_i \frac{\mathring{q}}{F} = \frac{r_i^2 - \tilde{\Omega}^2 + 2j\tilde{\Omega}\xi_e r_i}{\left(1 - \tilde{\Omega}^2 + 2j\tilde{\Omega}\xi_i\right)\left(r_i^2 - \tilde{\Omega}^2 + 2j\tilde{\Omega}\xi_e r_i\right) - k_i^2 r_i^2}, \tag{A.2}$$

where $\mathring{q}_i(\tilde{\Omega})$ is the Fourier transform of $q_i(t)$.

As a classical result (see e.g., [2]), it is possible to choose the electrical frequency ω_e and the damping ratio ξ_e such that the amplitude of the i-th resonance of the elastic structure is minimized and has a blunt shape, shown in Fig. 24(a). The optimal values of ω_e and ξ_e are:

$$\omega_e^{\text{op}} = \hat{\omega}_i \quad \Rightarrow \quad r_i^{\text{op}} = 1; \quad \xi_e^{\text{op}} = \frac{\sqrt{6}k_i}{4}. \tag{A.3}$$

Then, as in [2], a performance indicator of the RL-shunt can be defined as the difference, in dB, between the amplitude at the resonance of the mechanical oscillator without shunt (for instance, with the shunt in open-circuit) and the maximum amplitude of the blunt shunt with the optimal RL-shunt. Here, to simplify, we define the latter as the amplitude at the open circuit frequency, i.e., for $\Omega = \hat{\omega}_i$ ($\tilde{\Omega} = 1$). The optimal attenuation A_{dB} is then estimated with Eq. (A.2) as:

$$A_{\text{dB}} = 20 \log_{10} \frac{H_q|_{k_i=0}(\tilde{\Omega} = 1)}{H_q|_{\xi_e=\xi_e^{\text{op}}, r_i=1}(\tilde{\Omega} = 1)} = 20 \log_{10} \left(1 + \frac{k_i}{\xi_i\sqrt{6}}\right) \tag{A.4}$$

Eq. (A.4) suggests that the attenuation is solely function of the mechanical damping factor ξ_i and the piezoelectric coupling k_i, as shown in Fig. 24(b). Note that the above expression for A_{dB} is taken at the open circuit frequency and not at the frequency of the fixed points as in [2] to obtain a simpler expression whose numerical value is very close.

Appendix B: Regularization of the nonsmooth term and implementation in MANLAB

The numerical results in this work were all obtained using Manlab, which requires regularization of the nonsmooth term associated with the absolute value function of the piezoelectric voltage $|V|$. As a first step, we define a new variable y as:

$$y = |V| \quad \Longrightarrow \quad \begin{cases} y = -V & \text{if} \quad V < 0, \\ y = V & \text{if} \quad V > 0. \end{cases} \tag{B.1}$$

Then, the regularization is obtained through the following equation:

$$(y - V)(y + V) = \delta \quad \Longrightarrow \quad y^2 - V^2 - \delta = 0, \tag{B.2}$$

where $\delta \in \mathbb{R}$ is the regularization parameter. As seen in Fig. 25, if $\delta = 0$, the solution is equivalent to $y = |V|$. For a small value of δ, the angular point at $V = 0$ of the graph of the absolute value function is replaced by a smooth curve that gets closer to the nonsmooth exact one as δ approaches zero.

Upon obtaining the regularization, the two degree of freedom system in (2a,b) is implemented in MANLAB in the first order form considering four main variables (q, Q, v, w) and two auxiliary variables (V, y) [45]:

$$\begin{cases} \dot{q}_i = v, & \text{(B.3a)} \\ \dot{Q} = w, & \text{(B.3b)} \\ \dot{v} = -2\xi_i\hat{\omega}_i v - \hat{\omega}_i^2 q_i - \dfrac{\theta_i}{m_i C_{\text{pi}}} Q + \dfrac{F}{m_i} \cos \Omega t, & \text{(B.3c)} \\ \dot{w} = -2\xi_e\omega_e w - \omega_e^2 Q - \dfrac{\theta_i}{L C_{\text{pi}}} q_i - \dfrac{\beta}{L}\left(y + V\right), & \text{(B.3d)} \\ 0 = V - \dfrac{1}{C_{\text{p}i}}\left(Q + \theta_i q_i\right), & \text{(B.3e)} \\ 0 = y^2 - V^2 - \delta, & \text{(B.3f)} \end{cases}$$

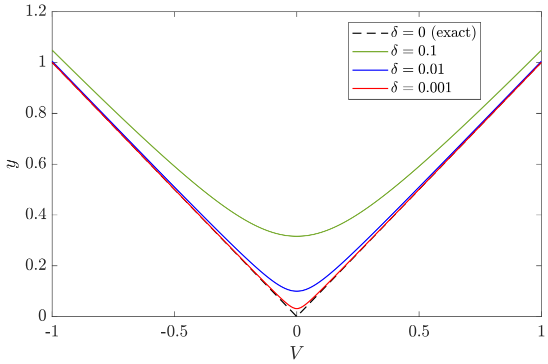

Fig. 25: Graph of the function $y = |V|$ and its regularized versions for different values of δ.

where Eqs. (B.3a,b,c,d) are the main equations and Eqs. (B.3e,f) are the auxiliary equations introduced to obtain the voltage V and the regularization variable y.

Appendix C: Tuning ratio for the 2:1 tuning

Following the reasoning used in [19], we consider the linear system (21a, b). Since the stiffness part is not diagonal, it is possible to compute its two dimensionless frequencies, which read:

$$\omega_1^2 = \frac{1 + \bar{r}_i^2 - \sqrt{\mathit{\Delta}}}{2}, \quad \omega_2^2 = \frac{1 + \bar{r}_i^2 + \sqrt{\mathit{\Delta}}}{2}, \tag{B.4}$$

with $\mathit{\Delta} = (1 - \bar{r}_i^2)^2 + 4\bar{k}_i^2\bar{r}_i^2$. Enforcing $\omega_2 = 2\omega_1$, one arrives to the following order 2 polynomial in $\bar{r}_i^2$:

$$4\bar{r}_i^4 + (25\bar{k}_i^2 - 17)\bar{r}_i^2 + 4 = 0, \tag{B.5}$$

that have two roots. r_i^* of Eq. (33) is the one which is smaller than 1, close to 0.5.

Conclusion

Conclusions

Main results

This thesis is part of a larger project interested in reducing the vibration of lifting surfaces. In the scope of this project, it was planned to make a demonstrator on a hydrofoil. Hydrofoils are lifting structures that are usually mounted at the boat hull to generate a lift force. Consequently, the contact area between the water and the boat is minimized, leading to the reduction of the drag force. The main problem that this thesis aims to solve is the strong vibration levels, in particular, induced flow vibrations, to which hydrofoils are subjected in certain flow regimes. Such high-level vibration levels can cause several problems, such as high-stress levels and fatigue, that can reduce the overall performance substantially. As conventional mechanical dampers cannot be easily implemented in such thin structures, the technique proposed in this project is based on the use of piezoelectric resonant shunt absorbers. This technique mainly consists of connecting a shunt circuit to the host structure through a piezoelectric patch. The latest is simply glued on the structure at relevant places to maximize the energy conversion from the mechanical domain to the electrical domain. The main novelty proposed in this thesis is the intentional addition of a nonlinear component in the shunt circuit to exploit some properties of nonlinearly coupled oscillators to enhance the absorber's performance. The main feature that this thesis focused on is the saturation phenomenon in which the oscillation amplitude remains constant as the excitation level increases. It should be noted that this, therefore, assumes an attenuation that is all the more effective as the excitation is high, which is of course impossible to achieve in the linear case. It should be also noted that the considered excitation considered is of sinusoidal type.

Another constraint of the project is to avoid a displacement or velocity feedbacks as was done in [147]–[151] which can be very difficult for applications involving the usage of the hydrofoil. Instead, the main circuit architecture of the nonlinear shunt circuits proposed in this thesis is composed of a resonant shunt (i.e., a resistor in series with an inductor) connected in series with a nonlinear voltage source. It was thus necessary to modify the initial quadratic nonlinearity to achieve saturation in practice. Based on the type of the introduced nonlinearity in the circuit, we considered three different designs. The first circuit has only a quadratic nonlinearity by drawing directly from theory, but due to practical limitations, it has performance degradations of the nonlinearity. The second design includes a modified nonlinearity that is a superposition of quadratic and cubic types in order to partially fix the problem. The last design includes a nonsmooth nonlinear component mathematically expressed by an absolute value function of the voltage across the piezoelectric patch. This circuit was initially motivated by a simpler realization and potentially supporting higher voltages.

First design: considering only quadratic nonlinearity

The theoretical analysis of the first design, discussed in chapter 2, aims to study the absorber performance and conclude guidelines for practical implementation. Adding a nonlinearity of quadratic type in series with the usual resonant circuit aims to create a 2:1 internal resonance between a given mechanical mode of the structure and an electrical mode associated with an electrical shunt circuit tuned at the order two subharmonic. Despite the apparent difference in the structure of the system, it is theoretically demonstrated that the primary resonance of the first harmonic of the displacement is replaced by an antiresonance associated with an amplitude saturation. The energy injected into the system is thus transferred to the subharmonic of the charge. The study of the design parameters, namely the electrical damping ratio ξ_e, the nonlinear gain β, and the modal piezoelectric coupling factor k_i showed that enhancing the attenuation relies on decreasing the ratio $\xi_e/(k_i\beta)$ as much as possible. In addition, numerical simulations have revealed much more complex behaviors where the symmetric feature of the analytical models considering only the resonant quadratic terms is lost. The main drawbacks are the violation of the saturation phenomenon due to the shifting of the antiresonance as the excitation level increases and the additional peak observed in the displacement frequency response near the primary resonance. The simulation also helped to attribute the cause to the nonresonant terms that admit a very high value which is unavoidable with this shunt design.
Thus, an antiresonance correction is proposed and numerically tested on a real structure that relies on properly tuning the inductance at each excitation level. This is possible since the antiresonance is characterized by a phase between the electrical and mechanical modes of $3\pi/2$. This way, the saturation is recovered; however, quasi-periodic regimes may appear.

The experimental proof of concept of the first design is discussed in chapter 3 in which the absorber is tested to attenuate the first bending mode of a cantilever beam structure excited with a monoharmonic sinusoidal forcing. The frequency responses of the first harmonic of the displacement u_{H1} and the subharmonic of the piezoelectric voltage $V_{\mathrm{H1/2}}$ are measured using a demodulation technique to validate the energy transfer between the harmonics. The quadratic nonlinearity in the circuit is generated using an analog multiplier. The high inductance is realized with a synthetic inductor which introduces a parasitic resistance, increasing ξ_e, which can be balanced by increasing the nonlinear gain

β, without the usage of a negative resistance.

The numerical results are validated experimentally by the excellent matching between the numerical and the experimental frequency responses. In addition, the effect of the design parameters is also experimentally validated, and the symmetry breaking of the frequency response with the antiresonance shifting is observed. The proposed antiresonance correction based on the relative phase between u_{H1} and $V_{\mathrm{H1/2}}$ discussed above is also verified. By comparing the performance of the designed nonlinear absorber with that of an optimized linear shunt, higher attenuation near antiresonance is obtained, although less efficient for broadband attenuation due to the appearance of an extra peak near the primary resonance.

Second design: saturation correction through a cubic nonlinearity

A more rigorous understanding of the effects of the nonresonant quadratic terms on the dynamics is required to obtain a better performance and propose a more efficient strategy to correct the saturation in practice. This is discussed in chapter 4 using the normal form approach. Namely, we considered a two degrees of freedom system equivalent to that obtained in the electromechanical basis discussed in chapter 2 where additional cubic nonlinearities are taken into account. The analysis with the normal form enabled the analytical estimation of the nonlinear normal modes (NNMs) of the system in the case of 2:1 internal resonance. These calculations reveal two families of backbone curves depending on the phase angle between the two oscillators, and in addition, the effect of the nonresonant quadratic terms is also illustrated. Namely, they induced a curvature of the backbone curves, which explains the loss of symmetry. Thanks to the obtained analytical expressions, we proposed a strategy to recover the symmetric property of the backbones by balancing the cubic resonant terms with the quadratic nonresonant terms so that the effect of the latter terms in the normal form basis is eliminated. By doing so, the symmetric property of the forced solution is preserved, and consequently, the saturation phenomenon is recovered. Numerical simulation of the proposed tuning suggests the saturation recovery up to a high excitation level.

Motivated by this result, a modified circuit was designed and experimentally tested in chapter 5 to damp the first bending mode of a hydrofoil structure. The quadratic and cubic nonlinearities are chosen proportional to the square and cubic of the voltage across the piezoelectric patch, and they are tuned by two gains β_q and β_c, to control the quadratic and cubic nonlinearities, respectively. In practice, only one out of four nonresonant terms of the normal form can be compensated. Hence this validation concentrates on the dominant one, which gives the simple relationship $\beta_c = 10/9\,\beta_q^2$. The measured frequency response of the first harmonic of the velocity and the subharmonic of the charge validated the recovery of the symmetric property of the response with the estimated tuning of β_c . In addition, the experimental results validated the recovery of the saturation phenomenon up to a certain excitation level is also verified.

Third design: resonant shunt circuit with nonsmooth component

The third design studied in this thesis involves introducing a nonlinear nonsmooth component in the shunt circuit. Initially, this idea arose from the fact that it quickly became apparent that the voltages involved in previous tests push op-amps to their limits. The proposed circuit was inspired by the so-called half-wave rectifier. Indeed, based on the antiresonance waveforms, it can be seen that the effect of the subharmonics produced by the nonlinear coupling is to dissymmetrize the voltage across the terminals of the piezoelectric patch. The idea is therefore to introduce in series with the piezoelectric, a semi-rectified voltage driven by its own voltage, and modulated by a gain to weight its effects.

The theoretical study is performed in chapter 6 in which the nonsmooth component is set to be proportional to the superposition of the piezoelectric voltage and its absolute value function. The nonsmooth component then enables a continuous switching of the stiffness associated with the electric circuit according to the voltage sign. In addition, introducing a nonsmooth term can create even harmonics, since it is not symmetric, in the same way as quadratic nonlinearities. Since the analytical treatment of the governing equations with the nonsmooth term can be very complicated, we simplified the analysis by studying the dynamics of a one degree of freedom oscillator, including the nonlinearity as a nonsmooth voltage source. A solution for the free oscillations of the system can then be obtained, and it demonstrates that their frequency is directly controlled by the gain β. An immediate interest in this result concerns one of the problems of shunts at low frequency: it becomes possible to use smaller inductances, which can be easier to realize in practice.

Considering the forced response with mono-harmonic sinusoidal excitation, the numerical results show a multi-harmonic response in which the harmonics admit a linear resonance shape near the resonance frequency $\bar{\omega}_e$. In addition, the amplitude of the harmonics appeared to be linear with respect to the excitation level. However, a strong nonlinear response of the superharmonics is obtained due to the strong nonlinearities presented by the nonsmooth term. The suggested linear behavior led to the approximation of the zeroth, first, and second harmonics by a linear oscillator. The energy distribution to each harmonic is quantified by a gain ϕ_p for the p-th harmonic. The approximation is then extended for the full system through the introduction of a modified piezoelectric coupling of the form $k_i\sqrt{\phi_p}$ lower than the initial coupling factor k_i. Two frequency tuning are then considered using β, a 1:1 tuning ($\bar{\omega}_e = \hat{\omega}_i$) and 2:1 tuning ($\bar{\omega}_e = \hat{\omega}_i/2$). The former case behaves linearly near the resonance frequency, while the latter comprises a transfer of energy towards the sub-harmonic by an internal resonance 2:1; however, the branches of the bifurcations admit a linear behavior with respect to the excitation. Thus, for the 2:1 internal resonance, the saturation phenomenon disappears. Optimal study is performed for either cases by considering a modified piezoelectric coupling $k_i\sqrt{\phi_1}$ for the 1:1 tuning case and $k_i\sqrt{\phi_2}$ for the 2:1 tuning. Contrary to linear resonant shunts, the inductance appeared explicitly in the expressions of the optimal attenuation A_{dB} for both cases. The main observation is that A_{dB} is reduced with the decrease of the inductance for the 1:1 tuning case in an opposite manner for the 2:1 tuning case. In addition, the 2:1 tuning case shows a lower performance with shorter attenuation bandwidth due to the substantial reduction of the coupling factor associated with $\sqrt{\phi_2}$.

The nonlinear shunt with the nonsmooth component is also validated experimentally, in which the two possible tunings, the 1:1 and 2:1 tunings, are considered. The shunt circuit is illustrated in which the nonsmooth component is analyzed with a diode. The absorber is applied to attenuate the first twisting mode of the hydrofoil. The experimental frequency response curves validated the numerical prediction in addition to the optimal parameters estimated in the theoretical analysis.

Perspectives

Presently, the various set-up for the nonlinear shunts has been studied theoretically and validated under very controlled conditions. In addition, the tests on the foil structure were not conducted in water medium. In the context of controlling the foil in more realistic conditions, the interactions with the fluid might behave very differently than the mono-frequency excitation used in this work. Moreover, the fluid is known to alter directly some parameters, such as the modal mass, which make the tuning even more challenging.

The first important step to be performed involves the experimental validations of the design of nonlinear shunts with hydrofoil placed in a water medium. The preliminary study to perform such a step should include a fluid-structure interaction analysis to analyze the vortex shedding in the laminar and turbulent flows and its effect on the vibrations and the piezoelectric coupling factor. In addition, a sensitivity analysis of the electromechanical modal parameters with respect to the water temperature and pressure might be necessary.

Regarding the nonlinear shunt circuit designs, some enhancements can be proposed. During experimental testing of 2:1 resonances, the observed circuit voltages quickly become very high. It was also necessary to maintain the excitations at levels compatible with the operational limits of the electronic components. They are probably not very representative of the levels in real conditions. Nevertheless, the attained voltages during the experiments were still far from the operating limits of the components(i.e., the operational amplifiers, the differential amplifier, and the multipliers), thus it will be useful to test the circuits in their full ranges (i.e., to consider higher excitation levels that leads to higher voltages). Indeed, at high levels of excitation, more complex responses was proven to appear (as in chapter 3), leading to detune the system and losing the saturation feature. However, thanks to the introduced cubic nonlinearity, one can find the right tuning of the cubic gain to lock the antiresonance at the resonance frequency and preserve the high performance, even at higher forcing levels. This is suggested in the following plot (see more discussion in Sec. 4 in chapter 5) in which, for the modal parameters considered, if one considers a low forcing level (between 0 and 0.35 mN), the value of the cubic gain $\beta_c = 0.001$, estimated analytically, will preserve the saturation. However, at higher forcing levels, thus attaining higher voltages in the circuit, one can slightly modify the cubic gain tuning to recover the saturation amplitude (for example, observe the minimum in Fig. 6.1(b) for $F = 0.49$mN with $\beta_c = 0.00093 < 0.001$).

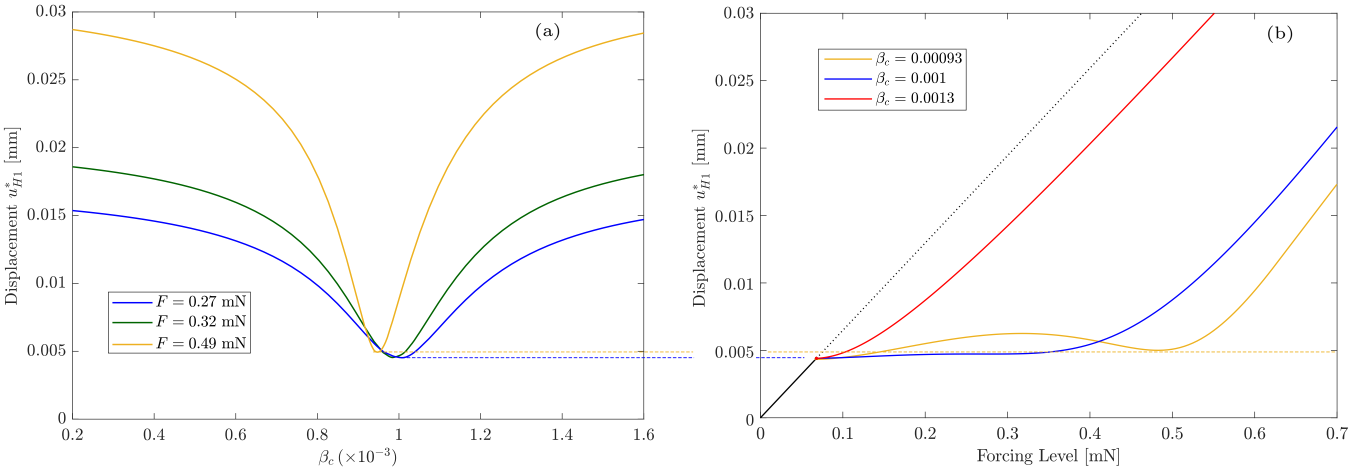

Figure 6.1: Choosing the right tuning of the cubic gain β_c as the excitation level F increases.

A first possibility of improvement would be to use operational amplifiers whose maximum voltages are higher. However, this option seems quite complex in implementation. Indeed, band gain products are generally less efficient and stability problems may result. This supposes moreover to have several power supplies: those intended for the power amplifiers, and those necessary for the mathematical functions such as the analogical multipliers.

Another problem concerns the inductor. Generally, it must have significant values, which justifies making it by a gyrator circuit like the Antoniou inductor. However, we have observed on several occasions that this circuit presents a parasitic resistance or even instabilities under conditions that are still poorly identified. They are all the more troublesome as they seem to be linked to internal defaults in the amplifiers themselves. Another option would be to change technology, using switching amplifiers, to solve the problem of voltage levels and to digitize part of the mathematical functions, allowing higher flexibility. In particular, the use of a quadratic nonlinearity requires a complex tuning that does not seem robust with respect to parametric variations.

It has already been verified that the resonances of the submerged foil were influenced by the speed of the flow, for example, which suggests that some form of resonance tracking will be needed. This type of problem has already been studied for nonlinear resonance plots. It is possible by automatic tuning with phase lock loop (PLL) to stabilize vibrations by forcing the resonance condition. It, therefore, seems possible to transpose these techniques to automate the adjustment of the nonlinear shunt.

The use of a nonsmooth nonlinearity turned out to have an unexpected behavior. Namely, It seemed relatively efficient to achieve a 2:1 internal resonance, but without the saturation feature. On this last point, it may be interesting to combine nonmooth nonlinearities with polynomial nonlinearities, starting by taking up the “diode” principle but substituting a quadratic branch for the linear branch. On the other hand, this circuit offers on the 1:1 resonance the possibility of making a tunable shunt in a simple way by playing on the slope of the linear part of the characteristic. This result makes it possible to use lower inductance values for the resonant shunts and possibly be an alternative approach for a tunable resonant shunt.

Bibliography

[1] B. Sahoo, R. K. Satpathy, and S. K. Panigrahi, "Analysis of a Turbine Blade Failure in a Military Turbojet Engine," *International Journal of Turbo and Jet-Engines*, vol. 33, Jan. 2016.

[2] A. Nienow and W. Bujalski, "The Versatility of Up-Pumping Hydrofoil Agitators," *Chemical Engineering Research and Design*, vol. 82, pp. 1073–1081, Sept. 2004.

[3] A. Posa, R. Broglia, and E. Balaras, "Flow over a hydrofoil in the wake of a propeller," *Computers & Fluids*, vol. 213, p. 104714, Dec. 2020.

[4] D. G. Hull, *Fundamentals of Airplane Flight Mechanics.* Berlin ; London: Springer, 2007.

[5] O. M. Faltinsen, *Hydrodynamics of High-Speed Marine Vehicles.* Cambridge ; New York: Cambridge University Press, 2005.

[6] E. J. Chae, D. T. Akcabay, A. Lelong, J. A. Astolfi, and Y. L. Young, "Numerical and experimental investigation of natural flow-induced vibrations of flexible hydrofoils," *Physics of Fluids*, vol. 28, p. 075102, July 2016.

[7] J. Hu, X. Ning, S. Sun, F. Li, J. Ma, and W. Zhang, "Fluid-structure coupled analysis of flow-induced vibrations in three dimensional elastic hydrofoils," *Marine Structures*, vol. 84, p. 103220, July 2022.

[8] A. H. Lee, R. L. Campbell, B. A. Craven, and S. A. Hambric, "Fluid–Structure Interaction Simulation of Vortex-Induced Vibration of a Flexible Hydrofoil," *Journal of Vibration and Acoustics*, vol. 139, p. 041001, Aug. 2017.

[9] I. E. Garrick and W. H. Reed, "Historical Development of Aircraft Flutter," *Journal of Aircraft*, vol. 18, pp. 897–912, Nov. 1981.

[10] M. A. Shubov, "Flutter Phenomenon in Aeroelasticity and Its Mathematical Analysis," *Journal of Aerospace Engineering*, vol. 19, pp. 1–12, Jan. 2006.

[11] C. Pandit Pagwiwoko and L. Jezequel, "Analysing Non-Linear Flutter Vibrations Using System Dynamic Approach," in *Noise and Vibration Control - From Theory to Practice* (E. Noroozinejad Farsangi, ed.), IntechOpen, Oct. 2019.

[12] J.-J. Sinou, "Flutter instability and active aeroelastic control with time delay for a two-dimensional airfoil," *European Journal of Mechanics - A/Solids*, vol. 92, p. 104465, Mar. 2022.

[13] L. Christiansen, T. Lehn-Schiøler, E. Mosekilde, P. Gránásy, and H. Matsushita, "Nonlinear characteristics of randomly excited transonic flutter," *Mathematics and Computers in Simulation*, vol. 58, pp. 385–405, Mar. 2002.

[14] Y. Watine, C. Gabillet, J.-A. Astolfi, L. Pernod, B. Lossouarn, and J.-F. Deü, "Vortex Induced Vibrations Analysis of a Cantilevered Blunt Plate by Proper Orthogonal Decomposition of TR-PIV and Structural Modal Analysis," in *ASME 2020 Fluids Engineering Division Summer Meeting*, 2020.

[15] J. Hu, Z. Wang, W. Zhao, S. Sun, C. Sun, and C. Guo, "Numerical Simulation on Vortex Shedding from a Hydrofoil in Steady Flow," *Journal of Marine Science and Engineering*, vol. 8, no. 3, 2020.

[16] "Luna Rossa AC75." www.lunarossachallenge.com.

[17] https://en.wikipedia.org/wiki/USS_Hercules_(PHM-2).

[18] Y. L. Young, C. M. Harwood, F. Miguel Montero, J. C. Ward, and S. L. Ceccio, "Ventilation of Lifting Bodies: Review of the Physics and Discussion of Scaling Effects," *Applied Mechanics Reviews*, vol. 69, p. 010801, Jan. 2017.

[19] E. Amromin, "Ships with ventilated cavitation in seaways and active flow control," *Applied Ocean Research*, vol. 50, pp. 163–172, Mar. 2015.

[20] F. Mohammed Arab, B. Augier, F. Deniset, P. Casari, and J. A. Astolfi, "Effects on cavitation inception of leading and trailing edge flaps on a high-performance hydrofoil," *Applied Ocean Research*, vol. 126, p. 103285, Sept. 2022.

[21] S. Frikha, O. Coutier-Delgosha, and J. A. Astolfi, "Influence of the Cavitation Model on the Simulation of Cloud Cavitation on 2D Foil Section," *International Journal of Rotating Machinery*, vol. 2008, pp. 1–12, 2008.

[22] A. Ducoin, J. André Astolfi, and J.-F. Sigrist, "An experimental analysis of fluid structure interaction on a flexible hydrofoil in various flow regimes including cavitating flow," *European Journal of Mechanics - B/Fluids*, vol. 36, pp. 63–74, Nov. 2012.

[23] P. D. Swales, A. J. Wright, R. C. McGregor, and R. Rothblum, “The Mechanism of Ventilation Inception on Surface Piercing Foils,” *Journal of Mechanical Engineering Science*, vol. 16, pp. 18–24, Feb. 1974.

[24] E. P. Rood, “Review—Mechanisms of Cavitation Inception,” *Journal of Fluids Engineering*, vol. 113, pp. 163–175, June 1991.

[25] D. T. Akcabay, E. J. Chae, Y. L. Young, A. Ducoin, and J. A. Astolfi, “Cavity induced vibration of flexible hydrofoils,” *Journal of Fluids and Structures*, vol. 49, pp. 463–484, Aug. 2014.

[26] G. Wang, Q. Wu, B. Huang, and Y. Gao, “Experimental investigation of the flow-induced vibration of hydrofoils in cavitating flows,” *Journal of Physics: Conference Series*, vol. 656, p. 012105, Dec. 2015.

[27] V. Temtching Temou, *Etude Expérimentale et Numérique Des Interactions Fluide-Structure Sur Des Hydrofoils Flexibles En Composite*. PhD thesis, Université de Bretagne Occidentale, 2020.

[28] B. Yang and X. Shu, “Hydrofoil optimization and experimental validation in helical vertical axis turbine for power generation from marine current,” *Ocean Engineering*, vol. 42, pp. 35–46, Mar. 2012.

[29] K. Kostas, A. Ginnis, C. Politis, and P. Kaklis, “Shape-optimization of 2D hydrofoils using an Isogeometric BEM solver,” *Computer-Aided Design*, vol. 82, pp. 79–87, Jan. 2017.

[30] N. Garg, Z. Lyu, T. Dhert, J. Martins, and Y. L. Young, “High-fidelity Hydrodynamic Shape Optimization of a 3-D Morphing Hydrofoil,” in *Fourth International Symposium on Marine Propulsors*, (Texas, USA), p. 13, 2015.

[31] M. Sacher, M. Durand, É. Berrini, F. Hauville, R. Duvigneau, O. Le Maître, and J.-A. Astolfi, “Flexible hydrofoil optimization for the 35th America’s Cup with constrained EGO method,” *Ocean Engineering*, vol. 157, pp. 62–72, June 2018.

[32] Y. Liao, J. R. Martins, and Y. L. Young, “3-D high-fidelity hydrostructural optimization of cavitation-free composite lifting surfaces,” *Composite Structures*, vol. 268, p. 113937, July 2021.

[33] N. Garg, B. W. Pearce, P. A. Brandner, A. W. Phillips, J. R. Martins, and Y. L. Young, “Experimental investigation of a hydrofoil designed via hydrostructural optimization,” *Journal of Fluids and Structures*, vol. 84, pp. 243–262, Jan. 2019.

[34] P. Ploe, *Surrogate-Based Optimization of Hydrofoil Shapes Using RANS Simulations*. PhD thesis, Université de Bretagne Loire, 2018.

[35] F. Gaugian, *Analyse Expérimentale et Simulation Numérique de l'interaction Fluide-Structure d'un Hydrofoil Élastique En Écoulement Subcavitant et Cavitant.* PhD thesis, Ecole Nationale Supérieure d'Arts et Métiers - Institut de Recherche de l'Ecole Navale, 2013.

[36] A. Lelong, *Etude Expérimentale Du Comportement Hydroélastique d'une Structure Flexible Pour Différents Régimes d'écoulement.* PhD thesis, Ecole Doctorale des sciences de la Mer - Institut de Recherche de l'Ecole Navale, 2016.

[37] A. Ducoin, *Etude Expérimentale et Numérique Du Chargement Hydrodynamique Des Corps Portants En Régime Transitoire Avec Prise En Compte Du Couplage Fluide Structure.* PhD thesis, Ecole Centrale de Nantes, 2008.

[38] P. Ausoni, M. Farhat, Y. A. Bouziad, J.-L. Kueny, and F. Avellan, "Kármán vortex shedding in the wake of a 2D hydrofoil: Measurement and numerical simulation," in *IAHR Int. Meeting of WG on Cavitation and Dynamic Problems in Hydraulic Machinery and Systems*, p. 15, 2006.

[39] P. Ausoni, M. Farhat, and F. Avellan, "Hydrofoil roughness effects on von kármán vortex shedding," in *2nd IAHR International Meeting of the Workgroup on Cavitation and Dynamic Problems in Hydraulic Machinery and Systems*, p. 4, 2007.

[40] C. Williamson and R. Govardhan, "Vortex induced vibrations," *Annu. Rev. Fluid Mech.*, p. 53, 2004.

[41] S. Krenk, "Frequency Analysis of the Tuned Mass Damper," *Journal of Applied Mechanics*, vol. 72, pp. 936–942, Nov. 2005.

[42] A. Javidialesaadi and N. E. Wierschem, "Optimal design of rotational inertial double tuned mass dampers under random excitation," *Engineering Structures*, vol. 165, pp. 412–421, June 2018.

[43] T. Igusa and K. Xu, "Vibration control using multiple tuned mass dampers," *Journal of Sound and Vibration*, vol. 175, pp. 491–503, 1994.

[44] M. Abé and Y. Fujino, "Dynamic characterization of multiple tuned mass dampers and some design formulas," *Earthquake Engineering & Structural Dynamics*, vol. 23, pp. 813–835, Aug. 1994.

[45] D. Chen, S. Huang, C. Huang, R. Liu, and F. Ouyang, "Passive control of jacket–type offshore wind turbine vibrations by single and multiple tuned mass dampers," *Marine Structures*, vol. 77, p. 102938, May 2021.

[46] A. Mayou and V. Denoël, "Asymptotic analysis of multiple mode structures equipped with multiple tuned mass dampers," *Journal of Sound and Vibration*, vol. 535, p. 117104, Sept. 2022.

[47] V. Laface, G. Alotta, G. Failla, C. Ruzzo, and F. Arena, “A two-degree-of-freedom tuned mass damper for offshore wind turbines on floating spar supports,” *Marine Structures*, vol. 83, p. 103146, May 2022.

[48] M. Auleley, O. Thomas, and C. Giraud-Audine, “Enhancement of a dynamic vibration absorber by means of an electromagnetic shunt,” *Journal of Intelligent Material Systems and Structures*, vol. 32, pp. 331–354, 2021.

[49] J. Wang, C. Lin, and B. Chen, “Vibration suppression for high-speed railway bridges using tuned mass dampers,” *International Journal of Solids and Structures*, vol. 40, pp. 465–491, Jan. 2003.

[50] H. Radmard Rahmani and C. Könke, “Seismic Control of Tall Buildings Using Distributed Multiple Tuned Mass Dampers,” *Advances in Civil Engineering*, vol. 2019, pp. 1–19, Sept. 2019.

[51] J. Brownjohn, E. Carden, C. Goddard, and G. Oudin, “Real-time performance monitoring of tuned mass damper system for a 183m reinforced concrete chimney,” *Journal of Wind Engineering and Industrial Aerodynamics*, vol. 98, pp. 169–179, Mar. 2010.

[52] M. Setareh, J. Ritchey, A. Baxter, and T. Murray, “Pendulum Tuned Mass Dampers for Floor Vibration Control,” *Journal of performance of ponstructed facilities*, vol. 20, 2006.

[53] S. Wang, G. Yang, L. Ji, C. Bi, and C. Zheng, “Multi-mode vibration attenuation of mistuned bladed disks by frictional tuned mass dampers array,” *Journal of Sound and Vibration*, vol. 536, p. 117176, Oct. 2022.

[54] E. Mrabet, M. Ichchou, and N. Bouhaddi, “Random vibro-acoustic control of internal noise through optimized Tuned Mass Dampers,” *Mechanical Systems and Signal Processing*, vol. 130, pp. 17–40, Sept. 2019.

[55] L. Zuo and S. Nayfeh, “Optimization of the individual stiffness and damping parameters in multiple-tuned- mass-damper systems,” *Journal of Vibration and Acoustics*, vol. 127, 2005.

[56] S. Salcedo-Sanz, C. Camacho-Gómez, A. Magdaleno, E. Pereira, and A. Lorenzana, “Structures vibration control via Tuned Mass Dampers using a co-evolution Coral Reefs Optimization algorithm,” *Journal of Sound and Vibration*, vol. 393, pp. 62–75, Apr. 2017.

[57] R. Greco and G. C. Marano, “Optimum design of Tuned Mass Dampers by displacement and energy perspectives,” *Soil Dynamics and Earthquake Engineering*, vol. 49, pp. 243–253, June 2013.

[58] G. Carlo Marano, R. Greco, and B. Chiaia, “A comparison between different optimization criteria for tuned mass dampers design,” *Journal of Sound and Vibration*, vol. 329, pp. 4880–4890, Nov. 2010.

[59] J. Bonet, A. J. Gil, and R. D. Wood, *Nonlinear Solid Mechanics for Finite Element Analysis: Dynamics.* Cambridge University Press, first ed., Mar. 2021.

[60] J. N. Reddy, *Theory and Analysis of Elastic Plates and Shells, Second Edition.* CRS Press, second edition ed., 2007.

[61] D. J. Inman, *Engineering Vibration.* Boston: Pearson, fourth edition ed., 2014.

[62] P. C. Muller and W. Schiehlen, *Linear Vibrations A Theoretical Treatment of Multi-Degree-of-Freedom Vibrating Systems.* Martinus nijhoff publishers, 1985.

[63] A. Beléndez, A. Hernández, A. Márquez, T. Beléndez, and C. Neipp, "Analytical approximations for the period of a nonlinear pendulum," *European Journal of Physics*, vol. 27, pp. 539–551, May 2006.

[64] S. Ghuku and K. Saha, "A Review on Stress and Deformation Analysis of Curved Beams under Large Deflection," *International Journal of Engineering and Technologies*, vol. 11, pp. 13–39, July 2017.

[65] O. Thomas, A. Sénéchal, and J.-F. Deü, "Hardening/softening behavior and reduced order modeling of nonlinear vibrations of rotating cantilever beams," *Nonlinear Dynamics*, vol. 86, pp. 1293–1318, Oct. 2016.

[66] C. Camier, C. Touzé, and O. Thomas, "Non-linear vibrations of imperfect free-edge circular plates and shells," 2009.

[67] J. Turner, "Non-linear vibrations of a beam with cantilever-Hertzian contact boundary conditions," *Journal of Sound and Vibration*, vol. 275, pp. 177–191, Aug. 2004.

[68] S. S. Antman, *Nonlinear Problems of Elasticity.* No. v. 107 in Applied Mathematical Sciences, New York: Springer, 2nd ed ed., 2005.

[69] F.-J. Elmer, "Nonlinear dynamics of dry friction," *Journal of Physics A: Mathematical and General*, vol. 30, pp. 6057–6063, Sept. 1997.

[70] S. Benacchio, C. Giraud-Audine, and O. Thomas, "Effect of dry friction on a parametric nonlinear oscillator," *Nonlinear Dynamics*, vol. 108, pp. 1005–1026, Apr. 2022.

[71] A. R. Plastino, R. S. Wedemann, E. M. F. Curado, F. D. Nobre, and C. Tsallis, "Nonlinear drag forces and the thermostatistics of overdamped motion," *Physical Review E*, vol. 98, p. 012129, July 2018.

[72] A. Nayfeh and D. Mook, *Nonlinear Oscillations.* John Wiley & Sons, inc., 1995.

[73] J. Guckenheimer and P. Holmes, *Nonlinear Oscillations, Dynamical Systems, and Bifurcations of Vector Fields*, vol. 42 of *Applied Mathematical Sciences*. New York, NY: Springer New York, 1983.

[74] I. Kovacic and M. J. Brennan, *The Duffing Equation: Nonlinear Oscillators and Their Behaviour*. Wiley, 2011.

[75] I. Vassilopoulou and C. J. Gantes, “Nonlinear dynamic phenomena in a SDOF model of cable net,” *Archive of Applied Mechanics*, vol. 82, pp. 1689–1703, Oct. 2012.

[76] B. Bodo, J. Armand Eyebe Fouda, A. Mvogo, and S. Tagne, “Experimental hysteresis in memristor based Duffing oscillator,” *Chaos, Solitons & Fractals*, vol. 115, pp. 190–195, Oct. 2018.

[77] A. M. Abou-Rayan, A. H. Nayfeh, D. T. Mook, and M. A. Nayfeh, “Nonlinear response of a parametrically excited buckled beam,” *Nonlinear Dynamics*, vol. 4, pp. 499–525, Oct. 1993.

[78] D. Jordan and P. Smith, *Nonlinear Ordinary Differential Equations*. Oxford: Clarendon Press, 1977.

[79] A. Givois, J.-J. Tan, C. Touzé, and O. Thomas, “Backbone curves of coupled cubic oscillators in one-to-one internal resonance: Bifurcation scenario, measurements and parameter identification,” *Meccanica*, vol. 55, pp. 481–503, Mar. 2020.

[80] J. M. Londoño, S. A. Neild, and J. E. Cooper, “Identification of backbone curves of nonlinear systems from resonance decay responses,” *Journal of Sound and Vibration*, vol. 348, pp. 224–238, July 2015.

[81] X. Liu, *Backbone Curve Analysis of Nonlinear Mechanical Systems*. PhD thesis, University of Sheffield, 2018.

[82] Y. Sun, A. Vizzaccaro, J. Yuan, and L. Salles, “An extended energy balance method for resonance prediction in forced response of systems with non-conservative nonlinearities using damped nonlinear normal mode,” *Nonlinear Dynamics*, vol. 103, pp. 3315–3333, Mar. 2021.

[83] T. Hill, S. Neild, and A. Cammarano, “An analytical approach for detecting isolated periodic solution branches in weakly nonlinear structures,” *Journal of Sound and Vibration*, vol. 379, pp. 150–165, Sept. 2016.

[84] R. Kuether, L. Renson, T. Detroux, C. Grappasonni, G. Kerschen, and M. Allen, “Nonlinear normal modes, modal interactions and isolated resonance curves,” *Journal of Sound and Vibration*, vol. 351, pp. 299–310, Sept. 2015.

[85] T. Hill, A. Cammarano, S. Neild, and D. Wagg, “Interpreting the forced responses of a two-degree-of-freedom nonlinear oscillator using backbone curves,” *Journal of Sound and Vibration*, vol. 349, pp. 276–288, Aug. 2015.

[86] S. Shaw and C. Pierre, “Non-linear normal modes and invariant manifolds,” *Journal of Sound and Vibration*, vol. 150, pp. 170–173, Oct. 1991.

[87] S. Shaw and C. Pierre, “Normal Modes for Non-linear vibratory systems,” *Journal of Sound and Vibration*, vol. 164, pp. 85–124, 1993.

[88] D. I. Caruntu, M. A. Botello, C. A. Reyes, and J. Beatriz, “Frequency–amplitude response of superharmonic resonance of second order of electrostatically actuated MEMS cantilever resonators,” *International Journal of Non-Linear Mechanics*, vol. 133, p. 103719, July 2021.

[89] A. Vakakis, *Analysis and Identification of Linear and Nonlinear Normal Modes in Vibrating Systems*. PhD thesis, California Institute of Technology, 1990.

[90] G. Kerschen, M. Peeters, J. Golinval, and A. Vakakis, “Nonlinear normal modes, Part I: A useful framework for the structural dynamicist,” *Mechanical Systems and Signal Processing*, vol. 23, pp. 170–194, Jan. 2009.

[91] T. L. Hill, A. Cammarano, S. A. Neild, and D. A. W. Barton, “Identifying the significance of nonlinear normal modes,” *Proceedings of the Royal Society A: Mathematical, Physical and Engineering Sciences*, vol. 473, p. 20160789, Mar. 2017.

[92] G. S. Agnes and D. J. Inman, “Performance of Nonlinear Vibration Absorbers for Multi-Degrees-of-Freedom Systems Using Nonlinear Normal Modes,” in *Normal Modes and Localization in Nonlinear Systems* (A. F. Vakakis, ed.), pp. 275–292, Dordrecht: Springer Netherlands, 2001.

[93] H. Yabuno and A. H. Nayfeh, “Nonlinear Normal Modes of a Parametrically Excited Cantilever Beam,” in *Normal Modes and Localization in Nonlinear Systems* (A. F. Vakakis, ed.), pp. 65–77, Dordrecht: Springer Netherlands, 2001.

[94] W. C. Xie, H. P. Lee, and S. P. Lim, “Nonlinear Dynamic Analysis of MEMS Switches by Nonlinear Modal Analysis,” *Nonlinear Dynamics*, vol. 31, pp. 243–265, 2003.

[95] C. E. Mazzilli, M. E. Soares, and O. G. Baracho Neto, “Non-linear normal modes of a simply supported beam: Continuous system and finite-element models,” *Computers & Structures*, vol. 82, pp. 2683–2691, Dec. 2004.

[96] C. Touzé, O. Thomas, and A. Huberdeau, “Asymptotic non-linear normal modes for large-amplitude vibrations of continuous structures,” *Computers & Structures*, vol. 82, pp. 2671–2682, Dec. 2004.

[97] C. Touzé and M. Amabili, “Nonlinear normal modes for damped geometrically nonlinear systems: Application to reduced-order modelling of harmonically forced structures,” *Journal of Sound and Vibration*, vol. 298, pp. 958–981, Dec. 2006.

[98] N. Srinil and G. Rega, “Two-to-one resonant multi-modal dynamics of horizontal/inclined cables. Part II: Internal resonance activation, reduced-order models and nonlinear normal modes,” *Nonlinear Dynamics*, vol. 48, pp. 253–274, Feb. 2007.

[99] S. Lenci and G. Rega, “Dimension reduction of homoclinic orbits of buckled beams via the non-linear normal modes technique,” *International Journal of Non-Linear Mechanics*, vol. 42, pp. 515–528, Apr. 2007.

[100] A. Vakakis, “Non-linear normal modes (nnms) and their applications in vibration theory: An overview,” *Mechanical Systems and Signal Processing*, vol. 11, pp. 3–22, Jan. 1997.

[101] L. Jezequel and C. Lamarque, “Analysis of non-linear dynamical systems by the normal form theory,” *Journal of Sound and Vibration*, vol. 149, pp. 429–459, Sept. 1991.

[102] A. H. Nayfeh and S. A. Nayfeh, “Nonlinear Normal Modes of a Continuous System With Quadratic Nonlinearities,” *Journal of Vibration and Acoustics*, vol. 117, pp. 199–205, Apr. 1995.

[103] A. F. Vakakis and O. Gendelman, “Energy Pumping in Nonlinear Mechanical Oscillators: Part II—Resonance Capture,” *Journal of Applied Mechanics*, vol. 68, pp. 42–48, Jan. 2001.

[104] E. Boroson, S. Missoum, P.-O. Mattei, and C. Vergez, “Optimization under uncertainty of parallel nonlinear energy sinks,” *Journal of Sound and Vibration*, vol. 394, pp. 451–464, Apr. 2017.

[105] V. Iurasov and P.-O. Mattei, “Bistable nonlinear damper based on a buckled beam configuration,” *Nonlinear Dynamics*, vol. 99, pp. 1801–1822, Feb. 2020.

[106] Y. Starosvetsky and O. Gendelman, “Response regimes of linear oscillator coupled to nonlinear energy sink with harmonic forcing and frequency detuning,” *Journal of Sound and Vibration*, vol. 315, pp. 746–765, Aug. 2008.

[107] G. Kerschen, Y. S. Lee, A. F. Vakakis, D. M. McFarland, and L. A. Bergman, “Irreversible Passive Energy Transfer in Coupled Oscillators with Essential Nonlinearity,” *SIAM Journal on Applied Mathematics*, vol. 66, no. 2, pp. 648–679, 2006.

[108] S. Tsakirtzis, P. N. Panagopoulos, G. Kerschen, O. Gendelman, A. F. Vakakis, and L. A. Bergman, “Complex dynamics and targeted energy transfer in linear oscillators coupled to multi-degree-of-freedom essentially nonlinear attachments,” *Nonlinear Dynamics*, vol. 48, pp. 285–318, Feb. 2007.

[109] O. V. Gendelman, “Targeted energy transfer in systems with external and self-excitation,” *Proceedings of the Institution of Mechanical Engineers, Part C: Journal of Mechanical Engineering Science*, vol. 225, pp. 2007–2043, Sept. 2011.

[110] G. Sigalov, O. V. Gendelman, M. A. AL-Shudeifat, L. I. Manevitch, A. F. Vakakis, and L. A. Bergman, “Resonance captures and targeted energy transfers in an inertially-coupled rotational nonlinear energy sink,” *Nonlinear Dynamics*, vol. 69, pp. 1693–1704, Sept. 2012.

[111] P.-O. Mattei, R. Ponçot, M. Pachebat, and R. Côte, “Nonlinear targeted energy transfer of two coupled cantilever beams coupled to a bistable light attachment,” *Journal of Sound and Vibration*, vol. 373, pp. 29–51, July 2016.

[112] D. M. McFarland, G. Kerschen, J. J. Kowtko, Y. S. Lee, L. A. Bergman, and A. F. Vakakis, “Experimental investigation of targeted energy transfers in strongly and nonlinearly coupled oscillators,” *Journal of the Acoustical Society of America*, vol. 118, no. 2, p. 10, 2005.

[113] E. Gourdon, N. Alexander, C. Taylor, C. Lamarque, and S. Pernot, “Nonlinear energy pumping under transient forcing with strongly nonlinear coupling: Theoretical and experimental results,” *Journal of Sound and Vibration*, vol. 300, pp. 522–551, Mar. 2007.

[114] O. Braydi, C. Gogu, and M. Paredes, “Robustness and reliability investigations on a nonlinear energy sink device concept,” *Mechanics & Industry*, vol. 21, no. 6, p. 603, 2020.

[115] E. Matta, “Seismic effectiveness and robustness of tuned mass dampers versus nonlinear energy sinks in a lifecycle cost perspective,” *Bulletin of Earthquake Engineering*, vol. 19, pp. 513–551, Jan. 2021.

[116] J. Luo, N. E. Wierschem, S. A. Hubbard, L. A. Fahnestock, D. Dane Quinn, D. Michael McFarland, B. F. Spencer, A. F. Vakakis, and L. A. Bergman, “Large-scale experimental evaluation and numerical simulation of a system of nonlinear energy sinks for seismic mitigation,” *Engineering Structures*, vol. 77, pp. 34–48, Oct. 2014.

[117] D. Bitar, E. Gourdon, C.-H. Lamarque, and M. Collet, “Shunt loudspeaker using nonlinear energy sink,” *Journal of Sound and Vibration*, vol. 456, pp. 254–271, Sept. 2019.

[118] B. Bergeot, S. Bellizzi, and B. Cochelin, “Passive suppression of helicopter ground resonance using nonlinear energy sinks attached on the helicopter blades,” *Journal of Sound and Vibration*, vol. 392, pp. 41–55, Mar. 2017.

[119] L. Sanches, T. A. M. Guimarães, and F. D. Marques, “Nonlinear energy sink to enhance the landing gear shimmy performance,” *Acta Mechanica*, vol. 232, pp. 2605–2622, July 2021.

[120] E. Gourc, S. Seguy, G. Michon, and A. Berlioz, "Delayed dynamical system strongly coupled to a nonlinear energy sink: Application to machining chatter," in *International Conference on Structural Nonlinear Dynamics and Diagnostics*, 2012.

[121] F. Georgiadis, A. F. Vakakis, D. McFarland, and L. A. Bergman, "Shock isolation through passive energy pumping in a system with piecewise linear stiffnesses," in *19th Biennial Conference on Mechanical Vibration and Noise, Parts A, B, and C*, vol. 5, pp. 1569–1574, 2003.

[122] C.-H. Lamarque, O. V. Gendelman, A. Ture Savadkoohi, and E. Etcheverria, "Targeted energy transfer in mechanical systems by means of non-smooth nonlinear energy sin," *Acta Mechanica*, vol. 221, pp. 175–200, 2011.

[123] C.-H. Lamarque, A. Ture Savadkoohi, and Z. Dimitrijevic, "Dynamics of a linear system with time-dependent mass and a coupled light mass with non-smooth potential," *Meccanica*, vol. 49, pp. 135–145, 2014.

[124] B. Youssef and R. I. Leine, "A complete set of design rules for a vibro-impact NES based on a multiple scales approximation of a nonlinear mode," *Journal of Sound and Vibration*, vol. 501, 2021.

[125] Z. Lu, Z. Wang, Y. Zhou, and X. Lu, "Nonlinear dissipative devices in structural vibration control: A review," *Journal of Sound and Vibration*, vol. 423, pp. 18–49, June 2018.

[126] H. Ding and L.-Q. Chen, "Designs, analysis, and applications of nonlinear energy sinks," *Nonlinear Dynamics*, vol. 100, pp. 3061–3107, June 2020.

[127] A. F. Vakakis, O. V. Gendelman, L. A. Bergman, A. Mojahed, and M. Gzal, "Nonlinear targeted energy transfer: State of the art and new perspectives," *Nonlinear Dynamics*, vol. 108, pp. 711–741, Apr. 2022.

[128] G. Habib, T. Detroux, R. Viguie, and G. Kerschen, "Nonlinear generalization of Den Hartog's equal-peak method," *Mechanical Systems and Signal Processing*, vol. 52–53, pp. 17–28, 2015.

[129] G. Raze and G. Kerschen, "Multimodal vibration damping of nonlinear structures using multiple nonlinear absorbers," *International Journal of Non-Linear Mechanics*, vol. 119, p. 103308, Mar. 2020.

[130] M. Vakilinejad, A. Grolet, and O. Thomas, "A comparison of robustness and performance of linear and nonlinear Lanchester dampers," *Nonlinear Dynamics*, vol. 100, pp. 269–287, Mar. 2020.

[131] S. J. Elliott, M. G. Tehrani, and R. S. Langley, “Nonlinear damping and quasi-linear modelling,” *Philosophical Transactions of the Royal Society A: Mathematical, Physical and Engineering Sciences*, vol. 373, Sept. 2015.

[132] M. Cirelli, M. Cera, E. Pennestrì, and P. P. Valentini, “Nonlinear design analysis of centrifugal pendulum vibration absorbers: An intrinsic geometry-based framework,” *Nonlinear Dynamics*, vol. 102, pp. 1297–1318, Nov. 2020.

[133] V. Mahe, A. Renault, A. Grolet, O. Thomas, and H. Mahe, “Dynamic stability of centrifugal pendulum vibration absorbers allowing a rotational mobility,” *Journal of Sound and Vibration*, vol. 517, p. 116525, Jan. 2022.

[134] V. Mahé, A. Renault, A. Grolet, H. Mahé, and O. Thomas, “On the dynamic stability and efficiency of centrifugal pendulum vibration absorbers with rotating pendulums,” *Journal of Sound and Vibration*, vol. 536, p. 117157, Oct. 2022.

[135] V. Mahe, A. Renault, A. Grolet, H. Mahe, and O. Thomas, “Subharmonic centrifugal pendulum vibration absorbers allowing a rotational mobility,” *Mechanical Systems and Signal Processing*, vol. 177, p. 109125, Sept. 2022.

[136] A. H. Nayfeh, *Nonlinear Interactions Analytical, Computational, and Experimental Methods.* John Wiley & Sons, inc., 2000.

[137] A. Grolet, Z. Shami, S. Arabi, and O. Thomas, “Experimental non-linear localisation in a system of two coupled beams,” in *Dynamical Systems -Theory and Applications*, 2019.

[138] M. Amabili, F. Pellicano, and A. F. Vakakis, “Nonlinear Vibrations and Multiple Resonances of Fluid-Filled, Circular Shells, Part 1: Equations of Motion and Numerical Results,” *Journal of Vibration and Acoustics*, vol. 122, pp. 346–354, Oct. 2000.

[139] A. Chaigne, C. Touzé, and O. Thomas, “Nonlinear vibrations and chaos in gongs and cymbals,” *Acoustical Science and Technology*, vol. 26, no. 5, pp. 403–409, 2005.

[140] O. Thomas, C. Touzé, and A. Chaigne, “Non-linear vibrations of free-edge thin spherical shells: Modal interaction rules and 1:1:2 internal resonance,” *International Journal of Solids and Structures*, vol. 42, pp. 3339–3373, June 2005.

[141] O. Thomas, C. Touzé, and É. Luminais, “Non-linear vibrations of free-edge thin spherical shells: Experiments on a 1:1:2 internal resonance,” *Nonlinear Dynamics*, vol. 49, pp. 259–284, July 2007.

[142] V. Guillot, A. Givois, M. Colin, O. Thomas, A. Ture Savadkoohi, and C.-H. Lamarque, "Theoretical and experimental investigation of a 1:3 internal resonance in a beam with piezoelectric patches," *Journal of Vibration and Control*, vol. 26, pp. 1119–1132, July 2020.

[143] J. Miles, "Parametric excitation of an internally resonant double pendulum," *Journal of Applied Mathematics and Physic*, vol. 36, p. 9, 1985.

[144] A. H. Nayfeh, D. T. Mook, and L. R. Marshall, "Nonlinear Coupling of Pitch and Roll Modes in Ship Motions," *Journal of Hydronautics*, vol. 7, pp. 145–152, Oct. 1973.

[145] G. Gobat, L. Guillot, A. Frangi, B. Cochelin, and C. Touzé, "Backbone curves, Neimark-Sacker boundaries and appearance of quasi-periodicity in nonlinear oscillators: Application to 1:2 internal resonance and frequency combs in MEMS," *Meccanica*, vol. 56, pp. 1937–1969, Aug. 2021.

[146] A. Nayfeh, "Parametric excitation of two internally resonant oscillators," *Journal of Sound and Vibration*, vol. 119, pp. 95–109, Nov. 1987.

[147] S. Oueini and H. Nayfeh, "Single-Mode Control of a Cantilever Beam Under Principal Parametric Excitation," *Journal of Sound and Vibration*, vol. 224, pp. 33–47, July 1999.

[148] S. Oueini, A. H. Nayfeh, and J. Pratt, "A Nonlinear Vibration Absorber for Flexible Structures," *Nonlinear Dynamics*, pp. 259–282, 1998.

[149] J. Pratt, S. Oueini, and A. Nayfeh, "Tefenol-D Nonlinear Vibration Absorber," *Journal of Intelligent Material Systems and Structures*, vol. 10, 1999.

[150] P. F. Pai, B. Rommel, and M. J. Schulz, "Dynamics Regulation of a Skew Cantilever Plate Using PZT Patches and Saturation Phenomenon," *Journal of Intelligent Material Systems and Structures*, vol. 11, pp. 642–655, Aug. 2000.

[151] P. F. Pai and M. J. Schulz, "A re"ned nonlinear vibration absorber," *International Journal of Mechanical Sciences*, p. 24, 2000.

[152] K. Aouali, *Quasiperiodic Arrays of Weakly Coupled Nonlinear Oscillators for Vibration Energy Harvesting by Electromagnetic or Electromagnetic-Piezoelectric Transductions*. PhD thesis, Université de franche-comté, 2021.

[153] L. Xiong, L. Tang, and B. R. Mace, "A comprehensive study of 2:1 internal-resonance-based piezoelectric vibration energy harvesting," *Nonlinear Dynamics*, vol. 91, pp. 1817–1834, Feb. 2018.

[154] X. Nie, T. Tan, Z. Yan, Z. Yan, and M. R. Hajj, “Broadband and high-efficient L-shaped piezoelectric energy harvester based on internal resonance,” *International Journal of Mechanical Sciences*, vol. 159, pp. 287–305, Aug. 2019.

[155] J. Curie and P. Curie, “Contractions et dilatations produites par des tensions électriques dans les cristaux hémièdres à faces inclinées,” *Compt. Rend*, vol. 93, pp. 1137–1140, 1881.

[156] G. Lippmann, “Principe de la conservation de l’électricité, ou second principe de la théorie des phénomènes électriques.,” *Journal de Physique Théorique et Appliquée*, vol. 10, pp. 381–394, 1881.

[157] S. O. R. Moheimani and A. J. Fleming, *Piezoelectric Transducers for Vibration Control and Damping.* Advances in Industrial Control, London: Springer, 2006.

[158] S. Harari, C. Richard, and L. Gaudiller, “New Semi-active Multi-modal Vibration Control Using Piezoceramic Components,” *Journal of Intelligent Material Systems and Structures*, vol. 20, pp. 1603–1613, Sept. 2009.

[159] K. Bendine, F. B. Boukhoulda, B. Haddag, and M. Nouari, “Active vibration control of composite plate with optimal placement of piezoelectric patches,” *Mechanics of Advanced Materials and Structures*, vol. 26, pp. 341–349, Feb. 2019.

[160] A. Faiz, D. Guyomar, L. Petit, and C. Buttay, “Semi-passive piezoelectric noise control in transmission by synchronized switching damping on voltage source,” *Journal de Physique IV*, vol. 128, pp. 171–176, Sept. 2005.

[161] M. Safaei, H. A. Sodano, and S. R. Anton, “A review of energy harvesting using piezoelectric materials: State-of-the-art a decade later (2008–2018),” *Smart Materials and Structures*, vol. 28, p. 113001, Nov. 2019.

[162] H. A. Sodano, D. J. Inman, and G. Park, “A Review of Power Harvesting from Vibration Using Piezoelectric Materials,” *The Shock and Vibration Digest*, vol. 36, pp. 197–205, May 2004.

[163] G. Park, C. R. Farrar, F. L. di Scalea, and S. Coccia, “Performance assessment and validation of piezoelectric active-sensors in structural health monitoring,” *Smart Materials and Structures*, vol. 15, pp. 1673–1683, Dec. 2006.

[164] W. Nelson, *Piezoelectric Materials: Structure, Properties and Applications (Materials Science and Technologies).* Nova Science Pub Inc, uk ed., 2010.

[165] J. Tichy, J. Erhart, E. Kittinger, and J. Přívratská, *Fundamentals of Piezoelectric Sensorics.* Springer Berlin, Heidelberg, 2010.

[166] D. Tan, P. Yavarow, and A. Erturk, "Resonant nonlinearities of piezoelectric macro-fiber composite cantilevers with interdigitated electrodes in energy harvesting," *Nonlinear Dynamics*, vol. 92, pp. 1935–1945, June 2018.

[167] A. Kovalovs, E. Barkanov, and S. Gluhihs, "Active control of structures using macro-fiber composite (MFC)," *Journal of Physics: Conference Series*, vol. 93, 2007.

[168] H. F. Tiersten, *Linear Piezoelectric Plate Vibrations.* Springer New York, NY, 1969.

[169] A. Lazarus, O. Thomas, and J.-F. Deü, "Finite element reduced order models for nonlinear vibrations of piezoelectric layered beams with applications to NEMS," *Finite Elements in Analysis and Design*, vol. 49, pp. 35–51, Feb. 2012.

[170] C. Galassi, M. Dinescu, K. Uchino, and M. Sayer, eds., *Piezoelectric Materials: Advances in Science, Technology and Applications.* Springer Dordrecht, 2000.

[171] O. Thomas, "Dynamique linéaire et non linéaire de structures élastiques et piézoélectriques. Instruments de musique, micro/nano systèmes électromécaniques, contrôle de vibration," HDR report, 2011.

[172] N. Hagood and A. von Flotow, "Damping of structural vibrations with piezoelectric materials and passive electrical networks," *Journal of Sound and Vibration*, vol. 146, pp. 243–268, Apr. 1991.

[173] O. Heuss, R. Salloum, D. Mayer, and T. Melz, "Tuning of a vibration absorber with shunted piezoelectric transducers," *Archive of Applied Mechanics*, vol. 86, pp. 1715–1732, Oct. 2016.

[174] B. Yan, K. Wang, Z. Hu, C. Wu, and X. Zhang, "Shunt Damping Vibration Control Technology: A Review," *Applied Sciences*, vol. 7, p. 494, May 2017.

[175] M. Berardengo, O. Thomas, C. Giraud-Audine, and S. Manzoni, "Improved resistive shunt by means of negative capacitance: New circuit, performances and multi-mode control," *Smart Materials and Structures*, vol. 25, no. 7, 2016.

[176] O. Thomas, J. Ducarne, and J.-F. Deü, "Performance of piezoelectric shunts for vibration reduction," *Smart Materials and Structures*, vol. 21, p. 015008, Jan. 2012.

[177] B. Gotz, O. Heuss, R. Platz, and T. Melz, "Optimal tuning of shunt parameters for lateral beam vibration attenuation with three collocated piezoelectric stack transducers," in *6th European Conference on Structural Control*, p. 12, 2016.

[178] J. Ducarne, O. Thomas, and J.-F. Deü, "Placement and dimension optimization of shunted piezoelectric patches for vibration reduction," *Journal of Sound and Vibration*, vol. 331, pp. 3286–3303, July 2012.

[179] P. Soltani, G. Kerschen, G. Tondreau, and A. Deraemaeker, "Piezoelectric vibration damping using resonant shunt circuits: An exact solution," *Smart Materials and Structures*, vol. 23, p. 125014, Dec. 2014.

[180] O. Thomas, J.-F. Deü, and J. Ducarne, "Vibrations of an elastic structure with shunted piezoelectric patches: Efficient finite element formulation and electromechanical coupling coefficients," *International Journal for Numerical Methods in Engineering*, vol. 80, pp. 235–268, Oct. 2009.

[181] D. Niederberger, A. Fleming, S. Moheimani, and M. Morari, "Adaptive multi-mode resonant piezoelectric shunt damping," *Smart Materials and Structures*, vol. 13, pp. 1025–1035, Oct. 2004.

[182] B. Lossouarn, M. Aucejo, and J.-F. Deü, "Multimodal vibration damping through a periodic array of piezoelectric patches connected to a passive network," in *SPIE Smart Structures and Materials + Nondestructive Evaluation and Health Monitoring*, 2015.

[183] D. Niederberger, A. Fleming, S. O. R. Moheimani, and M. Morari, "Adaptive multi-mode resonant piezoelectric shunt damping," *Smart Materials and Structures*, vol. 13, pp. 1025–1035, Oct. 2004.

[184] U. Yigit, E. Cigeroglu, and E. Budak, "Chatter reduction in boring process by using piezoelectric shunt damping with experimental verification," *Mechanical Systems and Signal Processing*, vol. 94, pp. 312–321, Sept. 2017.

[185] X. Liu, C. Wang, Y. Zhang, K. Wu, B. Dong, and L. Huang, "Extra sound attenuation via shunted piezoelectric resonators in a duct," *International Journal of Mechanical Sciences*, vol. 225, p. 107370, July 2022.

[186] B. Zhou, *Etude de l'amortissement Piézoélectrique Shunté Appliqué Aux Roues Aubagées Désaccordées.* PhD thesis, Ecole centrale de Lyon, 2012.

[187] H. Sun, Z. Yang, K. Li, B. Li, J. Xie, D. Wu, and L. Zhang, "Vibration suppression of a hard disk driver actuator arm using piezoelectric shunt damping with a topology-optimized PZT transducer," *Smart Materials and Structures*, vol. 18, p. 065010, June 2009.

[188] B. Zhou, F. Thouverez, and D. Lenoir, "Essentially nonlinear piezoelectric shunt circuits applied to mistuned bladed disks," *Journal of Sound and Vibration*, vol. 333, pp. 2520–2542, Apr. 2014.

[189] T. Silva, M. Clementino, C. De Marqui, and A. Erturk, “An experimentally validated piezoelectric nonlinear energy sink for wideband vibration attenuation,” *Journal of Sound and Vibration*, vol. 437, pp. 68–78, Dec. 2018.

[190] P. Soltani and G. Kerschen, “The nonlinear piezoelectric tuned vibration absorber,” *Smart Materials and Structures*, vol. 24, p. 075015, July 2015.

[191] G. Raze, A. Jadoul, S. Guichaux, V. Broun, and G. Kerschen, “A digital nonlinear piezoelectric tuned vibration absorber,” *Smart Materials and Structures*, vol. 29, p. 015007, Jan. 2020.

[192] C. Richard, D. Guyomar, D. Audigier, and G. Ching, “Semi-passive damping using continuous switching of a piezoelectric device,” in *Proceedings of SPIE Smart Structures and Materials Conference: Passive Damping and Isolation*, vol. 3672, pp. 104–111, 1999.

[193] S. M. Hoseyni, A. Aghakhani, M. Simsek, E. Lefeuvre, and I. Basdogan, “Multimodal piezoelectric energy harvesting on a thin plate integrated with SSHI circuit: An analytical and experimental study,” *TechRxiv*, 2022.

[194] D. Guyomar, Y. Jayet, L. Petit, E. Lefeuvre, Monn, and M. Lallart, “Synchronized switch harvesting applied to selfpowered smart systems: Piezoactive microgenerators for autonomous wireless transmitters,” *Sensors and Actuators A*, vol. 138, pp. 151–160, 2007.

[195] J. Ducarne, O. Thomas, and J.-F. Deü, “Structural Vibration Reduction by Switch Shunting of Piezoelectric Elements: Modeling and Optimization,” *Journal of Intelligent Material Systems and Structures*, vol. 21, pp. 797–816, May 2010.

[196] C. Richard, D. Guyomar, D. Audigier, and H. Bassaler, “Enhanced Semi-passive Damping Using Continuous Switching of a Piezoelectric Device on an Inductor,” in *Proceedings of SPIE Smart Structures and Materials Conference: Passive Damping and Isolation*, vol. 3989, pp. 288–299, 2000.

[197] L. Petit, E. Lefeuvre, C. Richard, and D. Guyomar, “A Broadband Semi Passive Piezoelectric Technique for Structural Damping,” in *Proceedings of SPIE Smart Structures and Materials Conference: Passive Damping and Isolation*, vol. 5386, pp. 414–425, 2004.

[198] E. Lefeuvre, A. Badel, L. Petit, C. Richard, and D. Guyomar, “Semi-passive Piezoelectric Structural Damping by Synchronized Switching on Voltage Sources,” *Journal of Intelligent Material Systems and Structures*, vol. 17, pp. 653–660, 2006.

[199] A. Antoniou, “Realisation of gyratqrs using operational amplifiers, and their use in RC-active-network synthesis,” *PROC.IEE*, vol. 116, p. 13, 1969.

[200] R. Riodan, “Simulated inductors using differential amplifiers,” *Electron. Lett.*, vol. 3, pp. 50–51, 1967.

[201] F. Viana and V. Steffen, Jr, “Multimodal vibration damping through piezoelectric patches and optimal resonant shunt circuits,” *Journal of the Brazilian Society of Mechanical Sciences and Engineering*, vol. 28, pp. 293–310, Sept. 2006.

[202] M. Vatavu, V. Nastasescu, F. Turcu, and I. Burda, “Voltage-Controlled Synthetic Inductors for Resonant Piezoelectric Shunt Damping: A Comparative Analysis,” *Applied Sciences*, vol. 9, p. 4777, Nov. 2019.

[203] C. Park and D. Inman, “Enhanced piezoelectric shunt design,” *Shock and Vibration*, vol. 10, pp. 127–133, 2003.

[204] A. J. Fleming, S. Behrens, and S. O. R. Moheimani, “Reducing the inductance requirements of piezoelectric shunt damping systems,” *Smart Materials and Structures*, vol. 12, pp. 57–64, Feb. 2003.

[205] J. Ducarne, *Modélisation et Optimisation de Dispositifs Non-Linéaires d’amortissement de Structures Par Systèmes Piézoélectriques Commutés.* PhD thesis, Conservatoire National des Arts et Métiers (CNAM), 2009.

[206] B. Lossouarn, M. Aucejo, J.-F. Deü, and B. Multon, “Design of inductors with high inductance values for resonant piezoelectric damping,” *Sensors and Actuators A: Physical*, vol. 259, pp. 68–76, June 2017.

[207] R. Darleux, B. Lossouarn, and J.-F. Deü, “Passive self-tuning inductor for piezoelectric shunt damping considering temperature variations,” *Journal of Sound and Vibration*, vol. 432, pp. 105–118, Oct. 2018.

[208] A. H. Nayfeh, *Perturbation Methods.* John Wiley & Sons, inc., 1973.

[209] A. H. Nayfeh, *Introduction to Perturbation Techniques.* John Wiley & Sons, inc., 1982.

[210] V. Mahe, *Improvements in the Design of Pendulum Absorbers to Reduce the Vibrations of Automotive Powertrains.* PhD thesis, Arts et Métiers Sciences et Technologies, 2022.

[211] M. Colin, O. Thomas, S. Grondel, and É. Cattan, “Very large amplitude vibrations of flexible structures: Experimental identification and validation of a quadratic drag damping model,” *Journal of Fluids and Structures*, vol. 97, p. 103056, Aug. 2020.

[212] B. Pratiher, “Vibration control of a transversely excited cantilever beam with tip mass,” *Archive of Applied Mechanics*, vol. 82, pp. 31–42, Jan. 2012.

[213] A. Mahmure, A. H. Sofiyev, N. Fantuzzi, and N. Kuruoglu, “Primary resonance of double-curved nanocomposite shells using nonlinear theory and multi-scales method: Modeling and analytical solution,” *International Journal of Non-Linear Mechanics*, vol. 137, p. 103816, Dec. 2021.

[214] W. Lacarbonara, A. Arena, and S. S. Antman, “Flexural vibrations of nonlinearly elastic circular rings,” *Meccanica*, vol. 50, pp. 689–705, Mar. 2015.

[215] V. Guillot, A. Givois, M. Colin, O. Thomas, A. Ture Savadkoohi, and C.-H. Lamarque, “Theoretical and experimental investigation of a 1:3 internal resonance in a beam with piezoelectric patches,” *Journal of Vibration and Control*, vol. 26, pp. 1119–1132, July 2020.

[216] A. Casalotti and W. Lacarbonara, “Nonlinear Vibration Absorber Optimal Design via Asymptotic Approach,” *Procedia IUTAM*, vol. 19, pp. 65–74, 2016.

[217] S. M. Osinaga, S. P. Machado, and M. Febbo, “An analytical model of the electromechanical coupling for a piezoelectric stepped buckled beam for energy harvesting applications,” *Mechanical Systems and Signal Processing*, vol. 179, p. 109355, Nov. 2022.

[218] H. Poincaré, “Les méthodes nouvelles de la mécanique céleste,” *Gauthiers-Villars*, 1892.

[219] H. Dulac, “Solutions d’un systéme d’equations différentielles dans le voisinage de valeurs singuliéres,” *Bulletin de la Société Mathématique de France*, vol. 40, pp. 324–383, 1912.

[220] A. H. Nayfeh, *The Method of Normal Forms.* Wiley-VCH, 2011.

[221] M. Haragus and G. Looss, *Local Bifurcations, Center Manifolds, and Normal Forms in Infinite-Dimensional Dynamical Systems.* Springer London, 2011.

[222] C. Touzé, “Normal form theory and nonlinear normal modes: Theoretical settings and applications,” in *Modal Analysis of Nonlinear Mechanical Systems* (G. Kerschen, ed.), vol. 555, pp. 75–160, Vienna: Springer Vienna, 2014.

[223] S. A. Neild and D. J. Wagg, “Applying the method of normal forms to second-order nonlinear vibration problems,” *Proceedings of the Royal Society A: Mathematical, Physical and Engineering Sciences*, vol. 467, pp. 1141–1163, Apr. 2011.

[224] P. B. Kahn, *Nonlinear Dynamics: Exploration Through Normal Forms.* Dover Publications, 2014.

[225] C. Touzé, O. Thomas, and A. Chaigne, “Hardening/softening behaviour in non-linear oscillations of structural systems using non-linear normal modes,” *Journal of Sound and Vibration*, vol. 273, pp. 77–101, May 2004.

[226] C. Touzé, “A normal form approach for nonlinear normal modes,” research, Publications du LMA, 2003.

[227] C. Touzé, O. Thomas, and A. Chaigne, “Non-linear oscillations of continuous systems with quadratic and cubic non-linearities using non-linear normal modes,” in *Second M.I.T. Conference on Computational Fluid and Solid Mechanics*, (Cambridge, USA), p. 5, 2003.

[228] C. Elphick, G. Iooss, and E. Tirapegui, “Normal form reduction for time-periodically driven differential equations,” *Physics Letters A*, vol. 120, pp. 459–463, Mar. 1987.

[229] S. A. Neild, A. R. Champneys, D. J. Wagg, T. L. Hill, and A. Cammarano, “The use of normal forms for analysing nonlinear mechanical vibrations,” *Philosophical Transactions of the Royal Society A: Mathematical, Physical and Engineering Sciences*, vol. 373, p. 20140404, Sept. 2015.

[230] A. H. Nayfeh, “On Direct Methods for Constructing Nonlinear Normal Modes of Continuous Systems,” *Journal of Vibration and Control*, vol. 1, pp. 389–430, Oct. 1995.

[231] C. Touzé, A. Vizzaccaro, and O. Thomas, “Model order reduction methods for geometrically nonlinear structures: A review of nonlinear techniques,” *Nonlinear Dynamics*, vol. 105, pp. 1141–1190, July 2021.

[232] A. Opreni, A. Vizzaccaro, A. Frangi, and C. Touzé, “Model order reduction based on direct normal form: Application to large finite element MEMS structures featuring internal resonance,” *Nonlinear Dynamics*, vol. 105, pp. 1237–1272, July 2021.

[233] A. Vizzaccaro, Y. Shen, L. Salles, J. Blahoš, and C. Touzé, “Direct computation of nonlinear mapping via normal form for reduced-order models of finite element nonlinear structures,” *Computer Methods in Applied Mechanics and Engineering*, vol. 384, p. 113957, Oct. 2021.

[234] R. Arquier, *Une Méthode de Calcul Des Modes de Vibrations Non Linéaires de Structures.* PhD thesis, Université de la Méditerranée - Aix-Marseille II, 2007.

[235] S. Karkar, *Méthodes Numériques Pour Les Systèmes Dynamiques Non Linéaires : Application Aux Instruments de Musique Auto-Oscillants.* PhD thesis, Aix-Marseille Université, 2012.

[236] L. Guillot, *De l’intérêt d’un Formalisme Quadratique Pour La Continuation Des Solutions d’un Système Dynamique et de Leurs Bifurcations - Applications Aux Instruments à Anche.* PhD thesis, Aix-Marseille Université, 2020.

[237] “MANLAB: An interactive path-following and bifurcation analysis software.” http://manlab.lma.cnrs-mrs.fr.

[238] L. Guillot, B. Cochelin, and C. Vergez, “A generic and efficient taylor series– based continuation method using a quadratic recast of smooth nonlinear systems,” *International Journal for Numerical Methods in Engineering*, vol. 119, pp. 261–280, 2019.

[239] L. Guillot, P. Vigué, C. Vergez, and B. Cochelin, “Continuation of quasi-periodic solutions with two-frequency harmonic balance method,” *Journal of Sound and Vibration*, vol. 394, pp. 434–450, 2017.

[240] L. Guillot, B. Cochelin, and C. Vergez, “A Taylor series-based continuation method for solutions of dynamical systems,” *Nonlinear Dynamics*, vol. 98, pp. 2827–2845, 2019.

[241] S. Karkar, B. Cochelin, and C. Vergez, “A high-order, purely frequency based harmonic balance formulation for continuation of periodic solutions: The case of non-polynomial nonlinearities,” *Journal of Sound and Vibration*, vol. 332, pp. 968–977, 2013.

[242] B. Cochelin and M. Medale, “Power series analysis as a major breakthrough to improve the efficiency of Asymptotic Numerical Method in the vicinity of bifurcations,” *Journal of Computational Physics*, vol. 236, pp. 594–607, 2013.

[243] B. Cochelin, “A path-following technique via an asymptotic-numerical method,” *Computers & Structures*, vol. 53, pp. 1181–1192, 1994.

[244] B. Cochelin, N. Damil, and M. Potier-Ferry, “Asymptotic–numerical methods and Pade approximants for non-linear elastic structures,” *International Journal for Numerical Methods in Engineering*, vol. 37, pp. 1187–1213, 1994.

[245] P. Vigué, C. Vergez, S. Karkar, and B. Cochelin, “Regularized friction and continuation: Comparison with Coulomb’s law,” *Journal of Sound and Vibration*, vol. 389, pp. 350–363, 2017.

[246] A. Ostrowski, *Solution of Equations and Systems of Equations: Pure and Applied Mathematics: A Series of Monographs and Textbooks*, vol. 9. Academic Press, 2016.

[247] M. Debeurre, A. Grolet, P.-O. Mattei, B. Cochelin, and O. Thomas, “Nonlinear Modes of Cantilever Beams at Extreme Amplitudes: Numerical Computation and Experiments,” in *Conference Proceedings of the Society for Experimental Mechanics Series*, Springer, 2022.

[248] J. Galan-Vioque, F. Almaraz, and E. Macias, “Continuation of periodic orbits in conservative and hamiltonian systems,” *Eur. Phys. J. Spec. Top.*, vol. 223, pp. 2705–2722, 2014.

[249] A. Lazarus and O. Thomas, “A harmonic-based method for computing the stability of periodic solutions of dynamical systems,” *Comptes Rendus Mécanique*, vol. 338, pp. 510–517, 2010.

[250] K. G. McConnell and P. S. Varoto, *Vibration Testing: Theory and Practice.* John Wiley & Sons, inc., 1995.

[251] A. Presas, D. Valentin, E. Egusquiza, C. Valero, M. Egusquiza, and M. Bossio, "Accurate Determination of the Frequency Response Function of Submerged and Confined Structures by Using PZT-Patches†," *Sensors*, vol. 17, p. 660, Mar. 2017.

[252] M. Colin, O. Thomas, S. Grondel, and É. Cattan, "Very large amplitude vibrations of flexible structures: Experimental identification and validation of a quadratic drag damping model," *Journal of Fluids and Structures*, vol. 97, p. 103056, Aug. 2020.

[253] V. Denis, M. Jossic, C. Giraud-Audine, B. Chomette, A. Renault, and O. Thomas, "Identification of nonlinear modes using phase-locked-loop experimental continuation and normal form," *Mechanical Systems and Signal Processing*, vol. 106, pp. 430–452, June 2018.

[254] G. Abeloos, F. Müller, E. Ferhatoglu, M. Scheel, C. Collette, G. Kerschen, M. Brake, P. Tiso, L. Renson, and M. Krack, "A consistency analysis of phase-locked-loop testing and control-based continuation for a geometrically nonlinear frictional system," *Mechanical Systems and Signal Processing*, vol. 170, p. 108820, May 2022.

[255] G. Abeloos, L. Renson, C. Collette, and G. Kerschen, "Stepped and swept control-based continuation using adaptive filtering," *Nonlinear Dynamics*, vol. 104, pp. 3793–3808, June 2021.

[256] T. Karaağaçlı and H. N. Özgüven, "Experimental Quantification and Validation of Modal Properties of Geometrically Nonlinear Structures by Using Response-Controlled Stepped-Sine Testing," *Experimental Mechanics*, vol. 62, pp. 199–211, Feb. 2022.

Chapter 7

Résumé étendu en Français

7.1 Introduction

7.1.1 Contexte et objectifs de la thèse

Les surfaces de levage sont devenues un domaine de recherche important en raison de leurs nombreuses applications dans le secteur industriel. Des exemples de telles applications impliquent des pales de turboréacteurs, des pompes, des hélices, des ailes d'avion et des hydrofoils de bateaux. Les surfaces de levage se réfèrent principalement à des structures minces conçues dans une géométrie spéciale (par exemple, des géométries de feuille ou de lame) qui peuvent conduire à un gradient de pression proportionnel au champ de vitesse dans le milieu fluide. Les performances de telles structures dépendent fortement de leurs aspects géométriques et matériels, qui doivent être optimisés pour répondre à un cahier des charges donné.

Une partie importante de l'amélioration des structures de levage implique la prise en compte des vibrations induites par l'écoulement sous des niveaux d'excitation élevés et certains régimes d'écoulement. Cela peut entraîner de la fatigue et de l'érosion et ainsi réduire la durée de vie de la structure et éventuellement conduire à une défaillance. De plus, dans les applications aérodynamiques et hydrodynamiques, des niveaux de vibration élevés peuvent réduire considérablement les performances et générer un niveau de bruit élevé. Un exemple célèbre dans la littérature est le phénomène de flottement, qui est une oscillation structurelle instable et auto-excitée qui peut entraîner des dommages dans les applications aéronautiques.

Ces problèmes ont conduit à initier le projet "Smart Lifting Surfaces" en collaboration entre l'Institut de Recherche de l'École navale (IRENav) de Brest, le Conservatoire National des Arts et Métiers (CNAM) de Paris, l'Institut Carnot Arts, le Laboratoire d'Ingénierie des Systèmes Physiques et Numériques (LISPEN) à Lille, et Laboratoire d'électrotechnique et d'électronique de puissance (L2EP) à Lille. Ce projet se concentre principalement sur les structures d'hydrofoils qui sont utilisées dans les applications marines. L'objectif principal était de proposer des méthodes nouvelles et pratiques pour réduire les vibrations des hydrofoils, qui peuvent être testées expérimentalement et dont le contrôle est simple à mettre en œuvre. La nouveauté repose sur l'utilisation de matériaux actifs, tels que des transducteurs piézoélectriques, qui peuvent modifier la dynamique dans le champ d'écoulement sans modifier sensiblement la géométrie de la structure. Ainsi, une telle approche peut réduire les contraintes de conception sur la géométrie de la structure pour optimiser les performances. De plus, cela peut conduire à la mise en œuvre d'amortisseurs de vibrations électroniques, qui peuvent représenter une solution efficace puisque les amortisseurs mécaniques classiques ne sont pas réalisables pour les corps portants légers en régime hydrodynamique.

A travers ce projet, deux grandes voies de recherche ont été suivies : la première porte sur l'étude de l'interaction fluide-structure dans le milieu eau pour étudier les délestages tourbillonnaires, représentés sur la Fig. 7.1, et leurs conséquences sur le vibrations de l'hydrofoil à différentes conditions ambiantes. De plus, l'intégration des patchs piézoélectriques et les couplages piézoélectriques dans le milieu aqueux ont été étudiés. La deuxième voie se concentre sur la conception de nouveaux absorbeurs de vibrations électroniques qui peuvent être mis en œuvre sur l'hydrofoil dans les régimes hydrodynamiques d'une part et facilement contrôlés dans des applications réelles d'autre part.

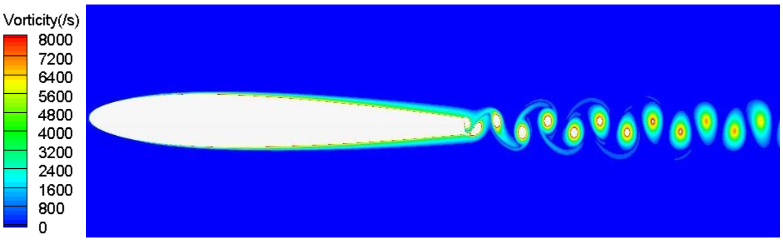

Figure 7.1: Rejets de vortex dans le sillage d'une structure d'hydrofoil.

Cette thèse fait partie du deuxième parcours du projet. Il se concentre sur la proposition de différentes conceptions d'amortisseurs de vibrations électromécaniques non linéaires. Ces absorbeurs sont composés d'un circuit électronique (appelé circuit shunt) relié à l'hydrofoil par l'intermédiaire d'un patch piézoélectrique. De tels absorbeurs seront appelés absorbeurs shunt piézoélectriques. L'objectif principal de cette thèse est l'utilisation intentionnelle des composants non linéaires dans le circuit shunt. L'idée derrière l'ajout de non-linéarités dans l'absorbeur est d'exploiter des caractéristiques particulières qui n'ont pas de contrepartie dans la théorie linéaire, principalement le phénomène de saturation. A travers cette thèse, une étude théorique détaillée est consacrée à l'analyse de la dynamique non linéaire des absorbeurs pour en déduire les lignes directrices pouvant être utilisées pour des implémentations pratiques. De plus, des essais expérimentaux sont effectués sur des structures de poutres et d'hydrofoils pour valider les absorbeurs proposés.

7.1.2 Hydrofoils

Les hydrofoils sont des surfaces portantes qui fonctionnent en milieu aquatique et sont utilisés depuis des décennies dans l'industrie maritime. L'utilisation d'hydrofoils vise à accroître l'efficacité des bateaux de plaisance, de voile ou de surf en améliorant le rapport entre la vitesse et la consommation d'énergie. Ils sont également utilisés dans différentes applications telles que les bateaux de surf. L'idée de base consiste à monter une structure en forme de feuille sur la coque du bateau pour créer une force de levage. Par conséquent, lorsque le bateau augmente sa vitesse, la coque du bateau est soulevée hors de l'eau, comme le montre la Fig. 7.2, et la zone de contact entre le bateau et l'eau est minimisée, ce qui réduit la force de traînée et le niveau d'énergie induit par les vagues et, par conséquent, la consommation d'énergie.

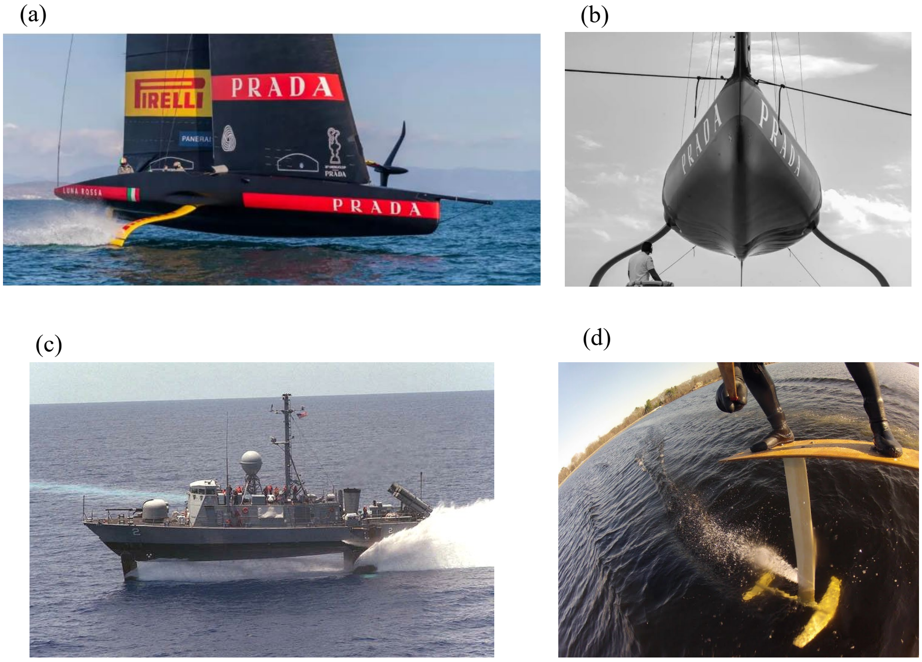

Figure 7.2: (a) et (b) voilier Luna Rossa AC75. (c) Bateau marin USS Hercules (PHM-2). (d) Planche à voile avec un hydrofoil.

7.2 Absorbeur piézoélectrique shunt : configurations linéaires et non linéaires

Les absorbeurs shunt piézoélectriques sont la principale technique utilisée dans cette thèse pour atténuer les vibrations. Cette technique a été présentée comme une extension électromécanique des amortisseurs mécaniques dans laquelle un circuit électronique dédié (appelé circuit shunt) est connecté à une structure élastique via un transducteur piézoélectrique lié à la structure hôte. Grâce aux effets piézoélectriques, l'énergie mécanique injectée dans la structure hôte peut être transformée en forme électrique puis dissipée ou contrecarrée dans le circuit shunt. Les principaux avantages de ces absorbeurs sont la facilité de réglage et de contrôle par rapport aux amortisseurs mécaniques. Ils sont également plus efficaces pour les structures légères où la taille et le poids sont des contraintes de conception.

7.2.1 Shunts piézoélectriques linéaires

Les deux architectures les plus simples des shunts piézoélectriques linéaires sont les shunts résistifs et résonnants, désignés respectivement par R-shunt et RL-shunt, comme le montre la Fig. 7.3. Le R-shunt permet de dissiper l'énergie en chaleur de Joule. En ce qui concerne le RL-shunt, puisque le patch piézoélectrique peut être modélisé électriquement comme un condensateur, un oscillateur à circuit RLC est alors formé, qui peut être réglé pour se comporter de manière analogue à un TMD dans lequel le mode de structure est remplacé par deux modes amortis. Ces architectures de shunts sont passives et colocalisées car la détection et l'actionnement sont servis simultanément par le patch piézoélectrique, ce qui leur confère l'avantage de stabilité de contrôle par rapport aux stratégies de contrôle actives. Comme pour les amortisseurs mécaniques, le R-shunt et le RL-shunt agissent à proximité d'une seule fréquence modale de la structure. Cependant, il est possible d'étendre les applications d'amortissement multimodal en utilisant des réseaux parallèles ou en série de shunts électroniques.

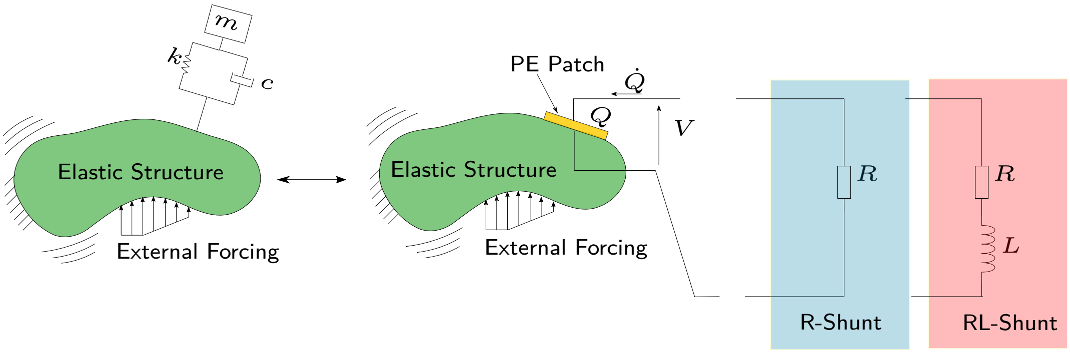

Figure 7.3: Schémas R-shunt et RL-shunt. Le patch PE désigne un patch piézoélectrique. Q, $\dot{Q}$ et V sont la charge dans l'électrode piézoélectrique, la dérivée temporelle de la charge (c'est-à-dire le courant) et la tension aux bornes du patch piézoélectrique.

Comme pour les amortisseurs mécaniques, le R-shunt et le RL-shunt agissent près d'une seule fréquence modale de la structure. Cependant, il est possible d'étendre les applications d'amortissement multimodal en utilisant des réseaux parallèles ou en série de shunts électroniques. Une autre limitation est le niveau élevé d'inductance requis pour le RL-shunt pour amortir les modes de basse fréquence. Par exemple, si l'on souhaite concevoir un shunt RL pour amortir un mode à une fréquence proche de

$\omega = 30 \times (2\pi)$rad/s avec une capacité piézoélectrique d'environ $C_p = 30$nF, une valeur d'inductance proche de $L = 1/(\omega^2 C_p) = 940$H est nécessaire pour obtenir une atténuation optimale. Une telle valeur d'inductance est très élevée pour être obtenue par l'inductance passive classique. Pour surmonter ce problème, des inducteurs synthétiques ont été proposés, qui sont principalement composés de composants électriques tels que des résistances, des condensateurs et des amplificateurs opérationnels.

7.2.2 Shunts piézoélectriques nonlinéaires

Les shunts piézoélectriques non linéaires sont une extension de la configuration linéaire qui vise à exploiter les caractéristiques non linéaires présentées dans la réponse dynamique. L'idée de base consiste à ajouter intentionnellement une source de tension non linéaire V_{nl} à un circuit RL-shunt, comme le montre la Fig. 7.4. L'idée d'utiliser les non-linéarités avec la méthodologie des shunts piézoélectriques a jusqu'à présent peu d'applications dans la littérature. Les principales applications concernaient la réalisation de puits d'énergie non linéaires (NES) de manière théorique et expérimentale, les absorbeurs de vibrations accordés non linéaires (NLTVA) et les shunts non lisses tels que la technique d'amortissement par commutation synchronisée (SSD).

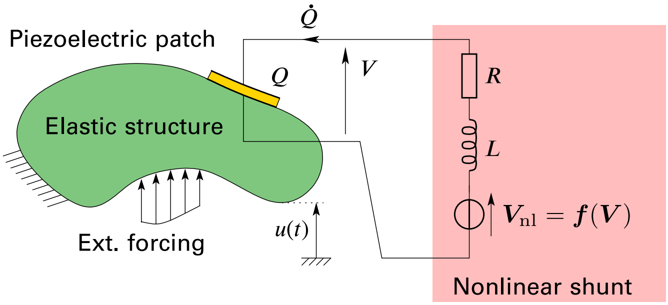

Figure 7.4: Schéma d'un circuit shunt non-linéaire avec une composante de source de tension non-linéaire V_{nl}.

Suite aux contributions ci-dessus, ce travail propose trois conceptions différentes d'absorbeurs shunt piézoélectriques non linéaires semi-passifs, en fonction de la tension non linéaire V_{nl}, introduite intentionnellement dans un shunt RL (voir Fig. 7.4). La nouveauté de cette thèse est d'exploiter le phénomène de saturation en utilisant la technique du shunt piézoélectrique. Le phénomène de saturation est expliqué dans la section suivante.

7.2.2.1 Phénomène de saturation

Le phénomène de saturation est l'idée centrale que cette thèse vise à exploiter pour améliorer l'atténuation. Ce phénomène est une caractéristique particulière d'un certain type de résonance interne, à savoir la résonance interne deux à un (2:1). Ce type de résonance interne est activé en présence d'un couplage non linéaire quadratique entre deux oscillateurs ayant des fréquences modales ω_1 et ω_2 comme suit :

$$\ddot{x}_1 + 2\mu_1\dot{x}_1 + \omega_1^2 x_1 + \alpha_1 x_1 x_2 = 0, \tag{7.1a}$$

$$\ddot{x}_2 + 2\mu_2\dot{x}_2 + \omega_2^2 x_2 + \alpha_2 x_1^2 = f\cos\Omega t. \tag{7.1b}$$

avec α_1 et α_2 les coefficients non linéaires quadratiques, (a_1, a_2) les amplitudes, et (γ_1, γ_2) les angles de phase. Pour activer la résonance interne 2:1, un réglage particulier de la fréquence modale tel que $\omega_2 = 2\omega_1$ doit être présenté. Lorsque l'on considère un forçage harmonique de fréquence d'excitation $\Omega \approx \omega_2$ et d'amplitude d'excitation F, un transfert d'énergie se produit du mode excité vers le sous-harmonique du mode basse fréquence oscillant à $\omega_1 = \Omega/2$. Ainsi la réponse de $x_1(t)$ et $x_2(t)$:

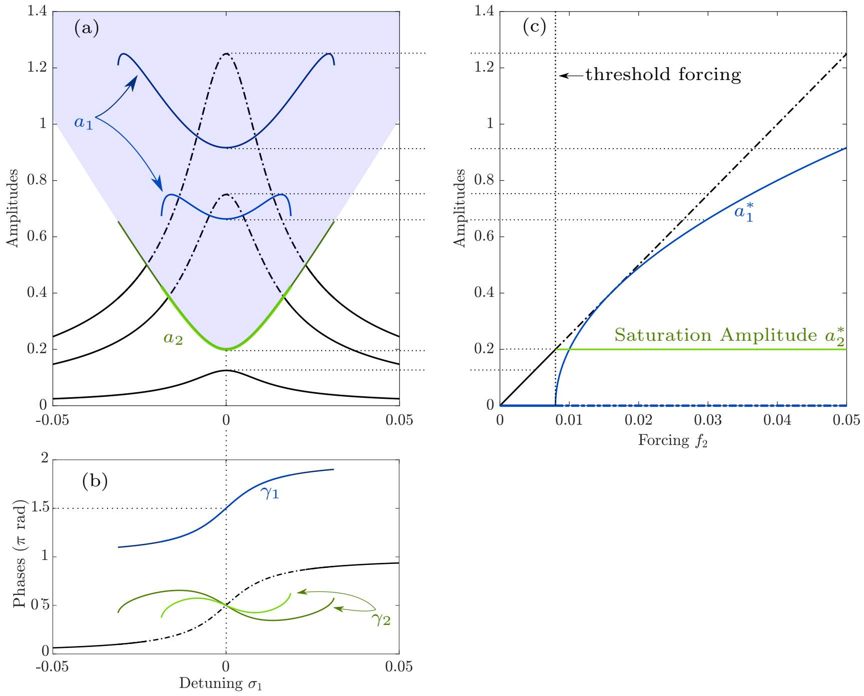

Figure 7.5: Réponse typique des amplitudes a_1 et a_2 et des phases γ_1 et γ_2 en résolvant (7.1a,b) pour $\omega_2 = 2\omega_1$. Les valeurs numériques sont $\alpha_1 = \alpha_2 = 0,1$, $\mu_1 = 0,005$, $\mu_2 = 0,01$. (a) et (b) montrent respectivement la réponse en amplitude et en phase par rapport au désaccord $\sigma_1 = \Omega - \omega_2$ pour les valeurs du forçage f ($f \in \{0,005; 0,03; 0,05\}$). (c) Réponse en amplitude à la fréquence de résonance ($\sigma_1 = 0$) par rapport au niveau d'excitation f. Dans les graphiques, les réponses linéaires de a_2 et γ_2 sont tracées en noir. Les lignes pleines et en pointillés indiquent respectivement les solutions stables et instables.

$$x_1(t) = a_1\cos\left(\frac{\Omega}{2}t - \frac{\gamma_1+\gamma_2}{2}\right), \quad x_2(t) = a_2\cos\left(\Omega t - \gamma_2\right), \tag{7.2}$$

La réponse présentée dans la Fig. 7.5a suggère qu'au-delà d'un niveau d'excitation seuil, la résonance linéaire est remplacée par une antirésonance dont l'amplitude est indépendante du niveau d'excitation comme le suggère la Fig. 7.5c. De plus, les résultats de la Fig. 7.5b suggèrent un verrouillage de la phase γ_1 à $3\pi/2$ à la fréquence d'antirésonance qui est utilisée pour désaccorder l'emplacement de l'antirésonance.

En définissant l'atténuation comme la réduction d'amplitude par rapport à l'amplitude de résonance linéaire correspondant à la réponse de $x_2(t)$ avec $\alpha_1 = \alpha_2 = 0$ (c'est-à-dire la différence d'amplitude entre les courbes verte et noire de la Fig. 1.6(c)), on peut conclure que le phénomène de saturation entraîne une atténuation croissante lorsque le forçage augmente au-delà d'une valeur seuil donnée, contrairement aux absorbeurs linéaires. Ainsi, l'atténuation peut être considérée comme dépendant de l'amplitude.

7.2.2.2 Conceptions d'absorbeurs proposées

Trois conceptions d'absorbeur shunt non linéaires proposées dans cette thèse en fonction de la composante de tension non linéaire V_{nl}, illustrées à la Fig. 7.4 :

- La première conception comprend uniquement une non-linéarité quadratique proportionnelle au carré de la tension piézoélectrique V telle que $V_{\text{nl}} = \beta V^2$ où β est un gain contrôlé. L'idée principale est d'activer la résonance interne 2:1 et d'exploiter ainsi le phénomène de saturation.

- La deuxième conception inclut des composants de tension non linéaires quadratiques et cubiques tels que $V_{\text{nl}} = \beta_q V^2 + \beta_c V^3$ où β_q et β_c sont respectivement les gains des non-linéarités quadratiques et cubiques. L'idée derrière l'ajout des non-linéarités cubiques est de corriger le phénomène de saturation violé en raison de la présence des inévitables termes non résonants quadratiques.

- La conception finale implique un comportement non lisse tel que $V_{\text{nl}} = \beta(V + |V|)$, réalisé par une diode dans le circuit shunt.

7.3 Première conception : avec non-linéarité quadratique

Cette section est consacrée à la conception théorique de l'absorbeur shunt avec une tension non linéaire quadratique proportionnelle au carré de la tension aux bornes du patch piézoélectrique ($V_{\text{nl}} = \beta V^2$), comme le montre la Fig. 7.6. L'idée principale est d'activer la résonance interne 2:1 et d'examiner ainsi le phénomène de saturation.

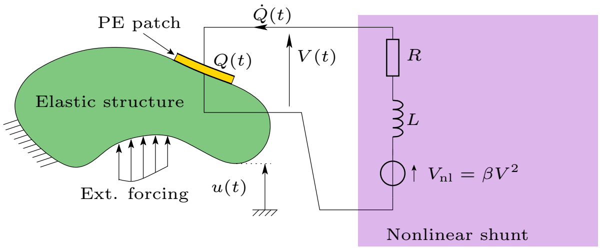

Figure 7.6: Circuit shunt non linéaire avec composante de tension quadratique.

7.3.1 Governing equations

En développant le vecteur de déplacement mécanique $u(t)$ sur cette base modale, tronquée au $i$ième mode seulement ($\boldsymbol{u}(t) = \boldsymbol{\Phi}_i q_i(t)$), les équations de gouvernance en termes de déplacement modal $q_i(t)$ et de la charge sur l'électrode piézoélectrique $Q(t)$ sont :

$$\ddot{q}_i + 2\xi_i\hat{\omega}_i\dot{q}_i + \hat{\omega}_i^2 q_i + \frac{\theta_i}{m_i C_{\text{p}i}} Q = \frac{F_i}{m_i}\cos\Omega t \tag{7.3a}$$

$$\ddot{Q} + 2\xi_e\omega_e\dot{Q} + \omega_e^2 Q + \frac{\theta_i}{LC_{\text{p}i}} q_i + \frac{V_{\text{nl}}}{L} = 0. \tag{7.3b}$$

avec F_i le forçage modal, m_i la masse modale, θ_i le facteur de couplage piézoélectrique, et ξ_i le taux d'amortissement mécanique, tout correspond au i-ième mode. $C_{\text{p}i}$ la capacité effective du patch piézoélectrique au voisinage de la $i$ième résonance, qui tient compte de l'effet statique de tous les modes autres que le i-ième. $\hat{\omega}_i^2 = \omega_i^2 + \theta_i^2/(C_{\text{p}i} m_i)$ est la fréquence de résonance en circuit ouvert avec ω_i est la résonance en court-circuit fréquence ($V = 0$), les deux correspondent au mode i-ième. De plus, la fréquence propre électrique et l'amortissement électrique facteur sont définis par :

$$\omega_e = \frac{1}{\sqrt{LC_{\text{p}i}}}, \qquad \xi_e = \frac{R}{2}\sqrt{\frac{C_{\text{p}i}}{L}} \tag{7.4}$$

Le facteur de couplage modal piézoélectrique électromécanique sans dimension k_i est également défini comme :

$$k_i = \frac{\hat{\omega}_i^2 - \omega_i^2}{\hat{\omega}_i^2} = \frac{\theta_i^2}{\hat{\omega}_i^2 C_{\text{p}i} m_i} \tag{7.5}$$

Par comparaison avec les équations présentées dans (7.1a,b), la résonance interne 2:1 peut être examinée en découplant linéairement (7.3a,b). Ceci est réalisé par expansion ($q_i(t)$, $Q(t)$) en termes de (x_1, x_2) sur une base modale électromécanique comme :

$$\begin{pmatrix} q_i(t) \\ Q(t) \end{pmatrix} = \sum_{k=1}^{2} \boldsymbol{\Psi}_k x_k(t) = \begin{pmatrix} -\varepsilon x_1(t) + x_2(t) \\ x_1(t) + \varepsilon x_2(t) \end{pmatrix} \text{ with } \varepsilon(k_i) \ll 1 \ (k_i < 0.25), \tag{7.6}$$

pour obtenir ce qui suit en substituant $V_{\mathrm{nl}} = \beta V^2$ et Eq. (7.6) in (7.3a, b) et en rappelant que $V = \frac{1}{C_{\mathrm{p}i}}(Q + \theta_i q)$:

$$\ddot{x}_1 + 2\xi_1\omega_1\dot{x}_1 + \omega_1^2 x_1 + g_{12}^1 x_1 x_2 + g_{11}^1 x_1^2 + g_{22}^1 x_2^2 = f_1 \cos \Omega t, \tag{7.7a}$$

$$\ddot{x}_2 + 2\xi_2\omega_2\dot{x}_2 + \omega_2^2 x_2 + g_{11}^2 x_1^2 + g_{12}^2 x_1 x_2 + g_{22}^2 x_2^2 = f_2 \cos \Omega t. \tag{7.7b}$$

avec g_{ij}^k les coefficients non linéaires quadratiques qui sont fonction de β et les paramètres modaux électromécaniques. On peut se rendre compte que le système obtenu dans (7.7a, b) est similaire à celui obtenu dans (7.1a, b) mais avec des termes supplémentaires, à savoir, $g_{11}^1 x_1^2$, $g_{22}^1 x_2^2$, $g_{12}^2 x_1 x_2$ et $g_{22}^2 x_2^2$ qui sont désignés par les termes non résonnants puisqu'ils éloignent le système de sa résonance. Les deux autres termes, $g_{12}^1 x_1 x_2$ et $g_{11}^2 x_1^2$ sont désignés par les termes de résonance qui sont responsables du fort transfert d'énergie à travers la résonance interne 2:1 (activée avec le réglage $\omega_1 = \omega_2/2$) et pour la réponse symétrique obtenue sur la Fig. 7.5. Notez que les termes non résonnants sont inévitables en raison de leur dépendance au couplage piézoélectrique qui doit toujours être présenté. Dans le cas de la résonance interne 2:1, le déplacement $\boldsymbol{u}(t)$ et la charge $Q(t)$ peuvent être récupérés en utilisant Eq. (7.6) comme :

$$\boldsymbol{u}(t) = \frac{\boldsymbol{\Phi}_i}{\sqrt{m_i}}\Big[-\varepsilon \underbrace{a_1 \cos\left(\frac{\Omega}{2}t - \frac{\gamma_1 + \gamma_2}{2}\right)}_{x_1(t) \to H1/2} + \underbrace{a_2 \cos\left(\Omega t - \gamma_2\right)}_{x_2(t) \to H1}\Big], \tag{7.8a}$$

$$Q(t) = \frac{1}{\sqrt{L}}\Big[\underbrace{a_1 \cos\left(\frac{\Omega}{2}t - \frac{\gamma_1 + \gamma_2}{2}\right)}_{x_1(t) \to H1/2} + \varepsilon \underbrace{a_2 \cos\left(\Omega t - \gamma_2\right)}_{x_2(t) \to H1}\Big]. \tag{7.8b}$$

On peut se rendre compte que le déplacement et la charge sont composés de la sous-harmonique H1/2 et de la première harmonique H1 due au transfert d'énergie. Puisque $\varepsilon << 1$ (dû au faible couplage piézoélectrique), la sous-harmonique H1/2 et la première harmonique H1 dominent respectivement la réponse de la charge et du déplacement. Ainsi, dans ce qui suit, les harmoniques dominantes ne seront représentées que dans les réponses en fréquence. Il est important de mentionner qu'en raison du dédoublement harmonique, la saturation présentée dans la réponse de a_2 (voir Fig. 7.5) est également observée dans la réponse H1 du déplacement.

7.3.2 Effect of the nonresonant terms

Pour examiner la saturation avec la réponse physique, le système (7.3a, b) est résolu directement à l'aide du logiciel de continuation MANLAB pour examiner les réponses en fréquence de la première harmonique du déplacement et de la sous-harmonique de la charge à valider l'occurrence de résonance interne 2:1. Les réponses en fréquence sont représentées sur la Fig. 7.7, estimées avec $\omega_e \approx \hat{\omega}_i/2$ et en considérant les paramètres électromécaniques modaux du premier mode de flexion de la structure de

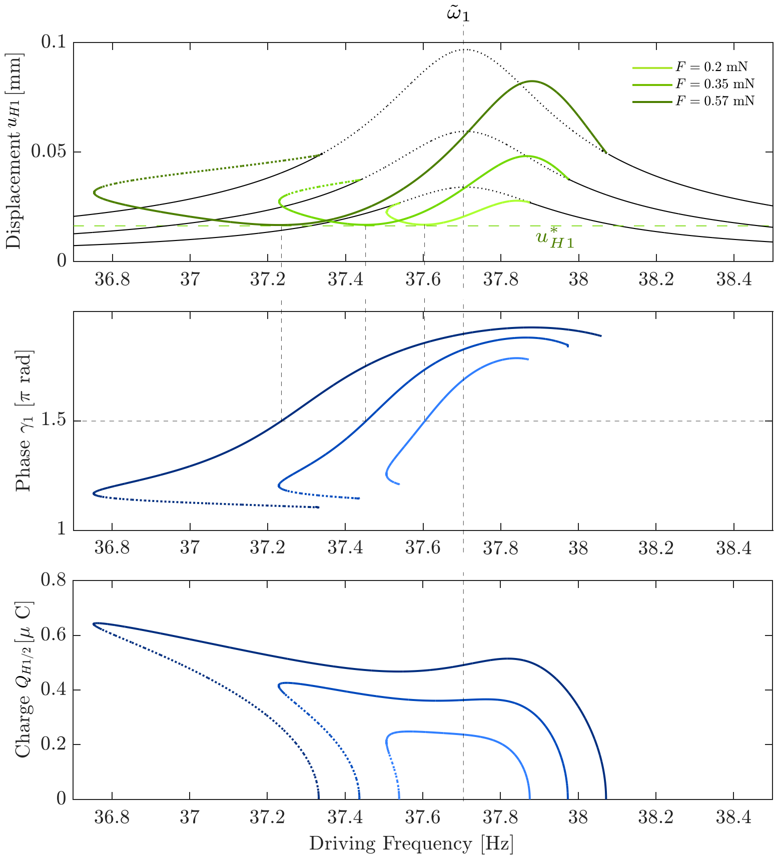

Figure 7.7: Réponse en fréquence de l'amplitude de la première harmonique de déplacement de la pointe du faisceau u_{H1}, de la sous-harmonique de charge $Q_{\mathrm{H1/2}}$ et de la phase γ_1, obtenue en résolvant (7.3a, b) en utilisant MANLAB pour plusieurs niveaux d'excitation. Les valeurs numériques sont $\beta = 0.012$, $r_1 = \omega_e/\hat{\omega}_1 = 0.52$, $\xi_e = 0.002$, et le coefficient d'amortissement mécanique est $\xi_1 = 0.005$. La réponse linéaire de déplacement est tracée en noir. Les lignes pleines et pointillées désignent respectivement les solutions stables et instables.

poutre représentée dans la Fig.7.9 (voir Tableau 7.1). Notez que pour le mode considéré l'indice $i = 1$ est remplacé.

Par rapport à la réponse typique de la Fig. 7.5, les résultats suggèrent le transfert d'énergie vers le sous-harmonique de la charge avec l'existence de l'antirésonace dans la réponse de déplacement. Cependant, à mesure que le niveau d'excitation augmente, l'antirésonance se déplace vers la gamme des basses fréquences, mais en atteignant la même amplitude u^*_{H1}. Ainsi, le phénomène de saturation est perdu à $\Omega \approx \hat{\omega}_i$. On peut également se rendre compte de l'existence de pic élevé à proximité de la résonance primaire. De plus, la réponse de la charge suggère un comportement d'adoucissement à des niveaux d'excitation élevés. De manière intéressante, la réponse de la phase γ_1 suggère un blocage à $3\pi/2$ à la fréquence d'antirésonance qui est une propriété observée sur la Fig. 7.5. En conclusion, la réponse suggère l'occurrence de la résonance interne 2:1 mais avec une réponse plus compliquée. Cela peut s'expliquer en examinant (7.7a, b), exprimé dans la base électromécanique qui suggère que l'un des termes non résinants, à savoir g_{11}^{1} est proportionnel à $1/C_{\mathrm{p}i}$ et atteint ainsi une très grande amplitude. Bien que cela ne soit pas résonnant, cela semble avoir un effet significatif sur la réponse, comme suggéré dans la Fig. 7.7.

7.3.3 Antiresonance correction and preserving the saturation

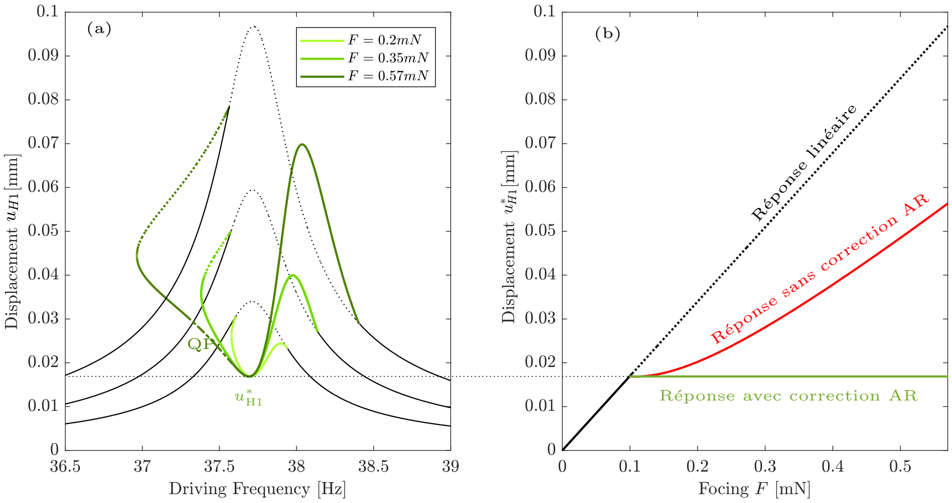

Figure 7.8: (a) Réponse en fréquence de la première amplitude harmonique du déplacement de la pointe du faisceau uH1, estimée en résolvant (7.3a, b) à l'aide de MANLAB, pour plusieurs niveaux d'excitation et avec correction AR. (b) Amplitude de la première harmonique du déplacement de la pointe du faisceau à la fréquence de résonance u_{H1}^{*} par rapport au niveau d'excitation, avec et sans correction AR. Les valeurs numériques sont $\beta = 0.012$ et $\xi_1 = 0.005$ La réponse linéaire de déplacement est tracée en noir. Les lignes pleines et pointillées/pointillées désignent, respectivement, les solutions stables et instables. QP fait référence à une réponse quasi-périodique, obtenue après une perte de stabilité due aux bifurcations de Neimark-Sacker.

Étant donné que la saturation est la principale caractéristique de l'absorbeur non linéaire conçu, une correction d'antirésonance (AR) est introduite pour empêcher le déplacement de l'antirésonance et ainsi la verrouiller à la fréquence de résonance. La motivation de cette correction est que l'amplitude de l'antirésonance atteint la même amplitude que celle indiquée pour la réponse en fréquence de u_{H1} sur la Fig. 7.7. Ainsi, un désaccord du circuit shunt (c'est-à-dire le choix de l'inductance appropriée dans le circuit) peut être choisi de sorte que le décalage soit contrebalancé à chaque niveau d'excitation. La procédure est effectuée numériquement avec MANLAB en estimant l'inductance requise à $\Omega = \hat{\omega}_i$ à laquelle l'amplitude de la première harmonique du déplacement u_{H1} atteint son minimum. Lors de l'identification de cette inductance, la réponse en fréquence de u_{H1} est obtenue, comme le montre la Fig. 7.8a. Les résultats suggèrent clairement que la correction AR permet le verrouillage de l'antirésonance à la fréquence de résonance et récupère ainsi la saturation comme le montre la Fig. 7.8b. Notez que le principal problème de cette correction AR est qu'elle n'est pas automatique et qu'elle conduit à l'apparition de régimes quasi-périodiques près de l'antirésonance.

7.3.4 Experimental verification

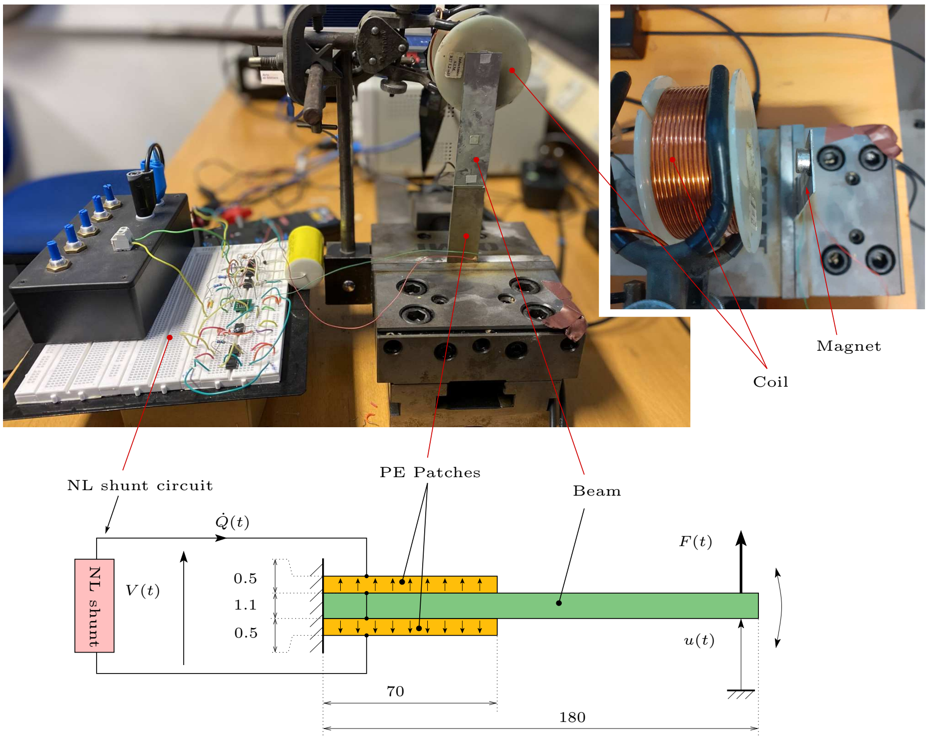

Figure 7.9: Montage expérimental. Les dimensions sont en mm. La largeur de la poutre et des patchs PE est 30,5 mm.

Les essais expérimentaux ont été menés sur une poutre en porte-à-faux avec deux patchs piézoélectriques (PE) PIC 151 symétriquement collé sur les deux faces d'une poutre en acier inoxydable, comme le montre la Fig. 7.9. Le circuit de shunt non linéaire est connecté à la structure avec les patchs PE en série et avec des polarisations opposées pour coupler le circuit de shunt électrique à la flexion de la poutre. Un actionneur électromagnétique sans contact composé d'une bobine fixe et d'un aimant fixé à la pointe de la structure est utilisé pour générer une force électromagnétique en induisant un courant dans la bobine. Une relation linéaire a été trouvée entre le courant I(t) induit dans la bobine et le forçage résultant F(t) tel que $F(t) = \alpha I(t)$, avec α une constante. Avant de mener les expériences avec le circuit shunt non linéaire, une analyse modale expérimentale a été effectuée pour identifier les

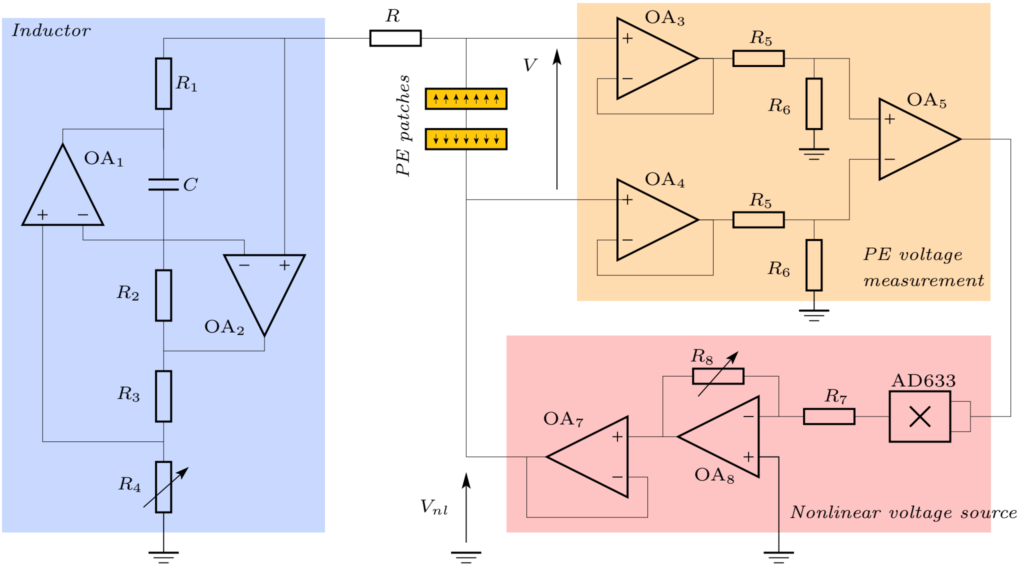

Figure 7.10: Conception de circuit shunt non linéaire.

paramètres modaux du système électromécanique testé. L'analyse modale expérimentale présentée ici consiste à exploiter le bénéfice du couplage piézoélectrique entre les domaines mécanique et électrique (c'est-à-dire la structure et le circuit shunt). En se concentrant sur un mode mécanique particulier de la structure (le $i$ième), la déformée modale est normalisée de sorte que sa valeur à la pointe de la poutre x_t, telle que $\Phi(x_t) = 1$. En considérant le déplacement transversal $u(t)$de la poutre à son extrémité et un point colocalisé forçant $F(t) = F_0 \cos \Omega t$ (voir Fig. 7.9), $u(t) = q_i(t)$ et $F_i = F_0$ in (7.3a, b). Différents tests expérimentaux ont été effectués, puis les fonctions de réponse en fréquence (FRF) obtenues ont été ajustées avec les fonctions analytiques correspondantes pour obtenir les paramètres modaux électromécaniques, qui sont rassemblés dans le Tableau 7.1.

Table 7.1: Paramètres modaux électromécaniques du premier mode de flexion de la poutre en porte-à-faux (indice i=1).

Parameters	$\omega_1/(2\pi)$ [Hz]	$\hat{\omega}_1/(2\pi)$ [Hz]	$\xi_1(\%)$	k_1	θ_1[mN/V]	$m_1[g]$	α [N/A]	$C_{\mathrm{p}1}$ [nF]
Value	36.6	37.51	0.5	0.2	0.8	8.8	0.6	32.45

Le circuit shunt non linéaire utilisé dans les expériences est illustré à la Fig. 7.10. Il se compose de trois sous-circuits : une inductance synthétique accordable pour réaliser la haute inductance (en bleu), le circuit de mesure de tension (en orange) et la source de tension non linéaire (en rouge) dans laquelle la non linéarité est réalisée par un multiplicateur analogique. L'inductance L et le gain non linéaire β peuvent être réglés respectivement en utilisant R_4 et R_8. Leurs valeurs numériques peuvent être estimées comme suit :

$$L = \frac{R_1 R_2 R_4 C}{R_3}, \quad \beta = \frac{R_8}{10R_7}\left(\frac{R_6}{R_5 + R_6}\right)^2. \tag{7.9}$$

7.3.5 Experimental results

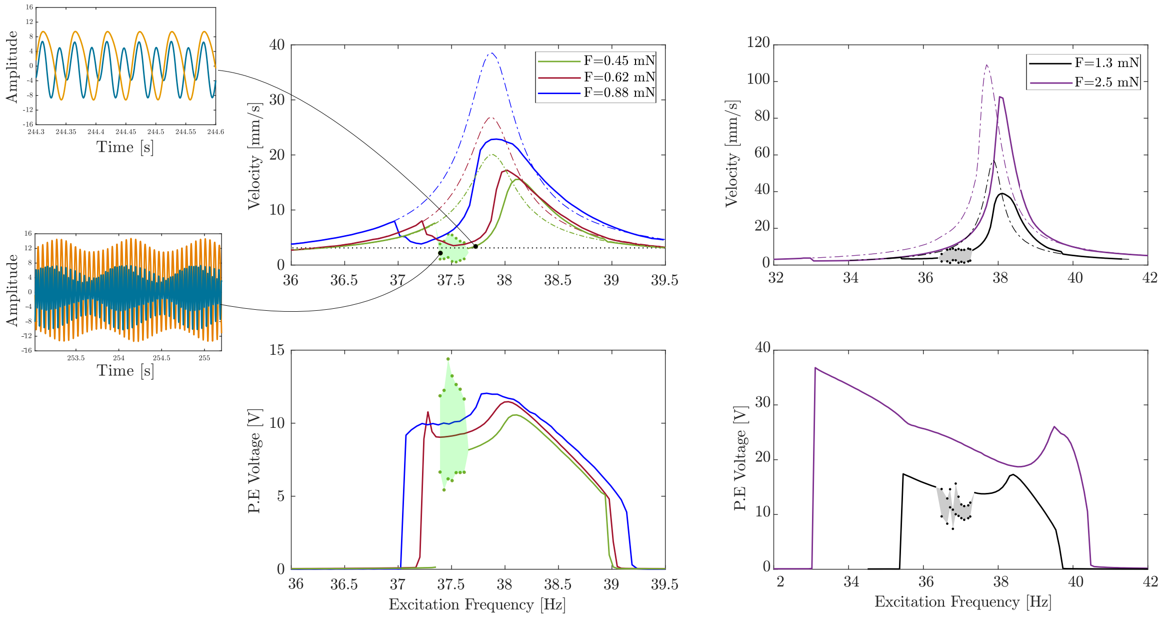

Figure 7.11: Résultats expérimentaux de v_{H1} (première ligne) et $V_{\mathrm{H1/2}}$ (deuxième ligne) pour plusieurs niveaux d'excitation F d'unité mN. Seules les données de balayage de la fréquence d'excitation sont représentées en traits pleins. Les mesures sont effectuées pour $\beta = 0.035$, $\xi_e = 0.002$, $\xi_1 = 0.005$ et $r_1 = \omega_e/\hat{\omega}_1 = 0.537$. Les régions ombrées représentent le régime quasi-périodique détecté. Les évolutions temporelles des réponses périodiques et quasi-périodiques sont également présentées. (la vitesse en bleu et la tension en orange)

Dans cette section, les réponses en fréquence mesurées expérimentalement de la première harmonique de la vitesse de pointe du faisceau v_{H1} et de la sous-harmonique de tension PE $V_{\mathrm{H1/2}}$ sont démontrées. La vitesse et la tension ont été respectivement mesurées à l'aide d'un vibromètre laser et d'une sonde de tension différentielle. Les réponses en fréquence sont présentées sur la Fig. 7.11 qui ont été estimées à l'aide de la méthode sinusoïdale avec démodulation. Les résultats valident le déplacement de l'antirésonance d'amplitude constante en plus du comportement d'adoucissement observé à des niveaux d'excitation élevés avec un pic élevé près de la résonance primaire.. De plus, l'existence d'un régime quasi-périodique au voisinage de l'antirésonance a également été validée. On peut aussi se rendre compte que les évolutions temporelles suggèrent clairement la réponse multi harmonique de la vitesse et de la tension qui peut être déduite de (7.8a, b).

Pour récupérer expérimentalement la saturation, la même correction AR présentée théoriquement est suivie d'un désaccord du circuit shunt à chaque niveau d'excitation. Dans les expériences, ceci est obtenu grâce au verrouillage des angles de phase γ_1 à $3\pi/2$ (voir Fig. 7.7) à la fréquence d'antirésonance. Cela a permis de déterminer l'inductance requise pour verrouiller l'antirésonance à la fréquence de résonance. Avec cette correction AR, la réponse en fréquence expérimentale de la vitesse a été estimée suggérant la récupération de la saturation comme le montre la Fig. 7.12 avec l'apparition de régimes quasi-périodiques. De plus, une atténuation élevée a été obtenue expérimentalement par rapport à la réponse linéaire.

Trois principaux problèmes sont restés dans l'absorbeur proposé : i) la correction d'antirésonance récupère la saturation mais n'est pas automatique, ii) le pic élevé près de la résonance primaire toujours présenté conduit à de faibles performances pour l'atténuation à large bande, iii) la correction AR conduit à l'apparition de régime quasi-périodique qui peut être un problème en termes de contrôle et de réglage du système. Pour ces raisons, une amélioration de l'absorbeur est proposée en ajoutant en plus une non-linéarité cubique dans le circuit shunt, qui est discutée dans la section suivante.

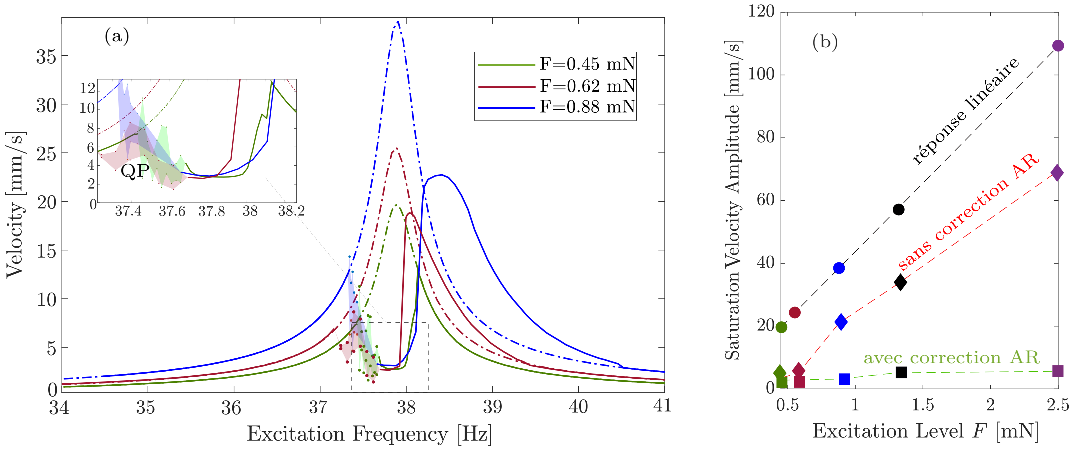

Figure 7.12: (a) Réponse en fréquence expérimentale de v_{H1} pour balayer la fréquence d'excitation pour plusieurs niveaux d'excitation avec la correction AR. (b) Amplitude de saturation antirésonance à la fréquence de résonance $\hat{\omega}_1$ en fonction du niveau d'excitation tracé pour trois cas différents : la réponse linéaire, avec $r_1 = \omega_e/\hat{\omega}_1 = 0.537$ fixe, et avec la correction AR. Les courbes sont estimées pour $\beta = 0.035$, $\xi_e = 0.002$, et $\xi_1 = 0.0055$. Les régions ombrées représentent le régime quasi-périodique (QP) détecté.

7.4 Deuxième conception : avec des non-linéarités quadratiques et cubiques

7.4.1 Motivation

Comme discuté dans la section précédente, le principal problème avec la conception de l'absorbeur est l'effet substantiel des termes quadratiques non résonnants qui conduisent à une réponse plus compliquée et entravent l'effet de saturation. De plus, la correction AR proposée n'était pas automatique. Pour résoudre ce problème de manière plus réaliste, une compréhension plus approfondie de l'effet des termes non résonnants est nécessaire. Ceci peut être réalisé avec la théorie de la forme normale qui stipule que les termes quadratiques non résonnants apparaissent comme des termes cubiques dans le système de forme normale du troisième ordre. Ainsi, l'idée était d'introduire une non-linéarité cubique dans le circuit, comme le montre la figure 7.13($V_{\mathrm{nl}} = \beta_q V^2 + \beta_c V^3$) tel que β_c soit correctement réglé pour annuler l'effet des termes quadratiques non résonnants et récupérer la saturation comme on le voit sur la Fig. 7.5. Dans ce qui suit une symétrie de la procédure est montrée, mais pour plus de détails, on peut se référer au chapitre 4.

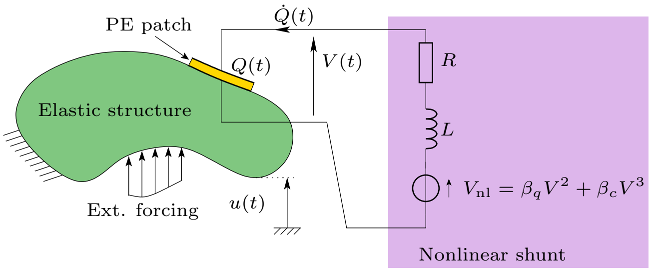

Figure 7.13: Circuit shunt non linéaire avec composante de tension quadratique et cubique.

7.4.2 Système de forme normale et solution libre

La première étape consiste à construire les principales équations gouvernantes dans la base du modèle électromécanique similaire à celle de (7.7a, b). La même procédure est suivie mais en incluant la non-linéarité cubique pour obtenir :

$$\begin{aligned}
&\ddot{x}_1 + 2\mu_1\dot{x}_1 + \omega_1^2 x_1 + g_{11}^1 x_1^2 + g_{12}^1 x_1 x_2 + g_{22}^1 x_2^2 \\
&\qquad + h_{111}^1 x_1^3 + h_{112}^1 x_1^2 x_2 + h_{122}^1 x_1 x_2^2 + h_{222}^1 x_2^3 = f_1 \cos\Omega t, \qquad (7.10a)\\
&\ddot{x}_2 + 2\mu_2\dot{x}_2 + \omega_2^2 x_2 + g_{11}^2 x_1^2 + g_{12}^2 x_1 x_2 + g_{22}^2 x_2^2 \\
&\qquad + h_{111}^2 x_1^3 + h_{112}^2 x_1^2 x_2 + h_{122}^2 x_1 x_2^2 + h_{222}^2 x_2^3 = f_2 \cos\Omega t. \qquad (7.10b)
\end{aligned}$$

La deuxième étape consiste à introduire un changement non linéaire de variables par une expansion polynomiale du troisième degré comme :

$$(X_p, Y_p = \dot{X}_p) \rightarrow \mathcal{P}_p^{(3)}(R_p, S_p = \dot{R}_p) \qquad (7.11)$$

Puis, en substituant Eq. 7.11 dans (7.10a, b), en négligeant f_1 et en fixant $f_2 = f$, en gardant les mêmes coefficients d'amortissement dans le processus de dérivation et après avoir effectué un peu d'algèbre avec le réglage $\omega_1 = \omega_2/2$ pour considérer la résonance interne 2:1, le système de forme normale en termes de $(R_p, S_p = \dot{R}_p)$ est obtenu comme :

$$\begin{aligned} &\ddot{R}_1 + 2\mu_1\dot{R}_1 + \omega_1^2 R_1 + g_{12}^1 R_1 R_2 + \alpha_1 R_1^3 \\ &\qquad + \alpha_2 R_1 R_2^2 + \alpha_3 R_1 \dot{R}_1^2 + \alpha_4 R_1 \dot{R}_2^2 + \alpha_5 R_2 \dot{R}_1 \dot{R}_2 = 0 \qquad (7.12a) \\ &\ddot{R}_2 + 2\mu_2\dot{R}_2 + \omega_2^2 R_2 + g_{11}^2 R_1^2 + \alpha_6 R_1^2 R_2 \\ &\qquad + \alpha_7 R_2^3 + \alpha_8 R_1 \dot{R}_1 \dot{R}_2 + \alpha_9 R_2 \dot{R}_1^2 + \alpha_{10} R_2 \dot{R}_2^2 = f\cos\Omega t \qquad (7.12b) \end{aligned}$$

avec $\alpha_m = f(g_{ij}^p, h_{ijk}^p)$. On peut se rendre compte que tous les termes quadratiques non résonnants ont été annulés dans (7.12a,b) et apparaissent comme des termes cubiques. En effet, seuls les termes quadratiques résonants subsistent puisqu'ils déterminent la dynamique essentielle dans le cas de la résonance interne 2:1.

Ayant le système de forme noraml, l'étape suivante consistait à annuler l'effet de tous les monômes cubiques dans le système de forme normale. Dans ce travail, la procédure proposée est d'obtenir la solution libre de (7.12a,b) (et donc les "backbone curves" montrant le changement de la fréquence de résonance sur l'amplitude d'oscillation). L'hypothèse principale est que puisque les "backbone curves" déterminent le squelette de la solution forcée (voir Fig. 7.14), la symétrisation de ces courbes en annulant les monômes cubiques symétrisera la solution forcée (similaire à celle de la Fig. 7.5) et ainsi récupérer la saturation. La solution libre de (7.12a,b) est déterminée à l'aide de la méthode des échelles multiples en définissant $\mu_1 = \mu_2 = f = 0$. La solution libre approchée s'écrit :

$$R_1(t) = a_1 \cos\left(\frac{\omega_{\mathrm{nl}}}{2}t + \frac{\phi_2 + k\pi}{2}\right) + O(\varepsilon), \qquad (7.13a)$$

$$R_2(t) = a_2 \cos\left(\omega_{\mathrm{nl}}t + \phi_2\right) + O(\varepsilon), \qquad (7.13b)$$

avec ϕ_2 le déphasage entre le mode excité et le forçage et $k \in \mathbb{Z}$ qui conduit à deux modes couplés distincts C+ et C- selon le déphasage entre les deux oscillateurs. $\omega_{\mathrm{nl}} = f(a_1, a_2)$ détermine l'équation des backbone curves qui se lit comme suit :

$$\omega_{\mathrm{nl2}} = \omega_2 + \Gamma_4\, p\, \frac{a_1^2}{a_2} + \Gamma_5 a_1^2 + \Gamma_6 a_2^2. \qquad (7.14)$$

avec Γ_4 ne dépend que des monômes quadratiques résonnants tandis que Γ_5 et Γ_6 dépendent des monômes quaratiques et cubiques non résonnants. Les expressions de Γ_k se trouvent au chapitre 4. Équilibrer les termes cubiques avec les termes quadratiques non résonnants nécessite que $\Gamma_5 = \Gamma_6 = 0$,

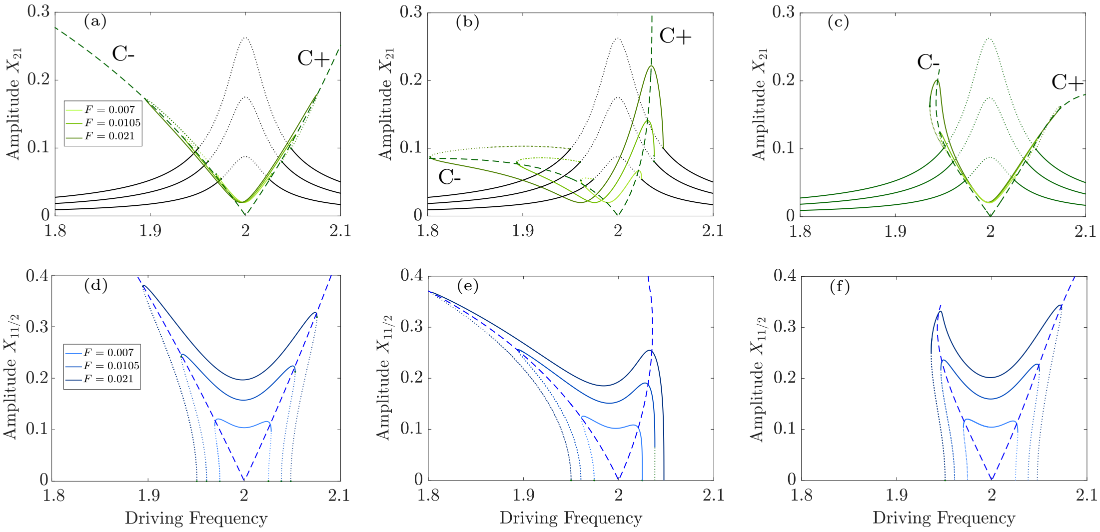

Figure 7.14: Réponse en fréquence de l'amplitude harmonique fondamentale X_{21} de $x_2(t)$ (la première ligne) et de l'amplitude sous-harmonique $X_{11/2}$ de $x_1(t)$ (la deuxième ligne) pour plusieurs niveaux d'excitation, calculés numériquement avec Manlab dans le cas $\sigma = 0$ (c'est-à-dire $\omega_2 = 2\omega_1$). La première colonne : seuls les termes de résonance quadratiques sont pris en compte ($g^1_{12} = g^2_{11} = 1$). La deuxième colonne : tous les termes quadratiques sont considérés avec des termes cubiques nuls ($g^1_{11} = g^1_{12} = g^2_{11} = 1$, $g^1_{22} = g^2_{12} = g^2_{22} = 0.1$). Troisième colonne : tous les termes quadratiques sont considérés avec les termes cubiques sont définis en fonction de (7.15a-d). Les coefficients d'amortissement sont $\mu_1 = 0.007$, $\mu_2 = 0.02$. La solution forcée découplée est tracée en noir et les solutions couplées sont tracées en vert et bleu. Les lignes pointillées et pleines indiquent les solutions stables et instables, respectivement. Les lignes pointillées désignent la solution libre couplée.

ce qui conduit à quatre ensembles de conditions sur les termes cubiques résonnants :

$$h^1_{111} = \frac{10}{9\omega_1^2}\left(g^1_{11}\right)^2 \tag{7.15a}$$

$$h^1_{122} = \left(\frac{8\omega_2^2 - 2\omega_1^2}{\omega_1^2(\omega_1^2 - 4\omega_2^2)}\right) g^1_{11} g^1_{22} - \frac{g^1_{12} g^2_{22}}{\omega_2^2} + \frac{2 g^1_{22} g^2_{12}}{\omega_1^2 - 4\omega_2^2}, \tag{7.15b}$$

$$h^2_{112} = \left(\frac{1}{\omega_1^2 - 4\omega_2^2}\right) (g^2_{12})^2 - \frac{2 g^2_{11} g^2_{22}}{3\omega_2^2} - \frac{g^1_{11} g^2_{12}}{\omega_1^2}, \tag{7.15c}$$

$$h^2_{222} = \left(\frac{8\omega_2^2 - 3\omega_1^2}{3\omega_1^2(\omega_1^2 - 4\omega_2^2)}\right) g^1_{22} g^2_{12} - \frac{10\left(g^2_{22}\right)^2}{9\omega_2^2} \tag{7.15d}$$

Pour tester le réglage proposé, le système (7.10a, b) est résolu avec MANLAB pour estimer respectivement les réponses en fréquence des amplitudes de la première et de la sous-harmonique de x_2 et x_1. La Fig. 7.14 montre trois cas différents : i) avec uniquement le quadratique résonant, ii) les termes quadratiques non résonnants sont également pris en compte, et iii) les termes cubiques sont considérés et accordés selon (7.15a-d). De plus, les "backbone curves" C+ et C- sont représentées.

Les résultats suggèrent clairement que l'accord des termes cubiques selon (7.15a-d) conduit à une réponse symétrique et à un blocage de l'antirésonance à la fréquence de résonance, récupérant ainsi la saturation.

7.4.3 Réglage de β_c

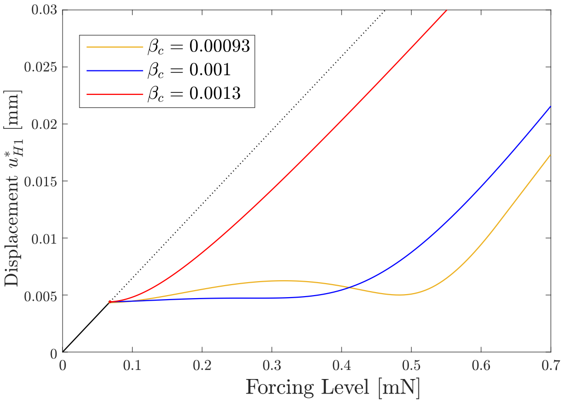

Figure 7.15: Amplitude de la première harmonique du déplacement de la pointe du foil évaluée à la fréquence de résonance, notée u^*_{H1}, en fonction de F pour trois valeurs différentes de β_c. Les tracés sont estimés pour $\beta_q = 0.03$, $\xi_e = 0.002$, $r_1 = \omega_e/\hat{\omega}_1 = 0.5055$. La réponse linéaire ($\beta_q = \beta_c = 0$) est indiquée en noir, avec les réponses stables et instables représentées respectivement par des lignes pleines et pointillées.

Pour estimer le réglage β_c requis pour une mise en œuvre pratique, rappelons qu'une seule condition cubique peut être satisfaite. La condition d'accord consiste à annuler l'effet du terme quadratique non résonnant le plus élevé, à savoir g^1_{11} et donc à satisfaire l'équation. (7.15) a qui conduit à l'accord suivant de β_c :

$$\beta_c = \frac{10}{9}\beta_q^2. \tag{7.16}$$

Ainsi, le réglage de β_c ne dépend que de β_q et la valeur de β_c doit toujours être positive. Pour valider la technique proposée, le système (7.3a, b) est résolu numériquement avec MANLAB en appliquant la condition de réglage dans Eq. (7.16) et en utilisant les paramètres modaux foil dans Tableau 7.2. La figure 7.15 montre la première amplitude harmonique du déplacement mesurée à la fréquence de résonance (notée u^*_{H1}) en fonction du niveau de forçage. Les résultats suggèrent qu'en choisissant le réglage dans Eq. (7.16) (voir la courbe bleue), la saturation peut être étendue jusqu'à des niveaux d'excitation élevés. Cette limite est due à la capacité de régler une seule condition cubique tandis que les trois autres termes cubiques de (7.15a-d) n'ont pas été réglés, créant un effet significatif à des niveaux d'excitauon élevés. Il convient de mentionner que la région de saturation peut être étendue à une excitation plus élevée en introduisant une petite correction à l'accord estimé de β_c (voir le minimum suggéré par la ligne jaune).

7.4.4 Validation expérimentale sur une structure d'hydrofoil

7.4.5 Montage expérimental

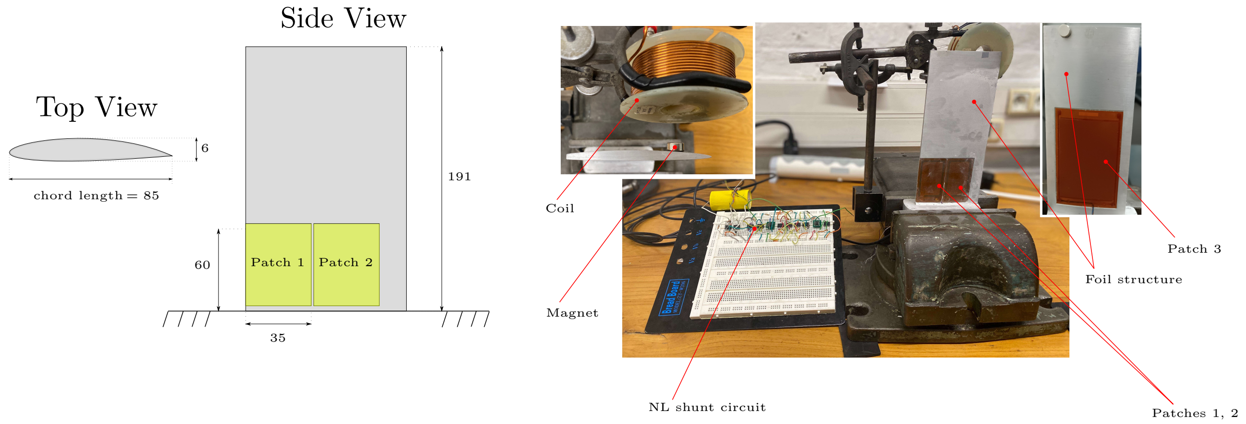

Figure 7.16: Montage expérimental. Les dimensions sont en mm. L'épaisseur des patchs en PE est de 1mm.

Table 7.2: Paramètres modaux électromécaniques du premier mode de flexion de la feuille (indice $i = 1$) par rapport au patch PE 2.

Parameters	$\check{\omega}_1/(2\pi)$ [Hz]	$\hat{\omega}_1/(2\pi)$ [Hz]	$\xi_1(\%)$	k_1	θ_1[mN/V]	$m_1[g]$	α [N/A]	$C_{\text{p}1}$ [nF]
Value	91.5	92.1	0.54	0.11	0.78	4.1	0.6	38

Les tests expérimentaux ont été menés sur une structure de feuille libre fixée à sa base dans un étau, comme le montre la Fig. 7.16. Trois patchs PE sont collés sur des cavités usinées sur les surfaces du foil : sur une face (notées patchs 1, 2), deux patchs piézoélectriques multicouches enduits polymère P-876.A15 DuraAct sont utilisés pour la transduction avec le premier mode de flexion, tandis qu'un composite macro-fibres M8557-F1 avec une orientation des fibres à 45 degrés est utilisé sur l'autre face (notée patch 3) pour un couplage avec le premier mode de torsion. Dans tous les tests de cet article, seul le patch 2 est utilisé puisque nous nous concentrons sur le premier mode de flexion. Par conséquent, le patch 2 est connecté au circuit shunt et les patch 1 et 3 sont court-circuités. Les trois patchs en PE proviennent du fabricant PI Ceramic. L'excitation mécanique est réalisée par une bobine interagissant avec un aimant fixé sur le foil. Les signaux mesurés sont la vitesse à la pointe de la feuille et la tension à travers le patch PE. L'analyse modale expérimentale et le protocole expérimental est la vente discutée pour celle de la première conception. Les paramètres électromécaniques modaux du premier mode de flexion de la feuille sont rassemblés dans le Tableau. 7.2.

Le circuit shunt non linéaire est illustré à la Fig. 7.17 qui est similaire à celui de la Fig. 7.10 mais avec une multiplication supplémentaire pour réaliser la non-linéarité cubique. L'inductance, β_q et β_c sont respectivement réglées avec les résistances variables R_4, R_8 et R_{10}. Pour satisfaire le réglage dans Eq. (7.16), R_{10} doit satisfaire :

$$R_{10} = \frac{10R_9}{9}\frac{R_6}{R_5 + R_6}\left(\frac{R_8}{R_7}\right)^2. \tag{7.17}$$

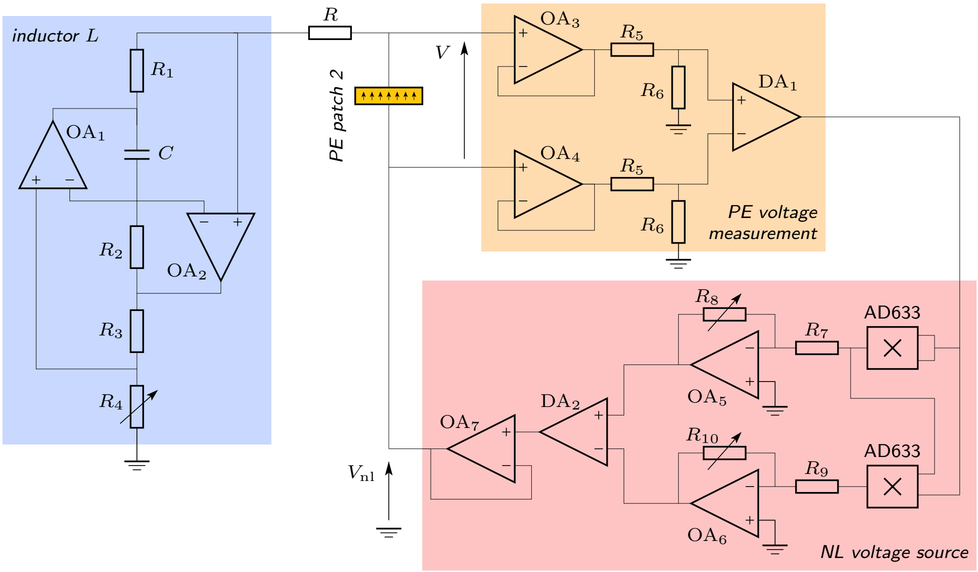

Figure 7.17: Conception de circuit shunt non linéaire avec non linéarité cubique.

7.4.6 Résultats expérimentaux

Pour valider expérimentalement la procédure, la réponse en fréquence de la première amplitude harmonique de la vitesse et la sous-harmonique de la tension PE ont été mesurées. Les résultats de la Fig. 7.18 montrent les réponses avec $\beta_c = 0$ et pour β_c accordés selon Eq. (7.16). Les résultats ont validé que l'accord cubique estimé peut verrouiller l'antirésonance à la fréquence de résonance et récupérer la saturation jusqu'à un niveau d'excitation élevé, conduisant à une atténuation élevée.

7.5 Troisième conception: avec une non-linéarité non lisse

Cette section est dédiée à l'illustration de la conception auto-absorbante dans laquelle un composant non lisse est intentionnellement ajouté au circuit électronique. Comme le montre la Fig. 7.19, l'élément non lisse V_{nl} est choisi pour être bilinéaire en termes de tension PE $V(t)$ de sorte que (c'est-à-dire ,

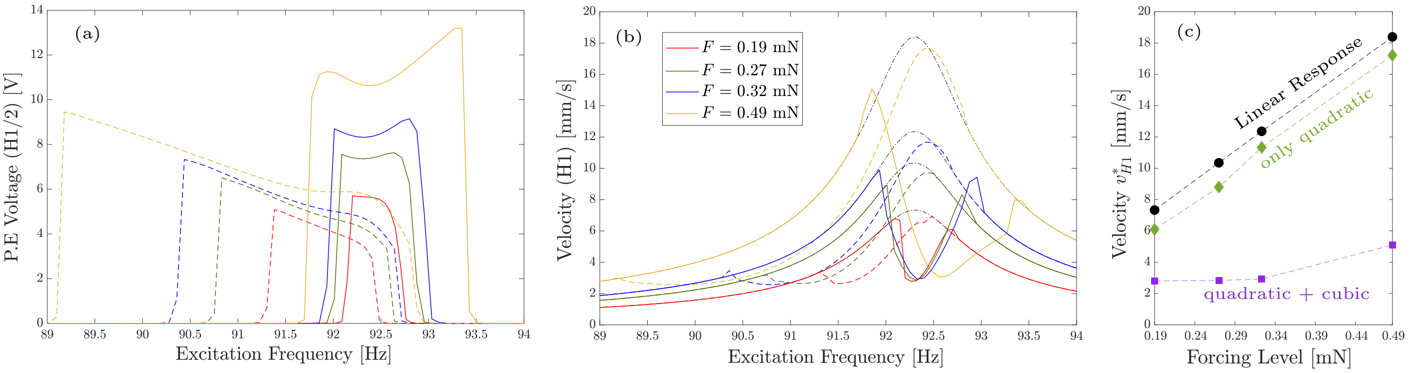

Figure 7.18: (b) et (a) montrent respectivement les réponses en fréquence mesurées expérimentalement des amplitudes de v_{H1} et $V_{H1/2}$ pour différents niveaux d'excitation, en considérant uniquement le terme non linéaire quadratique (lignes pointillées) et en considérant en plus un terme cubique (traits pleins) tel que β_c vérifie Eq. (7.16). Les résultats sont estimés avec $\xi_e = 0.002$, $\xi_1 = 0.0052$, $\beta_q = 0.03$, $\beta_c = 0.001$ et $r_1 = 0.5055$. La ligne pointillée noire indique la réponse linéaire mesurée expérimentalement de v_{H1} (c'est-à-dire, $\beta_q = \beta_c = 0$). (c) Amplitude de v_{H1} mesurée à la fréquence de résonance, notée v_{H1}^*, en fonction du niveau d'excitation.

$V_{\text{nl}} = \beta(V + |V|))$ avec β un gain sans dimension. Le but d'introduire une non-linéarité non lisse sous une telle forme est d'abord de générer des paires d'harmoniques dans le système, puisqu'il ne s'agit pas d'une fonction symétrique de V, d'activer éventuellement une résonance interne 2:1, puis d'utiliser de simples des composants électriques tels qu'une diode ou un transistor pour y parvenir.

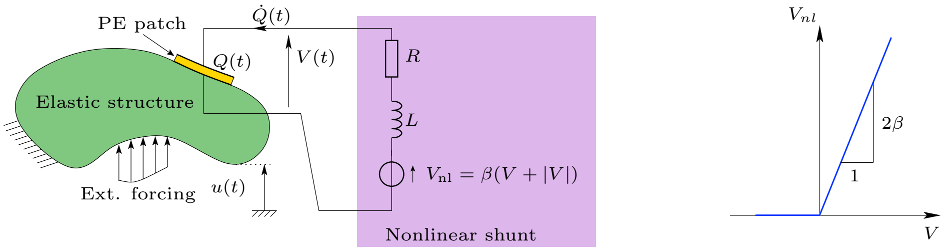

Figure 7.19: (a) Structure élastique couplée au circuit shunt non linéaire ; (b) graphe de la fonction $V \to V_{nl} = \beta(V + |V|)$.

7.5.1 Main equations

En substituant $V_{\mathrm{nl}} = \beta(V + |V|)$ dans Eq. (7.3)b, les équations gouvernantes en termes de déplacement modal $q_i(t)$ et la charge $Q(t)$ sont:

$$\ddot{q}_i + 2\xi_i\hat{\omega}_i\dot{q}_i + \hat{\omega}_i^2 q_i + \frac{\theta_i}{m_i C_{\mathrm{pi}}} Q = \frac{F_i}{m_i}\cos\Omega t, \tag{7.18a}$$

$$\ddot{Q} + 2\xi_e\omega_e\dot{Q} + \omega_e^2 Q + \omega_e^2\theta_i q_i - \beta\omega_e^2\left(Q + \theta_i q_i + |Q + \theta_i q_i|\right) = 0. \tag{7.18b}$$

Deux conclusions importantes peuvent alors être tirées : (i) les équations gouvernantes de (7.18a,b) sont bien non linéaires à cause du terme non lisse ($|V| \implies |Q + \theta_i q_i|$) qui n'apparaît que dans Eq. (7.18b) et crée une distorsion harmonique. (ii) bien que des non-linéarités soient présentes, (7.18a,b) *sont en fait entièrement linéaires en amplitude.* Cependant, il n'est pas toujours additif ou superposable, puisque $|x_1 + x_2| \neq |x_1| + |x_2|$ si $x_1x_2 < 0$ pour $x_1, x_2 \in \mathbb{R}$.

Pour donner une première analyse du comportement du système couplé (7.18a,b), nous ne considérons ici que l'Eq. (7.18b), nous excluons le couplage piézoélectrique (c'est-à-dire en fixant $\theta_i = 0$), et nous ajoutons un terme de forçage direct d'amplitude P, conduisant à :

$$\ddot{Q} + 2\xi_e\omega_e\dot{Q} + \omega_e^2 Q - \beta\omega_e^2\left(Q + |Q|\right) = P\cos\Omega t, \tag{7.19}$$

7.5.2 Free solution

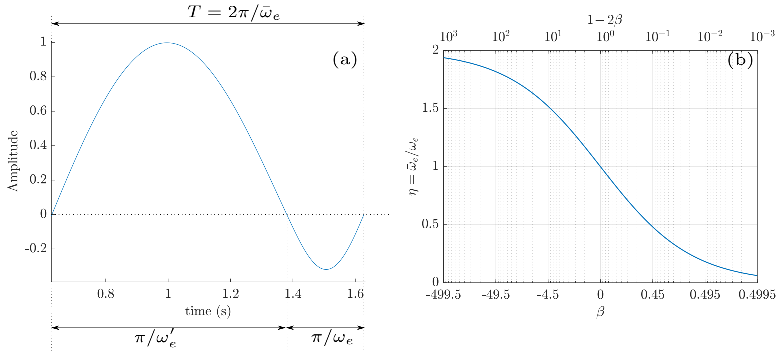

Figure 7.20: (a) Exemple de réponse libre de Eq. (7.19) sur une période. (b) Rapport $\eta = \bar{\omega}_e/\omega_e$ en fonction de β.

Pour analyser la réponse libre, nous fixons $P = 0$, et nous réécrivons Eq. (7.19) comme :

$$\ddot{Q} + 2\xi_e\omega_e\dot{Q} + \omega_e^2 Q = 0 \quad \text{if} \quad Q \leq 0, \tag{7.20a}$$

$$\ddot{Q} + 2\xi_e\omega_e\dot{Q} + \omega_e'^2 Q = 0 \quad \text{if} \quad Q \geq 0, \tag{7.20b}$$

avec $\omega_e' = \omega_e\sqrt{1-2\beta}$. Dans le cas conservateur ($\xi_e = 0$), Eqs. (7.20) suggèrent que la réponse libre est une succession d'une demi-période de sinus de période ω_e et d'une demi-période de sinus de fréquence ω_e', comme illustré Fig. 7.20(a) . Ensuite, la période d'oscillation peut être exprimée comme suit :

$$T = \frac{2\pi}{\bar{\omega}_e} = \frac{\pi}{\omega_e} + \frac{\pi}{\omega_e'}, \tag{7.21}$$

avec $\bar{\omega}_e$ la fréquence angulaire modifiée de la réponse libre due au terme non lisse, qui se lit :

$$\bar{\omega}_e = \underbrace{\frac{2\sqrt{1-2\beta}}{1+\sqrt{1-2\beta}}}_{\eta}\omega_e = \frac{2\sqrt{1-2\beta}}{1+\sqrt{1-2\beta}}\frac{1}{\sqrt{LC_p}}, \qquad \eta = \frac{\bar{\omega}_e}{\omega_e}, \tag{7.22}$$

avec η le rapport entre les fréquences naturelles modifiées ($\bar{\omega}_e$) et non modifiées (ω_e), tracées sur la Fig. 7.20(b). Eq. (7.22) prouve que *même si le comportement est non linéaire, la fréquence d'oscillation libre de Eq. (7.18b) ne dépend pas de l'amplitude.* De plus, Eq. (7.22) suggère qu'étant donné une fréquence de résonance électrique ω_e (c'est-à-dire, étant donné une inductance), la fréquence d'oscillation électrique modifiée $\bar{\omega}_e$ peut être ajustée selon la valeur de β. Cependant, *la valeur de β doit être inférieure à 1/2* pour éviter une réponse instable. Cette caractéristique est le principal avantage de ce circuit shunt non linéaire : en ajustant le paramètre non linéaire β, on peut accorder la fréquence du circuit électrique à une valeur particulière tout en fixant l'inductance à une valeur faible, ce qui est un avantage pour la mise en œuvre pratique.

7.5.3 Solution forcée

Pour analyser la réponse forcée, nous réécrivons Eq. (7.19) sous une forme adimensionnelle en introduisant les paramètres suivants :

$$\tilde{t} = \omega_e t, \quad \tilde{Q} = Q\frac{\omega_e^2}{P}, \quad \tilde{\Omega} = \Omega/\omega_e. \tag{7.23}$$

En utilisant les paramètres sans dimension dans Eq. (7.23), on obtient :

$$\ddot{\tilde{Q}} + 2\xi_e\dot{\tilde{Q}} + \tilde{Q} - \beta\left(\tilde{Q} + |\tilde{Q}|\right) = \cos\tilde{\Omega}\tilde{t}. \tag{7.24}$$

On peut se rendre compte que la solution de l'Eq. (7.24) ne dépend que du rapport d'amortissement ξ_e et du gain β. Par conséquent, *la forme de la courbe de résonance de l'Eq. (7.24) est indépendante du niveau d'excitation P* et peut être obtenue pour n'importe quelle valeur de P et $omega_e$ en utilisant la mise à l'échelle définie dans (7.23). Ceci est illustré sur la Fig. 7.21 en résolvant Eq. (7.19) pour différents niveaux d'excitation. On peut clairement observer que le terme non lisse crée un contenu harmonique complet dans lequel les harmoniques zéro (H0) et deuxième (H2) ont une contribution significative en plus de la première harmonique (H1), les harmoniques supérieures étant négligeables. L'observation la plus importante est que la forme de chaque harmonique, considérée séparément, semble proche de la réponse en fréquence d'un oscillateur linéaire au voisinage de sa fréquence de résonance, qui est obtenue ici au voisinage de la fréquence des oscillations libres, pour $\Omega = \bar{\omega}_e$. Contrairement au comportement quasi-linéaire décrit ci-dessus, le terme non linéaire non lisse peut générer une réponse superharmonique fortement non linéaire près de $\Omega = \bar{\omega}_e/2$ comme le montre la Fig. 7.22. Cela suggère que l'introduction du terme non lisse peut représenter une option pour l'application impliquant une résonance interne.

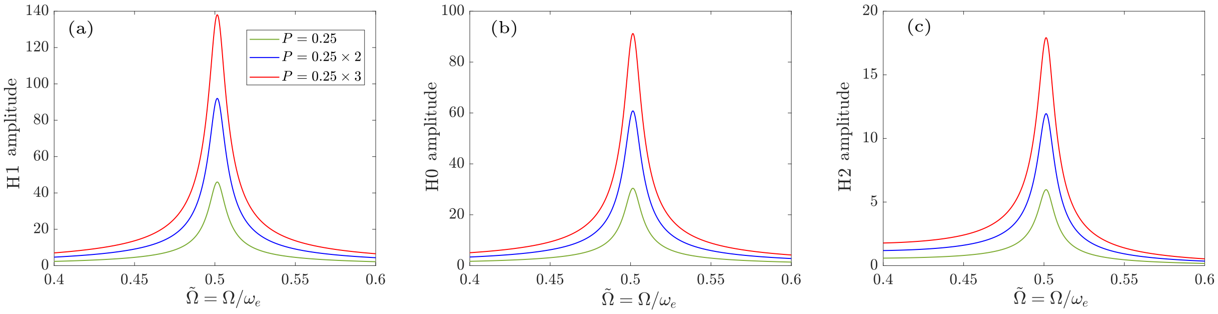

Figure 7.21: Harmoniques H1 (a), H0 (b) et H2 (c) des solutions périodiques de l'Eq. (7.19) au voisinage de la résonance primaire, en fonction de $\tilde{\Omega} = \Omega/\omega_e$ pour $\xi_e = 0.005$ et différents niveaux d'excitation P. Les valeurs numériques utilisées dans les simulations sont $\xi_e = 0.005$ et $\beta = 0.444$.

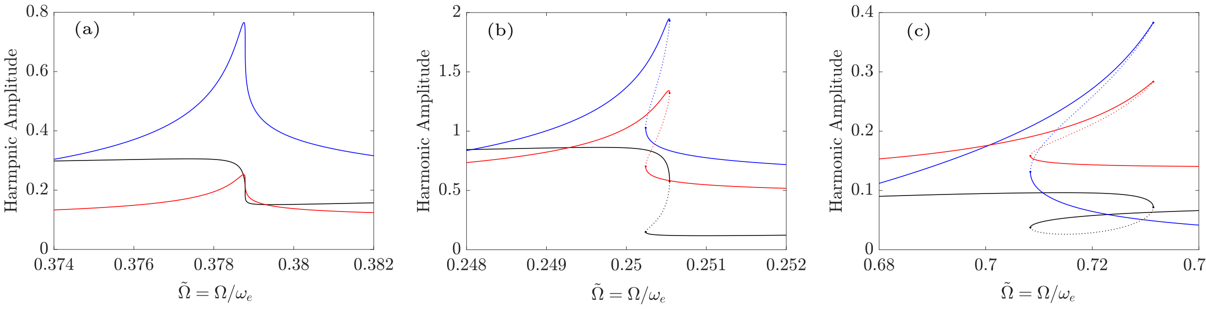

Figure 7.22: Harmoniques H0 (en rouge), H1 (en noir) et H2 (en bleu) des solutions périodiques de Eq. (7.19) au voisinage de la résonance superharmonique d'ordre deux. (a) $\beta = 0.3136$, (b) $\beta = 0.444$ et (c) $\beta = -3.883$. Les valeurs numériques sont $\xi_e = 0.005$ et $P = 0.1$. Les lignes pleines et pointillées indiquent les réponses stables et instables, respectivement.

7.5.4 Approximation avec un oscillateur linéaire

Comme indiqué dans la section précédente, la réponse en fréquence non linéaire des harmoniques semble similaire à la fonction de réponse en fréquence (FRF) d'un oscillateur linéaire proche de la résonance primaire. Ainsi, on cherche une approximation de Eq. (7.19) définie par l'oscillateur linéaire suivant, pour $p = 0, 1, 2$:

$$\ddot{Q}_p + 2\bar{\xi}_e\bar{\omega}_e\dot{Q}_p + \bar{\omega}_e^2 Q_p = \phi_p P \cos\Omega t, \tag{7.25}$$

où Q_p est la réponse approchée de la p-ième harmonique de $Q(t)$, $\bar{\xi}_e$ est le taux d'amortissement modifié dû au terme non lisse, et ϕ_p est un gain inconnu, correspondant au p-ième harmonique, introduit pour quantifier la différence entre les solutions analytique et numérique et à déterminer en ajustant la réponse en fréquence analytique de Q_p avec la réponse en fréquence numérique du p- ième harmonique.

Pour déterminer le rapport d'amortissement modifié $\bar{\xi}_e$, nous supposons et vérifions que le terme non lisse n'a aucun effet sur le coefficient d'amortissement (c'est-à-dire le terme multipliant $\dot{Q}$), et donc :

$$\bar{\xi}_e\bar{\omega}_e = \xi_e\omega_e \quad \Rightarrow \quad \bar{\xi}_e = \xi_e/\eta. \tag{7.26}$$

Étant donné que ϕ_p jouera un rôle important dans le processus d'optimisation décrit ci-après, une approximation polynomiale en termes de β est estimée pour chaque harmonique, grâce à la propriété de symétrie illustrée à la Fig. 7.23 (voir chapitre 6 pour plus de détails).

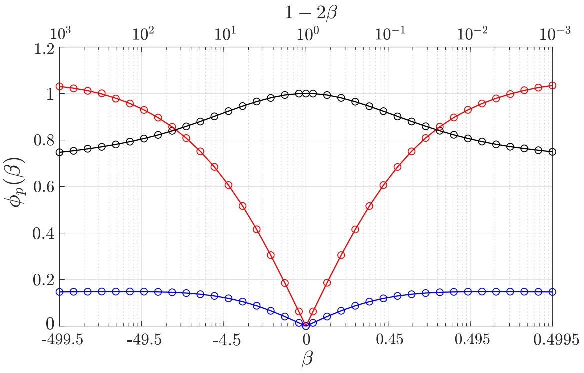

Figure 7.23: ϕ_p en fonction de β correspondant aux harmoniques H0 (rouge), H1 (noir) et H2 (bleu). Les cercles indiquent les valeurs estimées en ajustant les réponses analytiques et numériques pour chaque valeur de β, et les traits pleins indiquent les courbes polynomiales approchées.

7.5.5 Réponse du système complet : deux cas de réglage et une atténuation optimale

Dans cette section, deux cas de réglage sont étudiés : un réglage 1:1 avec $\bar{\omega}_e = \hat{\omega}_i$ et un cas de réglage 2:1 avec $\bar{\omega}_e = \hat{\omega}_i/2$, grâce à l'approximation discutée précédemment. L'étude impliquant la résolution (7.18a, b) avec MANLAB pour examiner la réponse et l'éventuelle activation de la résonance interne 2:1 pour le cas d'accord 2:1. Le cas d'accord 1:1 suggère de coupler la résonance mécanique avec l'harmonique H1. Étant donné que la réponse de l'harmonique H1 est entièrement linéaire près de la fréquence fondamentale, une fixation linéaire est alors couplée au mode mécanique à atténuer et une

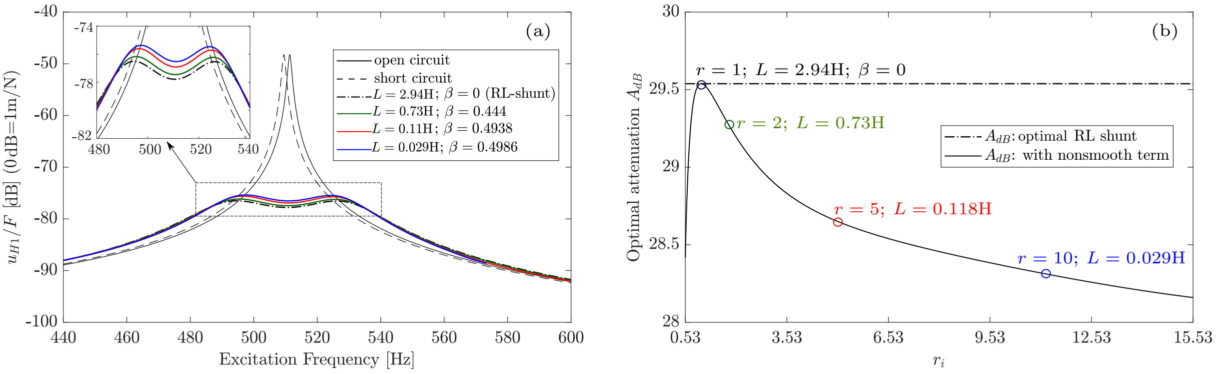

Figure 7.24: (a) Réponse en fréquence numérique de la première harmonique $u_{\mathrm{H}1}$ du déplacement $u(t)$, normalisée par rapport au niveau de forçage F, pour différentes valeurs du rapport r (ou l'inductance L) et en satisfaisant les conditions optimales . (b) Atténuation optimale pour le cas du shunt RL et le cas avec la composante non lisse avec un réglage 1:1. Les marqueurs circulaires sont les réponses en fréquence numériques d'atténuation obtenues pour chaque valeur de $r_i = \omega_e/\hat{\omega}_i = \frac{1}{\hat{\omega}_i\sqrt{LC_{\mathrm{pi}}}}$. Les paramètres modaux utilisés sont ceux rassemblés dans Table. (7.4).

réponse similaire à un amortisseur de masse accordé est attendue (voir Fig. 7.24) . L'idée principale est d'introduire un facteur de couplage piézoélectrique modifié $\bar{k}_i$ pour prendre en compte l'effet de la composante non résonnante qui se lit :

$$\bar{k}_i(\beta) = k_i\sqrt{\phi_1(\beta)}. \tag{7.27}$$

Ayant le couplage piézoélectrique modifié, une procédure d'optimisation est proposée (similaire à celle du shunt résonnant linéaire) dans laquelle les paramètres optimaux considérés sont le gain non lisse β et le rapport d'amortissement électrique (ou la résistance R), en imposant tout condition sur l'inductance. Les expressions des paramètres optimaux en plus de l'atténuation optimale A_{dB} sont rassemblées dans Table. 7.3. L'atténuation est définie comme la différence entre l'amplitude linéaire et l'amplitude avec le shunt non linéaire à la fréquence de résonance, mesurée en échelle de dB. Il est à noter que l'atténuation dépend de l'inductance dans le circuit, contrairement au cas du shunt résonnant linéaire, ce qui est logique puisqu'aucune condition sur l'inductance n'a été imposée. La figure 7.24(a) montre la réponse en fréquence de la première harmonique de déplacement pour le cas optimal pour différentes valeurs d'inductance. On peut voir que l'atténuation diminue légèrement pour un réglage d'inductance plus faible. Ceci est examiné plus en détail dans la Fig. 7.24(b) où il montre que l'inductance peut être réduite d'un facteur 100 par rapport à celle requise par le shunt linéaire mais sans perdre sensiblement les performances.

En ce qui concerne le cas d'accord 2:1, les résultats de la Fig. 7.25 suggèrent que l'activation de la résonance interne 2:1 est activée puisque la sous-harmonique de la charge répond par une bifurcation en fourche (PF). On peut se rendre compte que la réponse en déplacement ne présente pas la saturation et la réponse est bien linéaire avec le niveau d'excitation, similaire à celle d'un shunt résonnant linéaire. Les paramètres optimaux et les expressions d'atténuation optimales pour ce cas de réglage sont rassemblés dans Table. 7.3. Notez que l'optimisation pour le réglage 2:1 considère la modification du facteur de couplage piézoélectrique similaire à celui de l'équation. (7.27) mais avec ϕ_2 puisque la résonance mécanique est couplée à l'harmonique H2.

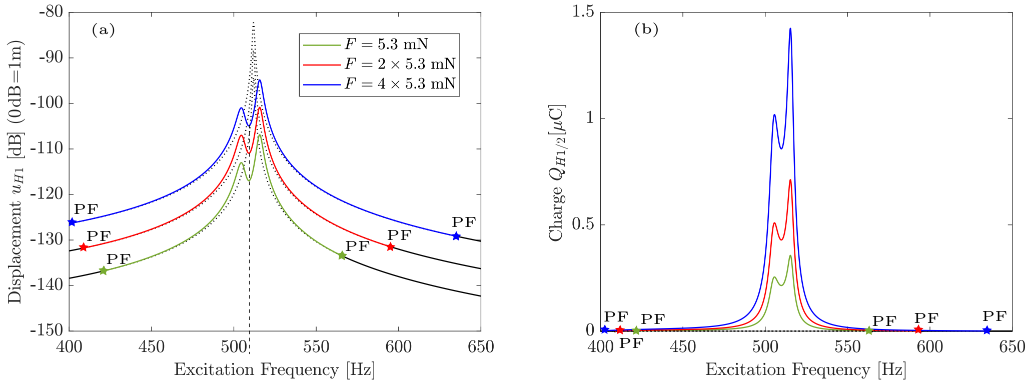

Figure 7.25: (a) et (b) montrent respectivement la réponse en fréquence numérique de u_{H1} et $Q_{\mathrm{H1/2}}$ pour les niveaux d'excitation croissants. La réponse linéaire est tracée en noir. Les réponses stables et instables sont représentées respectivement par des lignes pleines et pointillées. L'étoile violette indique la bifurcation de la fourche (PF). Les valeurs numériques utilisées sont $\beta = 0.444$, $R = 36\Omega$, $L = 2.948$H. Les paramètres modaux utilisés sont ceux rassemblés dans Table. 7.4.

Table 7.3: Paramètres optimaux et atténuation optimale pour les cas de réglage 1:1 et 2:1.

Cas	β optimal	R optimal	Atténuation optimale [dB]
1:1 tuning	$\beta^{\mathrm{op}} = \frac{1}{2}\left[1 - \left(\frac{1}{2r_i - 1}\right)^2\right]$	$R^{\mathrm{op}} = \frac{\sqrt{6}}{2C_{\mathrm{p}i} r_i^2 \hat{\omega}_i} k_i \sqrt{\phi_1^{\mathrm{op}}}$	$A_{\mathrm{dB}} = 20\log_{10}\left(1 + \frac{k_i}{\xi_i\sqrt{6}}\sqrt{\phi_1^{\mathrm{op}}}\right)$
2:1 tuning	$\beta^{\mathrm{op}} = \frac{1}{2}\left[1 - \left(\frac{r_i^*}{2r_i - r_i^*}\right)^2\right]$	$R^{\mathrm{op}} = \frac{\sqrt{6} r_i^*}{2C_{\mathrm{p}_i} r_i^2 \hat{\omega}_i} k_i \sqrt{\phi_2^{\mathrm{op}}}$	$A_{\mathrm{dB}} = 20\log_{10}\left(1 + \frac{k_i}{\xi_i\sqrt{6}}\sqrt{\phi_2^{\mathrm{op}}}\right)$

7.5.6 Validation expérimentale

La validation expérimentale a été effectuée pour atténuer le premier mode de torsion de la même structure d'hydrofoil illustrée à la Fig. 7.26. Dans ces tests, le patch 3 était couplé au circuit shunt tandis que les patchs 1 et 2 étaient en court-circuit. Même protocole expérimental comme indiqué précédemment a été utilisé. Les paramètres modaux électromécaniques ont été déterminés et rassem-

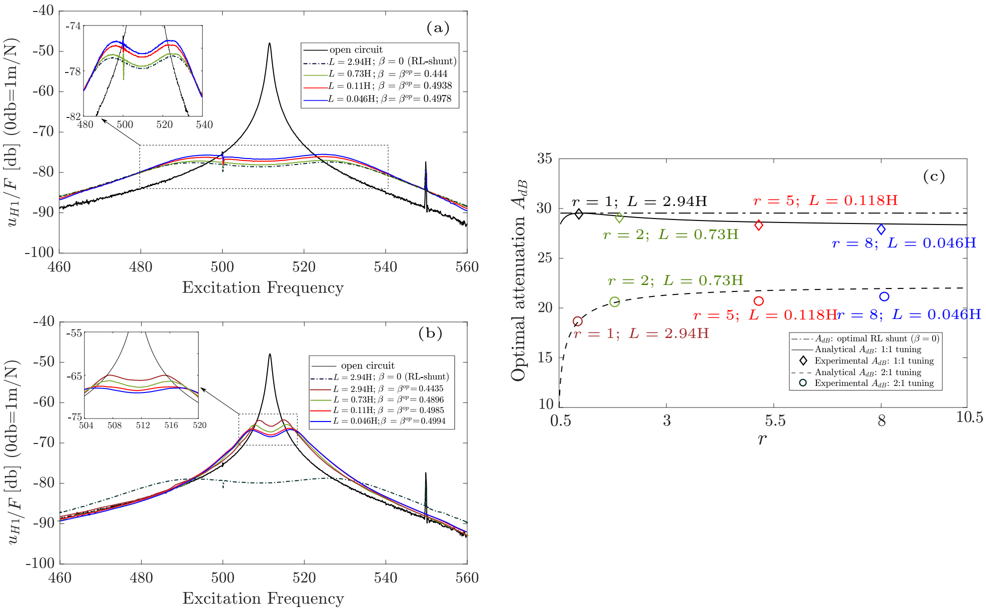

Figure 7.26: (a) et (b) montrent la réponse en fréquence expérimentale de la première harmonique de la vitesse u_{H1} pour différentes valeurs de l'inductance pour l'accord 1:1 et 2:1, respectivement. (c) Comparaison entre l'atténuation analytique optimale et celle mesurée expérimentalement pour les deux cas de réglage.

blés dans le Tableau. 7.4. Le composant non lisse est réalisé avec un circuit redresseur demi-onde avec une diode comme indiqué sur la Fig. 7.26. Les réponses en fréquence mesurées de la première harmonique du déplacement pour différentes valeurs d'inductance sont présentées sur les Figs. 7.26(a) et (b) pour les cas de réglage 1:1 et 2:1 respectivement. Les résultats valident la réponse similaire par rapport à celle du shunt résonnant linéaire avec la possibilité de régler une inductance beaucoup plus faible dans le circuit (une réduction d'un facteur 64 par rapport à celle requise par le shunt résonnant linéaire est obtenue dans les expériences). De plus, comme le montre la Fig 7.26(c), les expériences ont validé le comportement d'atténuation optimal, prédit théoriquement, en fonction de l'inductance.

Table 7.4: Paramètres modaux électromécaniques du premier mode de torsion.

Parameter	$\breve{\omega}/(2\pi)$	$\hat{\omega}/(2\pi)$	ξ	m	C_{p}	θ	k	$\psi(\boldsymbol{x}_m)$
Value	509.4 Hz	511.36 Hz	0.0012	10.42 g	32.8 nF	5.2 mN/V	0.0875	1

7.6 Conclusion

Cette thèse vise à atténuer les vibrations des hydrofoils à l'aide d'absorbeurs shunt piézoélectriques. Le procédé consiste à connecter la structure en feuille à un circuit électronique via un patch piézoélec-

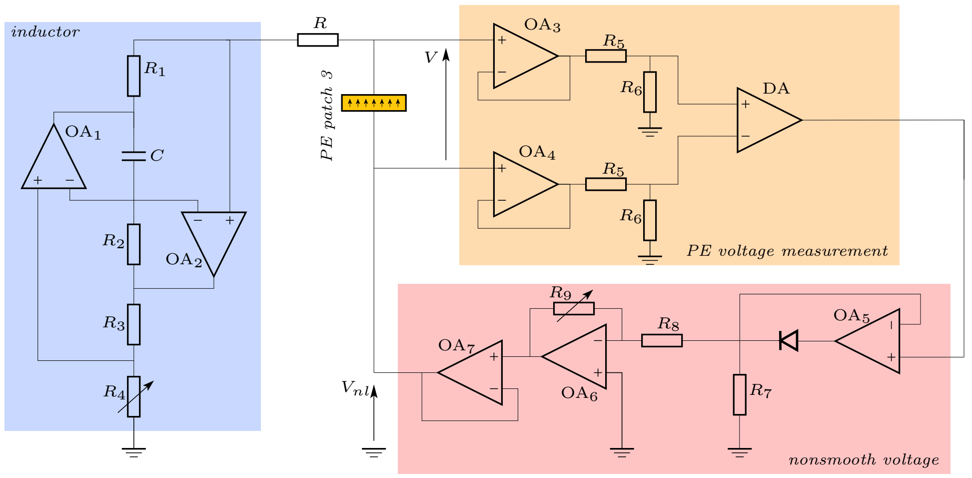

Figure 7.27: Schéma du circuit shunt avec composant non lisse.

trique. L'idée principale est d'introduire intentionnellement un composant non linéaire dans le circuit shunt pour améliorer l'atténuation. L'originalité principale de cette thèse est d'exploiter le phénomène de saturation en utilisant la méthode du shunt piézoélectrique. Pour ce faire, trois conceptions différentes ont été proposées. La première conception consiste à ajouter une composante de tension non linéaire quadratique proportionnelle au carré de la tension aux bornes du patch piézoélectrique ($V_{\text{nl}} = \beta V^2$). La saturation est conservée et validée expérimentalement sur une structure de poutre en porte-à-faux à l'aide d'une correction d'antirésonance non automatique. La seconde conception consistait à introduire en plus une non-linéarité cubique accordée grâce aux résultats suggérés par la théorie des formes normales. L'absorbeur a ensuite été testé expérimentalement sur une structure hydrofoil permettant de récupérer la saturation jusqu'à des niveaux d'excitation élevés et une atténuation élevée a été obtenue. La troisième conception consistait à introduire une non-linéarité non lisse pour activer la résonance interne 2:1 et être facilement analysée avec une diode. Les résultats ont montré que le circuit shunt peut alors être réglé avec le gain non lisse β avec un réglage à faible inductance, ce qui est un avantage pratique. Deux cas d'accord entre la fréquence de résonance électrique $\bar{\omega_e}$ et celle mécanique $\hat{\omega}_i$ ont été étudiés. Le cas d'accord 1:1 ($\bar{\omega}_e = \hat{\omega}_i$) a montré un comportement similaire par rapport à un shunt résonnant linéaire. De même, l'accord 2:1 ($\bar{\omega}_e = 1/2\hat{\omega}_i$) a également montré le même comportement mais avec l'activation de la résonance interne 2: 1 sans saturation. Des études d'optimisation ont ensuite été réalisées suggérant la possibilité d'accorder le circuit avec une très faible inductance par rapport à celle requise par le shunt résonnant linéaire, sans perdre beaucoup de performances.Les résultats ont ensuite été validés en appliquant l'absorbeur sur la structure de l'hydrofoil.

Arts Sciences et Technologies et Métiers

Zein Alabidin SHAMI

Vibration Control of Hydrofoil Structures with Nonlinear Piezoelectric Shunt Absorbers

HESAM UNIVERSITÉ

Résumé : Les hydrofoils sont des structures à surface portante qui sont montées sur la coque des bateaux afin d'augmenter le rapport entre la vitesse et la consommation d'énergie. Le concept de base consiste à générer une force de levage sur le corps du bateau, ce qui entraîne une réduction de la surface de contact avec l'eau et donc une diminution de la force de traînée. A des vitesses plus élevées, les hydrofoils sont soumis à des vibrations induites par l'écoulement qui peuvent conduire à des contraintes élevées et à la fatigue, diminuant ainsi leurs performances. Cette thèse a pour but d'atténuer ces vibrations en utilisant un absorbeur piézoélectrique non-linéaire en dérivation. Ces absorbeurs consistent à connecter un circuit électronique de dérivation à la structure de l'hydrofoil par transduction piézoélectrique. Dans ce travail, les circuits de dérivation consistent principalement en un circuit résonnant (c'est-à-dire une résistance en série avec une inductance) avec un composant non linéaire ajouté intentionnellement. Le but de l'ajout de la non-linéarité est d'exploiter certaines caractéristiques pour améliorer l'atténuation de l'absorbeur. La principale caractéristique prise en compte dans ce travail est le phénomène de saturation qui conduit à l'indépendance de l'amplitude d'oscillation par rapport au niveau d'excitation. Par conséquent, une forte atténuation des vibrations peut être atteinte à des niveaux d'excitation élevés. Ce travail propose différentes architectures de circuits non linéaires, incluant des non-linéarités quadratiques, cubiques et non lisses. Ces absorbeurs sont étudiés théoriquement et vérifiés expérimentalement avec une discussion détaillée sur leurs avantages, leurs performances et leurs limites.

Mots clés : Surfaces portantes, hydrofoils, absorbeurs de vibrations, absorbeurs piézoélectriques non linéaires en dérivation, phénomène de saturation.

Abstract : Hydrofoils are lifting surface structures that are mounted on the boats' hull to increase the speed to the power consumption ratio. The basic concept is based on generating a lift force on the boat body leading to a reduction of the contact area with the water and thus a lower drag force. At higher speeds, hydrofoils are subjected to flow-induced vibrations that can lead to high stresses and fatigue, lowering their performance. This thesis aims to attenuate those vibrations using the nonlinear piezoelectric shunt absorber. Those absorbers consist of connecting an electronic shunt circuit to the hydrofoil structure through piezoelectric transduction. In this work, the shunt circuits mainly consist of a resonant circuit (i.e., a resistor in series with an inductor) with a nonlinear component intentionally added. The purpose of adding the nonlinearity is to exploit some features to enhance the absorber attenuation. The main feature under consideration in this work is the saturation phenomenon that leads to the independence of the oscillation amplitude from the excitation level. Consequently, high vibration attenuation can be reached at high excitation levels. This work proposes different nonlinear circuit architectures, including quadratic, cubic, and nonsmooth nonlinearities. Those absorbers are studied theoretically and verified experimentally with a detailed discussion on their advantages, performance, and limitations.

Keywords : Lifting surfaces, hydrofoils, vibration absorbers, nonlinear piezoelectric shunt absorbers, saturation phenomenon.